



ÉCOLE
POLYTECHNIQUE
DE BRUXELLES



UNIVERSITÉ LIBRE DE BRUXELLES

Development and tests of JUNO electronics readout system and study of JUNO performance for core collapse supernova model discrimination

From JUNO back-end card hardware tests to statistical methods for supernova studies with JUNO

Thesis presented by Pierre-Alexandre PETITJEAN

in fulfilment of the requirements of the PhD Degree in Engineering Sciences and Technology ("Doctorat en Sciences de l'Ingénieur et Technologie")

Academic year 2024-2025

Supervisor: Professor Nicolas PAULY

Métrieologie nucléaire

Co-supervisor: Barbara CLERBAUX

Inter-University Institute For High Energies

Thesis jury :

Pascal VANLAER (Université libre de Bruxelles, Chair)

Yifan YANG (Université libre de Bruxelles, Secretary)

Nicolas PAULY (Université libre de Bruxelles, Supervisor)

Barbara CLERBAUX (Université libre de Bruxelles, Co-Supervisor)

Alberto GARFAGNINI (INFN-Università di Padova)

Mariangela SETTIMO (CNRS SUBATECH)

Abstract

Neutrinos are very elusive particles as they only interact with matter through weak interaction. Many uncertainties remain such as their mass ordering. The Jiangmen Underground Neutrino Observatory (JUNO), currently under construction in China, aims to determine the neutrino mass hierarchy and to measure oscillation parameters with sub-percent precision. The detector consists of 20 kilotons of liquid scintillator equipped with 17,612 20-inch photomultiplier tubes and 25,600 3-inch small photomultiplier tubes, providing a photocathode coverage of 77%. The electronics system is divided into two main parts: the front-end system, located underwater, which handles analog signal processing, and the back-end system, located outside water, which includes the data acquisition system and the trigger.

This thesis presents two main contributions to the JUNO experiment: the development of the Back-End Card for the photomultiplier tube readout system and the analysis of supernova model discrimination using neutrino detected with JUNO. The development of the Back-End Card addresses challenges such as signal integrity, mitigation of crosstalk, power distribution, and installation complexity. Through multiple design iterations and rigorous testing, the final design was optimized for mass production. By 2023, 180 Back-End Cards were produced, tested, and successfully installed as part of the JUNO detector, ensuring the system's reliable operation.

Supernovae are among the most significant cosmic events, producing essential elements and leaving behind remnants like neutron stars and black holes. Despite their importance, the mechanisms behind these stellar explosions are still not fully understood while neutrinos are playing a important role in the core collapse. By studying the neutrino production during the core collapse, one can learn valuable insights about the physics phenomena inside the star. Two likelihood methods—binned and unbinned—were employed to distinguish between different core-collapse supernova models. The unbinned method, particularly using the inverse beta decay channel, proved more effective by capturing fine details in time and energy distributions, crucial for model discrimination. The study showcases that 300 inverse-beta decay neutrino events in JUNO—corresponding to a supernova at a distance of at least 21 kpc—are sufficient to distinguish between these models with high accuracy.

These contributions illustrate JUNO's capacity to address key questions in neutrino physics. The first data taking runs are foreseen for Summer 2025.

Acknowledgments

First and foremost, I would like to express my deepest gratitude to Professor Pauly and Professor Clerbaux. Their guidance and support began with my master's thesis and have been invaluable throughout this PhD journey. Their expertise, insightful feedback, and unwavering encouragement have significantly shaped the direction and quality of my research. I am profoundly grateful for their willingness to take me under their wings, and for the opportunities they provided that allowed me to grow both as a researcher and as a scholar.

I am particularly grateful to my colleagues who have played a crucial role in the development and success of this thesis. Yifan Yang, your help in building the various setups for the electronics and your patience in teaching me so much about digital electronics has been invaluable. Your expertise and willingness to share your knowledge have greatly improved the technical aspects of my research. Special thanks to Marta Colomer, whose assistance with the supernova part of my thesis was crucial. Her insights, suggestions, and cooperation have enriched my understanding and were essential in completing this aspect of my research. I am also deeply grateful to Feng Gao, who joined me in the BEC work, allowing me to devote more time to the supernova part of my thesis. Her proactive approach and valuable contributions were key to the smooth and successful progress of my research. Your support was essential in balancing the different aspects of this project, and I greatly appreciate your dedication. I would also like to thank all three of you for your detailed comments on my thesis, which greatly improved it.

I would also like to acknowledge the staff of the Interuniversity Institute for High Energies (IIHE) for their assistance and support throughout my studies. Their efficiency and dedication ensured that the logistical aspects of my PhD experience ran smoothly. I am particularly grateful to Professor Favart and Professor Delendeker for their constant encouragement and support. Their belief in my work and their motivating words have been a source of strength throughout this journey.

I would like to express my sincere thanks to the members of the jury for their time and consideration of my thesis. Your expertise, insightful comments and thoughtful questions have contributed greatly to the quality of this thesis. I deeply appreciate your commitment and the effort you have put into reviewing my research. Your valuable feedback and constructive criticism will undoubtedly shape my future work. Thank you very much for your time and effort.

I would also like to extend my sincere gratitude to JUNO collaborators, whose contributions have been invaluable. I would like to thank Jianmeng Dong, whose expertise greatly assisted me in navigating complex aspects of the research. Your guidance and knowledge were essential in overcoming several key challenges. A heartfelt thank you to Zhaoyuan Peng, who not only offered significant help during my time in China but also made my experience there memorable. Your friendliness and the enjoyable basketball games we shared during our shifts provided a much-needed balance to the intense work schedule, making my time there both productive and enjoyable.

During my PhD, I also had the opportunity to engage in teaching activities, which have been an enriching experience. I would like to express my sincere thanks to Professor Delantsheer, Professor Dohet-Eraly, Professor Lessines, Professor Napov, and Professor Roland for allowing me to teach under their guidance. Their mentorship in the classroom has helped me grow as an educator and provided me with invaluable skills that I will carry forward in my career. The experience of teaching and interacting with students has been one of the most rewarding aspects of my PhD journey.

My sincere appreciation goes to my fellow PhD candidates and colleagues who have shared this journey with me. I am especially grateful to Ali, Andrea, Camille, Daniel, and Shuang, who spent countless weekends and evenings working alongside me. Your camaraderie and dedication were a tremendous source of motivation, and I am thankful for the support and shared experiences that made this journey more manageable and enjoyable.

A special thank you to my parents, whose unwavering support has been my foundation. To my dad, who always pushed me to achieve my best and took the time to read through my thesis, offering his invaluable feedback. Your dedication and belief in my abilities have been a driving force in my academic journey. To my mom, whose faith in me has never wavered, even during the most challenging times. Your constant encouragement and belief in my potential have given me the strength to keep going. I also want to express my gratitude to my little brother, who helped me during the confinement by assisting with the creation of Ethernet cables. Your help, especially during such a challenging time, was invaluable and truly appreciated.

I would also like to express my gratitude to the ULB Armwrestling Club, where I found a welcome release from the rigors of my academic work. Thank you to Daniel for bringing me to the club on Wednesday evenings, offering me a much-needed outlet after a hard day of work. It was there that I met Fred, whose guidance and encouragement helped me secure second place at the armwrestling Inter-Faculty Competition. The camaraderie and support I found at the club were essential in maintaining my well-being throughout this journey.

I would also like to express my appreciation for the PhD experience itself. This journey took me to incredible places, including China, France, Germany, Italy, and the UK, where I not only expanded my knowledge but also broadened my horizons. Traveling and interacting with diverse academic communities has been profoundly enriching. Moreover, it was at the BND Doctoral School where I met my soulmate, a life-changing encounter that I will cherish forever. This PhD journey has truly been transformative, both professionally and personally.

To all those who have contributed, in ways big and small, to the completion of this thesis, I offer my sincerest thanks.

Contents

Abstract

Acknowledgments

Part Introduction	3
Part I Neutrino physics and JUNO experiment	5
1 The standard model and the neutrino sector	7
1.1 The standard model of particle physics	7
1.2 Neutrino discovery	9
1.2.1 History	9
1.2.2 The solar neutrino problem	10
1.3 Neutrino oscillations in vacuum	11
1.3.1 Case of 2 flavor neutrino oscillations	12
1.3.2 Case of 3 flavor neutrino oscillations	15
1.4 Oscillation in matter	16
1.4.1 Neutrino effective potential in matter	16
1.4.2 Flavor evolution equation	17
1.4.3 Two-flavor case	18
1.5 Actual knowledge of neutrinos in the standard model	19
1.5.1 Neutrino mass hierarchy	19
1.5.2 Oscillation measurements	20
1.5.3 Other open questions	22
2 JUNO experiment	25
2.1 General description	25
2.1.1 Water Cherenkov pool (WC)	26
2.1.2 Top Tracker (TT)	28
2.2 Liquid scintillator	30
2.3 PMTs	32
2.3.1 Small PMT system	34
2.3.2 Large PMT system	36
2.4 Calibration	38
2.4.1 Energy scale calibration	39
2.4.2 Conceptual design of the calibration system	39
2.5 Summary	40
3 Neutrino physics with JUNO	43
3.1 Various sources of neutrinos	43
3.2 Various background sources	44

3.3	Reactor neutrinos	45
3.3.1	Neutrino mass ordering	46
3.3.2	Precision measurement of neutrino oscillation parameters	48
3.4	Supernova neutrinos and trigger strategy	49
3.5	Diffuse supernova neutrino background	51
3.6	Solar neutrinos with JUNO	52
3.7	Atmospheric neutrinos	53
3.8	Geo-neutrinos	54
3.9	Summary	55
Part II Test and development of the back-end card of JUNO		57
4	Large PMT readout electronic system	59
4.1	General description	59
4.1.1	Large PMT readout electronic system requirement	59
4.1.2	Large PMT electronic chain	60
4.2	Underwater electronics	62
4.2.1	High voltage unit and splitter board	64
4.2.2	The Global Control Unit (GCU)	65
4.3	Outside water electronics system	72
4.3.1	Low voltage power supply	72
4.3.2	Trigger system hardware	72
4.3.3	Trigger schemes	77
4.3.4	Synchronization and clock distribution scheme for trigger system	80
4.4	Data Acquisition and Detector Control System	82
4.4.1	Data Acquisition System (DAQ)	82
4.4.2	Detector Control System (DCS)	83
4.5	Summary	84
5	Development and design of the back-end cards	87
5.1	Conception study	87
5.1.1	Underwater aggregation principle	88
5.1.2	Specific implementation and protocol	88
5.1.3	First generation prototype	90
5.1.4	First generation prototype test	92
5.2	Design of initial proposal	94
5.2.1	Back-end card first version (BEC-V1)	94
5.2.2	Second version - BEC V2	96
5.3	The BX scheme and the 1F3 schemes	101
5.4	Back-end card version 3 (BEC-V3)	105
5.5	Final scheme (BEC-V4)	108
5.5.1	Design of BEC-V4.0	109
5.6	Function tests of the BEC V4	111
5.6.1	Testing strategies	111
5.6.2	Loop test	111
5.6.3	Interconnecting tests	114
5.6.4	Error capture	118
5.6.5	Final implementation (BEC-V4.1-2)	122
5.7	Summary	122
6	Production and installation	125
6.1	Peripheral design	125

6.1.1	Power supply design	125
6.1.2	Box design	126
6.1.3	Temperature monitoring	129
6.2	Mass production	133
6.2.1	Production and assembly	133
6.2.2	Combined tests with GCU	134
6.3	Installation and commissioning	143
6.3.1	Physical link test (BEC loop test)	143
6.3.2	Physical link test between BECs and GCUs	144
6.3.3	Light-off test	145
6.4	Summary	152
Part III Model discrimination of core collapse super nova with JUNO		153
7	Supernovae	155
7.1	The Supernova event SN1987A	155
7.2	Supernova spectral classification	156
7.3	Early stage of the life of star	156
7.4	Collapse dynamics and neutrino emission in supernovae	157
7.5	Core-collapse supernova models	161
7.5.1	General consideration on modeling of core-collapse supernova	161
7.5.2	Modeling in the market	164
7.5.2.1	Sukhbold (2015)	164
7.5.2.2	Bollig (2016)	165
7.5.2.3	Tamborra (2014)	165
7.5.2.4	Nakazato (2013)	166
7.5.2.5	Warren (2020)	166
7.5.2.6	Fornax (2021)	167
7.5.2.7	Summary of models used	168
7.6	Astrophysical implications	169
7.6.1	Nucleosynthesis in CCSN	169
7.6.2	Neutron star and black hole formation	171
7.7	Summary	172
8	Supernova model discrimination	173
8.1	Analysis tools	173
8.1.1	Expected value	173
8.1.2	Monte Carlo generator	175
8.1.3	Cross check of the data generation	178
8.2	Statistical Analysis Method	179
8.2.1	Hypothesis testing framework	179
8.2.2	Computation of $\Delta\chi^2$ for binned poisson data	179
8.2.3	Computation of likelihood for binned poisson data	180
8.2.4	Computation of likelihood for unbinned data	180
8.3	Model discrimination using binned likelihood analysis	181
8.3.1	Model discrimination using IBD channel	181
8.3.2	Model discrimination using νpES channel	183
8.4	Model discrimination using unbinned likelihood analysis	184
8.4.1	Discussion of the impact of the number of observed events	186
8.4.2	Impact of neutrino flavor transformation on model discrimination	187
8.4.3	Comparison with Hyper-Kamiokande	188

8.5	Summary and outlook	190
Part Conclusions		195
Part IV Appendices		197
Part Appendices		199
A	Additional event rate and Monte Carlo data 2D distributions for the analysis	199
A.1	Inverse- β Decay (IBD)	200
A.1.1	Adiabatic transformation using normal mass ordering (NMO)	200
A.1.2	Adiabatic transformation using inverted mass ordering (IMO)	202
A.2	Elastic neutrino-proton scattering (ν pES)	204
A.2.1	Adiabatic transformation using normal mass ordering (NMO)	204
A.2.2	Adiabatic transformation using inverted mass ordering (IMO)	206
B	The ΔL distributions	209
B.1	Binned Likelihood Model Discrimination Results	209
B.2	Inverse- β Decay (IBD)	210
B.2.1	Adiabatic transformation using normal mass ordering (NMO)	210
B.2.1.1	Number of observed events = 100	210
B.2.1.2	Number of observed events = 300	211
B.2.1.3	Number of observed events = 1000	212
B.2.1.4	Number of observed events = 3000	213
B.2.1.5	Number of observed events = 5000	214
B.2.2	HK comparison	215
B.2.3	Adiabatic transformation using inverted mass ordering (IMO)	216
B.2.3.1	Number of observed events = 100	216
B.2.3.2	Number of observed events = 300	217
B.2.3.3	Number of observed events = 1000	218
B.2.3.4	Number of observed events = 3000	219
B.2.3.5	Number of observed events = 5000	220
B.3	Elastic neutrino-proton scattering (ν pES)	221
B.3.1	Adiabatic transformation using normal mass ordering (NMO)	221
B.3.1.1	Number of observed events = 100	221
B.3.1.2	Number of observed events = 300	222
B.3.1.3	Number of observed events = 1000	223
B.3.1.4	Number of observed events = 3000	224
B.3.1.5	Number of observed events = 5000	225
B.3.2	Adiabatic transformation using inverted mass ordering (IMO)	226
B.3.2.1	Number of observed events = 100	226
B.3.2.2	Number of observed events = 300	227
B.3.2.3	Number of observed events = 1000	228
B.3.2.4	Number of observed events = 3000	229
B.3.2.5	Number of observed events = 5000	230

Acronyms

μ TCA Micro Telecommunications Computing Architecture.

ν eES elastic neutrino-electron scattering.

ν pES elastic neutrino-proton scattering.

ABC ASIC Battery Card.

ADC Analog-to-Digital Converter.

ADU Analog to Digital Unit.

AMC Advanced Mezzanine Cards.

ARA Askaryan Radio Array.

ASIC Application Specific Integrated Circuit.

ATX Advanced Technology Extended.

BEB Back-End aggregation Board.

BEC Back-End Card.

BER Bit-Error-Rate.

BXPMT BX-scheme Photo-Multiplier Tube.

CATIROC Charge And Time Integrated Read Out Chip.

CCSN Core Collapse Supernova.

CD Central Detector.

CDR Clock Data Recovery.

CE Collection Efficiency.

CLB Configurable Logic Block.

CMS Compact Muon Solenoid.

CTU Central Trigger Unit.

Cute-WR Compact Universal Timing Endpoint based on WR.

DAQ Data Acquisition.

DCR Dark Count Rate.

DCS Detector Control System.

DSNB Diffuse Supernova Neutrino Background.

DSP Digital Signal Processing.

EEPROM Electrically Erasable Programmable Read-Only Memory.

FADC Flash Analog-to-Digital Converters.

FEC Front-End Chip.

FPGA Field-Programmable Gate Array.

FTP cable Foiled Twisted Pair cable.

GBT GigaBit Transceiver.

GCU Global Control Unit.

GPIO General-Purpose I/O.

HP High-Performance.

HR High-Range.

HV High Voltage.

HVS High Voltage Splitter.

IBD Inverse- β Decay.

ILA Integrated Logic Analyzer.

IOB I/O Block.

ISI Inter-Symbol Interference.

JUNO Jiangmen Underground Neutrino Observatory.

LAB Linear AlkylBenzene.

LCU Link Control Unit.

LPC Low Pin Count.

LPMT Large Photo-Multiplier Tube.

LS Liquid Scintillator.

LUT Look-Up Table.

LVDS Low-Voltage Differential Signaling.

LVPECL Low Voltage Positive Emitter-Coupled Logic.

MAC Media Access Control.

MCP Micro Channel Plate.

MMC Modular Multifunction Counter.

MMCM Mixed-Mode Clock Manager.

NC Neutral-Current.

NEXT Near-End Cross Talk.

NMO Neutrino Mass Ordering.

NPP Nuclear Power Plants.

OEC Online Event Classification.

p.e. photo-electron.

PDE Photo-Detection Efficiency.

Phase-Locked Loop PLL.

PLA Polylactic Acid.

PLD Programmable Logic Device.

PMT Photo-Multiplier Tubes.

PoE Power over Ethernet.

PPS Pulse Per Second.

PRBS PseudoRandom Binary Sequence.

PROM Programmable Read-Only Memory.

PTP Precision Time Protocol.

PVs Process Variables.

QE Quantum Efficiency.

RMS Root Mean Square.

RMU Reorganize and Multiplex Unit.

SASI Standing Accretion Shock Instability.

SFP Small Form-factor Pluggable.

SM standard model.

SMA SubMiniature version A.

SPMT Small Photo-Multiplier Tube.

SRAM Static RAM.

TOF Time Of Flight.

TT Top Tracker.

TTC Trigger Timing and Control.

TTIM Trigger and Timing Interface Mezzanine.

TTS Transmit Time Spread.

UTP cable Unshielded Twisted Pair cable.

UWB UnderWater Box.

VFL Vertex Fitting Logic.

V/O virtual input/output.

WR White Rabbit.

Introduction

Introduction

The history of neutrino physics started with the study of the energy spectrum observed in radioactive beta decay. The observed spectrum was inconsistent with the conservation of energy principle at first. A new particle, the neutrino, was introduced to solve the problem by Pauli in 1930 [1]. The first detection of neutrinos occurred in 1956 through the work of Reines and Cowan [2]. Since then, neutrinos have remained a central focus of particle physics research.

Throughout the 20th century, the [standard model \(SM\)](#) of particle physics was developed and has been very successful in describing elementary particles and their interactions. However, the discovery of neutrino oscillations showing that neutrinos have masses highlighted a significant limitation of the minimal version of the [SM](#) as it assumes massless neutrino. This discovery was recognized in 2015 by awarding the Nobel Prize in Physics to Takaaki Kajita and Arthur B. McDonald [3]. Understanding the mechanism at the origin of the neutrino mass subsequently remains one of the hot challenges in modern physics.

In addition to the unresolved question of the neutrino mass mechanism, many other open questions remain about neutrinos. One of the critical issues is whether neutrinos are Majorana or Dirac particles. If neutrinos are Majorana particles, there would be their own antiparticles, a concept that could significantly impact our understanding of the matter-antimatter asymmetry in the universe. Another crucial question is the mass ordering of neutrinos—whether their mass hierarchy is normal or inverted. Determining this ordering is vital for understanding the process of neutrino mass generation and its implications for the fundamental laws of physics. Furthermore, the potential existence of sterile neutrinos adds another layer of complexity to neutrino research. Sterile neutrinos, which do not interact via the weak force like active neutrinos, could provide explanations for several anomalies observed in experiments and might play a role in the composition of dark matter.

Many detectors have been constructed to study neutrinos using different technologies, such as water Cherenkov detectors or [Liquid Scintillator \(LS\)](#) detectors. The detector used by Reines and Cowan was a [LS](#) detector of a few hundred kg [2]. As different neutrino interaction cross-sections are very low, very large detectors have to be built to measure neutrinos with enough statistics. The new generation of detectors went from only a few hundred kilograms to a kiloton scale. [Jiangmen Underground Neutrino Observatory \(JUNO\)](#) is an excellent example of this trend with its 20 kt of [LS](#) instrumented by thousands of photomultiplier tubes [4].

The JUNO experiment is a medium-baseline neutrino oscillation experiment currently under construction in China. One of the JUNO goals aims to accurately measure the energy spectrum of electron antineutrinos produced by nuclear reactors located at a distance of 52.5 kilometers in order to determine the neutrino mass hierarchy and to measure several neutrino oscillation parameters at the sub-percent level [5]. JUNO also plans to detect and study neutrinos from various other sources, including solar neutrinos, atmospheric neutrinos, and neutrinos produced in supernovae.

My work within the JUNO experiment collaboration focuses on three main areas. The first is the development and testing of the [Back-End Card \(BEC\)](#), a crucial component of the photomultiplier tube readout system that connects the front-end electronics to the trigger system. The second contribution is a study of the capability of JUNO to detect neutrino from a potential core collapse supernova. The development of methods for discriminating between different core collapse supernova models using JUNO data is presented. Lastly, the study of low level (L1) hardware triggers based on machine learning [6] has also been performed, a topic not covered in detail in this thesis.

This thesis is organized into three main parts. The first part provides an introduction to neutrino physics and the **SM**, then it provides a full summary of the JUNO project. Chapter 1 gives an overview at the **SM** and covers the neutrino sector, the discovery of neutrinos, the solar neutrino problem, and neutrino oscillations in both vacuum and matter. It also presents the current open questions in neutrino physics. Chapter 2 focuses on the JUNO experiment facility, detailing the design of the detector, including the water Cherenkov pool, top tracker, liquid scintillator, and calibration systems. The physics goals of JUNO, particularly concerning reactor neutrinos, supernova neutrinos, and various other sources, are explored in Chapter 3.

The second part delves into the technical developments and the different testing of JUNO's **BEC**. Chapter 4 provides a general description of the extensive PMT readout system and details the underwater and outside-water electronics. Chapter 5 presents the evolution of the design and the different prototypes of the **BEC**, highlighting the technical challenges and the developed solutions. Chapter 6 concludes this part by discussing the mass production, installation, and the commissioning of the **BEC**.

The third part of the thesis focuses on the possibility of discriminating between different modelings of mechanisms of **CCSN** by measuring neutrino fluxes with JUNO. Chapter 7 gives a quick overview of supernovae knowledge, including the supernova event SN1987A, and discusses the dynamics of core-collapse and the different modelings of the **CCSN**. Chapter 8 describes the different tools used for the analysis and gives the results for model discrimination using JUNO.

Part I

Neutrino physics and JUNO experiment

Chapter 1

The standard model and the neutrino sector

In this chapter, we provide a brief overview of the standard model of particle physics. We then present the neutrino sector, including a concise history of neutrino physics. Detailed calculations for neutrino oscillations are provided for both 2-flavor and 3-flavor schemes in vacuum. We also describe the matter effect on neutrino oscillations. Finally, the last section summarizes the current knowledge of the neutrino sector within the standard model.

Contents

1.1	The standard model of particle physics	7
1.2	Neutrino discovery	9
1.2.1	History	9
1.2.2	The solar neutrino problem	10
1.3	Neutrino oscillations in vacuum	11
1.3.1	Case of 2 flavor neutrino oscillations	12
1.3.2	Case of 3 flavor neutrino oscillations	15
1.4	Oscillation in matter	16
1.4.1	Neutrino effective potential in matter	16
1.4.2	Flavor evolution equation	17
1.4.3	Two-flavor case	18
1.5	Actual knowledge of neutrinos in the standard model	19
1.5.1	Neutrino mass hierarchy	19
1.5.2	Oscillation measurements	20
1.5.3	Other open questions	22

1.1 The standard model of particle physics

The actual theoretical formulation of the [standard model \(SM\)](#) was finalized in the middle of the seventies. The basis of the model is to link elementary particles among them, classify them into different classes or families, and connect them to the different interactions or forces described by the exchange of a virtual particle (boson). All these phenomena can be developed mathematically using the quantum field theory. In this description, each particle is a quantization of the field. So, the particles are classified according to the nature of their field of origin.

On one side, there are the gauge bosons responsible for each of the interaction fields. In the [SM](#), we have 3 distinguishable forces: the electromagnetic force, the weak interaction, and the strong interaction, while gravitation couldn't be yet accommodated in the SM. For each of the interactions corresponds to a force carrier

particle. For the electromagnetic force, it is the photon; for the weak interaction, the bosons W^\pm , and Z , and for the strong interaction, 8 gluons.

On the other side, we have the fermions. The fermions are classified into two types: the leptons and the quarks. Leptons are classified into two main categories: a charged one with a certain mass (electron-type) and a neutral mass-less one (neutrino-type). For quarks, the classification is done according to their charge: the up-type (charge $2/3$) and the down-type (charge $-1/3$). Together, fermions can be divided into three families according to their flavor. The first flavor family corresponds to the up (u) and down (d) quarks and the electron (e) and the electronic neutrino (ν_e); the second flavor family corresponds to the charm (c) and strange (s) quarks and the muon and the muonic neutrino (ν_μ); the last flavor family corresponds to the top (t) and bottom (b) quarks and the tau lepton (τ) and the tau neutrino (ν_τ). In total, there are thus 12 different fermions in the SM. To each of the 12 fermions corresponds an anti-particle of the same mass but with an opposite charge.

The fermions and the bosons can be differentiated based on their spin. The bosons have integer spin values, and the fermions have half integer spin values. The elementary particles that compose the stable matter are only formed with the first family: the u and d quarks and the electron. For example, the protons and the neutrons, which compose the nucleus of the atoms, are composed of 3 quarks: uud and udd, respectively. The elementary particles of the SM are presented in Figure 1.1.

In 2012, physicists at CERN discovered a new particle, the scalar boson H (spin 0), which was theoretically predicted to explain the masses of all elementary particles in the Universe by spontaneous symmetry breaking through the Brout-Englert-Higgs (BEH) mechanism.

In this thesis, we will focus more specifically on the neutrino sector. As can be seen in Figure 1.1, the absolute masses of the 3 neutrinos are unknown. In the minimal version of the SM, the ν masses are supposed to be zero. However, we know now that at least two of the three neutrinos should have non-zero masses as we observe the phenomena of ν -oscillations (described in Section 1.3). A more complex model is thus needed to describe this phenomenon. By studying the neutrino oscillations, we have a powerful tool to scrutinize the neutrino sector and discover new physics beyond the SM. The section below gives an overview of the neutrino sector and its unanswered questions.

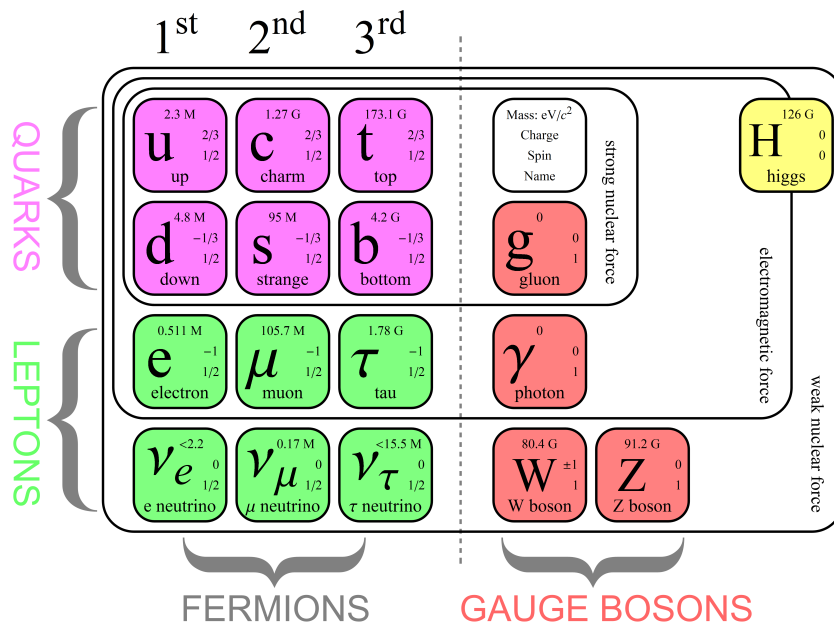
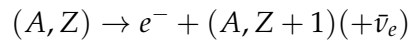


FIGURE 1.1: Actual knowledge of the SM extracted from reference [7].

1.2 Neutrino discovery

1.2.1 History

In the 1920s, it was already known that certain nuclei undergo beta decay, transforming into a nucleus of a different chemical element and emitting an electron:



In this equation, A is the number of nuclei inside the atom nucleus, and Z is the number of protons. Physicists initially believed that it was a two-body decay and thus expected the emitted electrons to have a discrete energy value due to the conservation of energy and momentum. Contrary to this expectation, measurements showed a continuous energy spectrum for the electrons, with the maximum energy matching the theoretical predictions [8, 9]. This unexpected result led some physicists, including Bohr, to speculate that energy might not be conserved at the subatomic level or might only be conserved "on average" [10].

In 1930, Pauli suggested an alternative explanation by introducing an additional undetected particle. This particle, produced during beta decay, was carrying away the missing energy. This hypothesis allows a continuous electron energy spectrum while still conserving energy [1]. Pauli initially called this particle the "neutron." However, after Chadwick discovered in 1932 the particle now known as the neutron [11], Pauli's particle was renamed as "neutrino".

Although Pauli was initially reluctant to publish his idea, it gained attention through discussions at various conferences. In 1934, Fermi published the first theoretical description of beta decay, including an analysis of how the electron spectrum's shape near the endpoint depends on the neutrino mass [12]. That same year, Bethe and Peierls provided the first theoretical estimate of the neutrino interaction cross-section based on the known beta decay lifetimes, establishing a limit of $\sigma < 10^{-44}$ cm² for 2.3 MeV neutrinos [13]. They concluded that such a particle would traverse approximately 10^{16} km of matter, leading them to think that no practically possible way exists to observe the neutrino [8].

During the next two decades, numerous experiments investigated beta decays with increasing precision, narrowing down alternative explanations for the continuous beta decay spectrum, yet failing to provide direct evidence for the existence of neutrinos. In the 1950s, Reines and Cowan proposed to use the nuclear fission reactor to measure the neutrino produced in it [14]. To reduce background interference, they planned to detect neutrinos via the spatial and temporal coincidence of signals from positrons and neutrons emitted in the [Inverse- \$\beta\$ Decay \(IBD\)](#) reaction ($\bar{\nu}_e + p \rightarrow n + e^+$) using a liquid scintillator detector [15]¹. It was only in 1956 that a refined experiment at the Savannah River nuclear reactor confirmed these observations, providing the first direct proof of neutrinos' existence [2, 16].

In the following years, the parity and helicity of the neutrino were measured by Wu and Goldhaber and their respective collaborators [17, 18]. In the 1950s, it was still uncertain whether neutrinos and antineutrinos were distinct particles, despite hints from double beta decay experiments [19]. Similarly, it was unclear if different types of neutrinos existed (i.e., different flavors, electron and muon neutrinos). This distinction was experimentally confirmed in 1962 when a beam of muon neutrinos produced by pion decay ($\pi^\pm \rightarrow \mu^\pm + (\nu_\mu/\bar{\nu}_\mu)$) generated muons, rather than electrons, in a nearby detector [[empty citation](#)].

Following the discovery of the τ lepton in 1975 [20], the existence of a corresponding neutrino, ν_τ , was widely anticipated. Experimental evidence for this particle was provided by the DONUT collaboration at Fermilab in 2001 [21]. Measurements of the Z boson's decay width at LEP indicate that no other species of weakly interacting neutrinos with a mass $m < m_Z/2 = 45.59$ GeV/ c^2 exist [22, 23].

¹The spatial and temporal coincidence of signals from positrons and neutrons emitted in the [Inverse- \$\beta\$ Decay \(IBD\)](#) is still used now in the JUNO experiment.

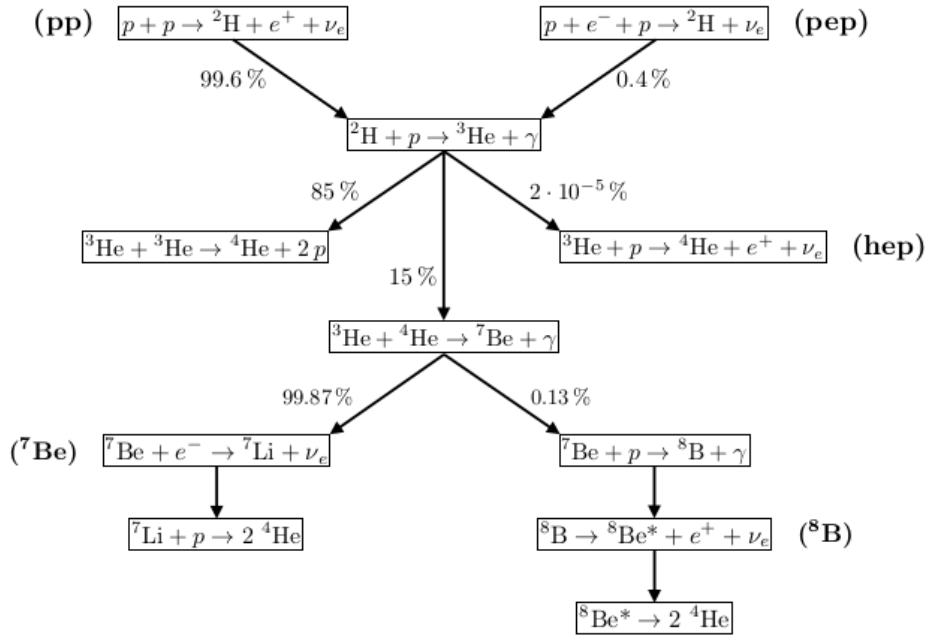


FIGURE 1.2: Reactions and branching ratios for the pp chain. Taken from [26].

1.2.2 The solar neutrino problem

The mechanism behind the sun's energy production remained a mystery until the twentieth century. Traditional energy sources known before the twentieth century, such as chemical or gravitational energy, could only account for a solar lifespan of several thousand to several million years, conflicting with geological and biological evidence. In 1920, Eddington proposed that the sun's energy might be generated through the nuclear fusion of hydrogen into helium [24]. This idea was further developed in the 1930s by Bethe and Critchfield, who suggested the proton-proton (pp) chain and the CNO cycle as potential fusion reactions in stars [25].

In both reaction chains, several intermediate steps involve the production of electron neutrinos through beta decays. The pp chain, depicted in Figure 1.2 is the primary energy production mechanism in the sun. About 0.26% of pp chain energy is emitted in the form of neutrinos.

Figure 1.2 illustrates the reaction steps and branching ratios of the pp chain. The CNO cycle, shown in Figure 1.3, produces neutrinos through similar reactions and is the dominant energy production process in heavier stars [12]. In both reaction chain, neutrinos are emitted which can be detected on earth.

Due to their weak interaction cross section, the produced neutrinos escape the sun without obstruction, providing insights into the ongoing fusion reactions. From the 1960s, several experiments aimed to measure the solar neutrino flux. These included radiochemical experiments, such as the Homestake experiment using chlorine and the GALLEX experiment using gallium, as well as water Cherenkov detectors like Kamiokande and Super-Kamiokande. All these experiments consistently detected a lower flux of solar neutrinos than predicted by the standard solar model, leading to the "solar neutrino problem" [27].

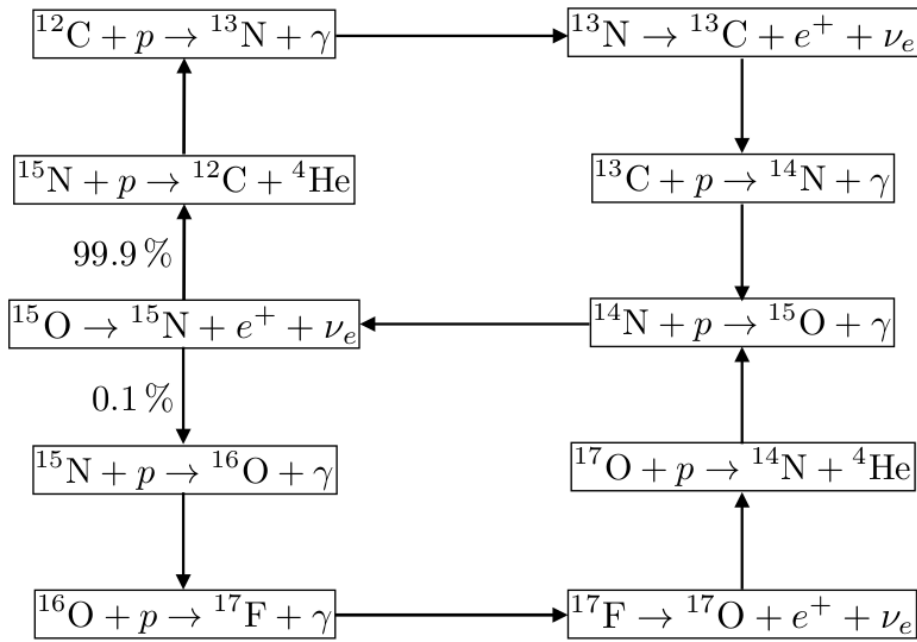


FIGURE 1.3: Reactions and branching ratios for the CNO cycle. Taken from [26].

This discrepancy was resolved in the early 2000s when the Sudbury Neutrino Observatory (SNO) demonstrated that neutrinos undergo flavor oscillations, changing from electron neutrinos to muon and tau neutrinos during their journey inside the sun core and mantle. This discovery not only resolved the solar neutrino problem but also provided the first direct evidence for neutrino oscillations, a phenomenon theoretically predicted by Pontecorvo, Maki, Nakagawa, and Sakata in the 1960s [28].

1.3 Neutrino oscillations in vacuum

The neutrinos produced via weak interaction are of a determined flavor state. The notations for the mass eigenstates are ν_1, ν_2, ν_3 and for the flavor eigenstates are ν_e, ν_μ, ν_τ . So a neutrino of a certain flavor can be expressed as a superposition of mass eigenstates²:

$$\begin{aligned}
 |\nu_e\rangle &= U_{e1} |\nu_1\rangle + U_{e2} |\nu_2\rangle + U_{e3} |\nu_3\rangle \\
 |\nu_\mu\rangle &= U_{\mu1} |\nu_1\rangle + U_{\mu2} |\nu_2\rangle + U_{\mu3} |\nu_3\rangle \\
 |\nu_\tau\rangle &= U_{\tau1} |\nu_1\rangle + U_{\tau2} |\nu_2\rangle + U_{\tau3} |\nu_3\rangle
 \end{aligned} \tag{1.1}$$

where $U_{e1} \dots U_{\tau3}$ are the 9 elements of the unitary PMNS matrix (Pontecorvo-Maki-Nakagawa-Sakata). A 3×3 unitary matrix contains 3 independent real numbers and one phase. The PMNS matrix can be written as:

$$U = \begin{pmatrix} c_{12}c_{13} & s_{12}c_{13} & s_{13}e^{-i\delta} \\ -s_{12}c_{23} - c_{12}s_{23}s_{13}e^{i\delta} & c_{12}c_{23} - s_{12}s_{23}s_{13}e^{i\delta} & s_{23}c_{13} \\ s_{12}s_{23} - c_{12}c_{23}s_{13}e^{i\delta} & -c_{12}s_{23} - s_{12}c_{23}s_{13}e^{i\delta} & c_{23}c_{13} \end{pmatrix} \tag{1.2}$$

The elements of the PMNS matrix are functions of the 3 mixing angles θ_{12} , θ_{13} and θ_{23} , with $c_{ij} =$

²This development is extracted from reference [29].

$\cos(\theta_{ij})$, $s_{ij} = \sin(\theta_{ij})$. We have also the Dirac phase δ . This phase is related to the CP violation³. To understand the oscillation phenomena, we derive in the following subsections, the formalism first for the two flavor case, and then the three flavor case.

1.3.1 Case of 2 flavor neutrino oscillations

We will first consider the case of two neutrino families in order illustrate easily the situation. We chose two neutrinos, for example here the electronic (ν_e) and the muonic (ν_μ) ones:

$$|\nu_i\rangle = \sum_{k=1}^2 U_{ik}^{2 \times 2} |\nu_k\rangle \quad (1.3)$$

where $i = e, \mu$ and $k = 1, 2$ for the mass eigen states. We can understand the mixing as a rotation of the coordinate system. This matrix can be written as:

$$U^{2 \times 2} = \begin{pmatrix} \cos \theta & \sin \theta \\ -\sin \theta & \cos \theta \end{pmatrix} \quad (1.4)$$

where θ is the mixing angle. We can express now the two weak eigenstates as a function of the mass eigenstates:

$$\begin{aligned} |\nu_e\rangle &= \cos \theta |\nu_1\rangle + \sin \theta |\nu_2\rangle \\ |\nu_\mu\rangle &= -\sin \theta |\nu_1\rangle + \cos \theta |\nu_2\rangle \end{aligned} \quad (1.5)$$

The mass eigenstates are solutions of the Schrödinger equation:

$$H |\nu_k\rangle = E_k |\nu_k\rangle = i\hbar \frac{d}{dt} |\nu_k\rangle \quad (1.6)$$

$E_k = \sqrt{m_k^2 c^4 + p_k^2}$ corresponds to the energy of the mass state k and the Hamiltonian can be expressed as:

$$H = \begin{pmatrix} E_1 & 0 \\ 0 & E_2 \end{pmatrix} \quad (1.7)$$

The solutions of the equation 1.6 are plane waves and when propagating in vacuum, the eigenstates can be written as:

$$|\nu_k(t)\rangle = e^{-i(E_k t - p_k x)} |\nu_k(0)\rangle = e^{-i\phi_k} |\nu_k(0)\rangle \quad (1.8)$$

with $\phi_k = E_k t - p_k x$. Now we will consider that we have at $t = 0$ a ν_e which is created:

$$|\nu_e(0)\rangle = |1\rangle \text{ and } |\nu_\mu(0)\rangle = |0\rangle \quad (1.9)$$

So the mass eigenstates are expressed as follows:

$$|\nu_1(0)\rangle = \cos \theta |1\rangle \text{ and } |\nu_2(0)\rangle = \sin \theta |1\rangle \quad (1.10)$$

³CP violation is a violation of charge conjugation and parity symmetries.

The evolution of the $|\nu_\mu\rangle$ is given by this formula:

$$\begin{aligned}
|\nu_\mu(t)\rangle &= -\sin\theta |\nu_1(t)\rangle + \cos\theta |\nu_2(t)\rangle \\
&= -\sin\theta e^{-i\phi_1} |\nu_1(0)\rangle + \cos\theta e^{-i\phi_2} |\nu_2(0)\rangle \\
&= -\sin\theta e^{-i\phi_1} \cos\theta |1\rangle + \cos\theta e^{-i\phi_2} \sin\theta |1\rangle \\
&= \frac{1}{2} \sin(2\theta) (e^{-i\phi_2} - e^{-i\phi_1}) |1\rangle
\end{aligned} \tag{1.11}$$

The probability of oscillation of the ν_e to ν_μ can be computed as:

$$\begin{aligned}
P_{\nu_e \rightarrow \nu_\mu} &= |\langle \nu_e(0) | \nu_\mu(t) \rangle|^2 \\
&= \frac{1}{4} \sin^2(2\theta) |e^{-i\phi_2 t} - e^{-i\phi_1 t}|^2 \\
&= \sin^2(2\theta) \sin^2\left(\frac{\phi_2 - \phi_1}{2}\right) \\
&= \sin^2(2\theta) \sin^2\left(\frac{\Delta\phi}{2}\right)
\end{aligned} \tag{1.12}$$

In the last equality, we pose $\Delta\phi = \phi_2 - \phi_1$. We will work in the ultra-relativistic limit i.e. $p \gg m_i$, with m_1 being the mass of the state $|\nu_1\rangle$ and m_2 is the mass of $|\nu_2\rangle$. We use natural units with $c = \hbar = 1$.

$$\begin{aligned}
E^2 &= p^2 + m^2 = p^2 \left(1 + \frac{m^2}{p^2}\right) \\
E &\approx p \left(1 + \frac{1}{2} \frac{m^2}{p^2}\right) = p + \frac{1}{2} \frac{m^2}{p}
\end{aligned} \tag{1.13}$$

We have used the Taylor expansion of the function square root trucked at the first order. We can express $\Delta\phi$:

$$\Delta\phi = (E_2 - p_2)t - (E_1 - p_1)t \approx \frac{m_2^2}{2p_2}t - \frac{m_1^2}{2p_1}t \approx \frac{m_2^2 - m_1^2}{2p}t \approx \frac{m_2^2 - m_1^2}{2E}t \tag{1.14}$$

The oscillation probability becomes:

$$P_{\nu_e \rightarrow \nu_\mu} = \sin^2(2\theta) \sin^2\left(\frac{m_2^2 - m_1^2}{4E}t\right) \tag{1.15}$$

If we use now the international unit system, h and c will appear:

$$P_{\nu_e \rightarrow \nu_\mu} = \sin^2(2\theta) \sin^2\left(\frac{(m_2^2 - m_1^2)c^4}{4hE}t\right) \tag{1.16}$$

We can also replace the travel time t by the travel distance L by using this $L = ct$:

$$P_{\nu_e \rightarrow \nu_\mu} = \sin^2(2\theta) \sin^2\left(\frac{(m_2^2 - m_1^2)c^3}{4hE}L\right) \tag{1.17}$$

If the units used for this formula are $[m^2] = \text{eV}^2/c^4$, $[E] = \text{GeV}$ and $[L] = \text{km}$, the oscillation probability $P_{\nu_e \rightarrow \nu_\mu}$ becomes:

$$P_{\nu_e \rightarrow \nu_\mu} = \sin^2(2\theta) \sin^2\left(1.27 \frac{\Delta m_{21}^2 L}{E}\right) \tag{1.18}$$

where $\Delta m_{21}^2 = m_2^2 - m_1^2$. In this case there is only one mixing angle θ , also labeled as θ_{12} .

Figure 1.4 shows the oscillation probability $P_{\nu_e \rightarrow \nu_\mu}$ for a 3 MeV neutrino as function of the distance. The

amplitude of the oscillations depends on the parameter θ . The period is a function of the ratio between the neutrino mass difference and the neutrino energy.

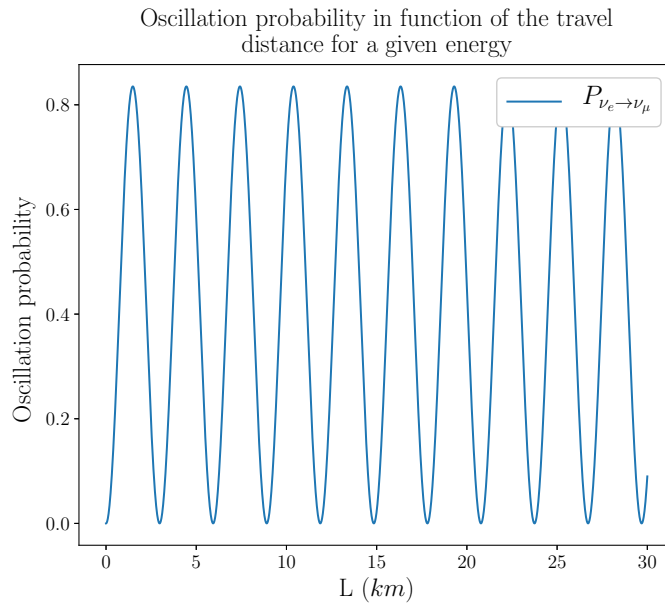


FIGURE 1.4: Graphic of the oscillation probability for ν_e to ν_μ as function of the distance L in kilometer. The parameters: Δm_{21}^2 and $\sin^2(\theta_{12})$ are taken from Table 1.8 and the neutrino energy is chosen at 3 MeV.

In Figure 1.5, we represent the normalized oscillation probability as a function of the variable E/L and we fix Δm_{21}^2 to 1 eV^2 .

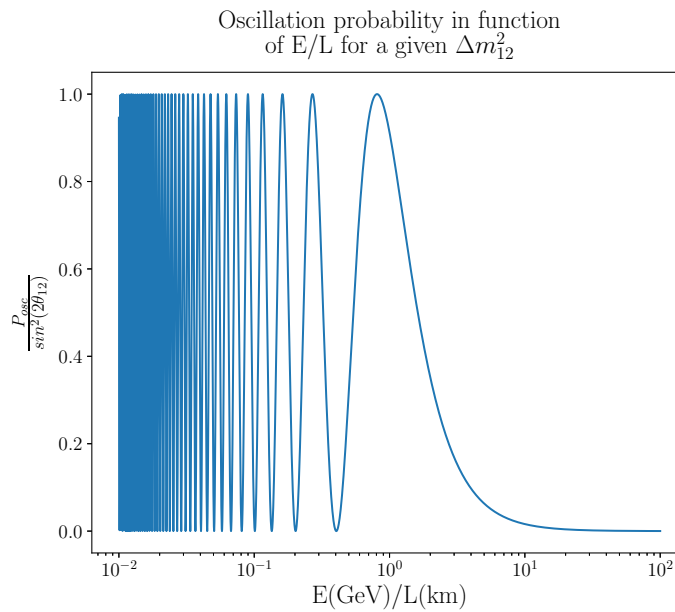


FIGURE 1.5: Graphic of the oscillation probability from the flavor state ν_e to ν_μ as a function of E/L ($\Delta m_{21}^2 = 1 \text{ eV}^2$).

1.3.2 Case of 3 flavor neutrino oscillations

The 2 flavor neutrino oscillation mechanism described in the previous section can be generalized to the case of 3 flavors. Starting from a ν_α at $t = 0$, the probability for this neutrino to oscillate into a ν_β at a time t is given by:

$$P_{\nu_\alpha \rightarrow \nu_\beta} = |\langle \nu_\alpha(0) | \nu_\beta(t) \rangle|^2 = \left| \sum_k U_{\alpha k}^* U_{\beta k} e^{-im_k^2 \frac{L}{2E}} \right|^2 \quad (1.19)$$

for $k = 1, 2, 3$ and U equals to the PMNS matrix defined at Equation 1.2. We will now compute the survival probability of one electronic neutrino (ν_e). The general expression for the survival probability is:

$$P_{\nu_e \rightarrow \nu_e} = \left| \sum_k U_{ek}^* U_{ek} e^{-im_k^2 \frac{L}{2E}} \right|^2 \quad (1.20)$$

$$= \sum_k U_{ek}^4 + \sum_{k=1}^3 \sum_{j>k}^3 U_{ek}^2 U_{ej}^2 (e^{-i\frac{\Delta m_{kj}^2 L}{2E}} + e^{i\frac{\Delta m_{kj}^2 L}{2E}}) \quad (1.21)$$

$$= c_{12}^4 c_{13}^4 + s_{12}^4 c_{13}^4 + s_{13}^4 + 2c_{13}^4 c_{12}^2 s_{12}^2 \cos\left(\frac{\Delta m_{21}^2 L}{2E}\right) \quad (1.22)$$

$$+ 2c_{13}^2 s_{13}^2 \left(c_{12}^2 \cos\left(\frac{\Delta m_{31}^2 L}{2E}\right) + s_{12}^2 \cos\left(\frac{\Delta m_{32}^2 L}{2E}\right) \right) \quad (1.23)$$

$$= 1 - c_{13}^4 \sin^2(2\theta_{12}) \sin^2\left(\frac{\Delta m_{21}^2 L}{4E}\right) \quad (1.24)$$

$$- \sin^2(2\theta_{13}) \left(c_{12}^2 \sin^2\left(\frac{\Delta m_{31}^2 L}{4E}\right) + s_{12}^2 \sin^2\left(\frac{\Delta m_{32}^2 L}{4E}\right) \right) \quad (1.25)$$

where $\Delta m_{31}^2 = m_3^2 - m_1^2$ and $\Delta m_{32}^2 = m_3^2 - m_2^2$. In the last expression, we can see that the oscillation frequency is a function of the mass square differences Δm_{21}^2 , Δm_{31}^2 and Δm_{32}^2 . We also know from neutrino oscillation measurements that $\Delta m_{21}^2 \ll \Delta m_{32}^2, \Delta m_{31}^2$.

Due to the small value of Δm_{21}^2 , we make the following approximation: $\Delta m_{31}^2 \approx \Delta m_{32}^2 \approx \Delta m_{fast}^2$. This leads to a two Δm^2 regimes approximation to simplify Equation 1.20. The probability of oscillation $P_{\nu_e \rightarrow \nu_e}$ can be rewritten as:

$$P_{\nu_e \rightarrow \nu_e} \approx 1 - c_{13}^4 \sin^2(2\theta_{12}) \sin^2\left(\frac{\Delta m_{21}^2 L}{4E}\right) \quad (1.26)$$

$$- \sin^2(2\theta_{13}) \sin^2\left(\frac{\Delta m_{fast}^2 L}{4E}\right) \quad (1.27)$$

$$= 1 - P_{slow} - P_{fast} \quad (1.28)$$

The fast oscillation regime is described by the parameters Δm_{32}^2 and Δm_{31}^2 . This part is also called the atmospheric neutrino oscillation. The slow oscillation regime is described by Δm_{21}^2 and is called the solar neutrino oscillation term. The survival probability $P_{\nu_e \rightarrow \nu_e}$ is represented in figure 1.6. The slow oscillation (red curve) corresponds to the 2 flavors case from section 1.3.1. The green curve in Figure 1.6 shows the oscillation due to the term in $\sin^2\left(\frac{\Delta m_{13}^2 L}{4E}\right)$ and $\sin^2\left(\frac{\Delta m_{23}^2 L}{4E}\right)$. These two sinuses have a frequency much higher than the red curve. As we can see in Table 1.8, Δm_{31}^2 and Δm_{32}^2 are in the range of $2 \times 10^{-3} \text{ eV}^2$ while the Δm_{21}^2 is more and less equal to $7 \times 10^{-5} \text{ eV}^2$.

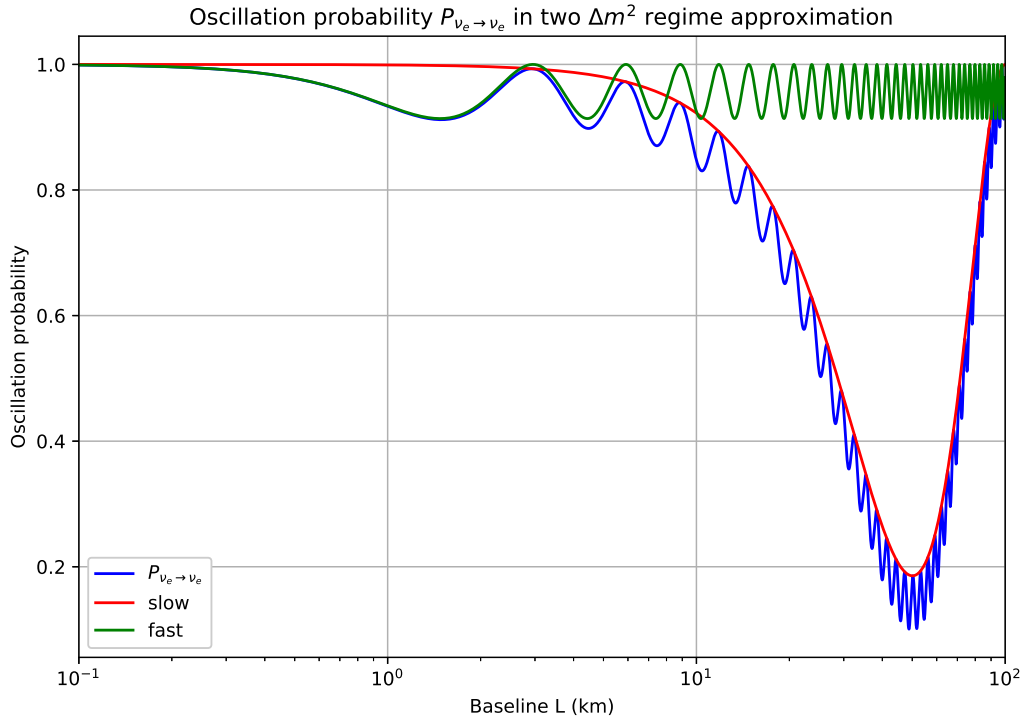


FIGURE 1.6: Graphic of the oscillation probability for ν_e remaining in the flavor state ν_e as a function of the distance L in kilometer for a neutrino of 3 MeV. The parameters: Δm_{21}^2 , Δm_{fast}^2 , $\sin^2(\theta_{12})$, $\sin^2(\theta_{23})$ and $\sin^2(\theta_{13})$ are from Table 1.8. The hypothesis of the normal neutrino mass hierarchy is used.

1.4 Oscillation in matter

The discussion presented in Section 1.3 was relevant for neutrinos propagating in vacuum. However, neutrinos also propagate through matter. Solar neutrinos, created in the center of the sun, have to travel across the sun before they can escape and reach the earth. Many of the atmospheric neutrinos have to propagate across a thick layer or even the entire earth before reaching the detector. Even reactor and accelerator neutrinos may have to cross thick layers of matter before being detected. This matter effect is called the Mikhaev, Smirnov, and Wolfenstein (MSW) effect [30]⁴.

1.4.1 Neutrino effective potential in matter

Neutrinos have an extremely low probability of interaction with matter. The presence of matter should only have a negligible effect on neutrino propagation. With the actual knowledge, we know that the coherent effect of forward scattering from many particles constituting the matter will affect neutrino propagation. The presence of an Effective Potential due to the presence of matter can describe this effect well. Electrons, protons, and neutrons compose the ordinary matter. The effective potential is built to take the contribution of the scattering from those target particles. The scattering interaction can proceed through Z^0 exchange, resulting in the effective potentials:

⁴This description and the development of the following is taken from lecture notes from Pr. Lipari [31].

$$\begin{aligned}
V_{\nu_\mu e} &= V_{\nu_\tau e} = V_{\nu_e e}^Z = -\frac{\sqrt{2}}{2}G_F N_e \\
V_{\nu_\mu p} &= V_{\nu_\tau p} = V_{\nu_e p} = +\frac{\sqrt{2}}{2}G_F N_p \\
V_{\nu_\mu n} &= V_{\nu_\tau n} = V_{\nu_e n} = -\frac{\sqrt{2}}{2}G_F N_n
\end{aligned} \tag{1.29}$$

where N_e, N_p, N_n is the electron, proton, and neutron density in matter, and G_F is the Fermi constant. ν_e can also scatter with electron through W processes leading to the effective potential for ν_e given as:

$$V_{\nu_e e} = V_{\nu_e e}^Z + V_{\nu_e e}^W = -\frac{\sqrt{2}}{2}G_F N_e + \sqrt{2}G_F N_e = \frac{\sqrt{2}}{2}G_F N_e \tag{1.30}$$

To compute the total effective potential, we need to perform the sum over the three contributions, giving, for example, $V_{\nu_e} = V_{\nu_e e} + V_{\nu_e p} + V_{\nu_e n}$. The different potential for ν_e compared to ν_μ and ν_τ plays a crucial role in the MSW effect:

$$V_{eff} \equiv V_{\nu_e} - V_{\nu_\mu} = V_{\nu_e} - V_{\nu_\tau} = +\sqrt{2}G_F N_e \tag{1.31}$$

This potential difference is proportional to the electron density N_e . For antineutrinos, the different potentials have a reversed sign:

$$V_{\bar{\nu}_\alpha} = -V_{\nu_\alpha} \tag{1.32}$$

1.4.2 Flavor evolution equation

To take into account the presence of matter, an effective Hamiltonian describes the flavor evolution. This Hamiltonian is constructed by summing up the vacuum Hamiltonian (H_0) and matter Hamiltonian (H_m), which includes the effective potential. This matter Hamiltonian, as seen above, changes signs for neutrinos and antineutrinos, leading to this definition for the effective Hamiltonian:

$$\begin{aligned}
H(\nu) &= H_0 + H_m \\
H(\bar{\nu}) &= H_0^* - H_m
\end{aligned} \tag{1.33}$$

Writing more explicitly for 3 different flavors of neutrinos as:

$$H(\nu) = U \begin{pmatrix} E_1 & 0 & 0 \\ 0 & E_2 & 0 \\ 0 & 0 & E_3 \end{pmatrix} U^\dagger + \begin{pmatrix} V_e & 0 & 0 \\ 0 & V_\mu & 0 \\ 0 & 0 & V_\tau \end{pmatrix} \tag{1.34}$$

where U is the PMNS matrix define at equation 1.2. This Hamiltonian enters a Schrödinger equation that controls the flavor evolution:

$$i \frac{d}{dt} \nu_\alpha = H \nu_\alpha \tag{1.35}$$

1.4.3 Two-flavor case

In the following, we will discuss the more straightforward case where ν_e is mixed with ν_μ and ν_τ and study the structure of the eigenvalues and eigenvectors in the matter as a function of the potential V . From Section 1.2.1, we know that the Hamiltonian in the vacuum is :

$$H_0 = \begin{bmatrix} \cos \theta & \sin \theta \\ -\sin \theta & \cos \theta \end{bmatrix} \begin{bmatrix} E_1 & 0 \\ 0 & E_2 \end{bmatrix} \begin{bmatrix} \cos \theta & -\sin \theta \\ \sin \theta & \cos \theta \end{bmatrix} \quad (1.36)$$

$$\sim \begin{bmatrix} \cos \theta & \sin \theta \\ -\sin \theta & \cos \theta \end{bmatrix} \begin{bmatrix} \frac{m_1^2}{2E} & 0 \\ 0 & \frac{m_2^2}{2E} \end{bmatrix} \begin{bmatrix} \cos \theta & -\sin \theta \\ \sin \theta & \cos \theta \end{bmatrix} \quad (1.37)$$

$$= \begin{bmatrix} \frac{m_1^2}{2E} \cos^2 \theta + \frac{m_2^2}{2E} \sin^2 \theta & \left(\frac{m_2^2}{2E} - \frac{m_1^2}{2E} \right) \cos \theta \sin \theta \\ \left(\frac{m_2^2}{2E} - \frac{m_1^2}{2E} \right) \cos \theta \sin \theta & \frac{m_1^2}{2E} \sin^2 \theta + \frac{m_2^2}{2E} \cos^2 \theta \end{bmatrix} \quad (1.38)$$

$$\begin{bmatrix} \frac{m_1^2 + m_2^2}{4E} + \frac{(m_1^2 - m_2^2) \cos 2\theta}{4E} & \frac{(m_2^2 - m_1^2) \sin 2\theta}{4E} \\ \frac{(m_2^2 - m_1^2) \sin 2\theta}{4E} & \frac{m_1^2 + m_2^2}{4E} + \frac{(m_2^2 - m_1^2) \cos 2\theta}{4E} \end{bmatrix} \quad (1.39)$$

$$= \frac{m_1^2 + m_2^2}{4E} \begin{bmatrix} 1 & 0 \\ 0 & 1 \end{bmatrix} + \frac{m_2^2 - m_1^2}{4E} \begin{bmatrix} -\cos 2\theta & \sin 2\theta \\ \sin 2\theta & \cos 2\theta \end{bmatrix} \quad (1.40)$$

where the first term does not affect the flavor evolution.

We can now add the matter Hamiltonian using the approximation $H_{\text{mat}} \approx \text{diag}(V_{\text{eff}}, 0)$ ⁵, that we can recast in the form:

$$H_{\text{mat}} = \frac{V_{\text{eff}}}{2} \begin{bmatrix} +1 & 0 \\ 0 & -1 \end{bmatrix} + \frac{V_{\text{eff}}}{2} \begin{bmatrix} 1 & 0 \\ 0 & 1 \end{bmatrix} \quad (1.41)$$

where V_{eff} is defined in equation 1.31. Adding the matter potential to the vacuum Hamiltonian one obtains:

$$H = H_0 + H_{\text{mat}} = \frac{\Delta m^2}{4E} \begin{bmatrix} -\cos 2\theta + \eta & \sin 2\theta \\ \sin 2\theta & +\cos 2\theta - \eta \end{bmatrix} + \frac{m_1^2 + m_2^2 + 2EV_{\text{eff}}}{4E} \begin{bmatrix} 1 & 0 \\ 0 & 1 \end{bmatrix} \quad (1.42)$$

where we have defined

$$\eta = \frac{2V_{\text{eff}}E}{\Delta m^2} = \frac{2\sqrt{2}G_F N_e E}{\Delta m^2} \text{ and } \Delta m^2 = m_2^2 - m_1^2 \quad (1.43)$$

By dividing and multiplying by $\sqrt{\sin^2 2\theta + (\cos 2\theta - \eta)^2}$ we can rewrite:

$$H = H_0 + H_{\text{mat}} = \frac{\Delta m^2}{4E} \begin{bmatrix} -\cos 2\theta + \eta & \sin 2\theta \\ \sin 2\theta & +\cos 2\theta - \eta \end{bmatrix} + \frac{m_1^2 + m_2^2}{4E} \begin{bmatrix} 1 & 0 \\ 0 & 1 \end{bmatrix} \quad (1.44)$$

$$\sim \frac{(\Delta m^2)_{\text{eff}}}{4E_v} \begin{bmatrix} -\cos 2\theta_m & \sin 2\theta_m \\ \sin 2\theta_m & +\cos 2\theta_m \end{bmatrix} \quad (1.45)$$

and where

$$\sin^2 2\theta_m = \frac{\sin^2 2\theta}{\sin^2 2\theta + (\cos 2\theta - \eta)^2} \text{ and } (\Delta m^2)_{\text{eff}} = \Delta m^2 \times \sqrt{\sin^2 2\theta + (\cos 2\theta - \eta)^2} \quad (1.46)$$

⁵The subtraction from the Hamiltonian of a term proportional to the unit matrix does not change the flavor evolution. The term leading to matter effect is then a matrix of the form $H_m \approx \text{diag}(V_{\text{eff}}, 0, 0)$. However, when the potential V_{eff} is comparable to the energy differences $|E_j - E_k| \approx \frac{|\Delta m_{jk}^2|}{2E_v}$, the flavor evolution is strongly modified and the $H_m \approx \text{diag}(V_{\text{eff}}, 0, 0)$ is not valid anymore [32].

Note that the term proportional to identity matrix does not contribute to the oscillation phenomenon. Finally, we can compute the oscillation probability of electron neutrinos to oscillate into muon neutrinos, $P_{\nu_e \rightarrow \nu_\mu}$ as:

$$P_{\nu_e \rightarrow \nu_\mu} = \sin^2 2\theta_m \sin^2 \left(1.27 \frac{(\Delta m^2)_{\text{eff}} L}{E} \right) \quad (1.47)$$

These formulae are useful to understand the following important consequences of the MSW effect:

1. long baselines or high matter densities are required to observe significant matter effects; in the limit $\eta \rightarrow 0$, the vacuum probabilities are retrieved
2. at the resonant condition $\cos 2\theta = \eta$, the oscillation phenomena can be significantly enhanced, even if the vacuum oscillation probability is minimal (i.e., θ is small)
3. the oscillation probabilities for neutrinos and antineutrinos can be different due to matter effects (because of the \pm sign in front of η), even if neutrino interactions with matter do not violate CP

1.5 Actual knowledge of neutrinos in the standard model

Neutrinos are among the most enigmatic particles in the universe, and several open questions continue to intrigue scientists:

1.5.1 Neutrino mass hierarchy

For the quarks and the charged leptons, we know that the mass hierarchy is normal. It means that the top quark is heavier than the charm quark and heavier than the up quark. The observation is the same for the other down-quarks and for the charged leptons. But for neutrinos, we do not know the mass ordering. To understand the situation, we use Figure 1.7, presenting the two possible mass orderings:

- normal ordering (NO): $m_1 < m_2 < m_3$
- inverted order (IO): $m_3 < m_1 < m_2$

The squared mass differences thus depend on the [Neutrino Mass Ordering \(NMO\)](#), from which they get their sign:

$$\begin{aligned} \Delta m_{21}^2 = m_2^2 - m_1^2 &\implies \Delta m_{21}^2 > 0, & \forall \text{NMO} \\ \Delta m_{32}^2 = m_3^2 - m_2^2 &\implies \Delta m_{32}^2 > 0, & \text{NMO} = \text{NO} \\ & & \Delta m_{32}^2 < 0, & \text{NMO} = \text{IO} \\ \Delta m_{31}^2 = m_3^2 - m_1^2 &\implies \Delta m_{31}^2 > 0, & \text{NMO} = \text{NO} \\ & & \Delta m_{31}^2 < 0, & \text{NMO} = \text{IO} \end{aligned}$$

The mass hierarchy will affect the oscillation probabilities. This impact will be used to determine the mass hierarchy by studying the neutrino oscillations.

Several ongoing and upcoming experiments aim to resolve this unknown. The determination of the [NMO](#) is a primary goal of different future experiments such as the [Jiangmen Underground Neutrino Observatory \(JUNO\)](#)

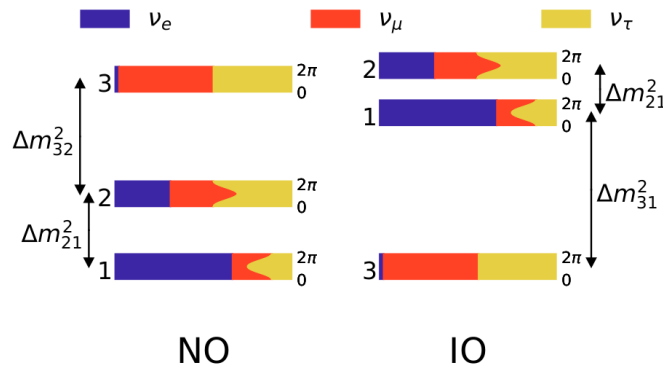


FIGURE 1.7: Neutrino mass ordering hypotheses: for the normal ordering (NO) on the left and inverted ordering (IO) on the right. Flavor contributions to the mass eigenstates are depicted by color. As the contributions depend on the weakly constrained CP-phase (δ_{CP}), different values are given for each mass eigenstate, with δ_{CP} increasing from bottom to top. Taken from [33].

[4] and the KM3NeT-ORCA [34] ones. Additionally, **Long Base Line (LBL)** experiments such as DUNE (Deep Underground Neutrino Experiment) [35] and T2HK (Tokai to Hyper-Kamiokande) [36] are also focused on resolving the NMO using matter effect on the oscillation of ν_μ created by accelerators.

1.5.2 Oscillation measurements

In addition to the **NMO**, neutrino oscillation experiments pursue the goal to constraint the values of the six parameters that govern the neutrino mixing, namely the mixing angles (θ_{12} , θ_{13} , θ_{23}), mass squared differences (Δm_{21}^2 , Δm_{32}^2 , Δm_{31}^2) and δ_{CP} . While significant progress was achieved, many questions remain unanswered, such as the actual value of δ_{CP} and the octant of θ_{23} .

By measuring neutrinos coming from natural and artificial sources, oscillation parameters are constrained. As each source produces neutrinos of different flavors and energies, each experiment is then constructed to constrain a particular set of parameters.

Measurement of θ_{13} Nuclear reactors produce a substantial flux of electron antineutrinos ($\bar{\nu}_e$) due to the fission of heavy elements such as ^{235}U , ^{238}U , ^{239}Pu , and ^{241}Pu . Several short-baseline reactor experiments have measured the value of θ_{13} via the $\bar{\nu}_e$ disappearance channel. In the early 2010s, three short-baseline experiments—Double Chooz, Daya Bay, and **Reactor Experiment for Neutrino Oscillations (RENO)**—provided the first measurements of θ_{13} .

An antineutrino flux deficit was first observed by the Double-Chooz collaboration [37] in 2011, confirming a non-zero value of θ_{13} . Soon after the results of Double-Chooz, the Daya Bay experiment reported a 5σ evidence of θ_{13} being non-zero [38]. The two results were later confirmed by the **RENO** experiment at 4.9σ [39]. Since then, increased statistics and experimental improvements have made θ_{13} the most accurately known neutrino mixing angle despite being the smallest neutrino mixing angle.

The Daya Bay experiment comprises eight antineutrino detectors spread across two near detector halls and one far detector hall. Those detectors monitor the antineutrino flux from six reactor cores composing the Daya Bay nuclear power plant. The two near halls are located 365 m and 505 m away from the reactor cores, while the far hall is about 1663 m away. The detectors use gadolinium-doped liquid scintillator technology. Later, Daya Bay published updated results, incorporating 1958 days of data, which refine the measurements of $\sin^2 2\theta_{13}$ and Δm_{32}^2 [40].

The **RENO** and the Double Chooz experiments, situated in South Korea and France, respectively, also use Gadolinium-doped liquid scintillator detectors. The **RENO** experiment consists of two detectors (one near detector and one far). They measure the antineutrino flux from six reactors. The far and near detectors are placed at 294 m and 1383 m from the reactor array, respectively. On the other hand, Double Chooz has two identically designed detectors with different average baselines of about 400 m and 1050 m from the two nuclear reactor cores of Chooz facility [41].

Measurement of θ_{12} and Δm_{21}^2 Solar experiments such as **Super-Kamiokande (SK)** [42], **Sudbury Neutrino Observatory (SNO)** [43] and **Borexino** [44] are used to constrain θ_{12} and Δm_{21}^2 . The ν_e produced in the Sun's core oscillates as they travel from their point of origin to the Earth. The observable spectra of neutrinos, dominated by 8B decays, are compared with the expectation of the Sun Standard Model and fitted to an oscillation model. In parallel, KamLAND [45], an experiment that measures the oscillations of electronic antineutrinos from nuclear reactors, is also sensitive to the measurement of solar parameters.

The **SK** detector is located in the Kamioka Mine in Japan and consists of a 50-kt water Cherenkov detector. It was the first experiment to provide strong evidence for the solution of the solar neutrino problem. Super-K has been collecting solar neutrino data since 1996, observing the flux of solar 8B decays [46]. **SNO** initially used a spherical heavy water tank located at a depth of 2092 m in the Vale Mine in Canada. It was also designed to measure the 8B solar spectrum and operated as the SNO experiment between 1999 and 2006. SNO experiment was using heavy water (D_2O) which allowed to distinguished the ν_e flux (measured using charged current $\nu + d \rightarrow p + p + e^-$) and the total ν flux (measured using through neutral current $\nu_x + d \rightarrow p + n + \nu_x$). Borexino, ran from 2007 to 2021 using a spherical liquid scintillator detector in the Gran Sasso Laboratory, and also contributed to the measurement of Δm_{12}^2 and θ_{12} presented in Reference [44].

KamLAND was the first experiment to measure the Δm_{21}^2 mass squared difference using reactor $\bar{\nu}_e$. The KamLAND detector uses a 1,000-ton liquid scintillator. This scintillator is enclosed in a 135 μm thick nylon sphere, surrounded by 1879 **Photo-Multiplier Tubess (PMTs)**. As the reactor antineutrinos travel an average distance of 180 km before being detected, KamLAND is called a **Long Base Line (LBL)**. It allows KamLAND to be sensitive to Δm_{21}^2 . KamLAND measured Δm_{21}^2 with a precision comparable to that one obtained from solar neutrino experiments. KamLAND measured the squared mass difference Δm_{21}^2 , the mixing angle $\tan^2 \theta_{12}$, for the number see Reference [47].

Measurement of θ_{23} and Δm_{32}^2 Several experiments have set constraints on the values of $\sin^2 \theta_{23}$ and Δm_{32}^2 through the ν_μ disappearance and ν_e appearance channels, particularly MINOS, NOvA, and T2K. In addition, neutrino telescopes such as **ANTARES**[48] and **IceCube** [49] are also involved in that measurement. The **ANTARES** neutrino detector consists of 12 vertical lines anchored to the Mediterranean sea floor, each 450 m long and spaced 65 m apart. Optical modules equipped with PMT are positioned along the lines to detect Cherenkov light from charged particles. These signals are transmitted via a 42 km electro-optical cable to a shore station for analysis [50]. Data collected by **ANTARES** between 2007 and 2010, spanning 863 days of live time, were used to measure atmospheric neutrino oscillation parameters. Muon tracks with energies as low as 20 GeV were reconstructed, showing a suppression of vertical up-going muon neutrinos. Oscillation parameters were extracted by fitting the event rate as a function of the neutrino energy to the reconstructed path through Earth. The results for Δm_{32}^2 are presented in Reference [51] under a two-flavor approximation and assuming maximal mixing.

The **IceCube** detector is a cubic-kilometer array of PMT embedded deep within the Antarctic ice. It is designed to detect neutrinos by capturing the Cherenkov light produced when neutrinos interact with ice. The **IceCube** detector consists of 78 strings, each equipped with 60 PMTs, deployed between 1,450 and 2,450 meters below the surface. The **DeepCore** extension, located in the central part of **IceCube**, lowers the detection threshold to approximately 10 GeV, enhancing its capability to study atmospheric neutrino oscillations [49]. Data from 953 days of operation, corresponding to more than 5,000 neutrino events, were used to measure atmospheric neutrino

oscillations. The oscillations were observed by fitting the ratio of the reconstructed neutrino energy to the zenith angle. The results of this analysis measured the oscillation parameters are given in Reference [52].

The MINOS (Main injector neutrino oscillation search) beam was produced at the Fermilab NuMI beamline [53]. The far detector was located 700 m underground in the Soudan mine (Minnesota, USA) for a baseline of 735 km. The near and far detectors were both segmented steel-scintillator tracking calorimeters to detect charged current $\nu_\mu + N \rightarrow \mu^- + X$ and $\bar{\nu}_\mu + N \rightarrow \mu^+ + X$. In 2013, MINOS performed the most accurate measurement of θ_{23} and Δm_{32}^2 [54]. T2K and NOvA were primarily designed to explore the neutrino sector by investigating the appearance of ν_e . However, they have also made, and will continue to make, important contributions to the study of ν_μ disappearance. J-PARC (Japan Proton Accelerator Research Complex) supplies 30 GeV protons to the T2K experiment. The neutrino beam, generated using the off-axis technique, has a narrow-band energy spectrum. Its energy is optimized to the oscillation maximum (around 600 MeV for T2K's 295 km baseline), which helps to minimize the high-energy component that contributes to background generation. T2K measure the neutrino beam flux at its far detector, Super-K [55].

On the other hand, NOvA studies the electron neutrino appearance in the muon neutrino beam generated thanks to Fermilab NuMI beamline [56]. The 222-ton near detector is placed in an underground cavern near the NuMI tunnel at Fermilab to help to measure beam backgrounds. The 14-kt far detector is constructed from 385,000 extruded PVC cells filled with liquid scintillator, which makes up 70% of the detector mass. It serves as a tracking calorimeter optimized for detecting electron neutrinos. The detector will be read out using 13,000 kilometers of optical wave-shifting fiber connected to avalanche photo-diodes. The NOvA experiment has been collecting data in the NuMI neutrino beam since 2014.

Constraints on δ_{CP} Charge-Parity (CP) symmetry in the lepton sector can be studied by examining differences between neutrino and antineutrino oscillations. Long-baseline accelerator neutrino experiments, like NOvA, and T2K, are effective in probing CP violation by observing ν_e appearance in ν_μ beams. These experiments have constrained δ_{CP} through ν_e and $\bar{\nu}_e$ appearance and ν_μ and $\bar{\nu}_\mu$ disappearance. However, their results show inconsistencies and lack of high significance. Upcoming experiments like DUNE and Hyper-K are essential to improve δ_{CP} measurements [57].

The NuFit group maintains an updated global analysis of neutrino oscillation measurements to determine the leptonic mixing matrix and the neutrino mass differences in the framework of the SM with 3 massive neutrinos. The most recent values of neutrino oscillation parameters are presented in Table 1.8 [58].

1.5.3 Other open questions

Neutrino masses The absolute mass of neutrinos is not known. The Karlsruhe Tritium Neutrino (KATRIN) experiment is a large-scale tritium-beta-decay experiment designed for the high-precision integral spectrum of the endpoint region of tritium beta decay. The goal of this experiment is to measure the absolute mass scale of neutrinos. The latest neutrino mass results of KATRIN, using the two first data-taking campaigns, are $m_\nu < 0.8$ eV at the 90 % confidence level [59].

Neutrino nature It is still uncertain whether neutrinos are Dirac or Majorana particles. If neutrinos are Majorana particles, they are their own antiparticles. This question has profound implications for the understanding of fundamental symmetries in physics, such as the matter-antimatter asymmetry in the universe.

Sterile neutrinos The existence of an additional neutrino family, named sterile neutrinos, as they would not interact via the weak force like the known neutrino types, is another open question. Evidence for sterile neutrinos would revolutionize the standard model of particle physics and provide insights into the nature of dark matter.

NuFIT 5.3 (2024)					
		Normal Ordering (best fit)		Inverted Ordering ($\Delta\chi^2 = 2.3$)	
		bfp $\pm 1\sigma$	3σ range	bfp $\pm 1\sigma$	3σ range
		without SK atmospheric data	$\sin^2 \theta_{12}$	$0.307^{+0.012}_{-0.011}$	$0.275 \rightarrow 0.344$
	$\theta_{12}/^\circ$	$33.66^{+0.73}_{-0.70}$	$31.60 \rightarrow 35.94$	$33.67^{+0.73}_{-0.71}$	$31.61 \rightarrow 35.94$
	$\sin^2 \theta_{23}$	$0.572^{+0.018}_{-0.023}$	$0.407 \rightarrow 0.620$	$0.578^{+0.016}_{-0.021}$	$0.412 \rightarrow 0.623$
	$\theta_{23}/^\circ$	$49.1^{+1.0}_{-1.3}$	$39.6 \rightarrow 51.9$	$49.5^{+0.9}_{-1.2}$	$39.9 \rightarrow 52.1$
	$\sin^2 \theta_{13}$	$0.02203^{+0.00056}_{-0.00058}$	$0.02029 \rightarrow 0.02391$	$0.02219^{+0.00059}_{-0.00057}$	$0.02047 \rightarrow 0.02396$
	$\theta_{13}/^\circ$	$8.54^{+0.11}_{-0.11}$	$8.19 \rightarrow 8.89$	$8.57^{+0.11}_{-0.11}$	$8.23 \rightarrow 8.90$
	$\delta_{CP}/^\circ$	197^{+41}_{-25}	$108 \rightarrow 404$	286^{+27}_{-32}	$192 \rightarrow 360$
	$\frac{\Delta m_{21}^2}{10^{-5} \text{ eV}^2}$	$7.41^{+0.21}_{-0.20}$	$6.81 \rightarrow 8.03$	$7.41^{+0.21}_{-0.20}$	$6.81 \rightarrow 8.03$
	$\frac{\Delta m_{3l}^2}{10^{-3} \text{ eV}^2}$	$+2.511^{+0.027}_{-0.027}$	$+2.428 \rightarrow +2.597$	$-2.498^{+0.032}_{-0.024}$	$-2.581 \rightarrow -2.409$
with SK atmospheric data		Normal Ordering (best fit)		Inverted Ordering ($\Delta\chi^2 = 9.1$)	
		bfp $\pm 1\sigma$	3σ range	bfp $\pm 1\sigma$	3σ range
	$\sin^2 \theta_{12}$	$0.307^{+0.012}_{-0.011}$	$0.275 \rightarrow 0.344$	$0.307^{+0.012}_{-0.011}$	$0.275 \rightarrow 0.344$
	$\theta_{12}/^\circ$	$33.67^{+0.73}_{-0.71}$	$31.61 \rightarrow 35.94$	$33.67^{+0.73}_{-0.71}$	$31.61 \rightarrow 35.94$
	$\sin^2 \theta_{23}$	$0.454^{+0.019}_{-0.016}$	$0.411 \rightarrow 0.606$	$0.568^{+0.016}_{-0.021}$	$0.412 \rightarrow 0.611$
	$\theta_{23}/^\circ$	$42.3^{+1.1}_{-0.9}$	$39.9 \rightarrow 51.1$	$48.9^{+0.9}_{-1.2}$	$39.9 \rightarrow 51.4$
	$\sin^2 \theta_{13}$	$0.02224^{+0.00056}_{-0.00057}$	$0.02047 \rightarrow 0.02397$	$0.02222^{+0.00069}_{-0.00057}$	$0.02049 \rightarrow 0.02420$
	$\theta_{13}/^\circ$	$8.58^{+0.11}_{-0.11}$	$8.23 \rightarrow 8.91$	$8.57^{+0.13}_{-0.11}$	$8.23 \rightarrow 8.95$
	$\delta_{CP}/^\circ$	232^{+39}_{-25}	$139 \rightarrow 350$	273^{+24}_{-26}	$195 \rightarrow 342$
	$\frac{\Delta m_{21}^2}{10^{-5} \text{ eV}^2}$	$7.41^{+0.21}_{-0.20}$	$6.81 \rightarrow 8.03$	$7.41^{+0.21}_{-0.20}$	$6.81 \rightarrow 8.03$
	$\frac{\Delta m_{3l}^2}{10^{-3} \text{ eV}^2}$	$+2.505^{+0.024}_{-0.026}$	$+2.426 \rightarrow +2.586$	$-2.487^{+0.027}_{-0.024}$	$-2.566 \rightarrow -2.407$

FIGURE 1.8: Most recent values of the neutrino oscillation parameters. The results shown in the table are obtained without (top) and with (bottom) the inclusion of the tabulated χ^2 data on atmospheric neutrinos provided by the Super-Kamiokande collaboration (SK-atm) [60]. The numbers in the 1st column are obtained assuming NO, and the second column assuming IO. Note that $\Delta m_{3l} = \Delta m_{31} > 0$ for NO and $\Delta m_{3l} = \Delta m_{32} < 0$ for IO. Taken from [58].

Chapter 2

JUNO experiment

Typical detectors for neutrino physics have two key characteristics: they are situated deep underground and have large active volumes. The underground location provides natural shielding against cosmic radiation, significantly reducing background noise. The large active volumes are essential to compensate for the low cross-section of the neutrino interactions, increasing the probability of capturing valuable events. This chapter will explore these design features optimized for the JUNO experiment.

Contents

2.1	General description	25
2.1.1	Water Cherenkov pool (WC)	26
2.1.2	Top Tracker (TT)	28
2.2	Liquid scintillator	30
2.3	PMTs	32
2.3.1	Small PMT system	34
2.3.2	Large PMT system	36
2.4	Calibration	38
2.4.1	Energy scale calibration	39
2.4.2	Conceptual design of the calibration system	39
2.5	Summary	40

2.1 General description

The Jiangmen Underground Neutrino Observatory (JUNO) project [4] is mainly focused on the measurement of the NMO with reactor anti-neutrinos. The detector must be situated at a specific distance from its source in order to optimize oscillation parameter measurements using anti-neutrino flux from nuclear reactors. The different reactors, mainly contributing to the neutrino flux measured by JUNO, need to be at the same distance from the central detector to avoid any cancellation effect due to the oscillation de-phasing. The location chosen is in the Jiangmen city, Guangdong province, in South China.

The detector is 52.5 km away from two Nuclear Power Plants (NPP): the Yangjian NPP and the Taishan NPP. The Yangjian facility has six nuclear reactor cores of 2.9 GW_{th} of thermal power, while Taishan has two cores of 4.59 GW_{th} each (4 cores were initially planned). The total thermal power generating the anti-neutrino flux studied with JUNO is 26.6 GW_{th}. All the cores of the Yangjian NNP are second generation pressurized water reactors, while the cores in Taishan are third-generation pressurized water reactors. The detector is composed of three different parts:

- A 20 kt **Liquid Scintillator (LS)** contained in a acrylic sphere, also called **Central Detector (CD)**
- A **Water Cherenkov (WC)** pool surrounding the **CD**, containing 35 kt of ultra-pure water
- A plastic scintillator detector, placed on top of the **CD** and the water pool. This detector is called **Top Tracker (TT)** and uses the scintillation strips from the OPERA experiment¹

The final vertical overburden for the CD center is 650 m [62], which is lower than the overburden presented in the conceptual design report [4]. Figure 2.1 presents a schematic view of the JUNO experimental hall and CD. The LS is contained in an spherical acrylic vessel of 35.4 m diameter. The 265 acrylic panels are designed to offer a high transparency in water (>96%). As the radioactive contamination was an important concern, the radio-purity level of the acrylic needs to be lower than 0.5 ppt for uranium and thorium. The acrylic vessel is maintained by a stainless steel structure inside the water pool. On the stainless steel structure, 17612 20-inch photomultiplier tubes, called **Large Photo-Multiplier Tube (LPMT)**, and 25600 3-inch PMTs, called **Small Photo-Multiplier Tube (SPMT)**, are used to collect the light coming from the inside of the CD. The combination of large and small PMTs allows a photo-cathode coverage² of about 77.9% of the CD. The photo-coverage is an important parameter to ensure the energy resolution of 3% required for the NMO measurement. Preliminary studies in JUNO [4] have shown that the required energy resolution ($\frac{\sigma}{E}$) to discriminate between the normal and inverted neutrino hierarchies at a 3 – 4 σ confidence level for about 6 years of the data record is 3% at an energy of 1 MeV. This goal puts strong constraints on the detector component quality, in particular on the PMTs. The layout of the PMT system has been optimized with an array of sPMTs placed in between the large PMTs, as shown in Figure 2.2.

2.1.1 Water Cherenkov pool (WC)

Around the detector, the TT and WC pool serve as vetoes to reduce the different backgrounds. The water Cherenkov pool is a cylinder of 43.5 m in diameter and 44 m in height containing 35 kt ultra-pure water. The purpose of the water Cherenkov pool is to detect Cherenkov light emitted by muons coming from outside the neutrino target (the LS). The PMTs collect the Cherenkov light emitted by the incoming charged particle.

The muons track length inside the water Cherenkov pool is short as the water thickness is limited. The challenge not only resides in the muon tagging but also their track reconstruction. The full photo-coverage of the water Cherenkov pool is the ideal solution. However by budget constraints, a total of 2400 20-inch PMTs are used to collect light inside the water Cherenkov pool. To capture the direction of the tagged event, PMTs are placed on the outer surface of the stainless steel structure, pointing in the direction of the water-pool.

We need ultra-pure water to avoid other background noises, such as the ones coming from the disintegration of the impurities in the water. It will also act as a passive shielding for neutrons and gammas originating from the rock around the detector. Additionally, radon from the surrounding rock will affect the purity of the water during the filling of the detector and the operation. To face this issue, a radon removal system is implemented using multi-stage degassing membranes during the filling. To avoid radon contamination during operation a specific film will cover the concrete of the pool to avoid infiltration inside the water.

As the PMTs of the CD and the water pool may be affected by Earth's magnetic field, circular coils surround the detector. The coils are designed to compensate the earth magnetic field to achieve 0.05 G in the CD PMT region and 0.1G in the water-pool PMT region.

¹The OPERA (Oscillation Project with Emulsion-tRacking Apparatus) experiment was designed to detect neutrino oscillations by observing the appearance of tau neutrinos from a beam of muon neutrinos. Conducted at the Gran Sasso Laboratory in Italy, the experiment used a high-intensity beam of muon neutrinos generated at CERN, 730 kilometers away. The OPERA detector consisted of layers of photographic emulsions interspersed with lead plates to perform precise tracking and identification of particles. In 2010, OPERA successfully detected the first tau neutrino (ν_τ) candidate. In total 5 ν_τ candidates were observed over a very small expected background, providing direct evidence for neutrino oscillations and contributing significantly to the understanding of neutrino physics [61].

²Photo-cathode coverage is the ratio of the surface covered by PMTs over the total surface of the detector.

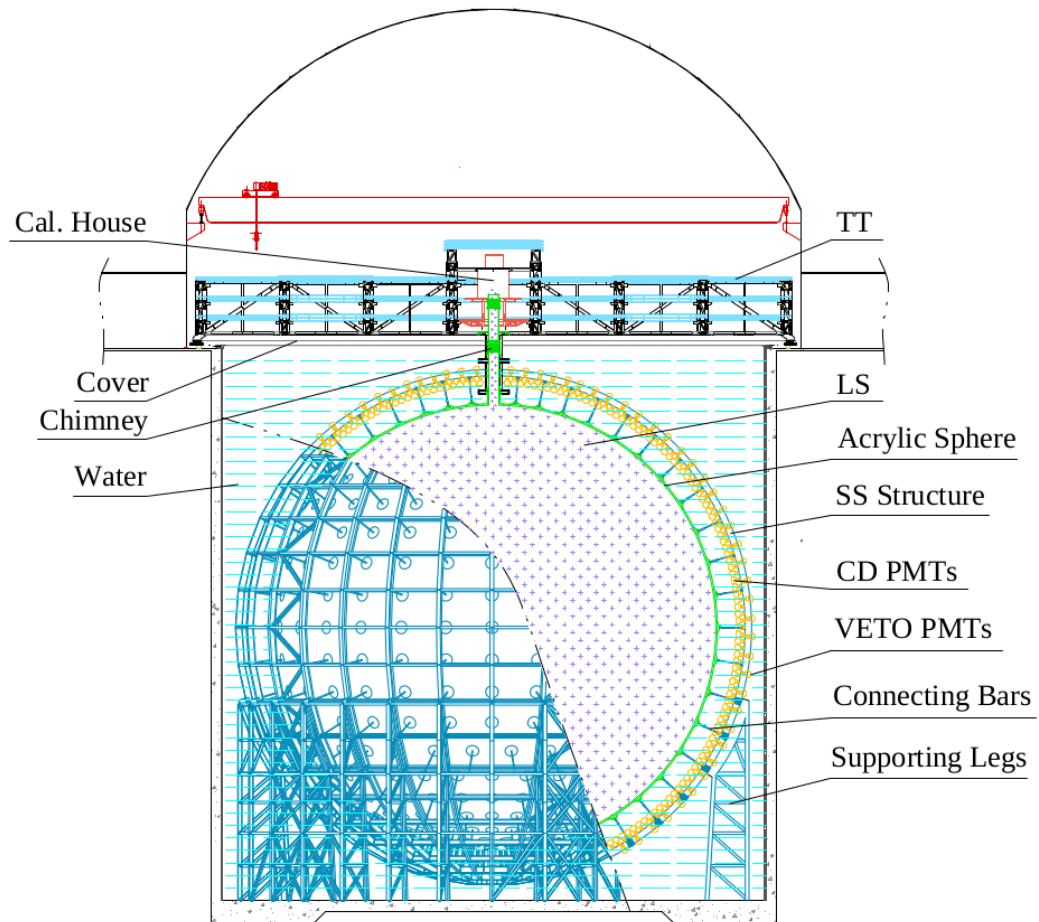


FIGURE 2.1: Schematic view of the JUNO experiment hall and central detector. Taken from [63].



FIGURE 2.2: LPMT and SPMT positioning. The SPMTs are positioned in the interstices of the LPMTs. Taken from [64].

2.1.2 Top Tracker (TT)

The role of the **TT** is to detect cosmic muons and to reconstruct their trajectory to study the cosmogenic background production. This helps to reduce the systematic errors in the neutrino mass ordering determination. The most problematic background is induced by cosmic muons generating ${}^9\text{Li}$ and ${}^8\text{He}$ unstable elements and fast neutrons, which could fake an IBD interaction inside the CD (see section 3.2 for details). Figure 2.3 presents schematically the most essential noise configurations. Panels (a) and (b) mainly concern ${}^9\text{Li}$ and ${}^8\text{He}$ production due to muon. In Panel (a), the muon track is partially contained in the central detector, while in Panel (b), the muon passes only by the water pool veto. The other case concerns the neutron production in the surrounding rock, shown in panel (c) [4, 65].

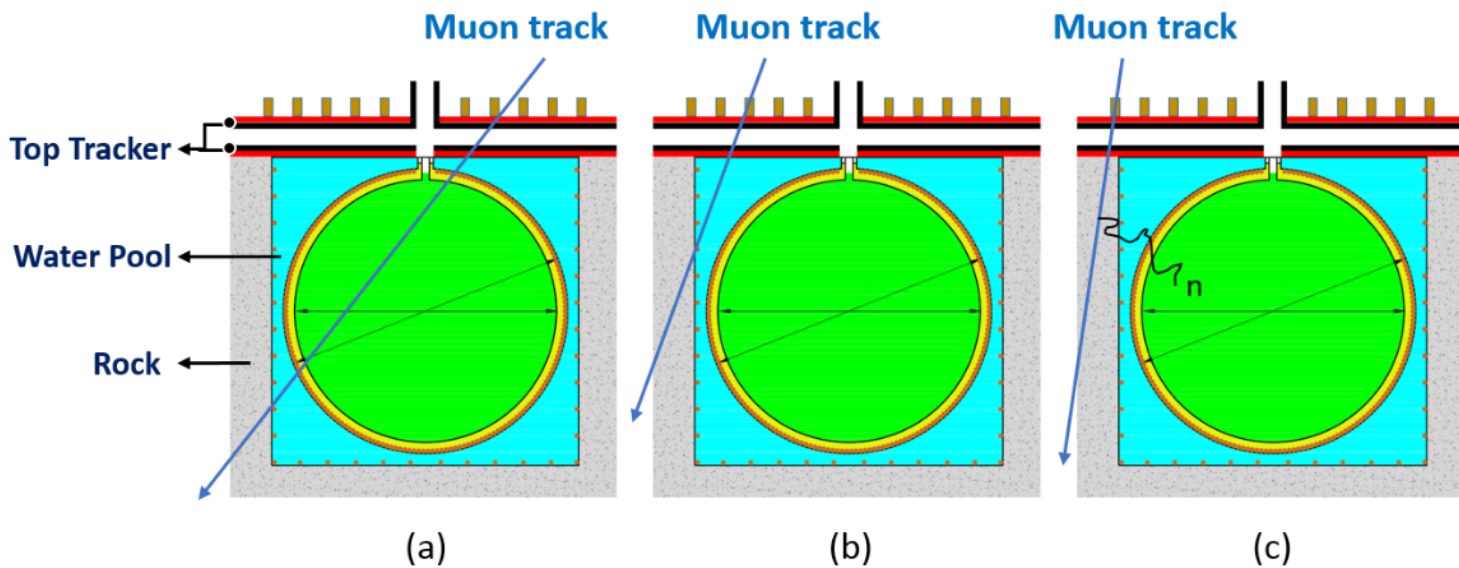


FIGURE 2.3: Different configurations for muon induced background. Taken from [4].

A TT module is made up of 64 strips of scintillator, with Wave Length Shifting (WLS) fibers at both ends connected to two 8×8 -channel photo-detectors housed in end-caps. Two perpendicular planes, each consisting of 4 TT modules, are combined to create a tracker wall that provides 2D track information, as shown in Figure 2.4a. The 8 TT modules are assembled to form a TT wall covering a surface area of $6.7 \text{ m} \times 6.7 \text{ m}$, and these walls are arranged in a 3×7 configuration to form a single layer of the TT. The TT consists of three layers and is installed above the WC pool.

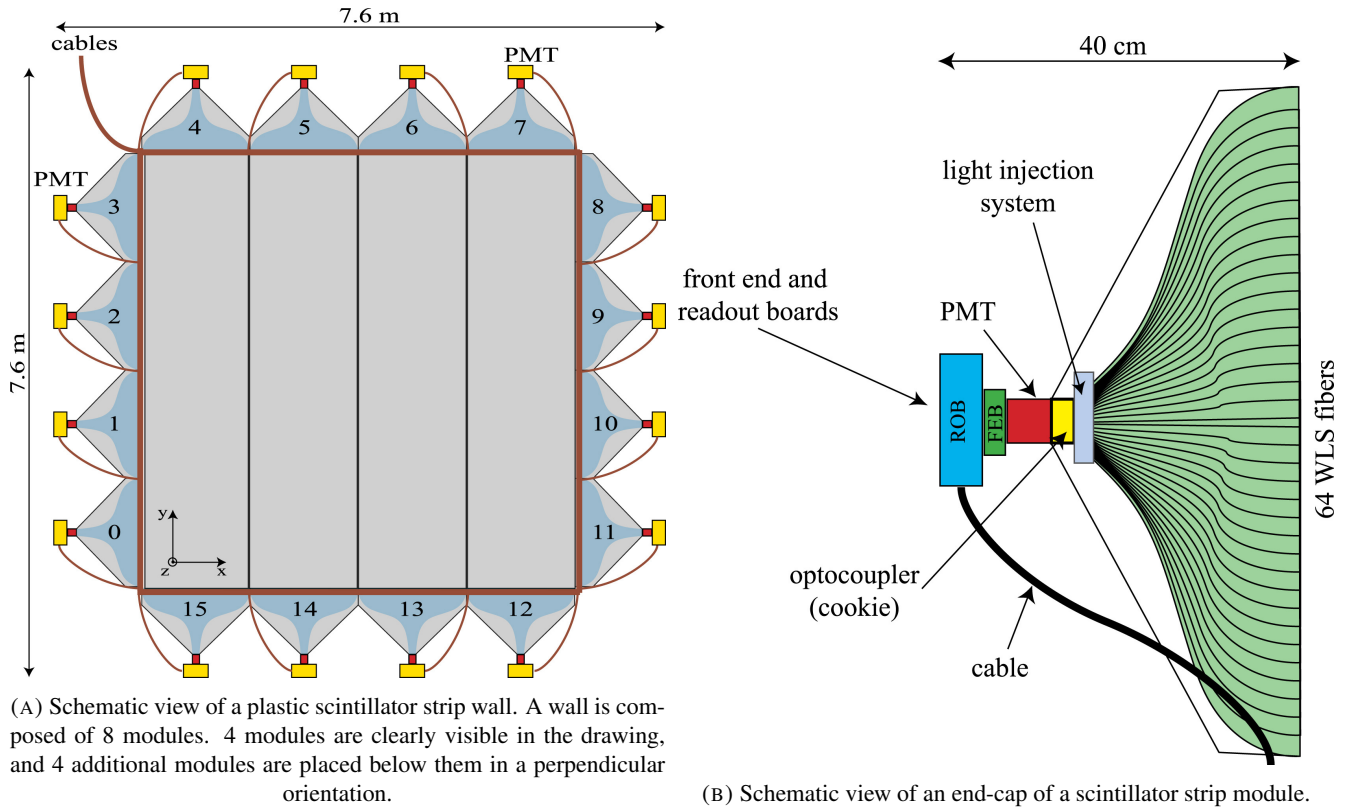


FIGURE 2.4: Top Tracker wall (on the left) and its readout system (on the right). Taken from [65].

To maximize the muon track reconstruction performance, the TT original electronics used for the Opera experiment have been modified, as a higher background induced by rock radioactivity is expected for JUNO. The PMT collects light coming from the optical fiber, and the dedicated electronics perform the signal processing. These electronics include a front-end board (FEB) and a readout board (ROB) installed in the end-cap, in yellow in Figure 2.4b. 16 end-caps are installed for on TT wall edges and are connected to a concentrator board. The concentrator board's role is to emit a first level trigger for muon events by performing $x - y$ coincidences in the same TT wall. The Concentrator Boards communicate with a Global Trigger Board, providing a three-layer TT trigger to the JUNO data acquisition system. The trigger rate of the TT after the Global Trigger Board is expected to be around 2 kHz, but it will be pushed down to a few Hz by an offline muon track reconstruction. Due to budget constraints, the TT does not cover the entire surface of the WC pool. A schematic view of the JUNO TT installed in the JUNO experiment hall is shown in Figure 2.5.

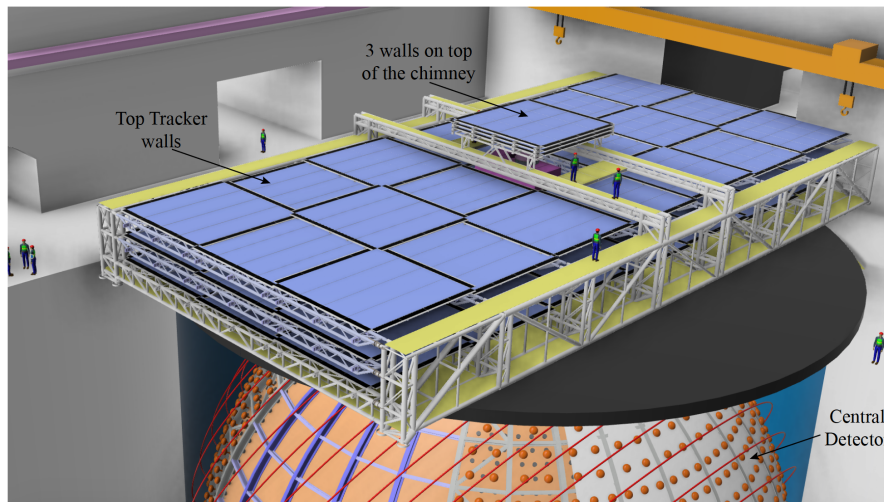


FIGURE 2.5: Schematic view of the Top Tracker on top of the Central Detector. Taken from [65].

2.2 Liquid scintillator

The **Linear AlkylBenzene (LAB)**-based LS is extensively used in different neutrino experiments, such as Borexino [44], Daya Bay [38], RENO [39], SNO+ [43] and, in the case that interests us, JUNO. The energy response of LS detectors is non-linear, partly due to the energy-quenching effect. The light output of LS is related to the energy deposit density $\frac{dE}{dr}$ per path length for a particle traversing the LS. An empirical model proposed by Birks [66] and generalized by Chou [67] is commonly used to describe this process:

$$\frac{dL}{dr} = S \frac{dE}{dr} \frac{1}{1 + k_B \frac{dE}{dr} + k_C \left(\frac{dE}{dr} \right)^2} \quad (2.1)$$

where L is the scintillation yield density, r is the path length, S is the absolute scintillation factor, $\frac{dE}{dr}$ is the energy deposit density, k_B is Birks' constant, and k_C is the second-order parameter. Both k_B and k_C depend on the LS material and the type of scattered particles (protons or electrons). From the previous equation, we can see that the light output is a non-linear phenomenon. As previously mentioned, the detector energy resolution is key for the JUNO physics goals, and thus, the energy non-linearity of JUNO needs to be precisely determined [68].

JUNO's liquid scintillator is an optimized mixture of three organic compounds. The solvent is **LAB** [69]. An additive of 2.5 g/L of 2,5-diphenyloxazole (PPO) serves as the primary fluor. Additionally, 1,4-bis(2-methyl styryl)benzene (bis-MSB) is included as a wavelength shifter at a concentration of 3 mg/L. A sketch of the energy transport in the liquid scintillator mixture is shown in Figure 2.6. This mixture has the required optical properties, such as light yield and transparency [69]. The energy transport process in the JUNO liquid scintillator involves several steps. LAB is excited through ionization and transfers this energy non-radiatively to PPO. The PPO then de-excites by emitting photons at 390 nm, which are absorbed by bis-MSB. Finally, the bis-MSB re-emits these photons at around 430 nm, leading to better transparency in the mixture and higher efficiency in the PMTs.

The JUNO liquid scintillator purification system is designed to enhance the optical and radio-purity properties of the scintillator mixture. The process, presented in Figure 2.7, begins with an alumina column purification. The alumina column aims to improve the transparency of **LAB** and to remove impurities. Following this, the distillation system is used to remove ^{238}U , ^{232}Th , and ^{40}K . The distillation is performed through partial vacuum

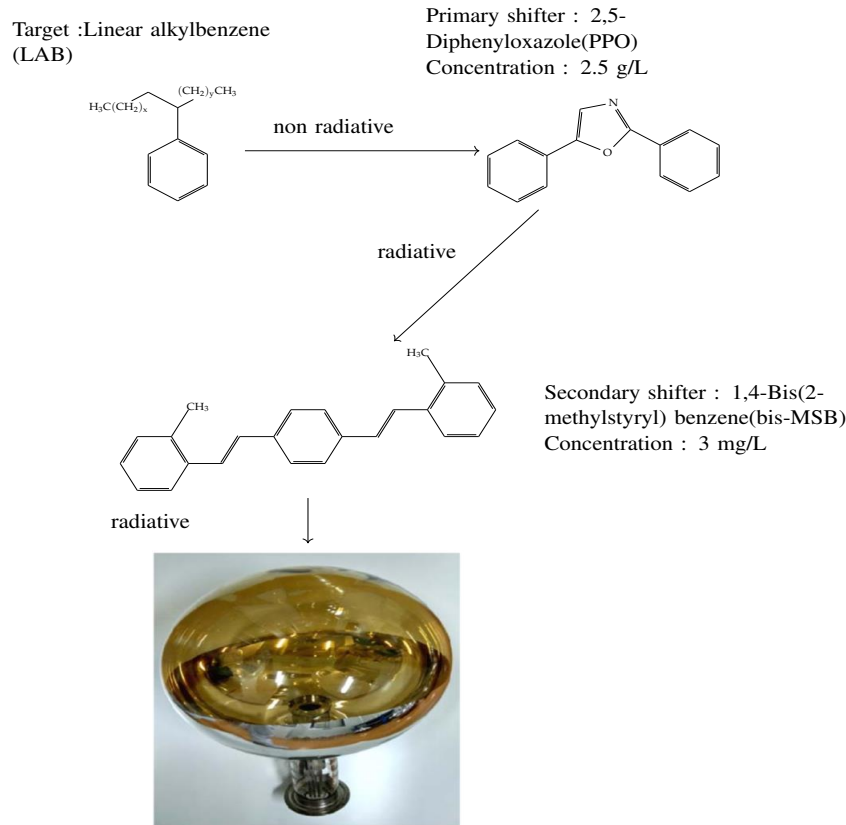


FIGURE 2.6: Principle of light transport and capture in the liquid scintillator used by JUNO.

distillation at 5 mbar, a technique validated by the Daya Bay pilot plant [70]. The next step involves the mixing system, where 2.5 g/L of PPO and 3 mg/L of bis-MSB are dissolved into the LAB to generate a master solution called LS. This process is carried out above ground, with PPO and bis-MSB being purified using an acid/water washing method. Then, the LS is sent underground.

When the LS arrives underground, it passes through the online purification system. Online purification is composed of two systems: water extraction and stripping columns. The water extraction system is employed to reduce the uranium and thorium concentration from the LS by fully mixing the LS with ultra-pure water using a turbine stirring. This step ensures that the concentrations of ^{238}U and ^{232}Th do not exceed 10^{-15} g/g required for neutrino mass ordering and 10^{-17} g/g required for solar neutrino measurements. The stripping column in a partial vacuum at 250 mbar is used to remove radioactive gases and gaseous impurities to purify the LS further. The first LS produced and tested shows a 95% purification efficiency for radon [70].

Following the purification process, the LS is sent to the OSIRIS detector for a final quality check [71]. The OSIRIS is a standalone detector that monitors the radiopurity of the LS while the JUNO CD is filled. Its primary purpose is to ensure ^{238}U and ^{232}Th concentrations in the LS meet requirements by detecting fast coincidence decays of ^{214}Bi - ^{214}Po and ^{212}Bi - ^{212}Po .

The OSIRIS detector features a 3-meter-wide cylindrical acrylic vessel inside a water-filled steel tank for radiation shielding. Located in a bypass of the main LS line, it samples approximately one-sixth of the processed LS. During the JUNO detector's LS filling, new LS is continuously added to the top of the OSIRIS vessel while monitored LS is drained from the bottom. Once the LS purity is validated, the Filling, Overflow, and Circulation (FOC) system fills the CD, replacing water in the acrylic vessel with LS.

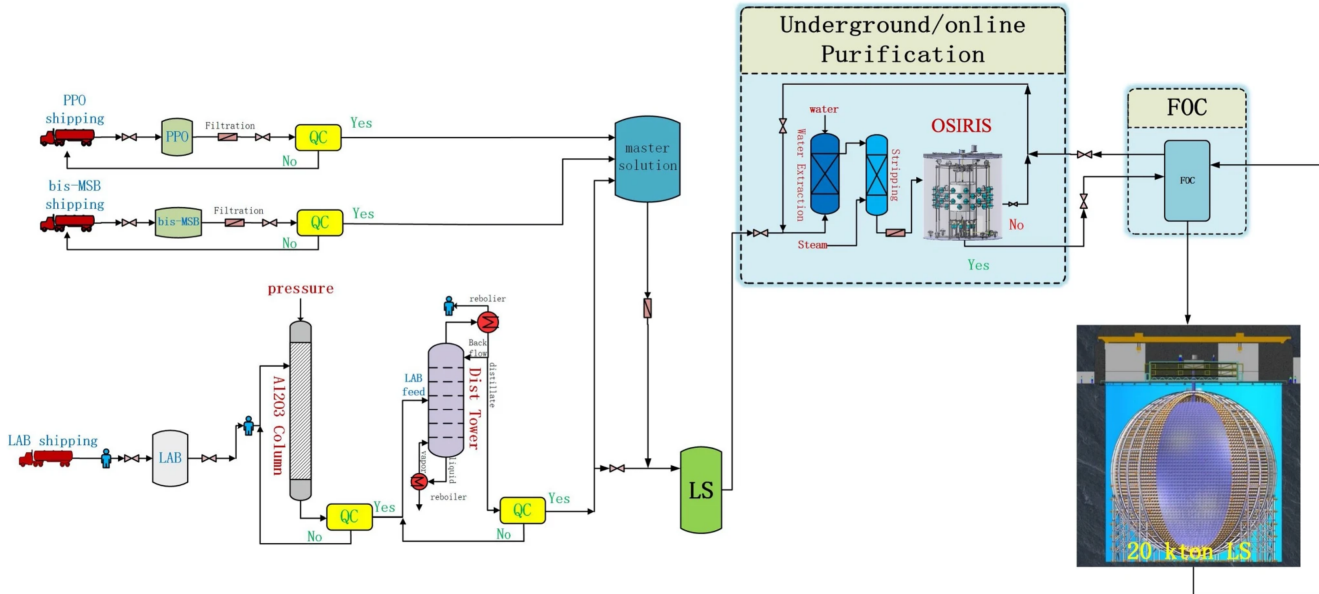


FIGURE 2.7: The JUNO scintillator system features four purification stages: Al_2O_3 column, distillation, water extraction, and steam stripping, along with storage and mixing tanks. OSIRIS is positioned as the final stage in the filling line to ensure the radiopurity of the product. After this, the liquid scintillator is transferred to the JUNO filling system (FOC). Taken from=[71].

2.3 PMTs

JUNO uses PMTs to collect the light emitted by the LS. An example of PMT is shown in Figure 2.8. We can describe a PMT as a vacuum tube consisting of an input window, a photocathode, focusing electrodes, an electron multiplier, and an anode sealed usually into an evacuated glass tube [72]. Two different electron multiplier technologies are used in JUNO. The electron multiplier technology shown in Figure 2.8 is called dynode. The dynode is an electrode where the film of material is deposited. This film is specifically studied for its secondary electron emission capabilities. The process of generating an electric signal from the incoming light follows the following steps in the case of dynode PMTs:

- Light passes through the input glass window and excites the electrons in the photocathode so that **photoelectron (p.e.)** are emitted into the vacuum
- These **p.e.** are accelerated by the electric field and focused by the focusing electrode, then directed onto the first dynode, where they are multiplied through secondary electron emission
- The secondary electron emission is repeated at each dynode in the electron multiplier
- A cluster of secondary electrons emitted from the last dynode are finally multiplied and extracted from the anode

The other electron multiplier technology used in JUNO is called **Micro Channel Plate (MCP)**. The MCP is composed of a two-dimensional array of parallel glass capillaries (channels), forming a thin disk. Each channel has an internal diameter ranging from 6 to 25 μm , with the inner walls treated to provide the appropriate electrical resistance and secondary emission properties. Each channel acts as an independent electron multiplier [72, 73]. MCPs are quite different in structure and operation from conventional discrete dynodes. This technology gives the following advantages: 1) compact and lightweight, 2) fast time response, 3) two-dimensional detection with high spatial resolution, 4) stable operation even in high magnetic fields, 5) Low power consumption.

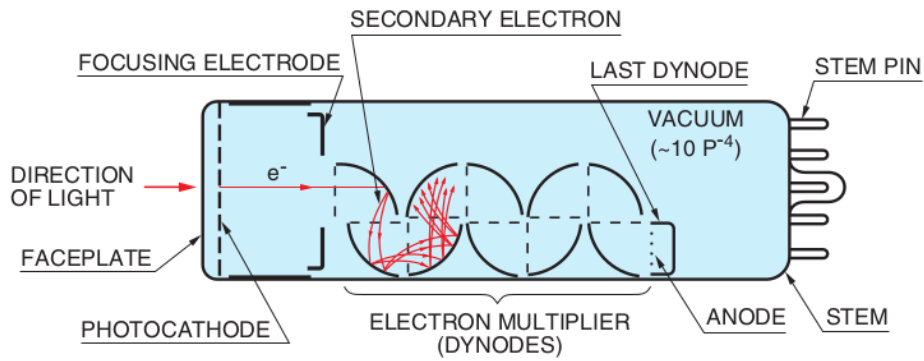


FIGURE 2.8: Example dynode PMT (i.e. Model THBV4_0201EA from Hamamatsu). Taken from [72].

To obtain sufficient gain, the MCP PMTs use two MCP. Figure 2.9 shows the structure and the gain mechanism of the MCP PMTs used in JUNO. The processes of the gain mechanism for this technology are as follows: the p.e. emitted from the photocathode enter the channels of the first MCP. The electrodes generate the voltage difference needed to accelerate the p.e. inside the micro-channel. As the tube is inclined, the p.e. bounce on the inner wall, where they are multiplied by means of secondary emission. This process is repeated along the second plate. Finally, a large number of electrons are collected by the anode generating the output signal.

JUNO experiment uses three different PMTs: 20-inch MCP-PMT from North Night Vision Technology Co. (NNVT), 20-inch dynode PMT from Hamamatsu Photonics K. K. (HPK), and 3-inch dynode PMT from HZC (Hainan Zhanchuang Photonics Technology). The technical drawings are presented in Figure 2.10.

Dual calorimetry The dual calorimetry in JUNO is developed to achieve high precision in neutrino energy measurements. The JUNO CD employs two independent readout systems: the LPMT system and the system SPMT. The LPMT system uses charge measurement performed through the reconstruction of PMT waveforms. On the other side, the SPMT system works in photoelectron counting mode to offer a robust and independent method for the energy deposit measurement.

To achieve a 3% energy resolution at 1 MeV and control the energy systematic uncertainties to the sub-percent level, we need to understand detector energy resolution behavior. This can be studied by collecting the deposited energy by identical events in the LS performed in two independent manners. This is precisely what dual calorimetry does. Let us study the energy resolution formula:

$$\frac{\sigma_E}{E} = \sqrt{\frac{\sigma_{\text{stochastic}}^2}{E} + \sigma_{\text{non-stochastic}}^2(E)} \quad (2.2)$$

In this formula:

- $\frac{\sigma_E}{E}$ represents the relative energy resolution
- $\sigma_{\text{stochastic}}$ denotes the stochastic term, which is inversely proportional to the square root of the energy, reflecting the statistical nature of the light collection process
- $\sigma_{\text{non-stochastic}}(E)$ is the non-stochastic term, which includes systematic uncertainties such as calibration errors, non-linearities, and non-uniformities at the level of the LS and the electronic system

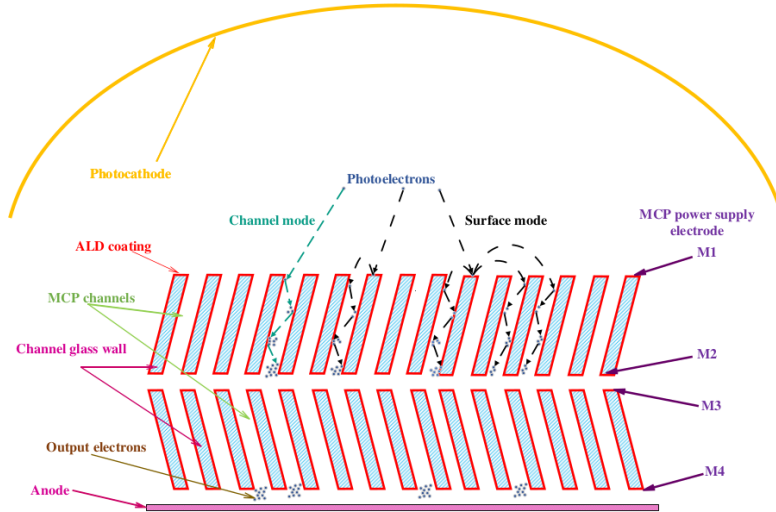


FIGURE 2.9: MCP-PMT structure: M1 and M3 are the input electrodes of MCPs, M2, and M4 are the output electrodes, and the four electrodes provide the potential differences during operation. The photoelectrons directly enter the channels (channel mode) or hit M1 to produce secondary electrons that enter the channels later (surface mode). After entering the MCP channel, the electron collides with the channel wall many times and is amplified in a series of such multiplications. Taken from [74].

The stochastic term drives the design requirements for high-light production and collection. JUNO achieves this by using a liquid scintillator with a high light yield (around 10^4 photons per MeV) and high transparency. Assuming that the number of p.e. per MeV follows a Poisson distribution, we can express the stochastic term as follows:

$$\sigma_{stochastic} = \sqrt{N_{pe}} \rightarrow \frac{\sigma_{stochastic}}{E} = \frac{\sqrt{N_{pe}}}{N_{pe}} = \frac{1}{\sqrt{N_{pe}}}$$

Assuming the non-stochastic term is 1% for the LPMT system, to achieve a 3% energy resolution, the light yield needed is over 1400 p.e. per MeV [75]. This requirement necessitates a liquid scintillator with a high light yield (around 10^4 photons per MeV), high transparency, and approximately 75.2% photocathode coverage for LPMTs [76, 77]. With this high light yield, meticulous calibration is needed to manage non-linearities, non-uniformities, and stability over time. 1% of non-stochastic terms is also a significant challenge as the current best value for non-stochastic terms is around 2% for other reactor neutrino experiments [78, 79, 80]. By comparing the correlated and the uncorrelated responses of LPMT and SPMT systems, the dual calorimetry method allows systematic errors to be corrected.

2.3.1 Small PMT system

The SPMTs system is designed to use 25,600 3-inch PMTs and to increase the photo-coverage of the CD by 3%. The structure of the SPMT is shown on the left of Figure 2.10. The SPMT readout system is introduced as an auxiliary readout system for JUNO, providing an independent energy estimator.

Readout electronics 128 SPMTs are connected to one [UnderWater Box \(UWB\)](#). Each SPMT UWB contains the following boards [63]:

- Two **High Voltage Splitter (HVS)** boards serve for 128 SPMTs, each board holding 8 HV units. The different HV units are grouped by two; for each pair, one unit powers 16 SPMTs, and the other serves as a backup.
- One front-end board, also called **ASIC Battery Card (ABC)** board, consisting of two key elements: the **Charge And Time Integrated Read Out Chip (CATIROC)** chips and the **Field-Programmable Gate Array (FPGA)**. Each CATIROC [81] provides an adjustable threshold common for 16 channels. It can perform the charge and time measurement channel by channel. The FPGA is responsible for the data capture, processing, and packaging. The FPGA can receive the sampled data with charge and time information from the CATIROC, forming the charge data stream. It can also register the signal passing the threshold (like a discriminator) directly and digitally, forming a digital **p.e.** counting output, i.e., the discriminator data stream. Moreover, the FPGA can perform the time measurement with high precision (1 ns), thus being able to record the time over threshold information of the signal pulse. The two data streams provide an almost **deadtime-less** readout.
- One global control unit responsible for powering and controlling the boards, transferring the data to the DAQ via Ethernet cables.

In total, 200 UWB, 400 splitter boards, 200 ABCs, and 200 GCUs will be produced for the SPMT system.

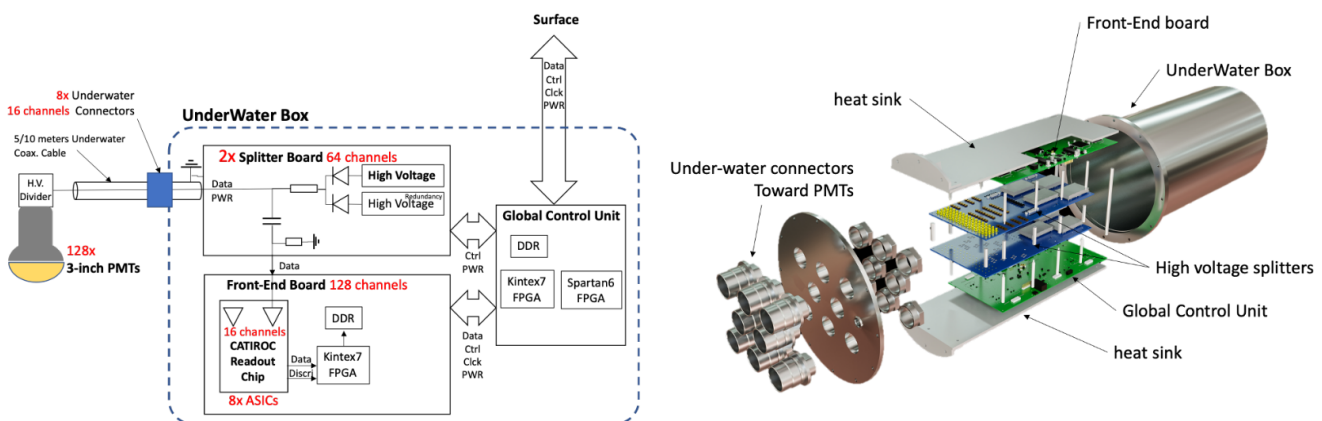


FIGURE 2.11: Schematic Overview of the JUNO SPMT system (left), and exploded view of the main components of the UWB (right). 128 3-inch PMTs are connected to a single UWB through eight 16-channel waterproof connectors. Each UWB contains two high-voltage splitter boards, one readout front-end board, and one control board (GCU). The latter two, which are shown in green, are thermally coupled to heat sinks that dissipate the heat through the lid of the UWB. The cables that connect the multi-channel receptacles to the splitter boards are not shown. Taken from [63].

2.3.2 Large PMT system

JUNO employs two types of 20-inch PMTs: approximately 5,000 dynode-PMTs from Hamamatsu Photonics K.K. (HPK) and around 15,000 MCP-PMTs from North Night Vision Technology (NNVT). An extensive R&D was conducted with NNVT to produce a new PMT design using the MCP technology [82, 83, 84, 85], maximizing the **Photo-Detection Efficiency (PDE)** and the energy resolution while having lower internal radioactivity. On the other side, HPK PMTs have good reliability and excellent **Transmit Time Spread (TTS)** compared to NNVT PMTs.

The performance of these PMTs significantly influences the overall energy resolution of the detector, mainly through parameters like the PDE³ and **Dark Count Rate (DCR)**. Additional factors, such as the timing and pulse shape parameters, are vital for event reconstruction and background reduction. As such, specific performance requirements for the 20-inch PMTs were established, listed in Table 2.1.

Parameter	HPK R12860-50 Average (limit)	NNVT GDB-6201 Average (limit)
Quantum efficiency	30.3% ($\geq 27\%$)	28.5% ($\geq 26.5\%$)
Collection efficiency	95.6%	98% ($\geq 96\%$)
Effective area ratio	96% (93%)	97% ($\geq 96\%$)
Gain	10^7	10^7
HV (for a 10^7 gain)	2000 V (≤ 2500 V)	2500 V (≤ 2800 V)
QE uniformity	5% ($\leq 15\%$ inside 70°) 20% ($\leq 30\%$ inside 80°)	8% ($\leq 10\%$)
TTS (FWHM)	2.7 ns (≤ 3.5 ns)	12 ns (≤ 15 ns)
P/V ratio	3 (≥ 2.5)	3.5
Pre-pulse ratio (80 ns window, main pulse ~ 160 p.e.)	0.8% ($\leq 1\%$)	0.5% ($\leq 1\%$)
After-pulse ratio (0.5 ~ 20 μ s window, main pulse ~ 160 p.e.)	10% ($\leq 15\%$)	10% ($\leq 15\%$)
Dark count rate (0.25 p.e., 22 $^\circ$ C)	10 kHz (≤ 50 kHz)	≤ 50 kHz (if $24\% \leq \text{PDE} \leq 27\%$) ≤ 60 kHz (if $27\% \leq \text{PDE} \leq 28\%$) ≤ 80 kHz (if $28\% \leq \text{PDE} \leq 29\%$) ≤ 100 kHz (if $29\% \leq \text{PDE}$)
Glass radioactivity		
²³⁸ U	< 400 ppb	< 75 ppb
²³² Th	< 400 ppb	< 75 ppb
⁴⁰ K	< 40 ppb	< 30 ppb

TABLE 2.1: Main acceptance criteria for JUNO 20-inch PMTs. Taken from [86].

A total of 22414 20-inch PMTs have been produced for the JUNO experiment. Based on the criteria of the selected 20-inch PMTs, presented in Table 2.1, a set of acceptance testing facilities was developed to realize semi-automatic PMT testing. A mass test program began in 2017 and finished in 2021 to assess the good quality of all accepted PMTs [86]. This system includes containers with shelf structures housing 36 drawer boxes, each serving as an individual measurement station. A scanning station system was designed and built aiming to use a reduced PMT sample (about 5% of all the PMTs) to perform photocathode uniformity tests.

To fully characterize the PMTs, the container stations test the following parameters: PDE, TTS, DCR, gain, Peak-to-Valley (P/V) ratio, fall time, rise time, and pre-pulse and after-pulse ratios. Figure 2.12 shows the results of the PDE obtained during the PMT tests. Figure 2.12a shows the distributions of the PDE of all the PMTs, and Figure 2.12b only for the MCP-PMTs. We can see from the test results that the MCP-PMTs from NNVT have a slightly better PDE on average than the HPK PMTs. We can also see in Figure 2.12b that, thanks to the R&D, the PDE of the NNVT PMTs increased during the production thanks to the improvement of both the **Quantum Efficiency (QE)** and **Collection Efficiency (CE)**. The NNVT PMTs are separated into two sets: High QE and Low QE PMTs. The mean value for Low QE PMTs is 26.8%, and 29.9% for High QE.

³The PDE is given by the formula: $PDE(\lambda) = QE(\lambda) \times CE \times E_{AR}$ where QE is the quantum efficiency, CE is the collection efficiency and E_{AR} is the effective area ration.

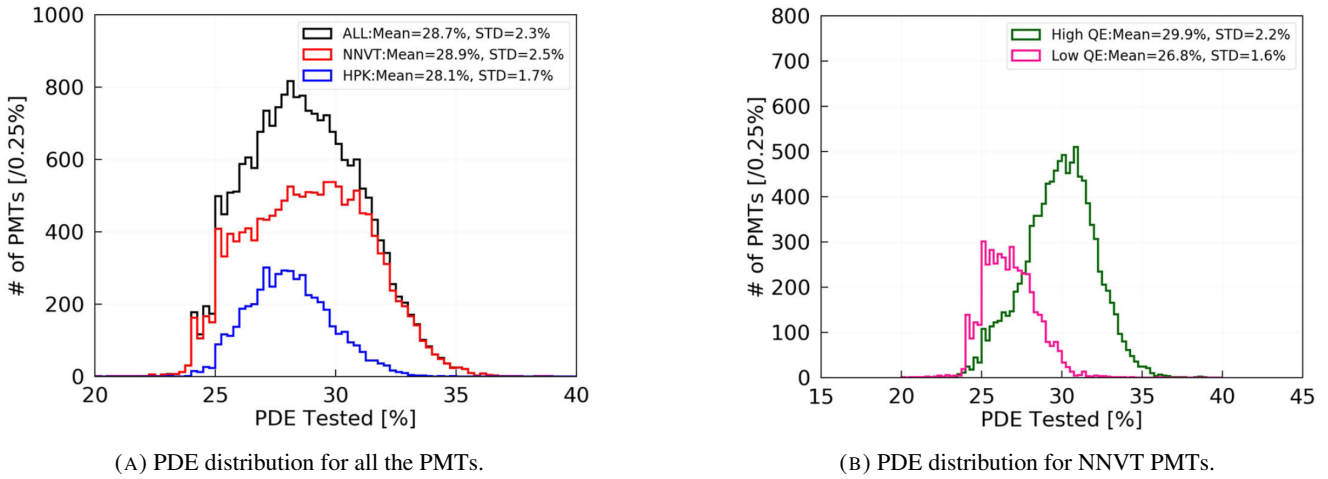


FIGURE 2.12: PDE distribution, taken from [86].

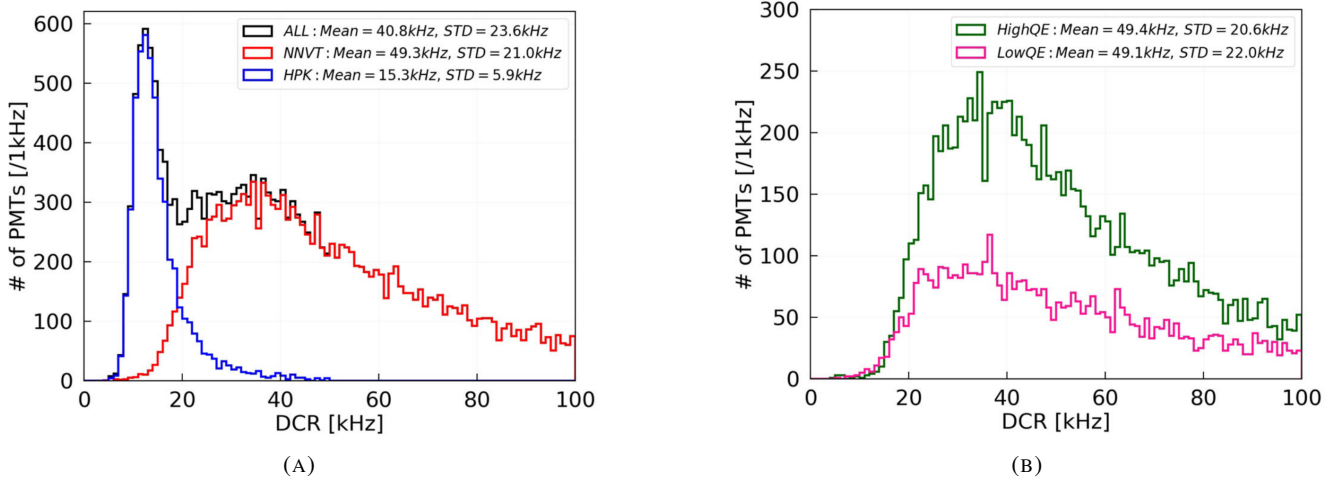


FIGURE 2.13: DCR distribution, taken from [86].

Another crucial key parameter is the DCR, as it directly impacts the electronics requirements. Figure 2.13a shows the DCR distributions for the two different types of PMTs. The distributions highlight a higher DCR for NNVT MCP-PMTs than for Hamamatsu PMTs. The average DCR for NNVT PMTs is 49 kHz, while for Hamamatsu PMTs, it is 15.3 kHz. The total mean value for all the PMTs is 40.5 kHz. Figure 2.13b shows that the DCR of High QE NNVT PMTs is not higher than the one for Low QE NNVT.

2.4 Calibration

To determine the neutrino mass ordering, the JUNO central detector must achieve a better than 1% energy linearity and a 3% effective energy resolution. To address the energy non-linearity and the spatial non-uniformity in detector response, multiple calibration sources and multi-dimensional scan systems have been developed. These tools allow precise correction and calibration, ensuring the detector meets the stringent requirements necessary to perform such accurate measurement.

2.4.1 Energy scale calibration

The calibration of the energy scale in the JUNO experiment addresses both physics and instrumental non-linearity. Physics non-linearity arises due to the quenching effect of the scintillator (see Birk's law in section 2.2) and the non-linearity of the Cherenkov light energy deposition. To calibrate this, a combination of radioactive sources (e.g., gamma and neutron sources) and a natural radioactivity background is used. The instrumental non-linearity originate from response variations in the PMTs and electronics. Instrumental non-linearity is addressed using dual calorimetry (see section 2.3).

A variety of radioactive sources are also employed in the calibration process to cover a broad range of energies and interactions. These sources provide a comprehensive energy range for calibration, covering both low and high-energy gammas, as well as neutrons that produce capture gammas [75].

Source	Type	Radiation
^{137}Cs	Gamma Source	0.662 MeV gamma
^{54}Mn	Gamma Source	0.835 MeV gamma
^{60}Co	Gamma Source	1.173 + 1.333 MeV gamma
^{40}K	Gamma Source	1.461 MeV gamma
^{68}Ge	Positron Source	0.511 + 0.511 MeV gamma
$^{241}\text{Am-Be}$	Neutron Source	Neutron + 4.43 MeV gamma
$^{241}\text{Am-}^{13}\text{C}$	Neutron Source	Neutron + 6.13 MeV gamma
(n, γ)p	Neutron Capture	2.22 MeV gamma
(n, γ) ^{12}C	Neutron Capture	4.94 MeV or 3.68 + 1.26 MeV gamma

TABLE 2.2: Radioactive sources used in JUNO calibration. Taken from [75].

2.4.2 Conceptual design of the calibration system

The calibration system is designed to ensure precise energy scale and resolution calibration. It includes several subsystems [75], shown in Figure 2.14:

Automatic Calibration Unit (ACU): the ACU deploys sources along the central vertical axis of the central detector (CD). It features multiple spools capable of unwinding and delivering sources with high positional accuracy. Regularly deployed sources include neutron sources, gamma sources, and pulsed UV lasers.

Guide Tube System (GT): the GT system loops around the acrylic sphere, deploying sources along a longitudinal circle. This system allows calibration at the detector boundary, where full absorption peaks are mixed with leakage tails.

Cable Loop System (CLS): the CLS deploys sources to off-axis positions within the detector. By adjusting cable lengths, sources can be positioned precisely to cover a significant fraction of the detector volume. An ultrasonic system ensures accurate positioning.

Remotely Operated Vehicle (ROV): The ROV can navigate almost the entire LS volume, providing flexibility for source deployment in regions not covered by other systems. It also utilizes ultrasonic positioning for precise calibration.

The calibration tasks are structured into comprehensive and periodic calibrations. The Comprehensive Calibration calibrations are performed at the start and a few times during the experiment's live time. They involve deploying the different radioactive sources, listed in Table 2.2, to a wide range of positions. Comprehensive calibration provides an extensive understanding of the detector's performance. In addition, periodic calibrations will be performed: weekly and monthly calibrations. The weekly calibrations monitor significant changes in detector

properties. Am-C (neutron source) sources and lasers are deployed along the axial axis, ensuring the energy scale remains stable and detecting any significant variations promptly. Monthly calibrations use the same Am-C sources and laser as weekly calibrations. The difference between the monthly and weekly calibration procedures is that during the first, the Am-C source moves in position outside the central axis thanks to the Cable Loop System and Guide Tube System. The monthly calibration focuses on maintaining the non-uniformity corrections.

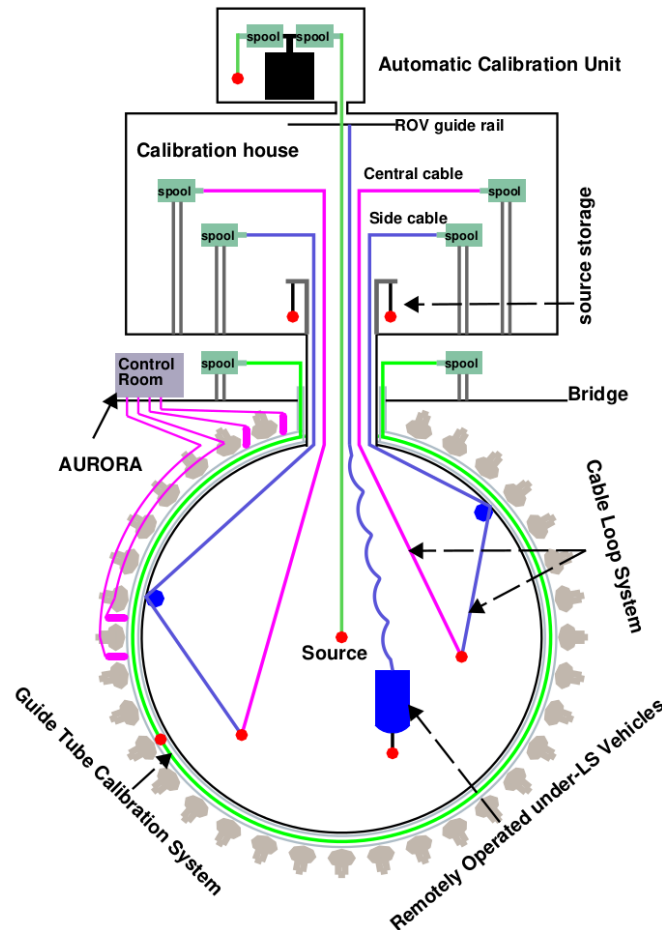


FIGURE 2.14: Overview of the calibration system. Taken from [75].

2.5 Summary

The JUNO experiment is a neutrino detector designed to precisely measure neutrino properties, focusing on NMO. Located in Jiangmen, South of China, JUNO is located a distance of 52.5 km of two NPPs to optimize reactor anti-neutrino detection. The central detector contains a 20-kiloton liquid scintillator within a 35.4-meter acrylic vessel, surrounded by a water pool and a top tracker situated above the central detector. The water Cherenkov detector and the top tracker serve as veto systems.

The liquid scintillator is a mixture of LAB, PPO, and bis-MSB, optimized for transparency and light yield. The liquid scintillator undergoes purification to minimize radioactive contamination, essential for reducing background noise and ensuring accurate measurements.

JUNO uses dual calorimetry with two PMT systems—20-inch LPMTs and 3-inch SPMTs—to achieve a 3% energy resolution at 1 MeV. The light emitted in the central detector is captured by 17,612 LPMTs and 25,600 SPMTs. The LPMTs use both dynode and MCP technology, they provide good time resolution and high photon detection efficiency required for the precise measurement of the incident neutrinos.

JUNO calibration system corrects the detector non-linear response and spatial non-uniformities using different radioactive sources and UV lasers. The hardware design of the calibration system includes the Automatic Calibration Unit, the Guide Tube System, the Cable Loop System, and the Remotely Operated Vehicle. Regular calibrations maintain energy scale stability and correct systematic uncertainties.

Chapter 3

Neutrino physics with JUNO

In this chapter, we will describe the different sources of neutrinos and the various backgrounds measured in JUNO. The different physics potentials across the different neutrino sources are then given. The results and Figures in this chapter are the ones officially communicated by the JUNO collaboration and were presented in the different collaboration papers.

Contents

3.1	Various sources of neutrinos	43
3.2	Various background sources	44
3.3	Reactor neutrinos	45
3.3.1	Neutrino mass ordering	46
3.3.2	Precision measurement of neutrino oscillation parameters	48
3.4	Supernova neutrinos and trigger strategy	49
3.5	Diffuse supernova neutrino background	51
3.6	Solar neutrinos with JUNO	52
3.7	Atmospheric neutrinos	53
3.8	Geo-neutrinos	54
3.9	Summary	55

3.1 Various sources of neutrinos

Across nature, many different phenomena produce neutrinos, and JUNO aims to measure some of them. The neutrino fluxes of the different sources are summarized in Figure 3.1. The x-axis represents the neutrino energy, ranging from μeV to EeV , and the y-axis represents the flux.

The curve for cosmological neutrinos (ν) is on the far left, showing a peak in flux at very low energies. A yellow curve represents solar neutrinos, giving events in the range of eV to MeV energies. The supernova 1987A burst spectrum is depicted by a red curve covering the 100 keV to 100 MeV range [87]. Reactor anti-neutrinos energy is situated in the 1.8 to 12 MeV interval. The background from old supernovae, also called **Diffuse Supernova Neutrino Background (DSNB)**, is shown as a magenta curve starting in the keV range and extending into the MeV range. Atmospheric neutrinos are represented by a green curve showing a broad peak at tens of MeV and a long tail towards TeV scale. Neutrinos from active galactic nuclei (AGN) are depicted by a pink curve peaking at very high energies. Finally, cosmogenic (GZK) neutrinos are shown as a brown curve extending from PeV to EeV energies.

JUNO is sensitive to neutrino events in the energy interval 100 keV-100 GeV, covering a large variety of neutrino sources. Table 3.1 provides a summary of the neutrino signals to which JUNO is sensitive, including the

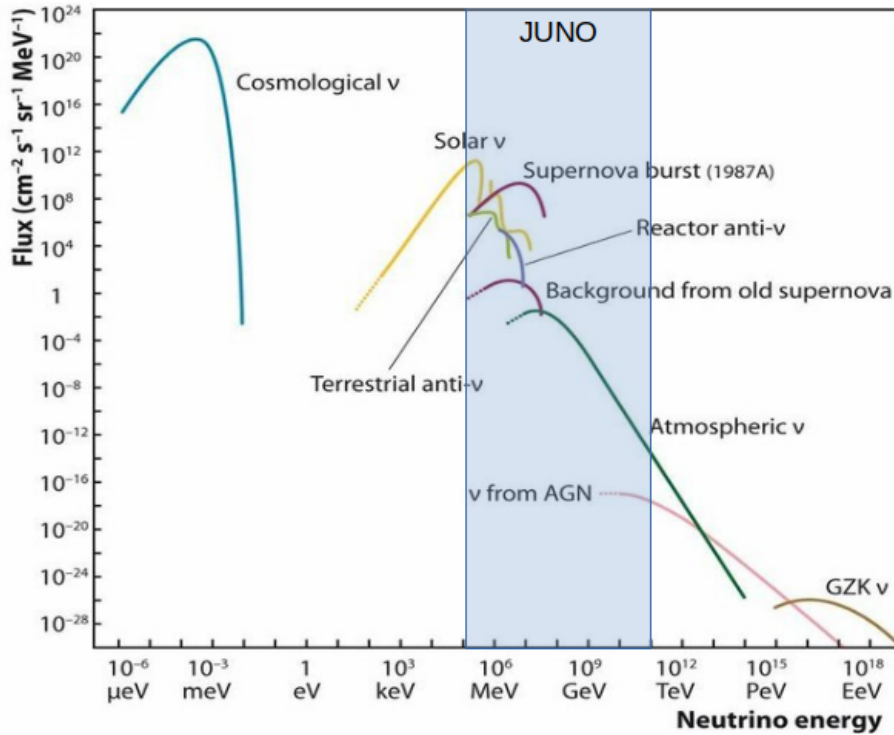


FIGURE 3.1: Neutrino flux as a function of their energy for different sources. Taken from [88].

expected signal rates and primary background sources corresponding to those signals. In the following section, we will describe the different physics achievable for those other sources and detail their different backgrounds.

Research	Expected signal	Energy region	Major backgrounds
Reactor antineutrino	60 IBDs/day	1.8–12 MeV	Radioactivity, cosmic muon
Supernova burst	5000 IBDs at 10 kpc 2300 elastic scattering	0.2–80 MeV	Negligible
DSNB (w/o PSD)	2–4 IBDs/year	10–40 MeV	Atmospheric ν
Solar neutrino	hundreds per year for ^8B	0.2–16 MeV	Radioactivity
Atmospheric neutrino	hundreds per year	0.2–100 GeV	Negligible
geo-neutrino	~ 400 per year	1.8–3.4 MeV	Reactor ν

TABLE 3.1: Summary of detectable neutrino signals in the JUNO experiment and the expected signal rates and major background sources.

3.2 Various background sources

In the relevant energy range for the JUNO experiment, the majority of backgrounds are either natural radioactive decay in the detector materials or so-called cosmogenics caused by atmospheric muons passing through the detector [5, 89]. During the passing atmospheric muon, the detector will be flooded with scintillation light due to the energy deposited by the muon. Hence, the detector will be vetoed during that time. Simulations considering the surrounding mountain profile are used to estimate muon rate and average energy [5, 89]. The expected muon flux is 0.004 Hz m^{-2} at an average energy of 207 GeV, leading to the CD to a rate of 4 Hz.

Muon induced background The cosmic muons and their shower particles generate photons by Bremsstrahlung (electromagnetic radiation due to the deceleration of those particles). The gammas produced in the rock can propagate to the LS, where they can interact, for example, with the Carbon nucleus. This interaction leads to an excited nucleus or generates a spallation neutron [90].

The spallation neutron production depends on the incident muon characteristics at the JUNO detector. Geant4 simulation was used to simulate the amount of neutrons generated by the muons and give $\approx 1.8\text{Hz}$ spallation neutrons in JUNO CD. Neutrons generated by muons passing through the JUNO LS will be tagged with almost 100% efficiency. Neutrons produced in water buffers can be tagged with an efficiency of 99.8% since their parent muons pass through the muon systems. Time veto after the tagged muons can reject tagged neutrons and suppress the possible correlated background [5].

In the LS, the ^{12}C nucleus can be excited due to the capture of Bremsstrahlung photon. When they decay, they can produce radioactive isotopes with atomic numbers $Z \leq 6$. Among these, ^9Li and ^8He are of particular concern due to their relatively long half-life time of 0.178 seconds and 0.119 seconds, respectively. These isotopes cause a significant background challenge in reactor analysis, as their decays can closely mimic the IBD signal [5] as they both emit a beta particle and a neutron in a manner similar to the IBD signal from reactor antineutrinos. Additionally, they are difficult to veto due to their long half-life time.

Natural radioactivity Natural radioactivity exists in the material of JUNO detector components and its surroundings. Particular care needs to be taken to select low radioactivity materials and design the passive shielding to control the radioactivity background. For the JUNO experiment, the radioactivity comes from various sources [5, 91]:

- $^{238}\text{U}/^{232}\text{Th}/^{40}\text{K}$ in the rocks around the detector hall
- $^{238}\text{U}/^{232}\text{Th}/^{40}\text{K}$ and ^{222}Rn dissolved in the water buffer
- $^{238}\text{U}/^{232}\text{Th}/^{40}\text{K}/^{60}\text{Co}$ in the stainless steel (vessel or strut)
- ^{222}Rn and ^{85}Kr in air
- $^{238}\text{U}/^{232}\text{Th}/^{40}\text{K}$ in the PMT glass
- $^{238}\text{U}/^{232}\text{Th}/^{40}\text{K}$ in the LS container (acrylic or polymer film)

Assuming the radioactivity of the rock at the JUNO experimental site is similar to that measured at the DYB site: $\approx 10\text{ ppm}$ for ^{238}U , $\approx 30\text{ ppm}$ for ^{232}Th and $\approx 5\text{ ppm}$ for ^{40}K . After fiducial volume cut ($R < 17.2\text{ m}$), the total singles rate reduces to 0.98 Hz.

There will be nitrogen flow on the top of the water pool and an anti-radon liner on the water Cherenkov pool walls to control Radon contamination into the water. A Monte Carlo simulation gives a 16 Hz rate in all LS volume if the Radon concentration in water is 0.2 Bq/m^3 . The rate will reduce to 1.3 Hz inside the volume with $R < 17.2\text{ m}$. Thus, the internal LS radio purity is essential to the JUNO experiment and will be well controlled.

3.3 Reactor neutrinos

The main goal of JUNO is the measurement of the **NMO** and neutrino oscillation parameters using anti-electron neutrinos from the Yangjian and Taishan nuclear power plants situated at a distance of 52.5 km from the detector.

The neutrino interaction is identified by observing the **Inverse- β Decay (IBD)** signal ($\bar{\nu}_e + p \rightarrow e^+ + n$). The reactor anti-neutrino interacts with a proton in the liquid scintillator, producing a positron (e^+) and a neutron. The positron quickly deposits its energy through ionization of the liquid scintillator and its annihilation, resulting in two 0.511-MeV γ -rays, which create the prompt signal. The neutron scatters within the detector until it thermalizes and is then captured by either a proton (99%) or a carbon nucleus (1%) within an average time of approximately 200 μ s. The absorption by a proton leads to the emission of a mono-energetic gamma of 2.2 MeV, while the gamma energy released by the carbon absorption is 4.95 MeV. The coincidental pair of prompt and delayed signals allows a clean selection of signal events and leads to a good background rejection.

The most significant backgrounds for the reactor neutrino program in JUNO are: i) the accidental coincidence background, ii) ${}^8\text{He}/{}^9\text{Li}$, iii) fast neutrons, and iv) ${}^{13}\text{C}(\alpha, n){}^{16}\text{O}$ reactions. To reduce the accidental and the ${}^{13}\text{C}(\alpha, n)$ (${}^{16}\text{O}$ backgrounds, a fiducial volume cut is used. By carefully choosing the energy selection, time coincidence, and vertex correlation of the prompt and delayed signals in the anti-neutrino selection, we improve the accidental background suppression. Finally, to reject the cosmogenic backgrounds such as ${}^8\text{He}/{}^9\text{Li}$ and fast neutrons, an optimization of the muon veto cuts is performed to maximize the detector live time and minimize the dead volume losses. With the knowledge of the different origins of the backgrounds, a set of preliminary anti-neutrino selection criteria can be listed below [5]:

- Fiducial volume: the interaction should be located inside the LS at a distance $R < 17.2$ m from the center of the detector, with the radius of the acrylic curve being 17.5 m.
- The prompt energy cut $0.8 \text{ MeV} < E_p < 12 \text{ MeV}$, E_p is the energy of the positron.
- The delayed energy cut $1.9 \text{ MeV} < E_d < 2.5 \text{ MeV}$ and $4.4 \text{ MeV} < E_d < 5.5 \text{ MeV}$, E_d is the delayed energy.
- The time interval between the prompt and delayed signal $\Delta T < 1.0$ ms. We reject the event if the delay between the detection of the energy due to the positron and the detection of the energy due to the neutron is too high.
- The prompt-delayed distance cut $R_{p-d} < 1.5$ m. R_{p-d} is the distance between the point of detection of the energy due to the positron and the detection point of the energy due to the neutron.
- Muon veto criteria:
 - for muons tagged by the Water Pool, a veto over the whole LS volume for 1.5 ms.
 - for good muon tracks in the central detector and water Cerenkov detector, veto over the detector volume within $R_{d2\mu} < 3$ m and $T_{d2\mu} < 1.2$ s. $R_{d2\mu}$ and $T_{d2\mu}$ are, respectively, the radius around the muon trajectory and the time of travel of the muon in the detector.
 - for the tagged, non-trackable muons in the CD, a veto over the whole LS volume for 1.2 s.

Table 3.2 summarizes the different cut and selection efficiency. The combined selection gives an 82.2 % efficiency and leads to 47.1 events per day [92].

3.3.1 Neutrino mass ordering

There are two possible methods to determine the neutrino mass hierarchy. The first one uses matter effects introduced by collective interactions of neutrinos with electrons in matter (experiments like NO ν A, T2k, Super-K or ORCA are sensitive to them), as explained in section 1.5. JUNO pursues a second method. It exploits an interference effect between the 3-flavor oscillations in the disappearance of electronic anti-neutrinos emitted from nuclear reactors [5, 93, 94, 95, 96, 97]. The interference manifests itself in a rapid oscillation pattern superimposed over the solar oscillation. The frequency of the pattern depends on the mass hierarchy, as shown in Figure 3.2.

Selection Criterion	Efficiency [%]	IBD Rate [day^{-1}]
All IBDs	100.0	57.4
Fiducial Volume	91.5	52.5
IBD Selection	98.1	51.5
Energy Range	99.8	-
Time Correlation (ΔT_{p-d})	99.0	-
Spatial Correlation (ΔR_{p-d})	99.2	-
Muon Veto (Temporal \oplus Spatial)	91.6	47.1
Combined Selection	82.2	47.1

TABLE 3.2: Summary of cumulative reactor anti-neutrino selection efficiencies. The indicated IBD rates, with baselines under 300 km, represent the anticipated daily events detected by JUNO, following the incremental application of selection criteria. Taken from [92].

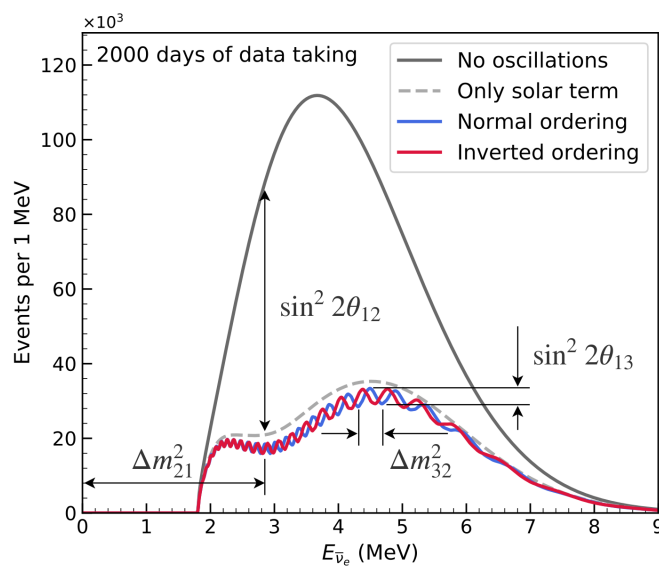


FIGURE 3.2: The expected anti-neutrino energy spectrum, weighted by the IBD cross-section, is presented with and without oscillation effects at the JUNO experiment for both normal and inverted mass ordering, assuming 2000 days of data collection. The dependence on the four oscillation parameters is illustrated. Taken from [63].

This method provides a clean determination of the mass hierarchy as it does not suffer from correlations with the leptonic CP-violation phase and the θ_{23} octant.

Figure 3.3 shows the oscillation probability for $\bar{\nu}_e \rightarrow \bar{\nu}_e$ as a function of the traveled distance L for the two hierarchy cases. The normal hierarchy is the blue curve, and the inverted hierarchy is the orange curve. In Figure 3.3a, we observe that JUNO distance corresponds to a minimum in the solar oscillation probability. The other experiments using reactor anti-neutrino are also represented. Figure 3.3b is a zoom of Figure 3.3b where we see that the phase offset between different NMO energy spectra is maximal around 52.5 km. In addition, the Figure 3.3b highlights the small difference between the normal ordering and the inverted ordering cases. This small difference in the oscillation patterns leads to the stringent requirement on the JUNO energy resolution to allow the discrimination between the two neutrino mass orderings.

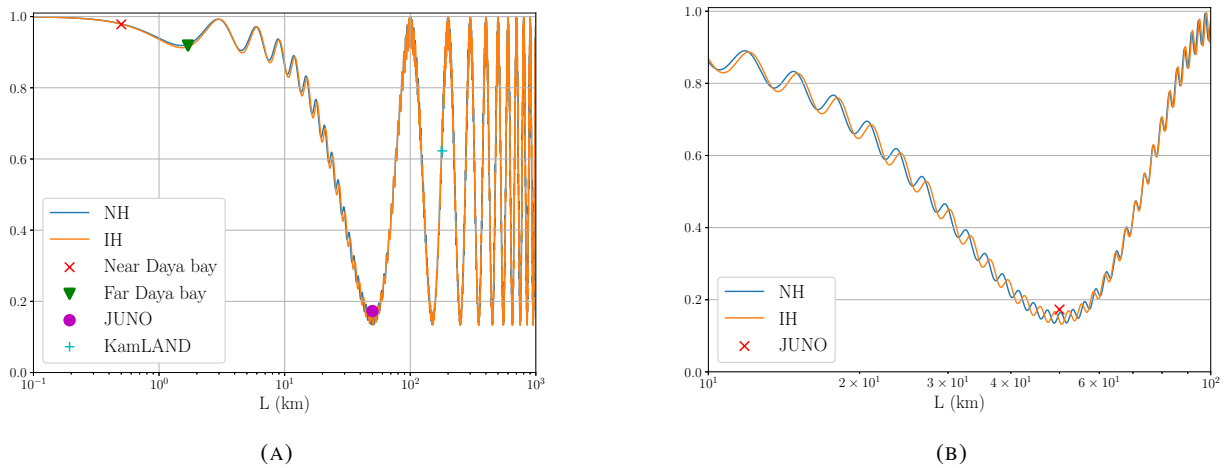


FIGURE 3.3: Graphic of the oscillation probability for $\bar{\nu}_e \rightarrow \bar{\nu}_e$ as a function of the distance L in kilometer for a neutrino of 3 MeV. The parameters: Δm_{21}^2 , Δm_{31}^2 , Δm_{32}^2 , $\sin^2(\theta_{12})$, $\sin^2(\theta_{23})$ and $\sin^2(\theta_{13})$ are from Table 1.8. The distances chosen by Daya Bay, KamLAND, and JUNO experiments are represented in left panel. On the right panel, we zoomed on the 10 km to 100 km region.

3.3.2 Precision measurement of neutrino oscillation parameters

JUNO aims to be the first experiment to observe the effects of solar and atmospheric oscillations simultaneously. Both effects can be seen in the anti-neutrino spectrum measured with JUNO, shown in Figure 3.2. The dashed line shows how the spectrum considering only the solar terms is influenced by both Δm_{21}^2 and $\sin^2 2\theta_{12}$, which cause the slow oscillation responsible for the reactor anti-neutrino disappearance. The fast oscillations (atmospheric oscillations) are superimposed to the slower oscillations and are driven by Δm_{32}^2 and modulated by $\sin^2 2\theta_{13}$. The fast oscillation effect is shown on the blue line and red line, representing the normal and inverted orderings, respectively. Measuring the oscillated reactor anti-neutrino spectrum with a resolution of 3% at 1 MeV will enable determining these four parameters simultaneously.

A new study was performed [98] that incorporates several important updates, including:

- Updated baselines and cosmogenic backgrounds that reflect slight adjustments made to the underground cavern's position during construction
- An IBD cross-section that includes all radiative corrections and neutron recoil effects
- A reactor anti-neutrino shape uncertainty consistent with expectations from the TAO experiment
- A data-driven scintillator non-linearity model inspired by the Daya Bay experiment
- The updated energy resolution from the JUNO physics paper
- The use of JUNO's full Monte Carlo simulation to model detector response effects such as non-uniformities and leakage
- The updated reactor configuration (8 cores instead of 10)

Taking into account those updates in the analysis, the sensitivity results are shown in Table 3.3. With six years of data taking by JUNO, the parameters Δm_{31}^2 , Δm_{21}^2 , and $\sin^2 \theta_{12}$ will be determined with world-leading precision of 0.2%, 0.3%, and 0.5%, respectively.

Parameter	Central Value	PDG2020	100 days	6 years	20 years
Δm_{31}^2 ($\times 10^{-3} \text{ eV}^2$)	2.5283	± 0.034 (1.3%)	± 0.021 (0.8%)	± 0.0047 (0.2%)	± 0.0029 (0.1%)
Δm_{21}^2 ($\times 10^{-5} \text{ eV}^2$)	7.53	± 0.18 (2.4%)	± 0.074 (1.0%)	± 0.024 (0.3%)	± 0.017 (0.2%)
$\sin^2 \theta_{12}$	0.307	± 0.013 (4.2%)	± 0.0058 (1.9%)	± 0.0016 (0.5%)	± 0.0010 (0.3%)
$\sin^2 \theta_{13}$	0.0218	± 0.0007 (3.2%)	± 0.010 (47.9%)	± 0.0026 (12.1%)	± 0.0016 (7.3%)

TABLE 3.3: A summary of precision levels for the oscillation parameters. The PDG2020 [99] is compared with 100 days, 6 years, and 20 years of JUNO data taking. No external constraint on $\sin^2 \theta_{13}$ is applied for these results. Taken from [98].

3.4 Supernova neutrinos and trigger strategy

Neutrinos play a crucial role during all stages of the stellar collapse and following explosion. The detection of 24 neutrino events from supernova 1987A by the Kamiokande-II, Irvine-Michigan-Brookhaven, and Baksan experiments confirmed the delayed neutrino-driven explosion mechanism for core-collapse supernovae. Despite this confirmation, the poor statistics from supernova 1987A made it impossible to determine supernova and neutrino parameters precisely. Future large neutrino detectors, such as Hyper-Kamiokande, JUNO, and DUNE, hold great promise in addressing this limitation. These detectors, using water Cherenkov, liquid scintillator, and liquid argon time projection chamber technologies, are capable of registering a much larger number of supernova neutrinos. The new generation of detectors will also enable the obtaining of detailed flavor information on CCSN neutrinos. Recent advances in numerical models offer better predictions of measurable CCSN neutrino features, enhancing our understanding of the CCSN mechanism (see Chapter 7 for details).

As shown in Figure 3.4, the total number of expected neutrino interactions, including all dominant channels, varies as a function of the CCSN distance. A CCSN at a distance of around 10 kiloparsecs (kpc) will result in approximately 10^4 observable neutrino interactions in JUNO. The red band represents the range of expected neutrino interactions according to the Garching model [100]. The x-axis shows the distance in kpc, while the y-axis on the left indicates the number of neutrino interactions in JUNO.

The blue lines show the probability density distribution of CC-SN distances according to different studies (Adams et al. [101], Ahlers et al. [102], and Mirizzi et al. [103]). The right y-axis provides the probability density. The dashed vertical line marks the position of the galactic center at 8.5 kpc.

Theoretical models of the CCSN mechanism identify three primary phases: the shock-breakout burst phase, the post-bounce accretion phase, and the proto-neutron star cooling phase. Detailed observations of these phases are critical, as they correspond to the dynamic stages of stellar collapse and explosion. The total energy, luminosity evolution, spectral distribution, and the mix of different SN neutrino flavors provide insights into the hydrodynamic conditions, dynamical processes, and characteristics of the progenitor star and its remnant. During the silicon burning phase, a significant number of MeV-energy neutrinos are produced via thermal processes and weak nuclear interactions. These so-called pre-supernova neutrinos are valuable for studying the late stages of stellar evolution and will provide an early warning for the CCSN neutrino burst.

JUNO, with its 20 kt liquid scintillator, is well-equipped to detect all flavors of O(10 MeV) postshock neutrinos. JUNO will significantly benefit from high statistics in two primary interaction channels: IBD and

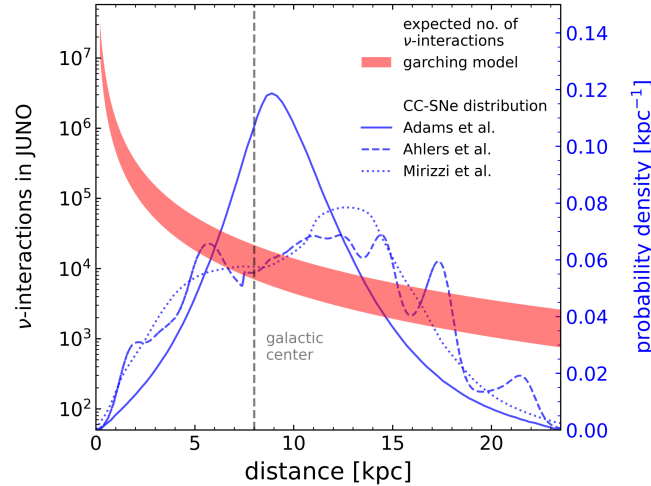


FIGURE 3.4: The expected number of neutrino interaction events in JUNO as a function of the distance to the CCSN (red curve). The galactic CCSN probability as a function of the distance is also shown (blue curves). Taken from [104].

Neutrino-Proton Elastic Scattering (νp ES). Additionally, Neutrino-Electron Elastic Scattering (νe ES) and various neutrino-carbon interactions (via Neutral Current (NC) and Charged Current (CC)) are notable, though with fewer statistics. The expected number of events for each channel, for a typical CCSN at a distance of 10 kpc, is presented in Table 3.4. The different channel characteristics are described in Chapter 8.

Interaction Chan.	Type	Num. evts (@10kpc)
$\bar{\nu}_e + p \rightarrow e^+ + n$	CC	~ 5000
$\nu + p \rightarrow \nu + p$	NC	~ 2000
$\nu + e^- \rightarrow \nu + e^-$	NC	~ 300
$\nu + {}^{12}\text{C} \rightarrow \nu + {}^{12}\text{C}^*$	NC	~ 300
$\nu_e + {}^{12}\text{C} \rightarrow e^- + {}^{12}\text{N}$	CC	~ 100
$\bar{\nu}_e + {}^{12}\text{C} \rightarrow e^+ + {}^{12}\text{B}$	CC	~ 100

TABLE 3.4: number of neutrino events in JUNO with their corresponding interaction channels for a typical CCSN at a distance of 10 kpc, where ν collectively stands for neutrinos and anti-neutrinos of all flavors.

JUNO’s front-end electronics will incorporate real-time waveform processing via FPGAs (for charge reconstruction and timestamp tagging) and a 2 GB DDR3 memory shared by three PMTs. The processed signal will be sent to the **Data Acquisition (DAQ)** in triggerless mode, while raw waveforms will be sent to **DAQ** upon validation by the global trigger electronics. This configuration minimizes the data loss even at high event rates (expected from nearby supernovae), as signals can be temporarily stored in the 2 GB memory.

A dedicated multi-messenger trigger system is designed to achieve an ultra-low detection threshold of $O(20 \text{ keV})$ [105]. This system aims to exploit JUNO as a neutrino telescope to play a significant role in the next-generation Supernova Early Warning System (SNEWS2.0) for multi-messenger astronomy [106]. Thanks to his lower threshold, it also allows the capture of more events in the νp ES channel, allowing the capture of additional phases of CCSN, such as neutrino trapping.

No SN neutrino burst has been observed since SN 1987A, and a recent analysis combining several independent studies predicts an expected rate of 1.63 ± 0.46 core-collapse SN per century [107]. Large neutrino detectors like Super Kamiokande-Gd, JUNO, Hyper-Kamiokande, and DUNE will be operational for several decades,

making it likely that we will obtain high-statistics measurements of neutrino signals from at least one galactic core-collapse SN in the coming decades.

3.5 Diffuse supernova neutrino background

Although CCSN within our galaxy are rare occurrences, they are frequent events across the observable Universe, emitting bursts of different flavor neutrinos. These neutrinos contribute to a persistent background flux known as the DSNB. The value of DSNB flux is estimated around $\sim 10 \nu \text{ cm}^{-2} \text{ s}^{-1}$ [108]. The precise flux and spectrum measurement of the DSNB lead to valuable information about the redshift-dependent supernova rate, the average supernova neutrino energy spectrum, and the fraction of core-collapse supernovae resulting in black hole formation.

DSNB signal The energy spectrum of DSNB events in JUNO can be described by:

$$\frac{dN_\nu}{dE_\nu} = N_p \times \sigma_\nu(E_\nu) \times c \int_0^\infty \frac{dN(E'_\nu)}{dE'_\nu} \times \frac{dE'_\nu}{dE_\nu} \times R_{\text{SN}}(z) \times \left| \frac{dt}{dz} \right| dz,$$

Where $N_p = 7.16 \times 10^{31}/(10 \text{ kt})$ is the number of protons in the JUNO LS target, $\sigma_\nu(E_\nu)$ is the energy-dependent cross-section for the IBD reaction, and the integral represents the differential DSNB flux. This flux is obtained by integrating the average supernova neutrino spectrum dN/dE'_ν along the line of sight, weighted by the core-collapse supernova rate $R_{\text{SN}}(z)$ over cosmic history. E'_ν denotes the emitted neutrino energy, while $E_\nu = E'_\nu/(1+z)$ is the redshifted energy detected. The term $\left| \frac{dt}{dz} \right|$ links redshift z to cosmic time t , accounting for the Universe's expansion history.

For simplicity, we assume the supernova neutrino spectra follow a Maxwell-Boltzmann distribution. The expected DSNB event rate and spectra are sensitive to the mean energy $\langle E_\nu \rangle$. The left panel of Figure 3.5 illustrates an example event spectrum for neutrino mean energy of 15 MeV, showing event numbers as a function of positron event energy over 10 years in a 17-kt fiducial volume.

Background rejection Detecting the DSNB signal involves overcoming various background sources. Reactor and atmospheric neutrinos create an irreducible background, limiting the DSNB observation window to the range of 10 to 30 MeV. Cosmic muons also generate background by generating β/n -emitting isotope in the CD and fast neutrons in the surrounding rock. A coincidence veto strategy mitigates these backgrounds after a thorough muon tagging and fiducial volume cut.

The most challenging background for DSNB detection in the CD comes from NC interactions of atmospheric neutrinos with ^{12}C . The neutron emitted combined with a prompt energy deposit mimics IBD signals. To estimate this background, a complex calculation is necessary to estimate NC event final-state distributions. This calculation requires considering both total cross-sections and residual nuclei de-excitation processes, using tools like the GENIE neutrino interaction generator [109] and the TALYS nuclear de-excitation tool [110]. Pulse-shape discrimination (PSD) capabilities of liquid scintillators can reduce the NC background to a manageable level. The right panel of Figure 3.5 illustrates the prompt energy spectra, with the DSNB signal dominating in the 11 to 22 MeV range. The residual atmospheric NC background rate can be further constrained by measuring the radioactive decay of final-state nuclei, reducing the background rate uncertainty to about 10%.

DSNB sensitivity JUNO's sensitivity to DSNB detection is assessed using an event counting analysis within the observation window, ignoring spectral details. Figure 3.6 shows the sensitivity as a function of the exposure,

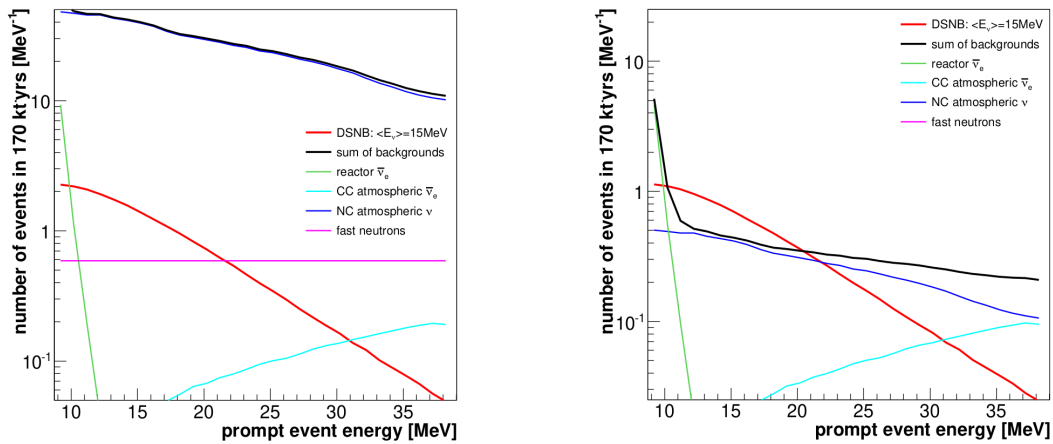


FIGURE 3.5: Prompt (e^+) energy spectra for the DSNB signal ($\langle E_\nu \rangle = 15$ MeV) and backgrounds as expected for JUNO. Left: After applying basic selection cuts, the background from atmospheric-neutrino NC reactions dominates across the entire observation window from 10 to 30 MeV. Right: By implementing pulse shape discrimination (PSD), the atmospheric neutrino NC and fast neutron backgrounds are significantly reduced. The DSNB signal becomes dominant in the range from 11 to approximately 22 MeV. Taken from [63].

influenced by the background rate uncertainty. For $\langle E_\nu \rangle \geq 15$ MeV, JUNO is expected to achieve 3σ evidence for the DSNB signal after 10 years.

3.6 Solar neutrinos with JUNO

Solar neutrinos are produced through thermonuclear reactions occurring in the sun core. These reactions can be categorized into two main processes: the proton-proton (pp) chain and the Carbon-Nitrogen-Oxygen (CNO) cycle, responsible for approximately 99% and 1% of solar neutrinos. Detecting solar neutrinos provides valuable insights into the sun interior composition. It helps improve our understanding of solar physics, such as the mechanisms governing solar dynamics and the solar metallicity problem. Recent experiments like Borexino have achieved significant milestones [112], including a comprehensive measurement of the pp-chain neutrinos and the first experimental evidence of neutrinos produced in the CNO cycle.

JUNO is a promising detector for solar neutrino research thanks to its large detection volume, excellent energy resolution, and low energy threshold. JUNO aims to make new measurements of the various components of the solar neutrino flux, particularly from the ^8B and ^7Be beta decays, which occur in the proton-proton chain. These measurements could provide a better understanding of the solar metallicity problem and the matter effects in neutrino oscillations [113].

For JUNO, the primary detection channel for solar neutrinos is the scattering with electrons. The main backgrounds for solar neutrino study include intrinsic natural radioactivity in the LS, gamma rays from external detector materials, and unstable isotopes produced by cosmic ray muons passing through the detector. Adequate shielding can suppress the external background with energies greater than 2 MeV to a negligible level, allowing the reduction of the analysis threshold to 2 MeV in a fiducial volume with a radius of 13 m. However, further reduction of the energy threshold is hindered by the high rate of cosmogenic ^{11}C decays in the LS.

In ten years of data taking, JUNO is expected to observe about 60,000 signal events and 30,000 background events above 2 MeV, assuming an intrinsic ^{238}U and ^{232}Th contamination level of 10^{-17} g/g inside the LS. Detailed studies and efforts in material selection and installation procedures are ongoing to maintain low background levels.

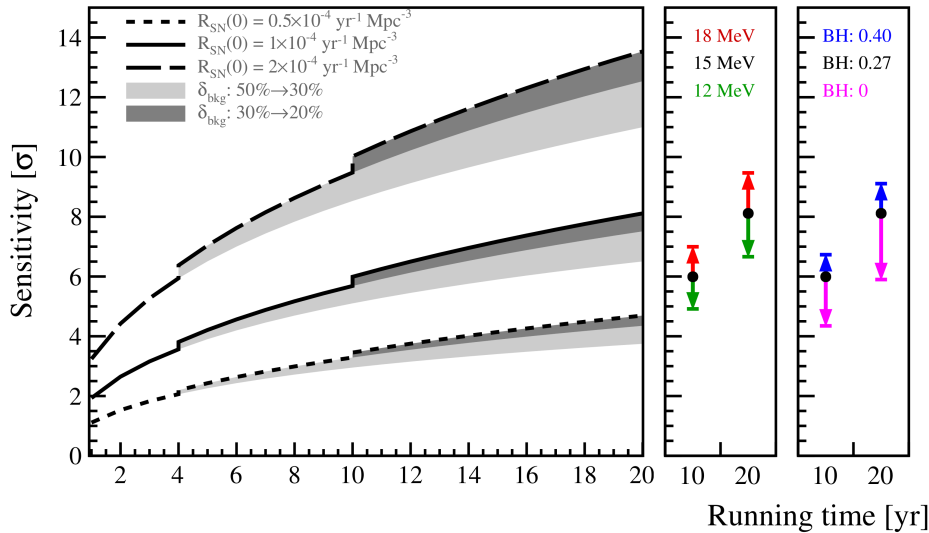


FIGURE 3.6: The discovery potential of the DSNB (σ) at JUNO as a function of the operational time is shown. The reference DSNB signal model is depicted by a solid black line in the left panel and by black circular points in both the middle and right panels. In the left panel, short and long dashed lines represent model variations with supernova (SN) rates ranging from $0.5 \times 10^{-4} \text{ yr}^{-1} \text{ Mpc}^{-3}$ to $2.0 \times 10^{-4} \text{ yr}^{-1} \text{ Mpc}^{-3}$. The dark grey and grey shaded areas indicate different levels of systematic uncertainty in the NC background. In the middle and right panels, the model variations based on the average SN energy (from 12 to 18 MeV) and the black hole formation fraction (from 0 to 0.40) are shown for data collected over 10 and 20 years, respectively. Taken from [111].

The expected spectra for 10 years of exposure are shown in Figure 3.7. However, overcoming the fundamental backgrounds to achieve a precision better than the 2.7% and 10% flux measurements established by Borexino will be a significant challenge.

3.7 Atmospheric neutrinos

Atmospheric neutrinos are essential for studying neutrino oscillation physics due to their wide range of baselines (approximately 15-13000 km) and energies (approximately 0.1 GeV to 10 TeV). These neutrinos, which include both neutrinos and anti-neutrinos of all flavors, pass through the earth and are affected by the MSW matter effect. This effect is critical for determining the neutrino mass ordering. JUNO's sensitivity to atmospheric neutrinos complements that of reactor neutrinos, with their combined sensitivity surpassing the purely statistical combination of their sensitivities.

Numerical simulations, which analyze atmospheric ν_μ and $\bar{\nu}_\mu$ events to evaluate their impact on the NMO, indicate that JUNO's sensitivity to the NMO can achieve 0.9σ for a 200 kt.-year exposure, assuming $\sin^2 \theta_{23} = 0.5$.

Figure 3.8 illustrates the atmospheric neutrino energy spectra reconstructed by the JUNO detector for ν_μ (in blue) and ν_e (in red). The data from JUNO are compared with existing measurements from Super-Kamiokande [60] and Fréjus [114] experiments. The HKKM14 [115] model predictions are also shown, both with and without oscillations, for ν_μ (blue dashed and solid lines) and ν_e (red dashed and solid lines). The comparison demonstrates JUNO's capability to achieve precise measurements in the same energy region as these established experiments, highlighting its potential to contribute significantly to atmospheric neutrino research. The details of the technics used to achieve the reconstruction of atmospheric neutrino is given in [116].

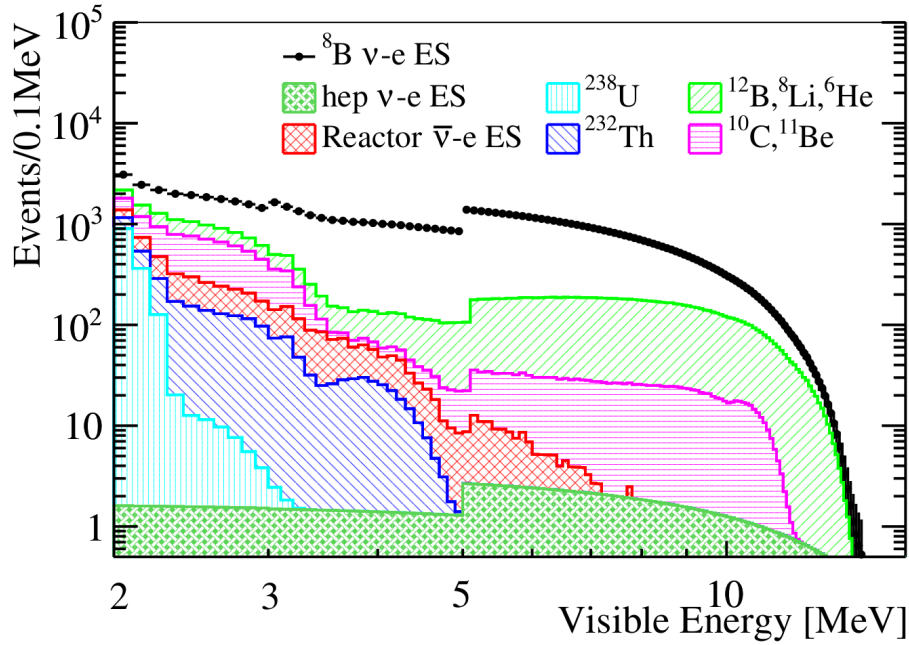


FIGURE 3.7: signal and background spectra over ten years of data collection have been obtained through simulation, taking into account all selection cuts and muon veto techniques. Due to the energy dependence of the fiducial volume, discontinuities are observed at 3 MeV and 5 MeV as a result. Taken from [113].

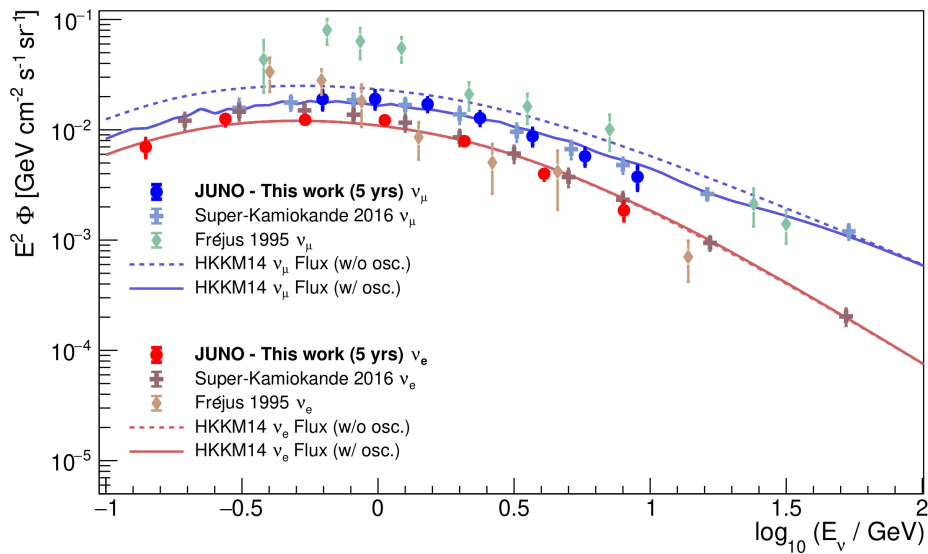


FIGURE 3.8: Atmospheric neutrino energy spectra reconstructed by the JUNO detector for ν_μ (blue color) and ν_e (red color), compared with Super-Kamiokande and Fréjus measurements in the same energy region [60, 114]. Taken from [63].

3.8 Geo-neutrinos

Geo-neutrinos are anti-neutrinos produced by the decay of long-lived radioactive elements within the earth. By measuring them we have a unique opportunity to study the earth interior physics, leading to knowledge on its radiogenic heat production, formation, and chemical composition. Geo-neutrinos from the decay chains of ^{238}U

and ^{232}Th can be detected via inverse beta decay on protons with a threshold of 1.8 MeV. Up to now, only two experiments, KamLAND [117, 47, 118, 119, 120] and Borexino [121, 122, 123, 124], have successfully measured geo-neutrinos. KamLAND detected a total of $168.8_{-26.5}^{+26.5}$ events, while Borexino measured $52.6_{-22.71}^{+98.46}$ events. Still, neither experiment has the sensitivity required to accurately determine the Th/U ratio, a critical parameter for understanding earth formation.

Some discrepancies exist between the results from KamLAND and Borexino. Borexino's results set stringent upper limits on the power of a hypothesized geo-reactor within the earth [125, 126, 127, 128]. KamLAND, on the other hand, estimated a radiogenic power of $12.4_{-4.9}^{+4.9}$ TW and favored geological models with lower concentrations of heat-producing elements [120]. Future experiments, such as JUNO, are designed to provide more definitive results on the earth radiogenic power and geo-neutrinos. With a detector volume at least 20 times larger than current detectors, JUNO is positioned to offer high-statistics measurements of geo-neutrinos, representing a significant advancement in this field.

The expected geo-neutrino signal at JUNO depends on the abundance and distribution of U and Th on earth. Sensitivity studies suggest that JUNO could detect geo-neutrinos with an expected signal of $39.7_{-2.5}^{+6.5}$ TNU (Terrestrial Neutrino Unit), where one TNU corresponds to one event detected per year by a detector with 100% efficiency and 10^{32} target protons (approximately 1 kt of liquid scintillator). This corresponds to measuring 400 geo-neutrinos per year, exceeding the total number detected by all previous experiments.

The crust within a 500 km radius around JUNO is expected to contribute more than 50% of the total geo-neutrino signal. Therefore, refined local geological models are crucial for accurately estimating the crustal signal and isolating the mantle signal. The primary challenge for JUNO's geo-neutrino measurements is the significant background from reactor anti-neutrinos, along with other non-antineutrino backgrounds such as cosmic muons, cosmogenic ^9Li - ^8He , fast neutrons, $^{13}\text{C}(\alpha,n)^{16}\text{O}$ reactions, and accidental coincidences.

Figure 3.9 shows the expected energy spectrum for IBD events in JUNO when searching for geo-neutrinos, with the geo-neutrino signal in red being overshadowed by the reactor anti-neutrino background. Considering JUNO's muon veto (17% exposure loss), IBD selection (80% efficiency), and detector response (3% energy resolution at 1 MeV), two methods were used to assess the potential precision of JUNO's geo-neutrino measurements. These methods yielded compatible results, estimating the precision of geo-neutrino measurements with a fixed chondritic mass Th/U ratio of 3.9 to be 17%, 10%, 8%, and 6% after 1, 3, 5, and 10 years of data taking, respectively [63]. Over several years, JUNO could also constrain the Th/U ratio in the observed geo-neutrino signal.

To improve the accuracy of geo-neutrino flux predictions, refined local geological models were developed. These models are based on the finding that geo-neutrino signals from U and Th within about 100 km of the detector contribute significantly to the total mantle signal. The South China Block surrounding JUNO was studied for density, crustal layer thickness, and chemical composition. JULOC (JUNO Local Crust) [129], a 3-D high-resolution crustal model, covers an area of $10^\circ \times 10^\circ$ around JUNO and uses seismic ambient noise tomography to provide information about the upper, middle, and lower crust. Based on U and Th abundances from over 3000 rock samples, JULOC suggests that the local upper crust has higher average U and Th abundances. In comparison, the middle and lower crust have lower abundances compared to global averages. The estimated crustal geo-neutrino signal by JULOC is 38.3 ± 4.8 TNU, compared to $28.2_{-2.5}^{+5.4}$ TNU based on a global crustal model. This demonstrates the potential of locally refined geological models to better isolate the mantle components.

3.9 Summary

Due to its unprecedented scale and precision, JUNO is an exceptional multipurpose detector with a rich physics program covering a wide energy range of 100 keV to 100 GeV. It covers different sources of neutrinos and their associated backgrounds. The primary neutrino source in the JUNO detector is reactor anti-neutrinos from nearby

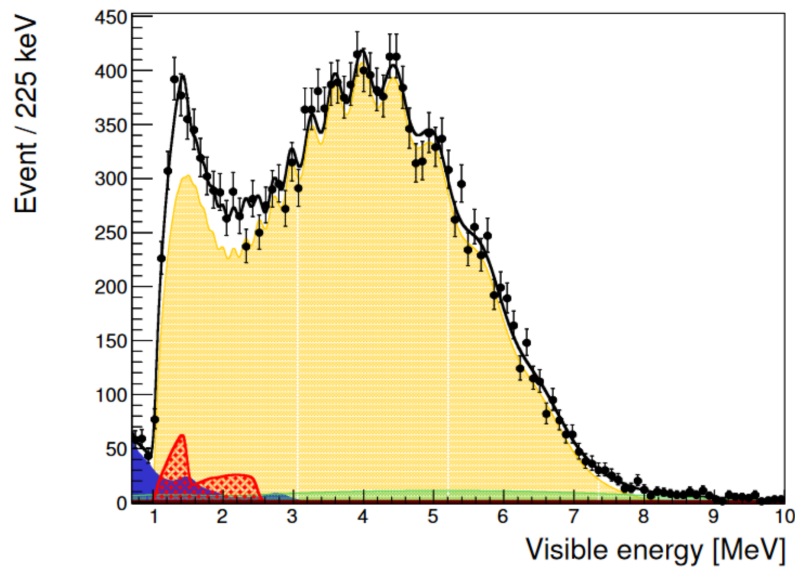


FIGURE 3.9: Expected energy spectrum for IBD events in JUNO when searching for geo-neutrinos. The reactor anti-neutrino background significantly overshadows the geo-neutrino signal (in red). Taken from [63].

nuclear power plants, which are detected via inverse beta decay. This detection is crucial for determining NMO and measuring neutrino oscillation parameters with high accuracy. JUNO is also sensitive to solar neutrinos, and atmospheric neutrinos. The study of solar neutrinos provides insights into solar dynamics and the composition of the solar core. On the other hand, atmospheric neutrinos are essential for understanding neutrino oscillations over long baselines and in the presence of matter effects, and provide additional NMO sensitivity.

To ensure accurate neutrino measurements, JUNO must carefully reduce various sources of background noise, such as natural radioactivity, cosmogenic isotopes, and neutron production. Background suppression techniques include energy threshold, fiducial volume radius, time coincidence, distance cut, muon vetoes, and precise calibration methods. They are used to reduce the contamination in the different parts of JUNO experiment.

JUNO has excellent capability to detect neutrinos from core-collapse supernovae. It can observe all flavors of post-shock neutrinos, providing valuable data on supernova dynamics and the explosion mechanism. With its large liquid scintillator volume, JUNO can obtain thousands of neutrino interactions from a supernova, depending on its distance. JUNO is also in good position to detect DSNB neutrinos, which originate from all past supernovae in the universe. The detection of the DSNB neutrinos provides insights into the supernova rate and the average energy spectrum of supernova neutrinos. JUNO uses pulse shape discrimination based on the liquid scintillator properties to enhance its sensitivity for DSNB detection, with the potential to achieve significant evidence after 10 years of operation.

JUNO will measure geo-neutrinos produced by radioactive decay inside the earth. These measurements will provide information about the internal heat production and composition of the earth. JUNO is expected to detect about 400 geo-neutrino events per year, significantly improving current measurements and refining geological models.

JUNO's advanced design, effective background suppression, and precise calibration make it a powerful tool for advancing our understanding of neutrino physics and the fundamental processes of the universe.

Part II

Test and development of the back-end card of JUNO

Chapter 4

Large PMT readout electronic system

In Chapter 2, we provided an overview of the main components of the JUNO experiment. In this chapter, we detail the operation of the LPMT readout system. We begin with a general description of the LPMT readout electronics, followed by an in-depth examination of both the underwater and outside electronic components. Finally, we will discuss the data acquisition system and the detector control system.

Contents

4.1	General description	59
4.1.1	Large PMT readout electronic system requirement	59
4.1.2	Large PMT electronic chain	60
4.2	Underwater electronics	62
4.2.1	High voltage unit and splitter board	64
4.2.2	The Global Control Unit (GCU)	65
4.3	Outside water electronics system	72
4.3.1	Low voltage power supply	72
4.3.2	Trigger system hardware	72
4.3.3	Trigger schemes	77
4.3.4	Synchronization and clock distribution scheme for trigger system	80
4.4	Data Acquisition and Detector Control System	82
4.4.1	Data Acquisition System (DAQ)	82
4.4.2	Detector Control System (DCS)	83
4.5	Summary	84

4.1 General description

To discriminate the [Neutrino Mass Ordering \(NMO\)](#), the nominal experimental setup must have an energy resolution of 3% at 1 MeV. To achieve the required energy resolution, the number of [photo-electron \(p.e.\)](#) collected by generated by the PMT needs to be more than 1400 per MeV. To achieve this amount of 1400 p.e./MeV, the JUNO experiment plays on two factors: the photo coverage and the [Photo-Detection Efficiency \(PDE\)](#). The photo-cathode total coverage of JUNO will be 78% with a total of 17612 LMPTs and 25600 SMPTs. The [PDE](#) of those PMTs is greater than 25% [4].

4.1.1 Large PMT readout electronic system requirement

The main tasks of the readout electronics are:

1. to receive and to digitize the analog signal from the PMTs, to transmit all the relevant information to the [Data Acquisition \(DAQ\)](#) without significantly losing data quality
2. to generate a trigger request/accept signal based on the PMT waveform data

The trigger accept signal is computed thanks to the global information of the different PMTs across the [CD](#). The trigger accept signal is then distributed to the front-end electronics. In case of positive trigger, the PMT data is sent to the DAQ. The electronics design, in terms of both hardware and firmware, is driven by the following key-points [4]:

- **Energy reconstruction:** optimization of the energy measurement of $\bar{\nu}_e$, especially at low energies, is crucial to achieving the neutrino mass ordering. The energy resolution is a function of the number of [p.e.](#) captured and amplified by the PMT. A higher number of [p.e.](#) lead to better energy resolution. The criteria is implemented on the [Analog-to-Digital Converter \(ADC\)](#), especially on ADC effective number of bits (ENOB). In our case the ADC ENOB is equal to 10. More details are given in section 4.2.
- **Reconstruction of the photon arrival pattern:** accurate measurement of the photon time pattern in the detector is crucial for determining event positions. This is particularly important for [IBD](#) events induced by $\bar{\nu}_e$ because (a) the detector's energy response is position-dependent, and (b) the spatial and temporal coincidences between prompt positron and delayed neutron events is crucial for the background suppression. The required time resolution is 1 ns as the PMT mean risetime for HPK PMTs is 6.9 ns and 4.9 ns for NNVN PMTs¹. The requirement is fulfilled on the ADC side using a sample rate of 1 Gsample/s.
- **Low dead time and dynamic acquisition rate:** during usual data-taking conditions, all type neutrino events (i.e. neutrinos from the reactor, solar neutrinos, geo-neutrinos, atmospheric neutrinos) need to be acquired with efficiency. An additional requirement on readout electronics is to be able to capture short episodes of very high trigger rates, such as neutrino bursts caused by supernovas. In a supernova burst, thousands of events are expected within seconds. Therefore, the electronics chain has to bear a high increase in its acquisition rate, from 1 kHz to 1 MHz, without significant data loss or dead time. As trigger decision frequency is 62.5 MHz and a 2GB DDR3 RAM is placed on the GCU, we achieve the goal of no data loss. The trigger decision rate is high enough to never have a overflow of the GCU buffer leading to a detector with no dead time.
- **Reliability:** The JUNO apparatus should exhibit a failure rate of less than 1% for channels over the initial six-year operational period. It is assumed that half of the failures originate from the PMTs, and thus less than 0.5% of electronic failures are permitted. The PCB design, choice of components, and firmware design have all been driven by the need to meet this stringent reliability requirement. As the underwater electronics cannot be accessed once the LS has been filled, meeting the aforementioned reliability criteria is of paramount importance for the front-end electronics.

4.1.2 Large PMT electronic chain

A scheme of the large PMT electronics is shown in Figure 4.1. The current design for the large PMT electronics splits the chain into two parts: underwater and outside water electronics. The underwater electronics have the front-end electronics function and are housed inside water-tight boxes called [UnderWater Box \(UWB\)](#), which are mounted on the stainless steel truss of the [CD](#). The connection from the [UWB](#) to the surface electronics is set up through three separate links: a power cable, a synchronous link (S-link), and an asynchronous link (A-link). The S-link, which interfaces with the trigger system via a CAT6 Ethernet cable, transmits the clock, trigger request, and trigger accept signals. A-link connects the front-end electronics to a Gbit enterprise switch via a CAT5e cable and is fully dedicated to the DAQ and the [Detector Control System \(DCS\)](#) connection.

¹Those are the mean values for the selected 20-inch PMTs extracted from Reference [86]

Each **UnderWater Box (UWB)** is positioned as close as possible to the PMTs to minimize the deteriorating effects of analog signal transmission over long cables. It processes data from three large PMTs and connects to each PMT via a 1.5 -3.5 m coaxial cable. However, underwater electronics have a significant constraint: they are not replaceable during operation. This limitation increases the reliability requirements for the electronics.

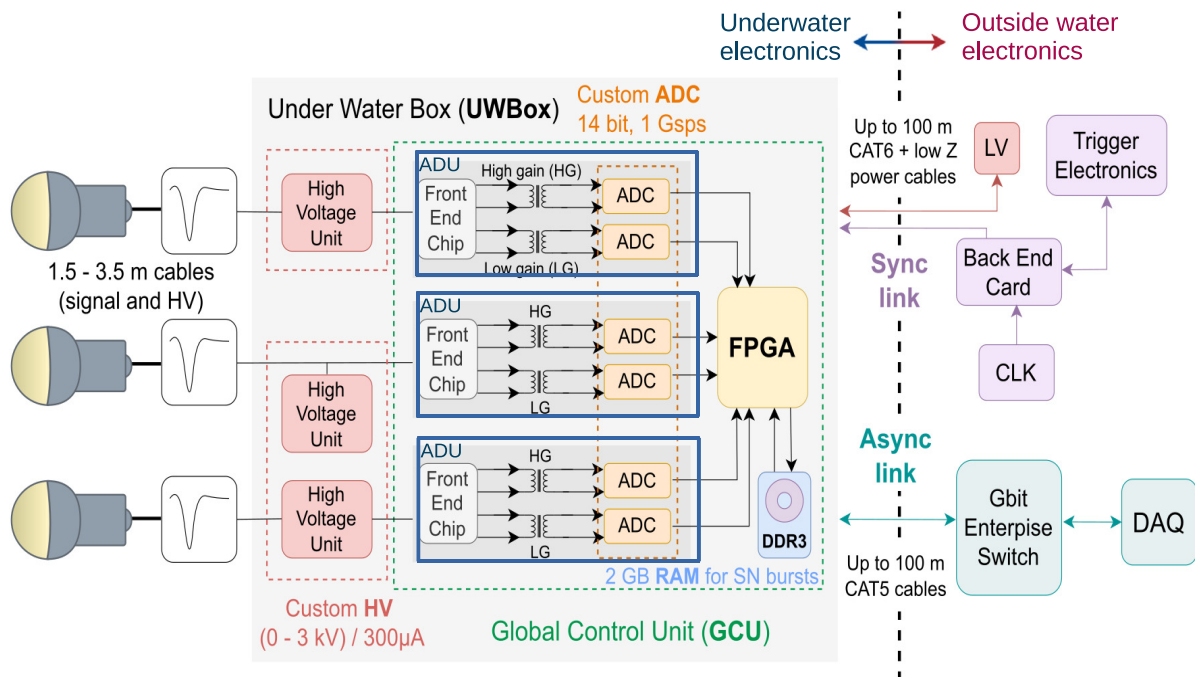


FIGURE 4.1: Final scheme of the large PMT readout system. The underwater electronics (PMTs and GCU) (left) is connected to the outside water electronics using two Ethernet cables and a dedicated low-impedance cable for power distribution. Taken from [130].

The whole JUNO electronic scheme works as the following :

- photons coming from different interactions in the detector are detected by the PMTs, resulting in negative pulses (waveform) on the PMTs output analog signal
- three PMTs are connected to one **UWB**, and the PMT analog signal is processed by a custom **Front-End Chip (FEC)**, which amplifies it with two different gains, and then digitizes by a 14-bit, 1 GS/s, custom **Analog-to-Digital Converter (ADC)**.
- the main FPGA analyzes the digitized waveform on the **Global Control Unit (GCU)**. The global trigger scheme requires that the FPGA generates the trigger requests and stores the waveform, waiting for a global trigger validation decision.
- from the **UWB**, the information from the single 'fired' PMT is sent to the **Back-End Card (BEC)** via the S-link and processed by the **Central Trigger Unit (CTU)** to generate the trigger decision.
- from the **CTU**, the trigger decision is distributed to all the **GCU**. Finally, the validated waveforms on **GCU** are sent to the DAQ event builder through the A-link.

4.2 Underwater electronics

The specifications for the front-end electronics are as follows:

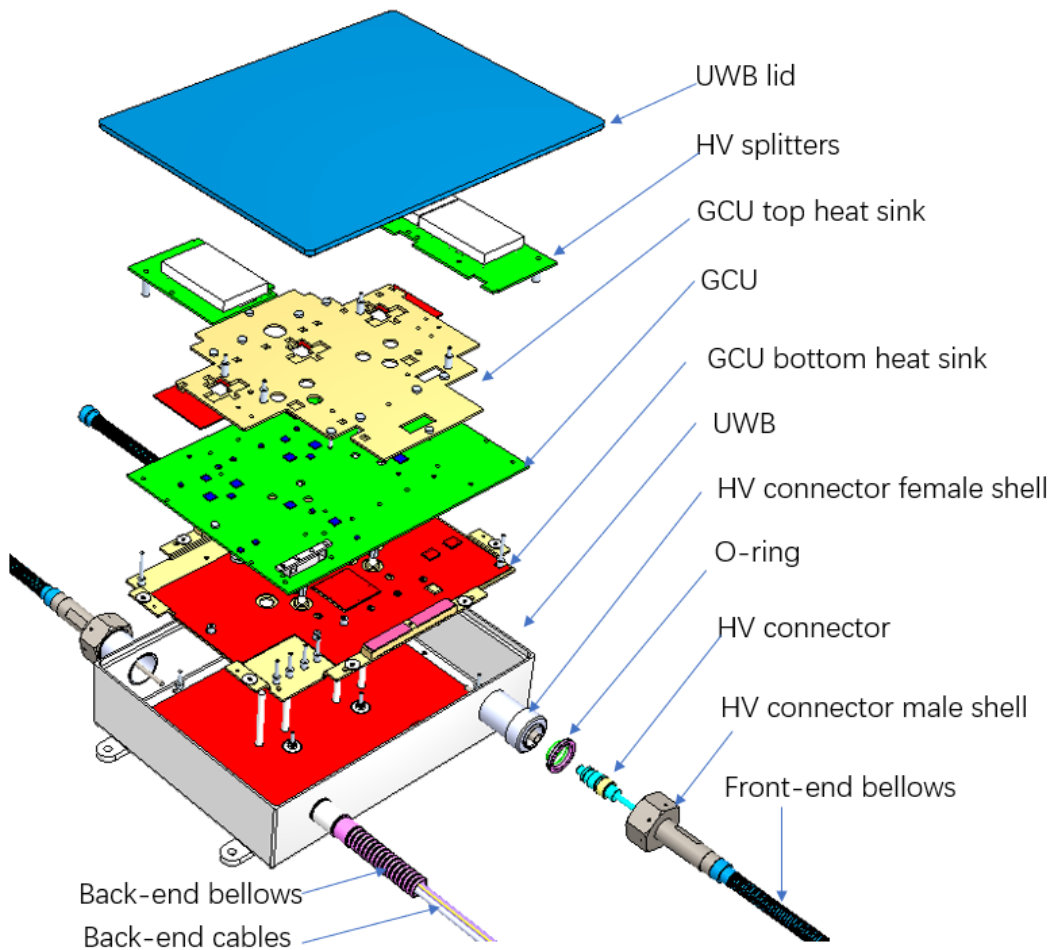
- High voltage communication: the communication between the front-end electronics and the PMTs must ensure the transmission of the PMT analog signal and the supply of the high voltage to the PMTs.
- Dynamic range: the electronics feature a dynamic range from 1 to 4000 p.e., with an amplitude dynamic range from 7.5 mV to 7.5 V (150 μ A to 150 mA), providing accurate measurements across a broad range the incoming PMT analog signals.
- Energy resolution: the required energy resolution for the [Analog to Digital Unit \(ADU\)](#) is 10 % for events in the range of 1 to 100 p.e., and 1 p.e. for events above 100 p.e, offering fine granularity for low signals and consistent accuracy for high-intensity signals.
- Each module includes 3 channels with a 1 Giga-sample per second (Gsp/s) 14-bit [Flash Analog-to-Digital Converters \(FADC\)](#), ensuring precise digitization of analog signals.
- Trigger: the electronics support both a global trigger system and a self-trigger mechanism, providing flexibility in the triggering scheme and allowing different testing procedures.
- Real-time charge and time calculation: the front-end electronics are equipped to calculate charge and timing information in real-time, allowing for rapid analysis and data processing
- Ethernet readout support: the connection to DAQ and the trigger system is performed by Ethernet cables, so the Ethernet interface needs to be implemented on the front-end electronics
- System synchronization, 8 ns clock alignment: the system synchronization ensures accurate timing with an 8 nanosecond clock alignment, allowing for precise event correlation
- Storage: the electronics include enough memory to handle trigger latency, Ethernet latency and long data from supernova events. The GCU design includes 2GB of DDR3 RAM memory for this.
- Safe remote reprogramming support: remote reprogramming is supported with safety measures to ensure secure and reliable firmware updates. As the front-end electronics are underwater, a solution needs to be foreseen to update the firmware when the electronics are installed
- Over-voltage protection and independent channel power control: each channel has over-voltage protection and independent power control to prevent damage and ensure stable operation
- Reliability: JUNO requires less than 1% channel failure during the first six years of operation, given less than 0.5% for electronic failures
- Power consumption: the power consumption for each PMT channel is limited to less than 10 W to maintain effective underwater cooling control.

To meet these specifications, the design incorporates two types of boards housed within the [UWB](#): 1) the [High Voltage \(HV\)](#) units, which are assembled on PCBs known as "splitter boards", and 2) the [GCU](#), the motherboard that supports the front-end electronics and two FPGAs (a Kintex-7 and a Spartan-6). Figure 4.2a shows the board assembly inside the [UWB](#), where the yellow Ethernet cable (CAT6) and the blue Ethernet cable (CAT5e) are soldered to the [GCU](#). The top of the [GCU](#) heat sink is in the background, the two-channel splitter board is on the left, and the one-channel splitter board is on the right.

Figure 4.2b provides an exploded view of the [UWB](#)'s interior. The cable connectors on the left and top right are used to connect to the PMTs, while the connector on the bottom right is for the back-end cables. As shown, the [GCU](#) is sandwiched between a top and bottom heat sink to ensure proper cooling [131].



(A) Underwater box. Taken from [131].



(B) Underwater box component.

FIGURE 4.2: The Global Control Unit and its underwater box.

4.2.1 High voltage unit and splitter board

The HV required by these PMTs is generated by the HV-Unit. This custom module converts a 24 V DC input into high DC voltage using a cascade of half-wave doublers (Cockcroft-Walton multipliers). This innovative system eliminates the need for high-voltage cables or connectors. The module has an embedded microcontroller that monitors all operations and provides an RS485 half-duplex interface to the GCU.

The two-channel version of the splitter board is shown on the left of Figure 4.3. The splitter board has a dual purpose: a) it acts as a motherboard for the HV-Units and distributes the high voltage to the PMTs, and b) it decouples the DC high voltage from the AC signal of the PMT. The schematic of the decoupling is shown in Figure 4.4. The splitter board specifications include noise levels below 0.1 p.e. and high-voltage withstanding capability exceeding 2000 V.

The high-voltage unit specifications are as follows:

- Range of HV: 800 V - 3000 V in steps of 0.5 V, offering fine-grained control over the output voltage for optimal PMT operation
- Ripple: 10 mV peak-to-peak, ensuring stable voltage output with minimal noise that could interfere with PMT signals
- HV long-term stability: 0.05%, providing consistent high voltage supply over extended periods and ensuring reliable PMT performance
- Temperature coefficient: 100 ppm/°C, maintaining voltage accuracy even in varying temperature conditions
- Maximum output current: 300 μ A, delivering sufficient current to support PMT operations under high voltage conditions

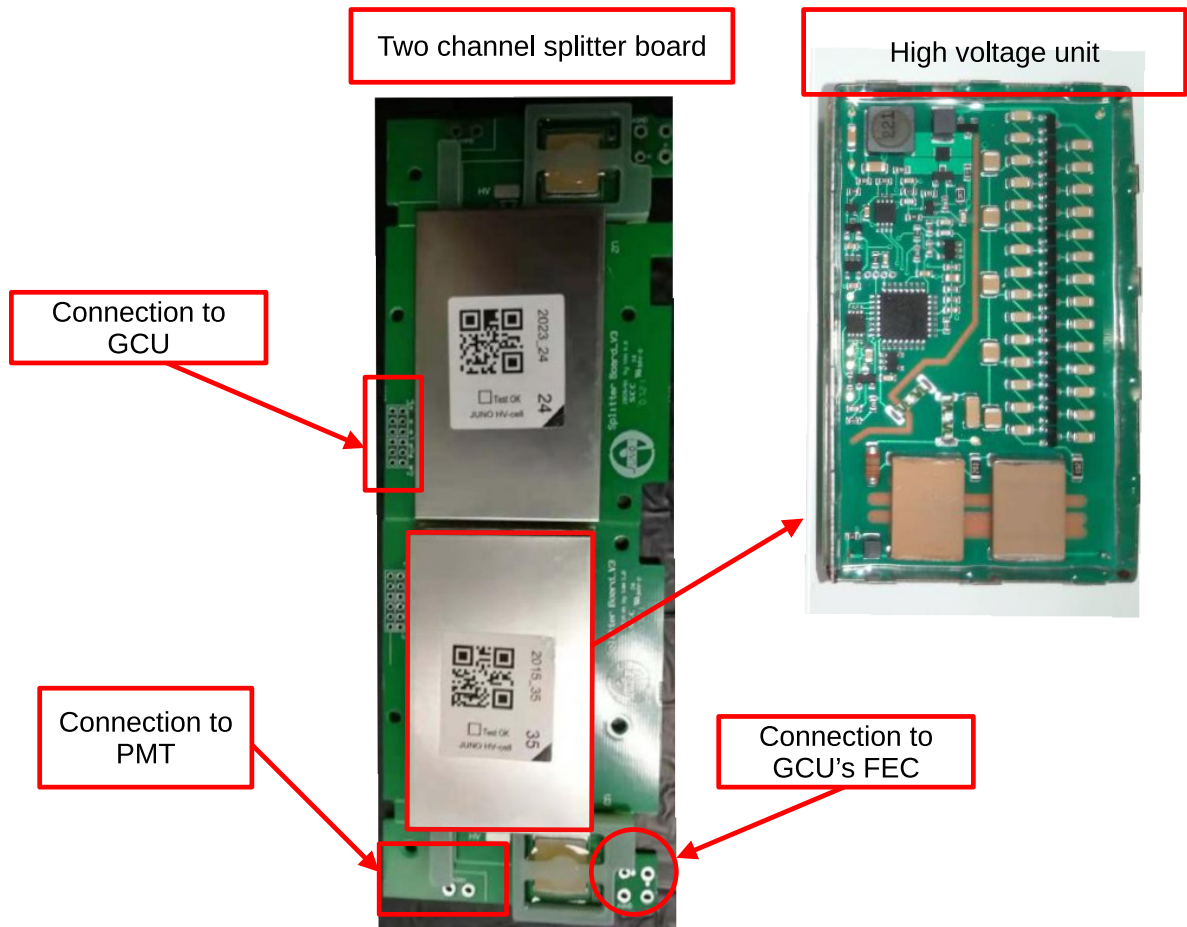


FIGURE 4.3: The two-channel splitter board (left) and the HV-Unit (right).

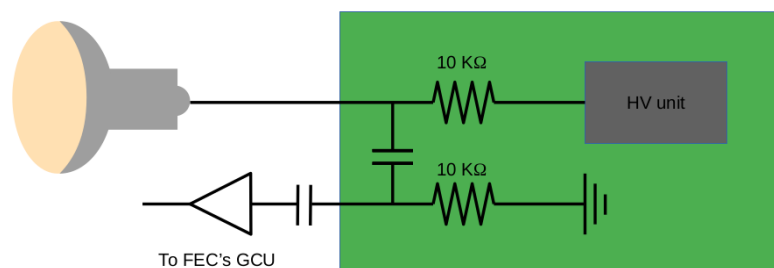
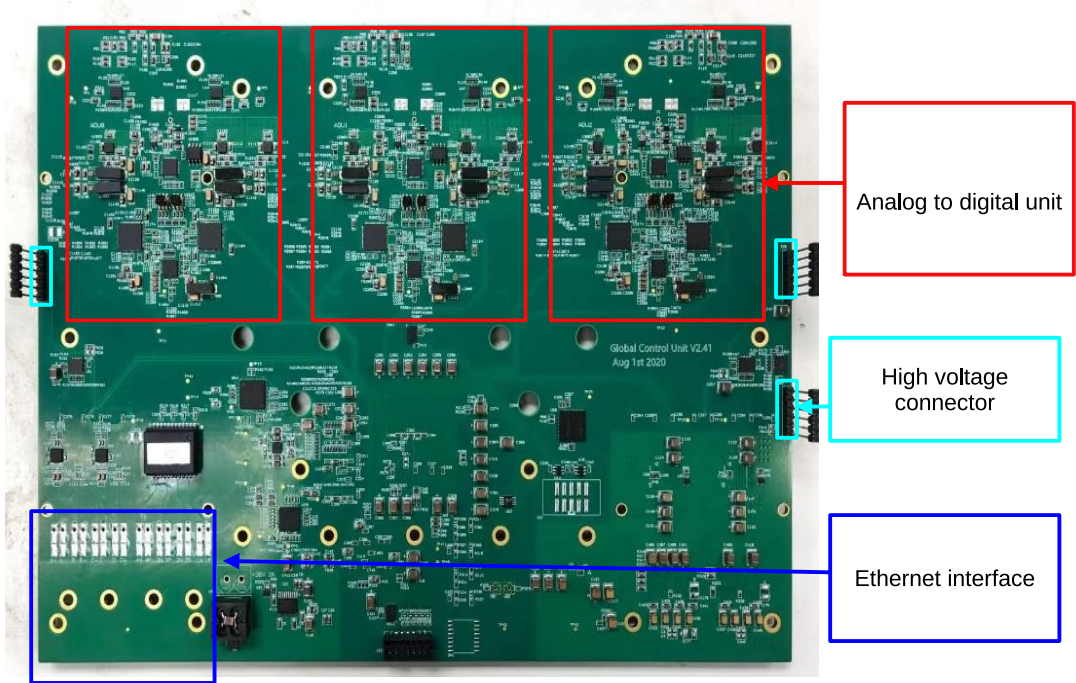


FIGURE 4.4: Splitter board decoupling scheme.

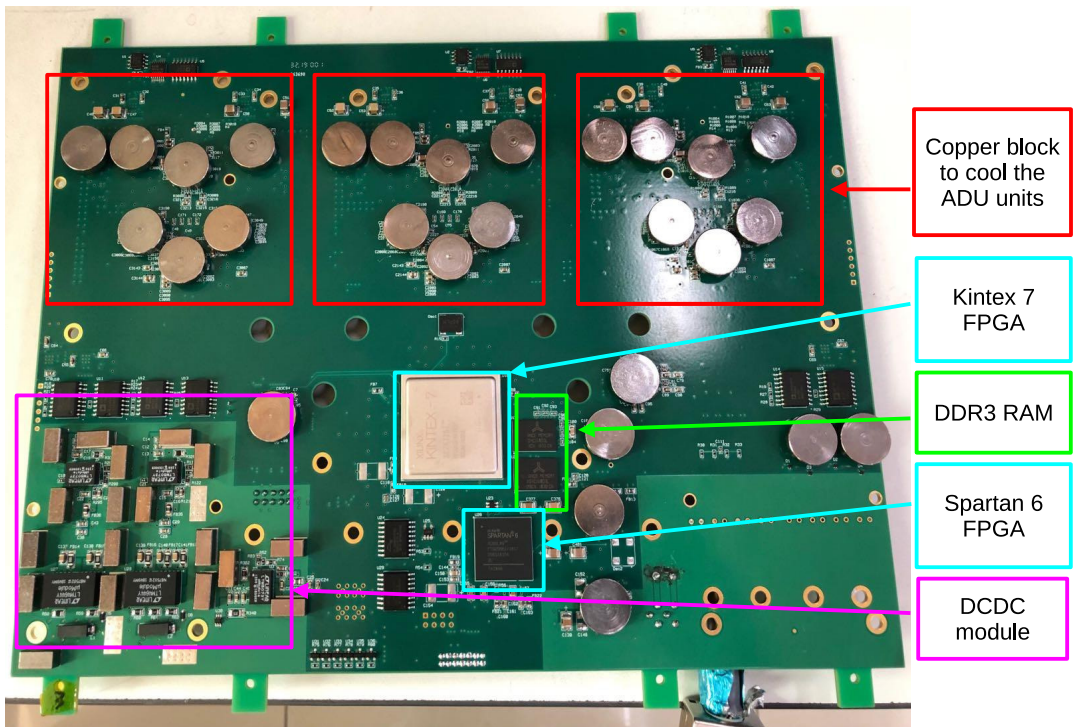
4.2.2 The Global Control Unit (GCU)

The **GCU** is a critical component of the JUNO readout electronics. It is responsible for acquiring the digital waveforms, generating local triggers, reconstructing time and charge information, and sending PMT waveform data to the DAQ upon trigger accept decision. An FPGA-based solution is particularly suitable for the demanding tasks of the JUNO front-end electronics. FPGA gives us more flexibility compared to **Application Specific Integrated Circuit (ASIC)** and a higher data rate compared to a micro-controller chip. A picture of the **GCU** board with its different modules and connection interfaces is shown in Figure 4.5. The **GCU** board and firmware development is

a joint effort from the Padova INFN and the IHEP electronic group. The parts detailed in this section are the ADU and its interface with GCU, an introduction to FPGA and their usage on the GCU, and finally, the implementation of S-link and A-link.



(A) Top view of the GCU.



(B) Bottom view of the GCU.

FIGURE 4.5: The Global Control Unit board with its main hardware component.

Analog to Digital Unit (ADU)

The ADU is the module on the GCU that performs the digital conversion of the PMT signal. The ADU board was developed in China, and it is a collaboration between the IHEP and Tsinghua University. From the underwater electronic requirements, the specific requirements for the ADU are the dynamic ranges and the energy resolution. To meet a wide dynamic range, two gains are implemented on the ADU for handling signals of varying intensities: one low gain range (8:1) and one high gain (1:1). The amplification on the ADU is performed by a custom current amplifier ASIC, called Front-End Chip (FEC).

The other requirements of the ADU are related to its FADCs. The FADCs digitize signals using a 14-bit resolution, providing precise signal representation. A sampling rate of 1 Gbps ensures high temporal resolution and capture of rapid signal changes on the FADC level. An effective number of bits (ENOB) of 10 guarantees high fidelity for input frequencies (f_{in}) up to 200 MHz at a sampling rate of 1 Gbps and an input level of -1.0 dBFS (decibels relative to full scale). Additionally, power consumption requirements are placed on the FADCs, with a maximum of 800 mW. Spurious-Free Dynamic Range (SFDR) is specified to be -68 dBc for input frequencies up to 200 MHz at 1 Gbps and -1.0 dBFS input level, thereby ensuring minimal harmonic distortion and spurious signals. The final requirement of the FADC with regard to differential non-linearity is that it should be less than ± 0.5 LSB, while the integral non-linearity must be less than ± 1 LSB.

In addition to those specifications from physics, two additional requirements on the ADU are needed: adjustable self-test pulse injection to perform tests and calibration of the electronic and over-voltage protection. The adjustable self-test pulse injection feature allows us to check the status of the entire electronics chain by generating a test pulse at the input of the FEC.

Since three PMTs are connected to a single GCU, three ADUs are on the GCU board. The path the PMT signal takes to the GCU is shown in Figure 4.6. As the ADU receives the charge (current signal) from one PMT, the FEC converts it into two voltage signals with two different gains. A balun converts the single-ended signal to a differential pair signal before entering the FADC.

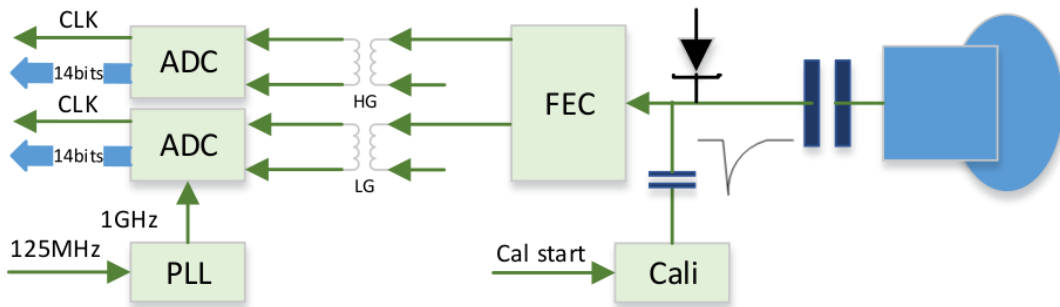


FIGURE 4.6: The working principle of the Analog to Digital Unit module on the GCU board.

The sampling clock of the FADC is generated by an external PLL (Phase-Locked Loop) mounted on the ADU. The Phase-Locked Loop receives the system clock of 125 MHz from the GCU and provides a low jitter (100 fs Root Mean Square (RMS)) 1 GHz clock to the FADC. Figure 4.7 shows FADC and FEC chips.

The Kintex-7 series, developed using a 28 nm process technology, offers superior integration and performance at a comparatively low cost. The Kintex-7 provides extensive **General-Purpose I/O (GPIO)** options with 350 **High-Range (HR)** pins and 125 **High-Performance (HP)** pins, meeting the demands of the on-board peripherals. Spartan-6 FPGA is built on a slightly older 45 nm process technology. The Spartan-6 series includes fewer **GPIO** and smaller memory blocks compared to the Kintex-7 series, but it adequately supports the system's fail-safe functionalities. The model of for the FPGAs used by GCU are XC7K325T for the Kintex-7 and XC6SLX16T-FTG256 for the Spartan-6.

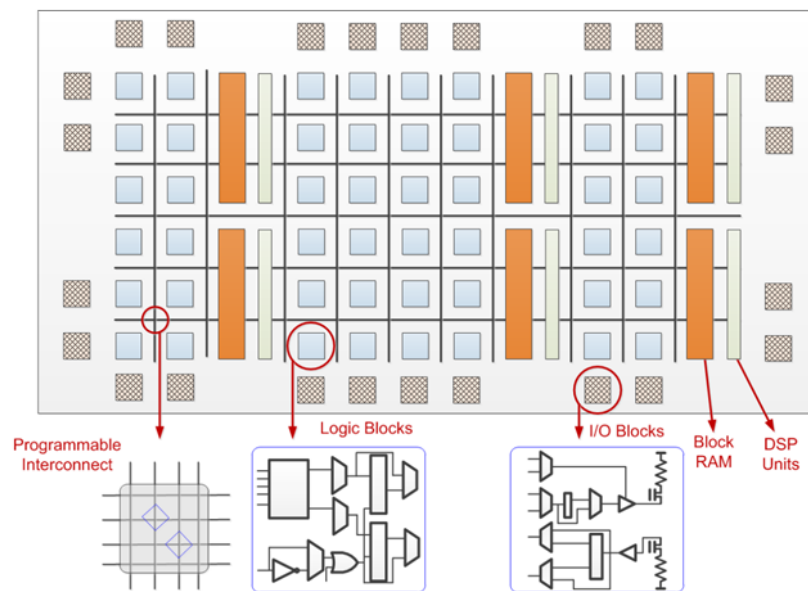


FIGURE 4.8: The basic architecture of an FPGA. Taken from [134].

Kintex-7 FPGA firmware structure The firmware structure of the Kintex-7 FPGA, shown in Figure 4.9, is meticulously designed to manage various subsystems and functionalities of the GCU efficiently. The clock generator module generates the necessary clock signals for all operations within the FPGA. The **Mixed-Mode Clock Manager (MMCM)**² inside FPGA use the local oscillator and **BEC** clock to generate the reference clock and the phase clock for the jitter cleaner (Si5345), respectively. Si5345 generates 4 clocks at 62.5MHz, for 3 LMX2581 and K7 FPGA. Each LMX2581 outputs 2 clocks at 1GHz for the ADCs, while the FPGA's **MMCM** generates most of the clocks required for internal logic. The 500MHz clock returned from the ADC is divided down to 125MHz for the ADC data sampling clock using **BUFIO** and **BUFR**. The red arrows in Figure 4.9 represent the clock signal.

The **ADU** block designed on the firmware is responsible for ADC **Low-Voltage Differential Signaling (LVDS)** data capture from the 6 ADC. The storage management component handles digital data storage within the FPGA. Three blocks are designed on the firmware to perform this: ring buffer, L2 buffers, and DDR controller. A ring buffer is designed to manage trigger latency and time domain crossing. The Level 2 (L2) buffer is designed to accommodate global trigger data packages. This buffer is structured to hold up to 16 events per channel across 6 channels, effectively managing a considerable amount of data simultaneously. Each event stored in the L2 buffer consists of 1000 data points, each occupying 2 bytes of memory, summing up to 2kB per event.

The data processing logic is at the heart of the FPGA's functionality. It processes the digital data obtained from the **ADU**, performing necessary computations, like computing the Time-Charge (T/Q) pair, handling the trigger accept, and making the HG/LG range decision. The basic encode/decode protocol between **BEC** and

²**Mixed-Mode Clock Manager (MMCM)** is a clock management block in Xilinx FPGAs, used for generating, conditioning, and phase-shifting clock signals, as well as reducing jitter and enabling dynamic reconfiguration.

GCU is modified **Trigger Timing and Control (TTC)**³ link protocol. Moreover, the synchronization PTP protocol principle is based on the IEEE 1588 protocol.

IPBus⁴ and TCP/IP⁵ mixed protocol to perform the **DAQ** and the **DCS** connection. The firmware also controls and monitors the high-voltage units that power the PMTs. HV-Unit can be accessed indirectly through dedicated forward ports of GCU by DCS commands. The IPBus protocol and IPBus user register interface implement all the control and status registers, including synchronization-related registers such as error counters and tap counters and DAQ configuration registers such as trigger latency.

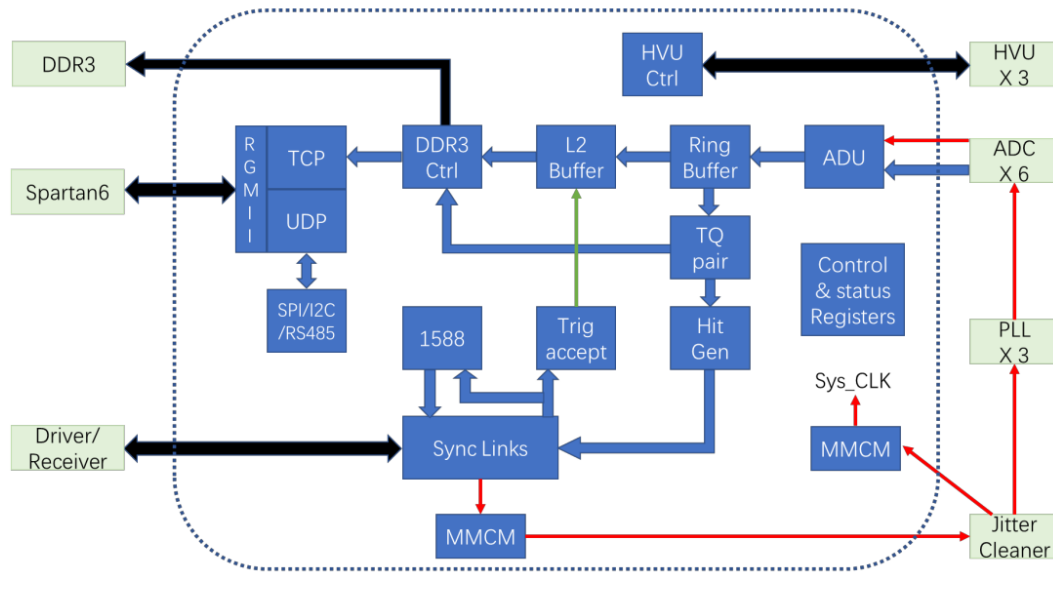


FIGURE 4.9: FPGA firmware logical structure.

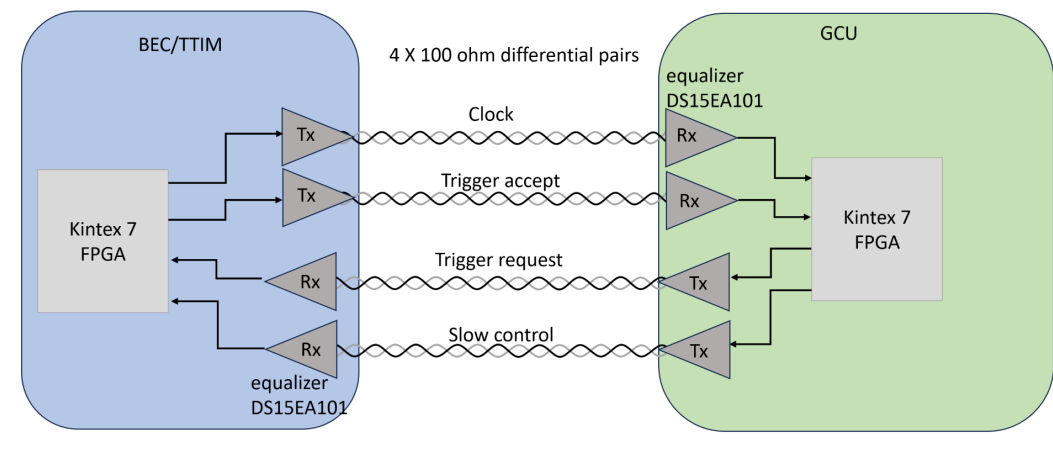


FIGURE 4.10: The synchronous link, all four pairs of a CAT6 cable.

³see section 6.2.2 for more details

⁴Developed collaboratively by CERN for the **Compact Muon Solenoid (CMS)** experiment, the IPBus was initially designed to control the trigger and readout systems of **Micro Telecommunications Computing Architecture (μ TCA)** or TCA-based hardware over Gigabit Ethernet. The IPBus operates on a simple Internet Protocol (IP) based control system, using UDP at the transport level.

⁵TCP/IP, or Transmission Control Protocol/Internet Protocol, is the fundamental communication protocol suite for the internet and networks. It comprises two primary protocols: TCP, which ensures reliable data transmission by confirming the delivery of packets and managing packet loss, and IP, which is responsible for addressing and routing packets to their destination across networks. TCP/IP provides a standardized method for transmitting data between devices.

The synchronous link As a critical component of the timing and trigger system, the synchronous link facilitates a communication channel between the front-end electronics and the back-end electronics. This channel provides simple, deterministic, and low-latency bidirectional communication. The physical medium consists of a standard CAT6 Foiled Twisted Pair cable (FTP cable). On the front-end electronic side, the twisted pairs are soldered directly onto the board, while on the BEC side, they are secured with RJ-45 connectors. The cables can extend up to 100 m, and LVDS scheme is employed to transmit signals over this distance. Signals are sent through the cable and recovered on-board by cable equalizer chips before reaching the FPGA.

The synchronous link utilizes all four twisted pairs of the Ethernet cable for bidirectional communication. Specifically, two pairs transmit data from the BEC to the GCU, and two pairs handle data transmission from the GCU back to the BEC. The direction from the BEC to the GCU sends two types of signals: one is a 62.5 MHz clock, and the other is the synchronization protocol operating at 125 Mbps. Conversely, for the GCU to BEC direction, the two pairs carry 125 Mbps signals; one is dedicated to the trigger request, and the other to slow control communications. The structure of this link is illustrated in Figure 4.10.

The asynchronous data readout and slow control link The asynchronous data readout and control for the GCU are managed via CAT5e UTP cables utilizing Ethernet readout with the IPBus and TCP/IP protocols. The DCS register is accessed via the UDP/IPBus core, which facilitates direct interactions with the system's control registers. DAQ flow is controlled using a commercial TCP/IP IP core, ensuring robust data handling.

GCU other on-board peripherals

DDR3 memory As mentioned in section 4.1.1, if the detector's event rate suddenly increases, normal readout operations through IPBus cannot import all the physics data that must be sent to the DAQ. Therefore, the GCU has a dedicated 2 GByte DDR3 Synchronous Dynamic RAM module. The memory can store about 1 second of continuous data, 0.3 second per channel. This allows the system to cope with a sudden increase in events, e.g., a supernova explosion and to read out all the data once the event rate returns to an average level.

Flash memory and EEPROM The GCU is equipped with two 256 Mbit flash memories, connected to each FPGA, and a 2 kbit Electrically Erasable Programmable Read-Only Memory (EEPROM). The smaller EEPROM memory stores network parameters, particularly the Media Access Control (MAC) address of both the Spartan-6 and Kintex-7. The content of the EEPROM can be accessed and modified via IPBus. The flash memories store the synthesized bitstream and automatically configure the FPGA after a power cycle. While the Xilinx Kintex-7 flash memory can always be re-configured, even at "run-time," the one connected to the Xilinx Spartan-6 should be programmed and fixed during the GCU production phase. Thus, the extra EEPROM memory is employed rather than saving the MAC address.

Clock jitter cleaner To enhance the sampling performance of the FADCs, the clock sent to the ADUs must have extremely low jitter characteristics. Therefore, the GCU utilizes a jitter attenuation chip capable of delivering ultra-low jitter clock signals at 90 fs RMS. Initially, the global clock transmitted by the BEC via the synchronous link is retrieved by the PLLs of two FPGAs. The first PLL is configured as a jitter cleaner, while the second PLL is used to extract the 125 MHz clock needed for the ADUs, among other functions. Before the clock is sent to the ADUs, it passes through an external ultra-low jitter cleaner chip. This cleaned clock is then returned to the FPGA and immediately forwarded to the ADCs for sampling.

4.3 Outside water electronics system

The underwater electronics are connected to two distinctive parts: the trigger system and the DAQ/DCS system. In this section, we describe the functioning of those two systems. For the trigger system, we detail the general trigger data flow, the hardware of the different boards, the timing protocol, and finally, the trigger schemes implemented in JUNO. The last part of the section describes the DAQ and DCS systems used in the experiment.

4.3.1 Low voltage power supply

A low-voltage power supply powers the UWB. Each UWB is provided with dedicated low-impedance power wires. The power supply used in the JUNO experiment must meet strong requirements to ensure good performance of the large PMT electronics. Here is a summary of the key specifications and features:

- Input: the power supply requires an input of 220 V AC
- Output: the power supply must provide $24 \times 36V$ ports for the UWB and one 12 V port for BEC with a maximum power rating of 40 W
- Voltage ripple: the voltage ripple must be below 5% to maintain stable voltage output with minimal noise interference
- Voltage accuracy: the voltage accuracy is crucial for precise operations and must be within 5%
- Protection function: the power supply has multiple protection functions to ensure operational safety: over-heat, overcurrent, and overvoltage protection
- Backups: several channels feature a hot backup, ensuring continuity of operation in the event of a primary channel failure
- Monitor: the power supply includes voltage and current monitoring and remote switch capability to provide accurate monitoring and control
- Cooling mode: the power supply is cooled by the airflow in the electronic room, requiring no additional cooling mechanisms
- Long-term reliability: the required mean time between failures is over 50,000 hours (approximately 6 years)

The low-voltage power supplies are installed in the cavern inside the electronics room.

4.3.2 Trigger system hardware

The diagram 4.11 illustrates the architecture and data flow of the JUNO trigger and synchronization system. Here is a detailed description:

1. Each GCU box manages three PMTs⁶ and generates the trigger request. To monitor the 20012 PMTs, 6681 GCU are used
2. Each BEC handles data from up to 48 GCU and, thanks to the Trigger and Timing Interface Mezzanine (TTIM), aggregates the trigger request from the GCU, then send the aggregated data to Reorganize and Multiplex Unit (RMU)

⁶For installation consideration, a very small amount of UWB are connected to one PMT or two PMTs.

3. **RMU** handles the data from 20 **BEC**; the 155 **BEC** feed into 8 **RMU**; **RMU** further organize and multiplex the data streams, preparing them for the **Central Trigger Unit (CTU)**
4. The **CTU** is the board responsible for generating the global trigger decisions; it receives processed data from the **RMU** and integrates inputs from other sources, such as Top tracker , and calibration systems

The following section describes the hardware of the different boards constituting the trigger system: **BEC**, **TTIM**, **RMU**, and **CTU**.

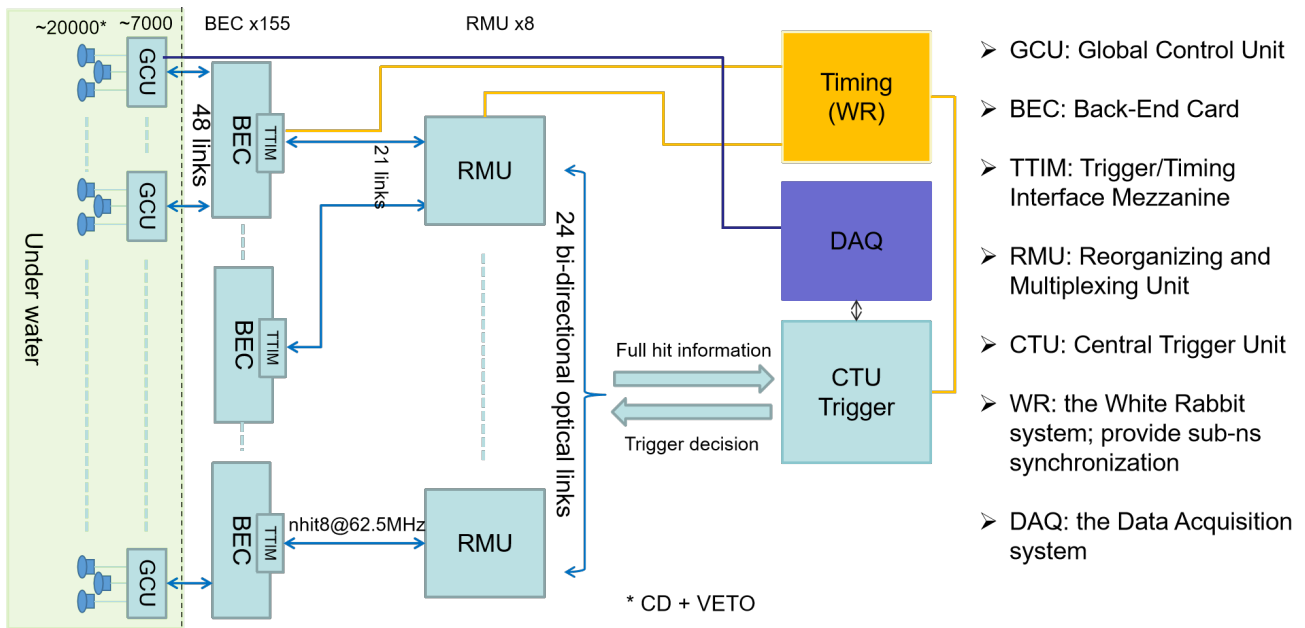


FIGURE 4.11: Schematic view of the JUNO trigger system. Taken from [135].

Back-End Card (BEC)

The **BEC** represents the first layer of the dry electronics, which is responsible for direct communication with the underwater electronics. The **BEC** is designed to root the incoming trigger request signal and **TTC** command from the **GCU** and distribute a 62.5 MHz clock signal to the **GCU**, and the trigger accepts the signal from the **CTU**. The **BEC** main channel then roots those four high-speed data links for 48 **GCU**s for 192 differential pairs on the PCB. To achieve that specification, we chose the following design of **BEC** composed of two types of modules: RJ45 mezzanine cards and baseboard.

Each RJ45 mezzanine card provides 8 physical RJ45 connection sockets and contains 16 equalizers, compensating for losses from propagation along the copper cables. This design allows for easy replacement in case of equalizer failure. A single **BEC** can connect up to 6 mezzanines. The baseboard provides power distribution and routes all the signals from the RJ45 mezzanine cards to the two FMC connectors used to plug the **TTIM** board.

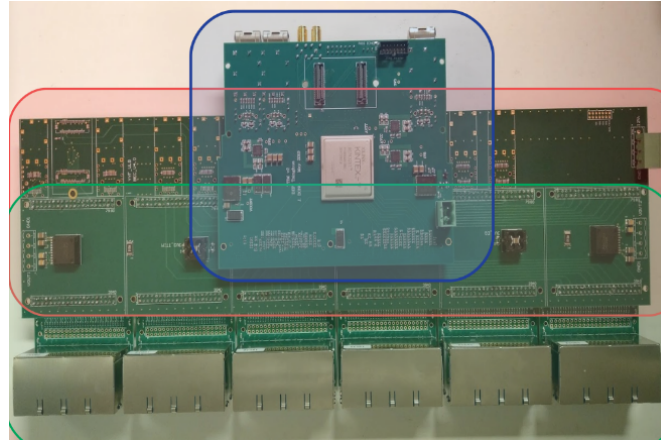


FIGURE 4.12: Picture of the back-end card. Trigger and Timing FMC is shown in the blue box; the red box represents the baseboard, and the green box contains 6 RJ45 mezzanine cards.

Trigger and Timing Mezzanine card (TTIM)

The **TTIM** board is an integral trigger and timing system component. It interfaces with 48 synchronous links originating from 48 different **GCU**. Each link comprises four input pairs, totaling 192 LVDS pairs per board. Beyond interfacing with the **GCU**, the **TTIM** is connected to the **RMU**, which links to the **CTU**. This connection utilizes bidirectional 1.25 Gbps optical links, essential for forwarding and receiving trigger information.

The board employs a Xilinx Kintex-7 FPGA, model XC7K325T-FFG900, ensuring it meets all operational requirements. The **TTIM** also implements a interface for a **White Rabbit (WR)** node. The **White Rabbit (WR)** is used for synchronizing to the global clock the **BECs** and the **GCUs**, and providing slow-control functionalities for the **BEC**. A block diagram of the **TTIM** board is illustrated in Figure 4.13.

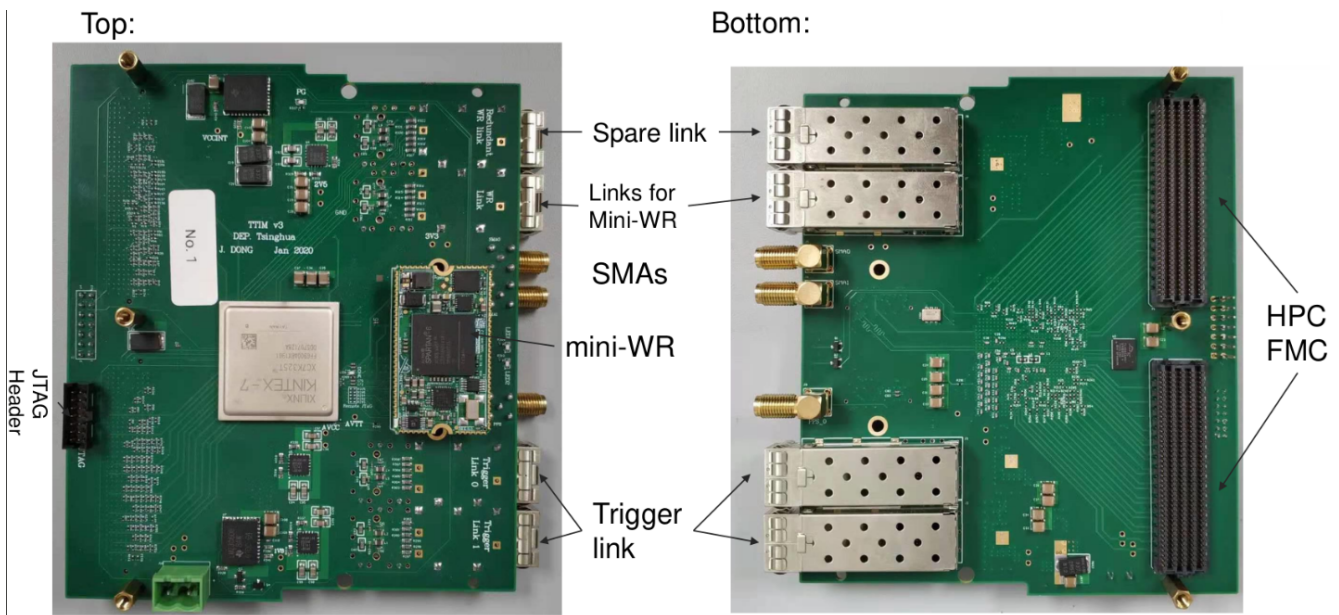


FIGURE 4.13: Top and bottom views of **TTIM** card.

Reorganize and Multiplex Unit (RMU)

The **RMU** [136] hosts three mezzanine cards responsible for data concentration tasks. Each mezzanine board has eight **Small Form-factor Pluggable (SFP)** cages. The mezzanine boards feature two distinct clocks and a programmable SPI flash⁷ for FPGA configuration. Based on a Kintex-7 FPGA, the mezzanine board utilizes all 8 serial links. The input data from the **BEC** are received through 7 links, aggregated into a single output stream, and then delivered to the **CTU**. This operation is performed on each of the three mezzanine optical link cards, so a **RMU** connects 21 **BEC** in total.

The **RMU** also includes three power distribution units to supply power to the mezzanine optical link cards. The control unit of the **RMU** is implemented by the μ SOP board [137], which provides control functions for the entire **RMU** environment. The μ SOP performs the slow control tasks and features two Ethernet ports, one of which implements the **WR** protocol to distribute the clock to the **RMU**. The **RMU**'s architecture, shown in 4.14, including its main modules, the μ SOP, and the optical mezzanine, is finalized and adopted in 2020 by the **JUNO** experiment.

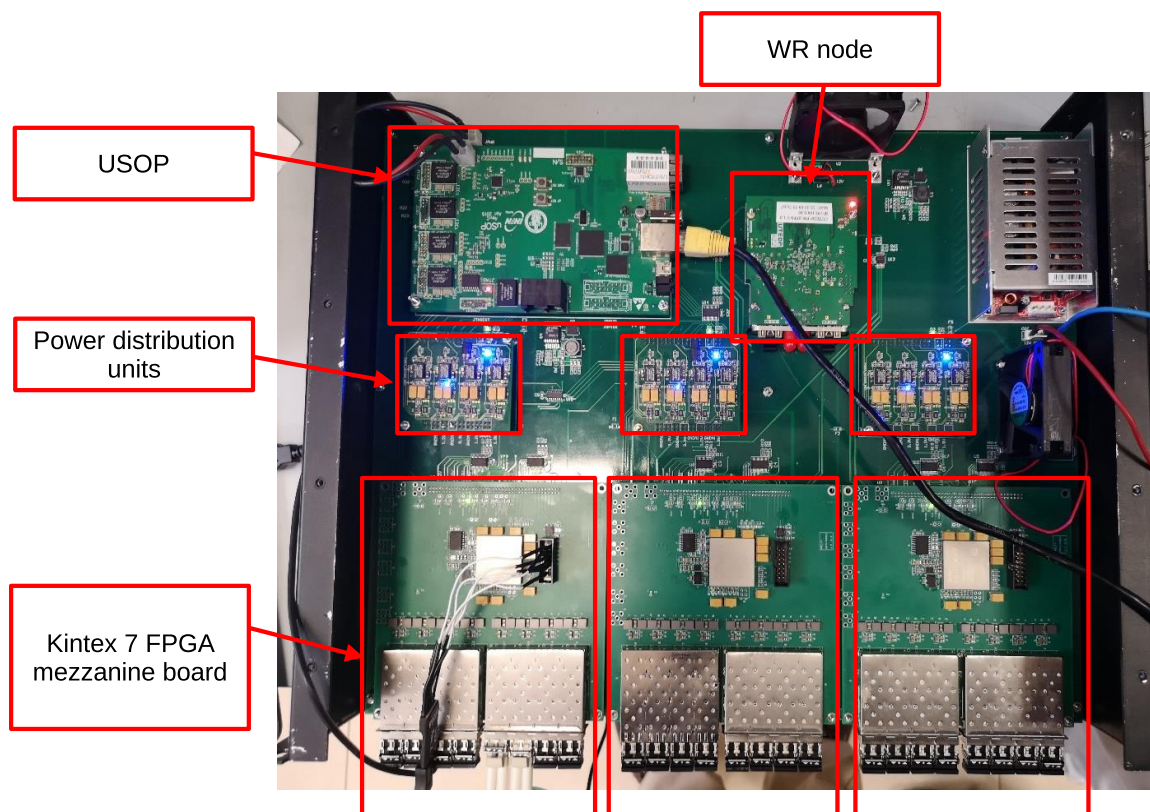


FIGURE 4.14: Picture of **RMU** board.

Central Trigger Unit (CTU)

The **CTU** is a pivotal **JUNO** hardware trigger system component. A picture of the **CTU** is shown in Figure 4.15. Its primary objective is to generate the trigger from **GCU** waveforms. The **CTU** utilizes at least twenty-four bi-directional optical links, each maintaining fixed latency, with a line rate of 5 Gbps to the **RMU**. The timing

⁷Programmable SPI flash is a type of non-volatile memory that can be programmed to store data, such as firmware or configuration settings, using the Serial Peripheral Interface (SPI) bus. It allows for easy updates and reprogramming of stored data in embedded systems.

synchronization is employing mini-White Rabbit (mini-WR) technology to ensure precise synchronization. The interface also connects to other systems and features large FPGAs to implement the Vertex Fitting Logics. Clock distribution and synchronization are also concerns at the CTU level. The CTU system clock comes from the mini-WR at 125 MHz, while the required system clock operates at 62.5 MHz. The system clock edge is aligned to the **Pulse Per Second (PPS)** signal to avoid phase uncertainty after a power cycle. The quality and skew between the PPS and the system clock are tested to ensure reliable operation.

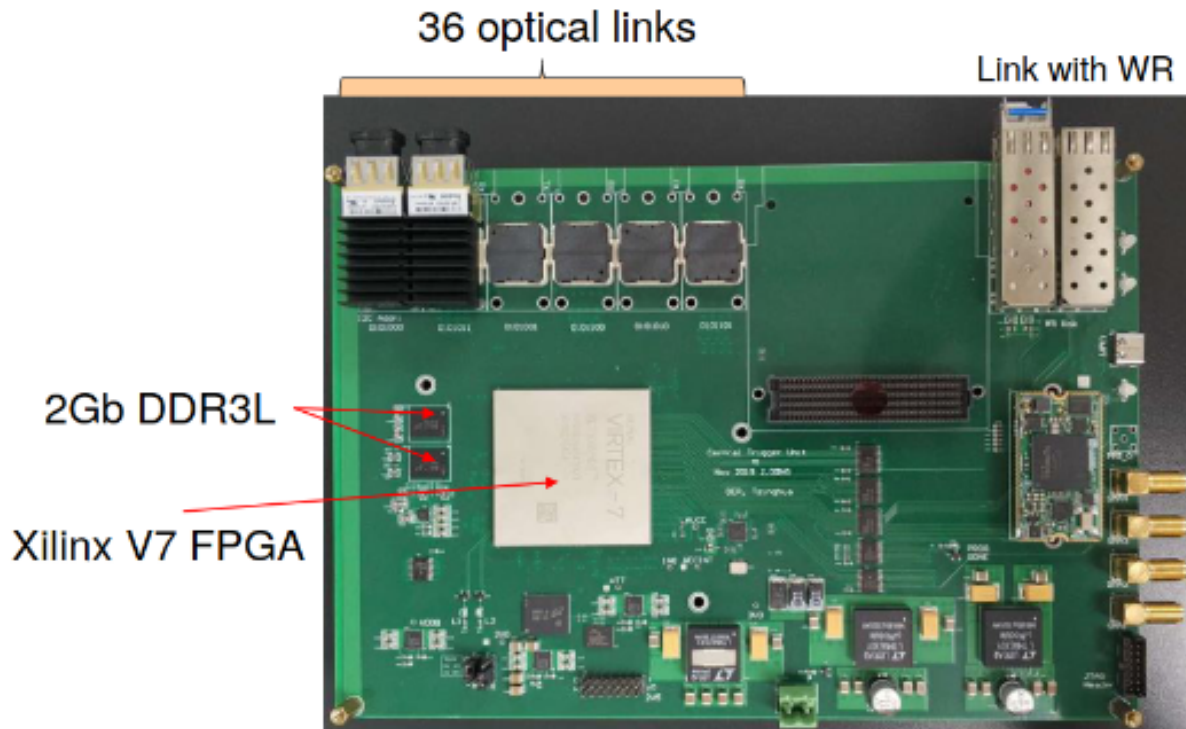


FIGURE 4.15: The Central Trigger Unit board.

CTU Firmware Architecture The firmware architecture of CTU, shown in Figure 4.16, in the JUNO experiment consists of several key modules, each responsible for specific functions:

- **RMU Links:**
 - connects to the RMU through 24 to 32 bi-directional 5 Gbps optical links
 - handles the reception of hit information from the RMU
 - maintains fixed latency after the power cycle
- **Trigger module:**
 - generates trigger accept waveform based on input data from the RMU and send back the trigger accept waveform to the RMU
- **WR interface:**
 - ensures synchronization of the local clock and system time with the global clock using the WR protocol
 - handles slow control commands
- **Clock and timestamp Generation (CLK/TIME):**

- generates clock signals for other modules
- produces timestamps to ensure synchronized operation across the system
- **Control registers:**
 - configures various modules of the CTU
 - sets operational parameters and monitor the status of system components
- **Other interfaces:**
 - connects the CTU to other systems such as calibration and monitoring (Calib, DAQ)
 - facilitates integrated operations and data flow
- **Monitor:**
 - tracks the FPGA's temperature and voltage levels
 - ensures the hardware operates within safe and optimal conditions

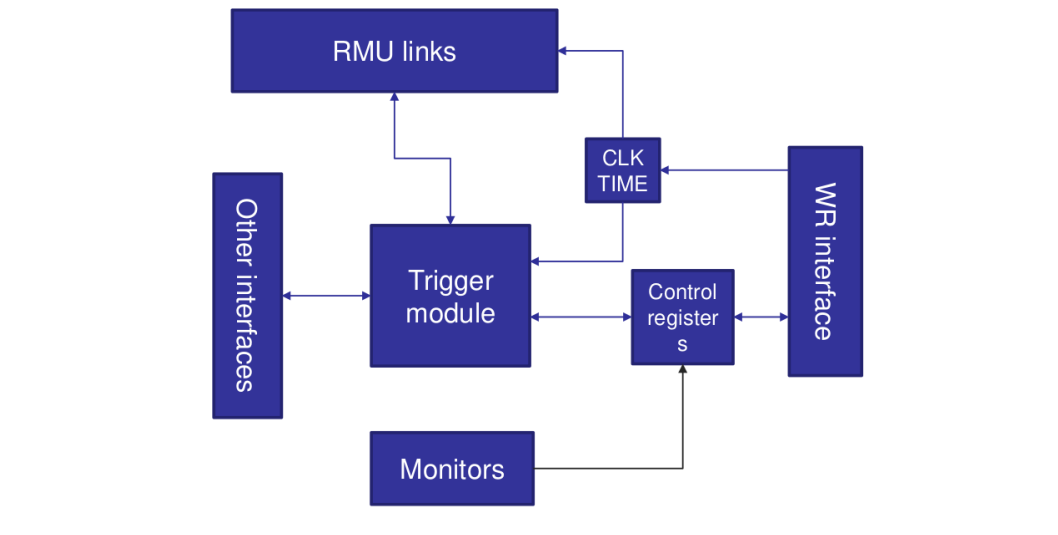


FIGURE 4.16: Firmware structure of the CTU.

4.3.3 Trigger schemes

A high-precision ADC and good time resolution are indispensable to achieve the energy resolution required by NMO physics. A global clock and triggering systems are crucial to ensure high-speed and efficient readout of the waveforms of 20,000 PMT signals. To convince about the necessity of triggering, let us perform a simple calculation to get the generated data in one second. The timing windows is $1 \mu\text{s}$, 16 is the number of bits⁸ for encoding the waveform on one time stamp, 40 kHz is the dark noise of the PMT⁹, and we have around 18 000 PMTs used for the CD. The product of these number gives us 11.5 Tbps bandwidth. Without triggering, this would be the amount of data needed to be handle by the online software, which is unnecessary and impractical. Data aggregation is also essential, as no computer can directly connect to and read out 20,000 analog signals. For example, with a global trigger algorithm, we can divide the data sent to the online software by 40.

⁸We use 14 bits from ADC and 2 more bits for the padding.

⁹From the PMT mass testing and characterization the mean DCR is 40 kHz [86].

Global Trigger The global trigger scheme relies on information from all PMTs to form a unified trigger decision that initiates the readout process for all instrumented PMTs. This scheme uses a synchronous link to transfer hit information from the front-end electronics to the CTU and to send validated trigger timestamps back to the front-end electronics. The global trigger is advantageous for energy reconstruction, as it records waveforms even for channels where PMT signals fall below individual thresholds, allowing the detection of low-charge p.e.. However, the global trigger is limited by the 1 Gbps bandwidth from the DAQ link. This limitation becomes critical during high-rate events such as a neutrino burst from a supernova explosion.

Decentralized Trigger In contrast, the decentralized trigger scheme operates through self-triggering channels at GCU level that locally save their charge and time information and transmit this data to the DAQ system. This scheme is beneficial during supernova neutrino bursts, where data rates can drastically increase. The threshold for triggering can be individually set for each channel, enabling precise extraction of digitized data for further analysis. The decentralized trigger supports the "QT readout" by storing self-triggered data in a local buffer and the "complementary DDR readout" by saving entire waveforms on external memory [138].

Global Trigger Algorithms Three trigger algorithms have been discussed for JUNO:

1. **Multiplicity trigger** Dark noise can be mistaken for actual neutrino events. To address this, the CTU employs a multiplicity threshold based on the number of fired PMTs to filter out dark noise. For instance, setting the multiplicity threshold around 400 effectively separates dark noise coincidence events from IBD neutrino events with a minimum deposit energy of 0.7 MeV. However, this method becomes less efficient for detecting solar neutrinos and supernova elastic scattering neutrinos, which exist at lower energy levels (as low as 0.2 MeV) and have a multiplicity distribution that overlaps with PMT dark noise. This overlap increases the readout rate, necessitating higher bandwidth and more expensive hardware. The multiplicity trigger counts the number of fired PMTs within a 300 ns trigger window. Figure 4.17 shows the dark noise event rate as a function of the number of fired PMTs for different dark noise frequencies and trigger windows. A high trigger threshold is required to reject coincidences from PMT dark noise, which can sacrifice the detection of low-energy events.

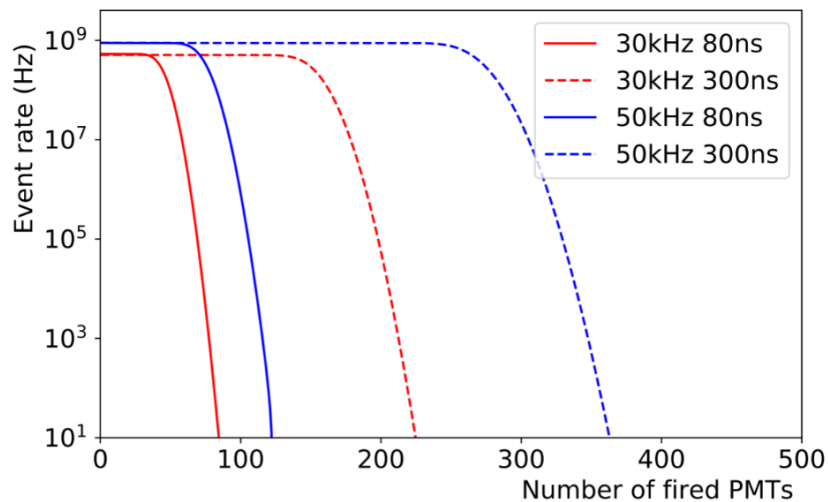


FIGURE 4.17: Dark noise event rate as a function of the number of fired PMTs. The full (dotted) lines use a time window of 80 ns (300 ns). Two dark noise frequencies (30 KHz and 50 KHz) are also considered [139].

2. **Vertex fitting trigger** To reduce the impact of PMT dark noise, a more sophisticated trigger scheme called vertex fitting [140] is implemented in the CTU. This method evaluates PMT information across all possible positions to find the most likely event vertex location. A charge weighted mean position algorithm is widely used in offline analyses to calculate the vertex position. Implementing a similar algorithm in the trigger system is very challenging. Unlike the multiplicity trigger, the vertex fitting method tests the PMT information with all possible positions and finds the most likely one among them. The vertex fitting concept is presented in Figure 4.18, and the detailed process contains the following aspects:

- Divide the whole detector volume into 179 cubic blocks. Since each block is treated as one position, the time difference caused by the dimension of the block should be negligible compared to the trigger window; on the other hand, a small block size will generate an unacceptable number of blocks. The size of the block should be optimized to compromise these two effects. The volume of the detector associated with one block is then a cube of $5 \times 5 \times 5\text{m}^3$.
- A **Time Of Flight (TOF)** correction map has been calculated and applied to the original PMT signals respectively for each VLF block. For events inside the block, the correction map could approximately compensate for the propagation time and merge the widely spread PMT hits to a much narrower time region; thus, a small trigger window could be applied.
- All local block trigger signals are logically "OR" to generate the final trigger.

The complete hit information from 8 RMU is used for vertex fitting. Although VFL modules are still under development, prototypes are being evaluated using Xilinx V5LX220 devices.

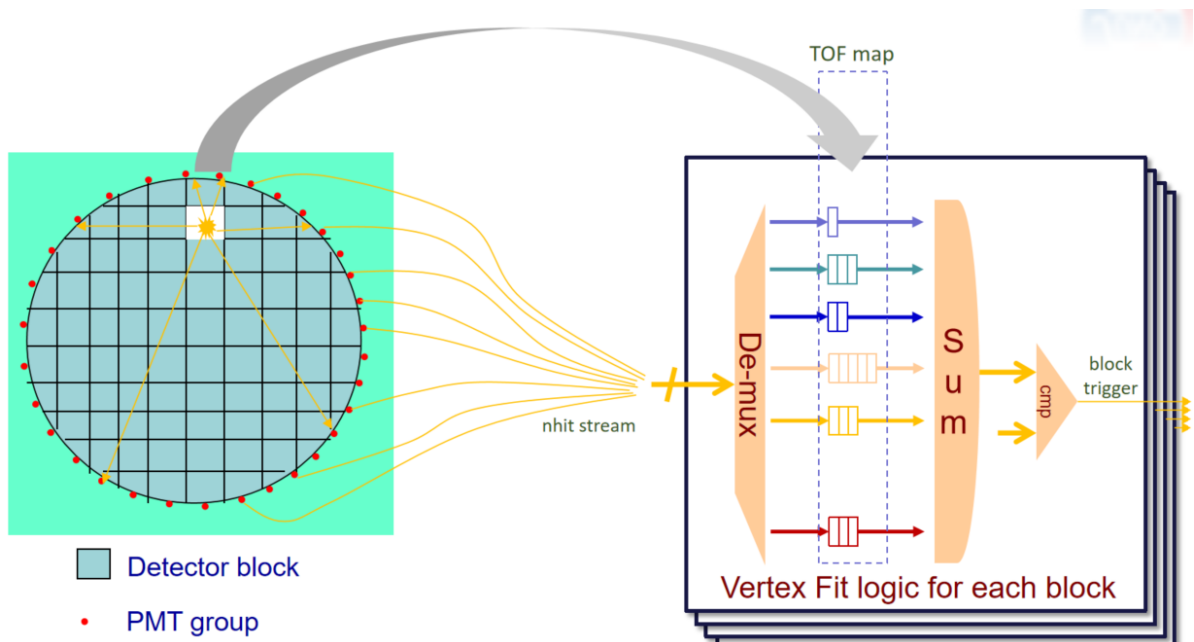


FIGURE 4.18: Vertex fitting concept in JUNO. On the left, an event occurs in the central detector's upper part, triggering several PMTs. On the right, a schematic view of the vertex fit logic, with corrections for the TOF for each PMT, before summing and sending to the trigger block. Taken from [140].

3. **Machine learning based trigger** We also study an alternative trigger to achieve a similar performance as the vertex fitting trigger but with fewer logic resources by using a firmware-implemented machine learning

model at the L1 trigger level. We treat the trigger decision as a classification problem and train a Multi-Layer Perceptron model to distinguish the signal events with an energy higher than a certain threshold from noise events. The technical details of the neural network development and training and its implementation in the hardware with the FPGA programming are detailed in [6].

4.3.4 Synchronization and clock distribution scheme for trigger system

The synchronization and clock distribution scheme is essential for ensuring high precision communication across all system components of JUNO experiment. This critical functionality is achieved by adopting **White Rabbit (WR)** technology. The **WR** was developed at CERN in collaboration with GSI Helmholtz Centre for Heavy Ion Research in Germany. The project began around 2006 as part of the effort to improve the synchronization of equipment used in particle accelerators. White Rabbit enhances the IEEE 1588 **Precision Time Protocol (PTP)** by providing sub-nanosecond accuracy and synchronization over Ethernet networks. It integrates Synchronous Ethernet and **PTP**, combining frequency and phase synchronization [4].

WR technology enables the distribution of a stable, low-jitter clock signal throughout the JUNO system, serving as a reference frequency crucial for the Front-End Electronics modules involved in waveform sampling and data processing. This system allows for sub-nanosecond phase alignment across the network and ensures that all **BEC**, **RMU**, and **CTU** nodes are synchronized with precision, leveraging **PTP** for consistent timestamp alignment across devices.

Despite the high synchronization capabilities of **WR**, the underwater setting of JUNO imposes significant constraints on its deployment. **WR**'s standard optical fiber implementation could be more suitable due to limited communication channels and the medium between the **BEC** and each Global Control Unit (**GCU**). To address this, JUNO has adapted its synchronization strategy to employ a hardware-based implementation of the IEEE 1588-2008 standard over Cat-5E copper cables. This method effectively maintains synchronization between global and local clocks within a window of \pm one clock period, providing a tailored solution that overcomes the environmental challenges of the experiment (IEEE Standard 1588-2008) [138].

The IEEE 1588-2008 standard [141] defines a protocol for precise clock synchronization, tailored explicitly for systems that use a multicast communication model between a master and timing nodes. In the JUNO experiment, this protocol is leveraged to address the synchronization needs between the back-end electronics and front-end electronics through a delay request-response mechanism. The specific steps involved in measuring and compensating the clock offset between the global time (t_{1g}) and the **GCU** local time (t_{1l}), ($t_{1g} - t_{1l}$) are depicted in Figure 4.19. The offset measurement and compensation procedure encompass eight critical steps:

1. Master timestamp Recording: the master logs the current timestamp (t_{1g}) and sends a synchronization message containing this timestamp to the slave.
2. Slave reception Time: the slave records the time of reception (t_{2l}) and computes the offset minus the delay from master to slave ($t_{1g} - t_{2l} = \text{offset} - \text{delay}_{ms}$).
3. Delay request: the slave sends a delay request back to the master and logs the transmission time (t_{3l}).
4. Master reception time: The master records the reception time (t_{4g}).
5. Master response: the master sends a delay response message containing the t_{4g} value.
6. Slave computation: upon receiving the delay response message, the slave calculates $t_{4g} - t_{3l} = \text{offset} + \text{delay}_{sm}$.
7. Offset computation: assuming $\text{delay}_{ms} = \text{delay}_{sm}$, the slave computes the offset as $\text{offset} = \frac{(t_{1g} - t_{2l}) + (t_{4g} - t_{3l})}{2}$.

8. Clock correction: finally, the slave adjusts its clock based on the calculated offset.

This protocol enables individualized offset correction procedures for each slave, allowing continuous alignment checks and adjustments throughout the experiment. The precision and stability of the clock signal are essential for the JUNO trigger system. This system coordinates the timing between components, such as the front-end electronics boards, BEC, RMU, and CTU, ensuring accurate event detection and processing. The efficiency of trigger decisions and the accuracy of timing information rely on this maintained synchronization of the different boards in the trigger scheme.

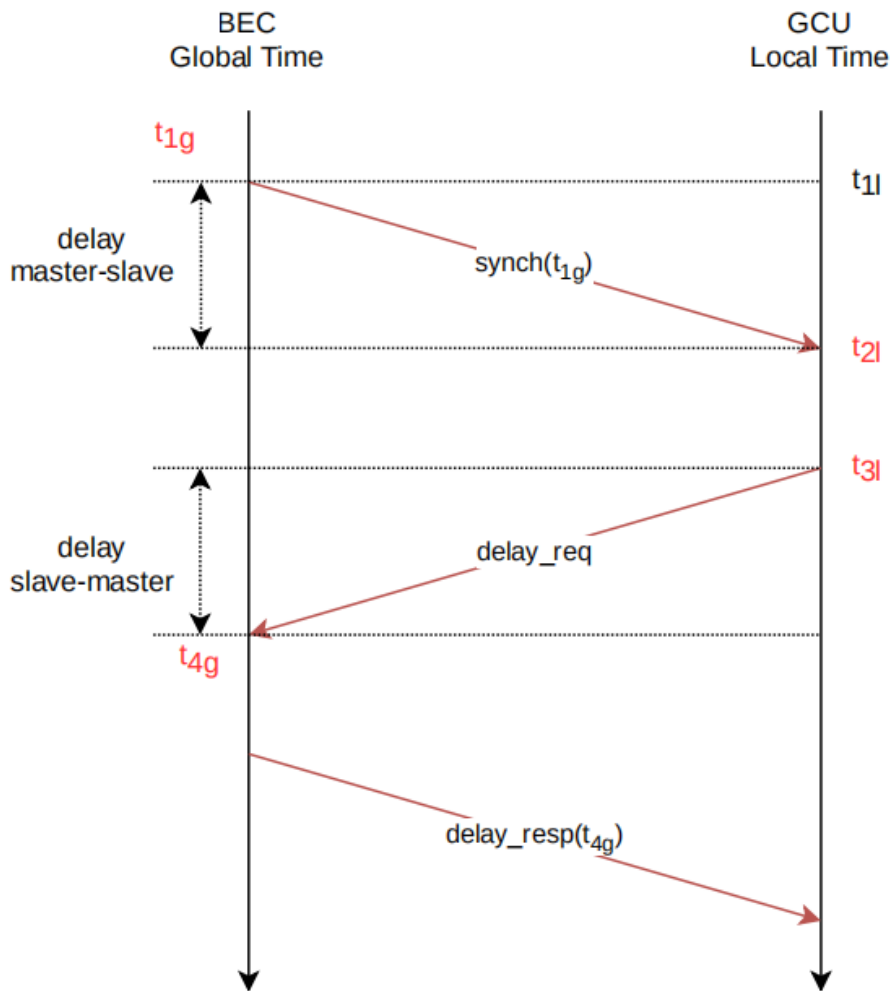


FIGURE 4.19: Illustration of the White Rabbit clock synchronization between BEC and GCU. Taken from [138].

Performances and limits of PTP The PTP has several inherent limitations [138, 141, 142] that affect clock alignment accuracy in the JUNO timing system. As PTP does not specify the clock frequency, lower clock frequencies lead to poorer time resolution. Another limiting factor is related to the time stamping. To achieve time synchronization in the nanosecond range, hardware-assisted time stamping is required due to the time-critical nature of this operation. Standard ethernet local area network rarely achieves better than microsecond level accuracy due to traffic-dependent packet latency. The best PTP performance over Ethernet is achieved with Deterministic Ethernet, which uses time scheduling to ensure low and bounded latency for critical messages. The JUNO timing system

relies on deterministic latency for its 20 012 channels. All message-based synchronization protocols suffer from asymmetry in the physical medium and data link layer implementation. PTP is no exception to this rule. The assumption that the delay from master to slave equals the delay from slave to master ($delay_{ms} = delay_{sm}$) is not valid in the presence of asymmetry.

4.4 Data Acquisition and Detector Control System

The **Data Acquisition (DAQ)** and **Detector Control System (DCS)** are critical components of the JUNO experiment, ensuring efficient data collection, processing, and monitoring. The DAQ system is responsible for handling the vast amounts of data generated by the PMTs, while the DCS oversees the operational status and environmental conditions of the detector. The following sections provide descriptions of the DAQ and DCS, highlighting their architecture, functionalities, and the technologies employed to meet the JUNO demands.

4.4.1 Data Acquisition System (DAQ)

The **Data Acquisition (DAQ)**, detailed in [4, 63, 143, 144], is designed to handle approximately 40 GBytes per second of triggered waveform data and trigger-less time and charge data through CAT5e Ethernet cables. This data comes from the 20012 20-inch PMTs (17612 in the Central Detector and 2400 in the water Cherenkov detector) and the 25600 3-inch PMTs. These events are built and processed by the **Online Event Classification (OEC)** algorithm and the software trigger to reduce the data rate by approximately 500 times. The resulting data is transferred to the cluster over an Internet connection with a bandwidth of 1 Gbps.

The JUNO electronics must be capable of handling close by supernova explosions, capturing over thousands of events within 10 seconds. The DAQ system must ensure lossless readout of these data and continuously monitor supernova bursts during detector calibration. The unified data flow is designed to read out the T/Q and PMT waveform data streams from the **GCU**, process, and store them on disks without any loss. The diagram 4.20 illustrates the hardware deployment showcasing the network infrastructure and interconnections between various components. The setup is divided into three main sections: the underground electronics room, the ground online computer room, and the control room.

In the underground electronics room, there are 6681 **GCU**, each designed to be linked to the DAQ thanks to an 1Gb link. In the cavern, 160 access switches, (48x1Gb and 4x10Gb ports), and eight aggregation switches (48x10Gb and 4x100Gb ports) are installed in the two electronics rooms. Each **GCU** is connected to the access switches via 1Gb connections, and the access switches are connected to the aggregation switches through 10Gb links.

The ground online computer room features two core switches with 64x100Gb ports each receiving the data from the 8 aggregation switches. This room also contains 128 computing nodes, each with 2 x 2.9G 16C CPUs, 384GB of memory, and 2 x 25Gb network interfaces. The computing nodes are connected to the core switches via 100Gb links. Additionally, there are four storage servers, each in a 4 Unit form factor¹⁰, connected to the core switches through 100Gb links, forming part of a disk array with a total capacity of 200TB. The room also includes four manage servers, also in a 4U form factor, connected to the core switches, and four management switches with 48x1Gb and 4x10Gb ports, which are connected to the core switches and other management servers via 10Gb links. The control room includes three control interfaces connected to the management switches via 1Gb links.

¹⁰The form factor refers to a hardware design characteristic that determines and specifies the size, shape, and physical dimensions of components, especially in electronics. It sets the structural parameters and constraints for how different components fit and interact within a system [145].

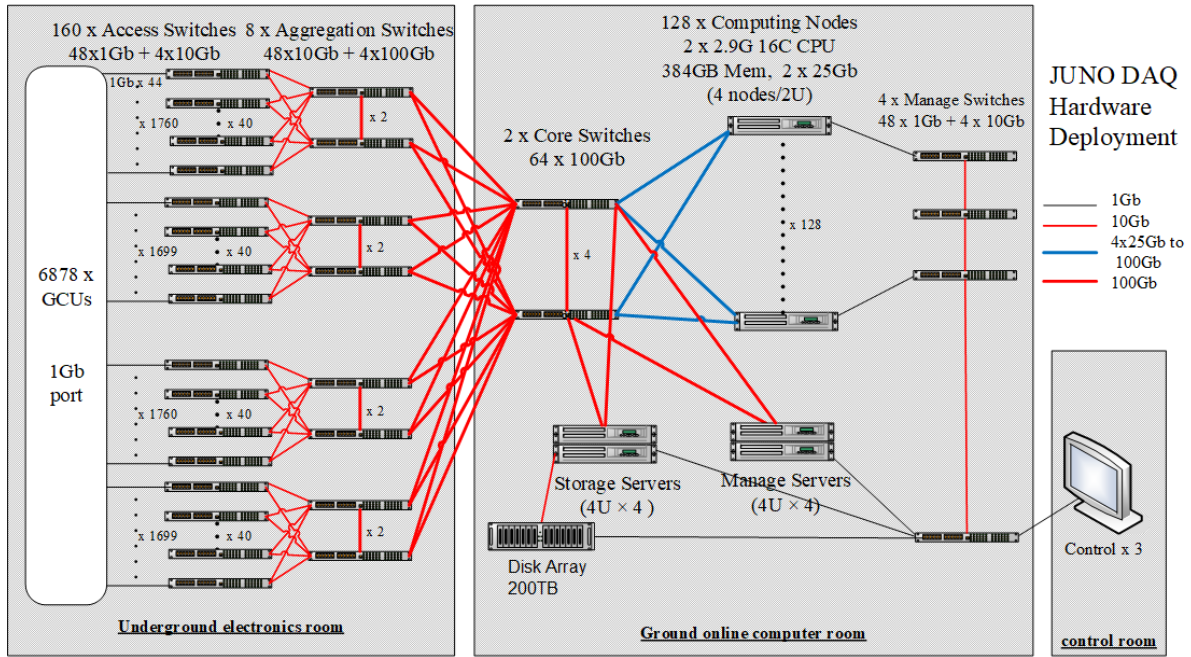


FIGURE 4.20: JUNO DAQ hardware deployment diagram. Taken from official JUNO documentation.

Online software plays a crucial role throughout the data acquisition in JUNO. Its responsibilities include distributing commands and configurations to all data flow software processes, as well as collecting and storing the data generated by these processes. Due to the extensive scale of the computing cluster, effective process management is essential. The JUNO DAQ system employs a centralized message topology microservice architecture [146], leveraging several advanced technologies to maintain efficient and reliable operation. The specifics of the online software and data flow software are detailed in the referenced articles [144, 147].

4.4.2 Detector Control System (DCS)

The remote monitoring system for the JUNO experiment plays a crucial role in ensuring the stable operation of the experimental environment, as well as the front-end and back-end hardware devices. Given the complexity and scale of JUNO, the system must allow precise monitoring and control [148]. The entire monitoring system is built using the Experimental Physics and Industrial Control System (EPICS)¹¹.

Environmental monitoring Environmental factors such as temperature and humidity in the experimental hall can significantly impact the stability and accuracy of the front-end hardware devices. Therefore, the monitoring system needs to continuously track these parameters across the entire facility, including experimental halls, laboratories, and various subsystems like the liquid scintillator and water systems. Currently, the system monitors approximately 200 temperature and humidity points, with plans to expand as more subsystems become operational. Additionally, other environmental variables such as air pressure and liquid levels will also be monitored [150].

Hardware device monitoring The PMTs and their associated electronics require comprehensive monitoring and control. There are 6681 GCU at the experimental site, necessitating 320 25-channel low-voltage power supply

¹¹EPICS: Experimental Physics and Industrial Control System, a software platform used for developing control systems in experimental physics [149].

units and 160 BEC¹². These components must be monitored for temperature, voltage, and current, totaling 140,000 Process Variables (PVs)¹³. The electronics hardware monitoring architecture is shown in Figure 4.21. Data from BEC and low-power voltage units are transmitted through dedicated elec-switches and GCU data are sent first to the DAQ switches. The elec- and DAQ switches handle the initial data flow, which is then passed to the DCS Switches for further processing. The Input/Output Controller (IOC)¹⁴ servers manage data and control commands. Finally, the users access the system through client interfaces, which allow for monitoring and controlling the DCS.

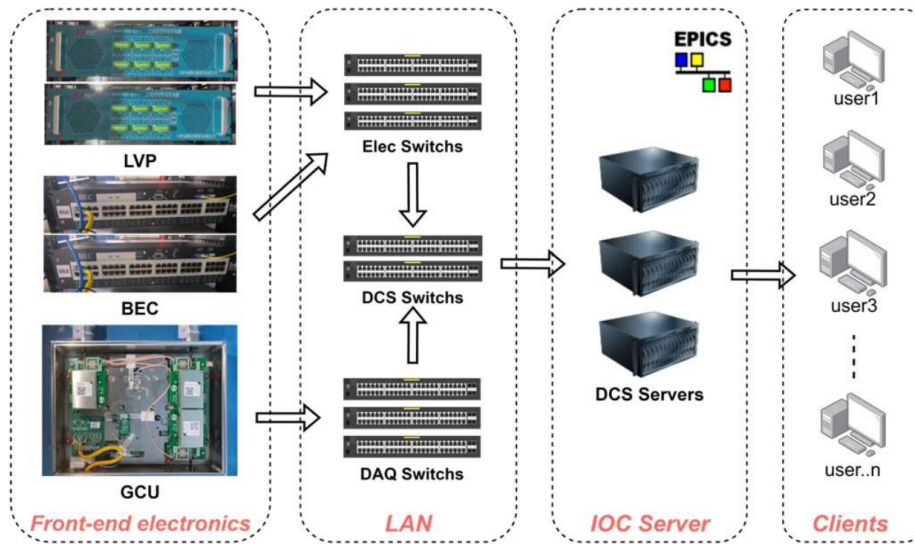


FIGURE 4.21: Electronics hardware monitoring architecture. Taken from [150].

Since 2023, the remote monitoring system has been operating reliably at JUNO. This system handles a significant amount of monitoring data and extended monitoring cycles. It employs MySQL and related components to form a distributed database cluster. The data tables are organized based on system and device types to facilitate data archiving and enable multi-node backups. To accommodate the large number of PVs, the data from front-end devices is archived in a local database through the PyEPICS interface [152]. A monitoring webpage, developed using PHP, provides users with an intuitive understanding of environmental and hardware device status. This webpage, along with categorized alarm modules, offers data query and alarm notification services. As new devices are introduced and subsystems become operational, related services are continually upgraded to enhance monitoring capabilities and ensure the safe and stable operation of experiments. More details are available in [150, 148].

4.5 Summary

This chapter provides a detailed overview of the LPMT readout electronics system in the JUNO experiment, essential for achieving the required energy resolution to determine the NMO.

The electronics system is designed to optimize energy reconstruction, to accurately measure photon arrival patterns, and to handle high data acquisition rates with minimal dead time, especially during events like supernova

¹²Here, we count the number of BECs used for LPMT and SMPT system combined.

¹³Process variables (PVs) are the different parameters that monitor and regulate the performance and safety of the detector components. In JUNO, the PVs include temperature, voltage, current, humidity levels, and LS operating parameters. A continuous tracking is needed to ensure optimal operating conditions, and any deviations from predefined thresholds trigger alarms or corrective actions.

¹⁴IOC is a core component in control systems, responsible for managing the communication between hardware devices and the control software [151].

bursts. The primary tasks of the readout electronics include receiving and digitizing analog signals from the PMTs and transmitting relevant data to the [Data Acquisition \(DAQ\)](#) system based on the trigger decision.

The LPMT electronics chain is split into underwater and outside water electronics. The underwater electronics, housed in watertight [UnderWater Box \(UWB\)](#), are positioned close to the PMTs to minimize signal loss. These units are not replaceable during operation, so they are designed to be highly reliable. The [UWB](#) connects to surface electronics via power cables and synchronous and asynchronous links. The front-end electronics in the [UWB](#) process data from three PMTs. The [Analog to Digital Unit \(ADU\)](#) digitizes the PMT signals with 14-bit accuracy at 1 GS/s. The digitized data are then processed by the [Global Control Unit \(GCU\)](#) FPGA. The [GCU](#) sends a trigger request signal to the [Back-End Card \(BEC\)](#). If the [GCU](#) receives a positive trigger accept signal, it sends the waveform to the [DAQ](#).

The outside water electronics is composed of the [DAQ](#), the trigger system, and the [Detector Control System \(DCS\)](#). The trigger system uses both global and decentralized triggers. The global trigger aggregates information from all PMTs to generate the trigger decision, while the decentralized trigger operates at the [GCU](#) level for high-rate events. The former trigger hardware includes the [BEC](#) equipped with the [TTIM](#), the [RMU](#) and the [CTU](#). The [BECs](#) are used as concentrators to collect and compensate the incoming trigger request signals. The [TTIM](#) aligns and sums them, then sends the result to the next stage (the [RMU](#)). Each [BEC](#) handles connections from up to 48 [GCUs](#), and distributes a 62.5 MHz system clock to the [GCUs](#). The [RMU](#) aggregates information from [BECs](#) using serialization methods and sends to the next stage, the [CTU](#). The latter generates the trigger decision by employing sophisticated trigger algorithms such as [PMT multiplicity](#) and [vertex fitting](#).

The synchronization and clock distribution system, based on White Rabbit technology, ensures precise timing across all components, which is critical for accurate event detection. Despite the challenges of the underwater environment, the system maintains sub-nanosecond synchronization using the IEEE 1588-2008 protocol. The [DCS](#) monitors environmental conditions and hardware status to ensure stable operation.

Chapter 5

Development and design of the back-end cards

In the previous chapter, we presented a general description of the JUNO electronics system and its final design, highlighted the importance of a data aggregation system. This system is essential for managing the large volume of signals from the 20,000 photomultiplier tubes. The back-end cards were specifically designed to fulfill this function. This chapter is divided into 6 sections: section 1-3 discuss the evolution of the design and the early prototypes used to verify the functionality of the proposed schemes. The last three sections detail the final prototype design and the various tests conducted before proceeding to mass production.

Contents

5.1	Conception study	87
5.1.1	Underwater aggregation principle	88
5.1.2	Specific implementation and protocol	88
5.1.3	First generation prototype	90
5.1.4	First generation prototype test	92
5.2	Design of initial proposal	94
5.2.1	Back-end card first version (BEC-V1)	94
5.2.2	Second version - BEC V2	96
5.3	The BX scheme and the 1F3 schemes	101
5.4	Back-end card version 3 (BEC-V3)	105
5.5	Final scheme (BEC-V4)	108
5.5.1	Design of BEC-V4.0	109
5.6	Function tests of the BEC V4	111
5.6.1	Testing strategies	111
5.6.2	Loop test	111
5.6.3	Interconnecting tests	114
5.6.4	Error capture	118
5.6.5	Final implementation (BEC-V4.1-2)	122
5.7	Summary	122

5.1 Conception study

The very initial concept for the JUNO electronics system was based on underwater aggregation. This approach was chosen to have lower number of cables running from underwater to above water, thus simplifying installation.

5.1.1 Underwater aggregation principle

In this initial design, a key component was the **Link Control Unit (LCU)**, which was designed to connect 32 **GCU**s to the above-water **Back-End aggregation Board (BEB)**. LCU primary functions included data aggregation, preliminary triggering, and clock synchronization. The design of the LCU was inspired by CERN's mature Optohybrid technology, which was originally developed for the CMS ¹ GEM ² detector upgrade.

The Optohybrid design was capable of controlling 24 front-end chips, each with 9 high-speed LVDS signals. For the LCU-GCU connection, a method similar to the **GigaBit Transceiver (GBT)** chip [155] was envisioned. The GBT is a high-speed serial data communication protocol used in various applications, particularly in particle physics experiments and high-energy physics research [156]. The chip, also designed by CERN, is used to connect front-end electronics to back-end circuits. It implements optical fiber for the back-end connection and three pairs of high-speed differential signal lines for each front-end chip, with each pair capable of reaching up to 320 Mbps. The back-end can achieve up to 4.8Gbps.

Given that JUNO is not a collider experiment, its trigger rate was expected to be much lower than the one of CMS. Therefore, the Optohybrid was chosen as a good candidate for the LCU to conduct initial experiments. However, while the Optohybrid connects to front-end chips via four high-density QSE connectors, the GCU and LCU could not be on the same board. HDMI cables were considered to address the high number of connections. An extension board was designed to fan out the LCU's QSE signals to 50 HDMI connectors, enabling the connection between the LCU and GCU.

The BEB role was to aggregate data further and provide interfaces with the clock system, trigger system, and DAQ system. This design also drew inspiration from the CMS GEM upgrade, utilizing a μ -TCA system [157]. The BEB was designed as an **Advanced Mezzanine Cards (AMC)** board to be inserted into the μ -TCA crate, using CERN's AMC13 for clock transmission and DAQ connection through the backplane. The BEB's front-end optical fiber would then connect to the trigger system. In this design version, a total of 6 **LCU**s are connected to one **BEB** through a fixed latency 4.8 Gbps link for trigger data transmission. A group of PMTs as the set of approximately 200 PMTs is connected to the same **BEB**. According to this subdivision, the detector is then decomposed into 84 groups of ~ 200 PMTs. The 84 **BEB** are plugged into 9 μ -TCA crates and are connected to the trigger and clock-distribution systems. Figure 5.1 shows the connection layout in this era.

The original concept foresaw to connect 32 **PMT** to one **UWB**. The **UWB** contained 6 different modules: splitter, **HV**, the **FEC**, **ADU**, **GCU**, and **LCU** represented in Figure 5.2. The splitter board is the blue rectangle, the high voltage unit the purple one, the **FEC** in yellow, the **LCU** in green, and the big red rectangle contains **ADU** and **GCU** modules. The **PMT** signals come to the splitter board and propagate to the **FEC**. The **FEC**, in the early development of JUNO electronics, has three gain levels and sends the different output signals to the **ADU** module. On the **GCU**, different complex signals are processed to generate the trigger request. The design plan is to connect 32 **GCU** to a **LCU**.

5.1.2 Specific implementation and protocol

The design of using three separate optical fiber links to connect under-water and outside water electronics is presented in Figure 5.3a. In this case, the fronted electronics have one dedicated optical fiber to connect with the **BEB**, one to connect to GbE switch or 10Gb switch for the DAQ link and the other one to connect to **WR**-system

¹The CMS (Compact Muon Solenoid) detector at CERN is a general-purpose detector at the Large Hadron Collider (LHC) designed to investigate a wide range of physics, including the search for the Higgs boson, extra dimensions, and particles that could make up dark matter. It uses a large solenoid magnet to bend the paths of charged particles. It consists of several layers of detection subsystems that provide detailed information on the particles produced in high-energy collisions. [153]

²The GEM (Gas Electron Multiplier) detector is a type of gaseous ionization detector used in particle physics for tracking and detecting charged particles. It employs thin polymer foils coated with a conductive material and perforated with a high density of holes, where the ionization electrons are multiplied, providing high spatial resolution and fast response times. [154]

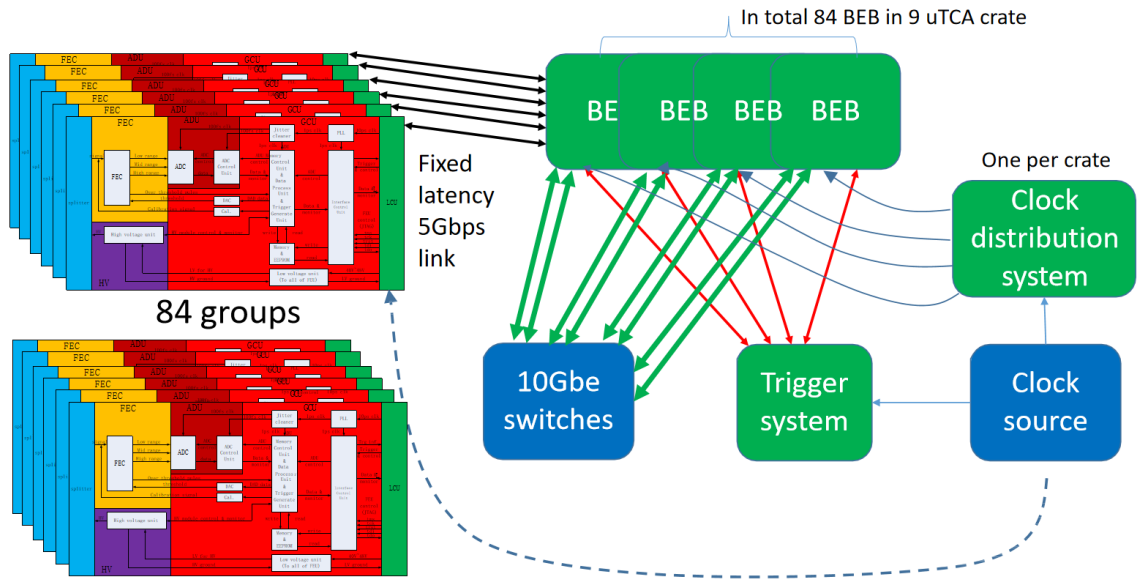


FIGURE 5.1: A LCU connects up to 32 GCU boards. Then, six LCU are connected to one BEB. The 192 PMTs connected to one BEB form a group. All the PMTs are divided into a total of 84 groups [158].

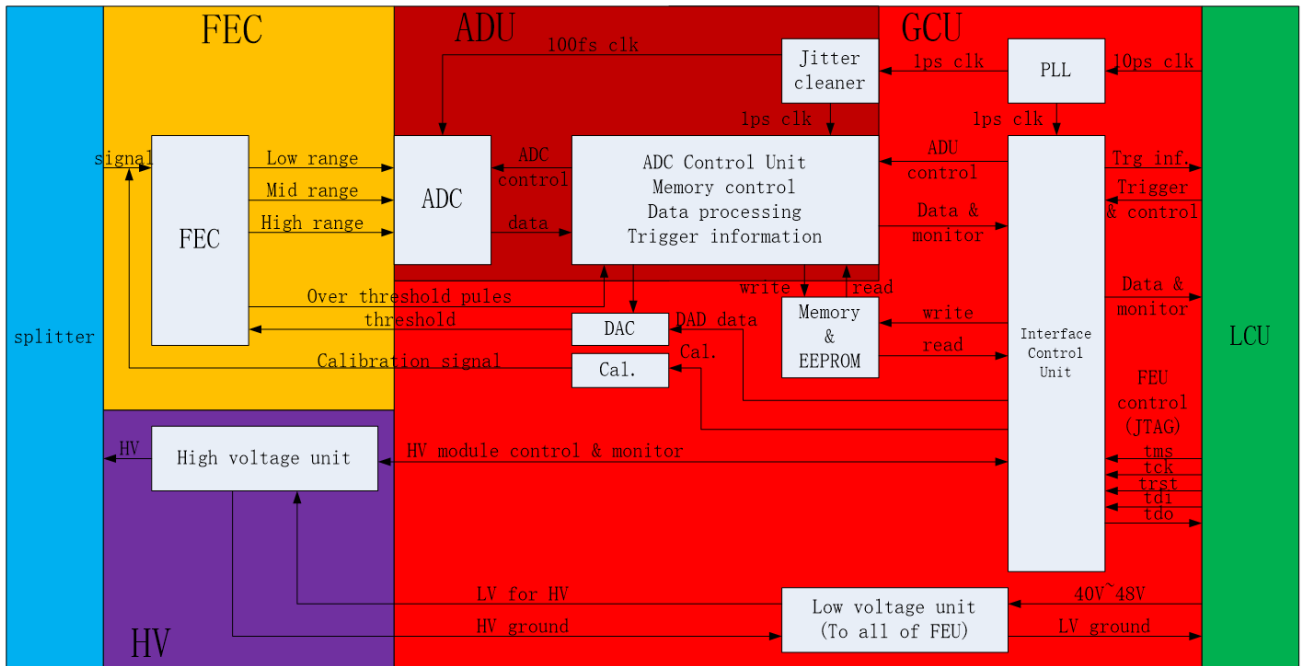


FIGURE 5.2: Underwater electronics: splitter board is in blue, FEC is drawn in yellow, ADU and GCU are red, and the LCU is in green. One LCU is connected to 32 PMTs [159].

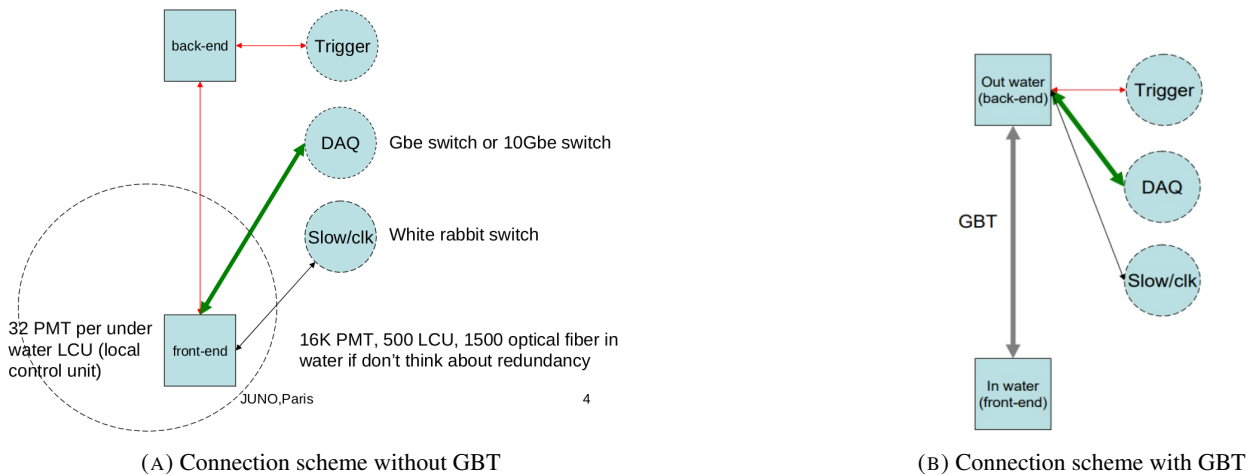


FIGURE 5.3: Connection logic between front end and backend with or without GBT-like protocol.

for cock and slow-control. In Figure 5.3a, the three links are represented by the red arrows for the trigger data transmission, the green arrows for the DAQ connection, and the black arrows for the slow control and clock link.

Another option is to connect underwater and outside water electronics with one link, as shown in Figure 5.3b. This solution has the significant advantage of reducing the number of wires and then facilitating the installation procedure. One possible approach is to use a GBT-like protocol to link LCU to the BEB. The LCU then uses an optical fiber to transmit GBT packet to the back-end electronics. The data going from the GBT-chip to the front-end electronics includes fixed-delay trigger signals, DAQ data, and slow control data.

The GBT-like protocol facilitates the communication between outside water and underwater electronics, ensuring efficient data transfer and consolidating critical information for further processing by the back-end electronics. By using optical fiber, we enhance data transmission reliability and speed. However, integrating multiple high-speed connectors on a single board requires careful design considerations to manage signal integrity and minimize channel interference. The design challenge lies in integrating 32 high-speed connectors on the same circuit board and 96 high-speed differential pairs to one FPGA (32 GCUs \times 3 pairs).

5.1.3 First generation prototype

The first versions of the LCU and BEB were built in 2016. This section gives the details of those two prototypes.

The link control unit (LCU) The LCU bandwidth requirement on the different links is presented as follows. The trigger link was designed as sending 10 bits every 300 ns, corresponding to a 30 Mbps bandwidth. The DAQ link required a 40 Mbps link per PMT. As 32 GCUs are connected to one LCU, the required bandwidth is 1.28 Gbps for the DAQ link. Finally, we need an extra 50 Mbps link for the slow control link. The combination of the requirement for DAQ, trigger, and slow control lead to a total of 1.36 Gbps per group of 32 GCU.

The LCU of the first-generation prototype comprises two boards – one Optohybrid V2 (shown in Figure 5.4a) and one connector extender board (shown in Figure 5.4b). We implement 200 differential pairs and 50 HDMI ports on the connector extender board to give the possibility to connect up to 50 GCUs to one LCU. For the LCU optohybrid V2 board key components, we get:

- 20 optical links to connect to outside water electronics

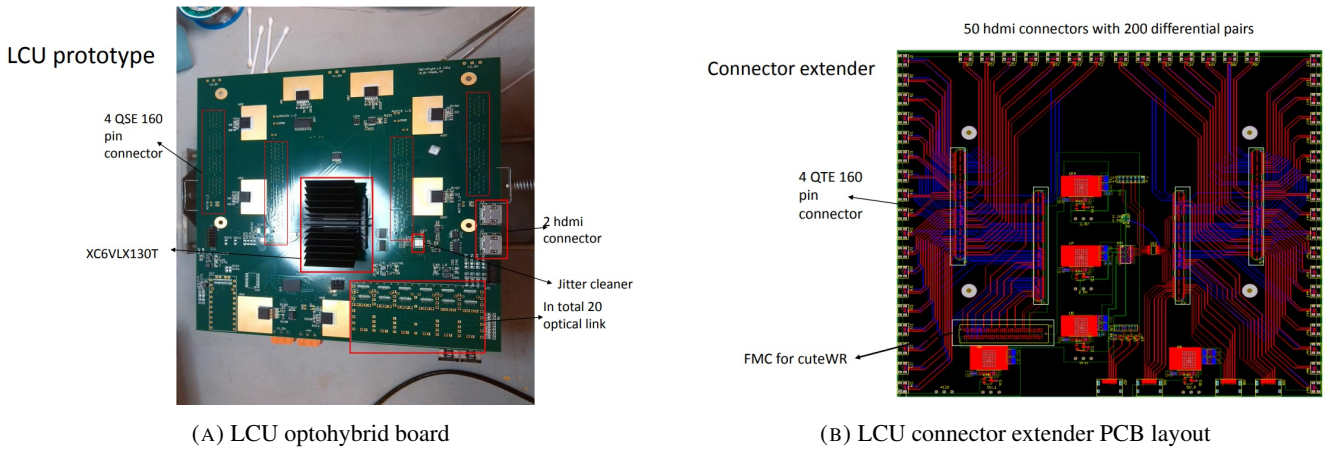


FIGURE 5.4: LCU boards prototypes.

- One XC6VLX130T **FPGA** to perform the protocol conversion and high-speed data transfer
- One jitter cleaner module
- 4 QSE 160 pin connectors to connect the **LCU** connector extender board

On the other side, the **LCU** connector extender board has the following:

- 4 QTE 160 pins connectors to connect the **LCU** optohybrid board
- One FMC connector for the **Compact Universal Timing Endpoint based on WR (Cute-WR)** [160]
- 50 HDMI connectors and 200 differential pairs strip on the PCB to connect to at least 32 **GCUs**

This design approach leverages proven concepts from the CMS GEM optohybrid. As the CMS GEM optohybrid does not provide an HDMI port, we adapted them to suit the specific requirements and objectives of the first-generation prototype. Using two separate boards, one Optohybrid V2 and one connected expansion board, allow for modularity and flexibility in testing and validation. **LCU** adopts the CMS GEM Optohybrid V2a and the connector expansion board. The Optohybrid V2a is crucial for handling optical signals and data processing, while the connector expansion board provides additional connectivity options.

Back-end Aggregation Board (BEB) The **BEB** prototype is shown in Figure 5.5. The **BEB** is primarily responsible for protocol conversion and optical fiber handling. For flexibility, the **BEB** is designed to receive the signal of up to 10 **LCUs** through an optical fiber link at 4.8 Gbps. The key components of the **BEB** are:

- Artix XC7A200T **FPGA** as the main computational unit
- Double-width **AMC** to connect to the μ -TCA crate
- **Modular Multifunction Counter (MMC)** to perform the different slow control of the board.
- 2 **HDMI** connectors to add additional options such as the multi-messenger trigger possibility.
- 1 **FMC** to connect the **WR**-system.

The main objective of this design is to validate the feasibility of the proposed solution.

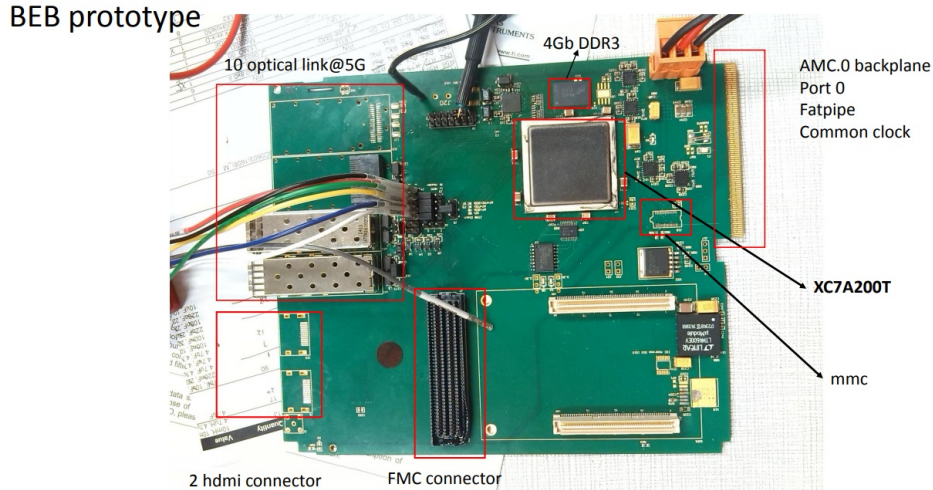


FIGURE 5.5: BEB prototype.

5.1.4 First generation prototype test

Initial testing focused on three main aspects: the LCU-GCU connection, the LCU-BEB connection, and the BEB's compatibility with the μ -TCA system, including the MMC design.

GCU-LCU link Figure 5.6 shows the simulation results for the GCU-LCU link. We have only simulated results here as GCU prototypes were unavailable at the moment. The simulation of the GCU-LCU link on the LCU board was performed using ANSYS electronics desktop suite [161]. ANSYS allows us to build a precise model of the board and then simulate the signal transmission inside the PCB and the different components of the board by using finite element methods. ANSYS simulation was used to model the transmission line from the Optohybrid's FPGA to the HDMI interface on the extension board. By injecting a PseudoRandom Binary Sequence (PRBS) data stream into the FPGA I/O, the eye diagram at the connected HDMI connector is observed.

An *eye diagram* is a graphical representation used to evaluate the performance of a digital communication system. By measuring the width of the eye, we can quantify the quality of the signal transmission. The eye shape of the *eye diagram* is obtained by overlaying multiple segments of a digital signal's waveform at the receiver end. We display the overlay of the signal waveform over a single time interval, corresponding to a one-bit period. The most crucial feature of the eye diagram is the eye-opening.

A clear and well-defined eye diagram indicates good signal integrity, with minimal distortion, noise, and jitter. Conversely, a distorted eye diagram with a small opening suggests problems with the signal transmission, such as reflections, attenuations, or interferences. The width of the eye-opening provides insight into the timing accuracy and synchronization capabilities of the transmission line. A narrow eye opening may indicate timing issues and potential bit errors.

By observing the eye diagram, shown in Figure 5.6, it was determined that the design could meet the requirements as the eye is open. While the highest requirement was 320 Mbps, the simulation used a 5 Gbps data stream.

LCU-BEB link A test was performed to verify the design functionality of the LCU-BEB link. Here, we want to check the bit error rate of the communication between these two boards. The LCU to BEB test involved a direct optical fiber connection, with the eye diagram observed using Vivado's online eye diagram function on the BEB. The eye diagram, shown in Figure 5.7, depicts a PRBS-7 data stream operating at a speed of 4.8 Gbps and is

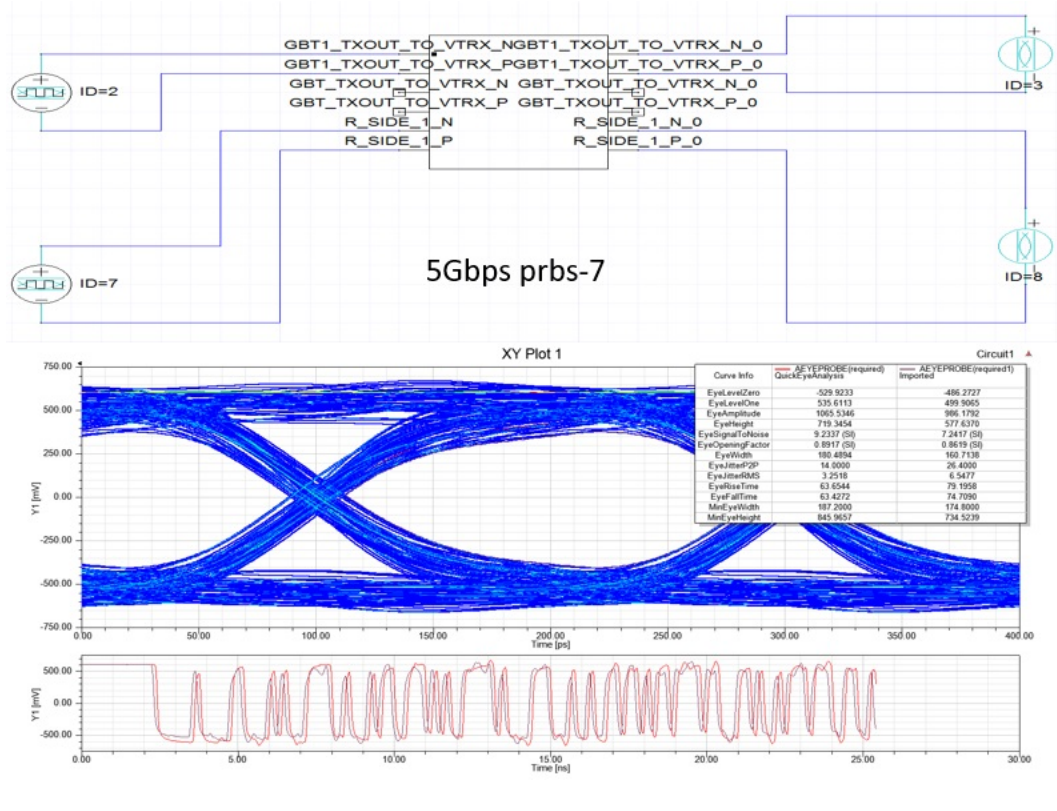


FIGURE 5.6: LCU to GCU simulation obtained with ANSYS software.

measured at the BEB output for a total exposure of 19 hours. The MMC design also proved successful, with the BEB being correctly recognized by the μ -TCA’s MCH and allocated power.

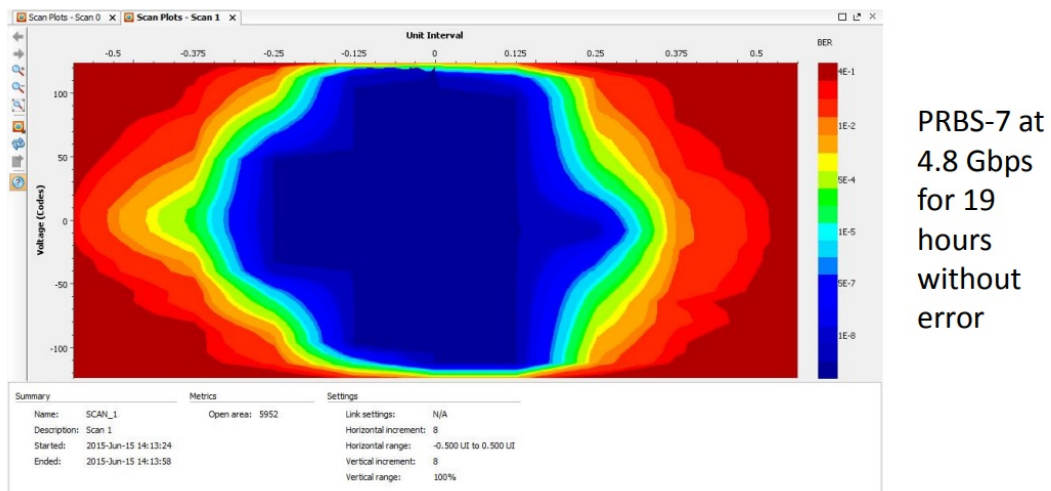


FIGURE 5.7: Eye diagram for the LCU-BEB connection results.

The design described in this section using the GCU-LCU-BEB scheme shows it is functionally feasible to concentrate the signal from PMTs in JUNO. However, this design brings a risk of losing 32 channels simultaneously by a failure of one LCU. If the 32 channels are concentrated, it will cause holes in the detector. The installation is complicated if the 32 channels are not connected to PMTs next to each other. In addition, the JUNO electronics group also needed clarification about the reliability and cost-effectiveness of optical fibers. Those reliability concerns lead to a transition from underwater aggregation to a fully above-water aggregation scheme.

5.2 Design of initial proposal

As mentioned in the previous section, there are different drawbacks to the underwater aggregation scheme. It was clear that a new scheme had to be developed. The new idea is to connect GCU to the surface through 100m Ethernet cables and then perform the aggregation in the electronics rooms.

The first challenge is whether the bandwidth of long network cables is sufficient, as 100m is the limit for data transmission over twisted copper cable without a relay. Data quality is important for global triggering, which requires a global clock and fixed-delay trigger request signals. Technically, we must ensure the transmission of 62.5 MHz clocks and 250 Mbps data over 100 m. A similar scheme was already used for another high-energy physics experiment: the [Askaryan Radio Array \(ARA\)](#) design [162]³. The ARA requirements are different: the bandwidth is lower, as the goal is to achieve 20 MHz clocks and 80 Mbps data stream, but the transmission is over 250 m in ARA instead of 100 m with JUNO. A second difference is that JUNO requires four pairs of lines (all the pairs inside an Ethernet cable), whereas ARA only uses three pairs. These different changes imply creating a new prototype for JUNO and performing tests on it.

5.2.1 Back-end card first version (BEC-V1)

The [Back-End Card \(BEC\)](#)-V1 was the prototype of the outside water aggregation era board. This section explains the details of its design development, the prototypes, and the tests performed on them.

Design As the design completely changes compared to the underwater aggregation era, we present in Figure 5.8 the first version of the scheme that uses BEC. This scheme is the first version of the BX scheme [164] detailed in section 5.3. The front-end electronic design also changes. The underwater box design gives its to the [BX-scheme Photo-Multiplier Tube \(BXPMT\)](#) design. The BXPMT consists of connecting the front-end electronics directly after the PMT to avoid any signal perturbation during the transmission between the PMT and the front end. Only one Ethernet cable links the BXPMT to the outside water electronics in this scheme. Since communication is performed through an Ethernet cable, a solution to compensate for the signal loss over the channel is required. To address this issue, a combination of equalizers and drivers is used. The primary function of the equalizer is to correct distortions and attenuation as the signal travels over the 100-meter Ethernet cable. The cable driver main function is to condition the signal before entering the transmission line to help the equalizer to ensure that the signal remains stable enough to overcome losses typically associated with long-distance transmission over Ethernet cable.

The connection between the BEC and the cable coming from GCU is performed using an RJ45 connector. In Figure 5.8, the green arrows represent the [Power over Ethernet \(PoE\)](#) signals. They are used for the DAQ. The red arrows are the data stream for the 62.5 MHz clock and the trigger accept signals (BEC to GCU) and the data stream for the trigger request (GCU to BEC). The GCU power is also brought to the GCU through the Ethernet cable. A power of 15 W is brought by the PoE pair and 5 W by the clock pair.

Prototype A BEC-V1 prototype was built in 2017. The primary to be done is to verify the 100 m high-speed transfer between GCU and BEC. The critical point is to test if the using of equalizers and drivers is sufficient to compensate for the transmission loss in the long cables. The BEC-V1 board is composed of the different components:

³The Askaryan Radio Array (ARA) experiment is designed to detect ultra-high energy neutrinos by observing the radio frequency signals produced when these neutrinos interact with Antarctic ice. Utilizing an array of antennas buried deep in the ice, ARA aims to capture the faint, short-duration pulses indicative of neutrino interactions to contribute to the understanding of cosmic particle acceleration and high-energy astrophysics [163].

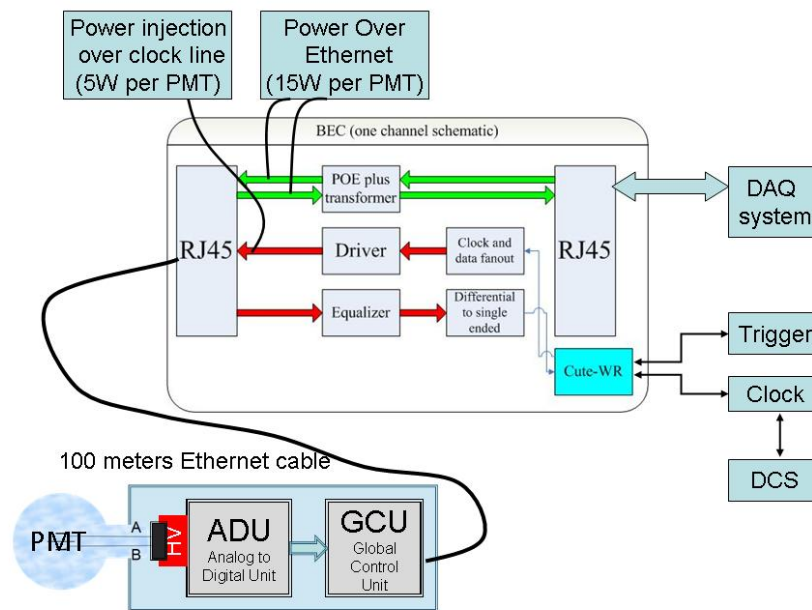


FIGURE 5.8: Logic usage of BEC-V1.

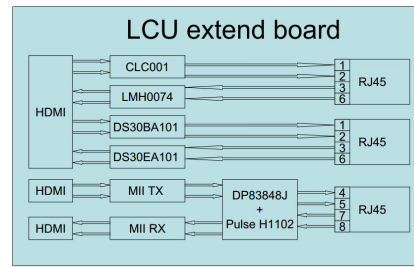
- The CLC001 [165] is a 3.3V cable driver for high-speed data transmission over long distances. It drives 75Ω transmission lines (Belden 8281 or equivalent) at data rates up to 622 Mbps. Its versatile input stage allows for various input levels, including direct LVDS and Low Voltage Positive Emitter-Coupled Logic (LVPECL) connections. It is used between the HDMI connector and the RJ45 connector.
- LMH0074 [166] is an equalizer used to compensate for the loss of the incoming signal.
- The DS30BA101 [167] is a high-speed differential buffer for cable driving, signal buffering, and signal repeating applications. Its fully differential signal path ensures good signal integrity and noise immunity. The DS30BA101 drives differential and single-ended transmission lines at data rates up to 3.125 Gbps.
- The DS30EA101 [168] is an adaptive cable equalizer optimized for equalizing data transmitted over copper cables [169]. The equalizer operates over data rates from 150 Mbps to 3.125 Gbps. It automatically apply the correct amplification and conditioning on the incoming signal. It can provide a gain up to 50 dB at 1.5 GHz.
- The DP83848J [170] is Commercial temperature, 10/100-Mbps Ethernet PHY transceiver in a 40-pin QFN package. Pulse H1102 is audio transformers/signal transformers [171]. They are used in addition to transmitting (TX) and receiving (RX) Media Independent Interface (MII), and are used for the PoE signal processing. In this scheme, the nominal link speed is 100 MHz.

Figure 5.9 shows the BEC-V1 board. We have two possibilities for connecting the RJ45 connector to the HDMI connector. This configuration offers two potential options: a) transmission using a pair consisting of a single-channel equalizer and cable driver, or b) using Ethernet packet communication through an Ethernet PHY transceiver and its interfaces. However, testing power injection and synchronizing pairs presents challenges due to the limitation of having only one channel available for synchronization.

Tests The bench test setup of the BEC-V1 is shown in Figure 5.10. We use the LCU from the previous underwater aggregation scheme to generate the PRBS-7 signal. The LCU is used here as a signal generator and emulates the



(A) BEC V1 prototype

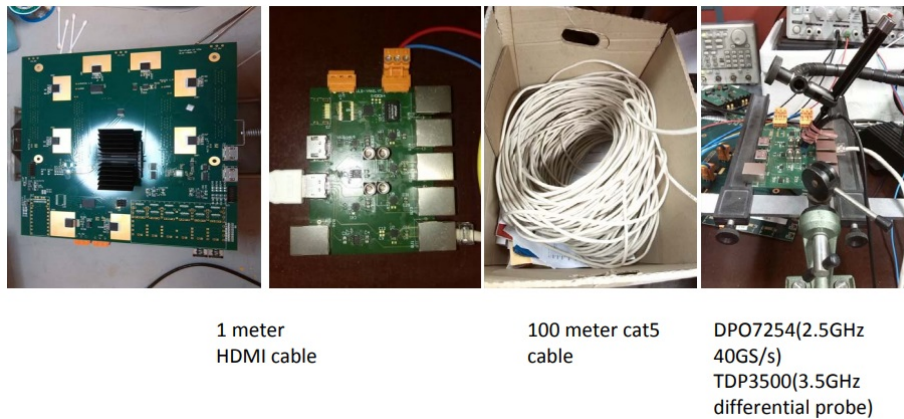


(B) BEC V1 logic

FIGURE 5.9: BEC V1.

GCU in our test, but it is not used in this new scheme. The signal is transmitted to a first BEC-V1 board through a 1m HDMI cable. We use this first BEC-V1 as it has RJ45 and HDMI ports, whereas LCU only has HDMI and optical ports. Then the signal is sent over 100 meter cat5e Ethernet cable to another BEC-V1. Finally, we will use a scope (DPO7254 from Tektronix [172]) to observe the resulting signal after the equalizer on the second BEC-V1.

By connecting one BEC-V1 to another BEC-V1 through 100 meter Ethernet cable, we can assess the performance of the cable driver/equalizer couple. An eye diagram obtained at the output of the equalizer of the receiving board is used to verify the feasibility of the solution using an Ethernet cable for the signal transmission between the underwater and outside water electronics. Figure 5.11 shows the eye diagram for unidirectional transmission, with a PRBS-7 signal working at 250 MHz. A fully open eye is shown here, which guarantees data transmission and receiving with a small amount of errors (no errors were detected for 24 hours).



1 meter HDMI cable

100 meter cat5 cable

DPO7254(2.5GHz 40GS/s)
TDP3500(3.5GHz differential probe)

FIGURE 5.10: Setup for LCU with BEC-V1 test. We are measuring the eye at the output of the equalizer.

5.2.2 Second version - BEC V2

The BEC-V1 was the first prototype and was used to verify the feasibility of transmission over 100 m Ethernet cable. This prototype successfully achieved 250Mbps unidirectional transmission. The BEC-V2.X prototypes are developed to test on bidirectional transmissions.

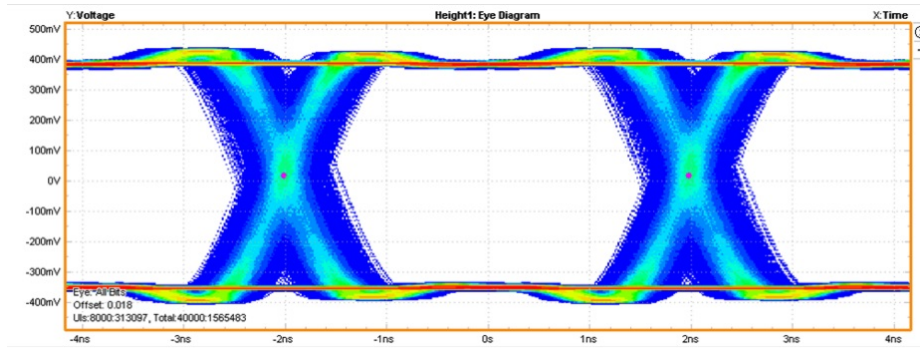


FIGURE 5.11: Eye diagram obtained at the output of the BEC-V1 link using Ethernet cable for a bandwidth of 250 MHz.

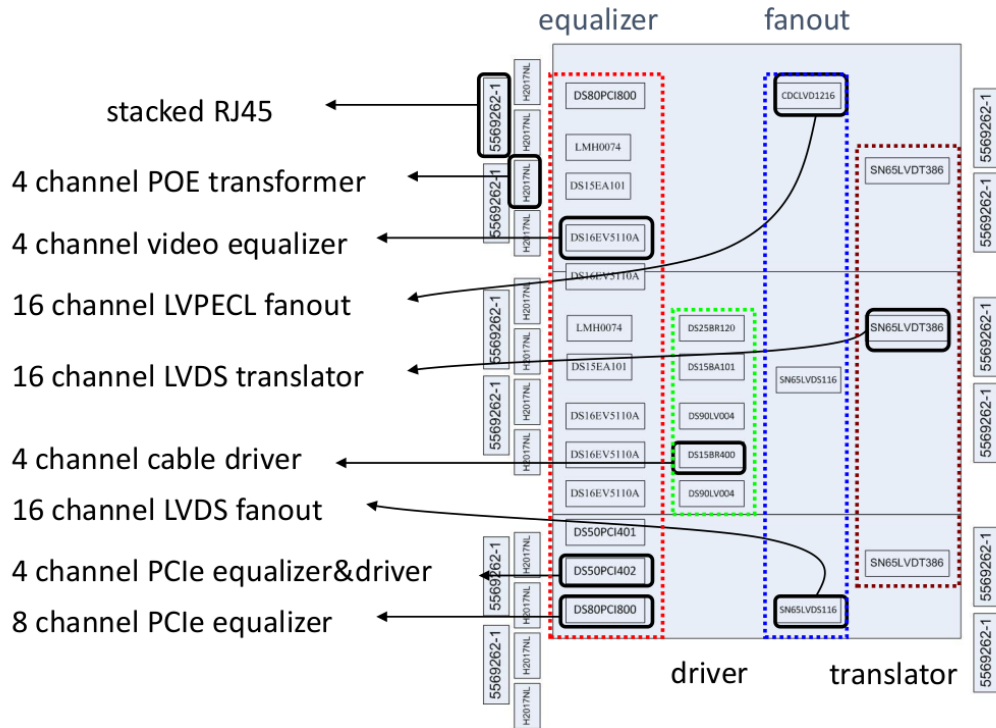
BEC V2.0

The BEC-V2.0 was designed with the following mindset: to test different equalizers and driver combinations that can be used for the BEC. The BEC-v2.0 prototype, presented in Figure 5.12a, is composed of the different blocks:

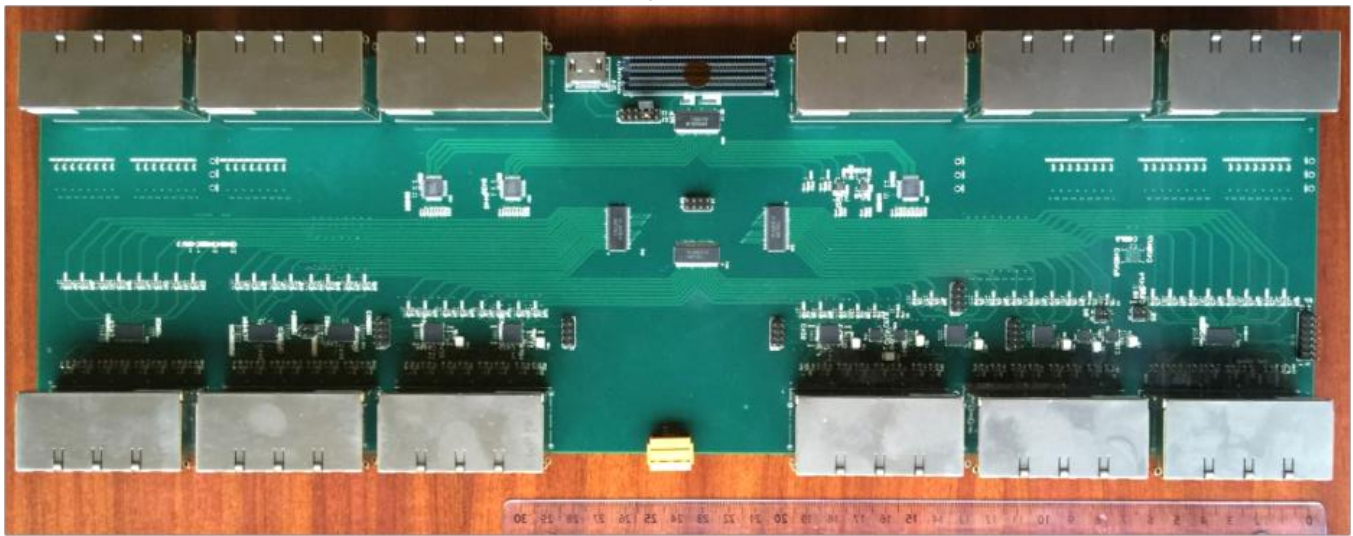
- 48 RJ45 and PoE transformer block: This block is designed to perform the interface between BEC and underwater electronics. The chip chosen for the PoE transformer is H2017NL [173], a 4-channel audio transformers.
- Equalizer Function: The signals travel long distances or encounter transmission mediums with frequency-dependent losses. An equalizer can compensate for signal distortions and attenuations, ensuring that the received signals maintain their integrity and quality. The equalizer block is composed, in addition of LMH0074 and DS15EA101 [174] chips used in BEC V1, a 4-channel video equalizer DS16EV5110A [175], a 4-channel PCIe equalizer&driver DS40PC402 [176], and the 8-channel PCIe equalizer DS8PCI800 [177].
- Driver Function: Cable drivers can amplify signals, helping them maintain strength over extended distances. For the driver block hardware, we kept the DS15BA101 [178], but we also had three other kinds of chips. The DS25BR120 [179], DS25BR400 [180] and DS90LV004 [181]. For example, DS15BR400 is a 4-channel LVDS Buffer/Repeater with pre-emphasis. High-speed data paths and flow-through pin-out inside the chip minimize internal device jitter. Additionally, the pre-emphasis overcomes Inter-Symbol Interference (ISI) jitter effects from lossy backplanes and cables.
- Fanout Function: A fanout function is required when a single signal needs to be distributed to multiple devices or components; in our case, the clock signal distribution is a good example. Using fanout logic helps to simplify the design by reducing the need to split signal paths from the source to each receiver. The hardware used here includes 16 channel LVPECL fanout CDCLCD1216 and 16 channel LVDS fanout SN65LVDS116 [182].
- Translator Function: When different system parts operate at various voltage levels or use different signaling standards, a translator function can bridge the gap, ensuring compatibility and seamless communication between these components. Here, a 16-channel LVDS SN65LVDT386 [183] chip is used.
- The other 48 RJ45 connectors to other part of the outside water electronics (DAQ, timing system, and trigger systems).

During the test of BEC-V2.0, the performance of the 4-channel video equalizer DS16EV5110A, 4-channel PCIe equalizer&driver DS40PC402, and the 8-channel PCIe equalizer DS8PCI800 did not meet the requirement in term

of bit error rate. The issue was coming from their power supply, which need to be cleaner to ensure the correct performance of different multi-channel equalizers.



(A) Block logic of BEC V2.0



(B) picture of BEC V2.0

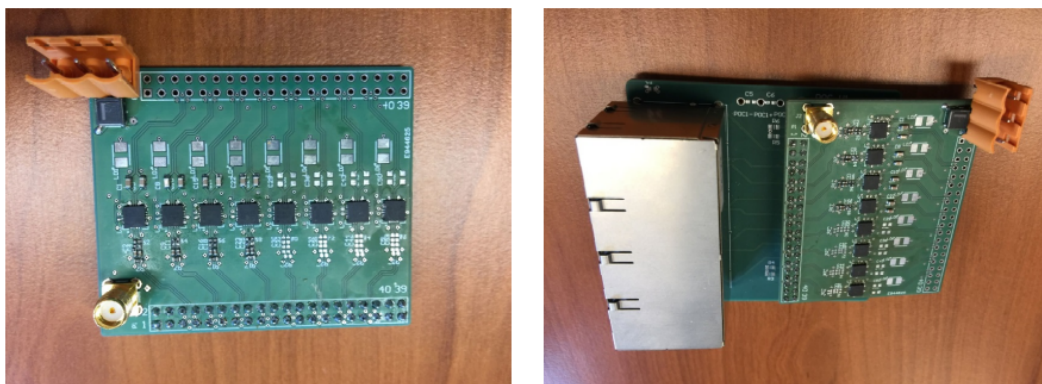
FIGURE 5.12: BEC-V2.0 block logic and prototype.

BEC V2.1 A new, smaller version of the BEC-V2.0 was built. This BEC-V2.1 has 16 channels compared to the 48 of BEC-V2.0. The BEC V2.1 is shown in Figure 5.13a. This version features an optimized power distribution system compared to BEC-V2.0 in order to solve the issue with bidirectional transmission observed on BEC-V2.0. The equalizer used is the DS16EV5110A. Those equalizers are not adaptive, which means the amplification factor is set depending on the length of the cable. Finally, the power optimization of BEC-V2.1 results in a lower ripple on



(A) Picture of BEC V2.1

(B) Picture of BEC V2.2



(C) BEC V2.3 is composed of a DS8 mezzanine board equipped with 8 DS15EA101 (on the left) and RJ45 board designed to receive the DS8 mezzanine card.

FIGURE 5.13: Prototypes of BEC-V2.1, BEC-V2.2 and BEC-V2.3.

the power supply compared to BEC-V2.0. However, some ultra-short pulses lower than 1 ns, also called glitches, persist and lead to the impossibility of data communication at 250 Mbps.

BEC V2.2 and V2.3 As the 250 Mbps was unachievable with BEC-V2.1, a new design, BEC-V2.2 (Figure 5.13b), was created, reverting to the single-channel equalizers used in BEC-V1. The results were positive for the single channel with adaptive equalizer DS15EA101, but due to glitches, 250 Mbps data communication can only be achieved in a single direction. At this point, we suspected that the loss of signal transmission was due to near-end crosstalk/ BEC-V2.3, shown in Figure 5.13c, was designed with additional debugging interfaces that allow each pair of Tx and Rx to be enabled separately. This design allows for a detailed investigation of the cross-talk issue.

Crosstalk study In a twisted pair cable, data is transmitted over two twisted wires around each other. This twisting helps to reduce electromagnetic interference from external sources, but some interference can still occur between the adjacent pairs. **Near-End Cross Talk (NEXT)** refers explicitly to the interference that occurs close to the source of the received signal or "near" the transmitting end of the cable. It is measured at the end where the signal is being received. The interference is unwanted because it can degrade the quality of the signal and potentially lead to errors in data transmission. The phenomena are shown in Figure 5.14a. The Tx signal denoted U_0 , is transmitted over the first twisted pair. Due to loss over the signal propagation, a reduced signal U_1 is got

at the transmission line end. On the other pair, the signal U_2 is sent over the transmission line, and as for the first pair, the signal is attenuated, but due to NEXT, the Rx signal, U_3 , is affected by the signal U_0 before entering the equalizer. If the coupling before the equalizer between the Rx signal and the Tx signals is too high, the data transmission can not be achieved.

The debugging method involved observing the equalizer output at the receiving end and comparing the outputs with and without the near-end Tx enabled. The setup is shown in Figure 5.14b to highlight the distortions. A 250 Mbps PRBS-7 signal is sent to the Fanout part of the BEC-V2.0. On the right side, the signal is sent to BEC-V2.3 by a Tx injector. The Tx injector is a simple RJ45 connector connected to the Tx pins of the BEC-V2.3, thanks to the jumper cable, which provides an easy way to connect/disconnect the injection. On the left side, the signal is sent to 3-6 receiving pairs of the BEC-V2.3 through 100 m cable. Eye diagrams of the Rx signal at the output of the equalizer on the DS8-mezzanine board, are performed for different configuration.

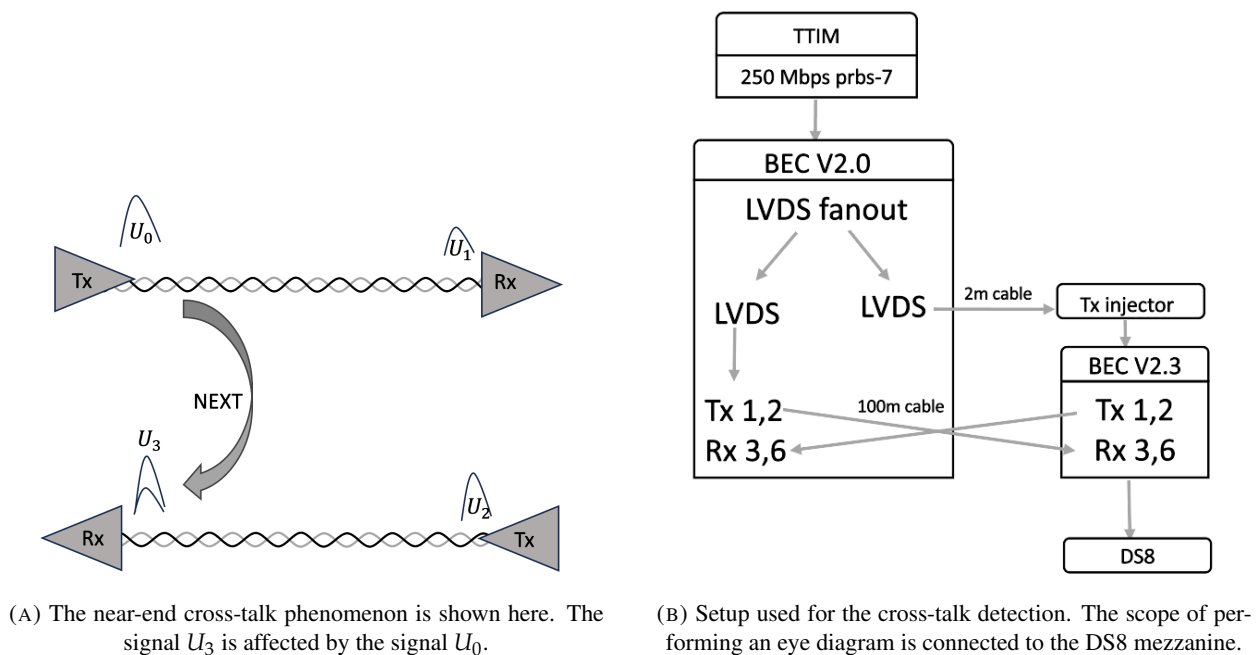


FIGURE 5.14: Cross-talk phenomenon and set up for the cross-talk detection.

Figures 5.15a and 5.15b show the eye diagrams with and without TX-injections. The eye in Figure 5.15b is closed, demonstrating that distortions of the Rx signal occur when the near-end Tx is enabled. To solve this problem, two steps must be involved: slowing down the Tx rising edge and adding a capacitor to the ground at the Rx end. This approach successfully mitigates the cross-talk issue allowing a successful bidirectional high-speed transmission.

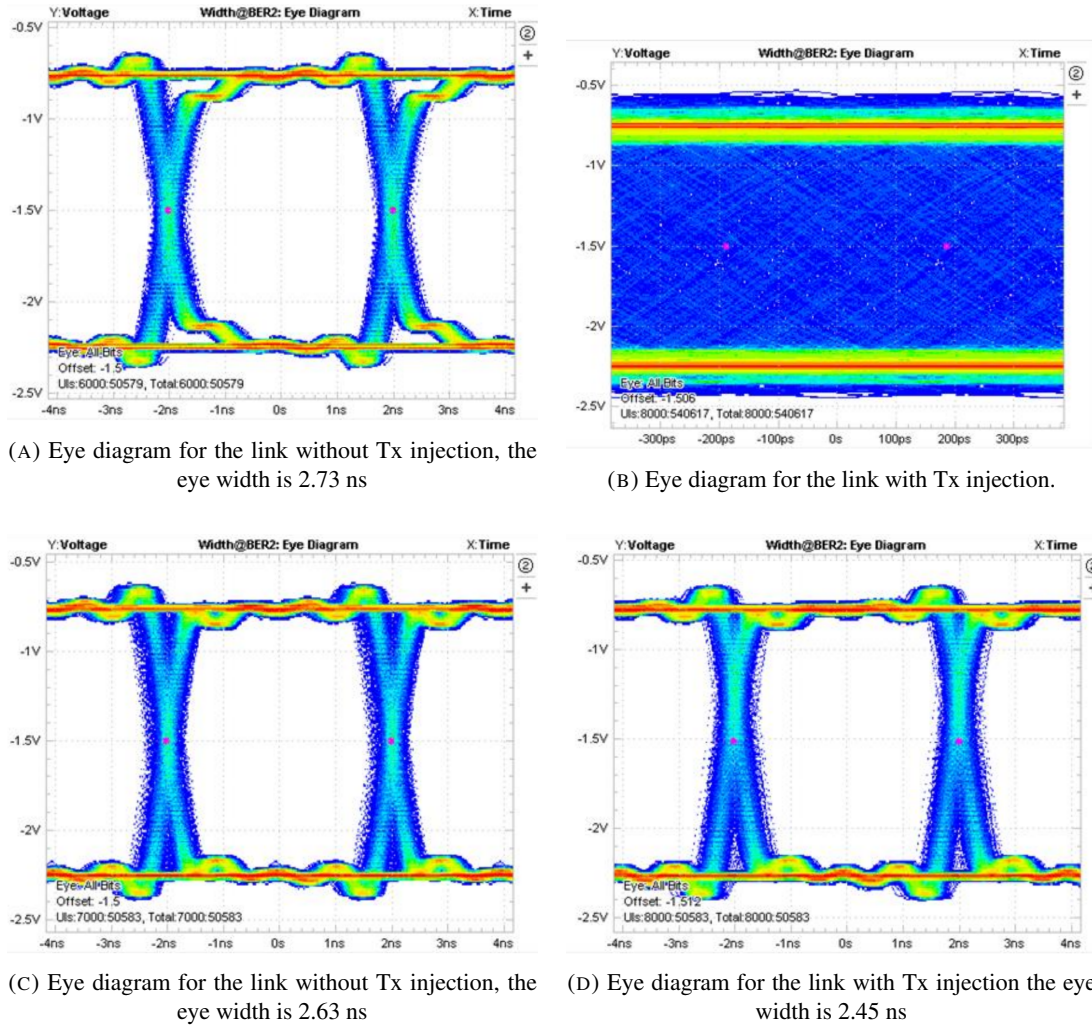


FIGURE 5.15: Figures (A) and (B) are eye diagrams obtained with the DS8 board without modification. For Figures (C) and (D), the DS8 mezzanine was modified with a capacitor.

5.3 The BX scheme and the 1F3 schemes

During the years 2016-2017, the option called the "BX scheme" was intensively studied. The BX scheme was characterized by its high level of integration, with all front-end electronics housed within the PMT base. This design offered advantages in terms of ease of sealing and compact packaging.

Previously, to accommodate the *Cute-WR*—which possesses only one FMC connector [160]—the BEC board required the implementation of "differential pair to single-ended" translator and fanout modules. The use of a fanout module compromises the individual control of the delay of each clock, reducing flexibility. Moreover, employing a translator results in a single-ended connection to the FPGA, which increases noise susceptibility. To address these issues, the *TTIM* was developed, featuring two FMC connectors to enhance functionality and reduce limitations. Compared to the scheme using BEC-V1 (illustrated in Figure 5.8), the *Cute-WR* board has been replaced by the *Trigger and Timing Interface Mezzanine (TTIM)* in response to the updated clock and trigger scheme requirements. This updated scheme requires a higher number of Input/Output (I/O) pins on the FMC connector, a shift from the configuration used in the development of BEC-V1 and BEC-V2.

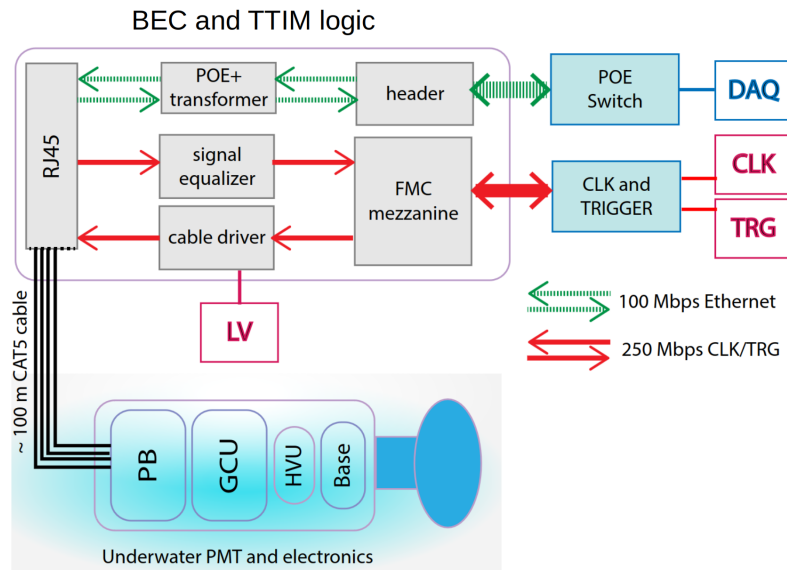


FIGURE 5.16: Logic of BX scheme taken from [164].

The various roles of the BEC are: 1) processing incoming signals from the GCU to ensure compatibility with the DAQ, 2) aggregating trigger requests from the GCU and distributing the clock signal, 3) powering the GCU, 4) managing slow control communications with the GCU. Regarding signal routing, four signals are managed on the BEC for each PMT electronics setup. These are divided into two sets: one set includes signals traveling from the GCU to the BEC, and the other includes signals from the BEC to the GCU.

The first set of signals is designed to work at 250 Mbps. Those ones are routed on the baseboard and then connected to the trigger and central clock system. In Figure 5.16, they are represented by red arrows as those high-speed signals are transmitted between BEC- TTIM and GCU through 100 m long Ethernet cables (the black lines in Figure 5.16).

The second set of signals is used for the DAQ link, the slow control, and the power supply of the underwater electronics. We keep the same design as BEC-V2 and use PoE transformer to power the GCU. The header technology is not fixed at this state. The link also provides the data transfer of the PMT waveform to the DAQ. This link works at a speed of 100 Mbps and uses standard Ethernet protocol. Those are represented by green arrows in Figure 5.16.

1F3 schemes The BX scheme also presented significant challenges. It required a large number of network cables, with each PMT needing its cable to the back-end. Moreover, the concentrated electronics in the PMT base posed potential heat dissipation problems. The 1F3 (1 Front-end for 3 PMTs) schemes were developed in response to the BX scheme challenge by: 1) to achieve lower power consumption, 2) to simplify the installation procedure, and 3) to reduce the number of cables required.

The reduced power consumption resulted from the 1F3 scheme's capability to decrease the number of GCU boards by a factor three. The 1F3 scheme hosts the front-end electronics inside the UWB connected to 3 PMTs via 3 short (about 1 m) coaxial cables. Minimizing power consumption is particularly important as active cooling is not designed for the water surrounding the electronics. The cooling mechanism for the electronic components within the BX scheme, which involves oil convection in the potting of the PMTs, poses significant concerns regarding the reliability of the electronics.

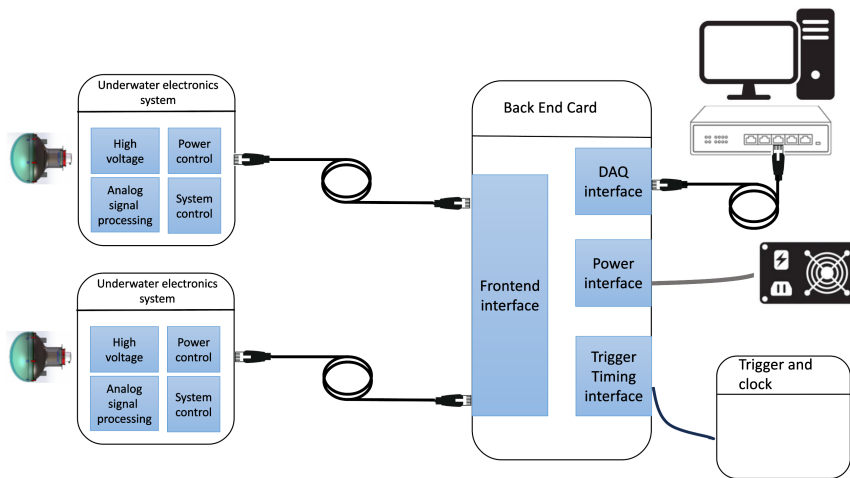
Another crucial aspect is the installation procedure. In the BX scheme, the PMTs and electronics form a unified unit. The installation of the PMTs, together with their long cable, would be very challenging. In addition, if

the electronics of one PMT are found to be defective during installation, they cannot be easily replaced. Conversely, in the 1F3 scheme, PMTs are installed first. Then, the corresponding electronics (underwater boxes) are installed once all the PMTs in a specific area around the central detector are in place. This approach facilitates the swift replacement of defective electronics during installation. However, the 1F3 scheme does have certain drawbacks compared to the BX scheme. For instance, in the 1F3 scheme, the ADU is not positioned directly after the PMT. Instead, the analog signal must propagate through a one-meter coaxial cable, which may introduce more noise than the digital signal transmission approach adopted in the BX scheme.

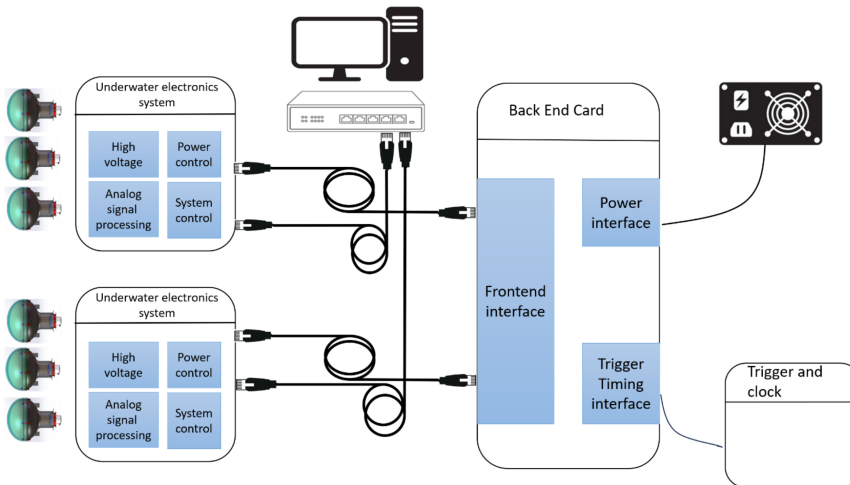
Figure 5.17 summarizes the different underwater and outside water electronics connection scheme versions. A simplified version of the BX scheme is shown in Figure 5.17a. One PMT is connected to one GCU, and one Ethernet cable links the GCU to the BEC. Different 1F3 designs were studied and are represented in panels 5.17b, 5.17c, and 5.21. The differences between the schemes lie in how the data link, trigger link, and power supply link are connected to the rest of the setup.

Figure 5.17b illustrates the 1F3 connection scheme. In this setup, one dedicated Ethernet cable handles event data and slow control information exchange over Gigabit Ethernet, while another cable connects the GCU to the BEC. In the cable linking the BEC and GCU, two pairs of wires are used for the data link, and the other two pairs are allocated for the power link. The uplink (GCU to BEC) carries a 250 Mbps signal for the trigger request, while the downlink (BEC to GCU) transmits a 250 Mbps signal containing the trigger acknowledge. For the power link, one pair is used for the 48V 15W positive connection, and the other pair for the 48V 15W negative connection. The signals on the BEC are routed as follows: trigger-related signals are directed to the TTIM, while power links are connected to power connectors and a commercial power supply. This configuration allows a single BEC to manage signals for up to 48 GCU units [184].

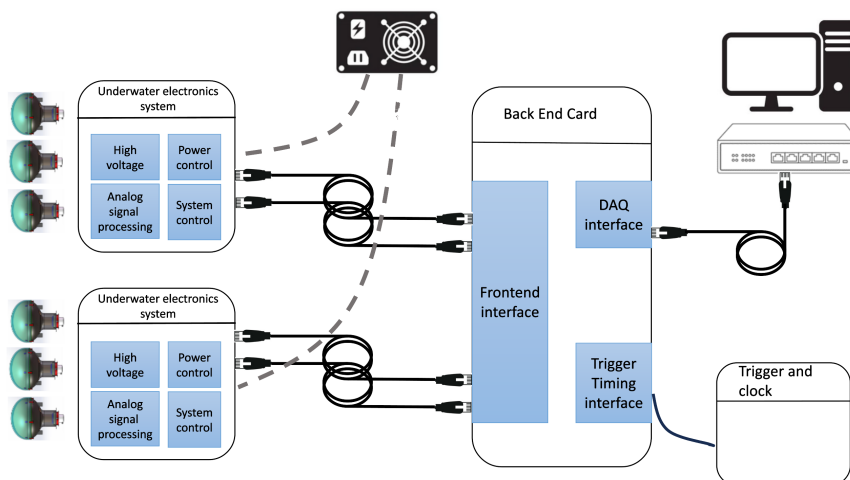
A second 1F3 scheme, 1F3RE, is also studied and shown in Figure 5.17c. In this case, two Ethernet cables connect one GCU to BEC, and a dedicated power cable is added to power the underwater system. Compared to the 1F3 design, the BEC is responsible, in addition of transmitting trigger and timing information, of the control command from the BEC to the GCU over fast/Giga bit Ethernet packet. The trigger-related signals are directed to the TTIM, while the event-related signals from the two cables are combined into a single RJ45 connector and connected to a commercial Gigabit Ethernet switch. Under normal operation, each pair of event links forms a Gigabit Ethernet connection. If one cable fails, the remaining cable continues to function as a Fast Ethernet link using the two remaining event links, thereby ensures redundancy. In the 1F3RE, a single BEC handles the signals of 24 GCU units [184].



(A) "BX scheme"



(B) "1F3 scheme"



(C) "1F3RE scheme"

FIGURE 5.17: Evolution of the different LMPT electronics schemes. The computer, the switch, and the power by the icon of the computer power supply represent the DAQ.

5.4 Back-end card version 3 (BEC-V3)

To test the BX and 1F3 schemes, a flexible BEC-V3 was designed and optimized to accommodate both configurations. This design incorporates a motherboard and mezzanine card structure where the mezzanines implement specific functional modules. The implemented interfaces on the BEC include the DAQ interface, the power interface, and the Trigger and Timing Input. The decision to move from a single board design to a baseboard with mezzanine cards was driven by several factors:

1. **Manufacturability:** integrating 48 equalizers on a single board would have made assembly extremely challenging
2. **Cost-effectiveness:** a modular design reduces the cost impact of component failures, as individual mezzanine cards can be replaced without discarding the entire board
3. **Thermal management:** smaller boards allow for better heat dissipation
4. **Reliability:** the modular design enhances overall system reliability by allowing easy replacement of faulty components
5. **Consistency:** using identical mezzanine cards ensures better channel-to-channel consistency
6. **Transportability:** smaller boards are less prone to damage during long-distance transportation

The various components of BEC-V3 are presented in Figure 5.19, and the PCB design is shown in Figure 5.18. The RJ45 connectors, shown in the green boxes in Figure 5.18, are used for interfacing the GCU with the BEC. These RJ45 connectors are arranged in six batches of eight, located on the top side of the board. Below these RJ45 connectors, the red boxes indicate the equalizer mezzanine cards. The up-link trigger request signals are conditioned through those equalizers to ensure signal integrity. Centrally positioned on the baseboard, two **Low Pin Count (LPC)** FMC connectors serve as interfaces to the **TTIM**. The board design supports 96 differential pairs linking top RJ45 connected from the **GCUs** to the FPGA on the **TTIM** to handle trigger requests and acknowledgment signals.

To enable future enhancements, 96 additional differential pairs are connected to the two LPC connectors, shown in the center of the board. These pairs are designated for handling the event data and slow control signals coming from the RJ45 connectors. After initial routing, these signals go through 0-Ohm resistors and a resettable fuse before being directed to the power connectors. This layout not only facilitates the critical evaluation of data and power injection systems but also enhances system reliability and serviceability.

The power connector designated for the BEC itself is located at the upper center of the baseboard. This separate configuration of the power supply for the underwater system allows the exploration and implementation of various grounding schemes, aiming to optimize the system stability and performance. On the PCB layout, specific areas are designated for different mezzanine cards (as shown in Figure 5.18).

Five types of mezzanines are developed to be plugged into the baseboard:

- Picture 5.19a shows the equalizer mezzanine; 6 of those ones can be plugged into one baseboard. The separated mezzanine card makes it possible to design a new board with a more powerful equalizer without changing the baseboard hardware, in case the one chosen here is insufficient.
- The translator mezzanine card is shown in picture 5.19b. The **TTIM** is currently unavailable, more information is needed regarding the number of I/Os on the **TTIM**. If necessary, the number of trigger-related signals can be reduced by half using a differential to single-ended translator.

- The mezzanine card highlighted in magenta on the BEC-V3 PCB layout, shown in picture 5.19c, serves as the fanout and cable driver. As the global trigger signal remains the same across all channels, we can obtain signals for the 48 channels by branching out from a single source. This approach reduces the I/O demand for the TTIM design. The trigger signals are also transmitted to the GCU through a 100-meter cable. While equalizers are on the GCU side, installing cable drivers on the BEC end might still be necessary to enhance transmission capacity. The cable driver and fanout mezzanine car are shown in picture 5.19c.
- Picture 5.19d is the RJ45 mezzanine card. The purpose of this mezzanine card is to combine the event data-related signals from two cables to one RJ45 connector. This card is designed to be plugged into the pin in the purple box in Figure 5.18.
- The last mezzanine card is a TTIM emulator. It is shown in picture 5.19e based on the microzed development board. This board has enough pins to perform a partial test, enough to verify the required functions of BEC.

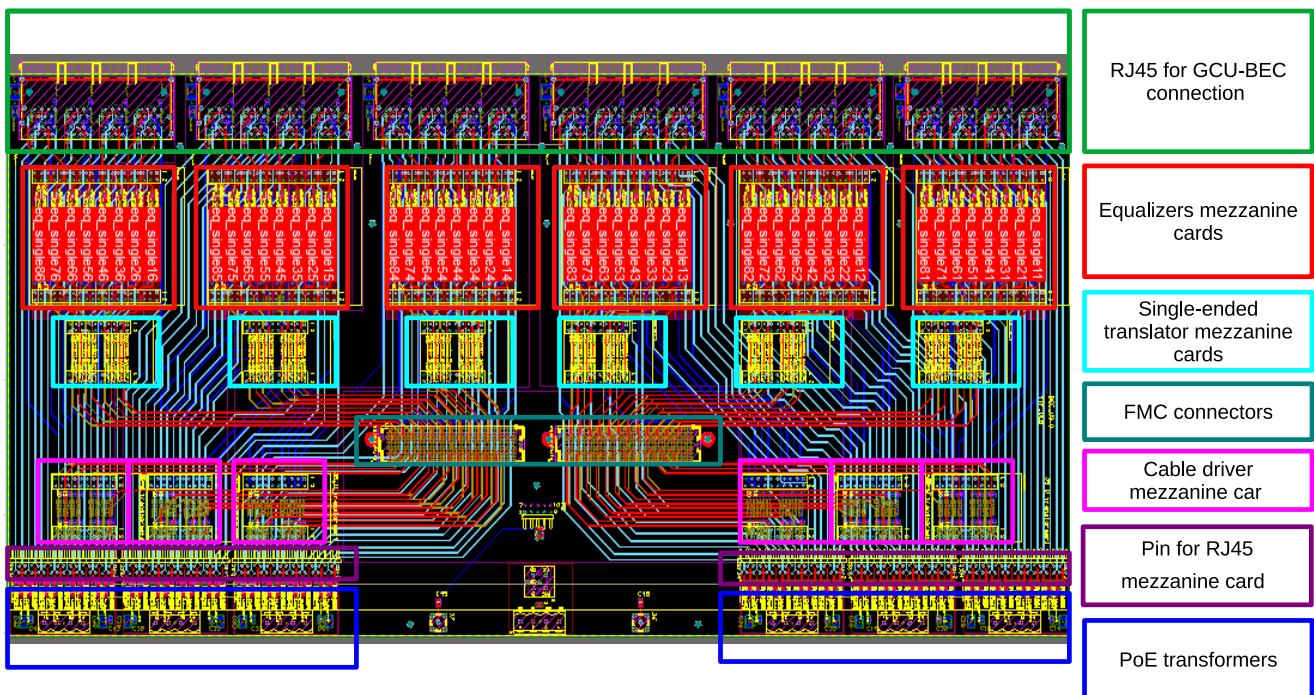


FIGURE 5.18: PCB layout of baseboard of BEC-V3

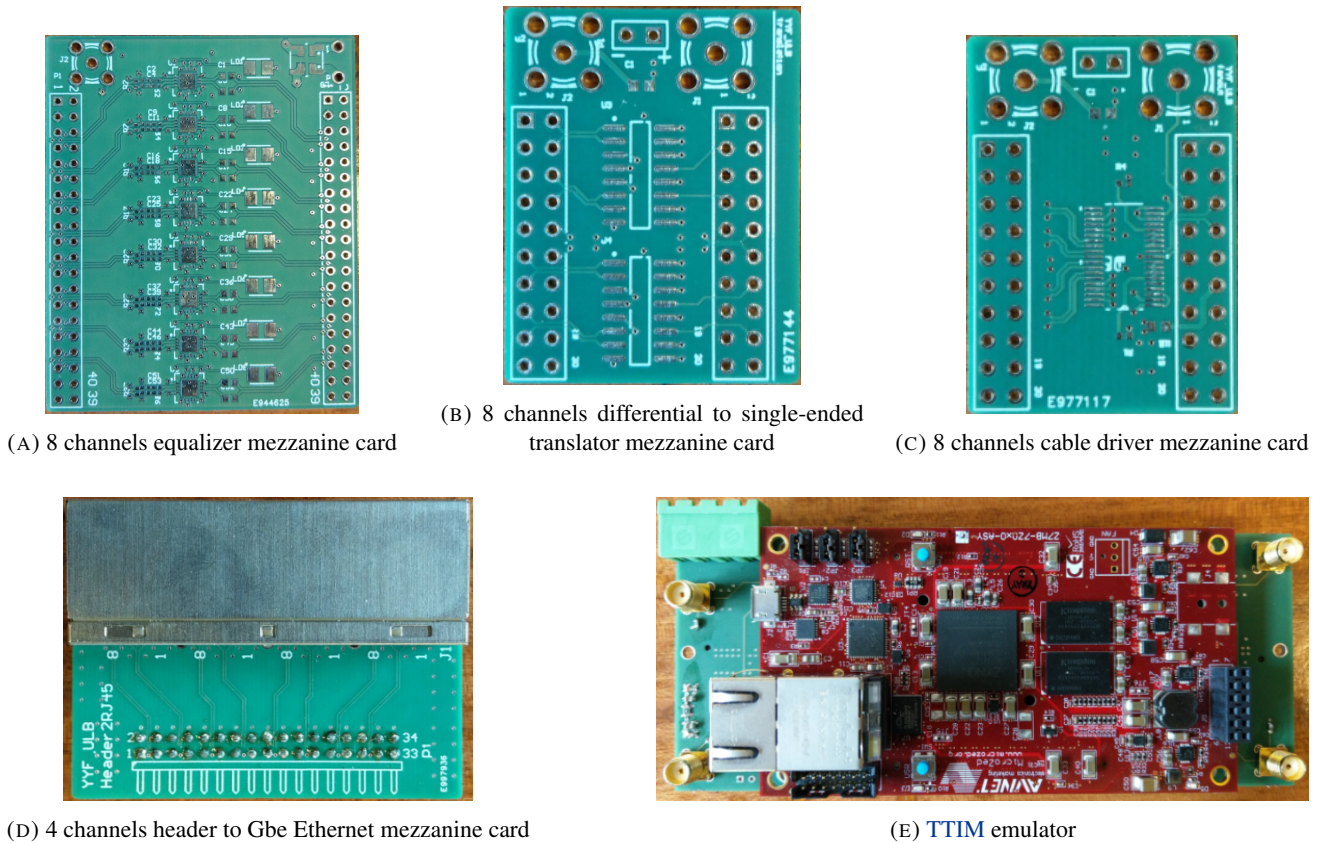


FIGURE 5.19: Different components of the BEC-V3. Images taken from [184].

The BEC-V3 design implemented several important features. Impedance control is implemented across all differential pairs, including those for power supply. Separate resettable fuse protection was provided for each power supply channel. Flexibility in grounding strategies was enabled by the separation of the back-end card and underwater electronics. Individual trigger request and acknowledgment connections were implemented via two FMC connectors for the TTIM connection.

Testing of BEC-V3 focused on three main aspects. 250 Mbps bi-directional trigger-related data transfer was performed, with emphasis on the synchronized link. The resulted eye diagram is shown on the right in Figure 5.20. The power supply delivery was tested to ensure that it correctly power the UWB. The 1 Gbps DAQ-related data transfer over combined asynchronous links was tested.

The test results for BEC-V3 were highly satisfactory, meeting all the specified requirements. This success validated the modular design approach and set the stage for the final iterations of the BEC design. The BEC-V3 and eye diagram of the synchronization test are shown in Figure 5.20.

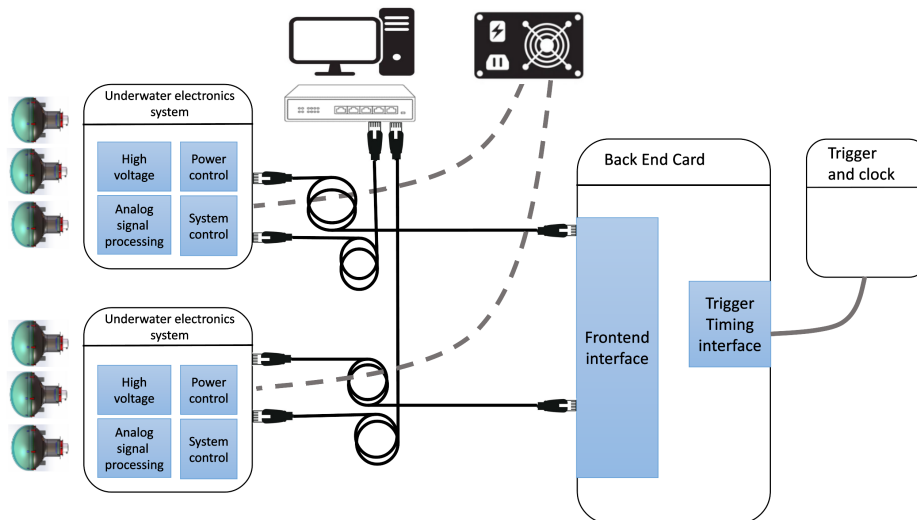


FIGURE 5.21: “1F3 final scheme”

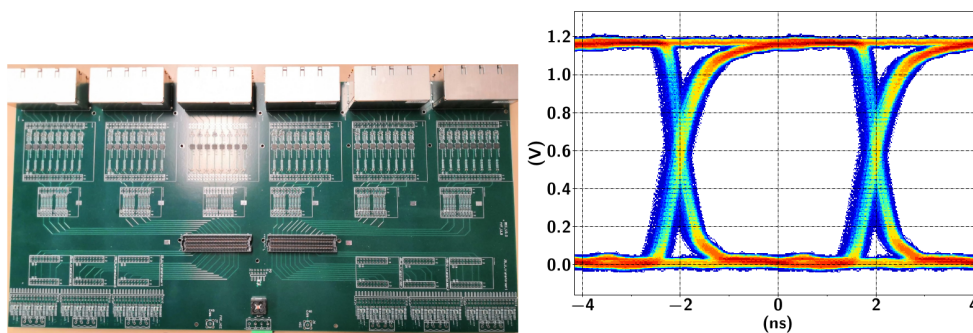


FIGURE 5.20: The left side is a picture of BEC-V3 without its mezzanine cards, and the right side is the eye diagram of the synchronization test. Image taken from BX scheme article [164].

5.5 Final scheme (BEC-V4)

An unexpected component issue in the GCU design necessitated the transition from BEC-V3 to BEC-V4. In all previous 1F3 schemes, the connection from BEC to GCU was designed as a single bidirectional 250Mbps link, with the clock embedded in the data transmitted to the GCU. The GCU was supposed to use a [Clock Data Recovery \(CDR\)](#) chip to extract the clock from this data stream. However, the selected CDR chip was discontinued, forcing a significant design change.

In the absence of the CDR chip on the GCU, it was no longer possible to recover the clock from the data stream directly. This led to desperate clock and trigger accept signals and resulted in a reduction in the global data transfer speed from 250 Mbps to 125 Mbps. Additionally, the IEEE 1588 Precision Time Protocol [185] was introduced for clock synchronization. Consequently, the revised scheme was adopted to align with the project timeline. In this final design, shown in Figure 5.21, the link from the underwater enclosure to the BEC-V4 is dedicated to carrying trigger and clock-related data. This adjustment required the doubling of the equalizer number and of the differential pair on the BEC in order to transmit all the data to the [TTIM](#). In this design, three separate cables connect the underwater electronics to the surface: one low-impedance cable to power the GCU, one CAT5E cable for the DAQ link, and a CAT6a cable for the trigger link connected to the BEC.

Despite these challenges, the BEC-V4 design maintains the successful baseboard and mezzanine card architecture of its predecessor. The main modifications included: a) the update of the FMC connectors from custom-defined LPC (Low Pin Count) to standard HPC (High Pin Count) to accommodate the increased number of I/O connections, b) management of the increased signal density, and c) the redesign the TTIM to accommodate the new connection scheme.

5.5.1 Design of BEC-V4.0

Six mezzanine cards and one TTIM are connected to one baseboard. The baseboard receives a 12 V external power supply and generates two separate 3.3 V for the six mezzanine cards and the TTIM. The baseboard is implemented with 192 signals connecting the six mezzanine cards. Compared to the BEC-V3, this design gives the following advantages: 1) double channel number in a smaller size, 2) more reliability, 3) more flexibility, and 4) higher adaptability to small combined tests. Each mezzanine card has 16 equalizers to compensate for the 16 incoming attenuated trigger request signals.

It is also implemented with 192 pairs of signals connected to the TTIM via 2 HPC FMC connectors. The TTIM follows FMC mezzanine specification, equipped with a Kintex 7 FPGA, used to communicate with the 48 GCUs and the next stage trigger system.

Baseboard design The baseboard has the following key features :

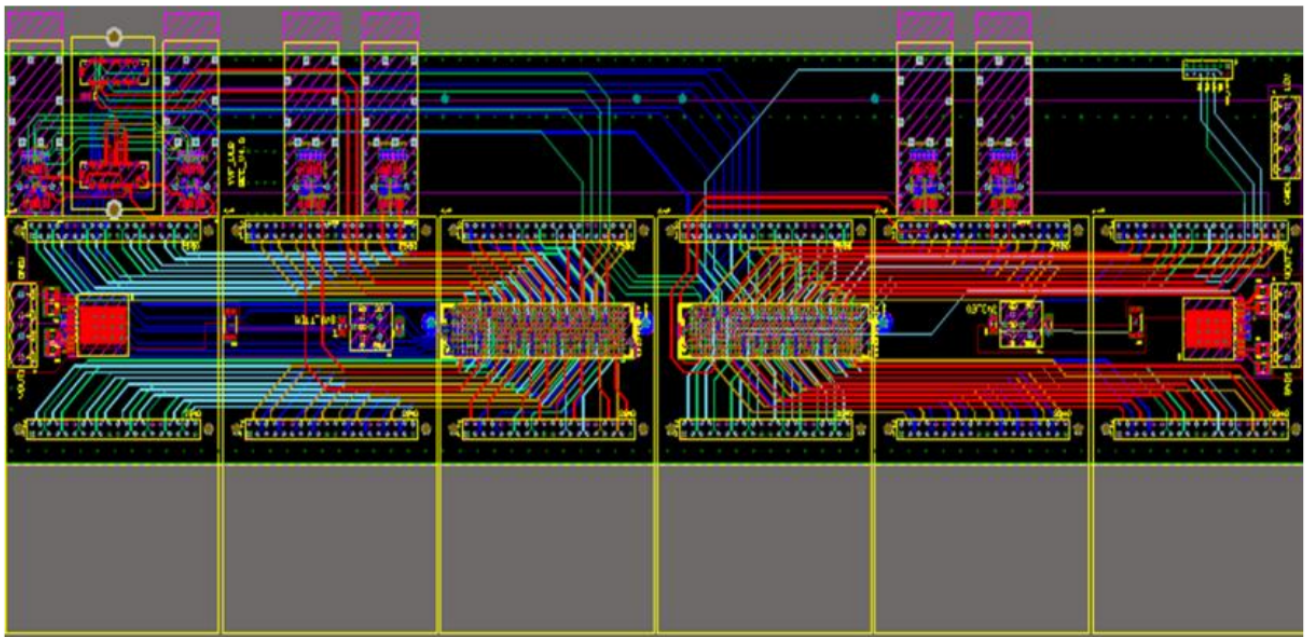
- PBC of 10.0 cm × 38.3 cm with 10 layers
- Supply power to TTIM and mezzanine separately. A 10 A filter protecting both of them
- 196 differential pairs with impedance control
- The minimum space between the differential pairs is being 4.5 times larger than the pitch

In addition, as some of the FMC's I/O was unused, we added the ability to connect small form-factor pluggable (SFP) modules and a mini White Rabbit (WR) board on the baseboard. The PCB layout of BEC-V4.0 is shown in Figure 5.22.

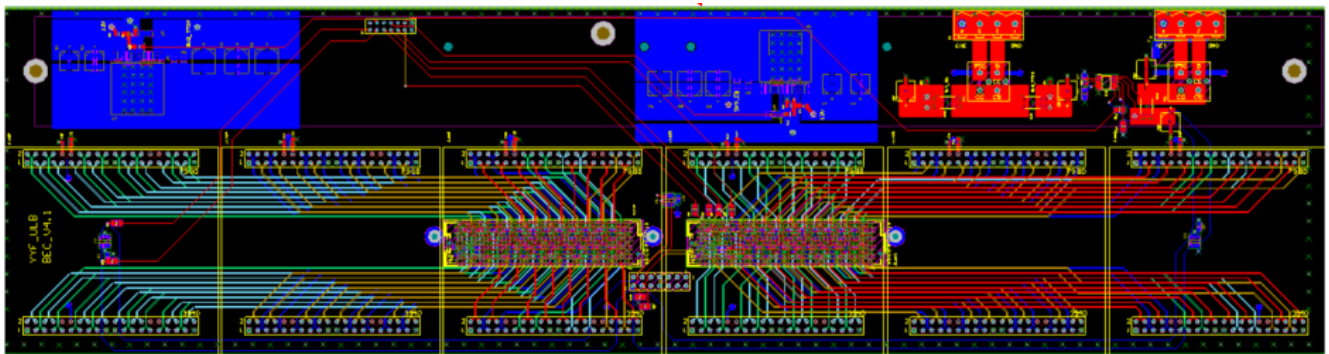
Mezzanine design The key points of the mezzanine card design are the following:

- PCB dimensions: 10.3 cm × 6.3 cm, 8 layers
- 16 DS equalizers per card
- 32 differential pairs with impedance control
- All equalizer inputs routed in stripline covered by solid ground and power planes
- Multi-channel design for all equalizers

A set of 8 RJ45 connectors is linked to the mezzanine card to establish connections with the UW electronics. Following the RJ45 connectors, the up-link trigger requests and slow control signals pass through equalizers. Subsequently, these signals are processed by the TTIM. All 96 channels are received from the TTIM on the down-link, encompassing the trigger accept and clock signals. The baseboard routes them to various mezzanines, from where they are sent to the UW electronics through the RJ45 connectors. The PCB layout of the mezzanine card is shown in Figure 5.23.

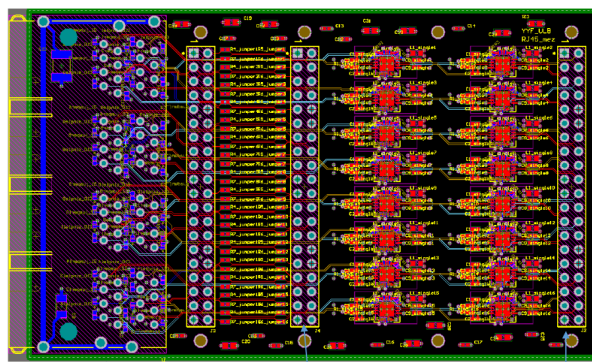


(A) PCB layout design for BEC-V4.0

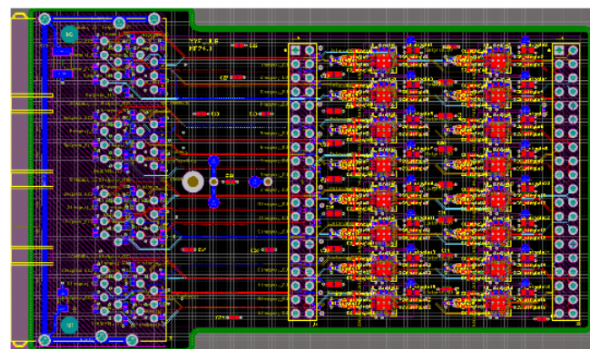


(B) PCB layout design for BEC-V4.1

FIGURE 5.22: PCB layout design for different baseboard versions.



(A) PCB layout design for mezzanine card V4.0



(B) PCB layout design for mezzanine card V4.1

FIGURE 5.23: PCB layout design for different mezzanine versions.

5.6 Function tests of the BEC V4

5.6.1 Testing strategies

Performing hardware tests on the JUNO experiment back-end card is essential for several reasons:

1. **Verification of functionality:** hardware tests ensure that each component of the back-end card works as intended. We have to validate the card's overall performance and confirm that it meets the specifications required for its role in the JUNO experiment. The specifications are detailed in section 4.3.2.
2. **Identification of defects or faults:** testing allows for the early detection of defects or faults in the hardware. We want to identify and address issues during the testing phase to prevent potential problems during the actual operations of the experiment, reducing the risk of data corruption or loss.
3. **Quality assurance:** hardware testing is a crucial step in quality assurance. It helps guarantee that the back-end card meets the reliability, accuracy, and stability standards.
4. **Performance optimization:** testing provides an opportunity to fine-tune the hardware for optimal performance. Through iterative testing, engineers can identify areas where improvements can be made to enhance the card's efficiency, speed, and overall capabilities.
5. **Compatibility testing:** the back-end card interfaces with various other components within the JUNO experiment. Hardware testing ensures compatibility with other devices and systems, avoiding integration issues that may arise during the experiment's operation.

To achieve these objectives, we have structured the testing process into two distinct phases. The first phase focuses on self-testing to evaluate the integrity and validity of the design. This phase is crucial for verifying that the individual components perform as expected separately, addressing the goals of functionality verification, quality assurance, and defect identification. By rigorously testing each component on its own during short-term and long-term tests, we ensure that the different components of the BEC are robust and reliable. This testing is performed mainly by loop test.

The second phase is dedicated to integrated testing, which involves the combination of various parts of the electronics scheme, referred as the interconnection test in the following. This phase fulfills with the goals of quality assurance, performance optimization, and compatibility testing. By evaluating the performance of the back-end card within the broader system, we can fine-tune its operation, ensure it meets the required standards, and verify its compatibility with other components in the JUNO experiment.

5.6.2 Loop test

To assess the hardware performance of the BEC, we employ a loop test, utilizing only the BEC/TTIM hardware. In this setup, the 48 upstream ports of a single BEC were connected in pairs using crossover cables. Each port has four differential pairs, two for transmitting and two for receiving. By injecting a PRBS signal into each Tx and checking for correct PRBS reception on each Rx, the functionality of every port could be verified. The test setup included: 1) A pattern generator producing four signals: two are directed to port_1 and two to port_2, 2) the signals were transmitted through the BEC and Ethernet cables, and 3) a pattern checker verified the received signals. Figure 5.24 illustrates the procedure of the loop test for two ports.

Firmware and software design To execute this straightforward test, several components on the TTIM firmware are necessary:

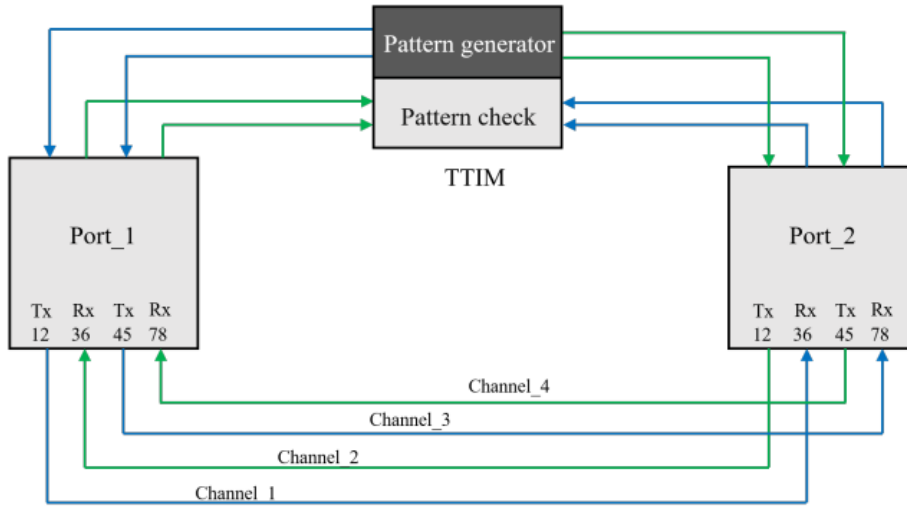


FIGURE 5.24: A PRBS IP core is implemented in the TTIM FPGA to generate and verify the PRBS data stream. Each port is connected to another port of the same BEC through an Ethernet cable. In the cable, we have four pairs; a line represents each pair. Taken from [186].

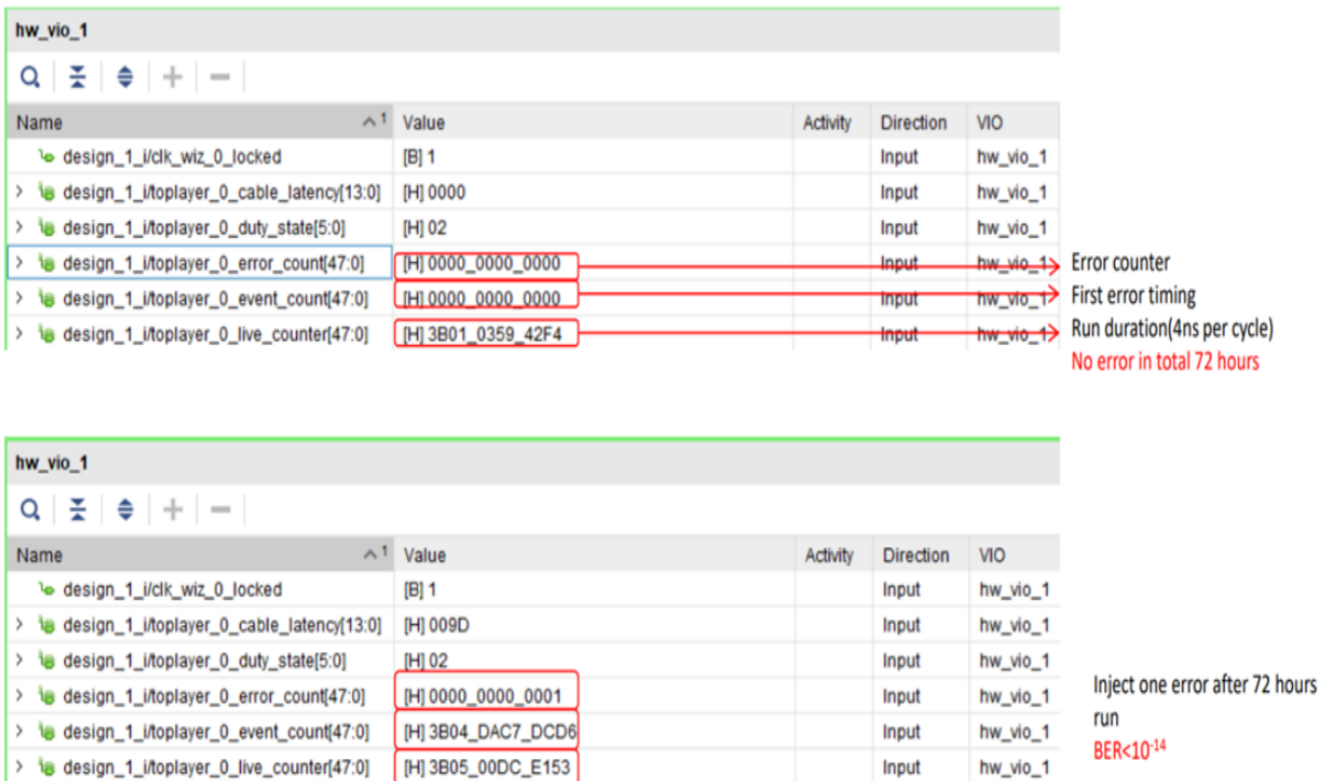


FIGURE 5.25: The top image shows the VIO, used to control the error number and the timing stamp when a first error occurs. We inject an error after 72 hours on the second image, and the VIO correctly captures the error. Taken from [186].

- A clock. The clock generate the different signals, and is used by the PRBS modules.
- PRBS modules that can be configured as generators or checkers.
- A [VIO](#) block to control the different parameters of the signals.
- [ILA](#) to output the different registers and signals.

An oscillator on the TTIM generates the clock. We use Input Buffer Differential Signaling (IBUFS) to convert the differential signal to a single signal. Then, the clock is distributed over the different blocks. Note that the clock comes from a white rabbit module in the final scheme to synchronize all the boards. For the pattern generator/checker, we will use a PRBS module [187]. Since our bandwidth is less than 10 Gbps, the PRBS-7 is the commonly used data stream to verify the physical link performance. The PRBS module can be configured to work as a checker or as a generator via the `CHK_MODE` attribute.

VIO core is a customizable core which monitors and drives internal FPGA signals in real-time [188]. The number and width of the input and output ports are customizable in size to interface with the FPGA design. Because the VIO core is synchronous to the design being monitored and driven, all design clock constraints applied to the design are also applied to the components inside the VIO core. Run time interaction with this core requires the use of the Vivado logic analyzer feature. The VIO is used here to control the speed of PRBS, clock, delay tabs, clock polarity, and bus to two [SubMiniature version A \(SMA\)](#) outputs. For example, Figure 5.25 shows the VIO output for the 72h test.

The last important block is the ILA block. ILA IP core is a logic analyzer core that can be used to monitor the internal signals of a design [189]. The ILA core includes many advanced features of modern logic analyzers, including Boolean trigger equations and edge transition triggers. The ILA is used here to store the different register values, like the error counters in our case.

Automatic loop test We use the PRBS IP core to generate the test data stream. A VIO core is used to configure the PRBS core. It governs parameters such as PRBS pattern and speed and facilitates the injection of artificial errors into the data stream. The PRBS errors are saved into a register. A clock counter running at the system clock records the timing stamp of the first error. Both the error and the timing stamp register are accessible from an ILA core. Thus, by monitoring the ILA core, we can quickly determine the link's performance during a specific period without the need for an external connection.

The test setup is shown in Figure 5.26a. The PC controls the FPGA via [VIO](#) and records the ILA values. We use a JTAG converter to link between the PC and the FPGA. Ethernet cables of various lengths are used to connect two successive ports. Another essential feature is the [SMA](#) connection from the FGPA output to the oscilloscope, which allows us to see the FPGA output signals. They allow us to perform an eye diagram at the FPGA output level. The power supply used for the BEC is a custom-made board.

As shown in Figure 5.26b, the signal is transmitted over the cables, then processed by the mezzanine's equalizer, and then returned to the FPGA. The pattern check is performed on the FPGA, and everything is stored and accessed thanks to TCL code that automatically saves the whole ILA status periodically. By analyzing the saved files, we can get the cross-section view of the link with a resolution of about 1Hz, which is enough to show the behavior and trend of the link.

The results are shown in Figure 5.27a for the loop test for BEC-V4.1 for 30 days. Blue lines are for CAT5E Ethernet cables of 20 m. Green lines are the results for the CAT6E Ethernet cables of 100 m, and cyan lines are the results for the CAT5E cables of 100 meters. The error is equal to zero, except for port 11. We draw the error as a function of the time for port 11 in Figure 5.27b. We see that the error jump occurs only once. If the error comes from a physical link, this error number will increase continuously, so we assume that some external noise-induced

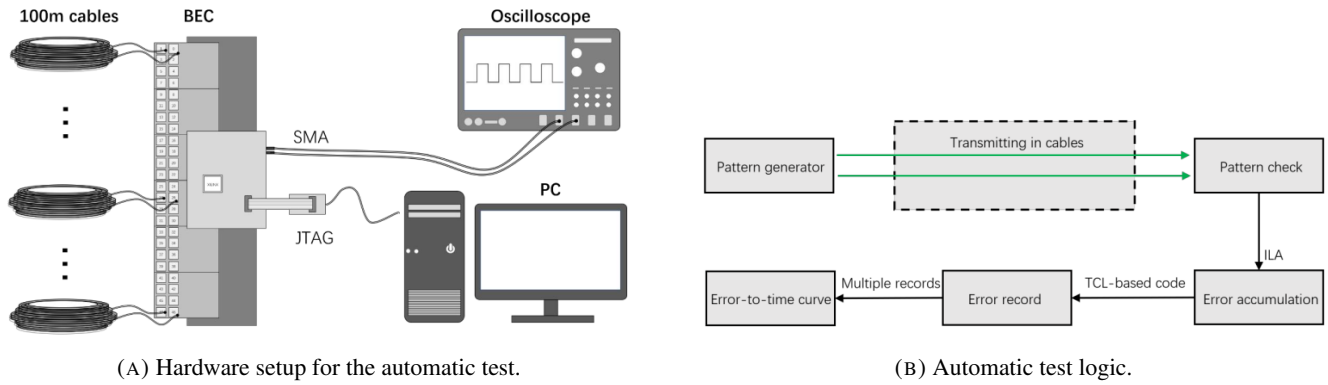


FIGURE 5.26: Automatic test for the BEC.

increases the number of errors. To verify this hypothesis, we performed an error capture test described in section 5.6.4.

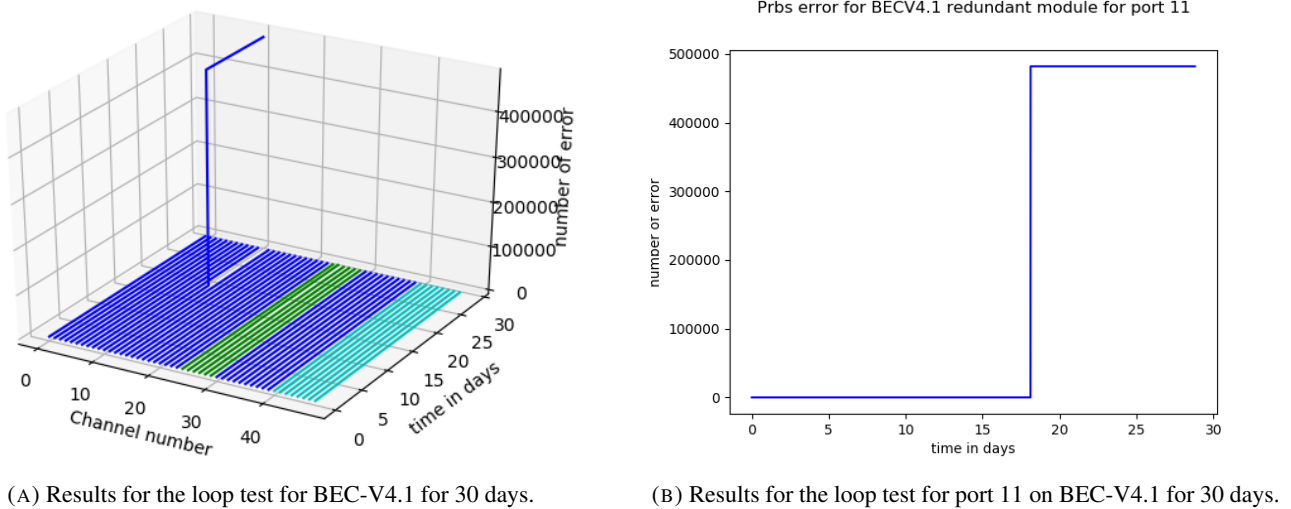


FIGURE 5.27: Result for the loop test for 30 days for BEC V4.1 . In the left pannel, the blue lines correspond to the results for 20 m CAT5E Ethernet cables. Green cables are the result of the CAT6 Ethernet cable of 100 meters, and cyan lines are the results of the CAT5E cable of 100 meters.

5.6.3 Interconnecting tests

As established in the previous section, while self-tests (loop test) are vital for verifying the individual functionality of components, comprehensive system testing is equally crucial given that the BEC forms part of a more extensive system. Therefore, it is essential to conduct tests that involve the BEC connected to other systems. At this stage of development, we primarily focus on the physical link test. A crucial aspect of the physical link test is to verify the hardware components without involving any software-based functionalities. This approach excludes any examination of software protocols, coding, or digital interfaces that manage data transmission beyond the physical layer. Such separation is crucial as it isolates hardware performance issues from software-related anomalies and thus facilitates targeted troubleshooting. The initial test involves connecting the BEC to another BEC. Subsequently, the BEC is tested in connection with a GCU. These tests are designed to validate the physical connectivity and performance of the BEC within the system.

During these tests, we evaluate various properties of the physical link, including signal strength, signal integrity, noise levels, and the ability to maintain a stable connection under varying conditions. These evaluations are critical to ensure the reliability of the BEC when interconnected with other boards. The assessments include checks for physical damage, wear, or manufacturing defects, along with measurements of the error rates.

Test with two BECs

One BEC will send the clock to the second BEC. The sending BEC is called the master, and the receiving one is called the slave. The slave is used here to emulate the GCU. Due to the limited availability of the mezzanines at that time, three mezzanines were plugged into each BEC, alternating between odd and even slots to ensure thorough hardware testing.

The first important point is the cable connection. We check the performance of the different cable lengths and types. In the setup, we use two different cable types: CAT5E [Unshielded Twisted Pair cable \(UTP cable\)](#) and CAT6 [Foiled Twisted Pair cable \(FTP cable\)/FTP cable](#). For the CAT6 FTP/FTP, only one cable of 100 m is used and is represented in light blue in Figures 5.28 and 5.29. The other is CAT5E with various lengths ranging from 10 m to 100 m. As the critical performance is for the 100 m cable, we will perform three tests to ensure that each port's performance is accessed for that cable.

The second important point is the clock distribution. It is performed by connecting Port 8 on the master board and Port 0 on the slave board via a 20-meter cable. The last important point is the power supply of those two BECs. In this case, both BECs use a programmable power supply. Using this kind of power supply guarantees good power quality and helps to remove the impact of the power supply quality on error occurrence.

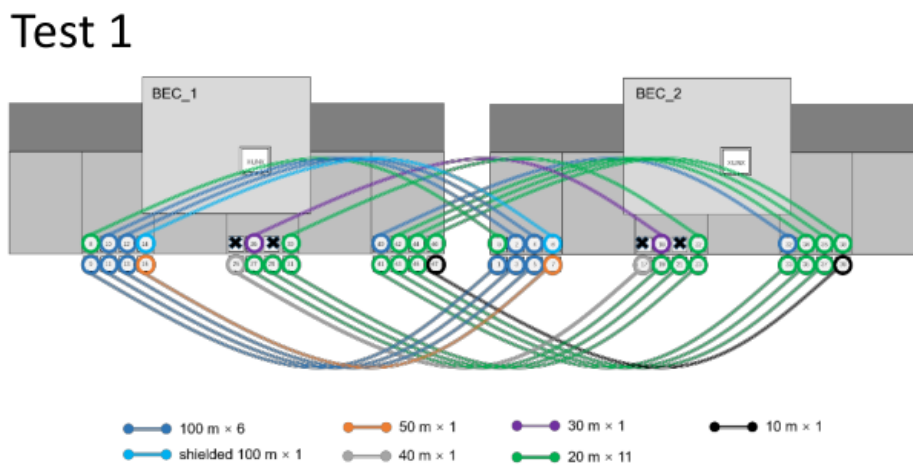


FIGURE 5.28: example for connection for two BECs test.

The results for the three different tests are shown in Figure 5.29. Only one channel in test 3 has 16 errors. We reject the error coming from the not-optimized sample point as the error is not continuously increasing. The external noise source hypothesis is also rejected, as no sharp jump is seen. Therefore we suppose this error comes from a bad connection between RJ45 Port on the BEC and the header of the cable.

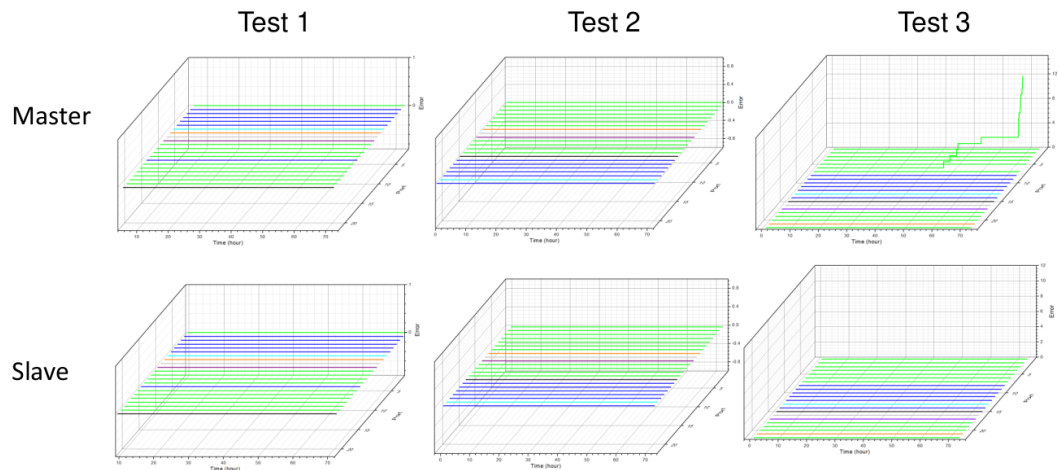


FIGURE 5.29: Error time curves for three "two BEC" test configurations. The master BEC results are shown in the first line, and the slave BEC results are shown in the bottom line.

Test with GCU

The objective of this test is identical to the previous one: to assess the physical link between the BEC and GCU. For the first time, we have access to two prototypes of the GCU, allowing us to replicate conditions as close as possible to the final system configuration.

In this setup, we use two types of 100 m cables: UTP and FTP. Both cables are encased in a metallic bellow and spooled over a length of 80 m. Specifically, GCU1 is connected via the FTP cable, and GCU2 through the UTP cable. Low-impedance cables (100 Ω) are employed for powering the GCU. This setup is shown in Figure 5.30. The different pairs of Ethernet cables are soldered directly onto the GCU board. During this phase of testing, all of the boards are housed outside their mechanical boxes, as these tests are scheduled for later during the mass production stage. Prior to discussing the results, it is important to outline the detail of four pairs of the Ethernet cable:

- Two pairs for downlink (pairs 1,2 and 4,5): one pair for 62.5 MHz clock signal, another for PRBS-7 data stream
- Two pairs for uplink (pairs 3,6 and 7,8): both transmitting PRBS7 data streams

All PRBS data streams operated at 125 Mbps to emulate the actual signal used in JUNO.

The error monitoring is conducted using **VI/O** implemented in the FPGA firmware of both the GCU and TTIM. The setup is constructed to capture both error counts and error timing, either on the TTIM FPGA or the GCU FPGA. The outputs from these **VI/Os** indicate that the system experienced problems after approximately 70 hours of operation, as depicted in the various sub-figures in Figure 5.32. Figure 5.32a shows the error counters for channels 3,6 and 7,8 on the link from GCU2 to TTIM. The output for pair 4,5 of GCU2, is shown in the first line of Figure 5.32b, highlighting where errors occurred, marked by the red line. The final Figure 5.32c displays the clock lock status for the GCU2, reporting no loss of clock throughout the entire run. The summary of the BER results is shown in Table 5.1.



FIGURE 5.30: Setup of BEC-GCU synchronization test. Two GCUs (on the left) are connected to the BEC-V4. The tests were performed in IHEP, and the picture is taken from [190].

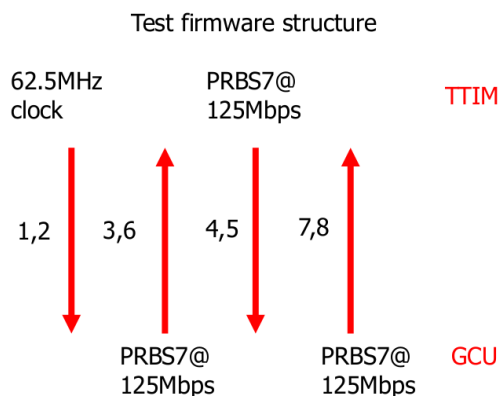


FIGURE 5.31: GCU-BEC link structure. Taken from [190].

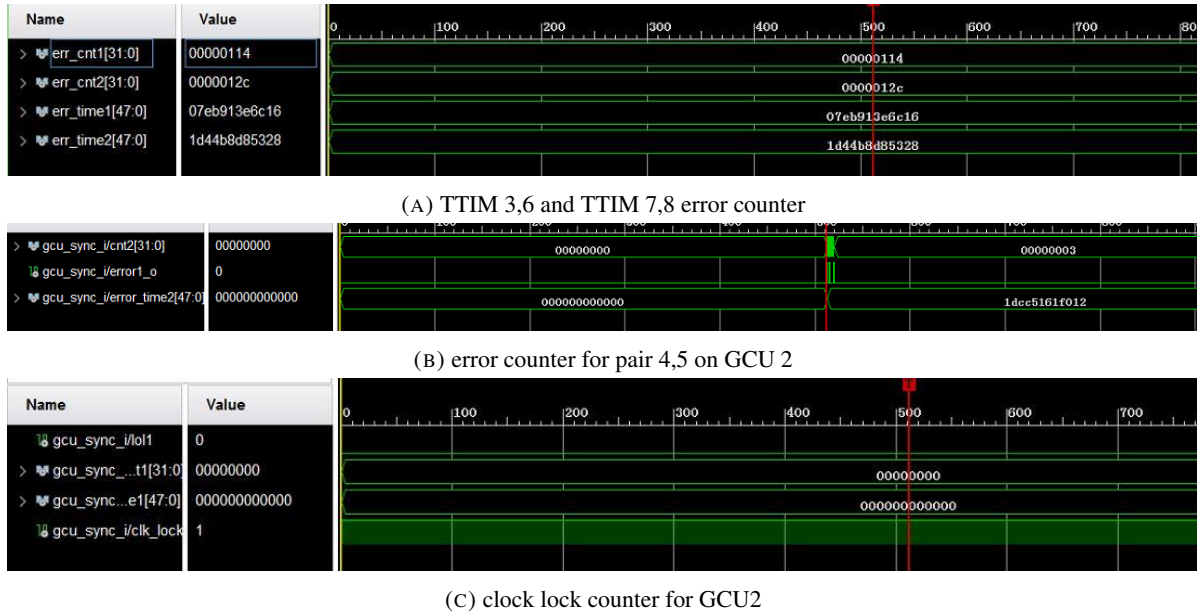


FIGURE 5.32: Results of the GCU-BEC synchronization tests. The results are obtained at the VIO, where we can observe the different error counters. Figure (A) show the error counter on pair 3,6 and 7,8 at the TTIM. Figure (B) is the error counter for pair 3,6 on the side of GCU 2 and shows no error. Figure (C) is the clock counter and synchronization status for GCU 2. The image are taken from [190].

Cable pair	BERs (60hours)		BERs (72hours)	
	GCU 1	GCU 2	GCU 1	GCU 2
1,2 (GCU1/2)	No loss of clock lock	No loss of clock lock	No loss of clock lock	No loss of clock lock
3,6 (TTIM)	1.11×10^{-14}	$< 3.70 \times 10^{-14}$	3.40×10^{-12}	4.57×10^{-9}
4,5 (GCU1/2)	$< 3.70 \times 10^{-14}$	$< 3.70 \times 10^{-14}$	$< 3.70 \times 10^{-14}$	2.09×10^{-10}
7,8 (TTIM)	$< 3.70 \times 10^{-14}$	$< 3.70 \times 10^{-14}$	3.70×10^{-12}	9.91×10^{-11}

TABLE 5.1: Summary of BER results for GCU-BEC connection perform in IHEP. Taken from [190].

5.6.4 Error capture

Error capture tests were implemented to investigate the source of occasional errors observed in the loop tests. The main goal was to determine whether errors originated from the Tx, Rx, or the transmission process itself. This distinction was crucial, as Tx or Rx errors would indicate design issues requiring optimization, while transmission errors would be more related to cable and environmental factors. Let us first discuss what can cause those errors and how to solve them by performing a quick theoretical overview.

Theoretical analysis In digital electronics, bit error measurement refers to assessing errors that occur during the transmission or processing of digital signals. Various factors can contribute to bit errors, and understanding these

errors from a theoretical point of view involves considering different aspects of the digital communication system. Here are some key theoretical concepts to explain errors in bit error measurement:

- External noise and interference:
 - Definition: noise refers to random variations in the signal, while interference introduces unwanted signals.
 - Effect on bit errors: both noise and interference can corrupt the digital signal, leading to misinterpretation of bits.
 - Potential solution: in case of noise or interference problems, we can add shielding on the cable, improving the grounding scheme, ...
- Signal-to-noise ratio (SNR):
 - Definition: SNR is the ratio of the signal power to the noise power.
 - Effect on bit errors: a low SNR implies a higher likelihood of errors, as the signal may be too weak compared to the noise.
 - Potential solution: we can play on this using different equalizers and playing on the amplitude to do the differential pair signal to improve the SNR.
- Channel characteristics:
 - Definition: the characteristics of the medium through which the digital signal travels (in our case, the copper cable inside the Ethernet cables, the copper strips on the different boards,...).
 - Effect on bit errors: channel impairments such as attenuation, distortion, and multi-path fading can introduce errors in the received signal.
- Bit rate and bandwidth:
 - Definition: bit rate is the number of bits transmitted per unit of time, while bandwidth is the frequency range available for signal transmission.
 - Effect on bit errors: high bit rates may increase the probability of errors, especially if the bandwidth of the channel is limited.
- Jitter and timing issues:
 - Definition: jitter refers to variations in the timing of signal transitions.
 - Effect on bit errors: timing discrepancies can lead to misinterpretation of bit values, causing errors in reception.
 - Potential solution: by adding different sampling points and playing on the rising edge sharpness on the FPGA firmware, we can easily solve this problem.

Setup and Results As previously discussed, we have outlined the various causes of error occurrence. The objective of this test is to capture errors and determine their origin during a BEC self-test (loop test). A BEC-V4 is connected via a 100-meter Ethernet cable, looping from one port back to another on the same device. To facilitate error capture, the FPGA firmware was modified to output the PRBS checker results on SMA output of the TTIM, enabling the use of these outputs as triggers for signal acquisition at various points in the setup.

The test setup displayed four different signals on the oscilloscope shown in Figure 5.33:

- Error indicator (green): this waveform, emanating from the PRBS checker, shows the occurrence of errors.

- Received PRBS data after equalizer (yellow): this shows the PRBS data post-100 meters of transmission and post-equalization.
- Delayed original PRBS data (pink): delayed by 500 ns to facilitate direct comparison with the received data, illustrating any discrepancies introduced during transmission.
- Received PRBS data before equalizer (blue): this waveform highlights the attenuation effects before the equalization process.

The green signal in Figure 5.33 shows the successful capture of error injected at the PRBS checker level. By comparing the pink delayed original data with the yellow received data post-equalizer, we confirmed the match between the two signals. Since the sent and the received data align, we conclude that the error originates from the injection at the FPGA level rather than from an external source.

A 72-hour test was subsequently conducted to observe long-term performance and error patterns, as presented in Figure 5.34. The same color codes are used as the one used in Figure 5.33. During this 72-hour test, the PRBS checker (green line) captured a transient error. To enhance clarity, the delayed version of the original data was overlaid on the received data post-equalizer. A sharp discrepancy, commonly referred to as a glitch, is visible in the yellow (Received PRBS data after equalizer) and blue (Received PRBS data before equalizer) signals within the red rectangle in Figure 5.34. The difference between the pink and yellow signals indicated that the error was due to external noise, as the glitch was present in the received data before equalization but absent in the original data.

To further investigate the impact of external noise, another experiment was conducted (see Figure 5.35). The setup included a green curve representing the error indicator from the PRBS checker, transmitted via an SMA cable connected to the TTIM, and a blue curve from a differential probe attached to a 100-Ohm terminator. This experiment simulated the impact of Electrical Fast-Transient⁴ noise by activating a load in a power socket adjacent to the TTIM power supply. The correlation between the activation of the load and the occurrence of errors, as shown in the figure, clearly indicates that these errors are not due to internal factors but are induced by external electrical noise sources.

Electrical Fast-Transients are a common noise source in data communications and can significantly affect data integrity. In the present study, we can conclude that external noise can induce error in the signal transmission. Given that perfect shielding is unattainable, bit errors will likely persist in data transfers using Ethernet cables. Therefore, integrating an error correction code into the communication protocol is recommended as an effective mitigation strategy.

⁴Electrical Fast-Transients are high-frequency bursts of electrical energy typically caused by switching processes or fault clearing in power circuits. Electrical Fast-Transient can induce voltage spikes in electrical lines, potentially disrupting or damaging electronic systems.

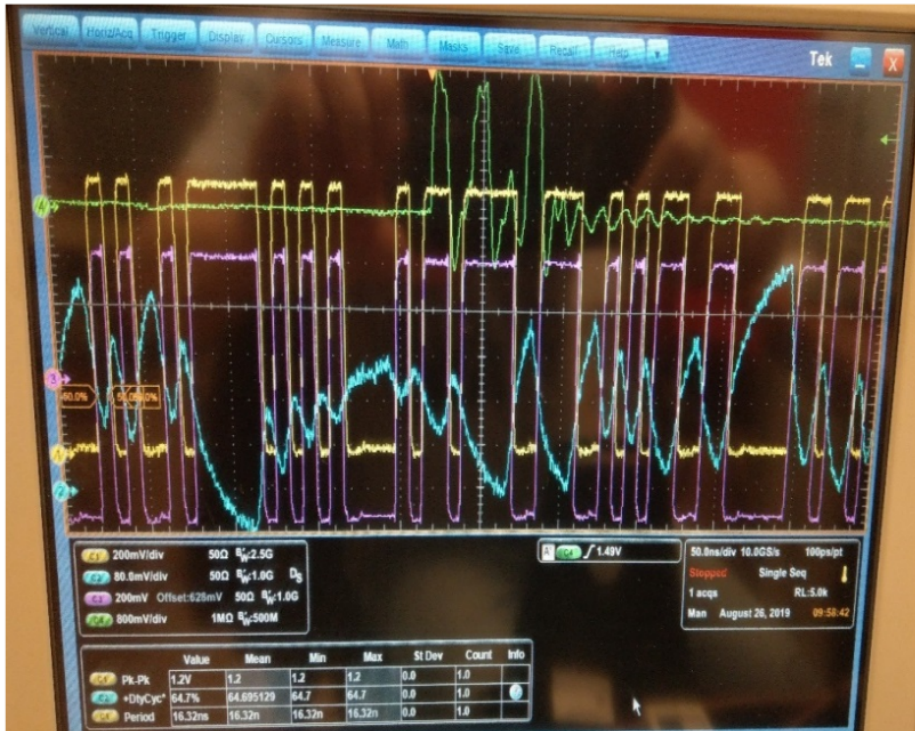


FIGURE 5.33: The four signals from the BEC error capture test. The green one is the error indicator from the PRBS checker; the yellow one is the received PRBS data (after equalizer) after 100 meter Ethernet cable; the pink one is a delayed version of the original PRBS data; it has been delayed for 500 ns to be able to compare with the received data after the long cable; the blue one is the received PRBS data before equalizer, on which we can clearly see the attenuation effect.



FIGURE 5.34: The errors are captured during a long-term test. In order to have a clear view, we have moved the delayed version of the original data to overlap with the received data after the equalizer.

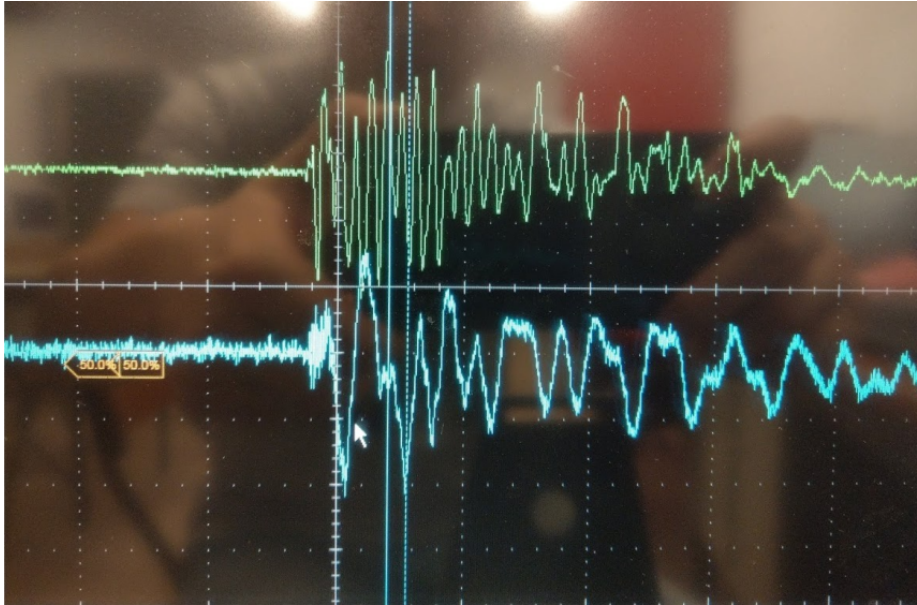


FIGURE 5.35: The green signal comes from an SMA cable connected to the TTIM and represents the error indicator of the PRBS checker. The blue signal is a differential probe connected to a 100-ohm terminator. By plugging a load in the adjacent power socket and supplying the BEC, an Electrical Fast-Transient is seen on the blue curve. The impact of Electrical Fast-Transient is seen on the PRBS checker. The Electrical Fast-Transient and the PRBS checker rise at the same time.

5.6.5 Final implementation (BEC-V4.1-2)

Based on the test results and further design reviews, BEC-V4.1 was developed in May 2020. This version included several enhancements:

1. Optimized routing of the DCDC power module
2. Addition of several TVS diodes for improved protection
3. Integration of three temperature sensors with I2C interface
4. Optimized mounting hole arrangement for better mechanical support and assembly

BEC-V4.2, finalized in April 2021, further refined the mounting hole optimization. This version became the basis for mass production, with 20 baseboards and 120 mezzanine cards manufactured, assembled, and thoroughly tested at Tsinghua University in Beijing and at ULB separately.

5.7 Summary

This chapter detailed the development and design of the BEC for the JUNO experiment. We started by describing the initial concept of underwater aggregation, and then we explained the design evolution. This evolution was not without its challenges, as we had to overcome practical issues such as signal integrity, power consumption, and installation complexity. The chapter explained the transition from underwater to above-water aggregation schemes, leading to the creation of various prototypes like BEC-V1 through BEC-V4.

Each prototype was thoroughly tested to assess its performance in real-world conditions. The focus was made on the evaluation of signal transmission over long Ethernet cables. The effectiveness of equalizers and drivers, as well as the overall reliability of the system, were assessed. The loop tests and interconnecting tests were developed to identify and address issues such as cross-talk and external noise interference. The final design, BEC-V4, was optimized for mass production, featuring a modular architecture that ensured ease of maintenance, cost-effectiveness, and reliability.

The chapter concludes with the successful implementation of BEC-V4.1 and BEC-V4.2, which were validated through extensive testing and prepared for mass production.

Chapter 6

Production and installation

In the previous chapter, we described the development and the test of the different BEC prototypes and the final prototype BEC-V4.2. The present chapter details the additional work needed to ensure the good functioning of the BEC in the JUNO experiment. First, we explain the design of the different peripherals required for the BEC. The mass production of the BEC is then given, and the different tests are performed at all the production stages. Finally, we describe the installation procedure and the different tests performed at the JUNO site.

Contents

6.1	Peripheral design	125
6.1.1	Power supply design	125
6.1.2	Box design	126
6.1.3	Temperature monitoring	129
6.2	Mass production	133
6.2.1	Production and assembly	133
6.2.2	Combined tests with GCU	134
6.3	Installation and commissioning	143
6.3.1	Physical link test (BEC loop test)	143
6.3.2	Physical link test between BECs and GCUs	144
6.3.3	Light-off test	145
6.4	Summary	152

6.1 Peripheral design

In addition to the BEC board design, two peripherals need to be designed: the power supply of the board and the mechanical box for installing the BECs in the electronic rooms.

6.1.1 Power supply design

As reliability is a major criterion for the JUNO electronic readout system, every component within a system must ensure uninterrupted functionality, especially in critical infrastructure where downtime can lead to significant losses. However, even the most robust systems are susceptible to power failures, disrupting operations and compromising performance. Implementing a redundant power supply scheme for JUNO BEC becomes imperative to mitigate this risk and to uphold operational continuity.

Loop test with redundant module The first requirement for the power supply is to use two [Advanced Technology Extended \(ATX\)](#) power supplies with a redundant module. A prototype was built using an ERDN20 [191] redundant module supplied by a [ATX](#) power supply and a programmable power supply for more convenience. An important point for us is the impact on [Bit-Error-Rate \(BER\)](#) of switching from one 12 V source to the other 12 V source. We build the setup shown in Figure 6.1b to perform the test. We connect one C3370 transistor [192] to the the positive terminal (+) of the programmable power supply. The transistor is used here as an interrupter controlled by the pulse generator. Thanks to the montage using the pulse generator, we switch on/off the signal received by port one on the redundant module every second. It means that the signal power of the BEC is successively coming from the [ATX](#) and the programmable power supply. Figure 6.1a shows the circuit schematic. The results obtained with the setup are similar to the one obtained in section 5.6.2.

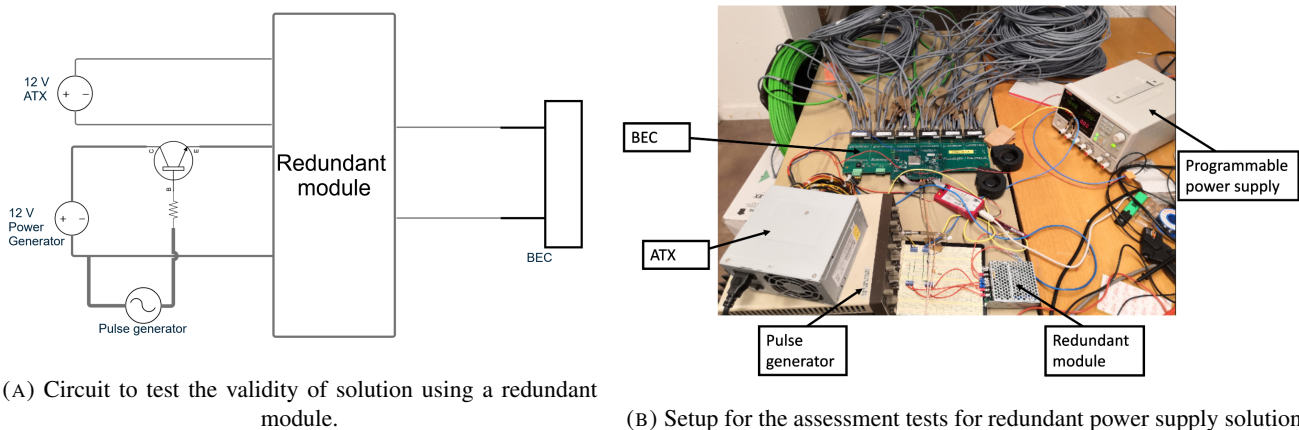


FIGURE 6.1: Setup and electrical circuit for redundant power supply of BEC.

However, due to noise considerations, the final design adopted the same power supply as the GCU. This change involves using a standard AC power source for both the GCU and BEC, which significantly reduces cable-induced noise. The GCU power supply already incorporates redundancy, eliminating the need for additional redundant modules in the BEC box.

6.1.2 Box design

To install the BEC and the related electronics in the rack in the electronic room, we need to place them in a rack-mounted steel box. This section explains the two main designs of the BEC box.

Box V1

We begin to design the mechanical support for the BEC system in 2019 based on the nVent-Schroff 1U 19-inch Wall Cabinet box. With the requirement for a redundant [ATX](#) power supply, we changed our design to a (larger) 2U box, with a special power supply connector installed on the back panel of the box and a small dedicated power board. The first version has the following elements inside:

- The BEC and the TTIM board
- Two [ATX](#) power supplies
- Three 8cmx8cm fans

- A power board

The functions of the power-board are the power distribution from the [ATX](#) power supply to the BEC and fans, the management of [ATX](#) failures, and the slow control of the BEC. Different views of the box-V1 are shown in figure 6.2. In practice, we find that there are few issues with this design:

1. There was no isolation between the box and the RJ45 connectors.
2. The BEC mounting holes are not distributed well enough to ensure the mechanical stability of the board inside the box. A solution has to be found as the box is transported to the JUNO site fully assembled.
3. The number of fans was too limited to ensure the proper cooling of the BEC in case of fan failure.

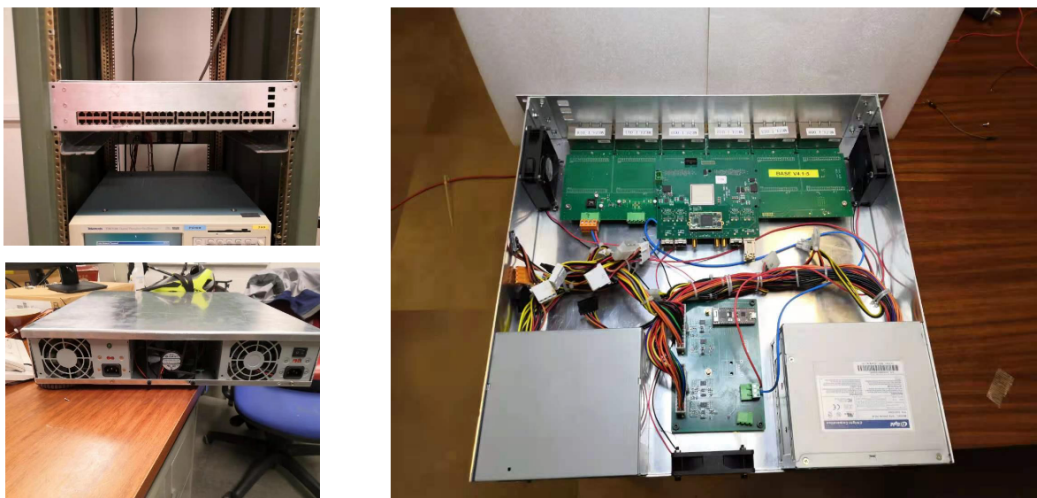


FIGURE 6.2: Box version 1. This version was tuned for power supply from two [ATX](#) modules.

Box V2

To enhance the [BER](#), the BEC now shares the same power supply as the [GCU](#), replacing the previously used [ATX](#) power supply. This change has removed the requirement for a redundant [ATX](#) power supply in the box design, as the redundancy is assured on the [GCU](#) power supply. However, to maintain flexibility, the option to use the [ATX](#) power supply as a backup remains integrated into the design. The revised design includes the following features:

- a 2U enclosure with dimensions of 45 cm by 60 cm
- five fans, each measuring 8 cm x 8 cm x 3 cm
- an updated power board
- new mounting holes to enhance stability and accommodate the updated power board
- openings on the back panel for both the primary power supply and [ATX](#) mounting
- modified support for the RJ45 connector and the debugging board.

The complete picture of the box is displayed in Figure 6.3. The power board has the following requirements. It receives a 12V input voltage, which is split in order to power the fans and the BEC separately. Several fuses and ferrite beads are added to protect the BEC from the possible shortage of fans and the noise of the fans during operation. Figure 6.4 shows the PCB layout of the power board. Additionally, the front panel of the box has been significantly modified from box version 1 and box version 2.

The front panel of the box is shown in Figure 6.5. A small debug board is mounted on the front panel above the RJ45 connectors. This board provides information about the status of the TTIM thanks to two LEDs and offers the possibility of programming the TTIM FPGA through the JTAG connection. A PPS interface is also added to access SMA output from the TTIM. Finally, the front panel has also two slots to install relays for optical fiber. One relay is used for the clock and trigger signal, and the other is used for multi-messenger triggers. We add printed supports in *Polylactic Acid (PLA)* to perform shielding on the RJ45 and on the debugging board to protect the hardware.

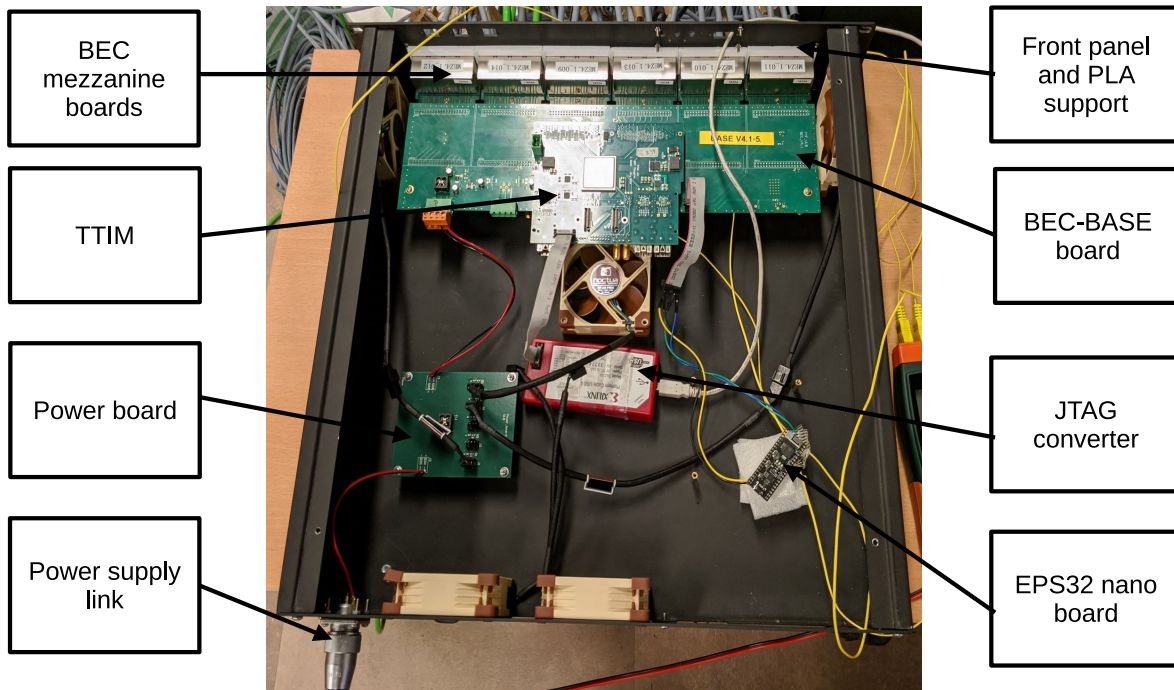


FIGURE 6.3: Box version 2. The BEC is locked in place thanks to screws and PLA RJ45 support (in white).



FIGURE 6.5: Picture of the different elements of the box's front panel.



FIGURE 6.4: Powerboard PCB layout.

6.1.3 Temperature monitoring

Ensuring optimal operating temperatures is crucial for maintaining performance and reliability. The cooling of BEC boards is pivotal in mitigating thermal issues during operation. This section presents the results of temperature monitoring tests conducted to evaluate the thermal behavior of BEC boards. The tests involve observing temperature variations over time and comparing the 3 temperature sensors (TMP100 [193]) on the baseboard with measurements obtained directly from 6 thermocouples placed on equalizers. Two additional thermocouples are placed outside the box. The thermocouples serve as a reference to calibrate the temperature sensors. The readout of the thermocouple is performed through the TC-08 thermocouple data logger [194].

Three temperature sensors on the baseboard monitor the heat generated by the equalizers, providing insight into the effectiveness of the cooling mechanism. This introduction sets the stage for a comprehensive examination of the cooling strategies employed and their implications on the reliability and performance of back-end boards in critical networking infrastructure. There is, however, a thin (8 mm) layer of air between the silicon and the equalizers, which might introduce differences between both measurements (see Figure 6.6). To have a reference in the first pro-typing testing, six thermocouples are attached to the equalizer 10 of each mezzanine (red squared in Figure 6.7).

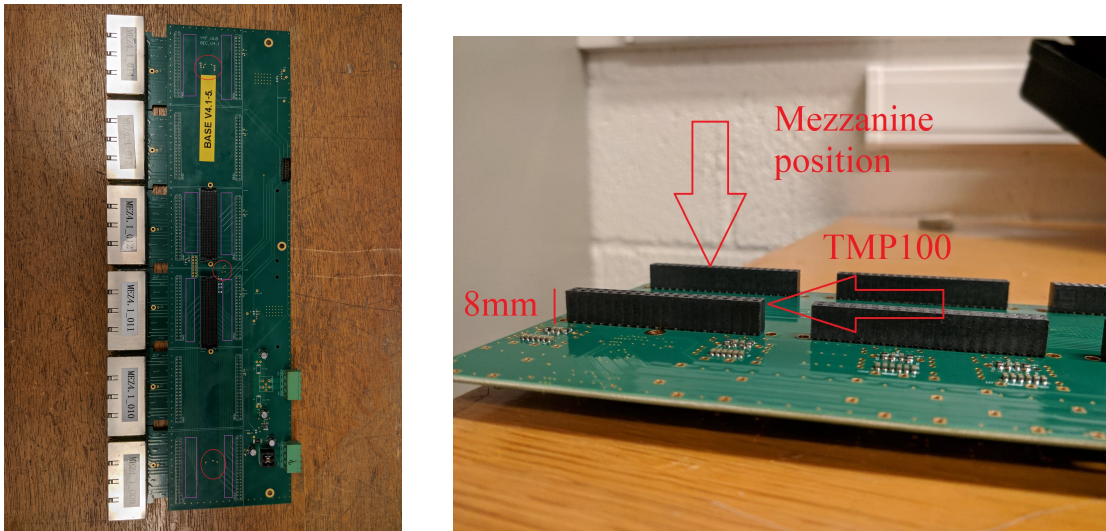


FIGURE 6.6: The left picture is the top side of the BEC V4.1, and the red circles are the position of the three TMP 100 IC. The right picture is the bottom side of the baseboard of BEC-V4.1, with no mezzanine card plugged in. The picture shows that the baseboard PCB and the mezzanine PCB are separated by 8 mm of air.

Continuous monitoring test

This test is performed to ensure the stability of temperature monitoring over a 14-day period. An ESP 32 nano board ¹ board is used to read the data of the three TMP100 IC mounted on the baseboard (blue hexagons IC3, IC4, and IC5 in Figure 6.7). The eight thermocouples are used here to reference the temperature measured by the TMP100 IC. On each mezzanine card, the thermocouple is placed on the same equalizer. Two other thermocouples are placed outside of the box, in front of fans 1 and 2, to monitor temperature outside of the box. The configuration of the different elements inside the box can be seen in Figure 6.7. Fans 1 and 3 push air inside the box, while fans 2, 4, and 5 pull air outside the box.

¹ESP32 is a series of the low-cost, low-power system on a microcontroller with integrated Wi-Fi and dual-mode Bluetooth [195].

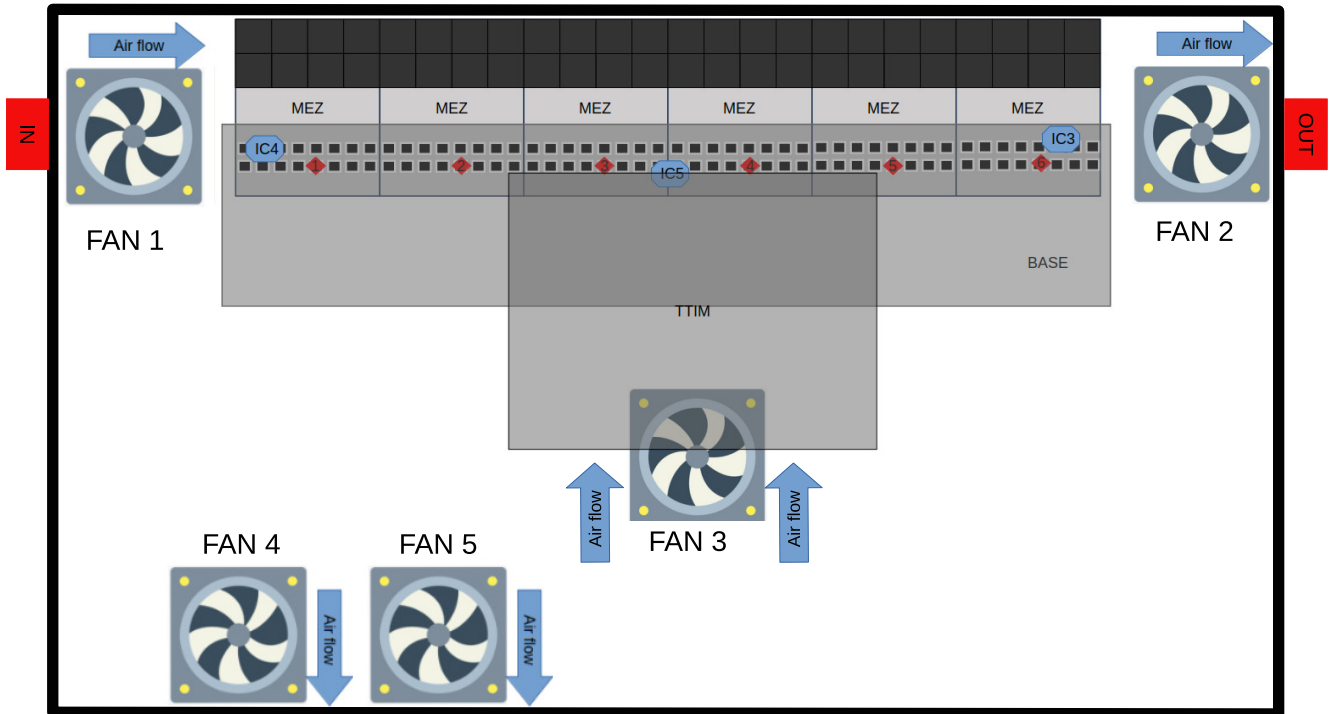
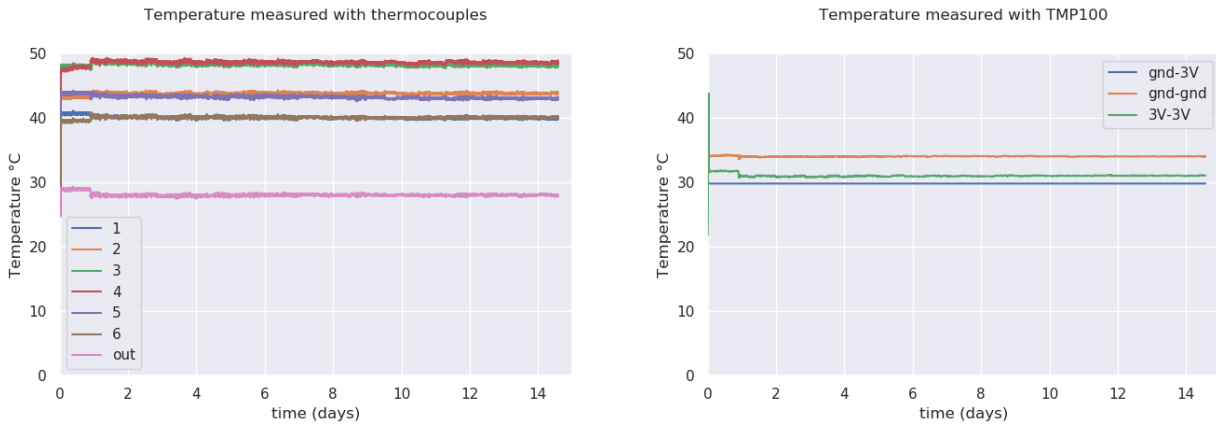


FIGURE 6.7: Schematic view of the BEC box. The blue hexagons are the three TMP 100 ICs on the baseboard. The thermocouples are the different red boxes. Six thermocouples are on the six mezzanines while two others are placed to the outside of the box.

We obtained the diagram of temperatures monitored by the three TMP100 IC sensors as shown in Figure 6.8b, and we can compare it to the temperature measured by the six thermocouples on the mezzanines as shown in Figure 6.8a. Both measurements show that the IC5 and thermocouples 3 and 4 are the hottest as they are in the center of the BEC. As we can see, the IC5 sensor is about seven degrees warmer than the other sensors, IC3 and IC4, which remain very close in temperature. The temperature profiles measured by the TMP 100 IC and the thermocouple are, therefore, consistent. These results confirm the appropriate solution of using the TMP100 IC on the baseboard to monitor the heat dissipation of the equalizers on the mezzanine.



(A) Temperature measured with thermocouples on the mezzanines

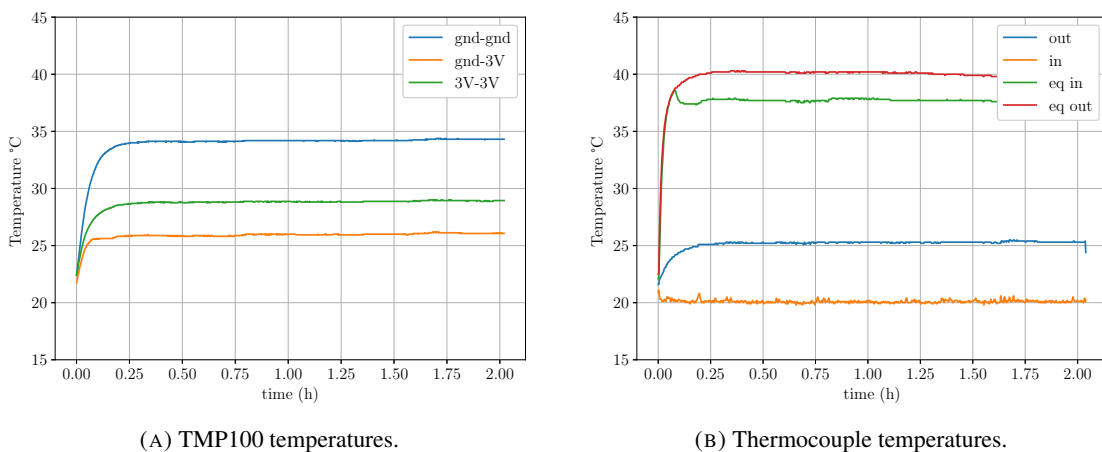
(B) Temperature from the 3 sensors on the baseboard, measured with TMP100 IC, GND-GND = IC5 (center), 3V-3V = IC3, GND-3V = IC4.

FIGURE 6.8: Temperature monitoring during 14 days.

Fan configuration test

We directly measure temperatures at four locations using a thermocouple (as shown in the right of Figure 6.7) to investigate the temperature differences between sensors on the baseboard and the thermocouples on the equalizers. The first spot, labeled "in" within the legend of Figure 6.9b, is outside the aluminum box where air enters fan number 1. The second spot, labeled "out", is outside the box where air exits fan number 2. The third spot, "eq 1", is positioned on the equalizers beneath IC4. The fourth spot, "eq 6", is positioned on the equalizers beneath IC3. The purpose of the following test is to check the cooling performance in case one or several fans are lost.

Fans 1 and 2 ON In the first experiment, we turn off all the fans except the two lateral fans (1 and 2 in Figure 6.7). This way, we expect to cool IC3 and IC4 the most, while IC5 would be the hottest sensor, as it receives the least airflow.



(A) TMP100 temperatures.

(B) Thermocouple temperatures.

FIGURE 6.9: TMP 100 and thermocouple temperatures. In panel (a), the correspondence between label and position on the BEC is GND-GND = IC5 (center), 3V-3V = IC3, GND-3V = IC4. For panel (b): out: temperature at fan 2. in: temperature at fan 1. "eq in": temperature at equalizers under IC4 (near fan 1). eq out: temperature at equalizers under IC3 (near fan 2).

As shown in Figure 6.9, the system stabilizes after 15 minutes. The TMP100 sensors read at a lower temperature than the thermocouple at the equalizer reads. IC4 sensor indicates a temperature 12°C lower than the one reported by "eq in". IC3 has a 10°C lower temperature than the one reported by "eq out". Moreover, the temperature of IC3 is 3°C higher than the one of IC4 because fan 2 is 3°C hotter than fan 1 according to the thermocouple measurement of "in" and "out". This differs from the previous test of section 6.1.3, where both temperatures were very close. It can be explained by the fact that the current experiment was done with the box placed on a table instead of a rack, allowing for better airflow. IC5 is 5°C and 8°C hotter than IC3 and IC4, respectively, as it has the worst airflow due to the geometry of the BEC.

Fans 1, 2 and 3 ON In the second one, we turn off all the fans except the two lateral and central fans (1, 2, and 3 in Figure 6.7). This way, we expect to cool IC3 and IC4 the most, while IC5 would still be the hottest sensor, even though it will receive more airflow thanks to fan number 3 compared to the previous experiment.

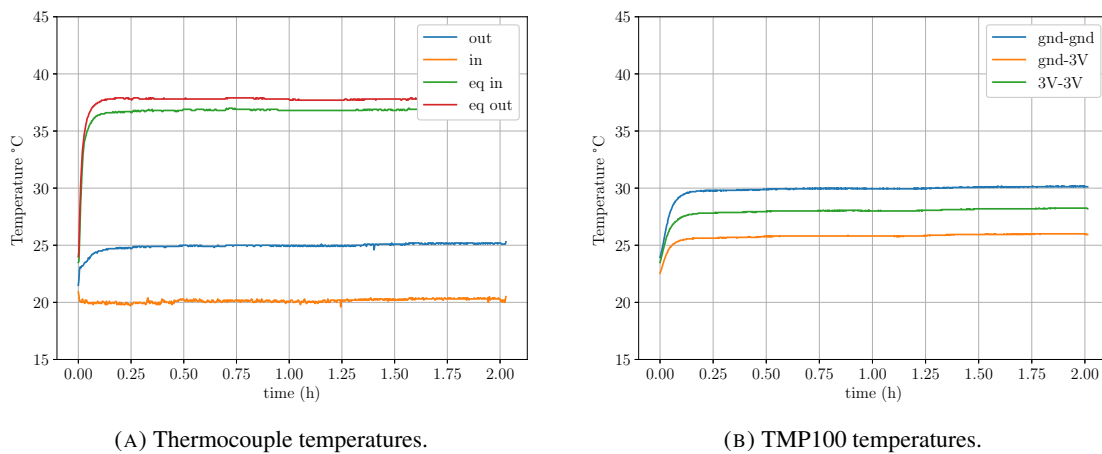


FIGURE 6.10: Thermocouple and ESP32 temperatures. In panel (a), the correspondence between label and position on the BEC is GND-GND = IC5 (center), 3V-3V = IC3, GND-3V = IC4. For panel (b): *out*: temperature at fan 2. *in*: temperature at fan 1. *eq in*: temperature at equalizers under IC4 (near fan 1). *eq out*: temperature at equalizers under IC3 (near fan 2).

In Figure 6.10, we observe the same trends as in the previous experiment. However, the *eq in* and *eq out* equalizers are almost at the same temperature (36.5°C and 37.5°C respectively), and the difference between IC4 and IC3 is 2°C instead of 3°C like before. Moreover, IC5 indicates a 4°C lower temperature than when fan number 3 was turned off. This allows us to conclude that the third fan helps cool all the equalizers, particularly the central ones.

6.2 Mass production

In this section, we describe the test performed during the mass production. At the production and assembly stages, only a loop test is performed. Then, all the BECs are shipped to a facility near Kunshan to join a combined test with GCUs.

6.2.1 Production and assembly

The manufacturing process for the BEC system involved several stages:

1. PCB production and component assembly:
 - conducted at PCB manufacturing facilities
 - initial tests for short circuits and open circuits
2. TTIM testing:
 - performed at Tsinghua University
 - check for the proper functionality of the TTIM board
3. Initial BEC system assembly:
 - integration of TTIM, baseboard, and mezzanine cards
 - 10-minute PRBS loop test using short crossover cables
 - pass criterion: No bit errors during the test
4. Box assembly:
 - conducted at Daxing facility
 - installation of the BEC system into the enclosure
 - another 10-minute PRBS loop test to verify functionality post-assembly

Optimal sampling point scan The standalone test during mass production is similar to the loop test performed in the assessment of the BEC prototype, as we aim to verify the physical link. The test uses a PRBS core on the TTIM FPGA, and it generates signals. A PRBS checker is used to verify the transmission over the line. To avoid external noise, we use a short cable (20 cm) to perform the test. In addition, before the run, we perform an eye diagram for all the 96 rx channels of the BEC. Those eyes are obtained by adjusting the delay tab, checking if an error occurs over a short period, and then changing the delay tab. A total of 62 delay tabs (IODELAY) are available in the TTIM firmware. Each delay tab is 78 ps. As we only have 62 steps of IODELAY, we can only cover about 4.8ns of the entire data eyes of 8ns. When the eye edge is inside our 62 steps, the measured eye width would be very small. This procedure pursues the goal of determining the optimal sampling point with the broadest error-free eye-opening.

Figure 6.11 shows the results for the 16 channels (8 RJ45 ports with two uplink pairs) of all 840 mezzanines. Each panel corresponds to the distribution of the partial eye width obtained after the test performed in Daxing. We get a mean for the partial eye width of 2.45 ns for all the channels tested, indicating good signal integrity for all channels. However, from the RX7 panel in Figure 6.11, we notice that one channel is far from the distribution; after a check, we see that it is channel 15 RX1 on BEC 77 (second mezzanine, equalizer on the channel 7 Rx1). After crosschecking from other tests, it seems this channel has no problem and passes the other tests.

6.2.2 Combined tests with GCU

The combined tests with GCU are performed in two phases. The first phase is performed in a facility near Kunshan from January 2022 to July 2022, and the second phase includes tests performed on the surface assembly building (SAB) and during the installation. This second phase is entirely performed on the JUNO site.

Kunshan facility tests Ensuring the reliability and performance of the LPMT electronics is vital for JUNO to achieve its energy resolution goals, especially considering that the underwater electronics boards and PMTs will be unreachable after installation. The mass production and testing of the 20-inch PMT readout electronics took place at a dedicated facility in Kunshan, China, as detailed by Coppini et al. [196] and Triozzi [197]. The testing

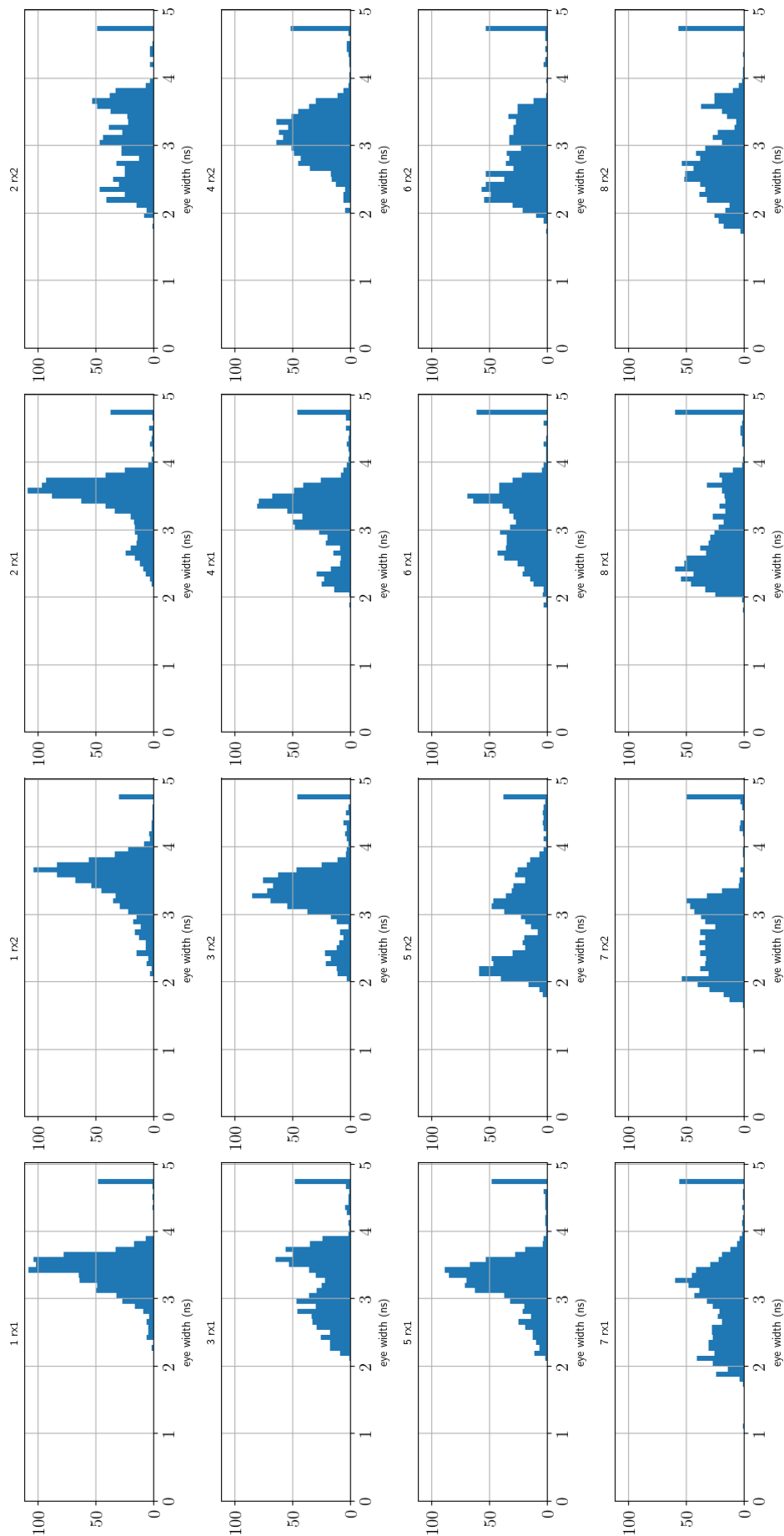


FIGURE 6.1.1: Distribution of partial eye width in ns for 140 BECs tested in Dashing.

in the Kushan facility primarily focused on assessing the GCU electronics and the GCU box sealing. These GCUs were interconnected with BECs and a DAQ system and involved four main components in the test sequence: 1) ping test, 2) linearity test, 3) stability test, and 4) slow control monitoring.

The first step of the test protocol is the ping test, which checks the connection of the GCUs to the network. The test uses the Linux ping command, as all the GCUs are connected to the same local network.

As described in section 4.2, the LPMT signal is processed by a FEC on the GCU, which provides two outputs with low and high gain. The two outputs of the FEC are then digitized by two custom FADCs. As the dynamic range of the FADCs is high, testing their linear response and measuring their gain factor is important. In this regard, an internal calibration unit is placed in the GCU. We can generate pulses with various amplitudes to test the FADCs using the calibration unit.

By using the internal calibration unit of the GCU, we generate a pulse to check the GCU hardware. In the stability test, we want to check if the different properties of the waveforms remain constant for several hours. We usually look at baseline consistency, amplitude, hit time, and FWHM.

A complete set of the sensors are installed on the GCU boards. We want to record the values of these parameters to monitor the state of the GCU. Key parameters available in the slow control link are, for example, the FPGA temperature, PMT HV values, HVU temperature, and internal voltages or currents,...

In addition to those tests, a specific test was performed to evaluate the hardware of the BEC. A partial check of the synchronous link can be performed by checking the idle packet on the slow control link. Each slow control packet has been coded with hamming code. By checking the correctness of the hamming coding, we can detect the error in the link.

Setup of the Kunshan combined test In the testing room, GCUs in batches of 40 were connected to the BECs to provide the clock to the tested boards through the synchronous link. For the asynchronous link, 40 GCUs were connected to a level 1 (L1) switch through a 1 Gb link, for a total of nine L1 switches; L1 switches were then connected to a level 2 (L2) switch through a 4x10 Gb link; the L2 switch was finally connected to the DAQ server via a 4x100 Gb optical link. The DAQ server consisted of a Dell PowerEdge C6400 [198], with a total of 24 cores and 48 threads, a 2.7 GHz processor, and 192 GB RAM—a dedicated local network communicated between the GCUs and the server. The BEC and the GCUs use the IPbus protocol to transmit the data to the DAQ. The implementation details can be found in [199]. The BEC is connected to the WR timing system. Through this connection, the BEC will send the TTC error results to the DAQ system. The TTC error data is taken in parallel every time the stability test is performed.

Figure 6.13 shows the facility where the tests are performed. On the right side of the picture is the shelf where the 40 UWB are stored during the test period. Their spooled cables surround the UWBs. Then, extension cables connect the end of the GCU cables to the electronics placed in a rack. The rack is shown on the left side of Figure 6.13. This rack contained the power supply for GCUs and BECs, as well as the L1 switch.

TTC connection between BEC and GCU The TTC connection between the BEC and GCU is a critical protocol of the JUNO experiment's trigger system. This connection serves multiple purposes:

1. Timing synchronization: it provides an accurate timing reference to ensure all GCUs are synchronized
2. Trigger distribution: it allows for the distribution of trigger decisions from the central trigger system to the GCUs
3. Control commands: it enables the transmission of control commands from the BEC to the GCUs for configuration and management

The physical link between the BEC and GCU is implemented using CAT6 Ethernet cables, which can span up to 100 meters in length. This long-distance connection poses significant challenges in terms of signal integrity and noise resistance.

The TTC protocol used in this connection is a modified version of the CERN TTC protocol [200], a bidirectional communication protocol. In the downstream direction (BEC to GCU), it carries timing information, trigger decisions, and control commands. In the upstream direction (GCU to BEC), it carries trigger requests and status information.

The protocol uses a fixed-latency, deterministic transmission scheme to ensure precise timing. The data is encoded using a robust error-detection coding scheme, which allows for the detection of transmission errors at the receiving end.

Using TTC decoding errors to detect physical link issues The process of using TTC decoding errors to detect physical link issues is an innovative "side-band" method developed to overcome the limitations of direct testing in the JUNO experimental environment. Here is a detailed description of this process:

1. Error Detection Coding: the TTC data is encoded at the transmitting end (either BEC or GCU) using an error detection code, such as Hamming code or Cyclic Redundancy Check (CRC); this encoding adds redundant information to the data stream, allowing for error detection at the receiving end.

2. Continuous monitoring: the TTIM (Timing and Trigger Interface Module) on the BEC continuously monitors the incoming TTC data from all connected GCUs; even when no active triggers or commands are being sent, the TTC link carries "idle" packets to maintain synchronization and allow for continuous link monitoring.

3. Decoding process: for each received TTC packet, the TTIM attempts to decode the data using the known error detection code; the decoding process is successful and matches the expected redundancy check, the packet is considered error-free; if the decoding process fails or the redundancy check does not match, a decoding error is flagged.

4. Long-term monitoring: by continuously monitoring TTC decoding errors over long periods, gradual degradation of link quality can be detected early; this allows for preventive maintenance before link issues affect data quality.

The advantage of this method is that it allows continuous monitoring of link quality without interrupting regular data taking. It leverages the existing TTC protocol, and it does not require additional test equipment or procedures. This side-hand method makes it an ideal solution for a complex experimental setup like JUNO, where direct access to equipment for testing may be limited once the installation is complete.

Results We will analyze the combined/production test in Kunshan. Each BEC is connected to 40 GCUs. We analyze the data received and decoded by the TTIM. The analysis procedure is the following:

- First, remove the runs lasting less than 40 minutes
- In every run, the channel will be marked as "error" if an error occurs at any time step
- We generated a table with the following color codes:
 - **NULL** : it means no GCU was connected on this port
 - **6824** : the GCU with ID number 6824 was connected, and this run layout is "error" labeled. The shade of the red color corresponds to the number of errors per hour

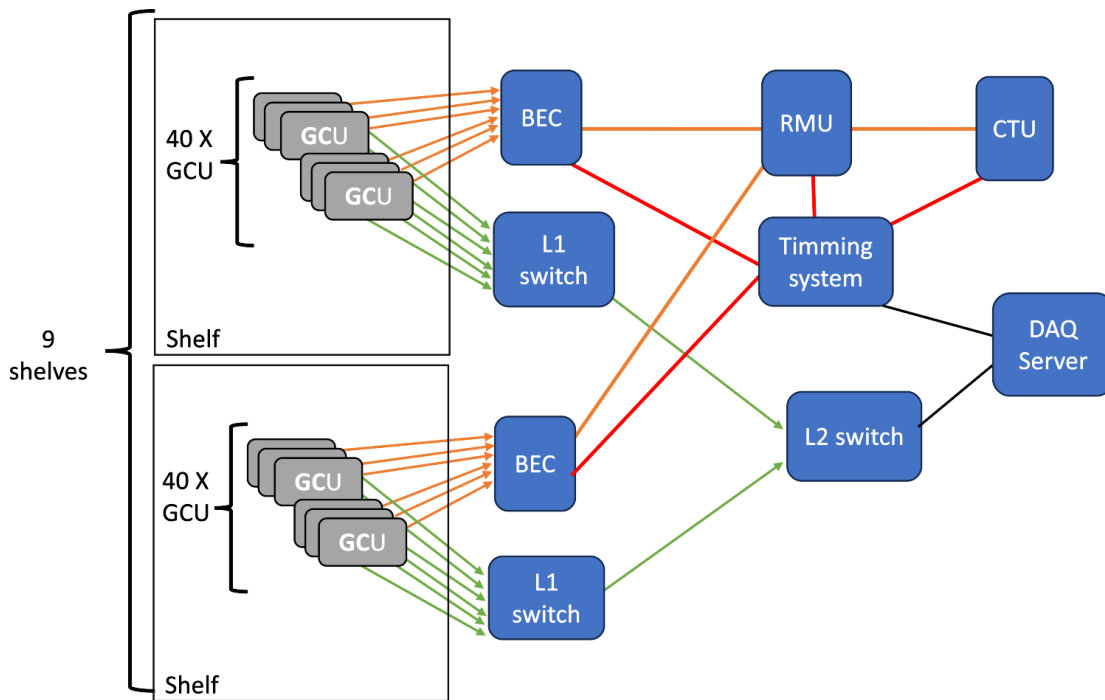


FIGURE 6.12: Logic used for the Kunshan test.

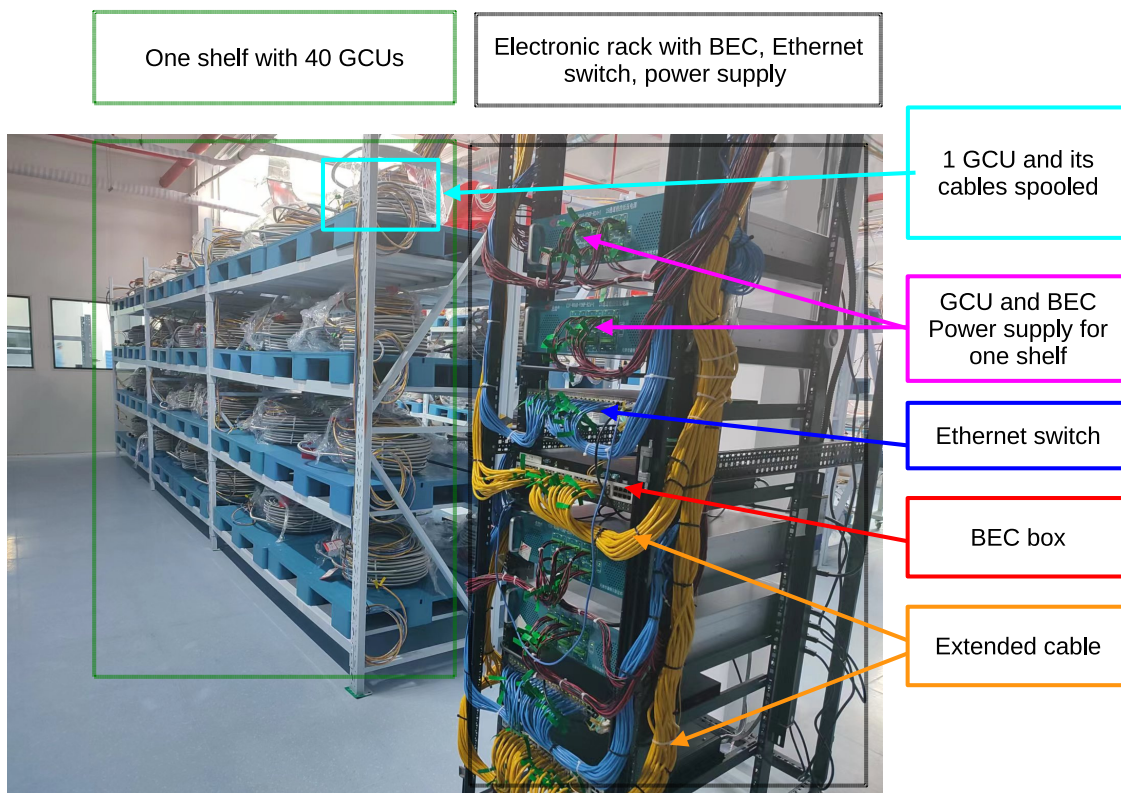


FIGURE 6.13: A shelf filled with UWBs in the Kunshan facility’s testing room. A rack with power supplies, switches, back-end, and trigger electronics is visible in the foreground. Taken from [196].

- We have these two colors for the test results for the last line of the tables:
 - **Pass**: this channel pass the test
 - **Err**: this channel did not pass the test, and future investigation is needed
- File corruption errors:
 - **4259**: TTC data are not available, but the temperature data are available
 - **NDA**: no data available; we do not have any data file for this run

Table 6.1 provides data from 40 channels of BEC No. 3. The first column records the dates of various runs conducted with this BEC, while the last column notes the duration of each run. The remaining columns represent the 40 channels; each cell within these columns indicates the ID of the GCU connected to the corresponding BEC channel during that run. To give an example, reading the cells in the Ch1 column for the run on 2022-02-10 at 23:21 shows that GCU 5950 was connected. This cell is highlighted in red to indicate that errors were detected during this run. The final row of the table provides a summary of the test history, where the pass/error threshold is defined as follows: a channel is considered to have passed if at least one run is error-free. In opposition, if all runs exhibit errors, the channel is marked as "Err" and targeted for further debugging.

Tables 6.2, 6.3, and 6.4 document the tests for BEC Nos. 49, 50, and 51, respectively. BEC No. 49 was tested from May 26 to May 28, 2022; BEC No. 50 from March 30 to April 3, 2022; and BEC No. 51 from March 17 to March 22, 2022. Throughout these periods, the facility functioned normally. It is notable that the BECs were changed frequently but not systematically. For example, BEC Nos. 49 and 51 each interfaced with only one set of GCUs, whereas BEC No. 50 interacted with two different sets.

A major concern is the inconsistency in test repeatability. For example, in Table 6.2, the run on May 26, 2022, at 17:40, shows no errors on channel 40, but the following tests alternated between error-free and error-present states. No changes in GCU connections were recorded during these tests, leaving the source of the errors unclear. This problem is not isolated to BEC No. 49; similar inconsistencies are observed in BEC No. 50 and 51. Specifically, on April 2, 2022, at 01:58, channel 36 of BEC No. 50 showed no errors, though the runs immediately before and after displayed errors. In the opposite order, on March 21, 2022, at 05:06, channel 5 of BEC No. 51 connected to GCU 4316, an error-free run; however, errors occurred in adjacent runs.

Another significant issue is the presence of tests where all channels are in an error state. For instance, the run on May 28, 2022, at 01:09, as shown in Table 6.2, is a typical example where all channels of BEC No. 49 were in an error state. A similar situation occurred in BEC No. 50 during the run on April 1, 2022, at 07:58, where 40 channels showed errors, while the previous and subsequent runs showed 39 channels with errors. These widespread errors across multiple channels suggest that external noise sources might have affected the setup. In the section detailing the error capture for loop tests (Section 5.6.4), we have already demonstrated that it is possible to detect error occurrences due to external noise. Although we cannot replicate the exact test in the Kunshan setup, we can compare the location of errors across two consecutive tests to infer the impact of external noise. The procedure to highlight this phenomenon is done by generating tables run-by-run, with Table 6.5 providing an initial example.

The first column of Table 6.5 lists the shelf number, the second column indicates the BEC number to which all GCUs on that shelf are connected, and the last column shows the duration of the run. The remaining columns present the results for the 40 BEC channels. It is noted that channels 33 to 40 were never connected to any BEC on shelves 8 and 9.

To determine the impact of external noise, we compare two tables from consecutive runs on May 28, 2022. Table 6.5 details the run at 01:09, showing all cells marked in red, with a deeper red for channels 1 to 5. According to the legend under the table, this indicates a higher error rate per hour for these channels compared to others. In contrast, Table 6.6 from the subsequent run at 16:10, where all BEC and GCU configurations remained unchanged, shows many channels error-free. This comparison leads us to conclude that an external disturbance particularly affects channels 1 to 5 during the run at 01:09.

run	ch 1	ch 2	ch 3	ch 4	ch 5	ch 6	ch 7	ch 8	ch 9	ch 10	ch 11	ch 12	ch 13	ch 14	ch 15	ch 16	ch 17	ch 18	ch 19	ch 20	ch 21	ch 22	ch 23	ch 24	ch 25	ch 26	ch 27	ch 28	ch 29	ch 30	ch 31	ch 32	ch 33	ch 34	ch 35	ch 36	ch 37	ch 38	ch 39	ch 40	Dur.	
2022-02-10-2321	5950	5672	5941	5980	5457	5539	5436	4833	6231	6129	4832	6724	4820	6090	5455	5481	5627	6203	5258	6105	6256	5542	5604	5205	5137	5290	6234	5292	6229	6171	5503	5861	5903	5259	5551	6494	5099	6728	5324	6394	1.23 h	
2022-02-11-0344	5950	5672	5941	5980	5457	5539	5436	4833	6231	6129	4832	6724	4820	6090	5455	5481	5627	6203	5258	6105	6256	5542	5604	5205	5137	5290	6234	5292	6229	6171	5503	5861	5903	5259	5551	6494	5099	6728	5324	6394	5.00 h	
2022-02-14-0131	4672	5670	4626	4511	6001	4606	15436	4371	4284	4625	4591	4910	5240	6094	4271	4327	5227	4638	4668	6166	4696	5553	5953	4258	5336	4878	5229	5471	5729	5273	15503	4530	5341	5781	5046	5788	5788	6149	5140	5626	5063	1.23 h
2022-02-14-0437	4672	5670	4626	4511	6001	4606	15436	4371	4284	4625	4591	4910	5240	6094	4271	4327	5227	4638	4668	6166	4696	5553	5953	4258	5336	4878	5229	5471	5729	5273	15503	4530	5341	5781	5046	5788	5788	6149	5140	5626	5063	4.00 h
2022-02-15-0255	4672	5670	4626	4511	6001	4606	15436	4371	4284	4625	4591	4910	5240	6094	4271	4327	5227	4638	4668	6166	4696	5553	5953	4258	5336	4878	5229	5471	5729	5273	15503	4530	5341	5781	5046	5788	5788	6149	5140	5626	5063	1.25 h
2022-02-15-0407	4672	5670	4626	4511	6001	4606	15436	4371	4284	4625	4591	4910	5240	6094	4271	4327	5227	4638	4668	6166	4696	5553	5953	4258	5336	4878	5229	5471	5729	5273	15503	4530	5341	5781	5046	5788	5788	6149	5140	5626	5063	3.98 h
2022-02-16-0124	4672	5670	4626	4511	6001	4606	5480	4371	4284	4625	4591	4910	5240	6094	4271	4327	5227	4638	4668	6166	4696	5553	5953	4258	5336	4878	5229	5471	5729	5273	5798	4530	5341	5781	5046	5788	5788	6149	5140	5626	5063	1.23 h
2022-02-17-0117	4672	5670	4626	4511	6001	4606	5480	4371	4284	4625	4591	4910	5240	6094	4271	4327	5227	4638	4668	6166	4696	5553	5953	4258	5336	4878	5229	5471	5729	5273	5798	4530	5341	5781	5046	5788	5788	6149	5140	5626	5063	1.23 h
2022-02-18-0025	4672	5670	4626	4511	6001	4606	5480	4371	4284	4625	4591	4910	5240	6094	4271	4327	5227	4638	4668	6166	4696	5553	5953	4258	5336	4878	5229	5471	5729	5273	5798	4530	5341	5781	5046	5788	5788	6149	5140	5626	5063	1.23 h
2022-02-18-0153	4672	5670	4626	4511	6001	4606	5480	4371	4284	4625	4591	4910	5240	6094	4271	4327	5227	4638	4668	6166	4696	5553	5953	4258	5336	4878	5229	5471	5729	5273	5798	4530	5341	5781	5046	5788	5788	6149	5140	5626	5063	4.98 h
2022-02-19-0045	4672	5670	4626	4511	6001	4606	5480	4371	4284	4625	4591	4910	5240	6094	4271	4327	5227	4638	4668	6166	4696	5553	5953	4258	5336	4878	5229	5471	5729	5273	5798	4530	5341	5781	5046	5788	5788	6149	5140	5626	5063	1.23 h
2022-02-19-0220	4672	5670	4626	4511	6001	4606	5480	4371	4284	4625	4591	4910	5240	6094	4271	4327	5227	4638	4668	6166	4696	5553	5953	4258	5336	4878	5229	5471	5729	5273	5798	4530	5341	5781	5046	5788	5788	6149	5140	5626	5063	5.00 h
2022-02-20-0101	4672	5670	4626	4511	6001	4606	5480	4371	4284	4625	4591	4910	5240	6094	4271	4327	5227	4638	4668	6166	4696	5553	5953	4258	5336	4878	5229	5471	5729	5273	5798	4530	5341	5781	5046	5788	5788	6149	5140	5626	5063	1.23 h
2022-02-20-0239	4672	5670	4626	4511	6001	4606	5480	4371	4284	4625	4591	4910	5240	6094	4271	4327	5227	4638	4668	6166	4696	5553	5953	4258	5336	4878	5229	5471	5729	5273	5798	4530	5341	5781	5046	5788	5788	6149	5140	5626	5063	4.98 h
2022-02-21-0137	4672	5670	4626	4511	6001	4606	5480	4371	4284	4625	4591	4910	5240	6094	4271	4327	5227	4638	4668	6166	4696	5553	5953	4258	5336	4878	5229	5471	5729	5273	5798	4530	5341	5781	5046	5788	5788	6149	5140	5626	5063	1.23 h
2022-02-21-0310	4672	5670	4626	4511	6001	4606	5480	4371	4284	4625	4591	4910	5240	6094	4271	4327	5227	4638	4668	6166	4696	5553	5953	4258	5336	4878	5229	5471	5729	5273	5798	4530	5341	5781	5046	5788	5788	6149	5140	5626	5063	4.98 h
2022-02-23-0221	4049	3916	3926	4103	3637	3715	3481	3701	3623	3751	3599	4073	3528	4200	4224	3561	3931	4202	4081	3584	3606	3678	3616	4128	3513	3706	3621	3514	3870	4099	3958	3629	3743	3498	3925	1.23 h						
2022-02-23-0353	4049	3916	3926	4103	3637	3715	3481	3701	3623	3751	3599	4073	3528	4200	4224	3561	3931	4202	4081	3584	3606	3678	3616	4128	3513	3706	3621	3514	3870	4099	3958	3629	3743	3498	3925	2.98 h						
2022-02-23-1744	4049	3916	3926	4103	3637	3715	3481	3701	3623	3751	3599	4073	3528	4200	4224	3561	3931	4202	4081	3584	3606	3678	3616	4128	3513	3706	3621	3514	3870	4099	3958	3629	3743	3498	3925	5.00 h						
2022-02-24-1641	4049	3916	3926	4103	3637	3715	3481	3701	3623	3751	3599	4073	3528	4200	4224	3561	3931	4202	4081	3584	3606	3678	3616	4128	3513	3706	3621	3514	3870	4099	3958	3629	3743	3498	3925	5.00 h						
2022-02-25-0323	4049	3916	3926	4103	3637	3715	3481	3701	3623	3751	3599	4073	3528	4200	4224	3561	3931	4202	4081	3584	3606	3678	3616	4128	3513	3706	3621	3514	3870	4099	3958	3629	3743	3498	3925	1.23 h						
2022-02-25-0546	4049	3916	3926	4103	3637	3715	3481	3701	3623	3751	3599	4073	3528	4200	4224	3561	3931	4202	4081	3584	3606	3678	3616	4128	3513	3706	3621	3514	3870	4099	3958	3629	3743	3498	3925	1.98 h						
2022-02-26-0318	4049	3916	3926	4103	3637	3715	3481	3701	3623	3751	3599	4073	3528	4200	4224	3561	3931	4202	4081	3584	3606	3678	3616	4128	3513	3706	3621	3514	3870	4099	3958	3629	3743	3498	3925	5.00 h						
2022-02-26-1702	4049	3916	3926	4103	3637	3715	3481	3701	3623	3751	3599	4073	3528	4200	4224	3561	3931	4202	4081	3584	3606	3678	3616	4128	3513	3706	3621	3514	3870	4099	3958	3629	3743	3498	3925	4.98 h						
2022-02-27-0331	4049	3916	3926	4103	3637	3715	3481	3701	3623	3751	3599	4073	3528	4200	4224	3561	3931	4202	4081	3584	3606	3678	3616	4128	3513	3706	3621	3514	3870	4099	3958	3629	3743	3498	3925	4.98 h						

TABLE 6.1: Table for BEC number 3.

run	ch 1	ch 2	ch 3	ch 4	ch 5	ch 6	ch 7	ch 8	ch 9	ch 10	ch 11	ch 12	ch 13	ch 14	ch 15	ch 16	ch 17	ch 18	ch 19	ch 20	ch 21	ch 22	ch 23	ch 24	ch 25	ch 26	ch 27	ch 28	ch 29	ch 30	ch 31	ch 32	ch 33	ch 34	ch 35	ch 36	ch 37	ch 38	ch 39	ch 40	Dur.
2022-05-26-1740	2080	1680	2624	1426	1921	2074	1998	1975	1307	2084	1076	2033	2059	2031	1330	1276	2721	2034	2020	2057	1860	1773	2076	1992	1640	2252	1651	1837	1756	1338	2263	1727	1967	2095	2291	1982	2554	2083	2714	1941	4.98 h
2022-05-27-1454	2080	1680	2624	1426	1921	2074	1998	1975	1307	2084	1076	2033	2059	2031	1330	1276	2721	2034	2020	2057	1860	1773	2076	1992	1640	2252	1651	1837	1756	1338	2263	1727	1967	2095	2291	1982	2554	2083	2714	1941	5.00 h
2022-05-27-2239	2080	1680	2624	1426	1921	2074	1998	1975	1307	2084	1076	2033	2059	2031	1330	1276	2721	2034	2020	2057	1860	1773	2076	1992	1640	2252	1651	1837	1756	1338	2263	1727	1967	2095	2291	1982	2554	2083	2714	1941	1.23 h
2022-05-28-0109	2080	1680	2624	1426	1921	2074	1998	1975	1307	2084	1076	2033	2059	2031	1330	1276	2721	2034	2020	2057	1860	1773	2076	1992	1640	2252	1651	1837	1756	1338	2263	1727	1967	2095	2291	1982	2554	2083	2714	1941	6.00 h
2022-05-28-1610	2080	1680	2624	1426	1921	2074	1998	1975	1307	2																															

Shelf	BEC	ch 1	ch 2	ch 3	ch 4	ch 5	ch 6	ch 7	ch 8	ch 9	ch 10	ch 11	ch 12	ch 13	ch 14	ch 15	ch 16	ch 17	ch 18	ch 19	ch 20	ch 21	ch 22	ch 23	ch 24	ch 25	ch 26	ch 27	ch 28	ch 29	ch 30	ch 31	ch 32	ch 33	ch 34	ch 35	ch 36	ch 37	ch 38	ch 39	ch 40	Dur.
S1	57	2413	2068	1892	2599	1952	2843	2008	3910	4783	2092	1923	2233	1994	2060	2100	2014	2732	2318	3845	1949	2072	1909	1735	1985	1797	1807	1995	2418	1940	2356	2889	2077	1954	2024	2400	2105	2002	2362	1922	1938	6.00 h
S2	146	1971	2552	2046	2547	1920	1947	1963	1864	2006	2044	2630	1893	1925	1664	1771	2969	1983	2052	1944	2013	1728	1833	1688	1813	1752	2236	1770	1827	1823	1848	1818	2234	1481	1534	1774	2917	1896	2558	1754	1905	6.00 h
S3	117	1748	2007	1988	1566	2533	1944	2698	1976	2055	1950	2868	2363	2416	2970	1775	2032	1616	2639	1869	1789	2232	2069	2670	6243	1722	2017	2371	1868	2425	1943	2230	2078	2050	2042	1776	1704	1877	1849	1795	2916	6.00 h
S4	122	2765	2073	1709	2306	2800	2548	1861	1810	1883	1533	2011	1619	2841	1881	1577	1804	1942	2009	6715	2410	2379	1880	1410	4431	2661	1891	2039	1755	1393	1934	2479	2015	2824	2409	2430	1834	1858	2881	2235	1570	6.00 h
S5	83	1744	2869	1653	1767	1724	1656	2085	2509	1945	2851	1636	2655	1737	2586	2784	1838	1812	1856	1802	1873	1917	1933	1919	1973	2010	2831	1980	2066	4130	2608	2037	2396	2431	2388	1978	2304	2414	2080	2082	2027	6.00 h
S6	8	2616	1673	1564	2544	2421	2587	1964	1825	2383	2001	1930	2104	2440	2893	2573	1500	2867	1915	2282	1931	2123	1907	2023	2522	2028	1946	2596	2089	2040	2081	1958	1959	2690	2276	2061	2550	2054	1960	1939	1968	6.00 h
S7	49	2090	1690	2624	1426	1921	2074	1998	1975	1307	2084	1076	2033	2059	2031	1330	1276	2721	2034	2020	2057	1860	1773	2076	1992	1640	2252	1651	1837	1756	1338	2263	1727	1967	2005	2291	1982	2554	2083	2714	1941	6.00 h
S8	123	1455	1458	2266	1395	1741	1449	1785	1840	3760	1409	1729	2810	2611	1434	1632	2764	2115	2309	1427	1415	1826	1132	1793	1429	1816	1540	1515	1387	1502	2770	1912	1601	NULL	6.00 h							
S9	71	1323	1119	1424	1681	1822	1620	1763	2146	1435	1850	1965	1591	1621	1231	1659	1747	2262	1116	1603	1441	1499	1576	1536	2019	1784	1555	1408	2099	1557	1296	1890	1562	NULL	6.00 h							

TABLE 6.5: Table for Run 2022-05-28-0109.

Shelf	BEC	ch 1	ch 2	ch 3	ch 4	ch 5	ch 6	ch 7	ch 8	ch 9	ch 10	ch 11	ch 12	ch 13	ch 14	ch 15	ch 16	ch 17	ch 18	ch 19	ch 20	ch 21	ch 22	ch 23	ch 24	ch 25	ch 26	ch 27	ch 28	ch 29	ch 30	ch 31	ch 32	ch 33	ch 34	ch 35	ch 36	ch 37	ch 38	ch 39	ch 40	Dur.
S1	57	2439	1478	1243	1824	2328	1416	1665	1095	1114	1986	1739	1927	1539	2219	7573	1333	1398	2240	2508	1513	2108	1420	1782	1625	2530	1599	1251	1798	1685	2106	2103	1648	1817	920	2774	2936	1786	2288	1473	2818	5.00 h
S2	146	2202	1245	1498	1289	1226	2207	1900	1791	2271	2398	1462	1460	1239	1430	2213	1281	1948	1263	1683	2322	1728	1833	1688	1813	1752	2236	1770	1827	1823	1848	1818	2234	1481	1534	1774	2917	1896	2558	1754	1905	5.00 h
S3	117	1748	2007	1988	1566	2533	1944	2698	1976	2055	1950	2868	2363	2416	2970	1775	2032	1616	2639	1869	1789	2232	2069	2670	6243	1722	2017	2371	1868	2425	1943	2230	2078	2050	2042	1776	1704	1877	1849	1795	2916	5.00 h
S4	122	2765	2073	1709	2306	2800	2548	1861	1810	1883	1533	2011	1619	2841	1881	1577	1804	1942	2009	6715	2410	2379	1880	1410	4431	2661	1891	2039	1755	1393	1934	2479	2015	2824	2409	2430	1834	1858	2881	2235	1570	5.00 h
S5	83	1744	2869	1653	1767	1724	1656	2085	2509	1945	2851	1636	2655	1737	2586	2784	1838	1812	1856	1802	1873	1917	1933	1919	1973	2010	2831	1980	2066	4130	2608	2037	2396	2431	2388	1978	2304	2414	2080	2082	2027	5.00 h
S6	8	2616	1673	1564	2544	2421	2587	1964	1825	2383	2001	1930	2104	2440	2893	2573	1500	2867	1915	2282	1931	2123	1907	2023	2522	2028	1946	2596	2089	2040	2081	1958	1959	2690	2276	2061	2550	2054	1960	1939	1968	5.00 h
S7	49	2090	1690	2624	1426	1921	2074	1998	1975	1307	2084	1076	2033	2059	2031	1330	1276	2721	2034	2020	2057	1860	1773	2076	1992	1640	2252	1651	1837	1756	1338	2263	1727	1967	2005	2291	1982	2554	2083	2714	1941	5.00 h
S8	123	1455	1458	2266	1395	1741	1449	1785	1840	3760	1409	1729	2810	2611	1434	1632	2764	2115	2309	1427	1415	1826	1132	1793	1429	1816	1540	1515	1387	1502	2770	1912	1601	NULL	5.00 h							
S9	71	1323	1119	1424	1681	1822	1620	1763	2146	1435	1850	1965	1591	1621	1231	1659	1747	2262	1116	1603	1441	1499	1576	1536	2019	1784	1555	1408	2099	1557	1296	1890	1562	NULL	5.00 h							

TABLE 6.6: Table for Run 2022-05-28-1610.

hypothesis, two experiments were conducted:

1. The first test was carried out directly at the Kunshan facility, where we removed the extension cable from one specific BEC and conducted a 6-hour test run. This test was conclusive, showing no errors on the connected ports.
2. The second test was performed in Brussels using the same setup for a loop test and included an eye diagram analysis for cable disposition. First, we connected port 1 of the BEC to port 2 using a 50-meter cable. The eye diagram was fully open, as depicted in Figure 6.15a. Then, we used two 20-meter cables connected via a female-to-female Ethernet extender, and the eye diagram for the same two ports showed a closed eye, as illustrated in Figure 6.15b.

These tests confirmed that the use of extension cables significantly impacted the signal quality and was a significant source of errors in the combined tests.

From the tests performed at the Kunshan facility, we cannot conclude that the BECs are fully functional in a combined test setting due to the presence of extension cables. The next step involves a self-test for each BEC upon their arrival at the JUNO site and after their installation in the electronic room. Subsequently, a combined test without extension cables is planned while the GCUs are installed on the CD. These tests are detailed in the following section.

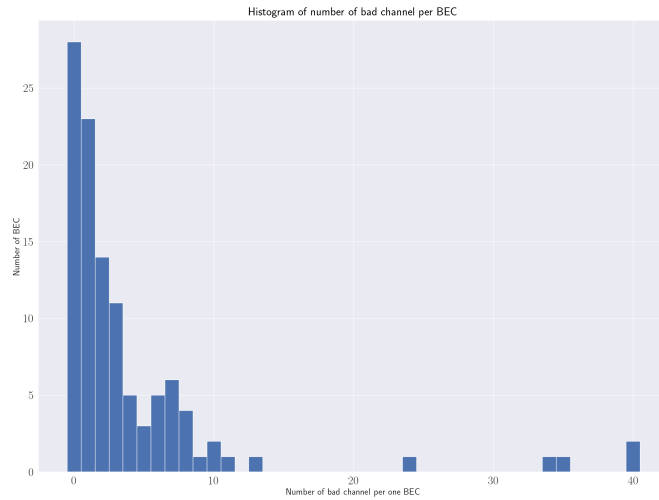
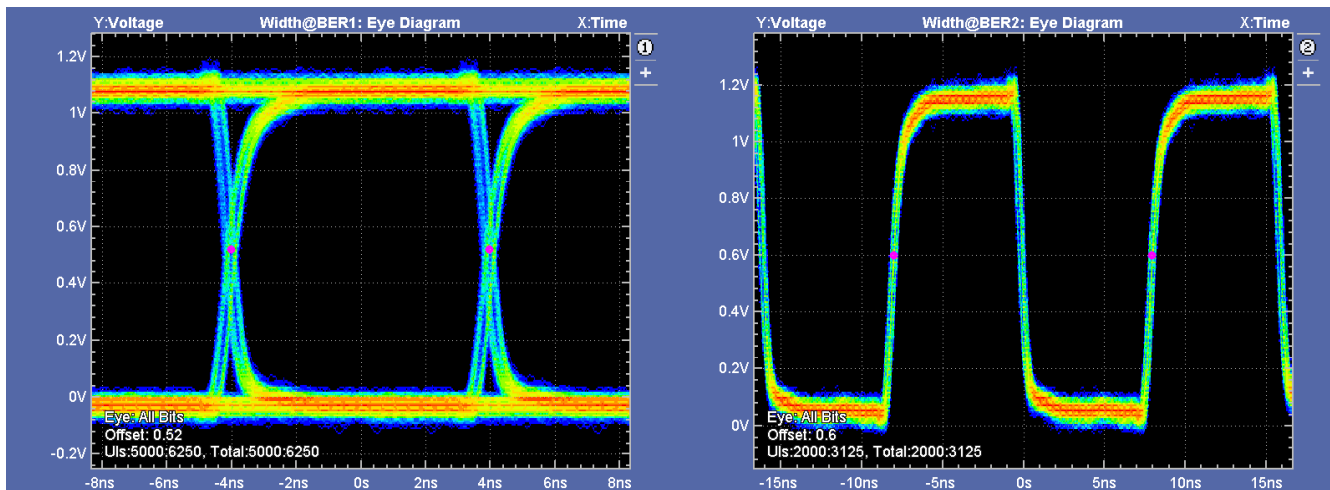
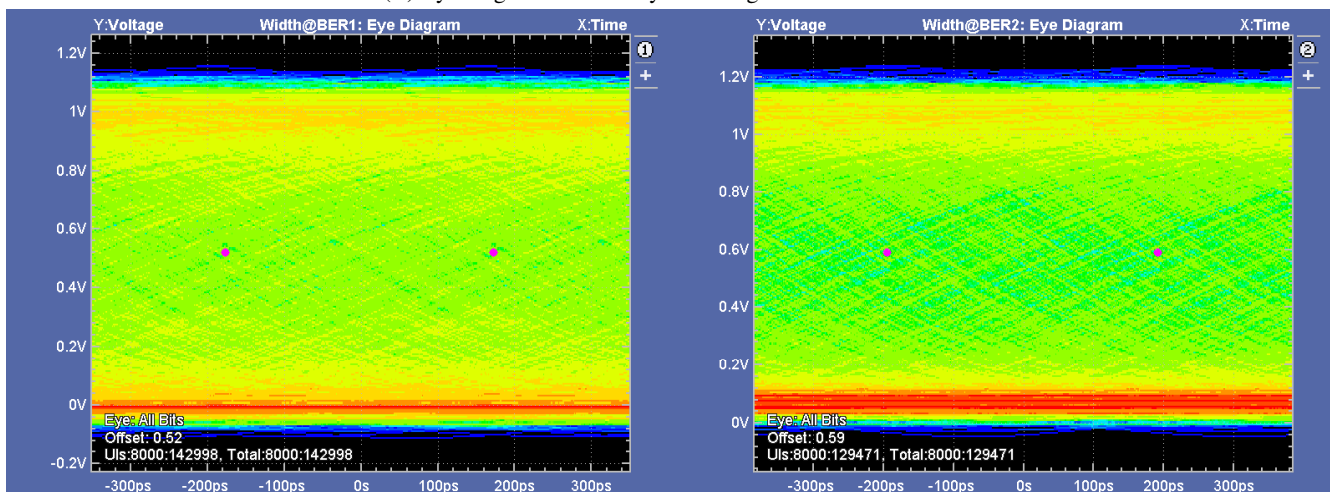


FIGURE 6.14: Results for 153 BECs over the 177 BECs tested from January 2022 to July 2022.



(A) Eye diagram obtained by removing the extension cable.



(B) Eye diagram obtained adding a cable extender and an extension cable.

FIGURE 6.15: Eye diagrams obtained with a loop test for BEC-V4. The purpose of those tests is to show the effect of extended cables on the error rate.

6.3 Installation and commissioning

The installation of the BEC in the electronic room in the Cavern of the JUNO detector was performed in September 2022. To ensure no damage appeared during the transport, we performed tests after the installations.

6.3.1 Physical link test (BEC loop test)

In September 2022, 164 BECs were installed in the two underground electronic rooms. The loop test using the PRBS signal was implemented for all the installed BECs, including 160 BECs for JUNO and 4 backups, in order to verify if any hardware damage happened during the different transportation. The setup is shown in Figure 6.16. The test for each BEC lasts for 10 minutes. Totally, 7 BECs out of 164 seemed to have some issues in this test:

1. Three BEC were unresponsive to ping commands; the mini-WR get loose on the TTIM during shipping; it is resolved by re-seating the Mini-WR
2. Four BEC experienced Mini-WR communication issues; it is resolved by removing common mode chokes see detail later
3. One channel on BEC No. 6 showed persistent errors; this BEC is relegated to backup status.

Common Mode Choke Voltage Drop Issue Common mode chokes are typically used in electronic systems to reduce electromagnetic interference (EMI) and improve the overall signal integrity. They work by suppressing common mode noise while allowing differential mode signals to pass through. In the case of the BEC system, specifically the Mini White Rabbit (Mini-WR) board, common mode chokes were initially included in the power supply path as a noise reduction.

The 3.3V power supply for the Mini-WR board is routed through a common mode choke before entering the PCB. This choke effectively acts as a small resistor in series with the power supply. Under normal operating conditions with a low current draw, the voltage drop across the choke is negligible. However, when the Mini-WR processes network packets, current consumption can suddenly increase. During high current draw situations, the voltage drop across the choke becomes substantial. This drop is significant enough to cause the voltage at the Mini-WR to fall below its required operating range. The voltage drop leads to clock unlocking issues on the Mini-WR and results in communication breaks and overall system instability. The problem has an intermittent nature, occurring only during periods of high network activity, and is particularly challenging to diagnose initially.

Solution to the Common Mode Choke Issue After identifying the root cause of the problem as the Common Mode Choke, the decision consists of removing the common mode chokes from all Mini-WR boards used on the BECs. There is no risk in removing the Common Mode Choke as the power supply for the Mini-WR comes from the TTIM. TTIM receives its power from the BEC baseboard, which already incorporates comprehensive filtering circuits, ensuring a clean power supply with minimal ripple. This analysis confirms that sufficient noise suppression is already in place without the need for additional common mode chokes.

Extensive testing is performed on the BEC and TTIM after removing the common mode chokes. Results show no packet loss and no clock unlocking issues in Tsinghua. The removal of the chokes eliminates the voltage drop issue during high current draw situations. The operation results in more stable operation of the Mini-WR, particularly during periods of high network activity. Following the successful testing, this modification is applied to all Mini-WR boards used in the JUNO experiment.



FIGURE 6.16: The setup for loop test in electronic room.

6.3.2 Physical link test between BECs and GCUs

The **UWB** installation starts in December 2022, where the installation of each JUNO subsystem has to be coordinated with each other. The sequence of installation of the **UWB** and other related systems is as follows: the acrylic vessel is installed one layer ahead of the **CD-LPMT**, and when the **CD-LPMT** is finished, the **CD-UWB** starts, followed by the **Veto-LPMT** and the corresponding electronics, and the **CD-SPMT**. So, the **UWB** installation is not continuous but centralized in conjunction with other systems. After each centralized installation of **UWB**, two large-scale tests are conducted on-site. One is the physical link test between **GCU** and **BEC**, and the other is the light-off test (commissioning test) related to all electronics. Figure 6.17 shows workers installing the **UWBs** on July 1, 2023. We can see the veto **LPMT** installed from layer 11 (top of the **CD**) to layer 8, while the **CD-LMPTs** are installed up to layer 4.

After the **UWB** is mounted on the steel frame, 3 installed **LPMTs** connect to it, as shown in Figure 6.17. Following that, the reflection tests are performed to check whether the connection between the **GCU** and the **PMTs** is in place by utilizing the reflection signals between the **UWB** and the **PMT**. Vacuum equipment is designed to test the correct sealing of the bellows. After that, the three cables from the **UWB** to the surface will be connected to the lower power supply, the **DAQ** switch, and the **BEC**, respectively, shown in figure 6.18. In order to verify that the surface electronics and **GCU** are working correctly, a final test of about 5 minutes is implemented, including the self-test of the **GCU** and the transmission rate test between the **BEC** and the **GCU**.

By May 2024, approximately 3150 **UWBs** have been installed (a total of around 7000 **UWBs** will be installed) and connected to 65 **BECs**, and all channels have been subjected to a final test. During these tests, the transmission test between **GCU** and **BEC** fails only once. By exchanging **GCU** and different **BEC** channels, it is confirmed that the problem comes from **UWB5901**. In order to not affect future use, the electronics group decides to uninstall this **UWB** and to replace it with a new **UWB**. After opening the **UWB** see Figure 6.19, we conclude that the transmission fails due to the squeezed yellow cable in the box.

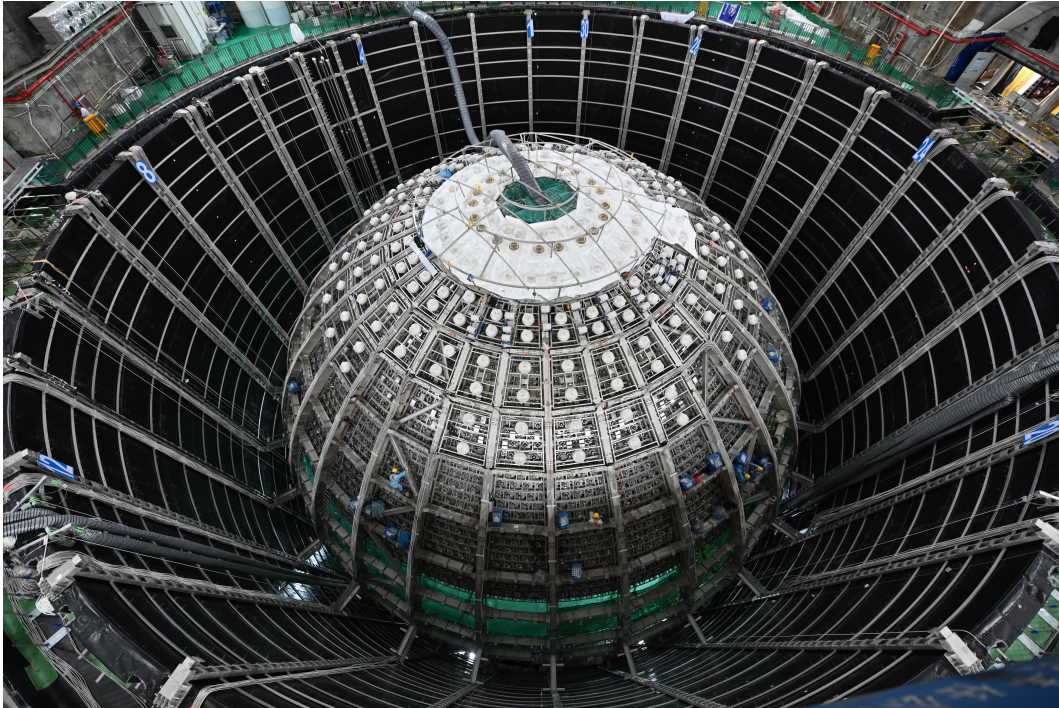


FIGURE 6.17: The CD detector with installed UWBs and PMTs taken on 01/07/2023.

6.3.3 Light-off test

The light-off test, also known as a dark run or background measurement, is a critical procedure in large-scale neutrino detection experiments like JUNO. Its primary purpose is to assess and characterize the detector's performance under conditions that closely mimic actual data-taking scenarios but without the presence of external light sources. Here is a detailed explanation of its purposes and importance:

- Light-off test gives us the opportunity to measure the intrinsic background noise of the detector system; understanding background noise is crucial for distinguishing genuine neutrino events from false signals; this knowledge allows for more accurate data analysis and event reconstruction
- It allows us to perform a verification that all components of the detection system are working together as intended; it ensures that the complex interplay between PMTs, electronics, trigger systems, and data acquisition systems works correctly in a real-world scenario
- During the light-off test, crosscheck of the PMT **Dark Count Rate (DCR)** measurement is performed; this baseline helps to set appropriate trigger thresholds and to understand the sensitivity limits of the detector
- Additionally to PMT **DCR** measurement, it is crucial to evaluate the noise contribution from the electronic readout chain, including amplifiers, digitizers, and data transmission systems
- Trigger system tests and optimizations need to be performed under realistic conditions as proper trigger configuration is essential for efficiently capturing neutrino events while rejecting background
- DAQ system testing is performed to verify its performance under full-scale operation to ensure that the system can handle the data rates expected during actual experiments without loss or corruption
- Calibration of time synchronization between the different electronics is checked and fine-tuned during the light-off tests



FIGURE 6.18: Three cables from UWBs to the lower power supply (Red/black pairs), the BEC (Yellow cable), and the DAQ switch (Blue cable).

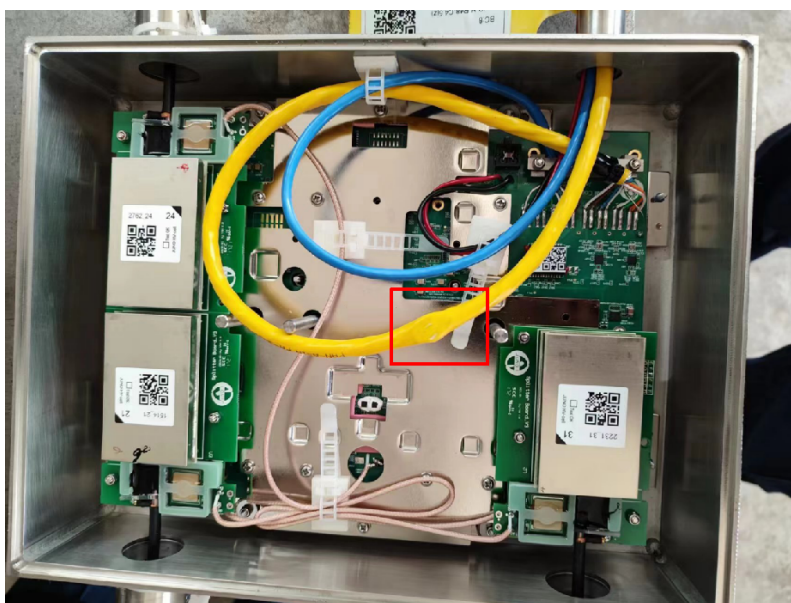


FIGURE 6.19: The yellow cable was squeezed in the UWU.

- Long-term stability is crucial for consistent data quality throughout the multi-year runtime of the experiment; the long-term stability is verified during the light-off tests
- During the light-off tests, rigorous identification of problematic channels is performed to allow us to conduct maintenance or recalibration before the start of actual data-taking
- The light-off tests serve as final validation before data-taking to provide confidence in the readiness of the experiment for scientific data collection

In the context of JUNO, the light-off tests are critical due to the experiment’s unprecedented scale and sensitivity requirements. These tests are an indispensable part of the commissioning process. By rigorously conducting and analyzing these light-off tests, the JUNO collaboration can optimize the detector’s performance, understand its limitations, and maximize its physics potential.

During the light-off tests, two levels of trigger decision-making have been implemented for the global trigger: BEC-level in the beginning phase and CTU-level. The progression from BEC-level trigger tests to complete CTU-level tests in the light-off scenario demonstrates the step-by-step validation of the entire trigger and data acquisition chain. This methodical approach ensures that each component of the system is thoroughly vetted before moving to full-scale operations.

As of May 2024, there have been two light-off tests: 1) BEC-level trigger decision-making on April 2023 and 2) nhits trigger using CTU-level trigger on 4th-5th September 2023.

BEC-level trigger decision-making on April 2023

Around 700 LPMTs, 232 GCUs, and 8 BECs are included in this light-off test. For one BEC, if the total nhits are above the threshold, all GCUs of this BEC are triggered. Figure 6.20 shows the data package format from GCU to DAQ. To validate the operational functionality of the trigger system, we utilize the error register value in the trailer to verify the clock signal transmission from the BEC to the GCU. By analyzing the count of triggered GCUs at specific timestamps, we examine the connection between the BEC and the GCU, the GCU, and the DAQ.

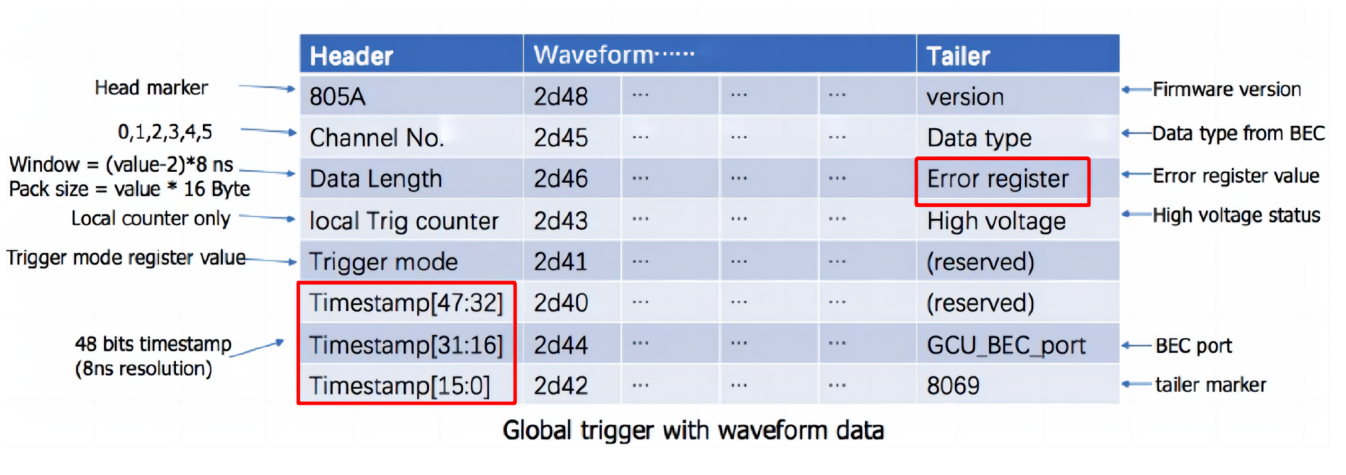


FIGURE 6.20: Global trigger data format from GCU.

Figure 6.21 represents the values from the error registers of all GCUs. During testing, an error value of zero indicates no issue with the clock link between the BEC and the GCU.

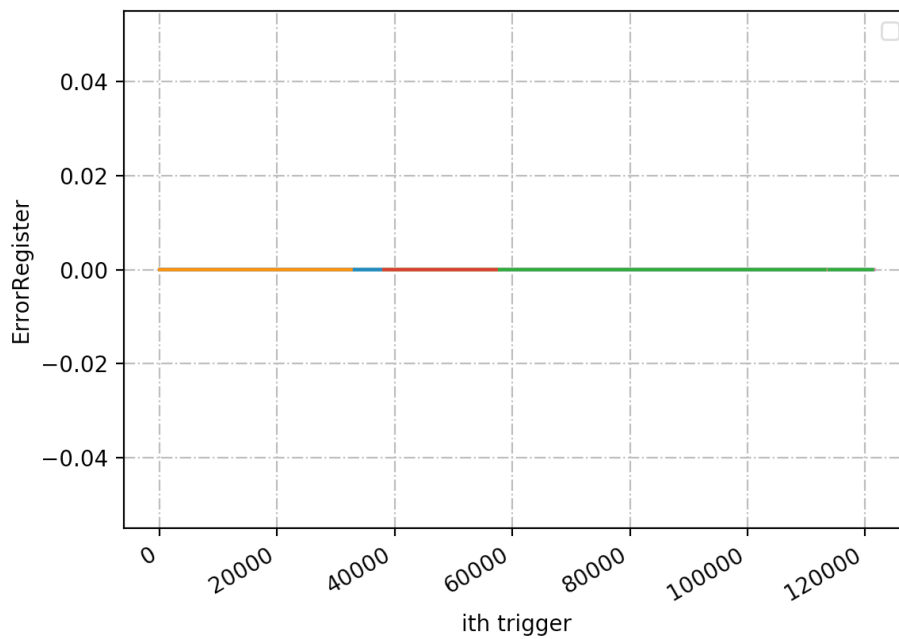


FIGURE 6.21: Error register value of all GCU in one run. The data here comes from 232 GCUs, with different colors indicating different GCUs. Due to the large amount of GCUs, the legend can not be shown here.

Another concern is that all the GCUs have a similar channel at each time. An example of this is presented in Figure 6.22, which illustrates the total number of triggered GCUs at each trigger time for the BEC. The BEC No 47 is connected with 23 GCUs, the same as the total number in Figure 6.22a. There are 3-time stamps where anomalies between the BEC-GCU-DAQ are observed. The anomalies involve the 3 GCUs shown in Figure 6.22b.

To investigate this issue, we analyze the variation of local trigger numbers on normal and problematic GCUs over time. The analysis result is shown in Figure 6.22. The local trigger number is recorded on the GCU. As every time stamp GCU receives a trigger, the local trigger number should increase by 1. In Figure 6.23a, within the highlighted box, there should have been six triggers for GCU3, but it registered only two, with a continuous local trigger number. This indicates that GCU received no trigger during this period, and there is a problem within the BEC and GCU links. Figure 6.23b shows the same situation as Figure 6.23a, with no triggers received for some time. Figure 6.23c shows that the trigger number increase of GCU18 is consistent with the reference GCU, but one data is lost, which means the problem occurs between the GCU and the DAQ.

A hypothesis that could explain this issue is that the GCU's RAM buffer is not large enough, resulting in data loss and that the buffer design needs to be updated. To visually check whether the anomaly occurs between the BEC and the GCU or between the GCU and the DAQ, we can compare the trigger number difference (TrgNdiff) between the GCU without anomaly and the GCU with anomaly at the same trigger time. If the maximum TrgNdiff is greater than 1, the GCU did not receive a trigger signal at least once. If the maximum TrgNdiff is 0, the problem occurs between the GCU and the DAQ.

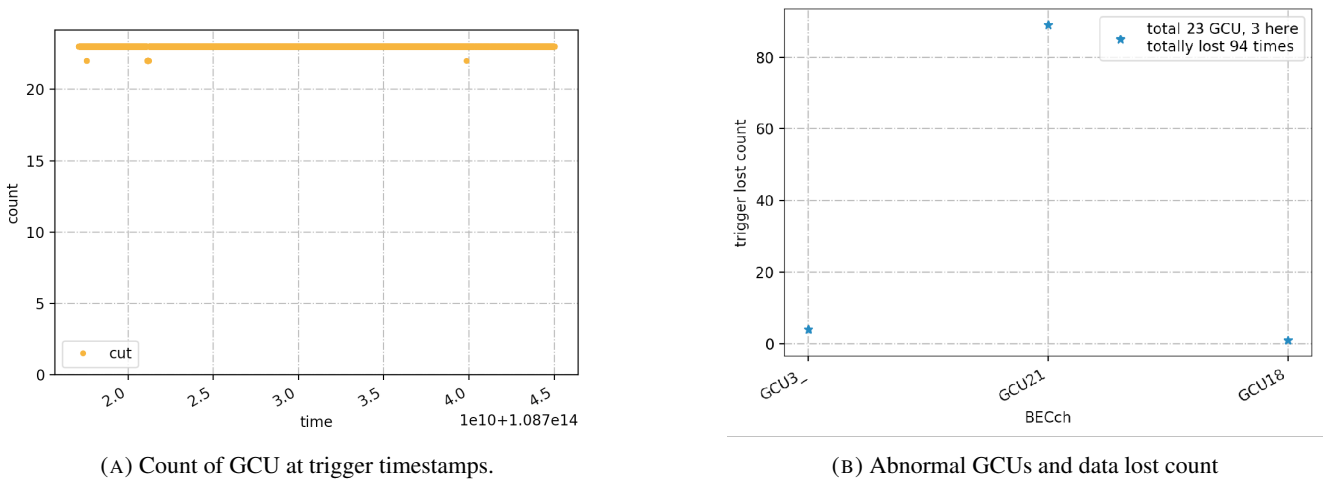


FIGURE 6.22: Left is the count of GCU at trigger timestamps, right is the abnormal GCU and data lost count.

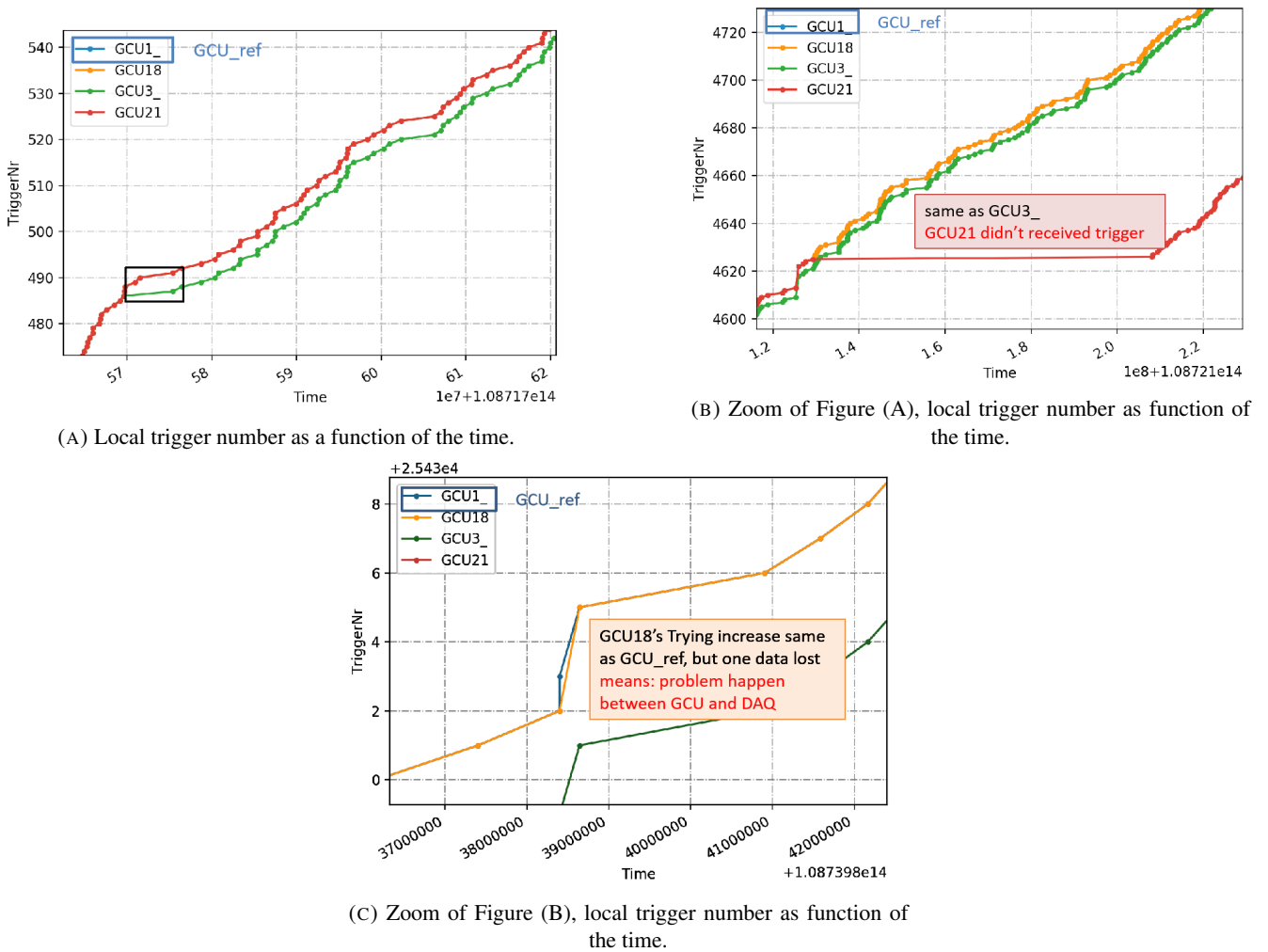


FIGURE 6.23: Local trigger numbers of normal/reference and anomalous GCUs over time. The line in blue correspond to the GCU taken as reference. The yellow, green and red curves are for the problematic GCUs.

Light-off test on September 2023

The light-off test of the period trigger and standard multiplicity trigger using CTU-level trigger happens on 4th-5th September 2023. 4787 CD-LPMTs, 1600 CD-GCUs, and corresponding 45 BECs, around 450 Veto-LPMTs, 155 Veto-GCUs, and corresponding 10 BECs attended this light-off test. The veto system and CD system are tested separately. The CTU and the RMU are implemented to trigger the system. The trigger request is sent to the CTU via the RMU and BEC. Then, the CTU generates a trigger validation and sends it back to all the Veto or CD GCUs (CD-GCUs were separated by 4 areas to do the test).

The period trigger is when the CTU generates a trigger signal at a specific interval, it allows us to evaluate the performance of the triggering system by comparing the frequency of the signals emitted by the CTU with the frequency of the data received by the DAQ. Figure 6.24 shows the constant frequency from DAQ, which is also the same as from the CTU of 200Hz. It concludes that no trigger is lost from the CTU sender.

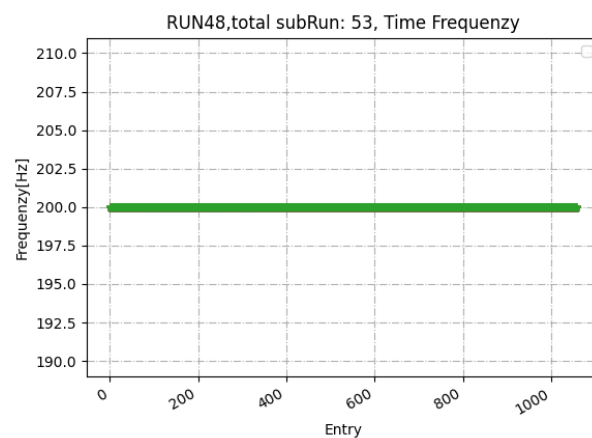


FIGURE 6.24: The frequency of the data received by the DAQ, the value is consistent as the CTU.

The same analysis as above is performed to check for any trigger loss between RMU-BEC-GCU-DAQ at a trigger time. The left of Figure 6.25 shows the minimum count of the triggered GCU in one sub-run. Every sub-run means 5s data. The right shows the difference in the local trigger number of the GCU for all sub-runs. It can be concluded that no data was lost between GCU and DAQ. Therefore, the data lost from the left figure is from the RMU-BEC-GCU link. Table 6.7 shows the total GCU numbers and the lost GCU numbers of the connected BEC ID in the i -th run, which gives the minimum GCU numbers on Figure 6.25. "Full" in the table represents all GCUs of this connected BEC lost at one trigger time. It means that the CTU sends the trigger decision signal to the RMU, but the RMU does not send it to the BECs. It concludes that the RMU is not stable initially and needs modification in the future.

The global trigger algorithms are vertex-fitting triggers or standard multiplicity triggers in the actual data-taking. This light-off test tests the standard multiplicity trigger (hits trigger). Figure 6.26 shows the total count of triggered GCUs and the trigger frequency in a few sub-runs with abnormal data and reference data. By comparing the upper and lower figures, the points marked in green show that the BEC-GCU link can handle a single high-frequency trigger. The points marked in red show that the BEC-GCU link is highly likely to lose the trigger signal. For sub-run 22 and sub-run 42, the high frequency might caused by environmental noise or transmission error, which needs to be checked for the next test. A total number of trigger GCUs smaller than expected might come from a non-match between the BEC latency of 8ms and the GCU memory buffer size. When the trigger decision with the timestamps after latency arrives at the GCU, the buffer is full and discards the old data. The BEC latency and the GCU buffer should be optimized.

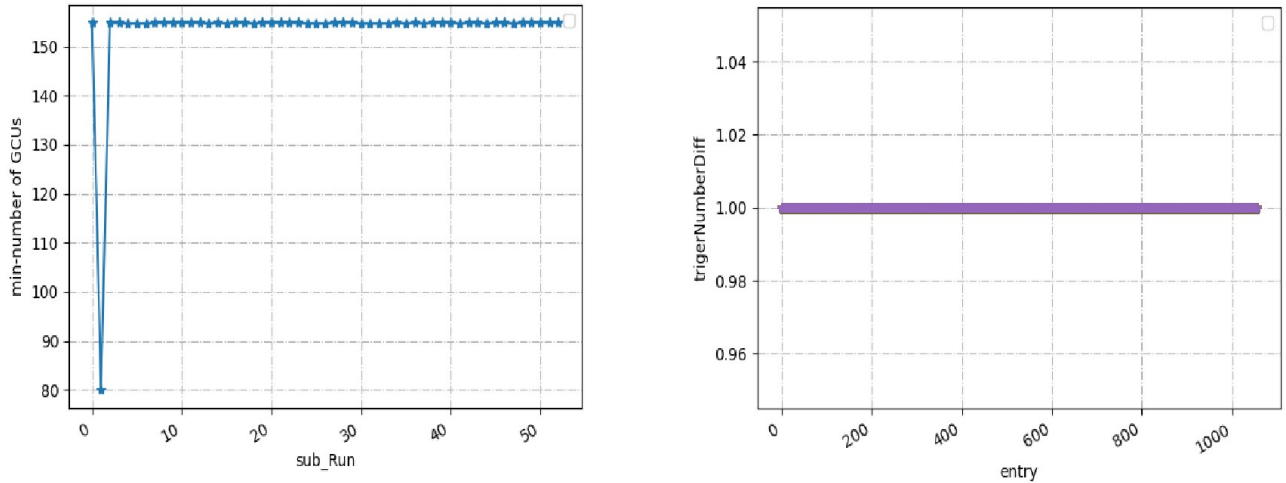


FIGURE 6.25: The total count of triggered GCU.

BEC-ID	Total number of GCU connected	Lost N: 0th	Lost N: 1th	Lost N: 2th	Lost N: 3th	Lost N: 4th	Lost N: 5th
121	10	-	-	Full	-	-	-
73	18	-	-	-	-	Full	-
23	13	-	Full	-	-	-	-
147	22	-	Full	Full	-	-	-
74	11	-	-	Full	Full	-	-
56	13	-	-	-	Full	Full	1
64	14	-	-	Full	Full	-	-
38	18	-	Full	Full	-	-	-
84	19	Full	Full	-	-	-	-

TABLE 6.7: The total GCU numbers and the lost GCU numbers of the connected BEC.

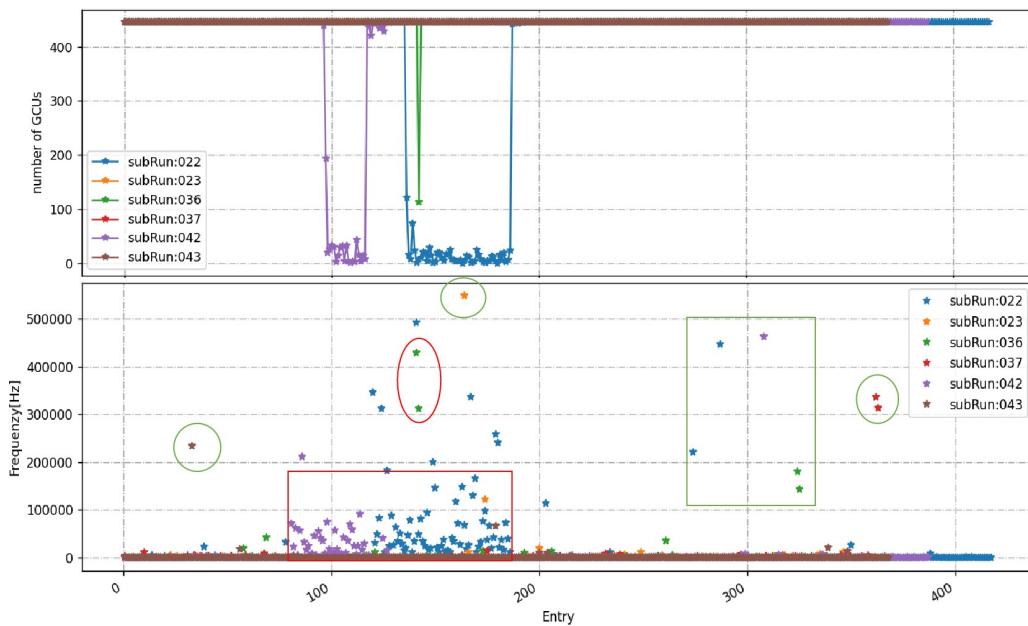


FIGURE 6.26: The total count of triggered GCU and trigger frequency for nhits trigger.

6.4 Summary

This present chapter outlines the detailed processes involved in the production, testing, and installation of the BEC for the JUNO experiment. The chapter begins with a description of the mass production phase, which involves careful planning and execution to ensure each BEC meet stringent quality standards. The production process encompassed PCB production, component assembly, and a series of tests to verify the functionality of each BEC unit.

Following production, each BEC undergoes a combined test with GCU at a dedicated facility in Kunshan. These tests were crucial in validating the physical link between the BEC and GCU, ensuring the integrity of signal transmission, and detecting any potential issues. A partial check of the synchronous link is performed by checking the idle packet on the slow control link. By checking the hamming code in the TTC protocol idle packet, we can detect the error in the link. The results presented here showed the influence of external components, such as extension cables, on the signal quality. To ensure the quality of their physical layer, all the BECs are tested again through a loop test after the test in the Kunshan facility.

Two significant light-off tests were performed up to May 2024. The first light-off test in April 2023 focused on BEC-level trigger decision-making, involving approximately 700 LPMTs, 232 GCUs, and 8 BECs. This stage was crucial for validating the operational functionality of the trigger system, particularly in ensuring that the clock signals transmitted from the BECs to the GCUs were functioning correctly. The second light-off test, conducted in September 2023, verified the working performance using the CTU-level trigger. This test involved a significantly larger scale, with 4787 CD-LPMTs and 450 Veto-LPMTs and their associated electronics. This light-off test demonstrated the system's ability to maintain a consistent trigger frequency for most of the GCUs. Only 3 GCUs showed synchronization errors due to limited buffer size implemented on the GCU firmware.

Overall, this chapter details the successful execution of the production, testing, installation, and commissioning processes for the BECs in the JUNO experiment.

Part III

Model discrimination of core collapse super nova with JUNO

Chapter 7

Supernovae

This chapter wants to give a summary of the actual knowledge about supernovae and describes some of the different existing models of their explosion. Firstly, we describe the SN1987A event, then give a quick description of the supernova classification based on the electromagnetic spectrum. Later, we detail the core collapse mechanism and the different models used in this thesis for model discrimination. Finally, the different astrophysical implications of the supernova are briefly described.

Contents

7.1	The Supernova event SN1987A	155
7.2	Supernova spectral classification	156
7.3	Early stage of the life of star	156
7.4	Collapse dynamics and neutrino emission in supernovae	157
7.5	Core-collapse supernova models	161
	7.5.1 General consideration on modeling of core-collapse supernova	161
	7.5.2 Modeling in the market	164
7.6	Astrophysical implications	169
	7.6.1 Nucleosynthesis in CCSN	169
	7.6.2 Neutron star and black hole formation	171
7.7	Summary	172

7.1 The Supernova event SN1987A

On February 24, 1987, the electromagnetic radiation from the explosion of the star Sanduleak 1 in the Large Magellanic Cloud reached Earth. This was a historically exceptional event. the [Core Collapse Supernova \(CCSN\)](#) event was observed much more precisely than any other previous ones, thanks to the advances of telescopes, the presence of the first neutrino detectors, and the better knowledge of the underlying theories. In addition to traditional electromagnetic measurements, two dozen neutrino events were associated with SN 1987A. The observations of these neutrinos were made from different locations in the world: 11 neutrinos were measured in Japan by Kamiokande II [201], 5 by the Russian detector Baksan [202], 8 by the American detector IMB [203] and 5 by the Italian detector LSD [204]. Although there may be false positives in this data, these neutrinos are the only neutrinos ever detected from a CCSN. Their analysis, and the fact that they arrived a few hours before the electromagnetic radiation, broadly confirms the gravitational supernova scenario developed by theorists.

7.2 Supernova spectral classification

The first classification of supernovas originates from the observation of their electromagnetic spectra (of the light emanating from them) at different wavelengths. Each class of supernovae is based on the presence or the absence of specific lines in their spectra (see Reference [205] for the details of the classification):

- Type I: the spectrum contains no hydrogen lines.
 - Type Ia: the spectrum contains silicon lines
 - Type Ib: the spectrum contains no silicon but contains helium, particularly He I.
 - Type Ic: neither silicon nor helium.
- Type II: Presence of hydrogen in the spectrum. Type II can be subdivided based on the shape of the light curve or specific characteristics.
 - Type II-P: The luminosity remains roughly constant (hence the designation P for "plateau") for a long period, which can be several months.
 - Type II-L: The luminosity decreases rapidly over time (much faster than linearly, despite the L for "linear").
 - Type II-n: The n for "narrow" designates narrow lines in the spectrum, while the vast majority of SN have broad lines due to the Doppler effect in an ejecta with very high velocity.
 - Type IIb: Intermediate between Type II and Type Ib, it is an SN with hydrogen, but very little. Woosley et al. (1987) proposed SN 1987A as a representative of this SN subtype.

Thousands of supernovas have been observed [206], among which about 70% are type II (all subtypes combined), 20% are type Ia, and 10% are type Ib or Ic. However, the spectral classification does not at all reflect the underlying physical mechanism. The classification of their explosion dynamics is divided into two classes: a) thermonuclear supernova, and b) CCSN, also called gravitational supernova.

Thermonuclear supernovae correspond to Type Ia supernovae in the electromagnetic classification. They are singular by their progenitor characteristic and explosion mechanism. Type Ia supernovae are always a binary system composed of a white dwarf that is primarily composed of carbon and oxygen and a companion, a lower mass star [12]. If the two stars orbit close enough to each other, the white dwarf will gain mass by capturing matter from the external layer of his companion star. When the white dwarf reaches Chandrasekhar mass limit (1.4 solar mass (M_{\odot})), the white dwarf can not hold its mass, and the thermonuclear explosion starts. The energy liberated by the explosion will eject the companion star and rip the white dwarf. Another scenario is when carbon fusion is delayed, and the white dwarf reaches its Chandrasekhar mass. The white dwarf could collapse and form a neutron star before exploding (see [207]). An alternative model proposes that two white dwarfs can be bound in a binary system, leading to a supernova. Reference [62] gives a review of different progenitor systems and explosion mechanisms of Type Ia supernovae.

Type Ib, Ic, and II supernovas are core-collapse supernovae. The section 7.4 presents in detail the explosion mechanism of the core-collapse supernova.

7.3 Early stage of the life of star

A massive star spends 90% of its lifetime fusing hydrogen into helium. These fusion reactions provide the energy source for the star, resulting in pressure that counteracts gravity and produces radiation, primarily in the form of

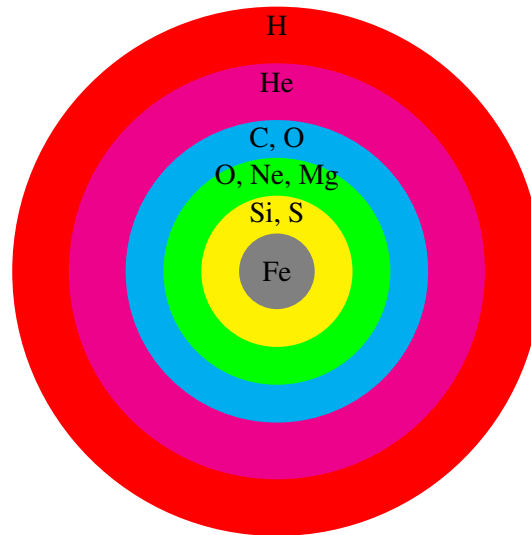


FIGURE 7.1: Onion-like structure of massive star at the end of its life. The layer dimensions are not to scale.

blackbody radiation. As long as the fusion of elements at the star's core generates radiation energy, the star is considered to be in its "living" phase.

Hydrogen fusion creates a relatively spherical helium core surrounded by an outer layer of hydrogen. The requirement to have helium fusion, leading to the formation of carbon and oxygen, is that the star is sufficiently massive, and the conditions of density and temperature at the core allow helium fusion. Thus, the star develops a carbon and oxygen core, with middle layers of helium and outer layers of hydrogen, which can continue to fuse.

The fusion of carbon leads to the production of neon and magnesium. The new core is then composed of oxygen, neon, and magnesium (O-Ne-Mg). If the star's mass is between 8 and 10 solar masses (M_{\odot}), it will explode at this stage as a specific supernova called electron capture CCSN. This mechanism leads to a less energetic explosion and, therefore, emits fewer neutrinos compared to higher mass iron core progenitor CCSN.

If the star's mass exceeds about $10 M_{\odot}$, silicon is produced through the fusion of neon and oxygen. Silicon fuses to produce iron and other elements in the iron group, particularly ^{52}Fe , ^{54}Fe , and ^{56}Ni , with ^{56}Fe being the most abundant. At this stage, the star resembles an onion-like structure, as depicted in Figure 7.1, with various concentric layers. Regardless of the star's mass, fusion stops at the iron group because these elements have the highest binding energies per nucleon. Fusion of the iron group would be endothermic and does not occur spontaneously.

Each successive fusion stage happens more rapidly. When the star becomes hot enough to spontaneously create neutrino-antineutrino pairs (typically during carbon fusion, see Heger [208]), energy is carried away by these neutrinos, leading to core contraction. The core contraction is characterized by an increased density and temperature, which is beneficial for nuclear fusion reactions. The time between the onset of silicon fusion and the core collapse is only a few days to a week.

7.4 Collapse dynamics and neutrino emission in supernovae

We present here the dynamics for the core collapse of stars with mass higher than $10 M_{\odot}$. The dynamical evolution from the core-collapse premise to the successful initiation of the supernova outburst can be divided into six stages as described in Figure 7.2. For details on the neutrino-driven explosion, see References [209, 210].

Before describing the dynamics we need to define few key elements. The first important concept is the **Equation of State (EoS)** which provides the relation between pressure, temperature, density, and composition of the stellar matter. On the neutrino emission point of view three regions are key. The first one is the **neutrinosphere** which corresponds to the region where the neutrinos are trapped. Outside of the neutrinosphere we have the cooling and the gain regions. The so called cooling region, is characterized by density where the neutrinos can escape, leading to a cooling of the star medium. On the other hand, the gain region is surrounding the cooling region. There, the density of the star medium is high enough to allow neutrino heating.

Initial core collapse Due to the production of iron group elements by the burning of silicon, the stellar core mass increases. The electron in the iron core are occupying higher energy states until they become relativistic. At the initial stage of the collapse, pressure is supported by relativistically degenerate electrons and, at higher densities, by neutrinos. The collapse occurs near neutral stability, leading to a homogeneous process where the mass within a given fractional radius remains constant.

The gravitational instability is triggered by electron captures on nuclei ($e^- + (A, Z) \rightarrow \nu_e + (A, Z - 1)$) and free protons ($e^- + p \rightarrow \nu_e + n$), and partial photo-dissociation of heavy nuclei into alpha particles and free nucleons. Those phenomena lower the effective adiabatic index¹ of the EoS below the critical value of about 4/3, necessary for gravitational stability. The initial collapse is marked on the top left panel of Figure 7.2 by the arrows pointing inward.

Neutrino trapping At the initial phase of the collapse mechanism, the electron neutrinos produced by these captures can escape freely. As the core is contracting, the density increases. When the threshold density of $10^{11} \text{ g cm}^{-3}$ is achieved, the mean free path for neutrino scattering off heavy nuclei becomes short enough that neutrinos begin to diffuse. The outward neutrino diffusion is slower than the accelerating infall of stellar material, leading to neutrino trapping. The inner core, subsonically collapsing, develops a homogeneous velocity profile. The maximum speed is found near the interface with the supersonically infalling outer core. The state for $t \sim 0.1 \text{ s}$ ($t=0$ being the start of the core collapse) is shown on the top right panel of Figure 7.2. M_{hc} represents the mass of the homologously collapsing inner core. At this point the matter density is high enough to trap the neutrino, this region is the neutrino sphere.

Bounce and shock formation Within approximately 10 milliseconds after the neutrino trapping (110 ms from the initial phase), the nuclear matter density is reached at the center, causing the dissolution of the heavy nuclei into a uniform medium. The inner core's collapse then halts abruptly due to incompressibility resulting from repulsion caused by nuclear forces between the nucleons. At this point, a phase transition to homogeneous nuclear matter stiffens the EoS. The resulting increase in the adiabatic index above 4/3 stabilizes the stellar matter.

However, the collapsing inner core overshoots its equilibrium state, causing it to bounce back and generate pressure waves. These waves steepen into a shock front as they transition to the supersonically infalling outer core. Due to the initial loss of electron neutrinos, the electron fraction at the center drops to between 0.25 and 0.27. As a result, the inner core's mass shrinks to below $0.5 M_{\odot}$, approximately defining the bounce-shock formation site. These dynamics are presented in the middle left panel in Figure 7.2. The shock is presented with arrows pointing outward, with the shock front presented with a continuous line at a distance of around 10 km from the star center.

Shock propagation and ν_e burst The newly formed shock begins to move outward (shown in the middle right panel of Figure 7.2). After around 0.2 s, the shock has propagated of around 90 km outward. During its propagation, it loses kinetic energy by generating photons, leading to the photodissociation of heavy nuclei into free

¹The adiabatic index (γ) is defined as $\gamma = \left. \frac{\partial \ln P}{\partial \ln \rho} \right|_s$, where s is entropy, P is pressure, and ρ is density. For a degenerate relativistic gas, γ equals 4/3. A value below 4/3 indicates insufficient pressure to counteract gravitational collapse, leading to instability.

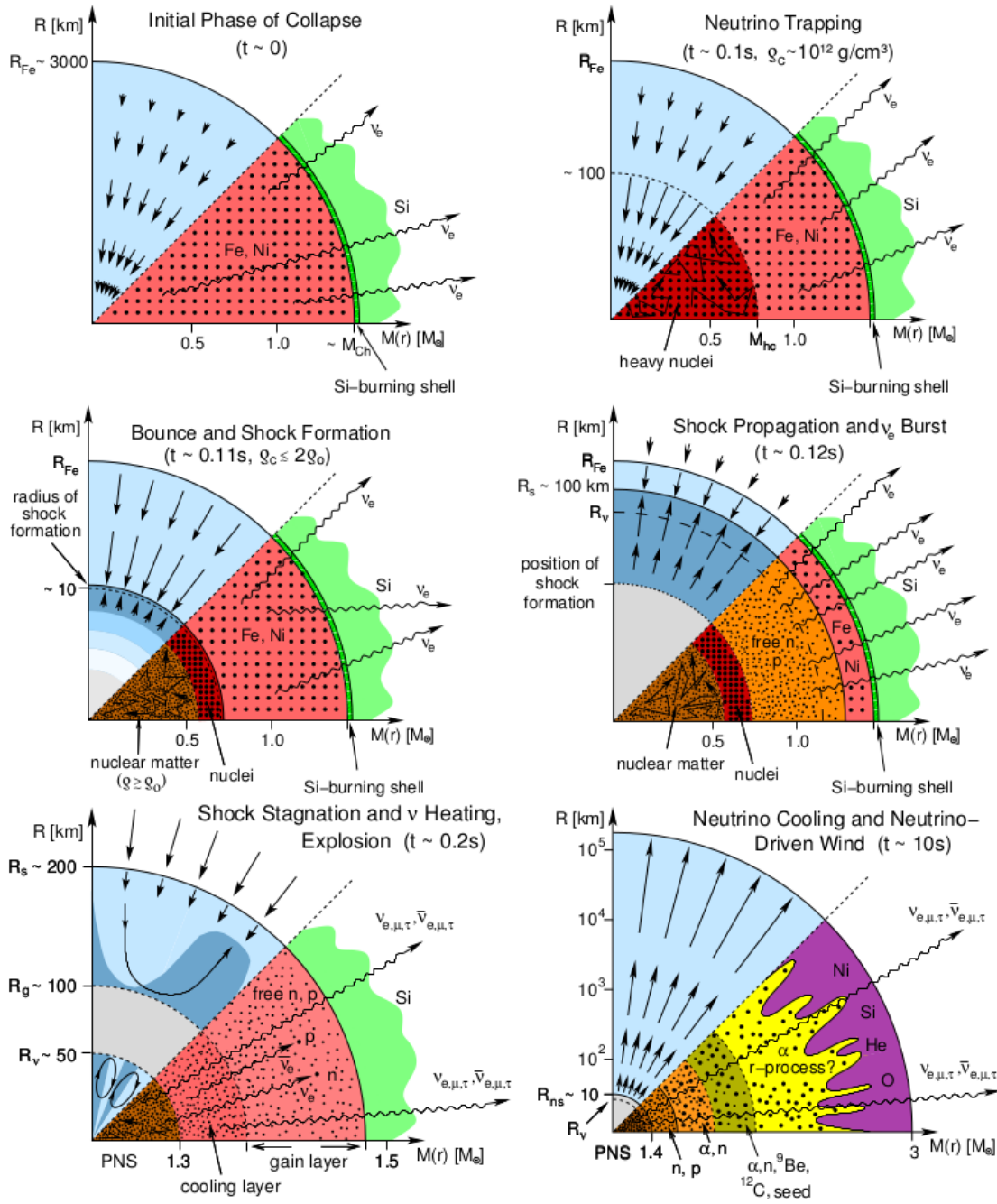


FIGURE 7.2: The six phases of neutrino production and their consequences on the dynamics of the core collapse are presented from left to right. The lower halves of the diagrams illustrate the composition of the stellar medium and the associated neutrino effects, while the upper halves depict the flow of stellar matter, represented by arrows. Arrows pointing inward indicate contraction or collapse, while outward-pointing arrows signify expansion or mass ejection. The radial distances R (in km) are displayed along the vertical axes, with the corresponding enclosed masses $M(r)$ (in M_{\odot}) shown on the horizontal axes. Important radii include the iron-core radius (R_{Fe}), shock radius (R_s), neutrinosphere radius (R_{ν}), gain radius (R_g), which separates the cooling and heating layers, and the proto-neutron star (PNS) radius (R_{ns}). The effective Chandrasekhar mass is denoted by M_{Ch} , while M_{hc} represents the mass of the homologously collapsing inner core. The central density is symbolized by ρ_c , and the nuclear saturation density is approximately $\rho_0 \approx 2.7 \times 10^{14} \text{ g/cm}^3$. Figure taken from [211].

nucleons. This disintegration continues as long as the shock remains within the stellar core. The free protons are then capturing electrons producing a large amount of electron neutrinos. As the neutrinosphere has a lower radius than the shock front, the neutrinos created between this two frontiers are suddenly released giving the called neutrino burst.

Shock stagnation, neutrino heating and accretion As the neutrinos escape the inner layer, they remove additional energy from the postshock layer. As velocities behind the shock turn negative (toward the center), the shock stalls and transitions into an accretion shock. The stagnation of the shock appends around 0.2 s after the start of the initial collapse. This is shown the lower left panel of Figure 7.2. The stalled shock receives energy by absorption of those escaping neutrinos by free protons and neutrons. This absorption occurs through interactions such as:



This process is called neutrino heating, electron neutrinos (ν_e) and antineutrinos ($\bar{\nu}_e$) depositing energy in the gain region between the gain radius and the shock.

If neutrino heating is sufficiently strong, it can push the shock outward, initiating a supernova explosion (bottom left panel of Figure 7.2). Non-radial fluid instabilities, such as buoyancy, convective overturn, and the **Standing Accretion Shock Instability (SASI)**, aid the neutrino-heating mechanism by expanding the shock, enlarging the gain region, and enhancing the efficiency of neutrino energy transfer compared to spherical conditions. If the pressure behind the shock, bolstered by turbulent pressure, exceeds the ram pressure of infalling material, runaway shock expansion can occur, driving the shock outward and resulting in a successful explosion.

Explosion phase As the shock propagates, it accelerates, especially in the less dense outer layers of the star. The interaction between the shock and the surrounding medium can produce complex structures and instabilities, leading to the mixing of stellar material. This mixing can transport heavy elements from the inner regions to the outer layers, enriching the interstellar medium as the supernova remnant expands and disperses. Once revived, the shock moves outward through the star, heating and compressing the stellar envelope layers. During the following ten seconds after the explosion, the proton-neutron star cools due to the emission of neutrino (bottom right panel of Figure 7.2).

CCSN neutrino signal CCSN are not a fully understood phenomenon and many projects aim to study them from different aspects. As the neutrinos play a crucial role in the explosion mechanism, it is key to measure on earth their signal. The CCSN neutrino signal can be divided into three phases: the neutronization (ν_e) burst, the accretion phase and the proton-neutron star cooling. As $\nu_{\mu/\tau}$ - $\bar{\nu}_{\mu/\tau}$ pairs are created in basically equal amounts through thermal processes and interact in a similar way with matter, they are designated as a single effective neutrino type ν_x , for easier handling. For ν_e and $\bar{\nu}_e$, their dynamics and interactions with matter remain different enough as to treat them separately [211].

1. **Neutronization burst:** during the core collapse, prior to the bounce, the emission of ν_e begins to increase as electron captures become energetically favorable in the dense layers and core. Following the bounce, the strong compression temporarily reduces the neutrino signal for a few milliseconds, and simultaneously, $\bar{\nu}_e$ emission starts to appear. After the ν_e burst ends (around 10 ms after the bounce), ν_x fluxes also begin to rise as neutrino-pair production becomes possible in the heated matter.
2. **Accretion phase:** following the neutrino burst and bounce, matter accumulates onto the core over several hundred milliseconds. The neutrino signal is sustained by the accretion flow, where ν_e are emitted due to electron capture on infalling electrons. During the early stages of accretion, the luminosity of ν_e and $\bar{\nu}_e$ is

nearly twice as strong as that of ν_x . After approximately 200 ms, the supernova explosion occurs, causing the luminosity to drop, which corresponds to the infall of the outer Si-O layers.

3. **Cooling:** after the supernova explosion, the proto-neutron star continues to emit neutrinos across all flavors. The luminosity gradually diminishes, reaching very low levels after approximately 10 seconds.

Each phase has thus its own signature, as can furthermore be seen on Fig. 7.3. Each of the phases bring different information and allow to study different physics related to CCSN.

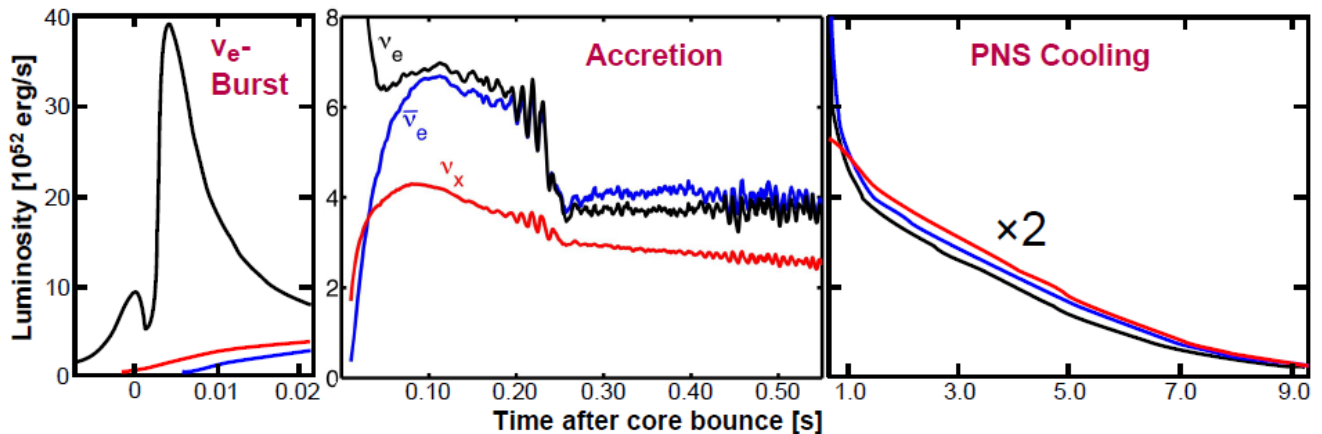


FIGURE 7.3: The neutrino luminosities (ν_e : black; $\bar{\nu}_e$: blue; ν_x , representing one type of ν_μ , $\bar{\nu}_\mu$, ν_τ , $\bar{\nu}_\tau$: red) during key phases of neutrino emission are illustrated. The left panel depicts the prompt burst of electron neutrinos, occurring milliseconds after the bounce ($t = 0$), as the shock breaks through the neutrino-transparent outer core layers. The middle panel shows the post-bounce accretion phase, before shock revival, as simulated in three dimensions [212]. In this phase, quasi-periodic variations in luminosity result from fluctuations in the mass accretion rate onto the neutron star, driven by violent non-radial motions due to hydrodynamic instabilities—specifically, the standing accretion-shock instability in the post-shock region. The right panel illustrates the gradual decline of neutrino luminosities over several seconds during the cooling phase of the newly formed neutron star. Taken from [213].

7.5 Core-collapse supernova models

7.5.1 General consideration on modeling of core-collapse supernova

The **progenitor** itself and the initial conditions of the core-collapse phenomenon have many associated uncertainties, both numerically and physically, arising from the complex phenomena created by the star outside of the equilibrium state. In this state, the star loses mass through stellar winds and energy through neutrinos. The mixing of the different layers described in Figure 7.1 is also poorly understood. Additionally, the inclusion of rotation or the magnetic field in progenitor models could significantly influence the star’s evolution. Furthermore, if the star belongs to a multi-body system (or, more generally, a multiple system), stellar evolution, particularly mass loss, can be profoundly affected and changes the problem.

Hydrodynamics and gravity are critical in CCSN mechanism. The collapse of the stellar core under gravity is described by hydrodynamic equations that account for fluid flows, shock waves, turbulence, and instabilities such as the **SASI**. The hydrodynamic equations describe the movement and behavior of the stellar material during the collapse. They must incorporate the conservation of mass, momentum, and energy. Additionally, the gravitational potential affects the matter’s infall and shock wave dynamics. At the high densities reached during the core

collapse, general relativistic effects become significant, necessitating relativistic corrections in simulations. Relativistic hydrodynamics involves solving the Einstein field equations coupled with the hydrodynamic equations.

When the stellar core collapses and rebounds, it creates a shock wave that propagates outward. This shock wave is responsible for heating and compressing the outer layers of the star, initiating nuclear reactions and leading to the supernova explosion. The dynamics of this shock wave, including its formation, propagation, and potential stalling in such dense media, are crucial aspects of the hydrodynamics in core-collapse supernovae.

During core collapse and the subsequent explosion, various instabilities can emerge, such as the Rayleigh-Taylor instability and the **SASI**. The Rayleigh-Taylor instability occurs when a lighter fluid pushes against a heavier fluid, generating turbulence and creating characteristic "mushroom-shaped" patterns in the flow [214]. However, when gas in the post-shock region is rapidly advected toward the gain radius, the growth of such buoyancy-driven instability can be suppressed. In these cases, the shock and post-shock flow may still develop non-radial asymmetries, with an increased oscillatory pattern. This phenomenon is known as **SASI** [215, 216].

SASI oscillations can trigger convective instabilities, leading to an expansion of the average shock radius and increasing the mass of the gain layer. The combined effects of these hydrodynamic instabilities prolong the advection time of matter through the neutrino heating region, enhancing neutrino energy deposition and supporting the neutrino-driven explosion mechanism. These instabilities contribute to turbulent flows, mixing different stellar layers and influencing the overall dynamics. Those turbulence's improve neutrino transport and energy deposition behind the shock, facilitating shock revival and favoring the explosion mechanism.

The Equation of state (EoS) describes how matter behaves at the extreme densities and temperatures present in the core of a collapsing star. The EoS must accurately represent the properties of nuclear matter, including phase transitions, such as the formation of a neutron-rich core or quark matter. An accurate EoS is critical for determining the core's response to compression and the resulting dynamics of the collapse and rebound.

During the collapse, the core density increases dramatically, reaching values of up to $10^{14} \text{ g cm}^{-3}$. At these densities, the nuclear matter becomes degenerate, and the repulsive component of the nuclear force leads to a stiffening of the EoS, halting the collapse and causing the core to bounce. The behavior of matter at such extreme conditions is influenced by the nuclear force, which includes short-range repulsion and longer-range attraction, as well as by the possible formation of exotic states of matter such as hyperons or quark-gluon plasma. These effects must be included in the EoS to model the core-collapse dynamics accurately.

Additionally, the EoS must account for the thermal and compositional state of the matter, including the contributions from electrons, positrons, photons, and neutrinos. EoS models can lead to variations in the mass and radius of the proto-neutron star, influencing the overall dynamics and the potential for explosion. Several equations of state are commonly used in supernova simulations, including:

- **Lattimer-Swesty EoS:** This EoS is based on a compressible liquid drop model and is widely used in core-collapse supernova simulations [217].

- **Shen EoS:** This EoS includes detailed nuclear physics and is derived from relativistic mean-field theory, providing accurate descriptions of dense matter [218, 219, 220].

- **SFHo EoS:** This EoS is optimized for supernova and neutron star applications, balancing between nuclear and observational constraints to provide realistic results for core-collapse scenarios [221].

Neutrino transport is crucial in core-collapse supernovae, as neutrinos are the primary mechanism for energy loss and transfer during the collapse and explosion. The Boltzmann equation describes the evolution of the neutrino distribution function in phase space, providing detailed information on neutrino interactions, including emission, absorption, and scattering processes.

Neutrino transport influences the proto-neutron star's cooling and the matter's heating behind the stalled shock, essential for shock revival. Neutrinos interact with matter through weak force interactions. During the core collapse, neutrinos are emitted via processes like electron capture on protons, pair production, and thermal emission. The Boltzmann transport equation includes these interactions and emissions, solved numerically, accurately describing these processes and their impact on the supernova dynamics. The main processes include:

- **Neutrino absorption:** Neutrinos can be absorbed by nucleons, such as $(\nu_e + n \rightarrow p + e^-)$ and $(\bar{\nu}_e + p \rightarrow n + e^+)$.

- **Neutrino scattering:** Neutrinos can scatter off nucleons and electrons, which affects their energy and momentum, influencing how energy is transported out of the core.

- **Neutrino emission:** This occurs through electron capture $(e^- + p \rightarrow n + \nu_e)$, and thermal emission from the hot core.

The different production and scattering processes are detailed in Table 7.1.

The neutrino transport equation must be solved in a multidimensional framework to capture the anisotropic nature of neutrino emission and absorption. This requires significant computational resources due to the complex interactions and the need to resolve fine details in the stellar environment. Accurate neutrino transport modeling is crucial for predicting the behavior of the stalled shock and the conditions required for its revival, ultimately determining the success of the supernova explosion.

Process	Reaction
Beta-processes (direct URCA processes)	
electron and ν_e absorption by nuclei	$e^- + (A, Z) \leftrightarrow (A, Z - 1) + \nu_e$
electron and ν_e captures by nucleons	$e^- + p \leftrightarrow n + \nu_e$
positron and $\bar{\nu}_e$ captures by nucleons	$e^+ + n \leftrightarrow p + \bar{\nu}_e$
"Thermal" pair production and annihilation processes	
Nucleon-nucleon bremsstrahlung	$N + N \leftrightarrow N + N + \nu + \bar{\nu}$
Electron-positron pair process	$e^- + e^+ \leftrightarrow \nu + \bar{\nu}$
Plasmon pair-neutrino process	$\tilde{\gamma} \leftrightarrow \nu + \bar{\nu}$
Reactions between neutrinos	
Neutrino-pair annihilation	$\nu_e + \bar{\nu}_e \leftrightarrow \nu_x + \bar{\nu}_x$
Neutrino scattering	$\nu_x + \{\nu_e, \bar{\nu}_e\} \leftrightarrow \nu_x + \{\nu_e, \bar{\nu}_e\}$
Scattering processes with medium particles	
Neutrino scattering with nuclei	$\nu + (A, Z) \leftrightarrow \nu + (A, Z)$
Neutrino scattering with nucleons	$\nu + N \leftrightarrow \nu + N$
Neutrino scattering with electrons and positrons	$\nu + e^\pm \leftrightarrow \nu + e^\pm$

TABLE 7.1: Most important neutrino production and scattering processes in supernova and proto-neutron star matter. N means nucleons, i.e., either n or p , $\nu \in \{\nu_e, \bar{\nu}_e, \nu_\mu, \bar{\nu}_\mu, \nu_\tau, \bar{\nu}_\tau\}$, $\nu_x \in \{\nu_\mu, \bar{\nu}_\mu, \nu_\tau, \bar{\nu}_\tau\}$. Taken from [213].

The inclusion of detailed neutrino opacities², as well as corrections for general relativistic effects, enhance the fidelity of these models. The role of different neutrino flavors and the impact of neutrino-driven convection and turbulence on the explosion dynamics is also subject to discussion. For example, the treatment of muon and tau neutrinos as separate species, rather than lumping them together, is one of the advances highlighted in the recent studies [222, 223]. To allow to solve the Boltzmann equation in 3D, different approximations can be applied. The ray-by-ray-plus approximation is a computational method used in multidimensional supernova simulations to handle neutrino transport. It treats each radial ray independently for neutrino transport calculations, simplifying

²Opacity refers to the measure of absorption and scattering of the neutrino in the medium.

the complex multidimensional problem while incorporating additional corrections to account for lateral energy transfers and interactions [224].

Another commonly used approximation involves solving the Boltzmann equation by employing a finite set of angular moments (integrals) of the neutrino phase-space distribution function. These moments are used to eliminate the momentum direction dependence of the Boltzmann equation. Since there is an infinite number of moments, and each level introduces more moments than equations, terminating the set at any level requires a closure relation. The closure relation is typically a function chosen to relate the available moments. Terminating at the first moment equation, which corresponds to the neutrino energy equation, leads to the diffusion approximation, while terminating at the second moment equation, corresponding to the neutrino momentum equation, results in the two-moment transport approximation [213].

Summary We can conclude that reference simulation towards which research tends would have:

- a progenitor as detailed as possible
- a solution of Einstein’s equations of general relativity for the space-time metric
- a three-dimensional (magneto-)hydrodynamic relativistic simulation
- a modern equation of state calculated from nuclear physics to describe interactions in the fluid
- a treatment of neutrinos by solving the Boltzmann equation, which implies, on the one hand, the treatment of neutrino transport (time-dependent) and, on the other hand, a detailed understanding of the weak interaction processes via which neutrinos interact.

7.5.2 Modeling in the market

In this section, we present the different models used in Chapter 8 for model discrimination. The set of models was chosen to cover the diversity of the CCSN models.

7.5.2.1 Sukhbold (2015)

As mentioned before, the CCSN involves a complex interplay of hydrodynamics, neutrino transport, and stellar physics. In the referenced study [225], the P-HOTB (Prometheus-Hot Bubble) code [226] was employed for the simulation. P-HOTB assumes spherical symmetry to simplify the computational process. This 1D simulation tracks the evolution from the onset of the stellar collapse, through core bounce, up to either a black hole formation or a successful explosion. A key aspect of these simulations is the exclusion of the high-density core of the proto-neutron star from direct hydrodynamical modeling. Instead, a contracting inner boundary is used to represent the shrinking core, with time-dependent neutrino luminosities and mean energies imposed at this boundary. This approach ensures that the feedback effects of neutrino emission on the explosion dynamics are taken into account. Calibration of the core model parameters is performed using well-studied supernovae such as SN 1987A and the Crab supernova (SN 1054). This calibration is crucial for tuning the simulations to match observed explosion energies and nucleosynthesis yields. The study also explores the influence of progenitor structure on the explosion outcome, emphasizing the importance of presupernova compactness in determining the star’s explodability.

The model data, referred to as Sukhbold_2015, is a 1D simulation using the Lattimer-Swesty EoS with incompressibility³ $K = 220$ MeV and a progenitor mass of $27 M_{\odot}$.

³The incompressibility coefficient K is the second order coefficient depending on the nucleon density in the Taylor expansion of the free baryon energy [217].

7.5.2.2 Bollig (2016)

The simulation presented in the paper [227] uses the Prometheus-Vertex Supernova Code. The Prometheus-Vertex SN code is a sophisticated tool used for both spherically symmetric (1D) and multidimensional (2D and 3D) simulations of core-collapse supernovae. It accurately simulates complex processes involved in these events, including the transport of neutrinos and the effects of general relativistic gravity [224].

The code employs a two-moment scheme for the transport of neutrinos and antineutrinos of all three flavors: electron neutrinos (ν_e), electron antineutrinos ($\bar{\nu}_e$) and heavy lepton neutrinos (ν_x). This scheme focuses on accurate modeling of neutrino interactions and energy transfer. For multidimensional simulations, the "ray-by-ray-plus" approximation is used to handle the complexity of neutrino transport in different directions [228, 224].

Although the hydrodynamics solver is Newtonian, the code incorporates an effective relativistic potential to account for the effects of general relativistic gravity. Relativistic redshifting is also included in the neutrino transport calculations to accurately model the energy and velocity dependencies [229].

The code includes a detailed set of neutrino opacities, which are crucial for accurately modeling neutrino interactions with matter. These opacities have been detailed and improved upon in various studies [224, 230, 231].

The interesting upgrades in the Prometheus-Vertex SN are the following:

- Separate treatment of neutrino species: the code now treats all individual types of muon and tau neutrinos and antineutrinos as separate species, rather than clustering them together into one representative heavy-lepton neutrino [232].
- Self-energy shifts: implementation of self-energy shifts for unbound neutrons and protons in their charged-current beta reactions with neutrinos has been added for more accurate modeling [232].
- Quasi-stationary convection: an optional treatment of quasi-stationary convection in 1D simulations through a mixing-length description allows for more accurate simulations of the convection processes within the proto-neutron star [233, 234, 235, 236].

The data used in this thesis are simulated in a 1D simulation with the different upgrades presented above, using the Lattimer equation of state [217] for a progenitor of $27M_{\odot}$. The results are presented in [227].

7.5.2.3 Tamborra (2014)

This model [237, 212] is a pioneer in three-dimensional supernova simulation incorporating advanced neutrino transport. It highlights the significant effects of the SASI. The SASI involves large-scale sloshing motions of the shock front, which may compete with neutrino-driven convection to facilitate explosions in multidimensional simulations. These effects are inherently multidimensional and are not observable in one-dimensional simulations of the same progenitors.

The simulation was conducted using the same Prometheus-Vertex code used for Bollig Models but in a 3D framework. The simulation utilizes a sophisticated set of neutrino interaction rates as described in reference [217]. It employs an effective potential to account for general relativistic corrections to Newtonian gravity [217].

In multidimensional simulations, the neutrino signal depends on the observer's direction relative to the progenitor, necessitating extensive post-processing to determine the directional dependence of the neutrino signal. Here, I use the fluxes in the "violet" observer direction identified in reference [237], which shows a particularly large amplitude of the SASI oscillations in the luminosity and mean energy of neutrinos.

For this study, we use simulation results of a $27 M_{\odot}$ progenitor from reference [237] that use the Lattimer-Swesty EoS with incompressibility $K = 220$ MeV.

7.5.2.4 Nakazato (2013)

The Nakazato model is a detailed one-dimensional core-collapse supernova simulation that includes sophisticated neutrino transport mechanisms. Developed by [238, 239, 240, 241], this model aims to provide accurate predictions of neutrino emissions from core-collapse supernovae by considering a variety of progenitor masses, metallicities, and equations of state.

The Nakazato model employs a general relativistic neutrino-radiation hydrodynamics code to simulate the collapse, bounce, and explosion of massive stars. This model incorporates detailed neutrino interactions and transport processes, allowing for precise calculations of the neutrino luminosities and spectra for different types of supernova progenitors.

The Nakazato model provides data for different progenitor masses, metallicities, and equations of state. The available progenitor masses are 13, 20, and $30 M_{\odot}$. The metallicities considered in the model are $Z = 0.004$ and $Z = 0.02$. The equations of state used in the model include the Lattimer-Swesty EoS with incompressibility $K = 180$ MeV and $K = 220$ MeV, as well as the Shen EoS. The data chosen to perform this analysis are simulated with a progenitor mass equal to $30 M_{\odot}$, metallicity equal to 0.02, and the Lattimer-Swesty EoS with incompressibility $K = 220$ MeV.

7.5.2.5 Warren (2020)

The simulation employed to generate those data uses the FLASH multi-physics simulation framework to conduct a series of 1D CCSN simulations using the Supernova Turbulence In Reduced-dimensionality (STIR) model [242, 243]. The goal of these simulations is to replicate the detailed thermodynamics and composition observed in 3D simulations, enabling us to make predictions about neutrino and gravitational wave signals from stellar core collapse.

FLASH is a highly versatile simulation code capable of handling a wide range of astrophysical problems [242]. It utilizes adaptive mesh refinement (AMR) to provide high-resolution simulations where needed, optimizing computational resources. In our study, we utilize the FLASH code with the STIR turbulence-driven explosion model, a new method for artificially driving CCSN explosions in 1D simulations.

Turbulence plays a critical role in the CCSN explosion mechanism, contributing significantly to the total pressure behind the shock and aiding in the explosion through turbulent dissipation and postshock heating [244, 245]. The STIR model uses the Reynolds-averaged Euler equations with mixing length theory as a closure to model the effects of turbulence. This model includes a primary free parameter, the mixing length parameter α_{Λ} , which scales the strength of convection. The parameter α_{Λ} has been fit to results from 3D simulations to accurately reflect the physical explosion mechanism in 1D simulations [243].

The paper Warren et al. [246] describes simulation performed with the parameter α_{Λ} equals to 1.23, 1.25, and 1.27. The value $\alpha_{\Lambda} = 0$ corresponds to a simulation without convection and turbulence, resembling a typical 1D simulation. Couch et al. (2020) [243] found that the best-fit value of α_{Λ} , when compared to convection seen in 3D simulations, is approximately 1.25. To account for uncertainties in theoretical models simulations with $\alpha_{\Lambda} = 1.23$ and $\alpha_{\Lambda} = 1.27$. Those values are obtained by fitting to 3D simulations and add other stellar evolution factors such as binarity and rotation [247]. The simulations in Warren et al. work exclusively use the SFHo EoS developed by Steiner et al. (2013) [221].

For neutrino transport, we use an explicit two-moment "M1" neutrino transport scheme with an analytic closure [248, 249, 250]. The M1 scheme is implemented in the FLASH code and assumes three neutrino flavors: electron neutrinos (ν_e), electron antineutrinos ($\bar{\nu}_e$), and a combined heavy-lepton neutrino species (ν_x), which includes both muon and tau neutrinos and their antineutrinos. The simulations incorporate velocity-dependent terms and inelastic neutrino-electron scattering, with 12 logarithmically spaced neutrino energy groups ranging from 1 to 300 MeV [250].

The validity of a 1D model is assessed by its ability to reproduce the results of comparable 3D simulations while making reasonable approximations of the physics involved. The STIR model has been shown to correctly predict key outcomes of the explosion (or its failure) in comparison with the 3D simulations of Burrows et al. (2019) [251]. Additionally, STIR reproduces the angle-averaged convective and thermodynamic structure of full 3D simulations closely [243].

The Warren simulated data chosen for this analysis use α_Λ equals to 1.23 and a progenitor of $27 M_\odot$.

7.5.2.6 Fornax (2021)

The Fornax software is a recent tool used to simulate CCSN. It uses 2D or 3D codes to simulate the evolution of the CCSN design to enhance the capture of the complex dynamics of supernovae. Fornax includes several advanced features:

- **Multidimensional capabilities:** Fornax supports both 2D and 3D simulations, allowing researchers to explore the full range of supernova dynamics.
- **Neutrino transport:** The software includes advanced neutrino transport algorithms, specifically the multi-group two-moment (MG2) transport scheme, that accurately models the emission, absorption, and scattering of neutrinos within the star.
- **AMR:** Fornax uses AMR to dynamically adjust the grid resolution, ensuring high accuracy in regions with complex physics while optimizing computational resources.
- **Parallel computing:** The software is designed to run efficiently on modern supercomputers, utilizing parallel computing techniques to handle the immense computational demands of 3D simulations.
- **Equation of state:** Fornax incorporates multiple equations of state, including Lattimer-Swesty, Shen, and SFHo, to provide flexibility in modeling different supernova progenitors.

With the multidimensional capabilities of Fornax software, models captured some aspects of the overturning convection that 1D models missed. However, the computational expense of these simulations meant that only a few runs could be performed each year, limiting the exploration of parameter space and physical behaviors. The transition to 2D simulations involved the following key advances:

- **Axisymmetric assumption:** 2D simulations adopted an axisymmetric approach (often referred to as cylindrical symmetry), where the system is symmetric around one axis. This allows for the modeling of fluid flows and other dynamic processes in a plane, effectively capturing radial and axial variations.
- **Computational techniques:** Enhanced computational techniques and algorithms were developed to handle the increased complexity of 2D models. These techniques included improved methods for solving the hydrodynamic equations and for modeling the interaction between neutrinos and matter.

- **Resource allocation:** The transition required more computational resources than for 1D models. Advances in computational power and the development of parallel computing methods allowed researchers to perform these more demanding simulations.
- **Capturing convection:** One of the critical improvements in 2D simulations was the ability to capture convection and other fluid instabilities. These processes are essential for understanding the energy transfer and explosion mechanisms in core-collapse supernovae.

The development of three-dimensional (3D) simulation capabilities represented a major leap forward. These models allowed for a more comprehensive exploration of core dynamics and explosion mechanisms. The transition from 2D to 3D simulations involved several advances:

- **Full spatial representation:** 3D simulations do not assume any symmetry, allowing for the modeling of all three spatial dimensions. This provides a more accurate representation of physical processes.
- **Complex turbulence:** 3D models can capture complex turbulent flows and instabilities that are inherently three-dimensional, providing deeper insights into the dynamics of the supernova core.
- **Advanced algorithms:** The development of more sophisticated numerical algorithms and increased computational power made it possible to handle the vast computational demands of 3D simulations.
- **Improved accuracy:** By eliminating symmetry assumptions, 3D simulations offer improved accuracy in predicting the behavior of supernovae, especially regarding the asymmetries observed in explosions.

2D simulations, while computationally feasible and useful for parameter exploration, impose an axisymmetric constraint that can limit accuracy. They are easier to run and require fewer computational resources, making them practical for initial studies and wide parameter sweeps. In contrast, 3D simulations provide a more complete and accurate representation of supernova dynamics. They capture the full complexity of turbulence and instabilities, allowing for more realistic modeling of the explosion mechanisms and asymmetries. However, they demand significantly higher computational resources and advanced algorithms, which can be a limiting factor for extensive parameter studies.

The Fornax simulation data chosen in this analysis used the 2D simulation with a progenitor mass of $26.99M_{\odot}$ with the LS-EoS.

7.5.2.7 Summary of models used

Table 7.2 gives the different parameters of the different models used in this thesis.

Model	Mass (M_{\odot})	Neutrino Transport Model	Software Used	Dimensio- nality	Equation of State	Key Parame- ters
Sukhbold	27	Time-dependent neutrino lumi- nosities and mean energies	Prometheus- Hot Bub- ble	1D	LS220 EoS	Calibration with SN 1987A and Crab SN
Bollig	27	Two-moment scheme	Prometheus -Vertex	1D	LS220 EoS	Ray-by- ray-plus approxima- tion
Tamborra	27	Advanced neu- trino transport	Prometheus -Vertex	3D	LS220 EoS	Random den- sity perturba- tions of 0.1%
Nakazato	30	General rela- tivistc neutrino- radiation hydro- dynamics	General relativistic code	1D	LS220 EoS	Metallicities: Z=0.004, Z=0.02
Warren /Couch	27	Two-moment M1 scheme	FLASH with STIR	1D	SFHo EoS	$\alpha_{\lambda}=1.23,$ 1.25, 1.27, Adaptive mesh refine- ment
Fornax	26.99	MG2 transport scheme	Fornax	2D	SFHo EoS	Adaptive mesh refine- ment

TABLE 7.2: Comparison of different CCSN models. The Lattimer-Swesty EoS with incompressibility $K = 220$ MeV EoS is written in Table as LS220 EoS.

7.6 Astrophysical implications

The following section examines the profound astrophysical implications of CCSN, offering a detailed exploration of the complex nucleosynthesis processes that produce elements heavier than iron and the dynamic mechanisms that result in the formation of dense remnants like neutron stars and black holes.

7.6.1 Nucleosynthesis in CCSN

CCSN are critical sites for nucleosynthesis, particularly for elements heavier than iron [252, 253, 254, 255]. CCSN involve complex nuclear processes that occur under extreme conditions. The relevant nucleosynthesis processes to be considered in this context are: the slow neutron capture process (s-process) [256, 257], the rapid neutron capture process (r-process) [258, 259], the proton capture process (p-process) [260, 261] and the neutrino-induced p-process (νp -process) [262].

Slow neutron capture process (s-process) The s-process, or slow neutron capture process, plays a significant role in nucleosynthesis within stars, particularly during the late stages of stellar evolution. It predominantly occurs

in the helium-burning zones of asymptotic giant branch (AGB) stars⁴. During the s-process, seed nuclei, typically iron, capture neutrons slowly enough that beta decays have time to occur between captures, allowing the production of heavier elements up to bismuth. This process is characterized by a steady neutron flux, which facilitates the formation of stable isotopes along the valley of beta stability in the chart of nuclei (see Figure 7.4) [252, 257].

Rapid neutron capture process (r-process) The r-process is responsible for producing approximately half of the elements heavier than iron. It involves the rapid capture of neutrons by atomic nuclei. This process requires environments with extremely high neutron density. Such conditions are found in the neutron-rich ejecta of CCSN, particularly in the regions outside the proto-neutron star [259].

The r-process proceeds through the rapid capture of neutrons by seed nuclei. Atomic nuclei capture neutrons rapidly before they have time to undergo beta decay. The neutron-rich nuclei then undergo beta decay (neutron converting to proton, emitting an electron and an antineutrino), moving the element up the periodic table. This process can form the heaviest elements, including uranium and thorium. The r-process path lies far from the line of stable isotopes, involving very neutron-rich isotopes. Initially, neutron capture occurs in a high-temperature, high-density environment. As the environment cools and expands, neutron captures slow, and beta decays continue to shape the final abundance pattern. The production of rich neutron elements through the r-process follows the red arrow in Figure 7.4.

Proton process (p-process) The p-process is an essential mechanism responsible for the synthesis of certain stable, proton-rich isotopes of elements heavier than iron, known as p-nuclides. Unlike the s-process and r-process, the p-process occurs through sequences of photodisintegration reactions (gamma captures) and captures of protons and alpha particles, predominantly in environments with high temperatures. One of the primary sites for the p-process is in CCSN. In a CCSN, the p-process takes place in the oxygen-neon (O-Ne) layers of a massive star during the supernova explosion. The p-process requires a pre-existing abundance of heavy nuclei, which are primarily produced by the s- and r-processes during the earlier evolutionary stages of the star. Once these nuclei are exposed to the intense gamma radiation in the supernova environment, they undergo a series of photodisintegration reactions leading to proton rich nuclei. This process is the orange arrow in Figure 7.4.

Neutrino-induced process (νp -process) In the νp -process, antineutrinos interact with free protons to produce free neutrons through the reaction $\bar{\nu}_e + p \rightarrow n + e^+$ [264]. These neutrons are then immediately captured by neutron-deficient nuclei, allowing for the synthesis of heavier elements. This process is essential for producing elements heavier than iron, particularly those with large number of protons compared to neutrons (yellow line in Figure 7.4), which are otherwise challenging to form through traditional nucleosynthesis processes like the r-process or s-process.

The νp -process is characterized by a sequence of reactions beginning with the formation of iron-group elements. Continued antineutrino absorptions generate free neutrons, which are rapidly captured by existing nuclei. This sequence allows the nucleosynthesis flow to bypass beta-decay points and continue to heavier nuclei. The significance of the νp -process lies in its ability to explain the observed abundances of certain isotopes, such as $^{92,94}\text{Mo}$ and $^{96,98}\text{Ru}$, which cannot be adequately accounted for by the classical r-process or s-process [265]. Moreover, this process operates in the innermost ejected layers of CCSN, making it a primary nucleosynthesis mechanism that does not depend on the initial heavy element content of the star. The presence of proton-rich matter with electron fraction higher than 0.5 in the supernova ejecta is a critical condition for the νp -process, ensuring that sufficient free protons are available for antineutrino capture and subsequent neutron production [264]. Moreover, this process operates in the innermost ejected layers of CCSN, making it a primary nucleosynthesis mechanism that does not depend on the initial heavy element content of the star.

⁴AGB stars are a class of stars that have completed core helium burning and are now burning helium in a shell around a core of carbon and oxygen. These stars are characterized by their large luminosity and significant mass loss through stellar winds[263].

Finally, this process, still poorly studied and understood, may also offer insights into the chemical evolution of galaxies, as it contributes to the abundance of elements observed in extremely metal-poor stars, providing evidence for early supernova events in the galaxy's history [265].

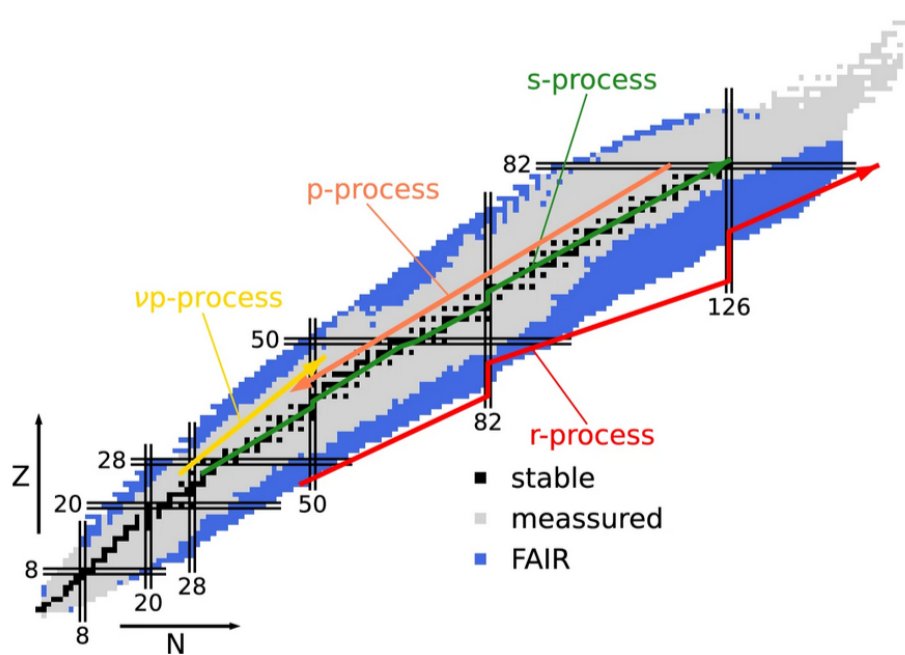


FIGURE 7.4: In the nuclear chart, each square represents an isotope, with horizontal rows corresponding to elements having the same number of protons, Z , but different numbers of neutrons, N . Stable isotopes are shown in black, while nuclei produced in laboratories are in grey. The light blue region marks exotic isotopes yet to be discovered. Colored lines schematically indicate various nucleosynthesis processes. Taken from [266].

7.6.2 Neutron star and black hole formation

CCSN are pivotal events in astrophysics, leading to the formation of compact remnants such as black holes and neutron stars. The fate of a collapsing massive star largely hinges on its progenitor mass and the intricate dynamics of the explosion mechanism.

For less massive progenitors, typically below $20 M_{\odot}$, the core-collapse process often results in the formation of a neutron star. These stars undergo gravitational collapse until nuclear densities are reached, at which point the collapse is halted by neutron degeneracy pressure. The energy released during the collapse is partly absorbed by the stellar envelope, potentially leading to a successful supernova explosion driven by neutrino heating. This mechanism is prevalent in less massive stars where the proto-neutron star does not reach the critical density for phase transition into quark matter, ensuring the formation of a stable NS [267, 268].

In contrast, more massive progenitors, typically exceeding $40 M_{\odot}$, are more likely to form black holes. The collapse of these stars can continue unabated due to their higher core masses, surpassing the neutron degeneracy pressure threshold. This leads to the formation of an event horizon and a subsequent black hole. For such progenitors, if the proto-neutron star mass reaches beyond the Tolman-Oppenheimer-Volkoff limit, a black hole forms either directly or after a brief period of NS existence. Additionally, failed supernovae, where the explosion mechanism is insufficient to expel the outer layers of the star, also result in black hole formation [269, 270].

An intriguing aspect of CCSN is the potential phase transition from hadronic matter to quark-gluon plasma

within the proto-neutron star. This phase transition can lead to a second hydrodynamic bounce, forming a hybrid star with a quark matter core if the conditions are favorable. The dynamics of this transition significantly influence the final remnant. In intermediate-mass stars (around $40\text{-}50 M_{\odot}$), this phase transition can either facilitate a successful supernova explosion, resulting in a hybrid star or continue to black hole formation if the proto-neutron star mass becomes unstable. The presence of a quark core can temporarily support the proto-neutron star, but if the accretion continues, it may ultimately lead to black hole formation due to the gravitational instability of the remnant [271, 272].

7.7 Summary

This chapter provides a comprehensive overview of the current knowledge of the CCSN phenomenon and the related available models. Up to now, only the SN1987A neutrinos have been detected on earth. A first classification of the supernova is based on their electromagnetic spectra related to the different nuclei fusions happening on the external layer. However, another classification exists based on their explosion mechanism. Two families of supernova explosions exist: thermonuclear and core-collapse supernova explosions. We focus on the second as it is the only one with an efficient neutrino production.

The core collapse mechanism is heavily dependent on the role of neutrinos. Neutrinos play a pivotal role in the creation of the shock inside the CCSN, as they induce core contraction by sapping energy from it. As the shock propagates through the stellar media, it loses energy and stalls. Ultimately, the shock is rejuvenated through neutrino energy deposition in higher density regions (neutrino heating), leading to the star exploding into a supernova.

The complete description of the CCSN mechanism requires an implementation of various physics. An ideal simulation should include a very detailed progenitor description, a modern equation of state based on nuclear physics, a 3D relativistic magneto-hydrodynamics solver, and precise treatment of the neutrino transport and propagation through the Boltzmann equation. However, due to limitations in computation power, various assumptions are required, leading to a large variety of models. Each model gives respectively more emphasis on different physics parameters, such as nucleosynthesis and the formation of compact remnants like neutron stars and black holes. This chapter highlights the intricate physical processes driving supernova explosions and presents ongoing efforts to model these events the most accurately.

Chapter 8

Supernova model discrimination

As motivated in the previous chapter, there are numerous CCSN models developed by various group. One of the main targets from the next explosion measurements is to constrain the available models in order to understand better the underlying CCSN physics. The following chapter describes the statistical analysis to perform this model discrimination and assesses the performance of the JUNO experiments to accomplish such a task.

Contents

8.1	Analysis tools	173
8.1.1	Expected value	173
8.1.2	Monte Carlo generator	175
8.1.3	Cross check of the data generation	178
8.2	Statistical Analysis Method	179
8.2.1	Hypothesis testing framework	179
8.2.2	Computation of $\Delta\chi^2$ for binned poisson data	179
8.2.3	Computation of likelihood for binned poisson data	180
8.2.4	Computation of likelihood for unbinned data	180
8.3	Model discrimination using binned likelihood analysis	181
8.3.1	Model discrimination using IBD channel	181
8.3.2	Model discrimination using νpES channel	183
8.4	Model discrimination using unbinned likelihood analysis	184
8.4.1	Discussion of the impact of the number of observed events	186
8.4.2	Impact of neutrino flavor transformation on model discrimination	187
8.4.3	Comparison with Hyper-Kamiokande	188
8.5	Summary and outlook	190

8.1 Analysis tools

In this section, we describe the different tools used for our analysis: the computation of the expected value and the Monte Carlo generator used in this study.

8.1.1 Expected value

The expected number of neutrino interactions in the JUNO detector at a specific time t for a given interaction channel ch can be estimated using the following integral:

$$N_{ch,\tilde{u}}(t) = n_{target} \int_{E_v \min}^{E_v \max} \int_{E_e \min}^{E_e \max} \frac{d\Phi(t, E_v)}{dE_v} \frac{d\sigma_{ch,\tilde{u}}(E_v, E_e)}{dE_e} dE_e dE_v \quad (8.1)$$

Here, E_v and E_e represent the energies of the incident neutrino and the outgoing particle, respectively. n_{target} is the number of targets constituting the detector, in our case the JUNO detector. This number changes following the channel used. The term $\Phi(t, E_v)$ denotes the neutrino flux obtained from the SNEWPY library [273]. SNEWPY library gives us access to different models. It also implements different transformation on the neutrino flux including matter effect, **Neutrino Mass Ordering (NMO)** and distance of the CCSN to the detector. The $\frac{d\sigma_{ch,\tilde{u}}(E_v, E_e)}{dE_e}$ refers to the differential cross-section for a neutrino of type \tilde{u} (i.e. $\nu_e, \bar{\nu}_e, \nu_\mu, \bar{\nu}_\mu, \nu_\tau, \bar{\nu}_\tau$) in the specified interaction channel. We obtain the different cross sections from the sntools library [274] (see next section for the details of the cross section implementation).

Similar to $N_{ch,\tilde{u}}(t)$, we can compute the event rate, $\frac{dN_{ch,\tilde{u}}(t)}{dE_e}$, using this integral :

$$\frac{dN_{ch,\tilde{u}}(t)}{dE_e} = n_{target} \int_{E_v \min}^{E_v \max} \frac{d\Phi(t, E_v)}{dE_v} \frac{d\sigma_{ch,\tilde{u}}(E_v, E_e)}{dE_e} dE_v \quad (8.2)$$

This formulation allows us to obtain the prediction of the time-energy distribution of the outgoing particles for a particular channel. Each of the 6 models presented in Table 7.2 predicts a different total number of events. Table 8.1 summarizes the d_{100} , d_{300} , d_{1000} , and d_{5000} values for different models, representing the distances at which 100, 300, 1000, and 5000 events would be observed in the detector for the IBD channel. For reference, the distance to the center of our galaxy is approximately 8.2 kpc [275].

Model	d_{100}	d_{300}	d_{1000}	d_{5000}
Warren	40.3	23.3	12.7	5.7
Tamborra	45.7	26.3	14.4	6.4
Nakazato	36.5	21.1	11.5	5.1
Bollig	41.2	23.8	13.	5.8
Fornax	48.2	27.8	15.2	6.8
Sukhbold	41.9	24.2	13.2	5.9

TABLE 8.1: d_{100} , d_{300} , d_{1000} , and d_{5000} in kpc for the different models used in this study. Parameters: Channel IBD, transformation = AdiabaticMSW_NMO, cut: 20-500 ms, 0.2-100 MeV.

We can then represent the event rate for the 6 models presented in Table 7.2 in a 2D plot as shown in Figure 8.1. The parameters chosen to compute the event rates displayed in Figure 8.1 are the following. We chose to present energy-time distribution of the positron emitted by IBD. The x-axis is the time in ms, y axis is the total energy of the positron in MeV, and the z-axis is the event rate. The distance is chosen for each model separately to achieve a normalization of the total number of event equal to 300, corresponding to a distance between 21 kpc and 27.8 kpc.

For the Tamborra model (panel A), the event rate exhibits the **SASI** phenomenon, characterized by periodic oscillations in the neutrino time distribution. The Nakazato model (panel E) is particularly distinct as the majority of events are concentrated in the 100-200 ms time window. A longer explosion time is seen for the Fornax model (panel F). Finally, for the Bollig (panel C) and Shukbold (panel D) models, the 2D plots show comparable energy-time distributions.

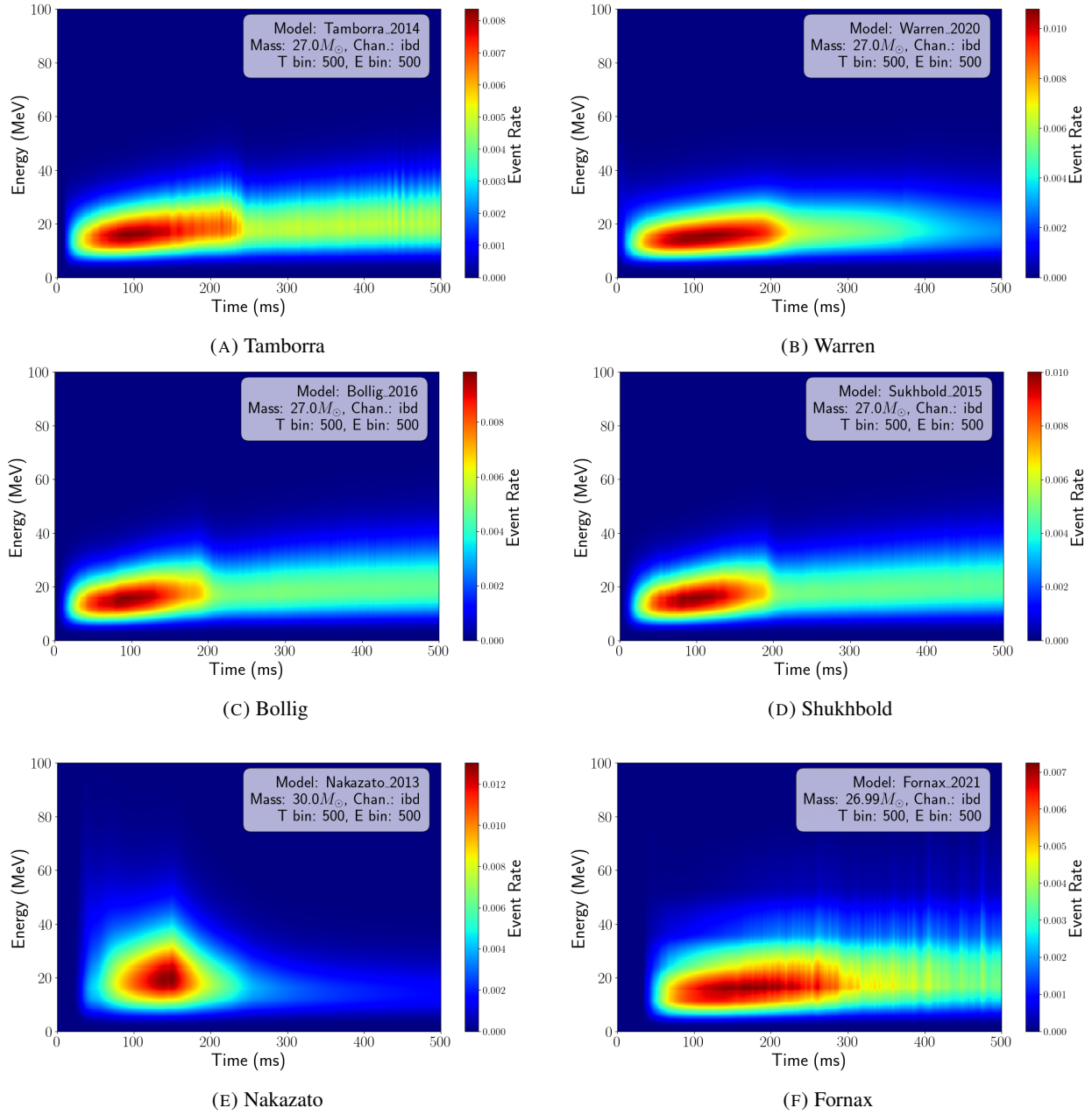


FIGURE 8.1: Expected event rate to be detected in JUNO for 6 different CCSN model for the IBD channel. The x-axis is the time in ms, while the y-axis is the total energy of the positron in MeV.

8.1.2 Monte Carlo generator

The Monte Carlo Generator used in this work is `sntools`. This generator is a well-known generator used for supernova neutrino. This python library allows us to calculate the number of neutrino interactions, $N_{ch,\bar{\nu}}(t)$, for various interaction channels [274]. The raw number of events in a given time bin t is generated using a Poisson distribution with an expected value corresponding to the event rate $\frac{dN_{ch,\bar{\nu}}(t)}{dE_e}$. Finally, the rejection sampling method is used to generate the outgoing particles.

`Sntools` employs a modular plug-in architecture that supports various input formats (thanks to its connection to the SNEWPY software) and interaction channels, as shown in Figure 8.2. The input format plug-ins handle the reading of data from input files and return the neutrino number luminosity as a function of time and energy. The

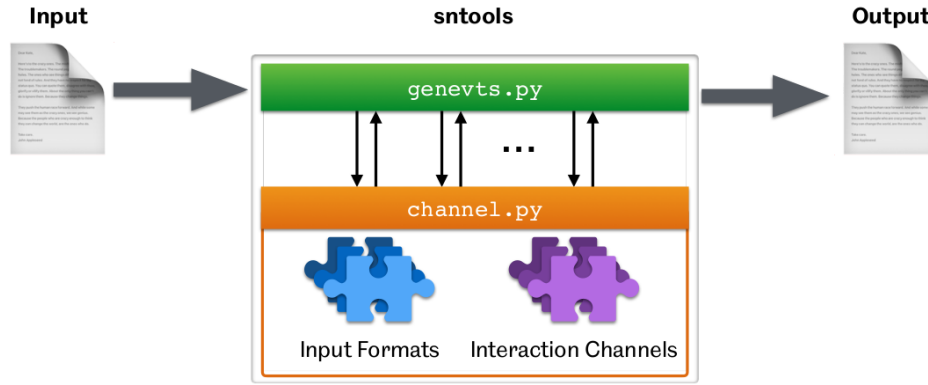


FIGURE 8.2: Structure of the sntools MC generator.

interaction channel interaction is defined by the channel plug-ins which define its properties. This channel plug-in gives the different functions to calculate the differential cross-section $\frac{d\sigma(E_\nu, E_e)}{dE_e}$ and the kinematically allowed energy range.

Detector materials and configurations sntools supports three detector materials: water, [Liquid Scintillator \(LS\)](#), and water-based LS. For the JUNO Central Detector [63], the geometry considered is a sphere with a radius of 17.7 m filled with 20 kton of LAB [274].

Interaction Channels All the interaction channels relevant to JUNO are implemented in sntools, namely: [Inverse- \$\beta\$ Decay \(IBD\)](#), neutrino-proton elastic scattering (νp ES), neutrino-electron elastic scattering (νe ES), ν_e and $\bar{\nu}_e$ interactions with ^{12}C , and the neutrino-carbon [Neutral-Current \(NC\)](#) for ν_e and $\bar{\nu}_e$.

- **IBD channel:** due to its relatively high cross-section and low energy threshold of approximately 1.8 MeV of the IBD channel, and thanks to the abundance of free protons in the JUNO central detector, the IBD channel (IBD; $\bar{\nu}_e + p \rightarrow n + e^+$) is the primary interaction channel for supernova neutrinos. The visible energy of IBD events is closely linked to the neutrino energy, leading to a good reconstruction of the $\bar{\nu}_e$ spectrum.

In sntools, the IBD process is implemented using the full tree-level cross-section calculated in reference [276], with radiative corrections from reference [277]. This calculation assumes the limit $m_e \rightarrow 0$, which is accurate within 0.1% above $E_e = 1$ MeV.

- **νp ES channel:** neutrino-proton scattering ($\nu + p \rightarrow \nu + p$) is an additional dominant channel. The energy deposited by the incident neutrino in the detector is relatively low (less than 1-2 MeV visible after maximum quenching).

This neutral-current interaction is possible for all (anti-)neutrino flavors. Sntools implements this process based on the predictions from Beacom, Farr, and Vogel [278], with the cross-section calculated directly from the SM of particle physics.

- **νe ES channel:** elastic neutrino-electron scattering ($\nu + e^- \rightarrow \nu + e^-$) is a subdominant interaction channel in liquid scintillator due to its lower cross-section and the lower energy spectrum of ν_e compared to $\bar{\nu}_e$. Although these events constitute only a small percentage of all interactions, their angular distribution is strongly forward-peaked, providing directional information pointing back to the supernova. Elastic scattering involves all neutrino flavors, but the cross-section is higher for ν_e and $\bar{\nu}_e$ compared to ν_μ and $\bar{\nu}_\mu$.

The modeling of this channel in sntools uses a tree-level cross-section from standard electroweak theory as calculated by 't Hooft [279], including one-loop electroweak, QCD corrections, and QED radiative corrections from reference [280].

- ν_e and $\bar{\nu}_e$ interactions with ^{12}C : the charged-current interactions of ν_e and $\bar{\nu}_e$ with ^{12}C nuclei are subdominant channel in LS. These channels are only sensitive to the high-energy tail of the supernova neutrino flux due to their high energy thresholds of approximately 17 MeV and 14 MeV, respectively, and the sharp energy dependence of their cross-sections. The implementation of those cross-section calculations is based on the work in reference [281].
- **Neutrino-carbon NC channel:** the neutral-current interactions of neutrinos with ^{12}C nuclei in LS produce $^{12}\text{C}^*$ in an excited state leading to the emission of a mono-energetic photon. This channel is equally accessible to neutrinos and antineutrinos of all flavors. Sntools implements this interaction based on theoretical calculations from [282].

To compare the different cross sections for different interaction channels in the LS detector, we have plotted all of them as a function of neutrino energy using SNOwGLoBES [283] in Figure 8.3. Since SNOwGLoBES does not provide the cross section for the $\nu p\text{ES}$ channel, it is not included in the Figure. The IBD cross section is shown as a black line, and we can see that it is significantly higher in the 5-20 MeV range compared to the other channels shown. Note as well the small value of the cross-sections, $\text{O}(10^{-40} \text{ cm}^2)$, which indicate the low probability of neutrinos interacting with matter particles.

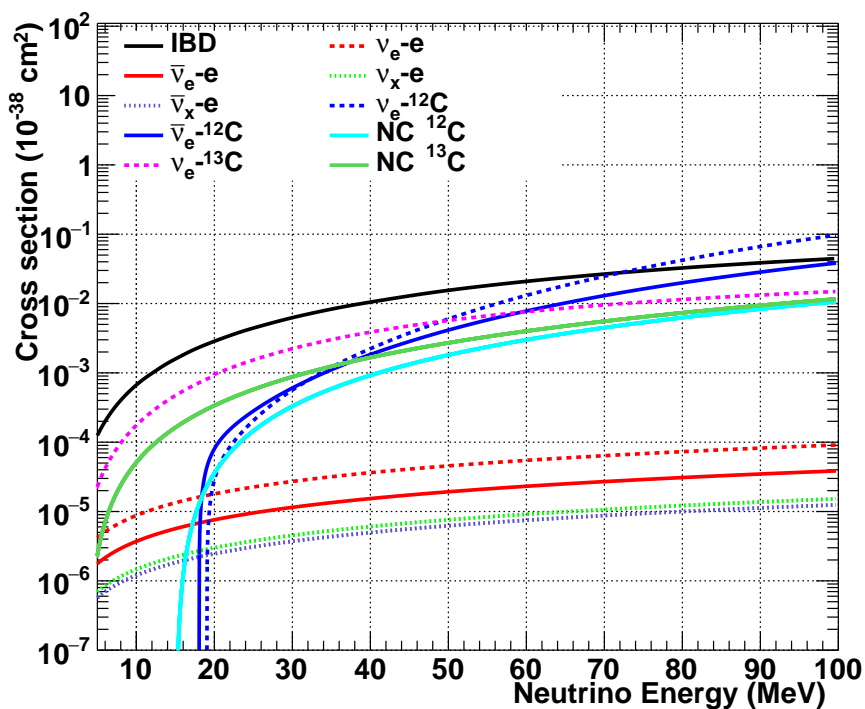


FIGURE 8.3: Cross sections for relevant processes in liquid scintillator detector. The $\nu p\text{ES}$ is not represented. Taken from [283].

Treatment of neutrino flavor conversion Thanks to its connections with SNEWPY, sntools allows the simulation of different neutrino flavor transformation scenarios between different transformations between the original neutrino flux produced in a supernova and the flux detected on Earth. Two specific transformations, `AdiabaticMSW_NMO` and `AdiabaticMSW_IMO`, assume that neutrinos pass through a gradually changing density profile as they exit the star, undergoing adiabatic flavor conversion via the MSW effect (see section 1.4) for normal ordering and inverted ordering, respectively. After the accretion phase, the shock front propagates outward, traversing the

region where adiabatic flavor conversion occurs, leading to a sudden change in matter and electron densities. This transition can significantly affect the flavor conversion processes [284].

8.1.3 Cross check of the data generation

To validate the accuracy of the data generation process, we compare the expected distributions with those ones generated by the Monte Carlo simulation using `sntools`. This comparison is shown in Figure 8.4a and uses the Nakazato 2013 supernova model for the IBD channel as a reference.

Figure 8.4a shows the expected event rate (Equation 8.2) for the IBD channel using `AdiabaticMSW_NMO` based on the Nakazato model. The top panel presents the time evolution of the expected number of events $N(t)$. The bottom left panel displays a 2D histogram of the expected interaction rates as a function of time and outgoing particle energy E_e . The bottom right panel shows the expected energy distribution $N(E_e)$ of the outgoing particles. The distance was chosen to have a total number of events for the event rate equal to 300.

Figure 8.4b presents the results from the Monte Carlo simulation using `sntools`. 1000 CCSN were simulated at a distance of 15 kpc, generating approximately 600,000 entries in the histogram. The central plot shows the 2D distribution of positron produced by IBD with the corresponding time (top) and energy (right) projections.

The comparison between the expected, in Figure 8.4a, and simulated, in Figure 8.4b, results shows good match in both temporal and energy distributions of the events. Slight differences in the distributions may result from statistical fluctuations in the Monte Carlo simulation or minor discrepancies in modeling parameters. This cross-check confirms that `sntools` generates data corresponding to the expected neutrino interaction distributions based on CCSN models. The crosscheck plots for the different channels and different flavor transformation used in this work are presented in appendix A.

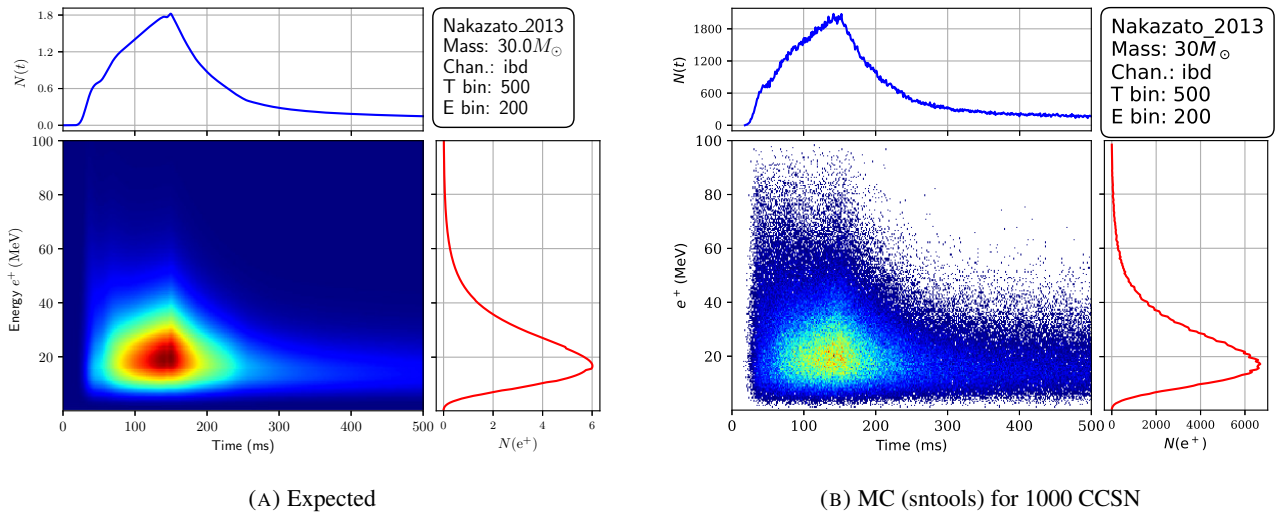


FIGURE 8.4: comparison of the expected and simulated distributions for the Nakazato 2013 model. (A) Expected distribution, (B) Monte-Carlo simulation using `sntools` for 1000 CCSN at 15 kpc. The histograms show the time evolution of events $N(t)$, the 2D histogram of interaction rates as a function of time and energy, and the energy distribution $N(E_e)$.

8.2 Statistical Analysis Method

In this work, we used hypothesis testing to evaluate the potential of CCSN model discrimination with the JUNO detector. To perform this, we construct a method that fits Monte Carlo data to expected value computed thanks to equation 8.2 for the different models. The definition of chi-squared (χ^2) and likelihood (L) functions are essential to quantify how the data fit models. The formulas used in this work are taken from [285].

8.2.1 Hypothesis testing framework

Hypothesis testing involves comparing two hypotheses:

- **Null hypothesis (H_0):** Represents the baseline model, defined as either no significant effect or as a parameter has a specific value.
- **Alternative hypothesis (H_1):** Represents a model either including the effect being tested or assuming that a parameter has a different value from the one proposed in the null hypothesis.

Then, by comparing the probability of measuring the null hypothesis over the alternative hypothesis, we can discriminate which hypothesis is the most probable.

8.2.2 Computation of $\Delta\chi^2$ for binned poisson data

When the number of events per bin is much lower than 1, the Gaussian approximation of the traditional χ^2 fails. To face this issue, the following $\Delta\chi^2$ static test is used. To compare two models, typically the null hypothesis model (H_0) and an alternative hypothesis model (H_1), the difference in χ^2 values, denoted as $\Delta\chi^2$, is computed:

$$\Delta\chi^2 = \chi_{H_0}^2 - \chi_{H_1}^2 \quad (8.3)$$

with the adapted χ^2 function given by:

$$\chi^2 = 2 \sum_{i=1}^N \left[\mu_i(\theta) - n_i + n_i \log \left(\frac{n_i}{\mu_i(\theta)} \right) \right] \quad (8.4)$$

where:

- n_i is the observed number of events in bin i (here the bin are a 2D bin function of the time and the energy),
- $\mu_i(\theta)$ is the expected number of events in bin i under the model with parameters θ ,
- N is the total number of bins.

A larger $\Delta\chi^2$ leads to a stronger preference for the alternative hypothesis.

8.2.3 Computation of likelihood for binned poisson data

For Poisson-distributed data, the likelihood function for a model is the product of Poisson probabilities over the N bins.

$$L(\theta) = \prod_{i=1}^N \exp(-\mu(\theta)) \frac{\mu(\theta)^{n_i}}{n_i!} \quad (8.5)$$

The log-likelihood function is given by:

$$\log L(\theta) = \sum_{i=1}^N [n_i \log(\mu_i(\theta)) - \mu_i(\theta) - \log(n_i!)] \quad (8.6)$$

The difference in the log-likelihoods of the two models, denoted as $\Delta \log L$, is computed as:

$$\Delta \log L = \log L_{H_1} - \log L_{H_0} \quad (8.7)$$

The likelihood ratio test is given by:

$$\Lambda = \frac{L_{H_0}}{L_{H_1}} \quad (8.8)$$

Taking the logarithm, we have:

$$\log \Lambda = \log L_{H_0} - \log L_{H_1} = -\Delta \log L \quad (8.9)$$

giving the $\Delta \log L$ used in this thesis to perform the model discrimination. In scenarios with low event counts per bin, $\Delta \log L$ provides a more accurate measure of the relative likelihood of the two hypotheses.

8.2.4 Computation of likelihood for unbinned data

Sometimes, the analysis uses the unbinned likelihood method as it can perform better than the binned likelihood analysis. This approach is practical when event counts are very low or when binned data might lead to a loss of information. The likelihood function for unbinned data is given by the product of the probability density functions evaluated for each of the N observed events:

$$L(\theta) = \prod_{i=1}^N f(x_i; \theta) \quad (8.10)$$

where:

- $f(x_i; \theta)$ is the probability density function for the i -th event, given the parameter θ . In our case, the event rate is $f(x_i; \theta) = \frac{dN_{ch, \bar{u}}}{dE_e}$, where $\frac{dN_{ch, \bar{u}}}{dE_e}$ is computed in Equation 8.2.
- N is the total number of observed events.

The log-likelihood function is then:

$$\log L(\theta) = \sum_{i=1}^N \log f(x_i; \theta) \quad (8.11)$$

To compare two hypotheses, the difference in the log-likelihoods, $\Delta \log L$, is computed the same way as Equation 8.9.

8.3 Model discrimination using binned likelihood analysis

In this section, we explore the effectiveness of model discrimination using the IBD or νpES channel separately for six different CCSN models. Cuts need to be applied to ensure that the comparison between the models is robust. Energy cuts are set in the range of 0.2 to 100 MeV. This approach is essential for the νpES channel, as νpES does not have a kinematic threshold. In the IBD channel, neutrinos must have an energy higher than 1.8 MeV to interact with this process. For the νpES channel, this threshold does not exist, and we can record lower-energy events. As the trigger has a 100% efficiency for events with energy above 0.2 MeV [140], we put the low energy cut at 0.2 MeV.

To discriminate models based on the same signal, we need to choose the exact time windows for the analysis. From the different models, we can see that more than 80% of the supernova signal is expected to occur within the first 500 ms after the core bounce. Moreover, not all models are simulated for extended time intervals. For instance, the Tamborra model is simulated from 10.5 ms to 551.5 ms. By setting the time cut in the range of 20 ms to 500 ms, we managed to take the bulk of the signal for the different models.

The different models predict different amount of events for a given distance as we can see in Table 8.1. The number of events expected is proportional to the inverse of the square of the distance between the supernova and the detector. In this study we decide to only perform the discrimination on the shape of the expected event rate energy-time distribution. We then decide to normalize the event rate to 300.

The cuts are applied on the data generated with `sntools` on the event rate. Additionally, the different data sets are created to have exactly the same number of events. In the case presented here, the size of the data set corresponds to 300 events.

After applying the time and energy cuts on the data and the normalization on the event rate, we compute the binned likelihood of each data set fitting the different models. Then, for each pair of models, we compute the ΔL . Figure 8.5 shows the binned ΔL distributions for the Tamborra and Warren models. Here, ΔL represents the difference in likelihood between the Tamborra model from 2014 and the Warren model from 2020, calculated as:

$$\Delta L = L_{\text{Tamborra}} - L_{\text{Warren}} \quad (8.12)$$

The orange distribution corresponds to data generated using the Warren model, while the blue distribution corresponds to data generated using the Tamborra model. The clear separation between these two distributions indicates discrimination between the Tamborra and Warren models. We can see a minimal overlap of the two distributions. This leads to the conclusion that good discrimination can be performed between these two models with the chosen parameters : progenitor mass equal to $27 M_{\odot}$, number of events equal to 300 for the IBD channel, and the cuts 20-500 ms for the time, 0.2-100 MeV for the energy. The following section presents the results of model discrimination across all six CCSN models using the binned likelihood method.

8.3.1 Model discrimination using IBD channel

Figure 8.6 displays the distribution of ΔL values for each model comparison. For example, the comparison between the Bollig and Sukhbold models shows overlapping ΔL distributions, indicating some level of confusion between these two models. The difficulty in distinguishing between the Bollig and Sukhbold models based on the IBD

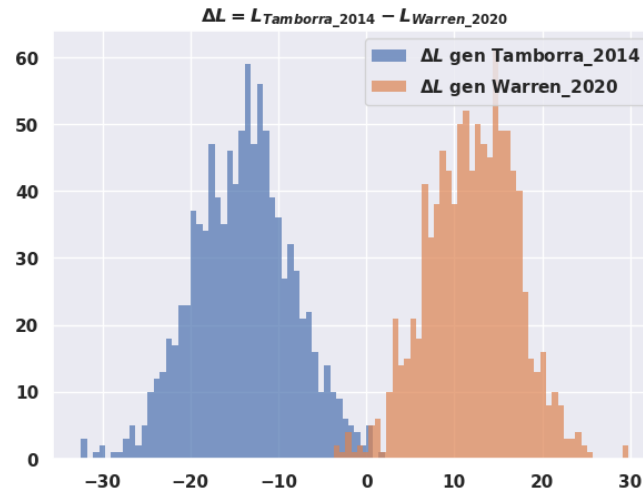


FIGURE 8.5: ΔL binned version in the case of IBD channel for the Tamborra and Warren models.

channel alone is expected as the two models are using the same simulation framework (Prometheus 1D framework as explained in the previous chapter).

The chosen method of presenting the results uses the accuracy tables. The likelihood given one data set (the model used to generate the data is called the true model) is computed for each of the six models. The reconstructed model is identified as the maximum likelihood given this data set. The accuracy is defined as the fraction of times that the true model is correctly reconstructed. Table 8.2 summarizes the accuracy of model discrimination by displaying the frequency with which the maximum likelihood (L) value was achieved for each model when compared to the generated data. For instance, in the first row of the table, we observe that for data generated using the Warren model, the maximum L value was correctly attributed to the Warren model in 979 out of 1000 CCSN simulations. In eight instances, the maximum L value was associated with the Tamborra model, in nine instances with the Bollig model, and four instances with the Sukhbold model. This indicates a high level of discrimination accuracy for the Warren model.

The results, shown in Figure 8.6 and Table 8.2, give good discrimination between the different models, except for the Bollig and Sukhbold models.

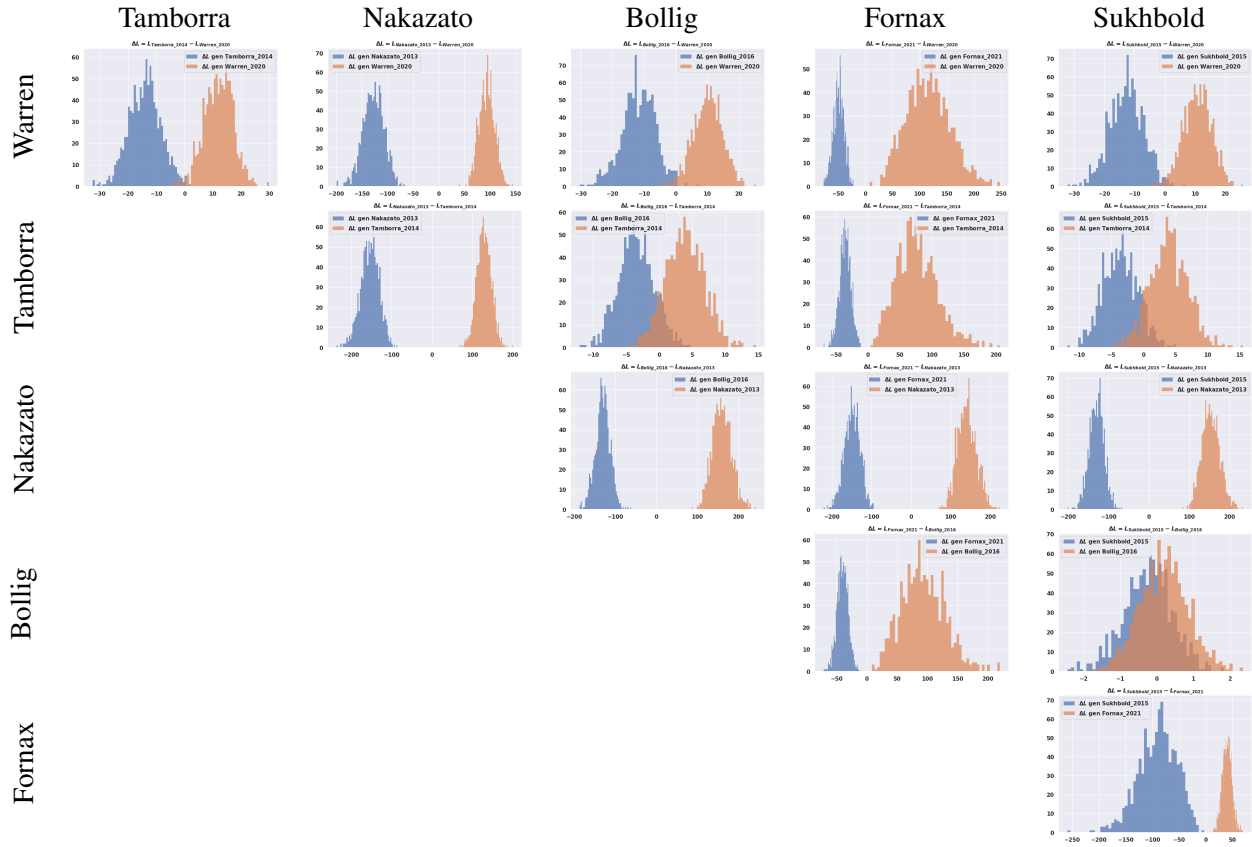


FIGURE 8.6: Binned ΔL distributions for the IBD channel for the 6 models considered. Parameters used are: number of observed events = 300, ebins=1000, tbins=500, number of CCSN=1000, transformation: AdiabaticMSW_NMO, channel: IBD, cut: 20-500 ms, 0.2-100 MeV

Model	Reconstructed Model					
	Warren	Tamborra	Nakazato	Bollig	Fornax	Sukhbold
Warren	97.9%	0.8%	0%	0.9%	0%	0.4%
Tamborra	0.4%	89.1%	0%	4.8%	0%	5.7%
Nakazato	0%	0%	100.0%	0%	0%	0%
Bollig	0.7%	9.6%	0%	55.5%	0%	34.2%
Fornax	0%	0%	0%	0%	100.0%	0%
Sukhbold	0.8%	8.6%	0%	32.7%	0%	57.9%

TABLE 8.2: Accuracy of the model discrimination for the binned likelihood in %. Parameters: number of observed events = 300, ebins=1000, tbins=500, number of CCSN=1000, transformation: AdiabaticMSW_NMO, channel IBD, cut: 20-500 ms, 0.2-100 MeV

8.3.2 Model discrimination using νpES channel

As the νpES channel is another dominant channel in LS, it is interesting to study it separately from IBD. Moreover, it is a complementary channel not accessible in water Cherenkov experiment, such as Hyper-Kamiokande to where the comparison presented in section 8.4.3, due to its low energy threshold. The results of the ΔL distribution are shown in Figure 8.7, and Table 8.3 is constructed the same way as Table 8.2. We can see a greater overlap of the ΔL distributions in Figure 8.7 compared to Figure 8.6. The results indicate a slightly reduced discrimination power

compared to the IBD channel. This is also seen in the accuracy table. This lower performance in the discrimination is explained as the νpES signals for all models are more similar to each other than those from the IBD channel.

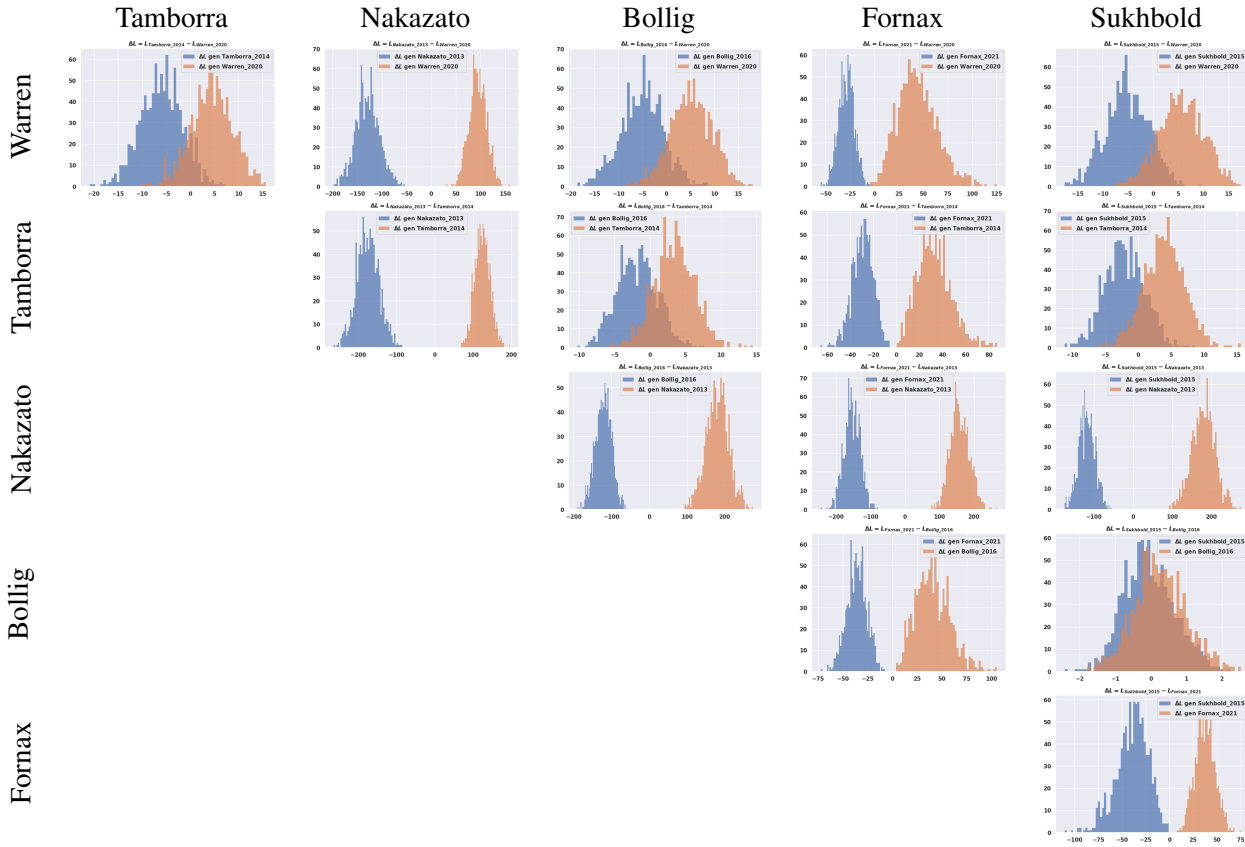


FIGURE 8.7: Binned ΔL distributions for the νpES channel for the 6 models considered. Parameters used are: number of observed events = 300, ebins=1000, tbins=500, number of CCSN=1000, transformation: AdiabaticMSW_NMO, channel: νpES , cut: 20-500 ms, 0.2-100 MeV

Model	Reconstructed Model					
	Warren	Tamborra	Nakazato	Bollig	Fornax	Sukhbold
Warren	80.8%	11.6%	0%	4.2%	0.1%	3.3%
Tamborra	7.8%	81.0%	0%	6.7%	0%	4.5%
Nakazato	0%	0%	100.0%	0%	0%	0%
Bollig	8.8%	22.1%	0%	39.5%	0%	29.6%
Fornax	0%	0%	0%	0%	100.0%	0%
Sukhbold	9.1%	19.5%	0%	26.3%	0%	45.1%

TABLE 8.3: Accuracy of the model discrimination for the binned likelihood in %. Parameters: number of observed events = 300, ebins=1000, tbins=500, number of CCSN=1000, transformation: AdiabaticMSW_NMO, channel: νpES , cut: 20-500 ms, 0.2-100 MeV

8.4 Model discrimination using unbinned likelihood analysis

This analysis is inspired from the work presented in Reference [286] where they use unbinned likelihood for CCSN model discrimination in the case of Hyper-Kamiokande detector. A comparison between the Hyper-Kamiokande

paper and the present analysis is given section 8.4.4.

In this section, we want to compare results obtained from the binned and unbinned likelihood methods for both the IBD and νpES channels. To implement the unbinned method, we need to find the optimal way to compute the expected value for each individual event. In this work, we chose to interpolate the histogram of expected values rather than directly calculating the event rates for every MC event. This decision was made to ensure higher computation efficiency, especially when dealing with large datasets. The interpolation is performed with the `scipy.interpolate.RegularGridInterpolator` method. It provides a smooth and continuous function that accurately represents the expected event rate [287].

Tables 8.4 and 8.5 present the accuracy of model discrimination using unbinned method for the IBD channel and νpES channel, respectively. The results from IBD channel, using the unbinned method, demonstrate an overall improvement in model discrimination accuracy over the binned methods. For the νpES channel, the unbinned method has more contrasted results as it provides better discrimination compared to the binned method for the Warren model but worse for Tamborra.

By its unbinned nature, the unbinned approach captures subtle variations in the time and energy distributions of the events that are otherwise smoothed out in the binned approach. These characteristics allow better discrimination between the different models. Based on these comparisons, it is obvious that the unbinned method offers overall a superior performance in terms of model discrimination for both the IBD and νpES channels. The increased accuracy of the unbinned method justifies its use in further analyses. Consequently, we adopt the unbinned method for all subsequent work.

Model	Reconstructed Model					
	Warren	Tamborra	Nakazato	Bollig	Fornax	Sukhbold
Warren	98.2%	0.6%	0%	0.7%	0%	0.5%
Tamborra	0.5%	89.4%	0%	4.9%	0%	5.2%
Nakazato	0%	0%	100.0%	0%	0%	0%
Bollig	7.0%	8.9%	0%	56.3%	0%	34.1%
Fornax	0%	0%	0%	0%	100.0%	0%
Sukhbold	0.9%	8.8%	0%	30.6%	0%	59.7%

TABLE 8.4: Accuracy of the model discrimination for the unbinned likelihood. Parameters: number of observed events = 300, number of CCSN=1000, transformation: `AdiabaticMSW_NMO`, channel IBD, cut: 20-500 ms, 0.2-100 MeV. The detailed ΔL distribution plots are presented in B.2.1.2.

Model	Reconstructed Model					
	Warren	Tamborra	Nakazato	Bollig	Fornax	Sukhbold
Warren	82.1%	8.1%	0%	5.0%	0.2%	4.6%
Tamborra	9.3%	73.4%	0%	9.6%	0.2%	7.5%
Nakazato	0%	0%	100.0%	0%	0%	0%
Bollig	11.3%	13.7%	0%	38.3%	0%	36.7%
Fornax	0%	0%	0%	0%	100.0%	0%
Sukhbold	9.8%	12.2%	0%	26.3%	0%	51.7%

TABLE 8.5: Accuracy of the model discrimination for the unbinned likelihood. Parameters: number of observed events = 300, number of CCSN=1000, transformation: `AdiabaticMSW_NMO`, channel νpES , cut: 20-500 ms, 0.2-100 MeV. The detailed ΔL distribution plots are presented in B.3.1.2.

8.4.1 Discussion of the impact of the number of observed events

The number of observed events depends on the model considered, and the distance of the CCSN. Table 8.6 presents the accuracy percentages for model discrimination using the unbinned likelihood method with 100 observed events. The results show that even with a smaller dataset Warren, Nakazato, and Fornax can be distinguished respectively 89.9%, 100.0%, and 99.4% of the time. However, the Tamborra model achieves only 72.5% accuracy, and Bollig and Sukhbold show no discrimination, with Bollig at 39.2% and Sukhbold at 44.3%.

Table 8.7 extends the analysis to 1000 observed events using the unbinned method, corresponding to a CCSN occurring at a distance slightly beyond the Galactic Center distance. In this scenario, we observe a notable improvement in discrimination accuracy across all models. Warren and Nakazato maintain perfect accuracy at 100.0%, while the discrimination power for Bollig increases to 72.4%, and Sukhbold shows a significant improvement, reaching 70.4%. These results suggest that if a supernova explosion occurs at around this distance, we can effectively discriminate even between closely related models.

Finally, Table 8.8 shows the discrimination accuracy with 5000 observed events using the unbinned method. As expected, accuracy improves further, with most models achieving near-perfect discrimination. Warren, Nakazato, and Fornax all reach 100.0% accuracy, while Bollig reaches 90.3% and Sukhbold reaches 92.8%.

These results demonstrate that the number of observed events naturally influences the accuracy of model discrimination, with higher event counts leading to improved performance. This confirms that the method works as expected, becoming more precise with larger datasets, and underscores its reliability for model discrimination in supernova analyses.

Model	Reconstructed Model					
	Warren	Tamborra	Nakazato	Bollig	Fornax	Sukhbold
Warren	89.9%	3.5%	0.0%	3.9%	0.0%	2.7%
Tamborra	6.7%	72.5%	0.0%	9.3%	1.2%	10.3%
Nakazato	0.0%	0.0%	100.0%	0.0%	0.0%	0.0%
Bollig	7.9%	16.4%	0.0%	39.2%	0.4%	36.1%
Fornax	0.1%	0.4%	0.0%	0.0%	99.4%	0.1%
Sukhbold	5.5%	16.4%	0.0%	33.4%	0.4%	44.3%

TABLE 8.6: Accuracy of the model discrimination for the unbinned likelihood. Parameters: number of observed events = 100, number of CCSN=1000, transformation: `AdiabaticMSW_NMO`, channel IBD, cut: 20-500 ms, 0.2-100 MeV. The detailed ΔL distribution plots are presented in B.2.1.1.

Model	Reconstructed Model					
	Warren	Tamborra	Nakazato	Bollig	Fornax	Sukhbold
Warren	100.0%	0.0%	0.0%	0.0%	0.0%	0.0%
Tamborra	0.0%	98.7%	0.0%	0.3%	0.0%	1.0%
Nakazato	0.0%	0.0%	100.0%	0.0%	0.0%	0.0%
Bollig	0.0%	0.4%	0.0%	72.4%	0.0%	27.2%
Fornax	0.0%	0.0%	0.0%	0.0%	100.0%	0.0%
Sukhbold	0.0%	0.7%	0.0%	28.9%	0.0%	70.4%

TABLE 8.7: Accuracy of the model discrimination for the unbinned likelihood. Parameters: number of observed events = 1000, number of CCSN=1000, transformation: `AdiabaticMSW_NMO`, channel IBD, cut: 20-500 ms, 0.2-100 MeV. The detailed ΔL distribution plots are presented in B.2.1.3.

Model	Reconstructed Model					
	Warren	Tamborra	Nakazato	Bollig	Fornax	Sukhbold
Warren	100.0%	0.0%	0.0%	0.0%	0.0%	0.0%
Tamborra	0.0%	100.0%	0.0%	0.0%	0.0%	0.0%
Nakazato	0.0%	0.0%	100.0%	0.0%	0.0%	0.0%
Bollig	0.0%	0.0%	0.0%	90.3%	0.0%	9.7%
Fornax	0.0%	0.0%	0.0%	0.0%	100.0%	0.0%
Sukhbold	0.0%	0.0%	0.0%	7.2%	0.0%	92.8%

TABLE 8.8: Accuracy of the model discrimination for the unbinned likelihood. Parameters: number of observed events = 5000, number of CCSN=1000, transformation: `AdiabaticMSW_NMO`, channel IBD, cut: 20-500 ms, 0.2-100 MeV. The detailed ΔL distribution plots are presented in B.2.1.5.

8.4.2 Impact of neutrino flavor transformation on model discrimination

As the [Neutrino Mass Ordering \(NMO\)](#) is unknown, we need to explore how different neutrino transformation scenarios affect model discrimination. We compare the results obtained using the `AdiabaticMSW_IMO` (Inverted Mass Ordering) transformation in Tables 8.9 and 8.10 with those ones obtained using the `AdiabaticMSW_NMO` (Normal Mass Ordering) transformation in Tables 8.4 and 8.5.

Model	Reconstructed Model					
	Warren	Tamborra	Nakazato	Bollig	Fornax	Sukhbold
Warren	89.2%	5.4%	0.0%	0.6%	0.0%	4.8%
Tamborra	5.0%	85.9%	0.0%	4.3%	0.0%	4.8%
Nakazato	0.0%	0.0%	100.0%	0.0%	0.0%	0.0%
Bollig	1.2%	6.9%	0.0%	68.9%	0.0%	23.0%
Fornax	0.0%	0.0%	0.0%	0.0%	100.0%	0.0%
Sukhbold	5.6%	5.6%	0.0%	23.1%	0.0%	65.7%

TABLE 8.9: Accuracy of the model discrimination for the unbinned likelihood. Parameters: number of observed events = 300, number of CCSN = 1000, transformation: `AdiabaticMSW_IMO`, channel IBD, cut: 20-500 ms, 0.2-100 MeV. The detailed ΔL distribution plots are presented in B.2.3.2.

True Model	Reconstructed Model					
	Warren	Tamborra	Nakazato	Bollig	Fornax	Sukhbold
Warren	91.6%	3.5%	0.0%	2.4%	0.0%	2.5%
Tamborra	5.2%	80.5%	0.0%	9.3%	0.0%	5.0%
Nakazato	0.0%	0.0%	100.0%	0.0%	0.0%	0.0%
Bollig	4.6%	9.1%	0.0%	49.2%	0.0%	37.1%
Fornax	0.0%	0.0%	0.0%	0.0%	100.0%	0.0%
Sukhbold	3.9%	6.7%	0.0%	28.6%	0.0%	60.8%

TABLE 8.10: Accuracy of the model discrimination for the unbinned likelihood. Parameters: number of observed events = 300, number of CCSN = 1000, transformation: `AdiabaticMSW_IMO`, channel νpES , cut: 20-500 ms, 0.2-100 MeV. The detailed ΔL distribution plots are presented in B.3.2.2.

When comparing these tables, we can see a clear dependence of the discrimination power on neutrino mass ordering. The `AdiabaticMSW_IMO` transformation (presented in Tables 8.9 and 8.10) generally shows worse discrimination between models compared to the `AdiabaticMSW_NMO` transformation (Tables 8.4 and 8.5).

A slight improvement is seen in the discrimination accuracy for the Bollig and Sukhbold models when using the `AdiabaticMSW_IMO` transformation. The accuracy for the Bollig model in the IBD channel increases to 68.9%, and for the Sukhbold model, it improves to 65.7%. In the case of the νpES channel, the Bollig model shows an accuracy of 49.2%, while the Sukhbold model reaches 60.8%.

8.4.3 Comparison with Hyper-Kamiokande

A similar study was conducted using the Hyper-Kamiokande detector, as reported in [286, 288]. Like our analysis with JUNO, they employed an unbinned likelihood approach. However, there are notable differences between the two studies. One significant distinction is that Hyper-Kamiokande used the Totani model. The Totani model, also known as the "Livermore model" or "Wilson model," is recognized for incorporating the late-time evolution of neutrino emission in supernova simulations. Although it has been surpassed by more recent models, it remains widely used due to its historical importance and its role in understanding the light curve of SN1987A [289]. The authors of the Hyper-Kamiokande analysis have used a progenitor of $20 M_{\odot}$ for this model.

In terms of model parameters, Hyper-Kamiokande paper uses slightly different values compared to our study. While both studies used the Tamborra model with the same parameters ($27 M_{\odot}$ and LS220 equation of

state), differences exist for the other models. For the Fornax model, they use $20 M_{\odot}$ progenitor while we use $30 M_{\odot}$. They also used a $20 M_{\odot}$ progenitor model with $\alpha_{\lambda} = 0.8$ for Warren model. The Nakazato model, another key model in their study, involved a $20 M_{\odot}$ progenitor with solar metallicity ($Z = 0.02$).

Another significant difference is the size and capability of the detectors. Hyper-Kamiokande has a 217 kt water Cherenkov detector, which is substantially larger than JUNO's 20 kt liquid scintillator detector. This size advantage allows Hyper-Kamiokande to detect more events and then to be sensitive to more distant CCSN. Additionally, Hyper-Kamiokande includes reconstruction and detector response effects in their analysis, which are not incorporated in our JUNO study yet. However, the most significant detector response impact comes from the trigger energy threshold, which has been taken into account. Moreover, the interaction channels utilized in each experiment differ due to the distinct detection media: Hyper-Kamiokande is a water Cherenkov detector and relies on channels like IBD, νe ES, and ν_e and $\bar{\nu}_e$ charged current interactions with ^{16}O . JUNO will be sensitive to channels such as IBD, νp ES, νe ES, and interactions with ^{12}C , including both charged current and neutral current interactions. Note that this work uses only IBD or only νp ES.

Tables 8.11 and 8.12 summarize the accuracy of model discrimination in both studies. Table 8.11 is adapted from Table 8.4, where the comparison was performed only for 5 models of Table 7.2 (ie Warren, Tamborra, Nakazato, Fornax, and Sukhbold). We remove Bollig model, as it is too close to Sukhbold model. The comparison between JUNO and Hyper-Kamiokande reveals that both experiments exhibit high accuracy in model discrimination, though with some notable differences. Both detectors identify the Warren model with similar accuracy ($\sim 98\%$), but HK slightly outperforms JUNO in distinguishing the Tamborra model, with a 98% identification rate compared to JUNO's 90.8%. This can be explained as in Hyper-Kamiokande the Tamborra model is not compared to other models using the Prometheus solver (Sukhbold in Table 8.11). In the JUNO analysis, all models use a progenitor of $\sim 27 M_{\odot}$, to avoid any correlation with the mass parameter. For the Nakazato and Fornax models, both detectors demonstrate near-perfect or perfect identification. The explanation behind this fact is that both Nakazato and Fornax models are very different compared to the other models presented in this analysis.

True Model	Reconstructed Model				
	Warren	Tamborra	Nakazato	Fornax	Sukhbold
Warren	98.2%	0.5%	0.0%	0.0%	1.3%
Tamborra	0.6%	90.8%	0.0%	0.0%	8.6%
Nakazato	0.0%	0.0%	100.0%	0.0%	0.0%
Fornax	0.0%	0.0%	0.0%	100.0%	0.0%
Sukhbold	0.5%	8.6%	0.0%	0.0%	90.9%

TABLE 8.11: Accuracy of the model discrimination for the unbinned likelihood. Parameters: number of observed events = 300, number of CCSN=1000, transformation: `AdiabaticMSW_NMO`, channel IBD, cut: 20-500 ms, 0.2-100 MeV. The detailed ΔL distribution plots are presented in B.2.2.

True Model	Reconstructed Model				
	Warren	Nakazato	Tamborra	Totani	Fornax
Warren	98.2%	0.2%	1.6%	0.0%	0.0%
Nakazato	0.1%	99.9%	0.0%	0.0%	0.0%
Tamborra	1.6%	0.0%	98.0%	0.2%	0.2%
Totani	0.0%	0.0%	0.0%	100.0%	0.0%
Fornax	0.0%	0.0%	0.0%	0.0%	100.0%

TABLE 8.12: Accuracy of the model discrimination for Hyper-Kamiokande. The size of data set is 300 events. They use a combination of the IBD, νe ES, $\nu_e + {}^{16}\text{O}$ CC, and $\bar{\nu}_e + {}^{16}\text{O}$ CC channels. The time cuts are 20-520 ms. Energy cut: kinetic energy of e^\pm must be higher than 5 MeV. Adapted from [286].

8.5 Summary and outlook

This chapter presents the challenges of distinguishing between different CCSN models using Monte-Carlo data simulating the CCSN signal at the JUNO detector. Two likelihood methods (binned and unbinned) are used to evaluate how well one can discriminate the models based on two key neutrino channels in LS experiments: IBD and νp ES. One explores the impact of different neutrino mass ordering scenarios as well as of the total observed event yield on the results.

The unbinned likelihood method performs overall better than the binned approach as it captures the fine details of the time and energy distributions, which are crucial for distinguishing between models. The IBD channel proves to be the most effective for model discrimination using the unbinned method. The νp ES channel also provides useful information, but its ability to distinguish between models is lower due to the similarity in the signals across different models.

This analysis reveals that neutrino mass ordering plays a significant role in model discrimination. The `AdiabaticMSW_NMO` scenario produces better results across both detection channels. However, the `AdiabaticMSW_IMO` scenario shows improved results when differentiating between the specific model pairs Bollig-Sukhbold. This finding highlights the importance to always include both mass ordering scenarios in supernova model discrimination analyses. The number of observed events is also a critical factor in improving discrimination accuracy.

An important future direction of this work is to perform an analysis that combines the two dominant channels, namely IBD and νpES . Then, this combination could be extended to other channels and neutrino experiments. Moreover, the current analysis uses MC information which does not incorporate all the realistic experimental effects. A more realistic analysis could be performed by taking into account the energy calibration and reconstruction as well as the selection efficiency (capability to separate the channels between them and from after-pulses or other noises). Another point to take into consideration would be that when dealing with low number of signal events, such as the analysis here considering only 100 events, different background sources may start to have a relevant contribution to the analysis. Conversely, in scenarios with a large number of events (a few thousands within one second), the detector may be affected by multiple simultaneous events (pileup), which will impact the reconstruction performance and selection efficiencies.

Conclusions

Conclusions

Neutrino physics is a quite recent and very active field. Neutrinos are crucial to our understanding of different physics phenomena. Many sources produce them in large quantities, such as nuclear reactors or supernovas. Key questions are still unanswered in neutrino physics, such as neutrino mass ordering and their absolute masses, the Majorana or Dirac nature of the neutrinos, and the search for sterile neutrino existence.

The JUNO experiment aims primarily to detect reactor electron antineutrinos with unprecedented accuracy in order to determine the neutrino mass ordering and to refine measurements of neutrino oscillation parameters. In addition, JUNO also contributes to measuring neutrinos from other sources, such as geo-neutrinos, solar neutrinos, and supernova neutrinos.

My contributions to the JUNO collaboration presented in this thesis cover electronic hardware development and preparation of the physics analyses. The contribution to the electronics system focuses on the [Back-End Card \(BEC\)](#) development and testing.

The [BEC](#) is a key component in the large PMT readout electronic system. It performs the link between the front-end electronics and the trigger system. Stringent requirements were put in place for the large PMT readout electronic system to allow precise measurements of neutrinos with JUNO. This system uses a high-end combination of FPGA boards, high-voltage modules, a sophisticated data acquisition system, and complex trigger algorithms. The front-end electronics are located underwater to ensure a precise digitization of the large PMT signals. The front-end electronics are placed into underwater boxes containing splitter boards, a high-voltage unit, and a global control unit. The global control unit is a FPGA board responsible for the digitization of incoming PMT signals, communicating with the trigger system by generating trigger requests and sending the digitized signal to the data acquisition system in case of positive trigger.

On the other hand, the outside-water electronics is composed of the trigger system, the data acquisition system, and the detector control system. The BEC is an FPGA board integrated in the trigger system. It receives the trigger request signal from up to 48 global control units and combines them to send to the following part of the trigger system. The trigger system sends the trigger accept signal to the [BEC](#), which is then distributed to the corresponding global control units. As an integral part of the large PMT readout electronic system design, the BEC development had to accommodate different requirements that changed over the duration of my thesis. Those changes lead to the design of multiple prototypes. The final design, BEC-V4.2, was deeply tested and then validated. The mass production of the 180 BECs (155 for the large PMT readout system, 5 for the small PMT system, and a few spare units) occurred from May 2021 and to October 2021.

After production, all BECs underwent a rigorous testing phase, including combined tests with global control units. Following these tests, all BECs were dispatched to the JUNO site for another round of self-testing before their installation. Currently, all BECs are installed in the two electronics rooms and connected to their corresponding global control units as the installation of the PMT and the global control unit progresses. The BECs are continuously tested during these installations, and the past light-off tests are used to assess their performance.

Additional work is still ongoing to optimize maintainability and to increase the debugging ease. A supplementary tool, using the ESP32 micro-controller, is under design to ease the diagnostic and the firmware deployment during the future testing and the commissioning phases of the BEC. From now on, BECs are undergoing the last commissioning steps as other light-off tests are foreseen, and the installation of the underwater electronics is being

finalized.

On the BEC side, my contribution includes participation on the design of the BEC, presented in Chapter 5. Additionally, I developed the automatic test procedures and conducted the analysis of the tests discussed at the end of Chapter 5. I was responsible for the design of the BEC box presented in Chapter 6. I also performed remote monitoring of the mass production and analyzed the data from the Kunshan test. Furthermore, I contributed to the analysis of the light-off tests.

Concerning the physics analysis preparation, I have worked on the topic of supernova neutrino detection in JUNO. The focus of these studies is the discrimination power between different [Core Collapse Supernova \(CCSN\)](#) models with the [Inverse- \$\beta\$ Decay \(IBD\)](#) and [elastic neutrino-proton scattering \(\$\nu\$ pES\)](#) channels in JUNO.

JUNO aims to study supernovae as astrophysical source of neutrinos. Supernovae, particularly CCSN, are crucial for understanding the life cycles of stars, the nucleosynthesis, and the mechanisms driving stellar explosions. Neutrinos play a fundamental role in the CCSN dynamics and allow for the final explosion. Various complex models have been developed by different research groups in order to accurately estimate the neutrino flux emitted during those events. Due to the complexity of the CCSN modeling, theorists have to perform approximations to ensure that simulations run in a fair amount of time. By precisely measuring neutrinos, we gain valuable insight into the dynamics of the CCSN and provide constraints to theorists to refine their models.

JUNO will be a sensitive supernova neutrino telescope, and this thesis assesses its discrimination power to CCSN models. We introduce the likelihood function and employ both binned and unbinned likelihood methods to perform the model discrimination. In this analysis, the discrimination is performed via the shape of the energy-time distribution. As the CCSN distance will in principle not be precisely known, we have to normalize the data and the expected event rate. We can conclude that models with significant differences can be discriminated by measuring 300 events over a time window covering 20 to 500 ms after the core bounce, which correspond to an observing distance between 21 kpc and 27.8 kpc. On the other hand, models using the same 1D simulation framework can not be discriminated when the analysis is limited 300 events. The next step of this analysis will be taking into account the detector performance. The data generated here do not take into account the effect of the different layers of the detector, such as PMT after-pulse, pile-up of channel classification, calibration, or reconstruction effect. Additionally, no background was considered in the present analysis. An extra improvement that will come from LS experiments with regard to water Cherenkov detectors, will be the addition of the [\$\nu\$ pES](#) channel.

A general combination of data from other detectors, such as Super-Kamiokande, can be conducted to extend the distance where the discrimination of the different models becomes possible. As a further development of Super-Kamiokande, Hyper-Kamiokande is a next-generation underground water Cherenkov detector with a central detector containing 217 kt of ultra-pure water, 8.4 bigger than its predecessor. Hyper-Kamiokande is planned to start the data-taking by 2027. A combination of data taken by one of those two experiments, in addition to JUNO data, will significantly increase the data for a single CCSN event and should lead to better model discrimination.

Currently, the installation of the PMTs and the underwater electronics is ongoing on the lower hemisphere of the detector. The water filling of the detector is planned to occur from December 2024 to January 2025. This is followed by filling the central detector with the liquid scintillator. The first physics run of JUNO is foreseen to start in August 2025.

Part IV

Appendices

Appendix A

Additional event rate and Monte Carlo data 2D distributions for the analysis

Contents

A.1	Inverse- β Decay (IBD)	200
A.1.1	Adiabatic transformation using normal mass ordering (NMO)	200
A.1.2	Adiabatic transformation using inverted mass ordering (IMO)	202
A.2	Elastic neutrino-proton scattering (ν pES)	204
A.2.1	Adiabatic transformation using normal mass ordering (NMO)	204
A.2.2	Adiabatic transformation using inverted mass ordering (IMO)	206

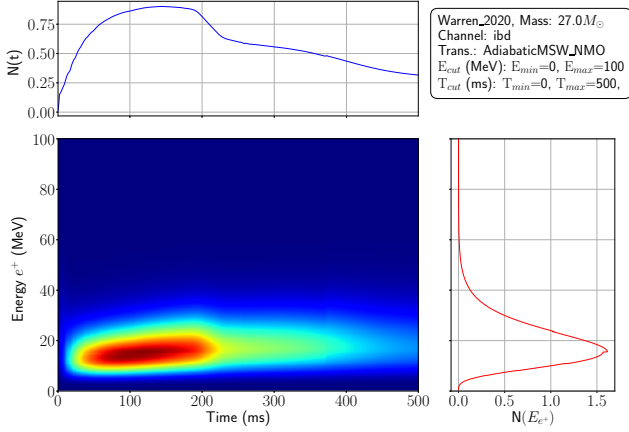
In this appendix, we validate the accuracy of the data generation process by comparing the expected event distributions with those generated by Monte Carlo simulations using `sntools` [274]. The left column of each figure presents the expected event rate in JUNO, while the right column shows the corresponding Monte Carlo data.

The left figures illustrate the expected event rate (as defined by Equation 8.2) for the different channels and flavor transformations for each supernova model. The event rate is represented on the z-axis. The x-axis represents time in seconds, and the y-axis shows the energy of the total outgoing particle (e^+ for IBD and p^+ for [elastic neutrino-proton scattering \(\$\nu\$ pES\)](#)). In each of these figures, the top plots show the time evolution of the expected number of events, $N(t)$. The left plots provide a 2D histogram of the expected interaction rates as a function of time and outgoing particle energy, E_e , while the bottom right panel presents the energy distribution, $N(E_e)$, of the outgoing particles. The distance was adjusted to yield a total event count of 300 for the expected event rate.

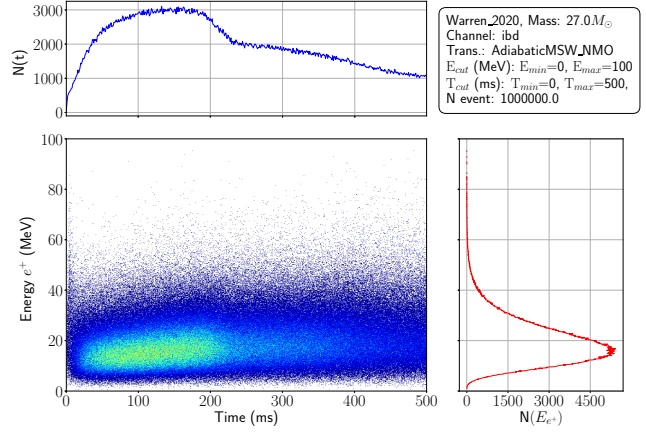
Figure 8.4b depicts the results from the Monte Carlo simulations, where 1000 core-collapse supernovae (CCSN) were simulated, producing around 1,000,000 entries in the histograms. The number of events in each energy-time bin is represented on the z-axis. The x-axis represents time in seconds, and the y-axis shows the total energy of the outgoing particle in MeV (e^+ for IBD and p^+ for [elastic neutrino-proton scattering \(\$\nu\$ pES\)](#)). The comparison between the expected results and the simulated results demonstrates a strong agreement in both the time and energy distributions of the events.

A.1 Inverse- β Decay (IBD)

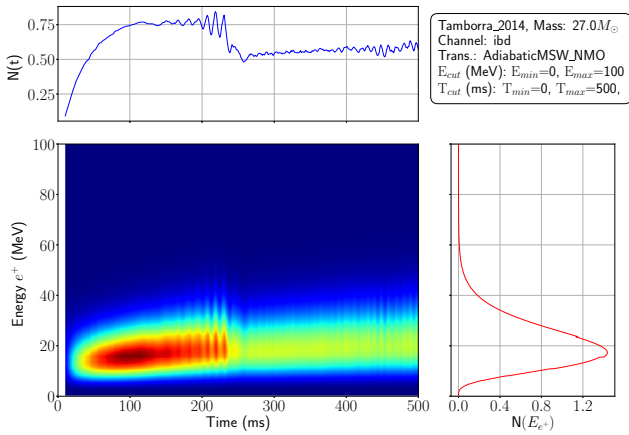
A.1.1 Adiabatic transformation using normal mass ordering (NMO)



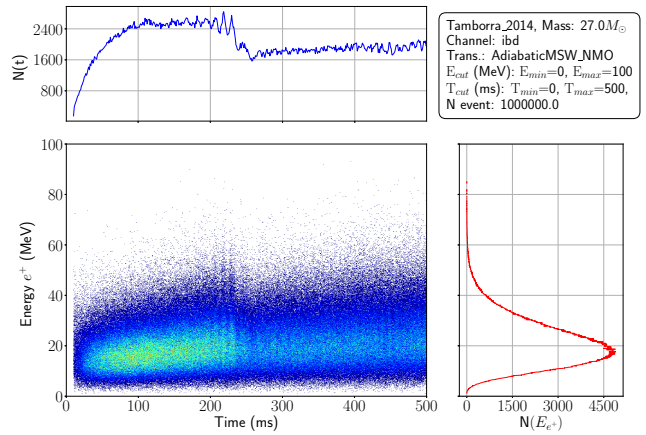
(A) Event rate in JUNO



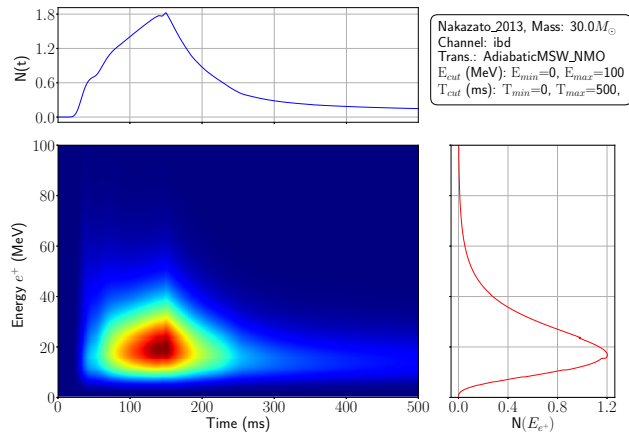
(B) MC data



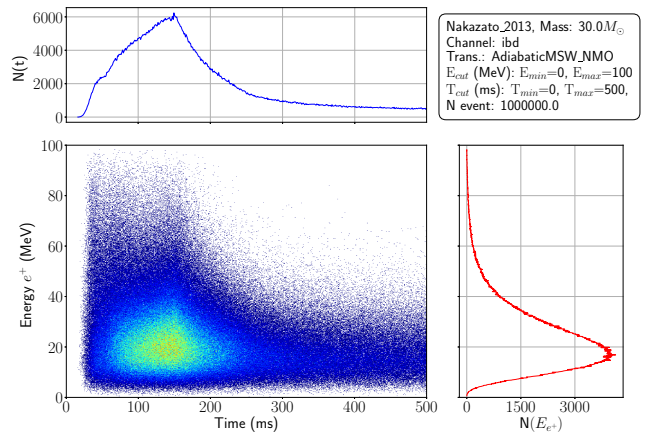
(A) Event rate in JUNO



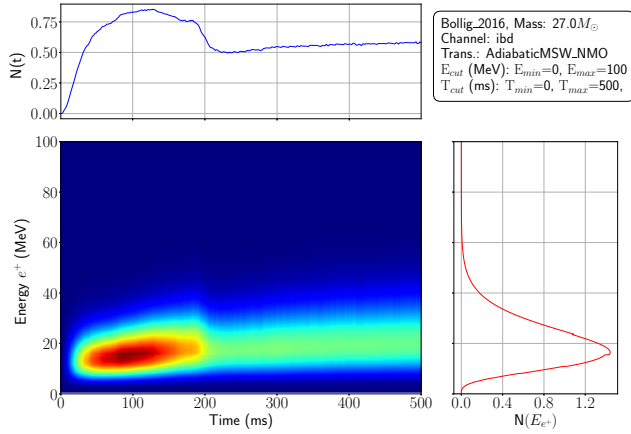
(B) MC data



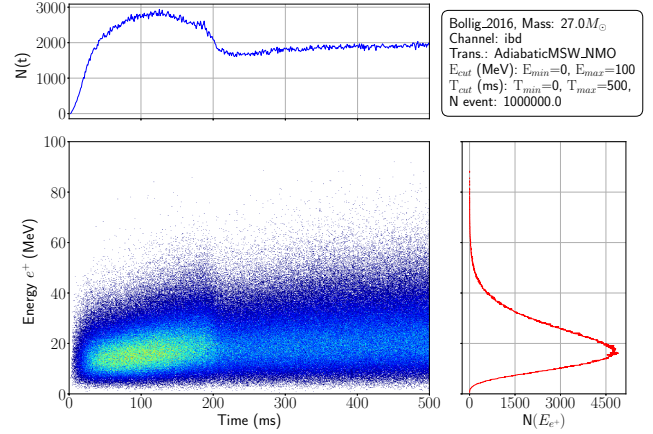
(A) Event rate in JUNO



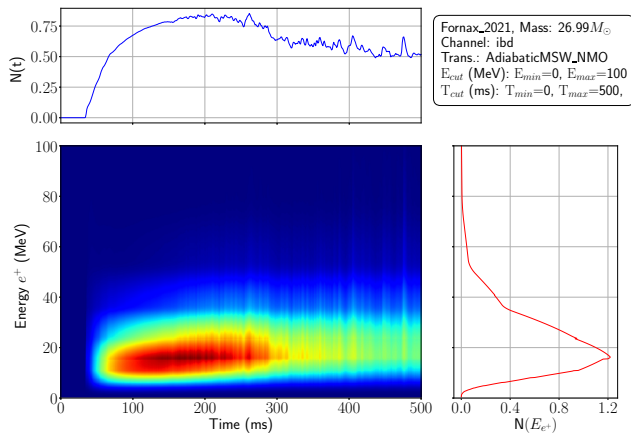
(B) MC data



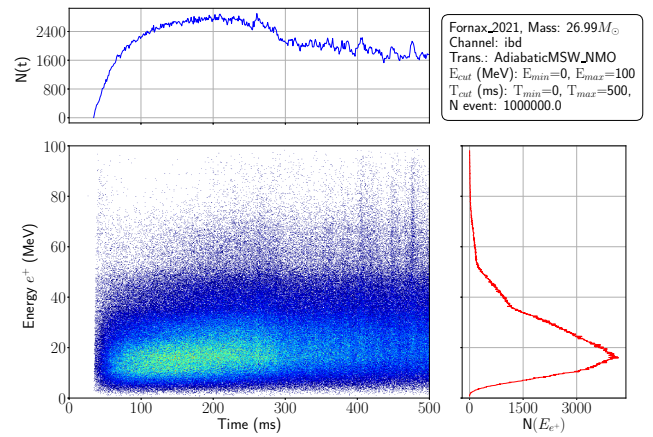
(A) Event rate in JUNO



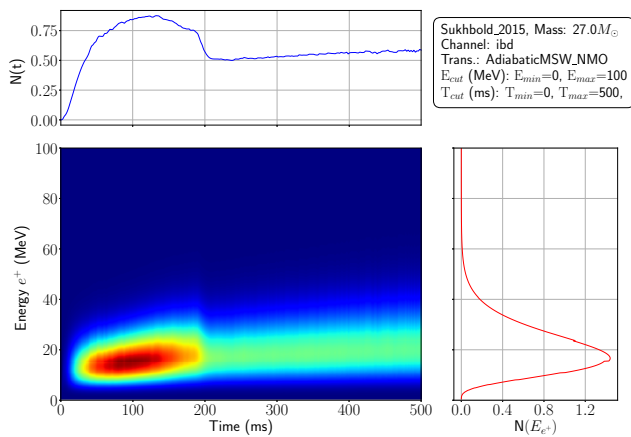
(B) MC data



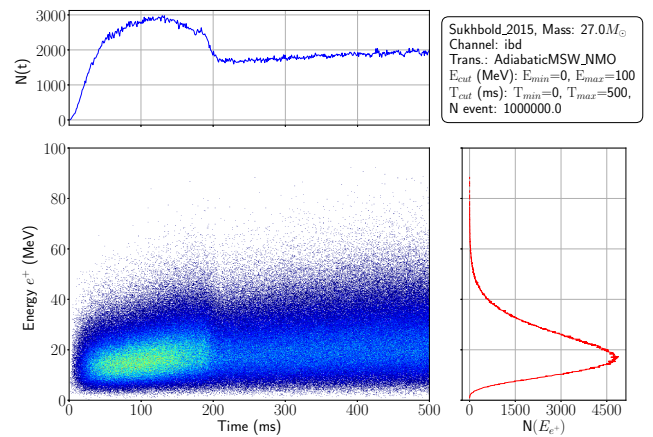
(A) Event rate in JUNO



(B) MC data

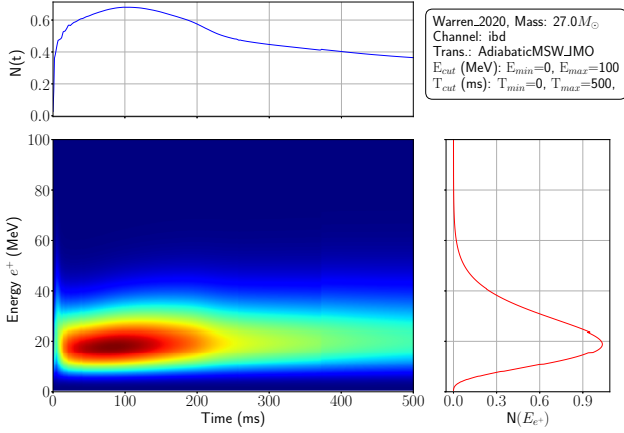


(A) Event rate in JUNO

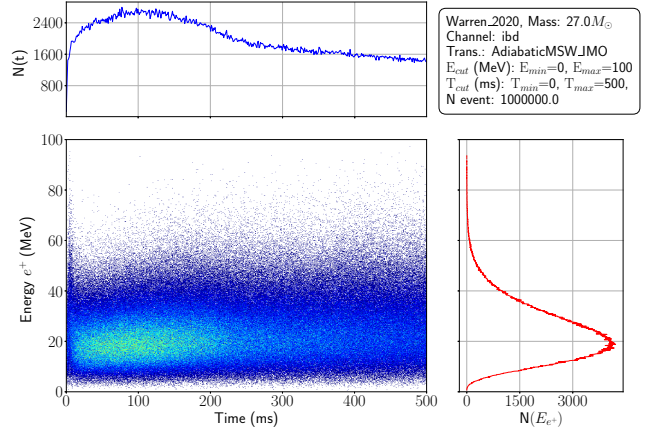


(B) MC data

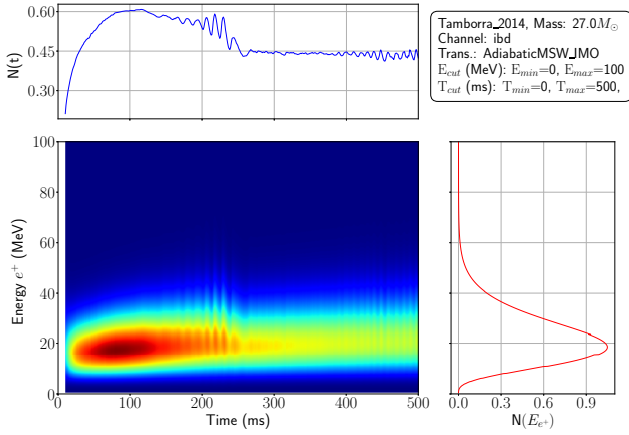
A.1.2 Adiabatic transformation using inverted mass ordering (IMO)



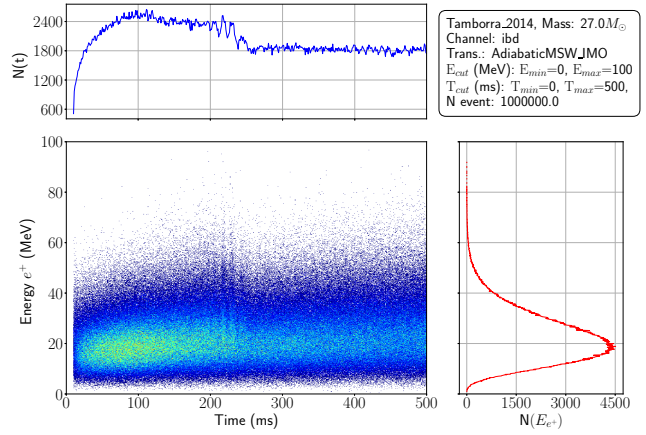
(A) Event rate in JUNO



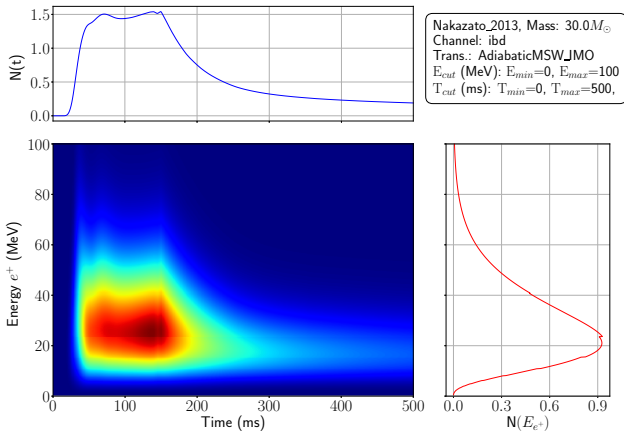
(B) MC data



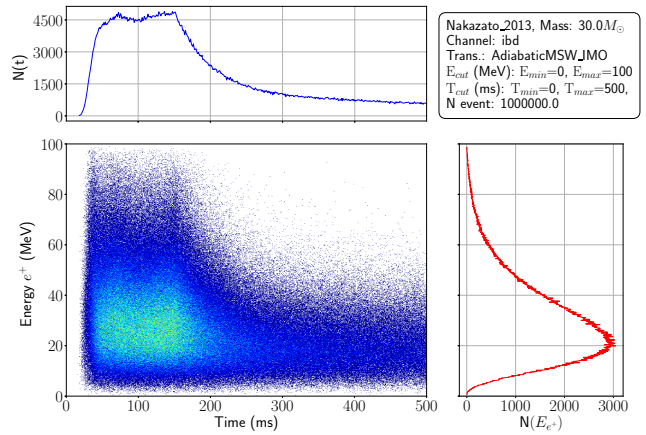
(A) Event rate in JUNO



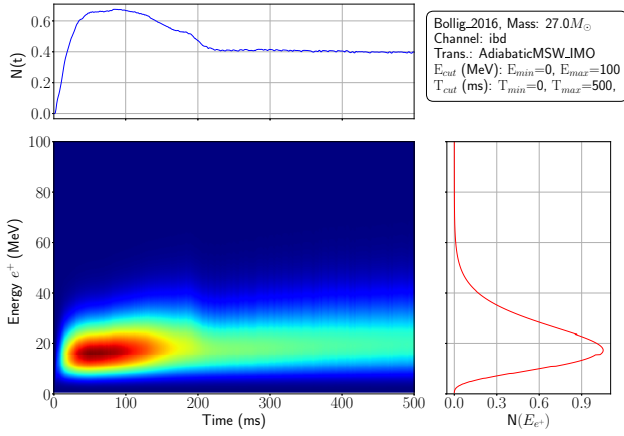
(B) MC data



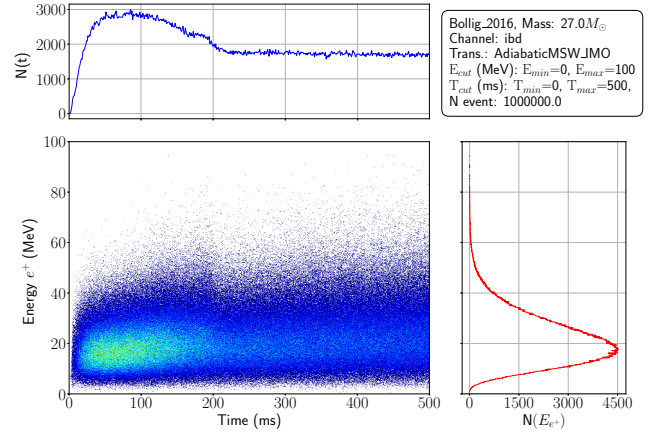
(A) Event rate in JUNO



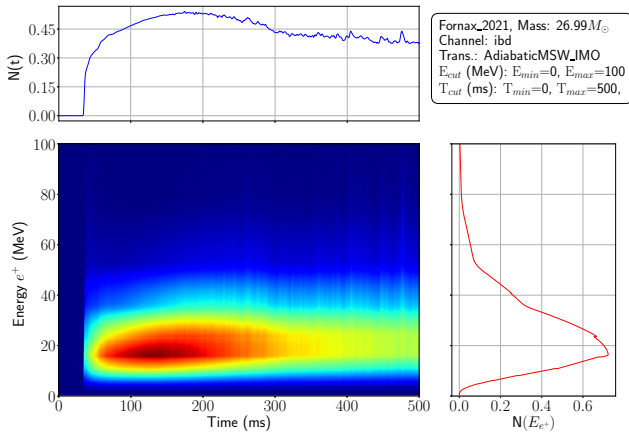
(B) MC data



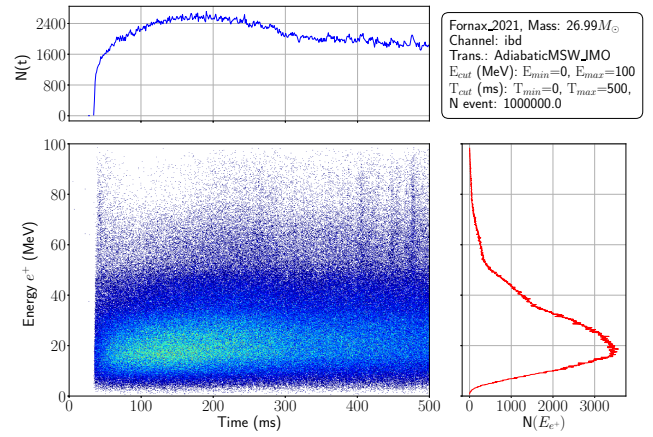
(A) Event rate in JUNO



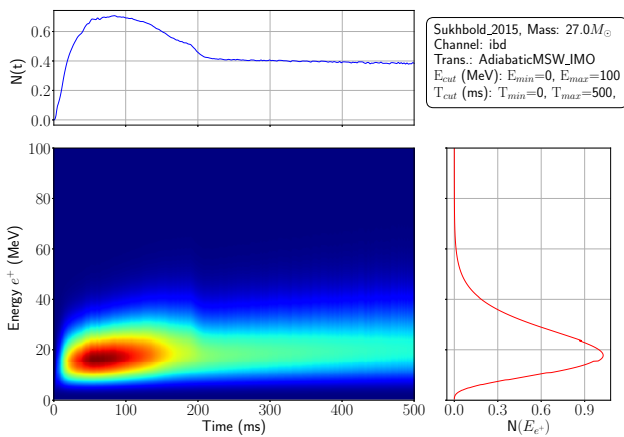
(B) MC data



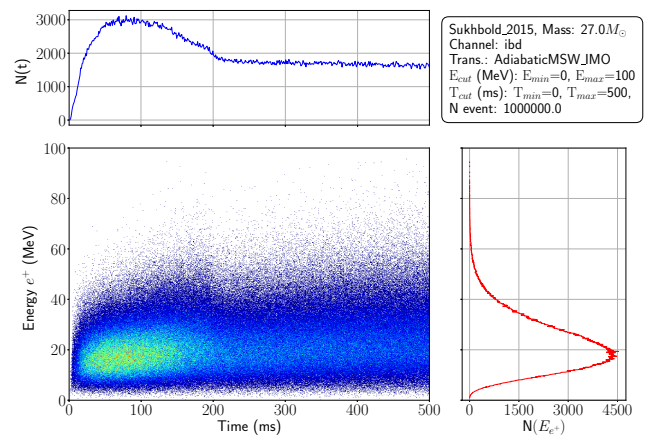
(A) Event rate in JUNO



(B) MC data



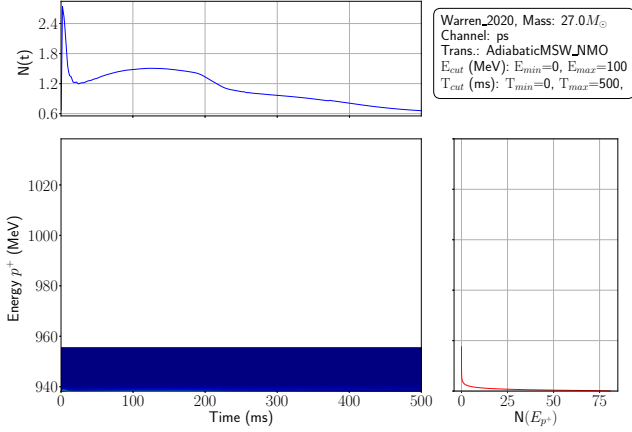
(A) Event rate in JUNO



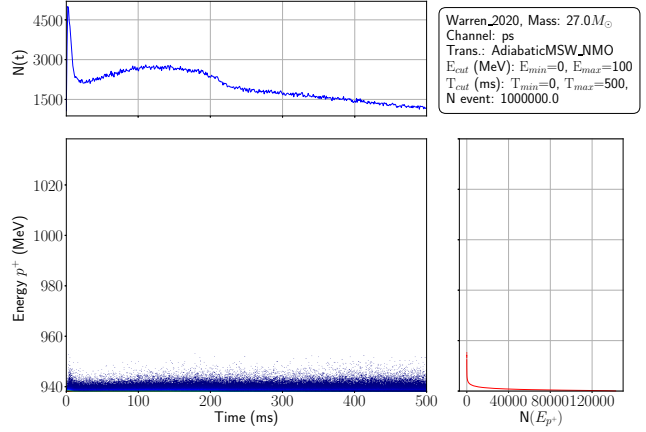
(B) MC data

A.2 Elastic neutrino-proton scattering (νp ES)

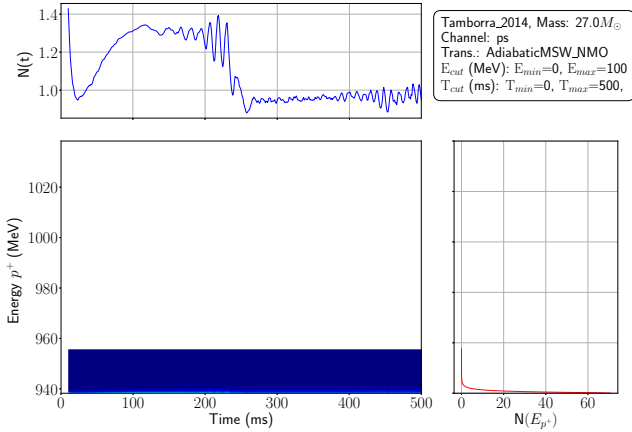
A.2.1 Adiabatic transformation using normal mass ordering (NMO)



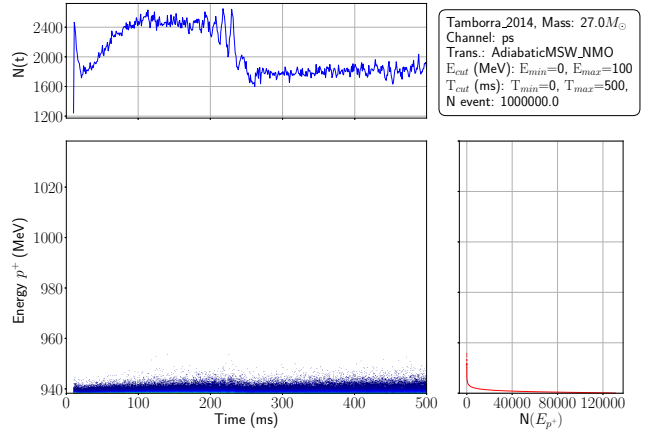
(A) Event rate in JUNO



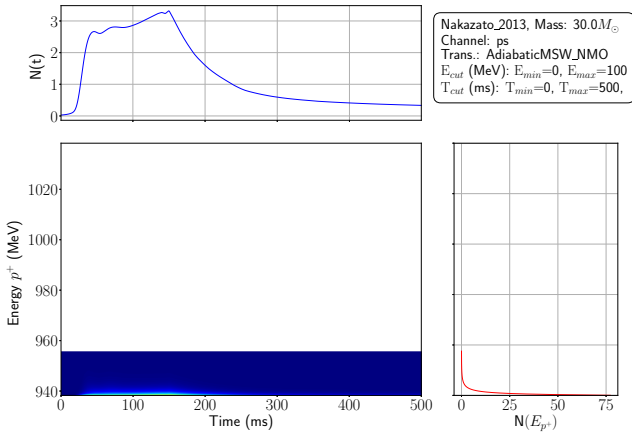
(B) MC data



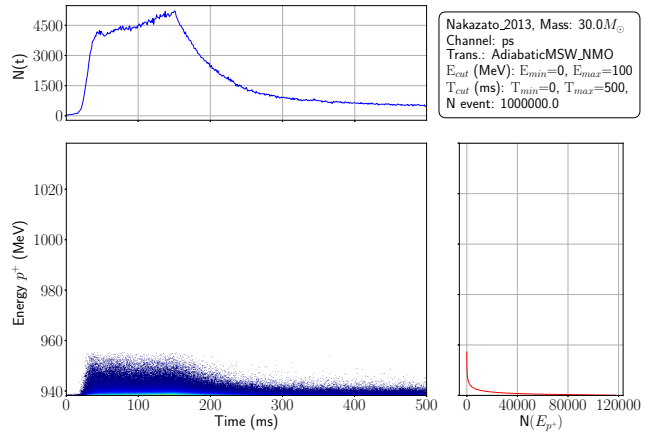
(A) Event rate in JUNO



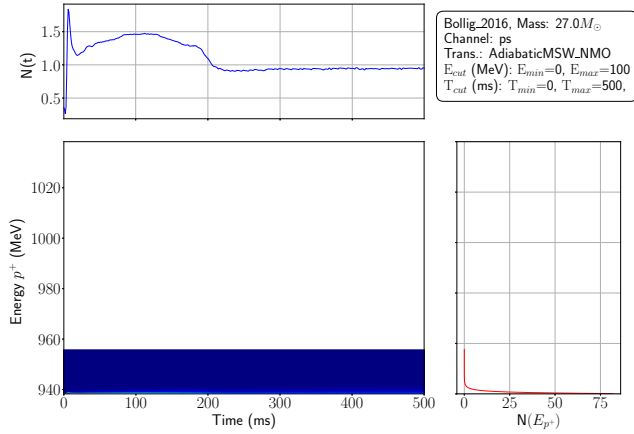
(B) MC data



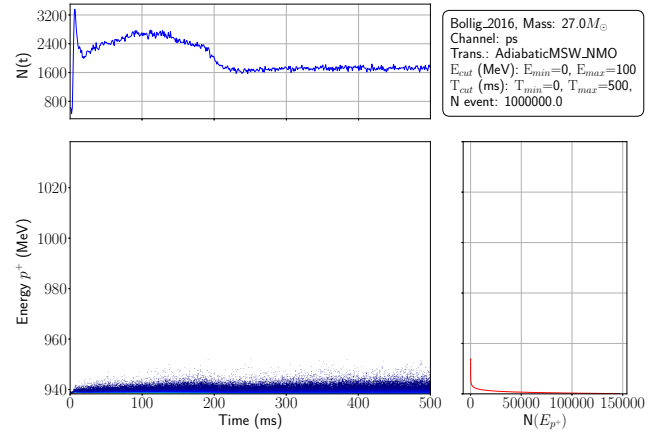
(A) Event rate in JUNO



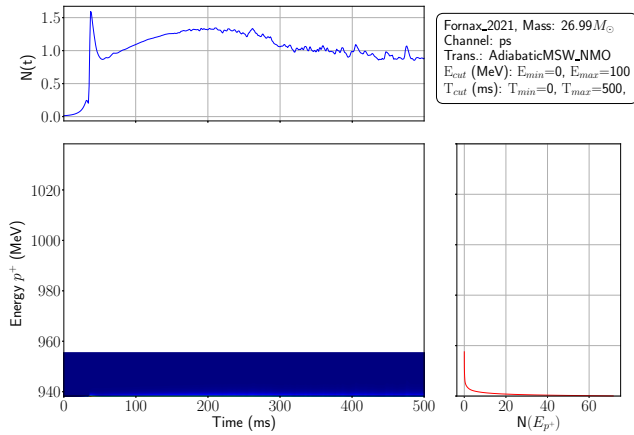
(B) MC data



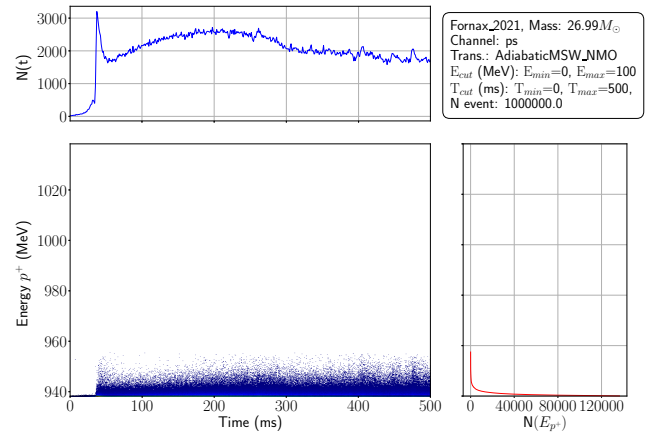
(A) Event rate in JUNO



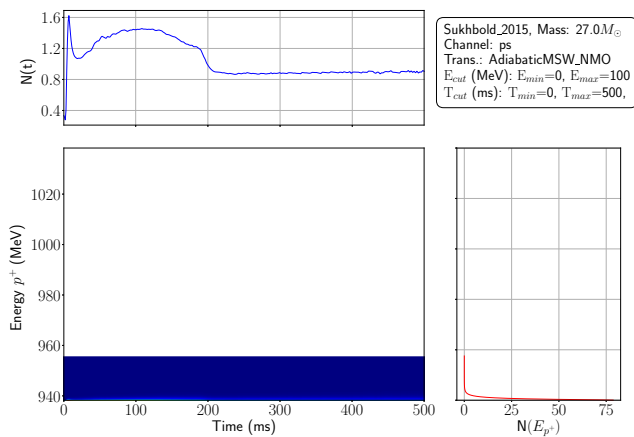
(B) MC data



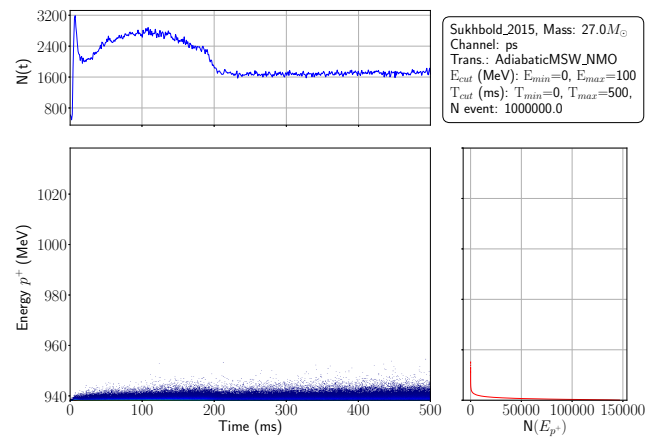
(A) Event rate in JUNO



(B) MC data

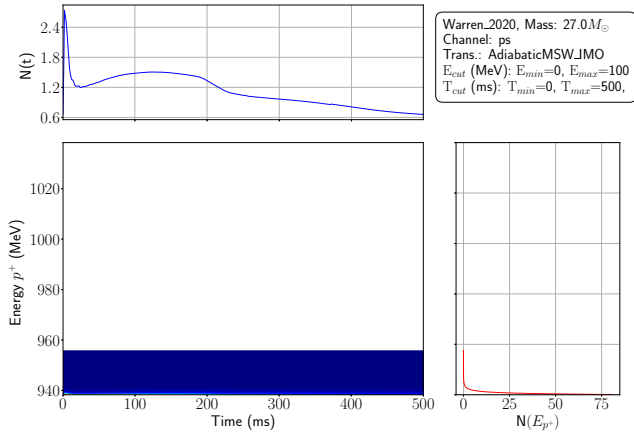


(A) Event rate in JUNO

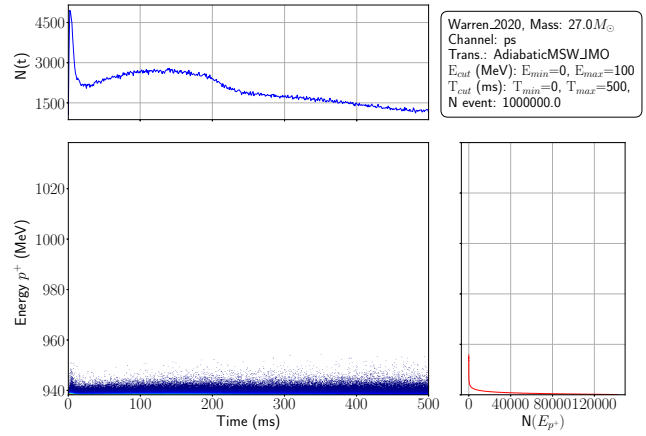


(B) MC data

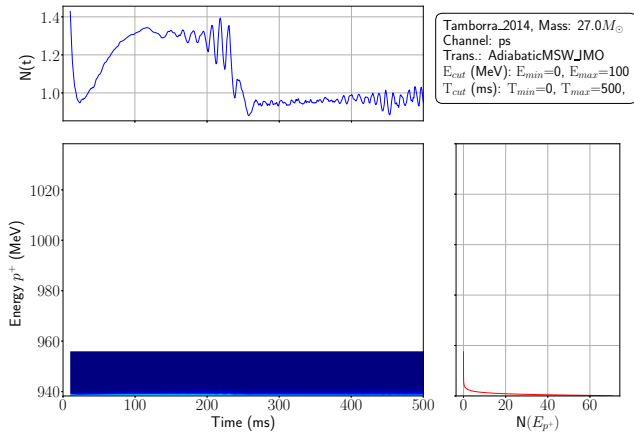
A.2.2 Adiabatic transformation using inverted mass ordering (IMO)



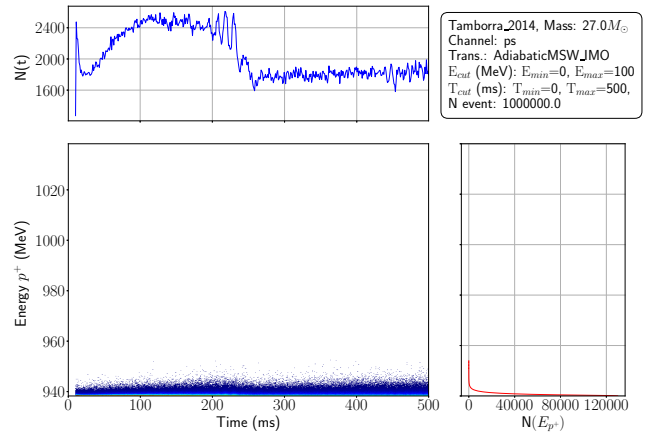
(A) Event rate in JUNO



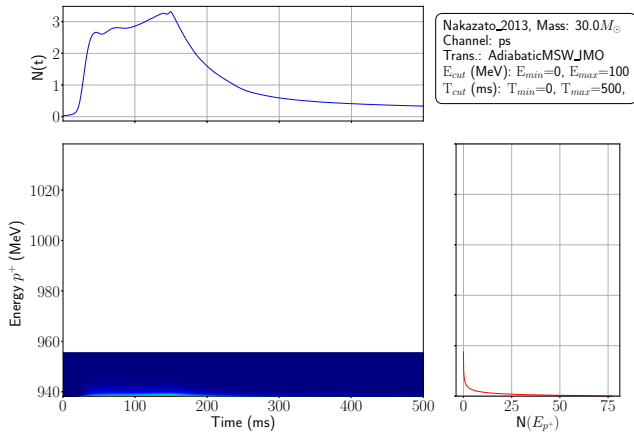
(B) MC data



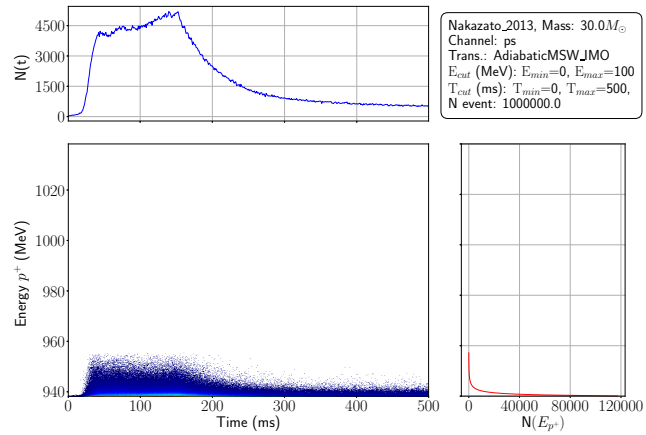
(A) Event rate in JUNO



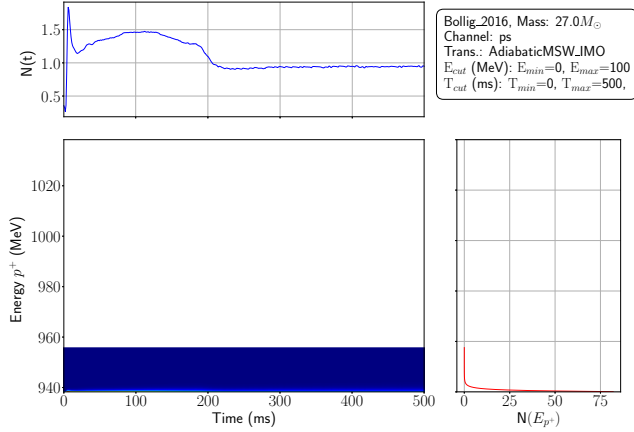
(B) MC data



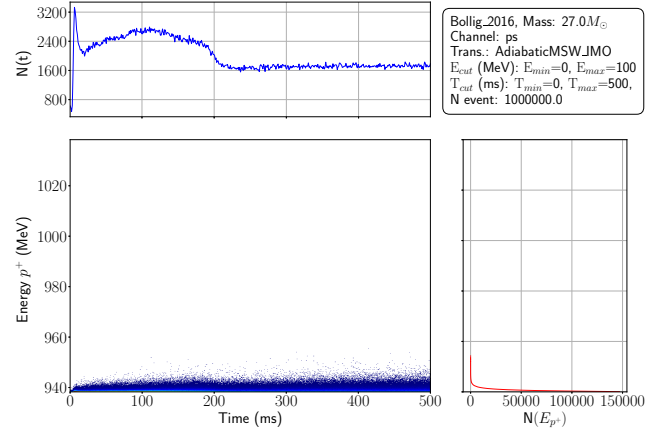
(A) Event rate in JUNO



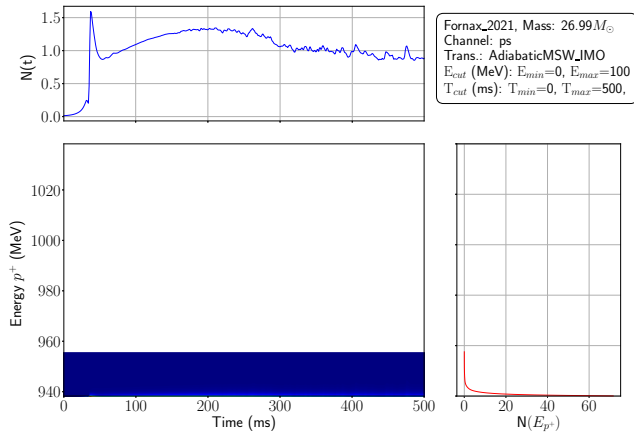
(B) MC data



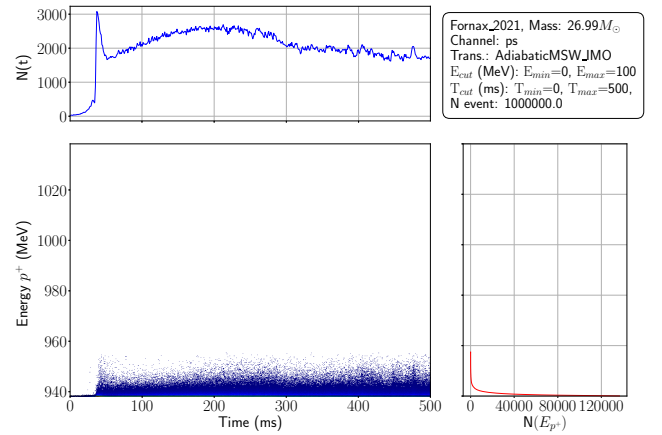
(A) Event rate in JUNO



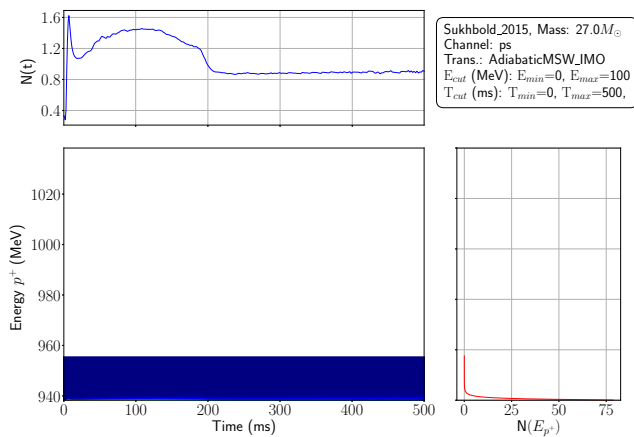
(B) MC data



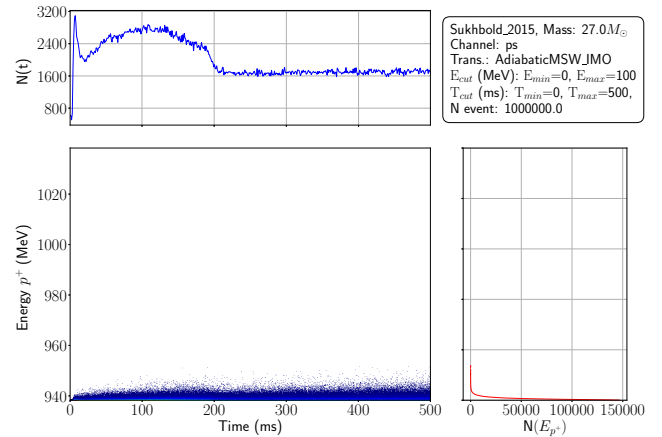
(A) Event rate in JUNO



(B) MC data



(A) Event rate in JUNO



(B) MC data

Appendix B

The ΔL distributions

Contents

B.1	Binned Likelihood Model Discrimination Results	209
B.2	Inverse- β Decay (IBD)	210
B.2.1	Adiabatic transformation using normal mass ordering (NMO)	210
B.2.2	HK comparison	215
B.2.3	Adiabatic transformation using inverted mass ordering (IMO)	216
B.3	Elastic neutrino-proton scattering (νpES)	221
B.3.1	Adiabatic transformation using normal mass ordering (NMO)	221
B.3.2	Adiabatic transformation using inverted mass ordering (IMO)	226

B.1 Binned Likelihood Model Discrimination Results

In this appendix, we present the ΔL distributions obtained for model discrimination across various core-collapse supernova (CCSN) models using the unbinned likelihood method. These distributions reflect the effectiveness of distinguishing between models based on event rates in the IBD and νpES channels. Energy cuts between 0.2 and 100 MeV, as well as time cuts between 20 and 500 ms, were applied uniformly across all models. Additionally, each dataset was normalized to ensure a fair comparison, with sizes of 100, 300, 1000, 3000, and 5000 events tested in the analysis.

The following figures display the ΔL distributions for each pair of models, highlighting the differences in likelihood and the potential for model discrimination across these different dataset sizes.

B.2 Inverse- β Decay (IBD)

B.2.1 Adiabatic transformation using normal mass ordering (NMO)

B.2.1.1 Number of observed events = 100

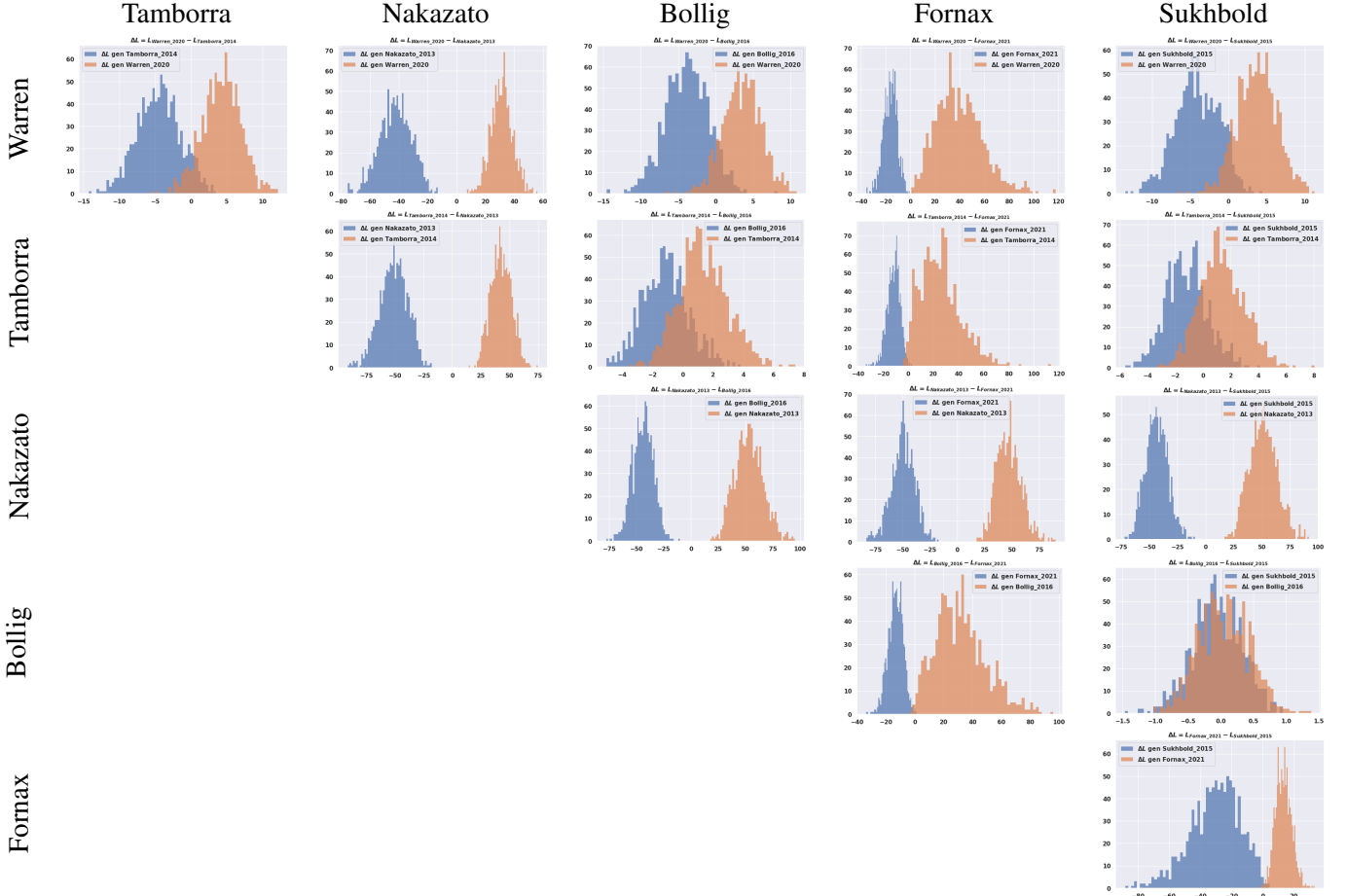


TABLE B.1: Uninned ΔL distributions for the 6 models considered. for the unbinned likelihood. Parameters: number of observed events = 100, number of CCSN = 1000, transformation: NMO, channel IBD, cut: 20-500 ms, 0.2-100 MeV.

Model	Reconstructed Model					
	Warren	Tamborra	Nakazato	Bollig	Fornax	Sukhbold
Warren	89.9%	3.5%	0.0%	3.9%	0.0%	2.7%
Tamborra	6.7%	72.5%	0.0%	9.3%	1.2%	10.3%
Nakazato	0.0%	0.0%	100.0%	0.0%	0.0%	0.0%
Bollig	7.9%	16.4%	0.0%	39.2%	0.4%	36.1%
Fornax	0.1%	0.4%	0.0%	0.0%	99.4%	0.1%
Sukhbold	5.5%	16.4%	0.0%	33.4%	0.4%	44.3%

TABLE B.2: Accuracy of the model discrimination for the unbinned likelihood. Parameters: number of observed events = 100, number of CCSN = 1000, transformation: NMO, channel IBD, cut: 20-500 ms, 0.2-100 MeV.

B.2.1.2 Number of observed events = 300

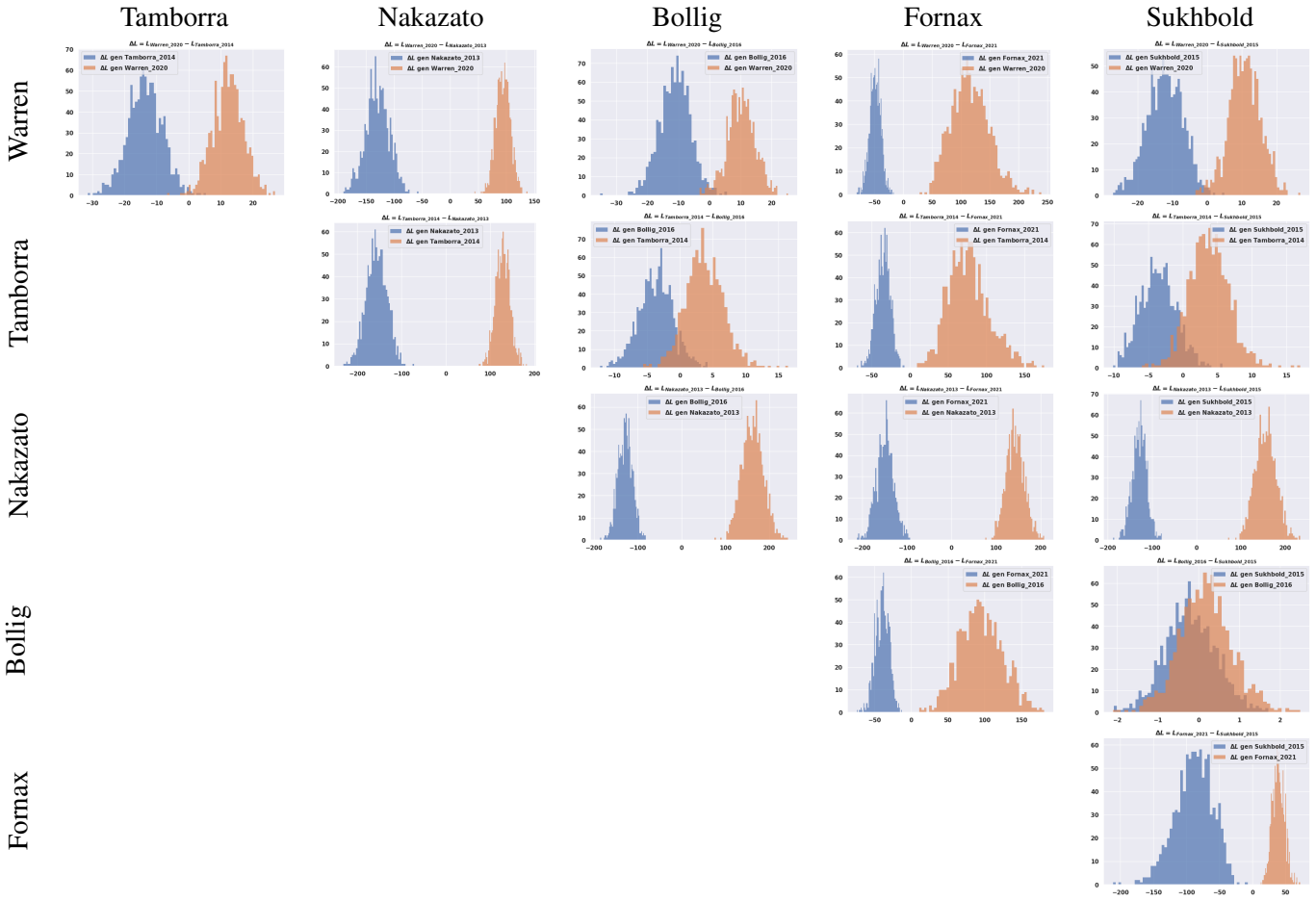


TABLE B.3: Uninned ΔL distributions for the 6 models considered. for the unbinned likelihood. Parameters: number of observed events = 300, number of CCSN = 1000, transformation: NMO, channel IBD, cut: 20-500 ms, 0.2-100 MeV.

Model	Reconstructed Model					
	Warren	Tamborra	Nakazato	Bollig	Fornax	Sukhbold
Warren	98.2%	0.6%	0%	0.7%	0%	0.5%
Tamborra	0.5%	89.4%	0%	4.9%	0%	5.2%
Nakazato	0%	0%	100.0%	0%	0%	0%
Bollig	7.0%	8.9%	0%	56.3%	0%	34.1%
Fornax	0%	0%	0%	0%	100.0%	0%
Sukhbold	0.9%	8.8%	0%	30.6%	0%	59.7%

TABLE B.4: Accuracy of the model discrimination for the unbinned likelihood. Parameters: number of observed events = 300, number of CCSN = 1000, transformation: NMO, channel IBD, cut: 20-500 ms, 0.2-100 MeV.

B.2.1.3 Number of observed events = 1000

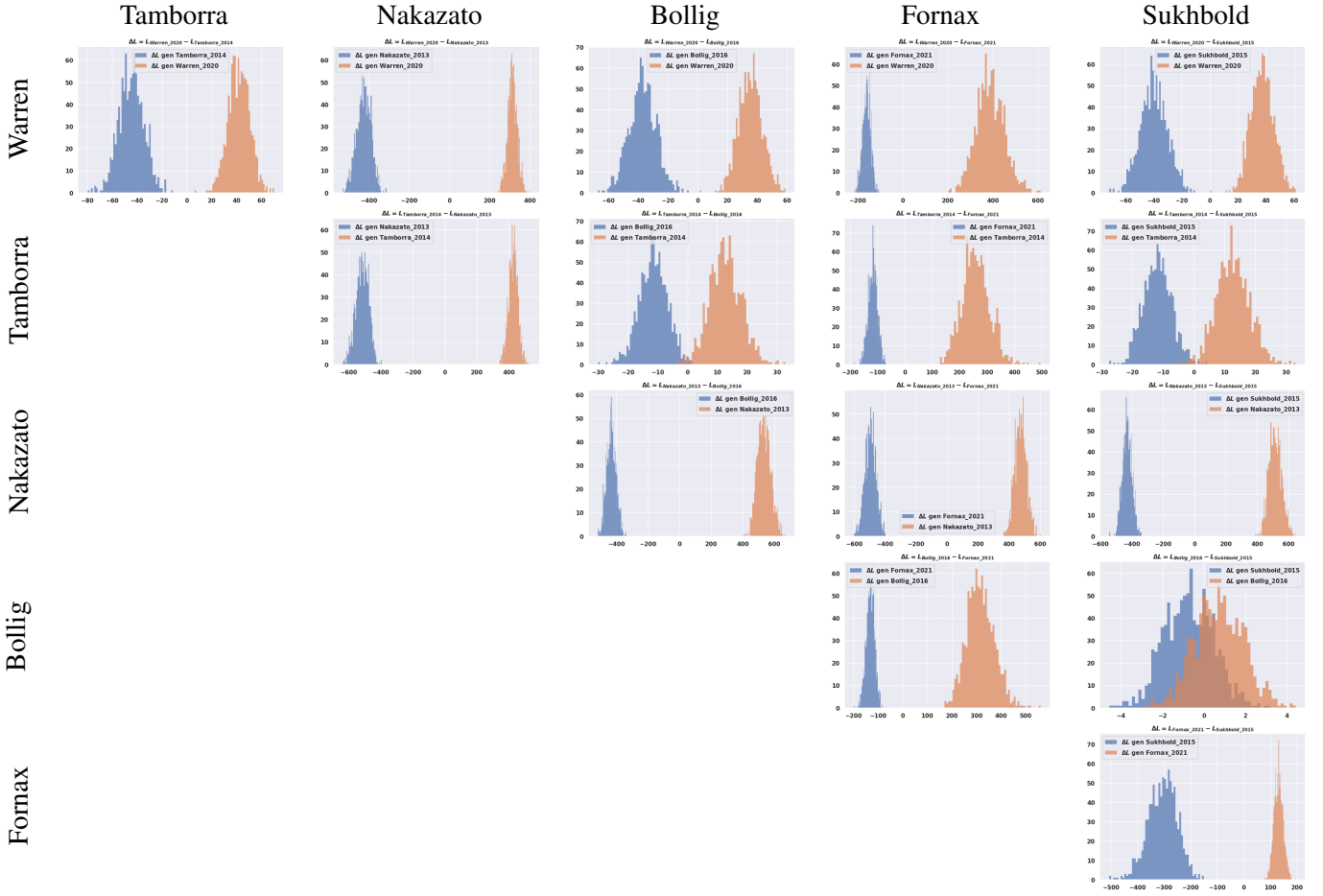


TABLE B.5: Uninned ΔL distributions for the 6 models considered. for the unbinned likelihood. Parameters: number of observed events = 1000, number of CCSN = 1000, transformation: NMO, channel IBD, cut: 20-500 ms, 0.2-100 MeV.

Model	Reconstructed Model					
	Warren	Tamborra	Nakazato	Bollig	Fornax	Sukhbold
Warren	100.0%	0.0%	0.0%	0.0%	0.0%	0.0%
Tamborra	0.0%	98.7%	0.0%	0.3%	0.0%	1.0%
Nakazato	0.0%	0.0%	100.0%	0.0%	0.0%	0.0%
Bollig	0.0%	0.4%	0.0%	72.4%	0.0%	27.2%
Fornax	0.0%	0.0%	0.0%	0.0%	100.0%	0.0%
Sukhbold	0.0%	0.7%	0.0%	28.9%	0.0%	70.4%

TABLE B.6: Accuracy of the model discrimination for the unbinned likelihood. Parameters: number of observed events = 1000, number of CCSN = 1000, transformation: NMO, channel IBD, cut: 20-500 ms, 0.2-100 MeV.

B.2.1.4 Number of observed events = 3000

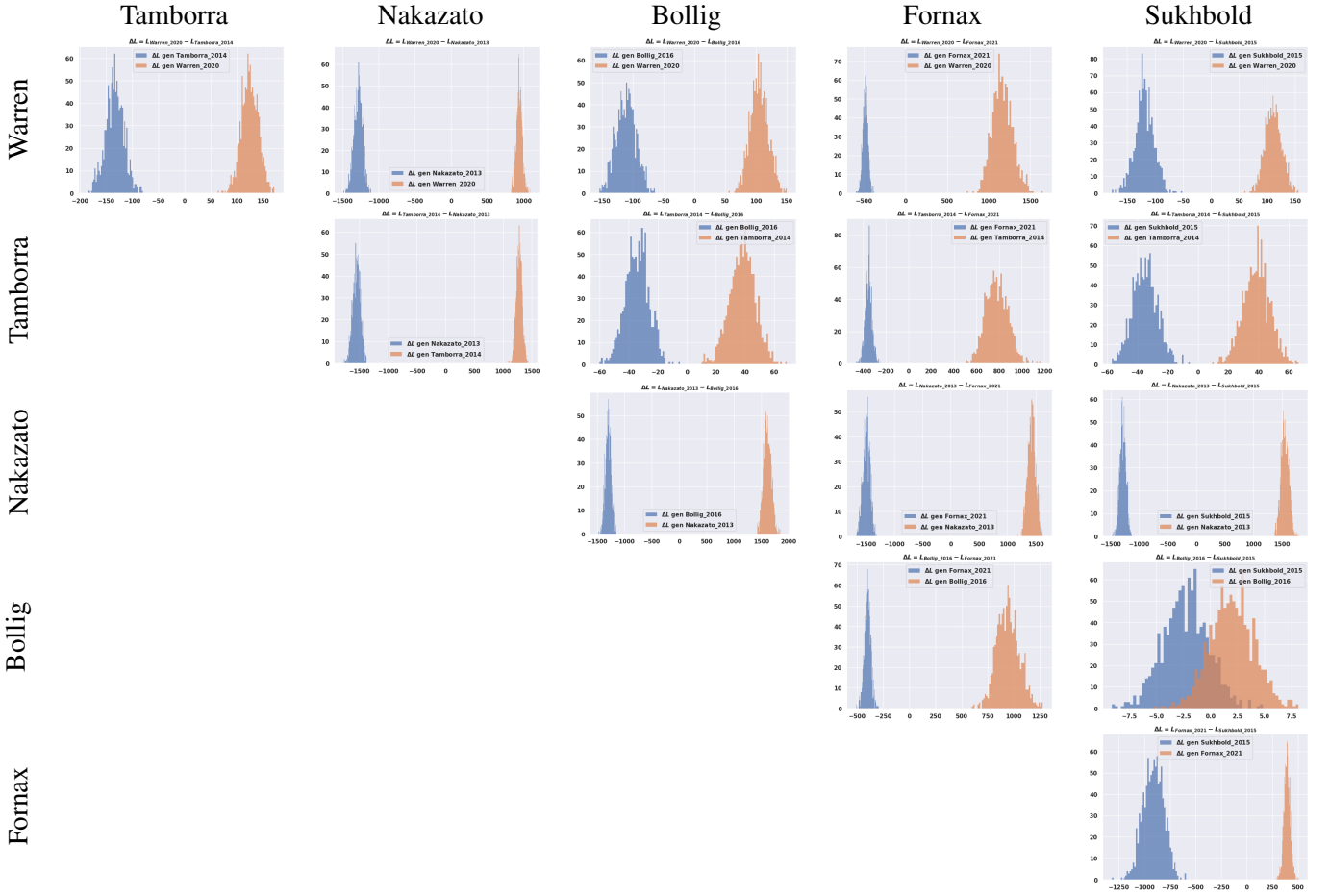


TABLE B.7: Uninned ΔL distributions for the 6 models considered. for the unbinned likelihood. Parameters: number of observed events = 3000, number of CCSN = 1000, transformation: NMO, channel IBD, cut: 20-500 ms, 0.2-100 MeV.

True Model	Reconstructed Model					
	Warren	Tamborra	Nakazato	Bollig	Fornax	Sukhbold
Warren	100.0 %	0.0 %	0.0 %	0.0 %	0.0 %	0.0 %
Tamborra	0.0 %	100.0 %	0.0 %	0.0 %	0.0 %	0.0 %
Nakazato	0.0 %	0.0 %	100.0 %	0.0 %	0.0 %	0.0 %
Bollig	0.0 %	0.0 %	0.0 %	83.4 %	0.0 %	16.6 %
Fornax	0.0 %	0.0 %	0.0 %	0.0 %	100.0 %	0.0 %
Sukhbold	0.0 %	0.0 %	0.0 %	13.3 %	0.0 %	86.7 %

TABLE B.8: Accuracy of the model discrimination for the unbinned likelihood. Parameters: number of observed events = 3000, number of CCSN = 1000, transformation: NMO, channel IBD, cut: 20-500 ms, 0.2-100 MeV.

B.2.1.5 Number of observed events = 5000

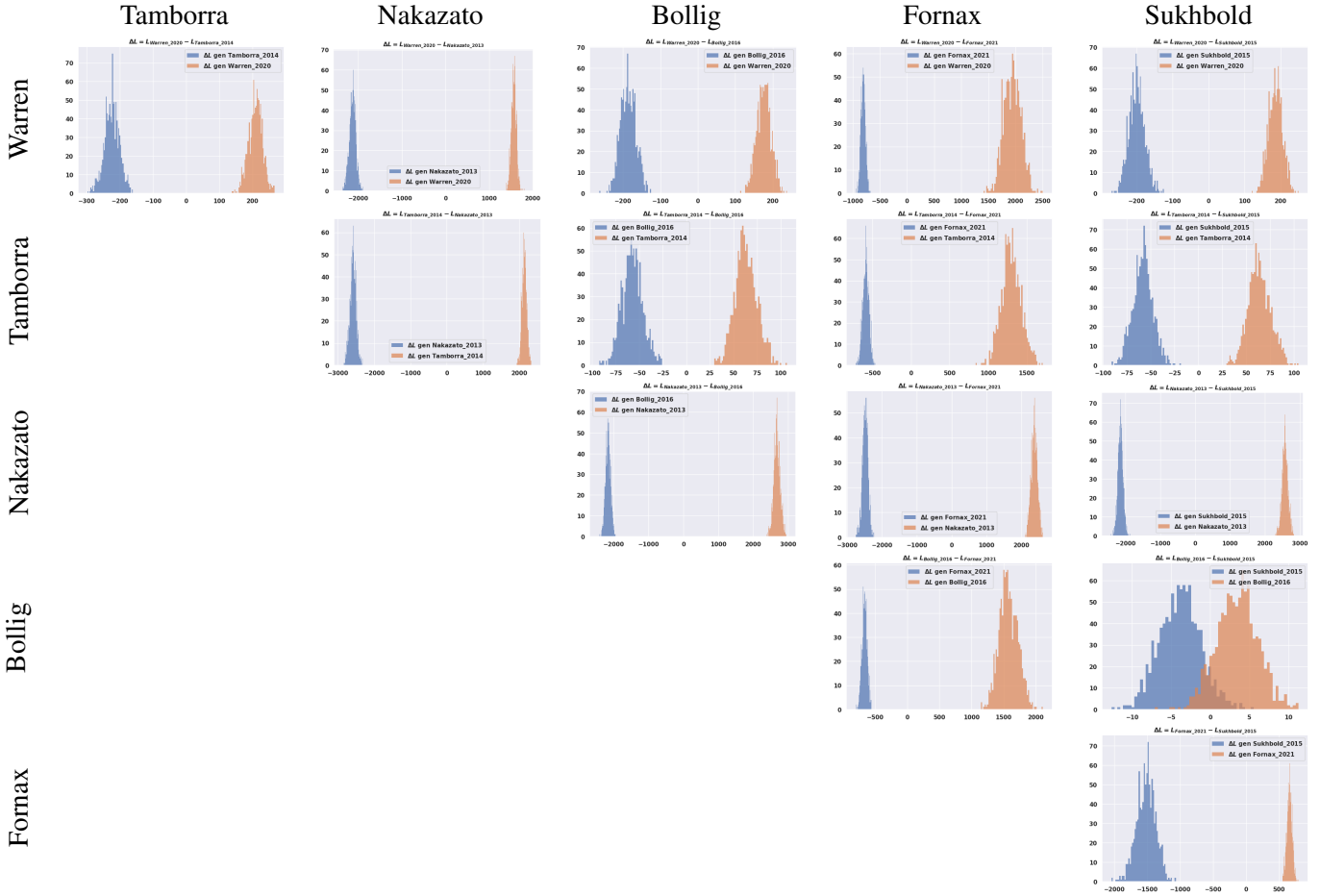


TABLE B.9: Uninned ΔL distributions for the 6 models considered. for the unbinned likelihood. Parameters: number of observed events = 5000, number of CCSN = 1000, transformation: NMO, channel IBD, cut: 20-500 ms, 0.2-100 MeV.

Model	Reconstructed Model					
	Warren	Tamborra	Nakazato	Bollig	Fornax	Sukhbold
Warren	100.0%	0.0%	0.0%	0.0%	0.0%	0.0%
Tamborra	0.0%	100.0%	0.0%	0.0%	0.0%	0.0%
Nakazato	0.0%	0.0%	100.0%	0.0%	0.0%	0.0%
Bollig	0.0%	0.0%	0.0%	90.3%	0.0%	9.7%
Fornax	0.0%	0.0%	0.0%	0.0%	100.0%	0.0%
Sukhbold	0.0%	0.0%	0.0%	7.2%	0.0%	92.8%

TABLE B.10: Accuracy of the model discrimination for the unbinned likelihood. Parameters: number of observed events = 5000, number of CCSN = 1000, transformation: NMO, channel IBD, cut: 20-500 ms, 0.2-100 MeV.

B.2.2 HK comparison

In this appendix, we present a comparison of model discrimination accuracy between the JUNO and Hyper-Kamiokande detectors. Both studies employed an unbinned likelihood approach, but key differences exist in the models, parameters, and detector characteristics. The analysis in this appendix focuses on the comparison between a reduced number of CCSN models used in the other analysis, with a fixed dataset size of 300 events, and the corresponding models in the Hyper-Kamiokande study.

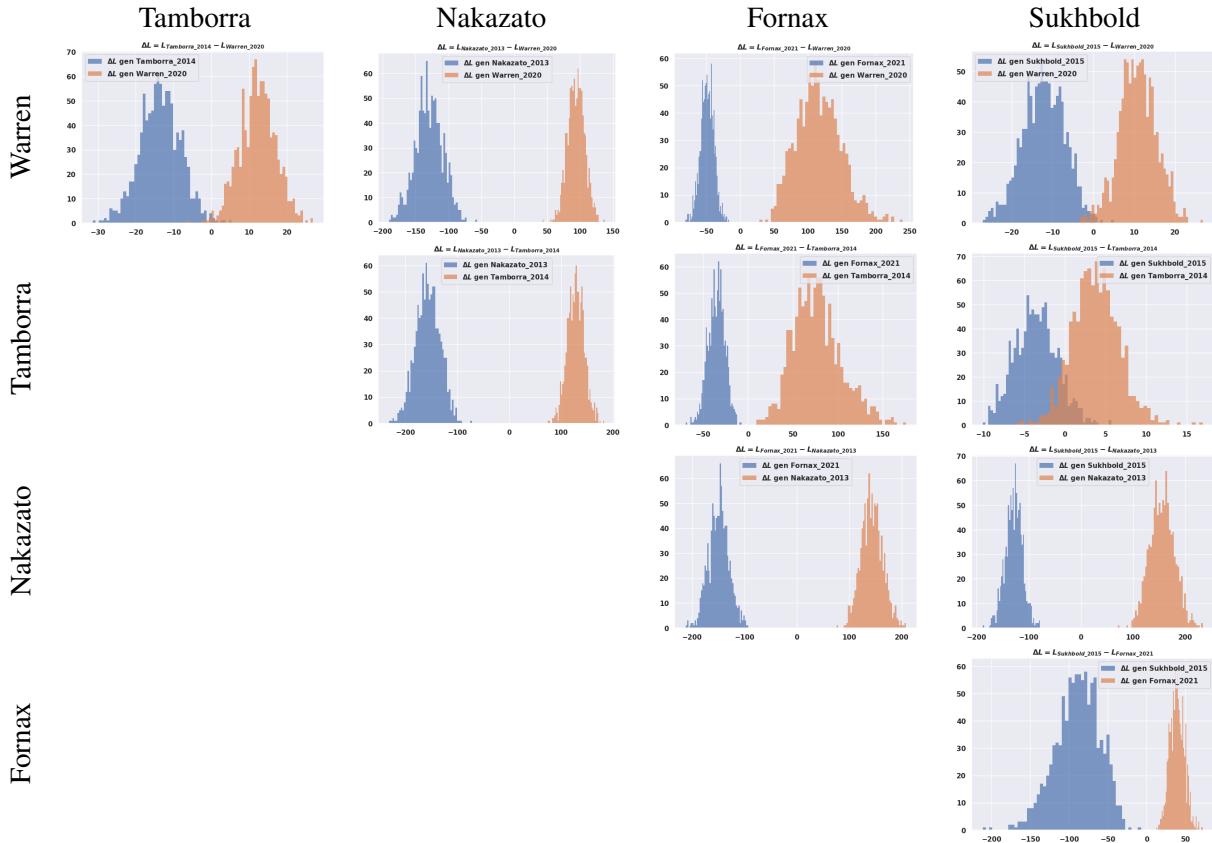


TABLE B.11: Unboxed ΔL distributions for the 5 models considered. Parameters: number of observed events = n , number of CCSN = 1000, transformation: NMO, channel: IBD, cut: 20-500 ms, 0.2-100 MeV.

True Model	Reconstructed Model				
	Warren	Tamborra	Nakazato	Fornax	Sukhbold
Warren	98.2%	0.5%	0.0%	0.0%	1.3%
Tamborra	0.6%	90.8%	0.0%	0.0%	8.6%
Nakazato	0.0%	0.0%	100.0%	0.0%	0.0%
Fornax	0.0%	0.0%	0.0%	100.0%	0.0%
Sukhbold	0.5%	8.6%	0.0%	0.0%	90.9%

TABLE B.12: Accuracy of the model discrimination for the 5 models likelihood. Parameters: number of observed events = n , number of CCSN = 1000, transformation: NMO, channel: IBD, cut: 20-500 ms, 0.2-100 MeV.

B.2.3 Adiabatic transformation using inverted mass ordering (IMO)

B.2.3.1 Number of observed events = 100

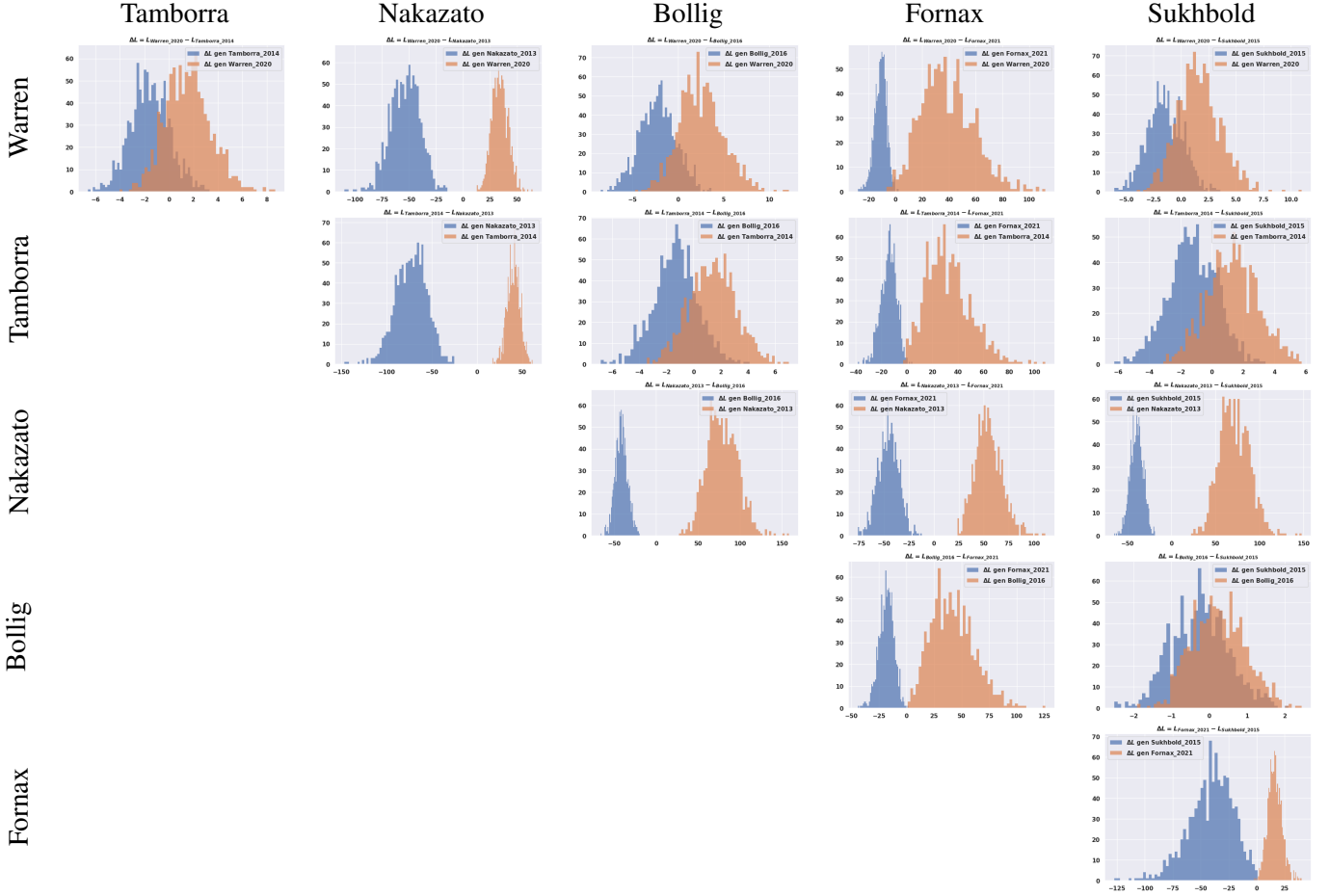


TABLE B.13: Uninned ΔL distributions for the 6 models considered. for the unbinned likelihood. Parameters: number of observed events = 100, number of CCSN = 1000, transformation: IMO, channel IBD, cut: 20-500 ms, 0.2-100 MeV.

True Model	Reconstructed Model					
	Warren	Tamborra	Nakazato	Bollig	Fornax	Sukhbold
Warren	67.7 %	14.5 %	0.0 %	4.6 %	0.8 %	12.4 %
Tamborra	12.3 %	65.3 %	0.0 %	13.0 %	0.4 %	9.0 %
Nakazato	0.0 %	0.0 %	100.0 %	0.0 %	0.0 %	0.0 %
Bollig	5.8 %	13.3 %	0.0 %	54.3 %	0.0 %	26.6 %
Fornax	0.0 %	0.5 %	0.0 %	0.0 %	99.5 %	0.0 %
Sukhbold	13.9 %	14.7 %	0.0 %	28.9 %	0.0 %	42.5 %

TABLE B.14: Accuracy of the model discrimination for the unbinned likelihood. Parameters: number of observed events = 100, number of CCSN = 1000, transformation: IMO, channel IBD, cut: 20-500 ms, 0.2-100 MeV.

B.2.3.2 Number of observed events = 300

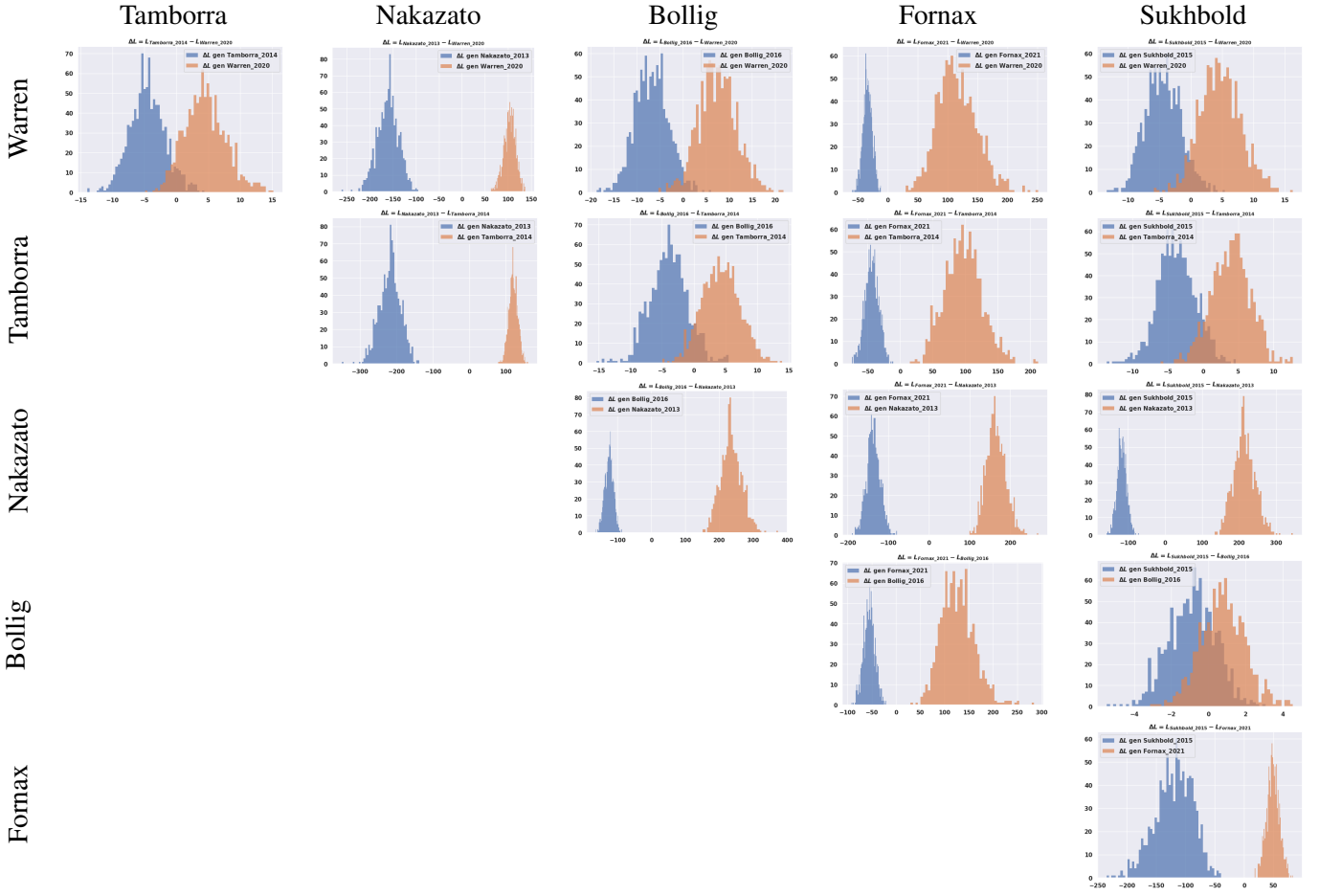


TABLE B.15: Uninned ΔL distributions for the 6 models considered. for the unbinned likelihood. Parameters: number of observed events = 300, number of CCSN = 1000, transformation: IMO, channel IBD, cut: 20-500 ms, 0.2-100 MeV.

Model	Reconstructed Model					
	Warren	Tamborra	Nakazato	Bollig	Fornax	Sukhbold
Warren	89.2%	5.4%	0.0%	0.6%	0.0%	4.8%
Tamborra	5.0%	85.9%	0.0%	4.3%	0.0%	4.8%
Nakazato	0.0%	0.0%	100.0%	0.0%	0.0%	0.0%
Bollig	1.2%	6.9%	0.0%	68.9%	0.0%	23.0%
Fornax	0.0%	0.0%	0.0%	0.0%	100.0%	0.0%
Sukhbold	5.6%	5.6%	0.0%	23.1%	0.0%	65.7%

TABLE B.16: Accuracy of the model discrimination for the unbinned likelihood. Parameters: number of observed events = 300, number of CCSN = 1000, transformation: IMO, channel IBD, cut: 20-500 ms, 0.2-100 MeV.

B.2.3.3 Number of observed events = 1000

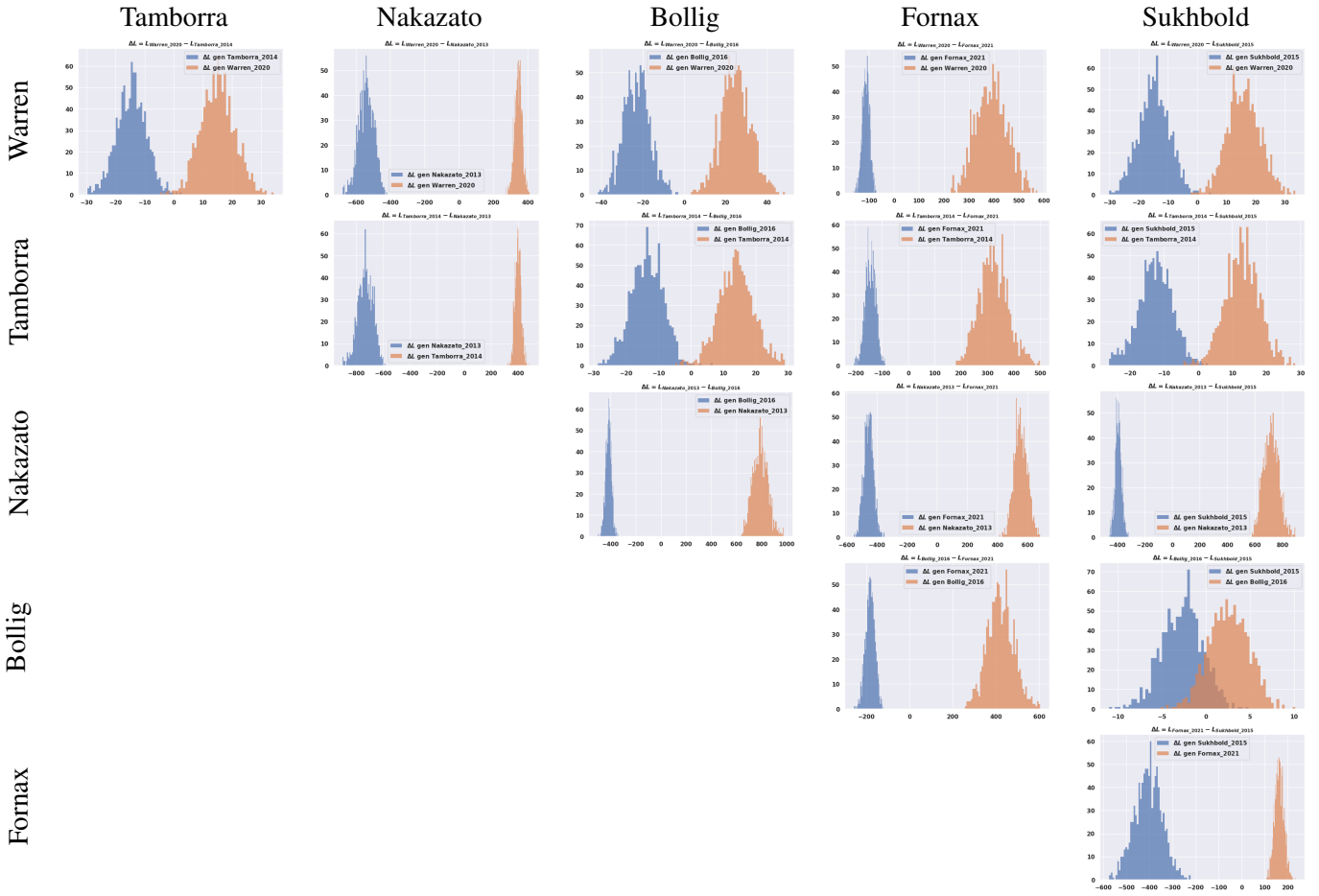


TABLE B.17: Uninned ΔL distributions for the 6 models considered. for the unbinned likelihood. Parameters: number of observed events = 1000, number of CCSN = 1000, transformation: IMO, channel IBD, cut: 20-500 ms, 0.2-100 MeV.

True Model	Reconstructed Model					
	Warren	Tamborra	Nakazato	Bollig	Fornax	Sukhbold
Warren	99.1 %	0.6 %	0.0 %	0.0 %	0.0 %	0.3 %
Tamborra	0.2 %	98.6 %	0.0 %	0.6 %	0.0 %	0.6 %
Nakazato	0.0 %	0.0 %	100.0 %	0.0 %	0.0 %	0.0 %
Bollig	0.0 %	0.2 %	0.0 %	86.8 %	0.0 %	13.0 %
Fornax	0.0 %	0.0 %	0.0 %	0.0 %	100.0 %	0.0 %
Sukhbold	0.3 %	0.4 %	0.0 %	11.8 %	0.0 %	87.5 %

TABLE B.18: Accuracy of the model discrimination for the unbinned likelihood. Parameters: number of observed events = 1000, number of CCSN = 1000, transformation: IMO, channel IBD, cut: 20-500 ms, 0.2-100 MeV.

B.2.3.4 Number of observed events = 3000

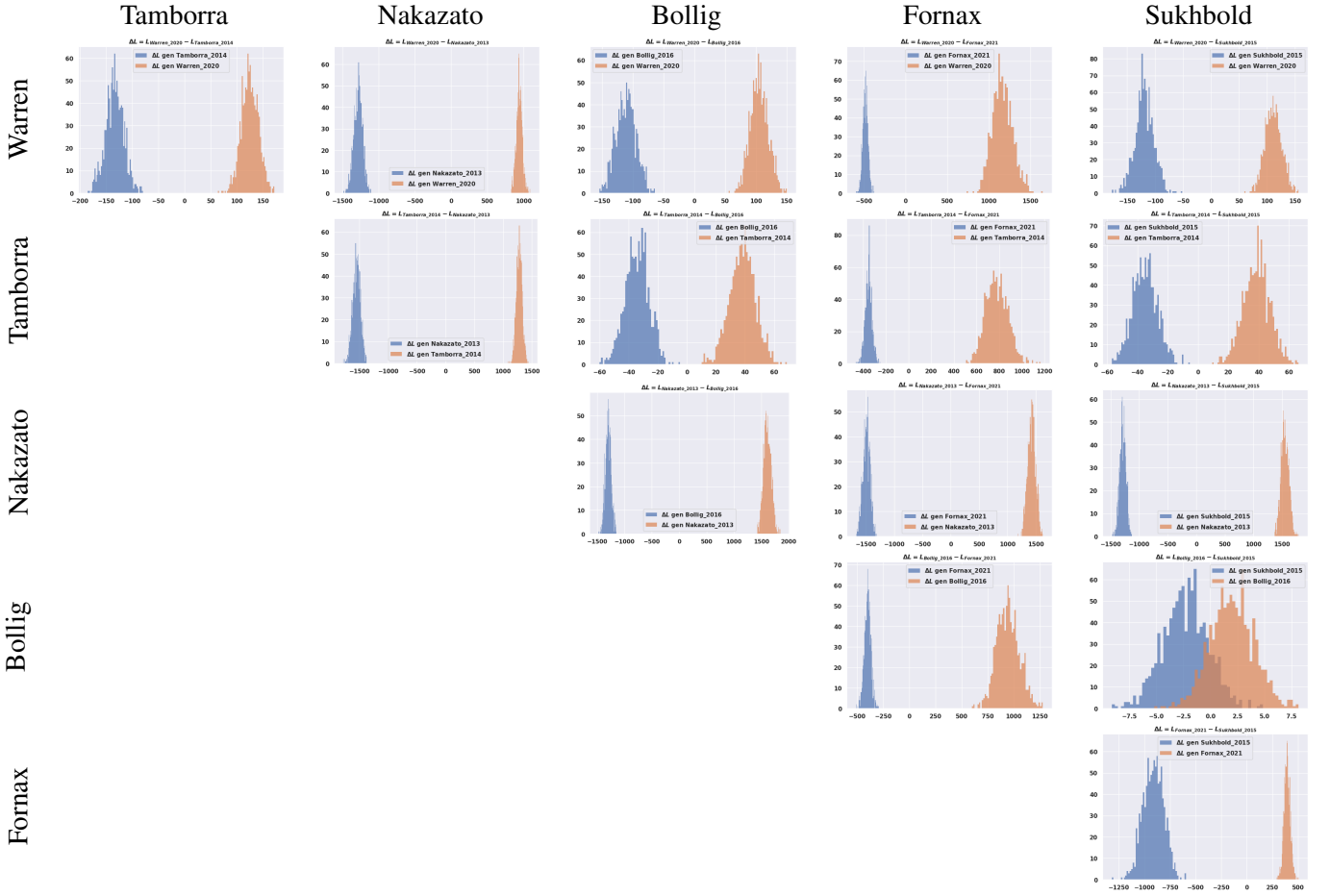


TABLE B.19: Uninned ΔL distributions for the 6 models considered. for the unbinned likelihood. Parameters: number of observed events = 3000, number of CCSN = 1000, transformation: NMO, channel IBD, cut: 20-500 ms, 0.2-100 MeV.

True Model	Reconstructed Model					
	Warren	Tamborra	Nakazato	Bollig	Fornax	Sukhbold
Warren	100.0 %	0.0 %	0.0 %	0.0 %	0.0 %	0.0 %
Tamborra	0.0 %	100.0 %	0.0 %	0.0 %	0.0 %	0.0 %
Nakazato	0.0 %	0.0 %	100.0 %	0.0 %	0.0 %	0.0 %
Bollig	0.0 %	0.0 %	0.0 %	83.4 %	0.0 %	16.6 %
Fornax	0.0 %	0.0 %	0.0 %	0.0 %	100.0 %	0.0 %
Sukhbold	0.0 %	0.0 %	0.0 %	13.3 %	0.0 %	86.7 %

TABLE B.20: Accuracy of the model discrimination for the unbinned likelihood. Parameters: number of observed events = 3000, number of CCSN = 1000, transformation: NMO, channel IBD, cut: 20-500 ms, 0.2-100 MeV.

B.2.3.5 Number of observed events = 5000

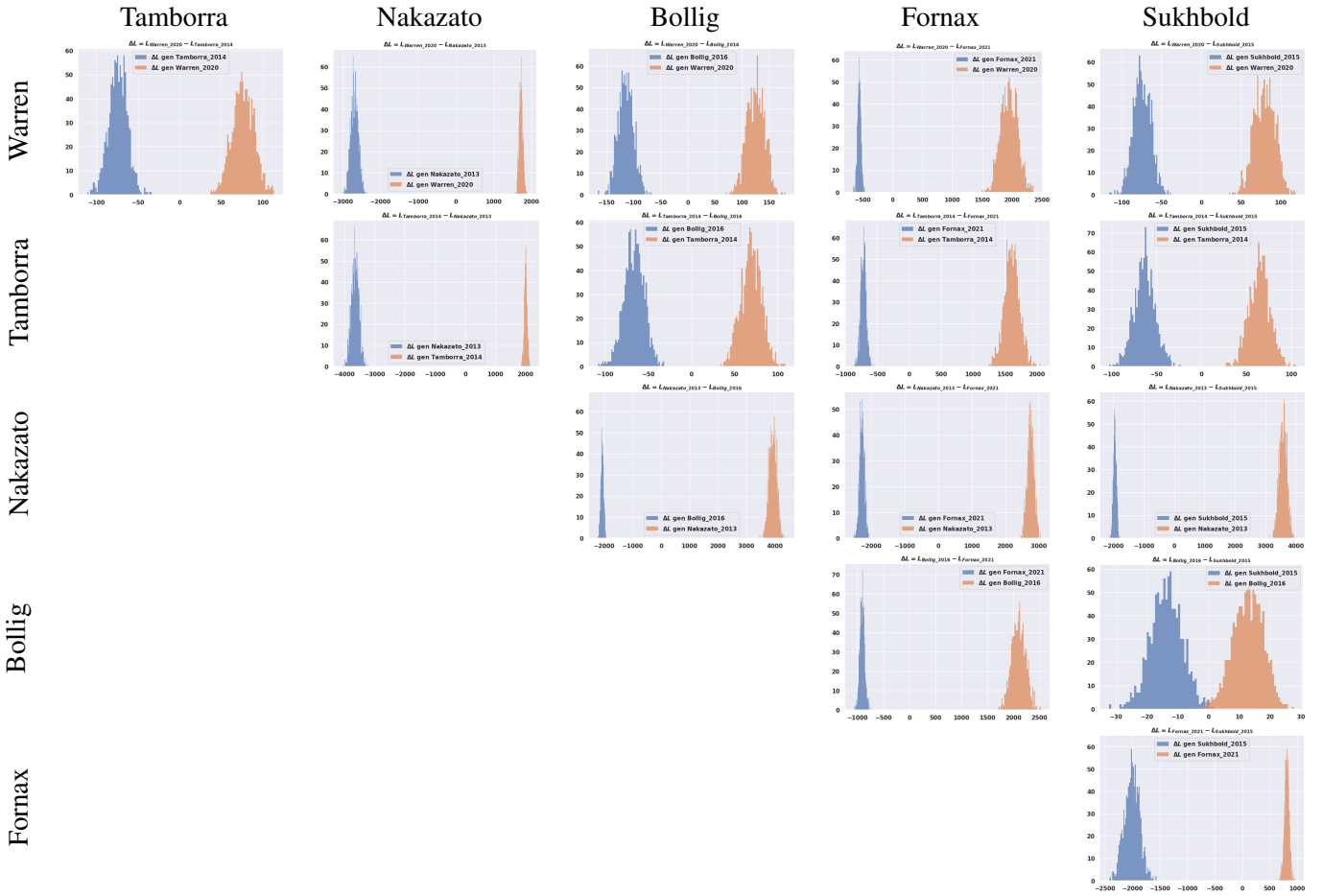


TABLE B.21: Uninned ΔL distributions for the 6 models considered. for the unbinned likelihood. Parameters: number of observed events = 5000, number of CCSN = 1000, transformation: IMO, channel IBD, cut: 20-500 ms, 0.2-100 MeV.

True Model	Reconstructed Model					
	Warren	Tamborra	Nakazato	Bollig	Fornax	Sukhbold
Warren	100.0 %	0.0 %	0.0 %	0.0 %	0.0 %	0.0 %
Tamborra	0.0 %	100.0 %	0.0 %	0.0 %	0.0 %	0.0 %
Nakazato	0.0 %	0.0 %	100.0 %	0.0 %	0.0 %	0.0 %
Bollig	0.0 %	0.0 %	0.0 %	99.4 %	0.0 %	0.6 %
Fornax	0.0 %	0.0 %	0.0 %	0.0 %	100.0 %	0.0 %
Sukhbold	0.0 %	0.0 %	0.0 %	0.2 %	0.0 %	99.8 %

TABLE B.22: Accuracy of the model discrimination for the unbinned likelihood. Parameters: number of observed events = 5000, number of CCSN = 1000, transformation: IMO, channel IBD, cut: 20-500 ms, 0.2-100 MeV.

B.3 Elastic neutrino-proton scattering (νpES)

B.3.1 Adiabatic transformation using normal mass ordering (NMO)

B.3.1.1 Number of observed events = 100

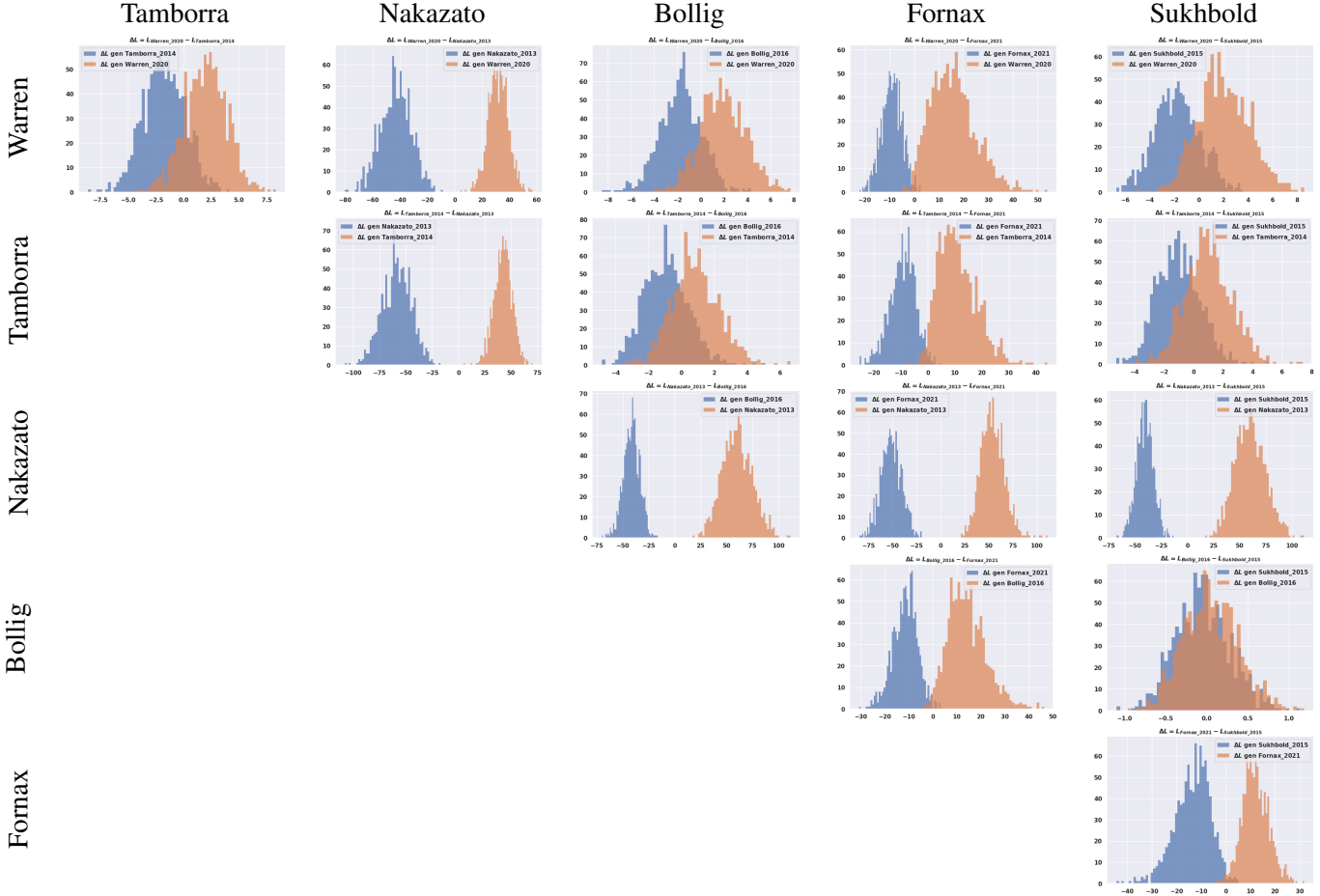


TABLE B.23: Uninned ΔL distributions for the 6 models considered. for the unbinned likelihood. Parameters: number of observed events = 100, number of CCSN = 1000, transformation: NMO, channel PS, cut: 20-500 ms, 0.2-100 MeV.

True Model	Reconstructed Model					
	Warren	Tamborra	Nakazato	Bollig	Fornax	Sukhbold
Warren	74.9 %	10.1 %	0.0 %	5.7 %	1.0 %	8.3 %
Tamborra	14.5 %	59.0 %	0.0 %	12.7 %	2.2 %	11.6 %
Nakazato	0.0 %	0.0 %	100.0 %	0.0 %	0.0 %	0.0 %
Bollig	11.9 %	18.1 %	0.0 %	33.7 %	0.5 %	35.8 %
Fornax	0.8 %	0.8 %	0.0 %	0.1 %	98.0 %	0.3 %
Sukhbold	12.8 %	15.8 %	0.0 %	24.9 %	0.7 %	45.8 %

TABLE B.24: Accuracy of the model discrimination for the unbinned likelihood. Parameters: number of observed events = 100, number of CCSN = 1000, transformation: NMO, channel PS, cut: 20-500 ms, 0.2-100 MeV.

B.3.1.2 Number of observed events = 300

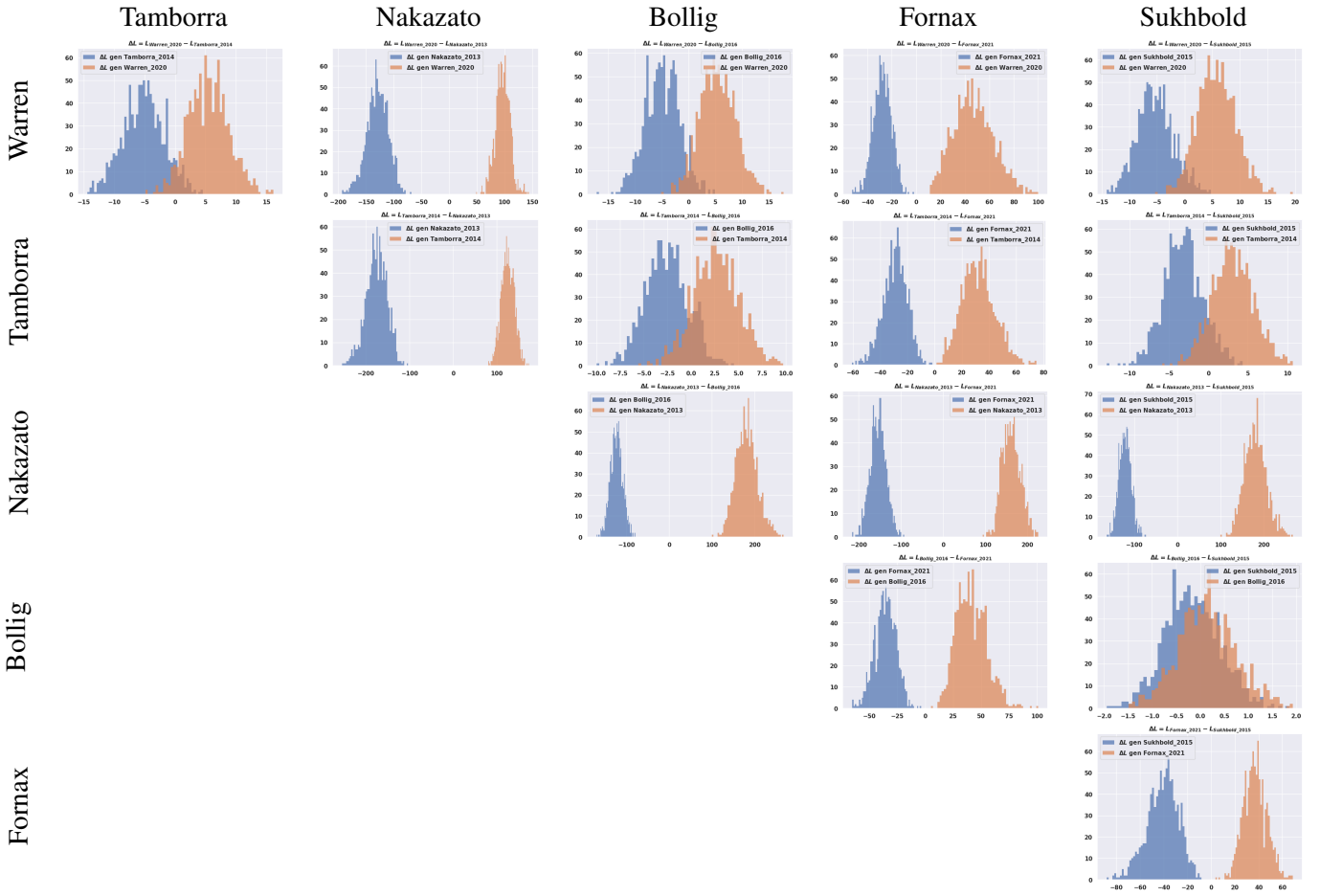


TABLE B.25: Uninned ΔL distributions for the 6 models considered. for the unbinned likelihood. Parameters: number of observed events = 300, number of CCSN = 1000, transformation: NMO, channel PS, cut: 20-500 ms, 0.2-100 MeV.

Model	Reconstructed Model					
	Warren	Tamborra	Nakazato	Bollig	Fornax	Sukhbold
Warren	82.1%	8.1%	0%	5.0%	0.2%	4.6%
Tamborra	9.3%	73.4%	0%	9.6%	0.2%	7.5%
Nakazato	0%	0%	100.0%	0%	0%	0%
Bollig	11.3%	13.7%	0%	38.3%	0%	36.7%
Fornax	0%	0%	0%	0%	100.0%	0%
Sukhbold	9.8%	12.2%	0%	26.3%	0%	51.7%

TABLE B.26: Accuracy of the model discrimination for the unbinned likelihood. Parameters: number of observed events = 300, number of CCSN = 1000, transformation: NMO, channel PS, cut: 20-500 ms, 0.2-100 MeV.

B.3.1.3 Number of observed events = 1000

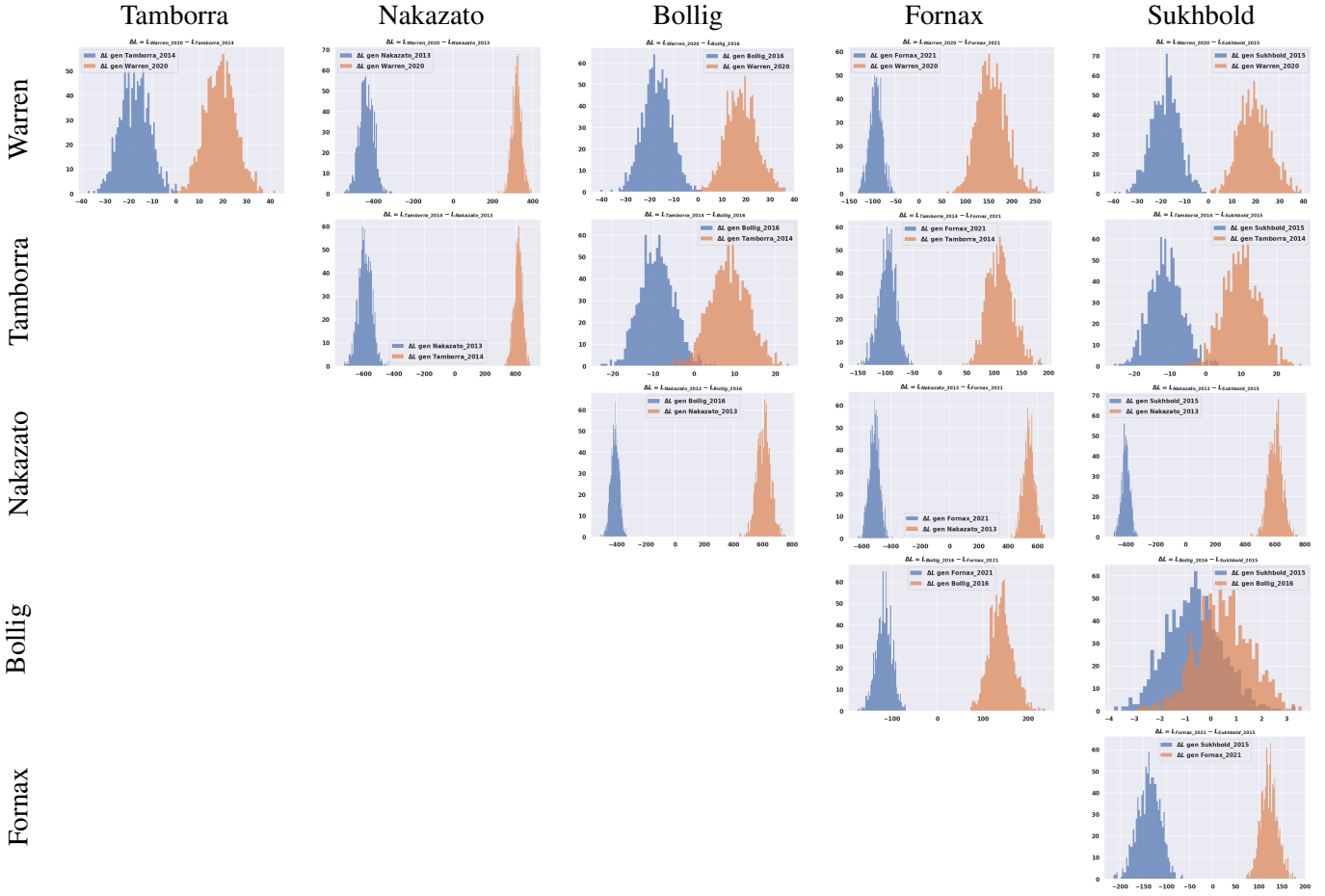


TABLE B.27: Uninned ΔL distributions for the 6 models considered. for the unbinned likelihood. Parameters: number of observed events = 1000, number of CCSN = 1000, transformation: NMO, channel PS, cut: 20-500 ms, 0.2-100 MeV.

True Model	Reconstructed Model					
	Warren	Tamborra	Nakazato	Bollig	Fornax	Sukhbold
Warren	99.7 %	0.2 %	0.0 %	0.0 %	0.0 %	0.1 %
Tamborra	0.3 %	97.0 %	0.0 %	2.0 %	0.0 %	0.7 %
Nakazato	0.0 %	0.0 %	100.0 %	0.0 %	0.0 %	0.0 %
Bollig	0.3 %	1.5 %	0.0 %	65.2 %	0.0 %	33.0 %
Fornax	0.0 %	0.0 %	0.0 %	0.0 %	100.0 %	0.0 %
Sukhbold	0.1 %	1.2 %	0.0 %	25.3 %	0.0 %	73.4 %

TABLE B.28: Accuracy of the model discrimination for the unbinned likelihood. Parameters: number of observed events = 1000, number of CCSN = 1000, transformation: NMO, channel PS, cut: 20-500 ms, 0.2-100 MeV.

B.3.1.4 Number of observed events = 3000

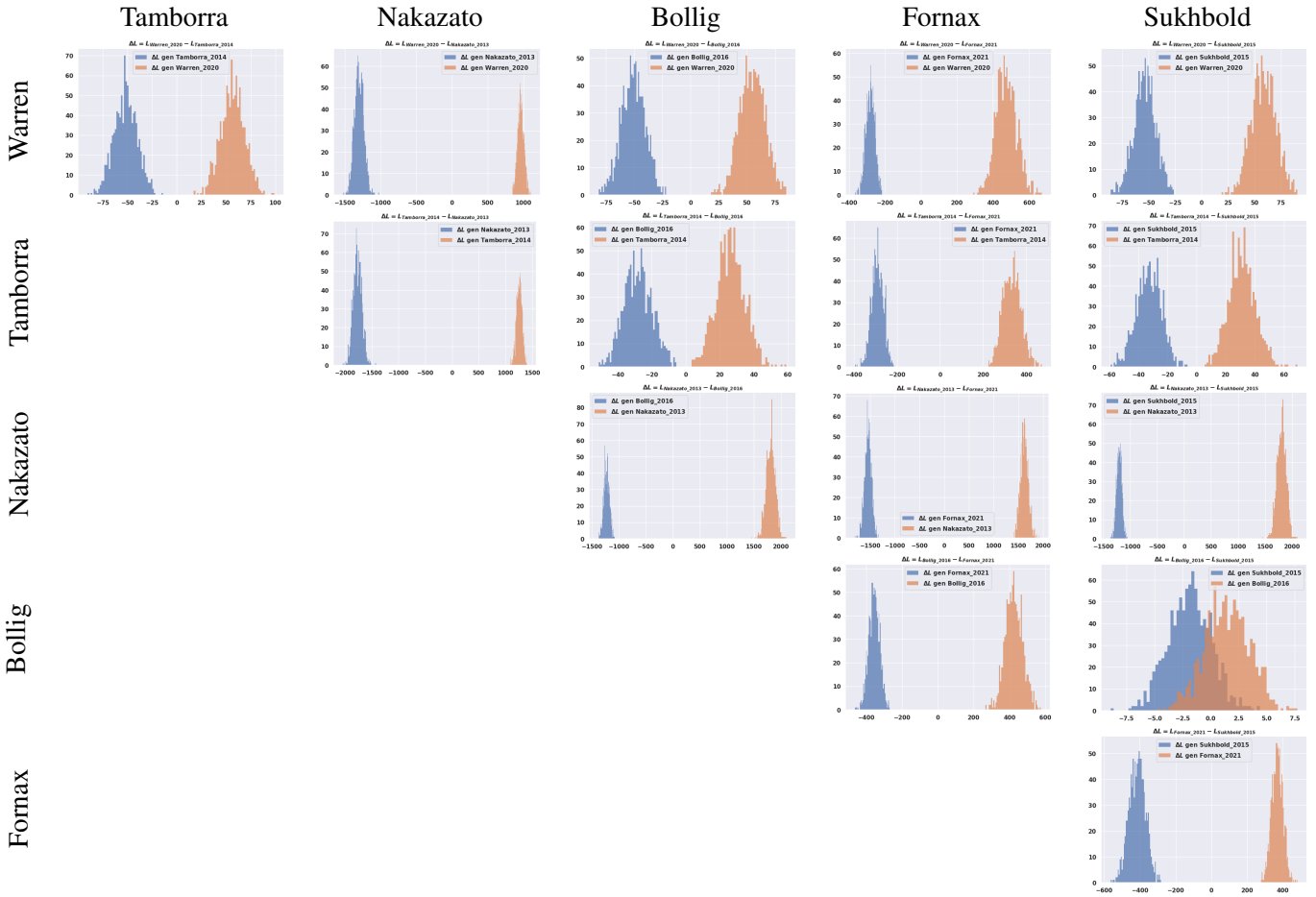


TABLE B.29: Uninned ΔL distributions for the 6 models considered. for the unbinned likelihood. Parameters: number of observed events = 3000, number of CCSN = 1000, transformation: NMO, channel PS, cut: 20-500 ms, 0.2-100 MeV.

True Model	Reconstructed Model					
	Warren	Tamborra	Nakazato	Bollig	Fornax	Sukhbold
Warren	100.0 %	0.0 %	0.0 %	0.0 %	0.0 %	0.0 %
Tamborra	0.0 %	100.0 %	0.0 %	0.0 %	0.0 %	0.0 %
Nakazato	0.0 %	0.0 %	100.0 %	0.0 %	0.0 %	0.0 %
Bollig	0.0 %	0.0 %	0.0 %	76.1 %	0.0 %	23.9 %
Fornax	0.0 %	0.0 %	0.0 %	0.0 %	100.0 %	0.0 %
Sukhbold	0.0 %	0.0 %	0.0 %	16.1 %	0.0 %	83.9 %

TABLE B.30: Accuracy of the model discrimination for the unbinned likelihood. Parameters: number of observed events = 3000, number of CCSN = 1000, transformation: NMO, channel PS, cut: 20-500 ms, 0.2-100 MeV.

B.3.1.5 Number of observed events = 5000

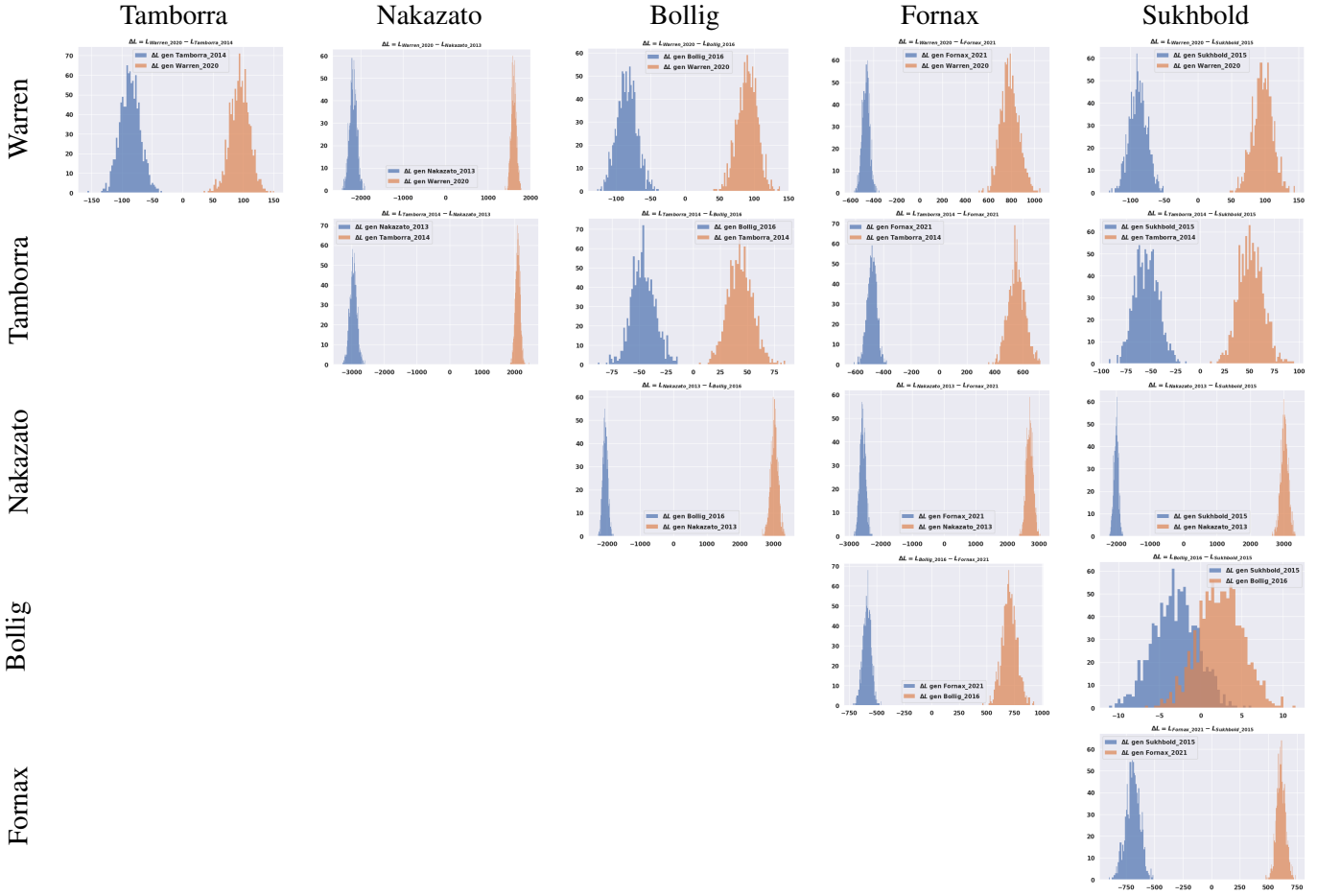


TABLE B.31: Uninned ΔL distributions for the 6 models considered. for the unbinned likelihood. Parameters: number of observed events = 5000, number of CCSN = 1000, transformation: NMO, channel PS, cut: 20-500 ms, 0.2-100 MeV.

True Model	Reconstructed Model					
	Warren	Tamborra	Nakazato	Bollig	Fornax	Sukhbold
Warren	100.0 %	0.0 %	0.0 %	0.0 %	0.0 %	0.0 %
Tamborra	0.0 %	100.0 %	0.0 %	0.0 %	0.0 %	0.0 %
Nakazato	0.0 %	0.0 %	100.0 %	0.0 %	0.0 %	0.0 %
Bollig	0.0 %	0.0 %	0.0 %	81.1 %	0.0 %	18.9 %
Fornax	0.0 %	0.0 %	0.0 %	0.0 %	100.0 %	0.0 %
Sukhbold	0.0 %	0.0 %	0.0 %	12.3 %	0.0 %	87.7 %

TABLE B.32: Accuracy of the model discrimination for the unbinned likelihood. Parameters: number of observed events = 5000, number of CCSN = 1000, transformation: NMO, channel PS, cut: 20-500 ms, 0.2-100 MeV.

B.3.2 Adiabatic transformation using inverted mass ordering (IMO)

B.3.2.1 Number of observed events = 100

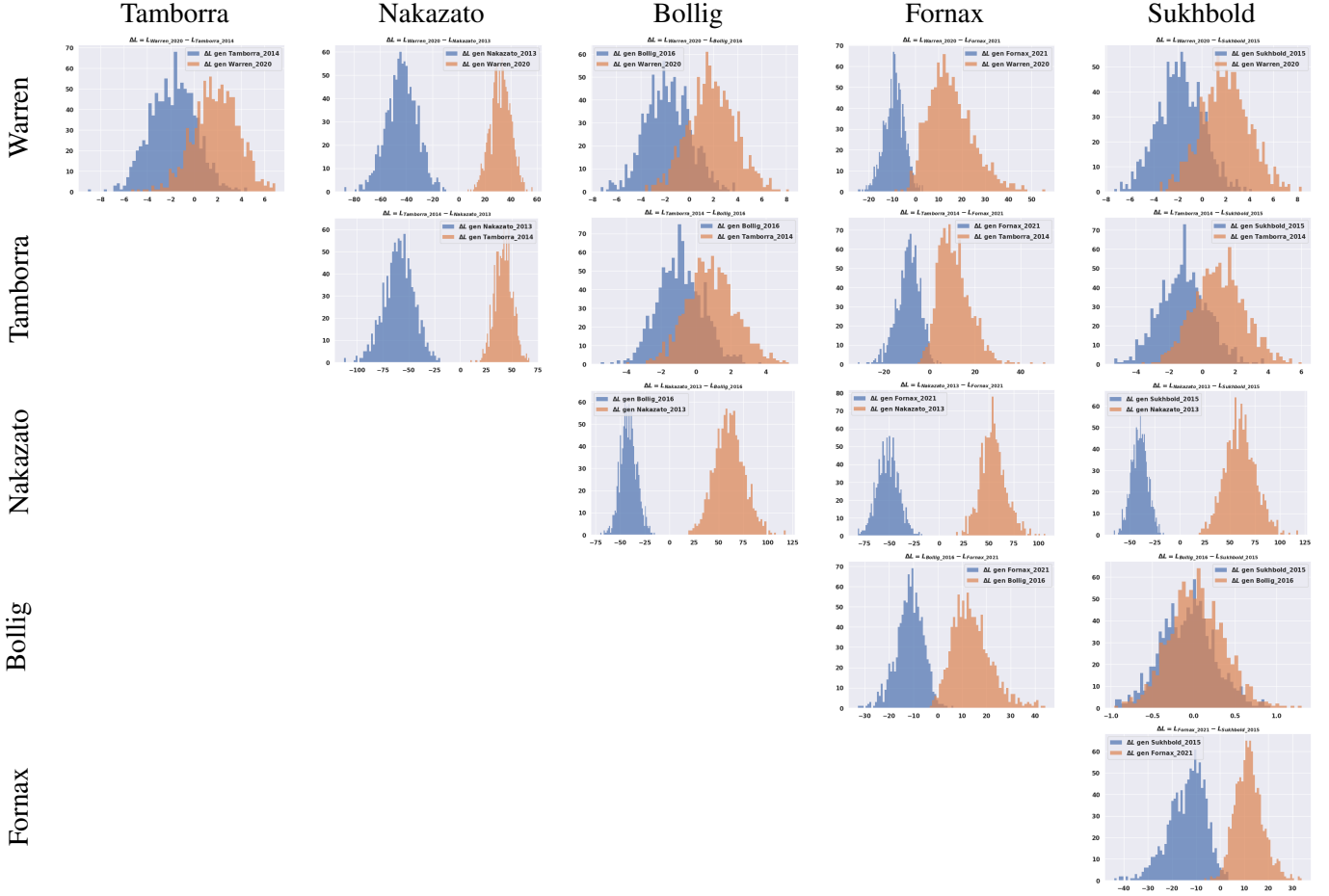


TABLE B.33: Uninned ΔL distributions for the 6 models considered. for the unbinned likelihood. Parameters: number of observed events = 100, number of CCSN = 1000, transformation: IMO, channel PS, cut: 20-500 ms, 0.2-100 MeV.

True Model	Reconstructed Model					
	Warren	Tamborra	Nakazato	Bollig	Fornax	Sukhbold
Warren	74.5 %	10.7 %	0.0 %	7.8 %	1.2 %	5.8 %
Tamborra	12.2 %	61.0 %	0.0 %	11.6 %	2.4 %	12.8 %
Nakazato	0.0 %	0.0 %	100.0 %	0.0 %	0.0 %	0.0 %
Bollig	12.0 %	19.3 %	0.0 %	31.1 %	0.7 %	36.9 %
Fornax	1.0 %	0.8 %	0.0 %	0.1 %	97.7 %	0.4 %
Sukhbold	12.2 %	16.1 %	0.0 %	26.1 %	1.0 %	44.6 %

TABLE B.34: Accuracy of the model discrimination for the unbinned likelihood. Parameters: number of observed events = 100, number of CCSN = 1000, transformation: IMO, channel PS, cut: 20-500 ms, 0.2-100 MeV.

B.3.2.2 Number of observed events = 300

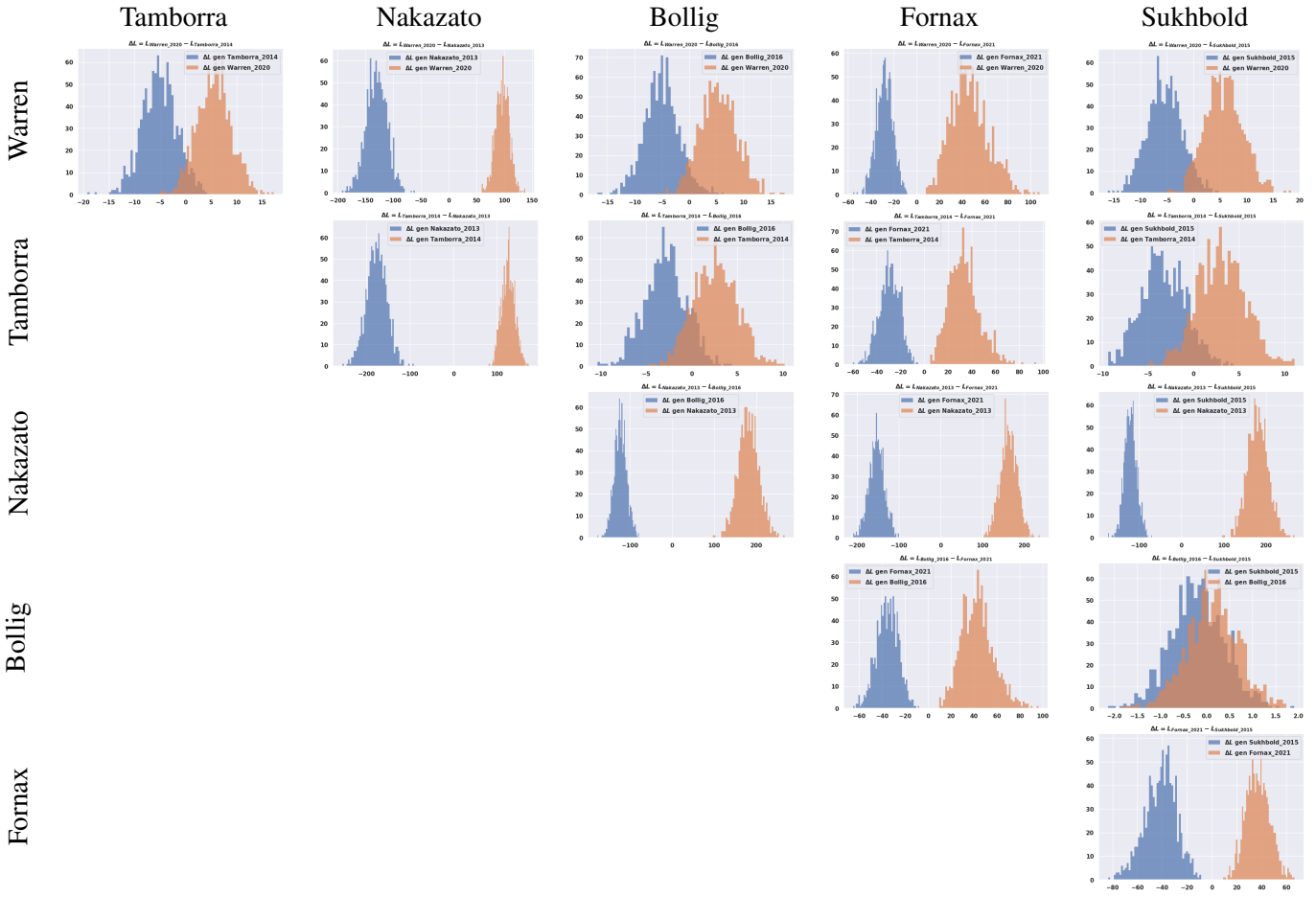


TABLE B.35: Uninned ΔL distributions for the 6 models considered. for the unbinned likelihood. Parameters: number of observed events = 300, number of CCSN = 1000, transformation: IMO, channel PS, cut: 20-500 ms, 0.2-100 MeV.

True Model	Reconstructed Model					
	Warren	Tamborra	Nakazato	Bollig	Fornax	Sukhbold
Warren	91.6%	3.5%	0.0%	2.4%	0.0%	2.5%
Tamborra	5.2%	80.5%	0.0%	9.3%	0.0%	5.0%
Nakazato	0.0%	0.0%	100.0%	0.0%	0.0%	0.0%
Bollig	4.6%	9.1%	0.0%	49.2%	0.0%	37.1%
Fornax	0.0%	0.0%	0.0%	0.0%	100.0%	0.0%
Sukhbold	3.9%	6.7%	0.0%	28.6%	0.0%	60.8%

TABLE B.36: Accuracy of the model discrimination for the unbinned likelihood. Parameters: number of observed events = 300, number of CCSN = 1000, transformation: IMO, channel PS, cut: 20-500 ms, 0.2-100 MeV.

B.3.2.3 Number of observed events = 1000

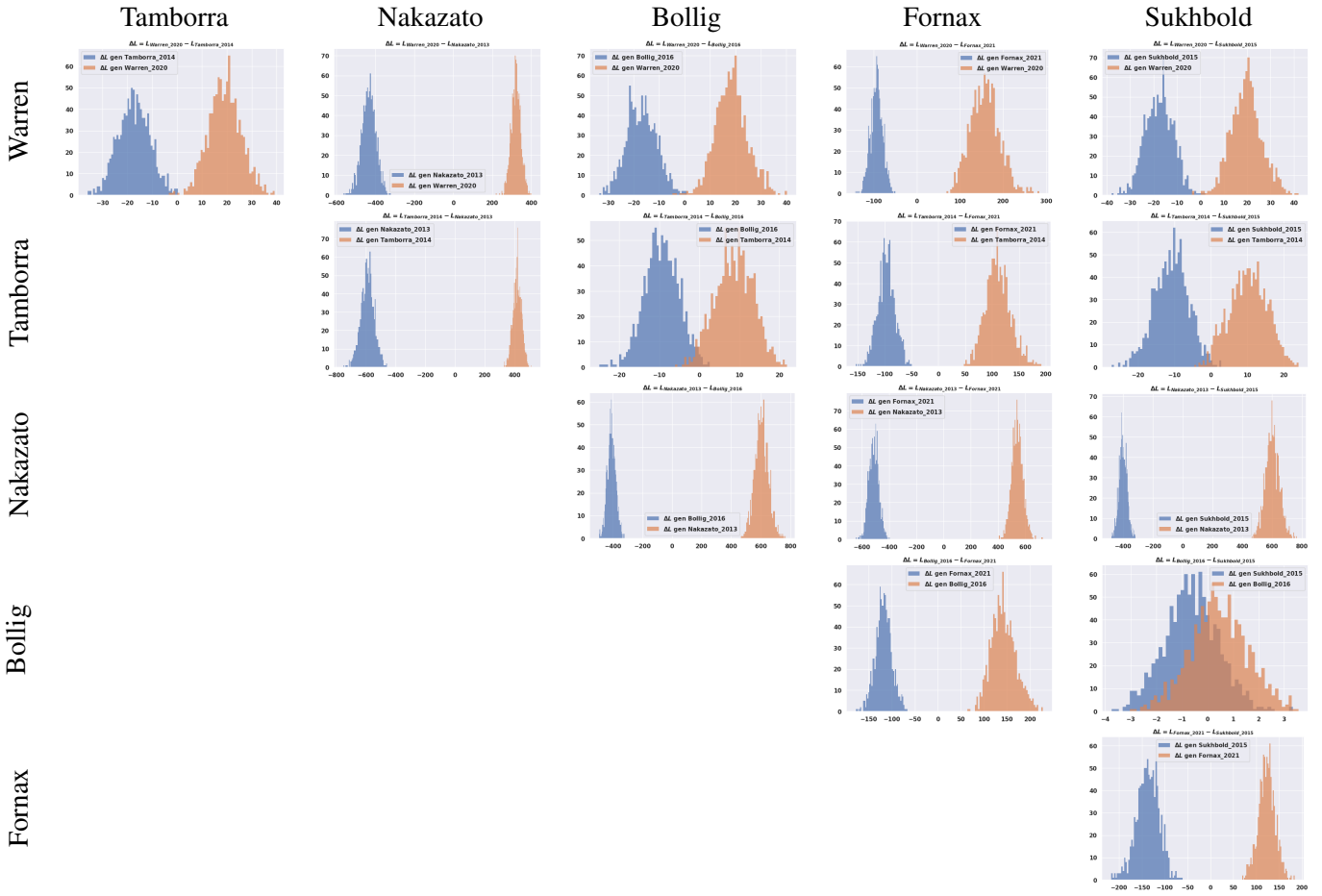


TABLE B.37: Uninned ΔL distributions for the 6 models considered. for the unbinned likelihood. Parameters: number of observed events = 1000, number of CCSN = 1000, transformation: IMO, channel PS, cut: 20-500 ms, 0.2-100 MeV.

True Model	Reconstructed Model					
	Warren	Tamborra	Nakazato	Bollig	Fornax	Sukhbold
Warren	99.4 %	0.2 %	0.0 %	0.3 %	0.0 %	0.1 %
Tamborra	0.1 %	96.3 %	0.0 %	3.1 %	0.0 %	0.5 %
Nakazato	0.0 %	0.0 %	100.0 %	0.0 %	0.0 %	0.0 %
Bollig	0.3 %	1.0 %	0.0 %	64.5 %	0.0 %	34.2 %
Fornax	0.0 %	0.0 %	0.0 %	0.0 %	100.0 %	0.0 %
Sukhbold	0.2 %	0.3 %	0.0 %	26.3 %	0.0 %	73.2 %

TABLE B.38: Accuracy of the model discrimination for the unbinned likelihood. Parameters: number of observed events = 1000, number of CCSN = 1000, transformation: IMO, channel PS, cut: 20-500 ms, 0.2-100 MeV.

B.3.2.4 Number of observed events = 3000

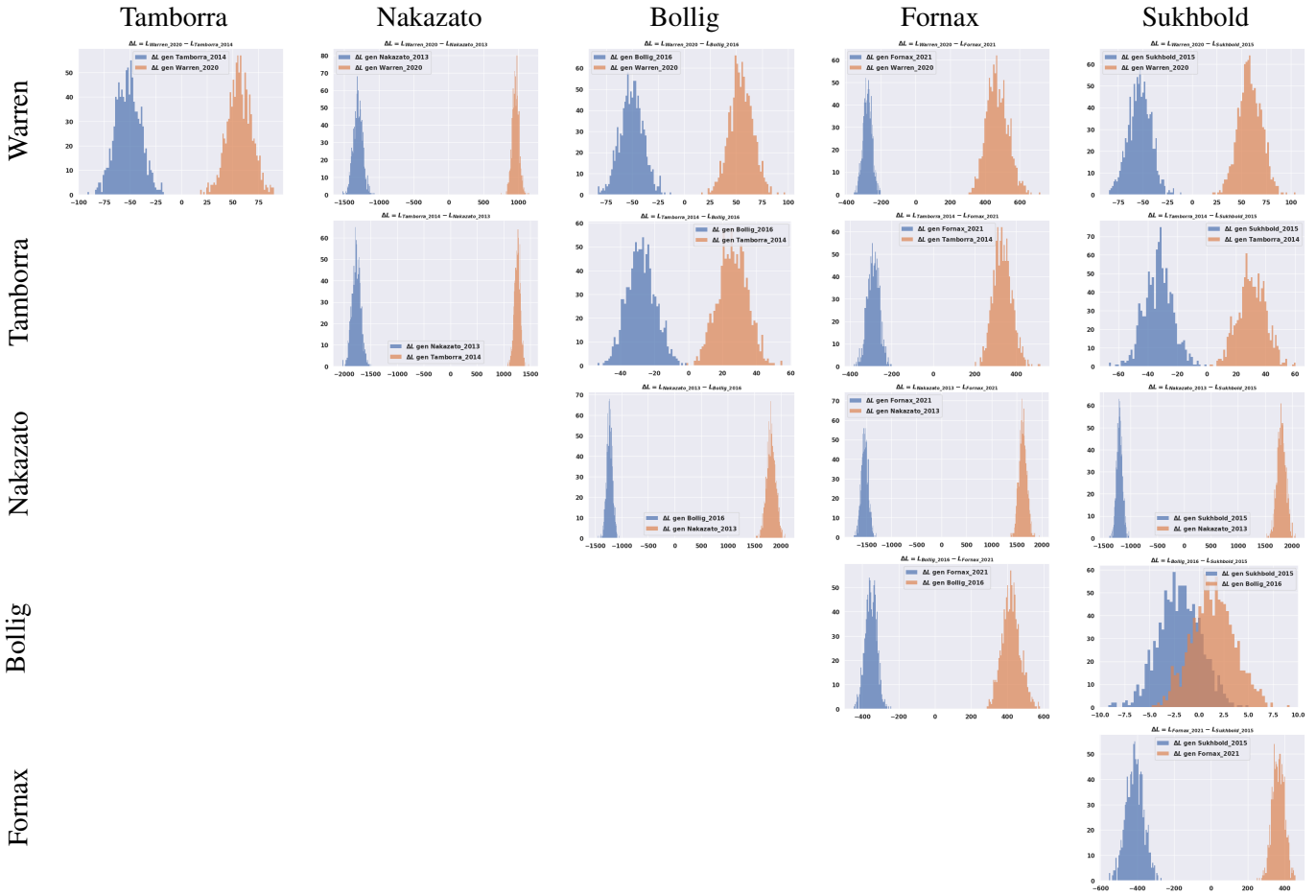


TABLE B.39: Uninned ΔL distributions for the 6 models considered. for the unbinned likelihood. Parameters: number of observed events = 3000, number of CCSN = 1000, transformation: IMO, channel PS, cut: 20-500 ms, 0.2-100 MeV.

True Model	Reconstructed Model					
	Warren	Tamborra	Nakazato	Bollig	Fornax	Sukhbold
Warren	100.0 %	0.0 %	0.0 %	0.0 %	0.0 %	0.0 %
Tamborra	0.0 %	99.9 %	0.0 %	0.1 %	0.0 %	0.0 %
Nakazato	0.0 %	0.0 %	100.0 %	0.0 %	0.0 %	0.0 %
Bollig	0.0 %	0.0 %	0.0 %	74.1 %	0.0 %	25.9 %
Fornax	0.0 %	0.0 %	0.0 %	0.0 %	100.0 %	0.0 %
Sukhbold	0.0 %	0.0 %	0.0 %	18.6 %	0.0 %	81.4 %

TABLE B.40: Accuracy of the model discrimination for the unbinned likelihood. Parameters: number of observed events = 3000, number of CCSN = 1000, transformation: IMO, channel PS, cut: 20-500 ms, 0.2-100 MeV.

B.3.2.5 Number of observed events = 5000

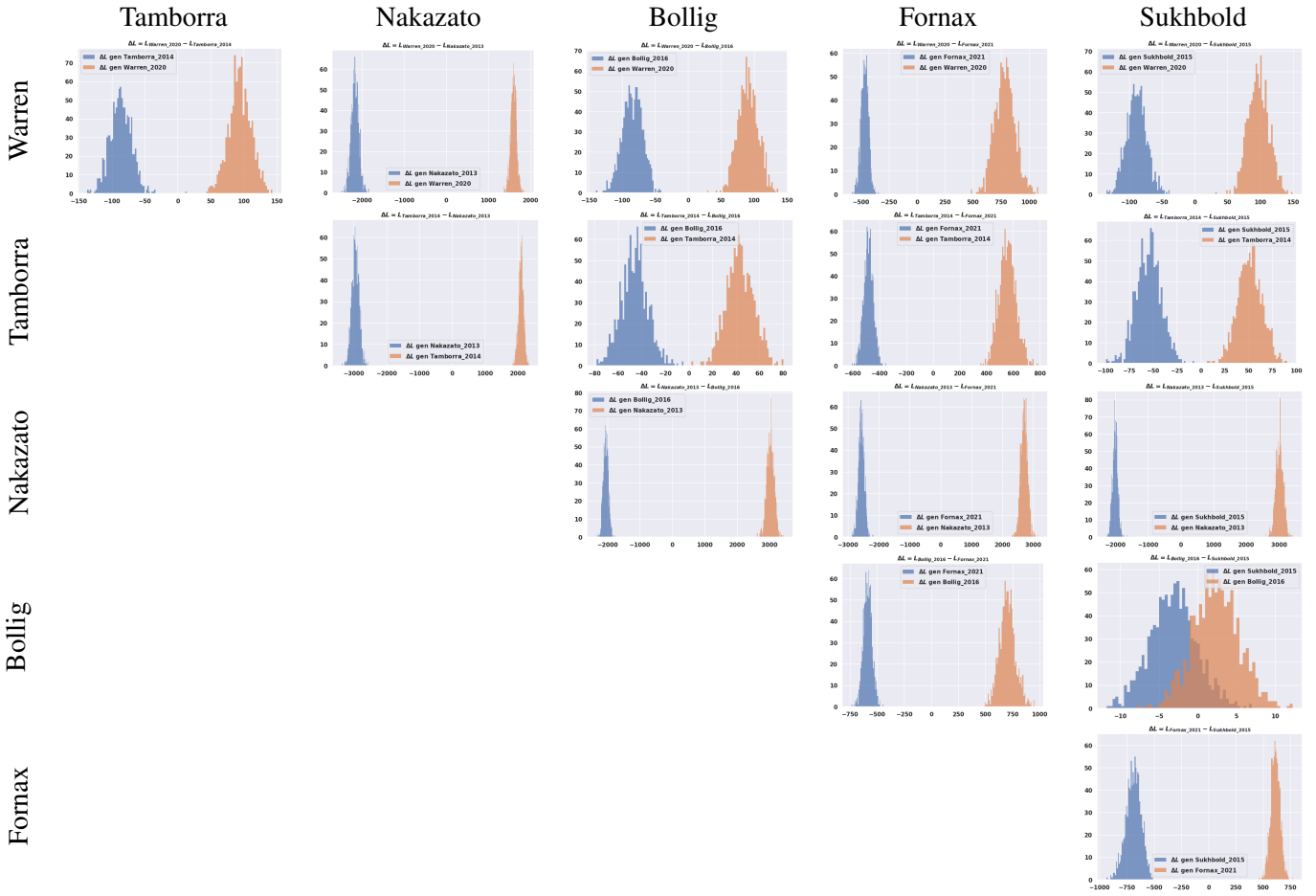


TABLE B.41: Uninned ΔL distributions for the 6 models considered. for the unbinned likelihood. Parameters: number of observed events = 5000, number of CCSN = 1000, transformation: IMO, channel PS, cut: 20-500 ms, 0.2-100 MeV.

True Model	Reconstructed Model					
	Warren	Tamborra	Nakazato	Bollig	Fornax	Sukhbold
Warren	100.0 %	0.0 %	0.0 %	0.0 %	0.0 %	0.0 %
Tamborra	0.0 %	100.0 %	0.0 %	0.0 %	0.0 %	0.0 %
Nakazato	0.0 %	0.0 %	100.0 %	0.0 %	0.0 %	0.0 %
Bollig	0.0 %	0.0 %	0.0 %	78.5 %	0.0 %	21.5 %
Fornax	0.0 %	0.0 %	0.0 %	0.0 %	100.0 %	0.0 %
Sukhbold	0.0 %	0.0 %	0.0 %	14.4 %	0.0 %	85.6 %

TABLE B.42: Accuracy of the model discrimination for the unbinned likelihood. Parameters: number of observed events = 5000, number of CCSN = 1000, transformation: IMO, channel PS, cut: 20-500 ms, 0.2-100 MeV.

Bibliography

- [1] W. Pauli. *Pauli letter collection: Letter to Lise Meitner*. Typed copy. 1930.
- [2] F. Reines and C. L. Cowan. “The Neutrino”. In: *Nature* 178 (1956), p. 446. DOI: [10.1038/178446a0](https://doi.org/10.1038/178446a0).
- [3] Nobel Foundation. URL: https://www.nobelprize.org/nobel_prizes/physics/laureates/2015/ (visited on 09/04/2018).
- [4] T. Adam et al. *JUNO Conceptual Design Report*. 2015. arXiv: [1508.07166](https://arxiv.org/abs/1508.07166) [physics.ins-det].
- [5] Fengpeng An et al. “Neutrino physics with JUNO”. In: *Journal of Physics G: Nuclear and Particle Physics* 43.3 (2016), p. 030401. DOI: [10.1088/0954-3899/43/3/030401](https://doi.org/10.1088/0954-3899/43/3/030401).
- [6] Barbara Clerbaux et al. “Study of Using Machine Learning for Level 1 Trigger Decision in JUNO Experiment”. In: *IEEE Transactions on Nuclear Science* 68.8 (2021), p. 2187. DOI: [10.1109/TNS.2021.3085428](https://doi.org/10.1109/TNS.2021.3085428).
- [7] *Standard model*. 2016. URL: https://cosmology.education/images/standard_model.png (visited on 09/04/2018).
- [8] H. Bethe and R. Peierls. “The "Neutrino"”. In: *Nature* 133 (1934), p. 532. DOI: [10.1038/133532a0](https://doi.org/10.1038/133532a0).
- [9] L. Meitner and W. Orthmann. “Über eine absolute Bestimmung der Energie der primären β -Strahlen von Radium E”. In: *Zeitschrift für Physik* 60 (1930), p. 143. DOI: [10.1007/BF01339819](https://doi.org/10.1007/BF01339819).
- [10] N. Bohr. “Faraday lecture: Chemistry and the quantum theory of atomic constitution”. In: *Journal of the Chemical Society* (1932), p. 349. DOI: [10.1039/JR9320000349](https://doi.org/10.1039/JR9320000349).
- [11] J. Chadwick. “Possible Existence of a Neutron”. In: *Nature* 129 (1932), p. 312. DOI: [10.1038/129312a0](https://doi.org/10.1038/129312a0).
- [12] John Whelan and Jr. Iben Icko. “Binaries and Supernovae of Type I”. In: *The Astrophysical Journal* 186 (1973), p. 1007. DOI: [10.1086/152565](https://doi.org/10.1086/152565).
- [13] E. Fermi. “Versuch einer Theorie der β -Strahlen. I”. In: *Zeitschrift für Physik* 88 (1934), p. 161. DOI: [10.1007/BF01351864](https://doi.org/10.1007/BF01351864).
- [14] “The Reines-Cowan experiments: Detecting the Poltergeist”. In: *Los Alamos Science* 25 (1997), p. 4.
- [15] C. L. Cowan et al. “Large Liquid Scintillation Detectors”. In: *Physical Review* 90 (1953), p. 493. DOI: [10.1103/PhysRev.90.493](https://doi.org/10.1103/PhysRev.90.493).
- [16] F. Reines and C. L. Cowan. “Detection of the Free Neutrino”. In: *Physical Review* 92 (1953), p. 830. DOI: [10.1103/PhysRev.92.830](https://doi.org/10.1103/PhysRev.92.830).
- [17] C. S. Wu et al. “Experimental Test of Parity Conservation in β Decay”. In: *Phys. Rev.* 105 (1957), p. 1413. DOI: [10.1103/PhysRev.105.1413](https://doi.org/10.1103/PhysRev.105.1413).
- [18] M. Goldhaber, L. Grodzins, and A. W. Sunyar. “Helicity of Neutrinos”. In: *Phys. Rev.* 109 (1958), p. 1015. DOI: [10.1103/PhysRev.109.1015](https://doi.org/10.1103/PhysRev.109.1015).
- [19] E. J. Konopinski and L. M. Langer. “The Experimental Clarification of the Theory of β -Decay”. In: *Annual Review of Nuclear Science* 2 (1953), p. 261.
- [20] Martin L. Perl et al. “Evidence for anomalous lepton production in $e^+ - e^-$ annihilation”. In: *Phys. Rev. Lett.* 35 (1975), p. 1489. DOI: [10.1103/PhysRevLett.35.1489](https://doi.org/10.1103/PhysRevLett.35.1489).
- [21] K. Kodama and others (DONUT Collaboration). “Observation of tau neutrino interactions”. In: *Phys. Lett. B* 504 (2001), p. 218. DOI: [10.1016/S0370-2693\(01\)00307-0](https://doi.org/10.1016/S0370-2693(01)00307-0).

- [22] S. Schael et al. “Precision electroweak measurements on the Z resonance”. In: *Phys. Rept.* 427 (2006), p. 257. DOI: [10.1016/j.physrep.2005.12.006](https://doi.org/10.1016/j.physrep.2005.12.006).
- [23] M. Tanabashi and others (Particle Data Group). “Review of Particle Physics”. In: *Physical Review D* 98 (2018), p. 030001.
- [24] A. S. Eddington. “The Internal Constitution of the Stars”. In: *The Scientific Monthly* 11.4 (1920), p. 297.
- [25] H. Bethe. “Energy Production in Stars”. In: *Physical Review* 55 (1939), p. 434. DOI: [10.1103/PhysRev.55.434](https://doi.org/10.1103/PhysRev.55.434).
- [26] Samoil M. Bilenyk, C. Giunti, and W. Grimus. “Phenomenology of neutrino oscillations”. In: *Prog. Part. Nucl. Phys.* 43 (1999), p. 1. DOI: [10.1016/S0146-6410\(99\)00092-7](https://doi.org/10.1016/S0146-6410(99)00092-7).
- [27] Dan Maoz, Filippo Mannucci, and Gijs Nelemans. “Observational clues to the progenitors of Type-Ia supernovae”. In: *Ann. Rev. Astron. Astrophys.* 52 (2014), p. 107. DOI: [10.1146/annurev-astro-082812-141031](https://doi.org/10.1146/annurev-astro-082812-141031).
- [28] W. Hillebrandt et al. “Towards an understanding of Type Ia supernovae from a synthesis of theory and observations”. In: *Front. Phys. (Beijing)* 8 (2013), p. 116. DOI: [10.1007/s11467-013-0303-2](https://doi.org/10.1007/s11467-013-0303-2).
- [29] Barbara Clerbaux. “Physique des particules”. Phys-F416, ULB. 2017.
- [30] L. Wolfenstein. “Neutrino oscillations in matter”. In: *Phys. Rev. D* 17-9 (1978), p. 2369. DOI: [10.1103/PhysRevD.17.2369](https://doi.org/10.1103/PhysRevD.17.2369).
- [31] P. Lipari. “Introduction to neutrino physics”. In: *2001 CERN - CLAF School of High-energy Physics*. Università di Roma. CERN, 2003, p. 115. DOI: [10.5170/CERN-2003-003.115](https://doi.org/10.5170/CERN-2003-003.115).
- [32] David Dooling et al. “Matter effects in four-neutrino mixing”. In: *Physical review. D, Particles and fields* 61.7 (2000), p. 1. DOI: [10.1103/PhysRevD.61.073011](https://doi.org/10.1103/PhysRevD.61.073011).
- [33] Pablo F. de Salas et al. “Neutrino Mass Ordering from Oscillations and Beyond: 2018 Status and Future Prospects”. In: *Frontiers in Astronomy and Space Sciences* 5 (2018). DOI: [10.3389/fspas.2018.00036](https://doi.org/10.3389/fspas.2018.00036).
- [34] A. Kappes. *KM3NeT: A Next Generation Neutrino Telescope in the Mediterranean Sea*. 2007. DOI: <https://doi.org/10.48550/arXiv.0711.0563>.
- [35] James Strait. “DUNE Physics”. In: *17th International Workshop on Neutrino Factories and Future Neutrino Facilities*. 2015. DOI: [10.3390/instruments5040031](https://doi.org/10.3390/instruments5040031).
- [36] T. Ishida. “T2HK: J-PARC upgrade plan for future and beyond T2K”. In: *15th International Workshop on Neutrino Factories, Super Beams and Beta Beams*. 2013. arXiv: [1311.5287](https://arxiv.org/abs/1311.5287) [hep-ex].
- [37] Y. Abe et al. “Indication of Reactor $\bar{\nu}_e$ Disappearance in the Double Chooz Experiment”. In: *Phys. Rev. Lett.* 108 (2012), p. 131801. DOI: [10.1103/PhysRevLett.108.131801](https://doi.org/10.1103/PhysRevLett.108.131801).
- [38] F.P. An et al. Daya Bay Collaboration. “The detector system of the Daya Bay reactor neutrino experiment”. In: *Nucl. Instrum. Methods A* 811 (2016), p. 133.
- [39] J.K. Ahn et al. RENO Collaboration. “Production and optical properties of Gd-loaded liquid scintillator for the RENO neutrino detector”. In: *Nucl. Instrum. Methods A* 707 (2013), p. 45. DOI: [10.1016/j.nima.2012.12.121](https://doi.org/10.1016/j.nima.2012.12.121).
- [40] D. Adey et al. “Measurement of the Electron Antineutrino Oscillation with 1958 Days of Operation at Daya Bay”. In: *Phys. Rev. Lett.* 121 (2018), p. 241805. DOI: [10.1103/PhysRevLett.121.241805](https://doi.org/10.1103/PhysRevLett.121.241805).
- [41] H. de Kerret and Y. et al. Abe. “The Double Chooz antineutrino detectors”. In: *The European Physical Journal C* 82 (2022). DOI: [10.1140/epjc/s10052-022-10726-x](https://doi.org/10.1140/epjc/s10052-022-10726-x).
- [42] Yoichiro Suzuki. “The Super-Kamiokande experiment”. In: *Eur. Phys. J. C* 79.4 (2019), p. 298. DOI: [10.1140/epjc/s10052-019-6796-2](https://doi.org/10.1140/epjc/s10052-019-6796-2).
- [43] M. C. Chen. “The SNO liquid scintillator project”. In: *Nucl. Phys. B Proc. Suppl.* 145 (2005), pp. 65–68. DOI: [10.1016/j.nuclphysbps.2005.03.037](https://doi.org/10.1016/j.nuclphysbps.2005.03.037).

- [44] Borexino Collaboration et al. “Final results of Borexino Phase-I on low-energy solar neutrino spectroscopy”. In: *Physical Review D* 89.11 (June 25, 2014). Publisher: American Physical Society, p. 112007. DOI: [10.1103/PhysRevD.89.112007](https://doi.org/10.1103/PhysRevD.89.112007).
- [45] P. Aliani et al. “KamLAND and the determination of neutrino mixing parameters in the post SNO-NC era”. In: *New J. Phys.* 5 (2003), p. 2. DOI: [10.1088/1367-2630/5/1/302](https://doi.org/10.1088/1367-2630/5/1/302).
- [46] Y. Suzuki. “Solar neutrino results from Kamiokande and Super-Kamiokande”. In: *Conf. Proc. C* 960613 (1996), p. 73.
- [47] S. Abe and et al. “Precision Measurement of Neutrino Oscillation Parameters with KamLAND”. In: *Physical Review Letters* 100 (2008), p. 221803. DOI: [10.1103/PhysRevLett.100.221803](https://doi.org/10.1103/PhysRevLett.100.221803). eprint: [0801.4589](https://arxiv.org/abs/0801.4589).
- [48] Elena V Korolkova, ANTARES collaboration, et al. “The Status of the ANTARES experiment”. In: *Nuclear Physics B-Proceedings Supplements* 136 (2004), p. 69.
- [49] M. G. et al. Aartsen. “IceCube-Gen2 - The Next Generation Neutrino Observatory at the South Pole: Contributions to ICRC 2015”. In: (2015). arXiv: [1510.05228](https://arxiv.org/abs/1510.05228) [astro-ph.IM].
- [50] E. et al. Aslanides. *A deep sea telescope for high-energy neutrinos*. 1999. arXiv: [astro-ph/9907432](https://arxiv.org/abs/astro-ph/9907432).
- [51] S. et al. Adrián-Martínez. “Measurement of atmospheric neutrino oscillations with the ANTARES neutrino telescope”. In: *Physics Letters B* 714 (2012), p. 224. DOI: [10.1016/j.physletb.2012.07.002](https://doi.org/10.1016/j.physletb.2012.07.002).
- [52] M.G. Aartsen et al. “Neutrino oscillation studies with IceCube-DeepCore”. In: *Nuclear Physics B* 908 (2016), p. 161. DOI: [10.1016/j.nuclphysb.2016.03.028](https://doi.org/10.1016/j.nuclphysb.2016.03.028).
- [53] Pn Adamson et al. “The NuMI neutrino beam”. In: *Nuclear Instruments and Methods in Physics Research Section A: Accelerators, Spectrometers, Detectors and Associated Equipment* 806 (2016), p. 279. DOI: <https://doi.org/10.1016/j.nima.2015.08.063>.
- [54] Justin Evans. *The MINOS experiment: results and prospects*. 2013. arXiv: [1307.0721](https://arxiv.org/abs/1307.0721) [hep-ex]. URL: <https://arxiv.org/abs/1307.0721>.
- [55] K. Kaneyuki. *T2K experiment*. 2005. DOI: [10.1016/j.nuclphysbps.2005.04.001](https://doi.org/10.1016/j.nuclphysbps.2005.04.001).
- [56] D. S. et al. Ayres. “The NOvA Technical Design Report”. In: (2007). DOI: [10.2172/935497](https://doi.org/10.2172/935497).
- [57] Peter B. Denton. “Probing CP Violation with Neutrino Disappearance Alone”. In: *Phys. Rev. Lett.* 133 (3 2024), p. 031801. DOI: [10.1103/PhysRevLett.133.031801](https://doi.org/10.1103/PhysRevLett.133.031801).
- [58] Ivan Esteban et al. “The fate of hints: updated global analysis of three-flavor neutrino oscillations”. In: *Journal of High Energy Physics* 2020.9 (2020). DOI: [10.1007/jhep09\(2020\)178](https://doi.org/10.1007/jhep09(2020)178).
- [59] M Aker, M Balzer, and D et al. Batzler. “KATRIN: status and prospects for the neutrino mass and beyond”. In: *Journal of Physics G: Nuclear and Particle Physics* 49 (2022), p. 100501. DOI: [10.1088/1361-6471/ac834e](https://doi.org/10.1088/1361-6471/ac834e).
- [60] E. Richard et al. “Measurements of the atmospheric neutrino flux by Super-Kamiokande: Energy spectra, geomagnetic effects, and solar modulation”. In: *Phys. Rev. D* 94 (5 2016), p. 052001. DOI: [10.1103/PhysRevD.94.052001](https://doi.org/10.1103/PhysRevD.94.052001).
- [61] Osamu Sato. “OPERA Results”. In: *Nucl. Phys. B Proc. Suppl.* 253-255 (2014), p. 147. DOI: [10.1016/j.nuclphysbps.2014.09.036](https://doi.org/10.1016/j.nuclphysbps.2014.09.036).
- [62] Zheng-Wei Liu, Friedrich K. Röpke, and Zhanwen Han. “Type Ia Supernova Explosions in Binary Systems: A Review”. In: *Research in Astronomy and Astrophysics* 23.8 (2023), p. 082001. DOI: [10.1088/1674-4527/acd89e](https://doi.org/10.1088/1674-4527/acd89e).
- [63] “JUNO Physics and Detector”. In: *Progress in Particle and Nuclear Physics* 123 (2022), p. 103927. DOI: [10.1016/j.pnpnp.2021.103927](https://doi.org/10.1016/j.pnpnp.2021.103927).
- [64] Clément Bordereau. “Performances of the 3” PMT front-end electronics in the JUNO experiment and study of its impact on charge and time measurements.” PhD thesis. 2022. URL: <http://www.theses.fr/2022BORD0462>.

- [65] Angel Abusleme et al. “The JUNO experiment Top Tracker”. In: *Nuclear Instruments and Methods in Physics Research Section A: Accelerators, Spectrometers, Detectors and Associated Equipment* 1057 (2023), p. 168680. DOI: [10.1016/j.nima.2023.168680](https://doi.org/10.1016/j.nima.2023.168680).
- [66] J.B. Birks. *The Theory and Practice of Scintillation Counting*. Pergamon, Oxford, 1964.
- [67] C. N. Chou. “The Nature of the Saturation Effect of Fluorescent Scintillators”. In: *Phys. Rev.* 87.5 (1952), pp. 904–905. DOI: [10.1103/PhysRev.87.904](https://doi.org/10.1103/PhysRev.87.904).
- [68] Masheng Yang et al. “Measurement of proton quenching in a LAB-based liquid scintillator”. In: *Radiation Detection Technology and Methods* 3.1 (2018). DOI: [10.1007/s41605-018-0049-z](https://doi.org/10.1007/s41605-018-0049-z).
- [69] A. Abusleme et al. “Optimization of the JUNO liquid scintillator composition using a Daya Bay antineutrino detector”. In: *Nuclear Instruments and Methods in Physics Research Section A: Accelerators, Spectrometers, Detectors and Associated Equipment* 988 (2021), p. 164823. DOI: [10.1016/j.nima.2020.164823](https://doi.org/10.1016/j.nima.2020.164823).
- [70] P. Lombardi et al. “Distillation and stripping pilot plants for the JUNO neutrino detector: Design, operations and reliability”. In: *Nuclear Instruments and Methods in Physics Research Section A: Accelerators, Spectrometers, Detectors and Associated Equipment* 925 (2019), p. 6. DOI: <https://doi.org/10.1016/j.nima.2019.01.071>.
- [71] Angel Abusleme et al. “The design and sensitivity of JUNO’s scintillator radiopurity pre-detector OSIRIS”. In: *The European Physical Journal C* 81.11 (2021). DOI: [10.1140/epjc/s10052-021-09544-4](https://doi.org/10.1140/epjc/s10052-021-09544-4).
- [72] Hamamatsu Photonics. “PHOTOMULTIPLIER TUBES Basics and Applications”. In: fourth. Hamamatsu Photonics, 2020, p. 26.
- [73] Lin Chen et al. “Optimization of the electron collection efficiency of a large area MCP-PMT for the JUNO experiment”. In: *Nuclear Instruments and Methods in Physics Research Section A: Accelerators, Spectrometers, Detectors and Associated Equipment* 827 (2016), p. 124. DOI: <https://doi.org/10.1016/j.nima.2016.04.100>.
- [74] Jun Weng et al. *Single electron charge spectra of 8-inch high-collection-efficiency MCP-PMTs*. 2024. arXiv: [2402.13266](https://arxiv.org/abs/2402.13266) [physics.ins-det].
- [75] Angel Abusleme et al. “Calibration strategy of the JUNO experiment”. In: *Journal of High Energy Physics* 2021.3 (2021). DOI: [10.1007/jhep03\(2021\)004](https://doi.org/10.1007/jhep03(2021)004).
- [76] Yang Han. “Dual Calorimetry for High Precision Neutrino Oscillation Measurement at JUNO Experiment”. PhD thesis. 2021. URL: <https://theses.hal.science/tel-03295420>.
- [77] Victor Lebrin. “Towards the Detection of Core-Collapse Supernovae Burst Neutrinos with the 3-inch PMT System of the JUNO Detector”. 2022NANU4080. PhD thesis. 2022. URL: <http://www.theses.fr/2022NANU4080>.
- [78] F. P. An et al. “Observation of Electron-Antineutrino Disappearance at Daya Bay”. In: *Physical Review Letters* 108.17 (2012). DOI: [10.1103/physrevlett.108.171803](https://doi.org/10.1103/physrevlett.108.171803).
- [79] Y. Abe et al. “Improved measurements of the neutrino mixing angle θ_{13} with the Double Chooz detector”. In: *Journal of High Energy Physics* 2014.10 (2014). DOI: [10.1007/jhep10\(2014\)086](https://doi.org/10.1007/jhep10(2014)086).
- [80] J. H. Choi et al. “Observation of Energy and Baseline Dependent Reactor Antineutrino Disappearance in the RENO Experiment”. In: *Phys. Rev. Lett.* 116 (21 2016), p. 211801. DOI: [10.1103/PhysRevLett.116.211801](https://doi.org/10.1103/PhysRevLett.116.211801).
- [81] Selma Conforti et al. *CATIROC: an integrated chip for neutrino experiments using photomultiplier tubes*. 2021. eprint: [2012.01565](https://arxiv.org/abs/2012.01565) (physics.ins-det). URL: <https://arxiv.org/abs/2012.01565>.
- [82] Feng Gao et al. “Time Performance of large area 20 inch MCP-PMTs”. In: *2017 IEEE Nuclear Science Symposium and Medical Imaging Conference (NSS/MIC)*. 2017, p. 1. DOI: [10.1109/NSSMIC.2017.8532598](https://doi.org/10.1109/NSSMIC.2017.8532598).
- [83] Lin Chen et al. “A new large area MCP-PMT for high energy detection”. In: *Scientific Reports* 13.1 (2023). DOI: [10.1038/s41598-023-47818-x](https://doi.org/10.1038/s41598-023-47818-x).

- [84] Yao Zhu et al. “Study of Time Characteristic Test Method of the Fast Timing MCP-PMT”. In: *2019 IEEE Nuclear Science Symposium and Medical Imaging Conference (NSS/MIC)*. 2019, p. 1. DOI: [10.1109/NSS/MIC42101.2019.9059973](https://doi.org/10.1109/NSS/MIC42101.2019.9059973).
- [85] Qi Wu et al. “The Status of the 20 inch MCP-PMT and its APR Test Result”. In: *2019 IEEE Nuclear Science Symposium and Medical Imaging Conference (NSS/MIC)*. 2019, p. 1. DOI: [10.1109/NSS/MIC42101.2019.9059825](https://doi.org/10.1109/NSS/MIC42101.2019.9059825).
- [86] Angel Abusleme et al. “Mass testing and characterization of 20-inch PMTs for JUNO”. In: *The European Physical Journal C* 82.12 (2022). DOI: [10.1140/epjc/s10052-022-11002-8](https://doi.org/10.1140/epjc/s10052-022-11002-8).
- [87] W. David Arnett et al. “Supernova 1987A”. In: *Annual Review of Astronomy and Astrophysics* 27.1 (1989), p. 629. DOI: [10.1146/annurev.aa.27.090189.003213](https://doi.org/10.1146/annurev.aa.27.090189.003213).
- [88] Kohta Murase. “Active Galactic Nuclei as High-Energy Neutrino Sources”. In: *Proceedings of Science ICRC2017* (2018), p. 009. DOI: [10.22323/1.306.0009](https://doi.org/10.22323/1.306.0009).
- [89] Cheng Zha. “Muon-induced spallation neutrons in the JUNO central detector”. In: *Journal of Physics G: Nuclear and Particle Physics* 43.9 (2016), p. 095003. DOI: [10.1088/0954-3899/43/9/095003](https://doi.org/10.1088/0954-3899/43/9/095003).
- [90] Y.-F. Wang et al. “Predicting neutron production from cosmic-ray muons”. In: *Phys. Rev. D* 64 (1 2001), p. 013012. DOI: [10.1103/PhysRevD.64.013012](https://doi.org/10.1103/PhysRevD.64.013012).
- [91] Angel Abusleme et al. “Radioactivity control strategy for the JUNO detector”. In: *Journal of High Energy Physics* 2021.11 (2021). DOI: [10.1007/jhep11\(2021\)102](https://doi.org/10.1007/jhep11(2021)102).
- [92] The JUNO Collaboration. *Potential to Identify the Neutrino Mass Ordering with Reactor Antineutrinos in JUNO*. 2024. arXiv: [2405.18008](https://arxiv.org/abs/2405.18008) [hep-ex]. URL: <https://arxiv.org/abs/2405.18008>.
- [93] S.T. Petcov and M. Piai. “The LMA MSW solution of the solar neutrino problem, inverted neutrino mass hierarchy and reactor neutrino experiments”. In: *Physics Letters B* 533.1 (2002), p. 94. DOI: [10.1016/s0370-2693\(02\)01591-5](https://doi.org/10.1016/s0370-2693(02)01591-5).
- [94] Shao-Feng Ge et al. “Determination of mass hierarchy with medium baseline reactor neutrino experiments”. In: *Journal of High Energy Physics* 2013.5 (2013). DOI: [10.1007/jhep05\(2013\)131](https://doi.org/10.1007/jhep05(2013)131).
- [95] Yu-Feng Li et al. “Unambiguous determination of the neutrino mass hierarchy using reactor neutrinos”. In: *Physical Review D* 88.1 (2013). DOI: [10.1103/physrevd.88.013008](https://doi.org/10.1103/physrevd.88.013008).
- [96] A. B. Balantekin et al. “Neutrino mass hierarchy determination and other physics potential of medium-baseline reactor neutrino oscillation experiments”. In: *Proceedings, 2013 Community Summer Study on the Future of U.S. Particle Physics: Snowmass on the Mississippi (CSS2013): Minneapolis, MN, USA, July 29-August 6, 2013*. 2013. arXiv: [1307.7419](https://arxiv.org/abs/1307.7419) [hep-ex].
- [97] R. N. Cahn and al. “White Paper: Measuring the Neutrino Mass Hierarchy”. In: *Proceedings, 2013 Community Summer Study on the Future of U.S. Particle Physics: Snowmass on the Mississippi (CSS2013): Minneapolis, MN, USA, July 29-August 6, 2013*. 2013. arXiv: [1307.5487](https://arxiv.org/abs/1307.5487) [hep-ex].
- [98] Angel Abusleme et al. “Sub-percent precision measurement of neutrino oscillation parameters with JUNO*”. In: *Chinese Physics C* 46.12 (2022), p. 123001. DOI: [10.1088/1674-1137/ac8bc9](https://doi.org/10.1088/1674-1137/ac8bc9).
- [99] P.A. Zyla et al. “Review of Particle Physics”. In: *PTEP* 2020.08 (2020), p. 083C01.
- [100] L. Hüdepohl. “Ph.D. Thesis Technische Universität München”. neutrino model data can be made available upon request at <http://mpa-garching.mpg.de/ccsnarchive/>. PhD thesis. 2013.
- [101] S. M. Adams et al. “Observing the next galactic supernova”. In: *The Astrophysical Journal* 778 (2013), p. 164. eprint: [1306.0559](https://arxiv.org/abs/1306.0559) (astro-ph.HE).
- [102] M. Ahlers, P. Mertsch, and S. Sarkar. “Cosmic ray acceleration in supernova remnants and the FERMI/PAMELA data”. In: *Physical Review D* 80 (2009), p. 123017. arXiv: [0909.4060](https://arxiv.org/abs/0909.4060) [astro-ph.HE].
- [103] A. Mirizzi et al. “Supernova neutrinos: production, oscillations and detection”. In: *La Rivista del Nuovo Cimento* 39 (2016), p. 1. arXiv: [1508.00785](https://arxiv.org/abs/1508.00785) [astro-ph.HE].

- [104] Thilo Birkenfeld. “Reconstruction of the neutrino energy spectra of galactic Core-Collapse Supernovae with the Jiangmen Underground Neutrino Observatory”. Presented to the Faculty of Mathematics, Informatics, and Natural Sciences for the degree of Doctor of Natural Sciences. PhD thesis. Aachen, Germany: RWTH Aachen University, 2023.
- [105] Iwan Morton-Blake et al. “Extending JUNO’s Astrophysical Reach with a Low-Energy Multi-Messenger Trigger System”. In: *Proceedings of 38th International Cosmic Ray Conference — PoS(ICRC2023)*. Sissa Medialab, 2023, p. 1585. DOI: [10.22323/1.444.1585](https://doi.org/10.22323/1.444.1585).
- [106] S. Al Kharusi et al. “SNEWS 2.0: a next-generation supernova early warning system for multi-messenger astronomy”. In: *New J. Phys.* 23.3 (2021), p. 031201. DOI: [10.1088/1367-2630/abde33](https://doi.org/10.1088/1367-2630/abde33).
- [107] Karolina Rozwadowska, Francesco Vissani, and Enrico Cappellaro. “On the rate of core collapse supernovae in the milky way”. In: *New Astron.* 83 (2021), p. 101498. DOI: [10.1016/j.newast.2020.101498](https://doi.org/10.1016/j.newast.2020.101498). arXiv: [2009.03438](https://arxiv.org/abs/2009.03438) [astro-ph.HE].
- [108] J. F. Beacom. “The Diffuse Supernova Neutrino Background”. In: *Annual Review of Nuclear and Particle Science* 60 (2010), p. 439.
- [109] C. Andreopoulos et al. “The GENIE neutrino Monte Carlo generator”. In: *Nuclear Instruments and Methods in Physics Research Section A: Accelerators, Spectrometers, Detectors and Associated Equipment* 614.1 (2010), p. 87. DOI: [10.1016/j.nima.2009.12.009](https://doi.org/10.1016/j.nima.2009.12.009).
- [110] Arjan Koning, Stephane Hilaire, and Stephane Goriely. “TALYS: modeling of nuclear reactions”. In: *The European Physical Journal A* 59.6 (2023). DOI: [10.1140/epja/s10050-023-01034-3](https://doi.org/10.1140/epja/s10050-023-01034-3).
- [111] Angel Abusleme et al. “Prospects for detecting the diffuse supernova neutrino background with JUNO”. In: *Journal of Cosmology and Astroparticle Physics* 2022.10 (2022), p. 033. DOI: [10.1088/1475-7516/2022/10/033](https://doi.org/10.1088/1475-7516/2022/10/033).
- [112] D. Basilico et al. “Final results of Borexino on CNO solar neutrinos”. In: *Physical Review D* 108.10 (2023). DOI: [10.1103/physrevd.108.102005](https://doi.org/10.1103/physrevd.108.102005).
- [113] A. Abusleme and et al. “Feasibility and physics potential of detecting ^8B solar neutrinos at JUNO”. In: *Chinese Physics C* 45.2 (2021), p. 023004. DOI: [10.1088/1674-1137/abd92a](https://doi.org/10.1088/1674-1137/abd92a).
- [114] K. Daum et al. “Determination of the atmospheric neutrino spectra with the Fréjus detector”. In: *Zeitschrift für Physik C Particles and Fields* 66.3 (1995), p. 417. DOI: [10.1007/bf01556368](https://doi.org/10.1007/bf01556368).
- [115] S. Abe et al. “Precision Measurement of Neutrino Oscillation Parameters with KamLAND”. In: *Physical Review Letters* 100.22 (2008). DOI: [10.1103/physrevlett.100.221803](https://doi.org/10.1103/physrevlett.100.221803).
- [116] Giulio Settanta et al. “Atmospheric neutrino spectrum reconstruction with JUNO”. In: *Proceedings of European Physical Society Conference on High Energy Physics — PoS(EPS-HEP2019)*. EPS-HEP2019. Sissa Medialab, 2020, p. 041. DOI: [10.22323/1.364.0041](https://doi.org/10.22323/1.364.0041).
- [117] T. Araki and et al. “Experimental investigation of geologically produced antineutrinos with KamLAND”. In: *Nature* 436 (2005), p. 499. DOI: [10.1038/nature03980](https://doi.org/10.1038/nature03980).
- [118] A. Gando and et al. “Partial radiogenic heat model for Earth revealed by geoneutrino measurements”. In: *Nature Geoscience* 4 (2011), p. 647. DOI: [10.1038/ngeo1205](https://doi.org/10.1038/ngeo1205).
- [119] A. Gando and et al. “Reactor On-Off Antineutrino Measurement with KamLAND”. In: *Physical Review D* 88.3 (2013), p. 033001. DOI: [10.1103/PhysRevD.88.033001](https://doi.org/10.1103/PhysRevD.88.033001).
- [120] H. Watanabe. *Geoneutrino measurement with KamLAND*. https://indico.cern.ch/event/825708/contributions/3552210/attachments/1930535/3197332/HirokoWatanabe_NGS2019.pdf. 2019.
- [121] G. Bellini and et al. “Observation of Geo-Neutrinos”. In: *Physics Letters B* 687 (2010), p. 299. DOI: [10.1016/j.physletb.2010.03.051](https://doi.org/10.1016/j.physletb.2010.03.051).
- [122] G. Bellini and et al. “Measurement of geo-neutrinos from 1353 days of Borexino”. In: *Physics Letters B* 722 (2013), p. 295. DOI: [10.1016/j.physletb.2013.04.030](https://doi.org/10.1016/j.physletb.2013.04.030).

- [123] M. Agostini and et al. "Spectroscopy of geoneutrinos from 2056 days of Borexino data". In: *Physical Review D* 92.3 (2015), p. 031101. DOI: [10.1103/PhysRevD.92.031101](https://doi.org/10.1103/PhysRevD.92.031101).
- [124] M. Agostini and et al. "Comprehensive geoneutrino analysis with Borexino". In: *Physical Review D* 101.1 (2020), p. 012009. DOI: [10.1103/PhysRevD.101.012009](https://doi.org/10.1103/PhysRevD.101.012009).
- [125] J. M. Herndon. "Feasibility of a nuclear fission reactor at the center of the earth as the energy source for the geomagnetic field". In: *Journal of Geomagnetism and Geoelectricity* 45.5 (1993), p. 423. DOI: [10.5636/jgg.45.423](https://doi.org/10.5636/jgg.45.423).
- [126] J. M. Herndon. "Substructure of the inner core of the earth". In: *Proceedings of the National Academy of Sciences* 93.2 (1996), p. 646. DOI: [10.1073/pnas.93.2.646](https://doi.org/10.1073/pnas.93.2.646).
- [127] V. D. Rusov and et al. "Geoantineutrino spectrum and slow nuclear burning on the boundary of the liquid and solid phases of the earth's core". In: *Journal of Geophysical Research: Solid Earth* 112.B9 (2007), p. 203. DOI: [10.1029/2005JB004212](https://doi.org/10.1029/2005JB004212).
- [128] R. Meijer and W. Westra. "The feasibility and implications of nuclear georeactors in earth's core-mantle boundary region". In: *South African Journal of Science* 104 (2008), p. 111. URL: https://scielo.org.za/scielo.php?script=sci%5C_abstract&pid=S0038-23532008000200008.
- [129] R. Gao et al. "JULOC: A local 3-D high-resolution crustal model in South China for forecasting geoneutrino measurements at JUNO". In: *Physics of the Earth and Planetary Interiors* 299 (2020), p. 106409. DOI: [10.1016/j.pepi.2019.106409](https://doi.org/10.1016/j.pepi.2019.106409).
- [130] Vanessa Cerrone et al. "Validation and integration tests of the JUNO 20-inch PMT readout electronics". In: *Nuclear Instruments and Methods in Physics Research Section A: Accelerators, Spectrometers, Detectors and Associated Equipment* 1053 (2023), p. 168322. DOI: <https://doi.org/10.1016/j.nima.2023.168322>.
- [131] Yangfu Wang et al. "Thermal management for the underwater frontend and readout electronics of JUNO 20-inch PMTs". In: *Radiat. Detect. Technol. Methods* 7.3 (2023), p. 418. DOI: [10.1007/s41605-023-00401-4](https://doi.org/10.1007/s41605-023-00401-4).
- [132] *Xilinx Kintex-7*. URL: <https://www.xilinx.com/products/boards-and-kits/device-family/nav-kintex-7.html>.
- [133] *Xilinx Spartan-6*. URL: <https://www.xilinx.com/products/boards-and-kits/dk-s6-embd-g.html>.
- [134] HardwareBee. *The Ultimate Guide to FPGA Architecture - HardwareBee*. [Accessed 19-08-2024]. URL: <https://hardwarebee.com/the-ultimate-guide-to-fpga-architecture/>.
- [135] Feng Gao et al. "The status of the back-end card for the JUNO experiment". In: *Journal of Instrumentation* 19.05 (2024), p. C05046. DOI: [10.1088/1748-0221/19/05/C05046](https://doi.org/10.1088/1748-0221/19/05/C05046).
- [136] A. Aloisio et al. "The Reorganize and Multiplex (RMU) front-end trigger optical bridge for the JUNO experiment". In: (2017), p. 1. DOI: [10.1109/NSSMIC.2017.8533064](https://doi.org/10.1109/NSSMIC.2017.8533064).
- [137] A. Aloisio et al. "uSOP: A microprocessor-based service-oriented platform for control and monitoring". In: *2016 IEEE-NPSS Real Time Conference (RT)*. 2016, p. 1. DOI: [10.1109/RTC.2016.7543085](https://doi.org/10.1109/RTC.2016.7543085).
- [138] Filippo Marini. "Development and Testing of the large PMTs Front-End Electronics for the JUNO Experiment". PhD thesis. Università degli Studi di Padova, 2021.
- [139] X. Fang et al. "Capability of detecting low energy events in JUNO central detector". In: *Journal of Instrumentation* 15.03 (2020), P03020. DOI: [10.1088/1748-0221/15/03/p03020](https://doi.org/10.1088/1748-0221/15/03/p03020).
- [140] Guanghua Gong et al. "The Global Trigger with Online Vertex Fitting for Low Energy Neutrino Research". In: vol. ICALEPCS 2015. 2015, Australia. DOI: [10.18429/JACoW-ICALEPCS2015-THHB2003](https://doi.org/10.18429/JACoW-ICALEPCS2015-THHB2003).
- [141] *IEEE Standard for a Precision Clock Synchronization Protocol for Networked Measurement and Control Systems*. 2008. DOI: [10.1109/IEEESTD.2008.4579760](https://doi.org/10.1109/IEEESTD.2008.4579760).

- [142] Agilent Technologies. *Understanding Precision Time Protocol (IEEE 1588)*. Tech. rep. 2011. URL: <https://literature.cdn.keysight.com/litweb/pdf/5990-7066EN.pdf>.
- [143] Fei Li Tingxuan Zeng and Kejun Zhu. “JUNO DAQ Readout and Event Building Research”. In: *IEEE Transactions on Nuclear Science* 66.7 (2019), p. 1217. DOI: 10.1109/tns.2018.2885986.
- [144] Yinhui Wu et al. “The Online Software of JUNO Data Acquisition System”. In: *Submitted to 'IEEE Transactions on Nuclear Science'* (2024), p. 1. DOI: 10.1109/TNS.2024.3470334.
- [145] Wikipedia contributors. *Form factor (design) — Wikipedia, The Free Encyclopedia*. [Accessed 29-09-2024]. 2024. URL: [https://en.wikipedia.org/wiki/Form%5C_factor%5C_\(design\)](https://en.wikipedia.org/wiki/Form%5C_factor%5C_(design)).
- [146] Jin Li et al. “An SOA-Based Design of JUNO DAQ Online Software”. In: *IEEE Transactions on Nuclear Science* 66.7 (2019), p. 1199. DOI: 10.1109/tns.2019.2907367.
- [147] Chao Chen et al. “Design and Development of JUNO DAQ Data Flow Software”. In: *Submitted to 'IEEE Transactions on Nuclear Science'* (2024).
- [148] Mei Ye and Ziguo Han. “Framework Upgrade of the Detector Control System for JUNO”. In: *Proceedings of the 16th Int. Conf. on Accelerator and Large Experimental Control Systems ICALEPCS2017* (2018), Spain. DOI: 10.18429/JACOW-ICALEPCS2017-MODPL04.
- [149] The EPICS Collaboration. *Experimental Physics and Industrial Control System*. 2021. URL: <https://epics-controls.org/>.
- [150] Shenghui Liu et al. “Remote Monitoring System of DCS for JUNO”. In: *IEEE Transactions on Nuclear Science* (2024).
- [151] EPICS Collaboration. *EPICS Input/Output Controller (IOC)*. Accessed: 2024-07-08. 2024. URL: <https://ntrl.ntis.gov/NTRL/dashboard/searchResults/titleDetail/DE200241280.xhtml>.
- [152] Matthew Newville et al. *PyEpics: Python interface to EPICS Channel Access*. Accessed: 2024-07-08. 2023. URL: <https://pypi.org/project/pyepics/>.
- [153] S. Chatrchyan et al. “The CMS experiment at the CERN LHC”. In: *Journal of Instrumentation* 3.08 (2008), S08004. DOI: 10.1088/1748-0221/3/08/S08004.
- [154] Fabio Sauli. “GEM: A new concept for electron amplification in gas detectors”. In: *Nuclear Instruments and Methods in Physics Research Section A: Accelerators, Spectrometers, Detectors and Associated Equipment* 386.2-3 (1997), p. 531. DOI: 10.1016/S0168-9002(96)01172-2.
- [155] Paulo Moreira, A Marchioro, et al. *The GBT: A proposed architecture for multi-Gb/s data transmission in high energy physics*. 2007. URL: <https://cds.cern.ch/record/1091474/files/p332.pdf>.
- [156] Paulo Moreira et al. *The GBT project*. 2009. URL: <https://cds.cern.ch/record/1235836/files/p342.pdf>.
- [157] BT Khai et al. “ μ -TCA DAQ system and parallel reading in CANDLES experiment”. In: *IEEE Transactions on Nuclear Science* 66.7 (2019), p. 1174.
- [158] Yifan Yang. *Backend electronics consideration*. https://juno.ihep.ac.cn/cgi-bin/Dev_DocDB/ShowDocument?docid=944.
- [159] Xianshan Jiang. *The progress of the JUNO electronics*. https://juno.ihep.ac.cn/cgi-bin/Dev_DocDB/ShowDocument?docid=841.
- [160] *CUTE White Rabbit*. http://www.synctechonology.cn/EN_detaile.aspx?id=39.
- [161] Inc. Ansys. *Ansys Electronics Desktop*. Software package. 2023. URL: <https://www.ansys.com/products/electronics/ansys-electronics-desktop>.
- [162] K. Hanson et al. “An extended-range Ethernet and clock distribution circuit for distributed sensor networks”. In: *Journal of Instrumentation* 7.01 (2012), p. C01086. DOI: 10.1088/1748-0221/7/01/C01086.

- [163] P. Allison et al. “Design and Initial Performance of the Askaryan Radio Array Prototype EeV Neutrino Detector at the South Pole”. In: *Astroparticle Physics* 35 (2012), p. 457. DOI: [10.1016/j.astropartphys.2011.11.010](https://doi.org/10.1016/j.astropartphys.2011.11.010).
- [164] M. Bellato et al. “Embedded readout electronics R&D for the large PMTs in the JUNO experiment”. In: *Nuclear Instruments and Methods in Physics Research Section A: Accelerators, Spectrometers, Detectors and Associated Equipment* 985 (2021), p. 164600. DOI: [10.1016/j.nima.2020.164600](https://doi.org/10.1016/j.nima.2020.164600).
- [165] *CLC001 datasheet*. <https://www.ti.com/lit/ds/symlink/clc001.pdf?ts=1723109510576>.
- [166] *LMH0074 datasheet*. <https://www.ti.com/lit/ds/symlink/lmh0074.pdf?ts=1723124939316>.
- [167] *DS30BA101 datasheet*. <https://www.ti.com/jp/lit/ds/symlink/ds30ba101.pdf?ts=1723125073468>.
- [168] *DS30EA101 datasheet*. <https://www.ti.com/lit/ds/symlink/ds30ea101.pdf?ts=1723125162699>.
- [169] *National Semiconductor Introduces Lowest-Power, Easy-to-Use Cable Extender Chipset* — news.thomasnet.com. <https://news.thomasnet.com/fullstory/national-semiconductor-introduces-lowest-power-easy-to-use-cable-extender-chipset-510487>. [Accessed 15-03-2024].
- [170] *DP83848J datasheet*. <https://www.ti.com/lit/ds/symlink/dp83848t.pdf?ts=1723127020673>.
- [171] *Pulse H1102 datasheet*. <https://www.mouser.be/datasheet/2/447/H1102NL-2904957.pdf>.
- [172] *DPO7000 Series*. <https://www.tek.com/en/datasheet/dpo7000-series>.
- [173] *Pulse H2017NL datasheet*. <https://www.mouser.be/datasheet/2/447/H2017NL-3071710.pdf>.
- [174] *DS15EA101 datasheet*. <https://www.ti.com/lit/ds/symlink/ds15ea101.pdf?ts=1723128831781>.
- [175] *DS16EV5110A datasheet*. <https://www.ti.com/lit/ds/symlink/ds16ev5110.pdf>.
- [176] *DS40PC402 datasheet*. <https://www.ti.com/lit/ds/symlink/ds90c402.pdf>.
- [177] *DS80PCI800 datasheet*. <https://www.ti.com/lit/ds/symlink/ds80pci800.pdf>.
- [178] *DS15BA101 datasheet*. <https://www.ti.com.cn/cn/lit/ds/symlink/ds15ba101.pdf>.
- [179] *DS25BR120 datasheet*. <https://www.ti.com/lit/ds/symlink/ds25br120.pdf?ts=1723129339990>.
- [180] *DS25BR400 datasheet*. <https://www.ti.com/lit/ds/symlink/ds25br400.pdf?ts=1723129414789>.
- [181] *DS90LV004 datasheet*. <https://www.ti.com/lit/ds/symlink/ds90lv004.pdf?ts=1723092895404>.
- [182] *SN65LVDS116 datasheet*. <https://www.ti.com/lit/ds/symlink/sn65lvds116.pdf?ts=1723129898281>.
- [183] *SN65LVDT386 datasheet*. <https://www.ti.com/lit/ds/symlink/sn65lvdt388a.pdf?ts=1723064040156>.
- [184] Yifan Yang and Barbara Clerbaux. *Design of a common verification board for different back-end electronics options of the JUNO experiment*. 2018. arXiv: [1806.09698](https://arxiv.org/abs/1806.09698) [physics.ins-det].
- [185] John C Eidson and John Tengdin. “IEEE 1588 standard for a precision clock synchronization protocol for networked measurement and control systems and applications to the power industry”. In: *Proc. Distributech* (2003), p. 4.

- [186] Barbara Clerbaux et al. “Automatic Test System of the Back-End Card for the JUNO Experiment”. In: *IEEE Transactions on Nuclear Science* 68.8 (2021), p. 2121. DOI: [10.1109/tns.2021.3085369](https://doi.org/10.1109/tns.2021.3085369).
- [187] Xilinx Corporation. *AMD Adaptive Computing Documentation Portal* — docs.xilinx.com. [Accessed 09-02-2024]. URL: https://docs.xilinx.com/v/u/en-US/xapp884_PRBS_GeneratorChecker.
- [188] Xilinx Corporation. *Virtual Input/Output (VIO)* — [xilinx.com](https://www.xilinx.com). [Accessed 09-02-2024]. URL: <https://www.xilinx.com/products/intellectual-property/vio.html>.
- [189] Xilinx Corporation. *Integrated Logic Analyzer (ILA)* — [xilinx.com](https://www.xilinx.com). [Accessed 09-02-2024]. URL: <https://www.xilinx.com/products/intellectual-property/ila.html>.
- [190] J. Hu and J. Dong. *GCU V22 Hardware Design*. https://juno.ihep.ac.cn/cgi-bin/Dev_DocDB/ShowDocument?docid=4978. [Accessed 19-03-2024]. 2019.
- [191] *ERDN20-MEAN WELL Switching Power Supply Manufacturer* — [meanwell.com](https://www.meanwell.com). [Accessed 25-03-2024]. URL: <https://www.meanwell.fr/content/files/pdfs/productPdfs/MW/ERDN20/ERDN20-spec.pdf>.
- [192] *C3370 transistor*. <https://www.web-bcs.com/transistor/tc/c0/C3370.php>.
- [193] *TMP100 datasheet*. <https://www.ti.com/lit/ds/symlink/tmp101.pdf?ts=1723298555067>.
- [194] *TC-08 thermocouple data logger*. <https://www.picotech.com/data-logger/tc-08/thermocouple-data-logger>.
- [195] *Nano ESP32 datasheet*. <https://docs.arduino.cc/hardware/nano-esp32/>.
- [196] Alberto Coppi et al. “Mass testing of the JUNO experiment 20-inch PMT readout electronics”. In: *Nuclear Instruments and Methods in Physics Research Section A: Accelerators, Spectrometers, Detectors and Associated Equipment* 1052 (2023), p. 168255. DOI: <https://doi.org/10.1016/j.nima.2023.168255>.
- [197] Riccardo Triozzi. *Mass testing of Large-PMT electronics at Kunshan for the JUNO experiment*. 2022. DOI: [10.22323/1.414.1062](https://doi.org/10.22323/1.414.1062).
- [198] *PowerEdge C6400*. https://i.dell.com/sites/csdocuments/Product_Docs/en/poweredge-c6400-c6420-technical-guide.pdf.
- [199] J. Hu et al. *LPMT GCU Kintex 7 Firmware Review*. [Accessed 29-04-2024]. 2023. URL: https://juno.ihep.ac.cn/cgi-bin/Dev_DocDB/ShowDocument?docid=10362.
- [200] A. Aloisio et al. “A FPGA-based emulation of the Timing Trigger and control receiver for the LHC experiments”. In: *2011 IEEE Nuclear Science Symposium Conference Record* (2011), p. 794. DOI: [10.1109/NSSMIC.2011.6154541](https://doi.org/10.1109/NSSMIC.2011.6154541).
- [201] K. Hirata et al. “Observation of a neutrino burst from the supernova SN1987A”. In: *Physical Review Letters* 58.14 (1987), p. 1490. DOI: [10.1103/PhysRevLett.58.1490](https://doi.org/10.1103/PhysRevLett.58.1490).
- [202] E.N. Alexeyev et al. “Detection of neutrinos from the SN1987A explosion in the LMC using the Baksan underground scintillation telescope”. In: *Physics Letters B* 205.2-3 (1988), p. 209.
- [203] R.M. Bionta et al. “Observation of a neutrino burst in coincidence with supernova 1987A in the Large Magellanic Cloud”. In: *Physical Review Letters* 58.14 (1987), p. 1494.
- [204] V.L. Dadykin et al. “Detection of a rare event on 23 February 1987 by the neutrino radiation detector under Mont Blanc”. In: *Soviet Journal of Experimental and Theoretical Physics Letters* 45 (1987), p. 593.
- [205] Massimo Turatto. “Classification of Supernovae”. In: *Supernovae and Gamma-Ray Bursters*. Ed. by Kurt W. Weiler. Berlin, Heidelberg: Springer Berlin Heidelberg, 2003, p. 21. DOI: [10.1007/3-540-45863-8_3](https://doi.org/10.1007/3-540-45863-8_3).
- [206] J. Leaman et al. “Nearby supernova rates from the Lick Observatory Supernova Search - I. The methods and data base”. In: *Monthly Notices of the Royal Astronomical Society* 412.3 (2011), p. 1419.

- [207] Ramon Canal, Jordi Isern, and Javier Labay. “The origin of neutron stars in binary systems.” In: *Annual Review of Astronomy and Astrophysics* 28 (1990), p. 183. DOI: [10.1146/annurev.astro.28.1.183](https://doi.org/10.1146/annurev.astro.28.1.183).
- [208] Alexander Heger et al. “Nucleosynthesis in Stellar Explosions from Early Stars”. In: *Astronomical Society of the Pacific Conference Series* 458 (2012).
- [209] H. -Thomas Janka et al. *Core-Collapse Supernovae: Reflections and Directions*. 2012. arXiv: [1211.1378](https://arxiv.org/abs/1211.1378) [astro-ph.SR].
- [210] Hans-Thomas Janka. “Neutrino-Driven Explosions”. In: *Handbook of Supernovae*. Springer International Publishing, 2017, p. 1095. ISBN: 9783319218465. DOI: [10.1007/978-3-319-21846-5_109](https://doi.org/10.1007/978-3-319-21846-5_109).
- [211] H JANKA et al. “Theory of core-collapse supernovae”. In: *Physics Reports* 442.1–6 (2007), p. 38. DOI: [10.1016/j.physrep.2007.02.002](https://doi.org/10.1016/j.physrep.2007.02.002).
- [212] Irene Tamborra et al. “Neutrino emission characteristics and detection opportunities based on three-dimensional supernova simulations”. In: *Physical Review D* 90.4 (2014). DOI: [10.1103/physrevd.90.045032](https://doi.org/10.1103/physrevd.90.045032).
- [213] Hans-Thomas Janka. “Neutrino Emission from Supernovae”. In: *Handbook of Supernovae*. Springer International Publishing, 2017, p. 1575. ISBN: 9783319218465. DOI: [10.1007/978-3-319-21846-5_4](https://doi.org/10.1007/978-3-319-21846-5_4).
- [214] H.J. Kull. “Theory of the Rayleigh-Taylor instability”. In: *Physics Reports* 206.5 (1991), p. 197. DOI: [https://doi.org/10.1016/0370-1573\(91\)90153-D](https://doi.org/10.1016/0370-1573(91)90153-D).
- [215] John M Blondin, Anthony Mezzacappa, and Charles DeMarino. “Stability of standing accretion shocks, with an eye toward core-collapse supernovae”. In: *The Astrophysical Journal* 584.2 (2003), p. 971.
- [216] L. Scheck et al. “Multidimensional supernova simulations with approximative neutrino transport: II. Convection and the advective-acoustic cycle in the supernova core”. In: *Astronomy and Astrophysics* 477.3 (2007), p. 931. DOI: [10.1051/0004-6361:20077701](https://doi.org/10.1051/0004-6361:20077701).
- [217] James M. Lattimer and F. Douglas Swesty. “A generalized equation of state for hot, dense matter”. In: *Nuclear Physics A* 535.2 (1991), p. 331. DOI: [https://doi.org/10.1016/0375-9474\(91\)90452-C](https://doi.org/10.1016/0375-9474(91)90452-C).
- [218] H. Shen et al. “Relativistic equation of state of nuclear matter for supernova and neutron star”. In: *Nuclear Physics A* 637.3 (1998), p. 435. DOI: [10.1016/s0375-9474\(98\)00236-x](https://doi.org/10.1016/s0375-9474(98)00236-x).
- [219] H. Shen et al. “Relativistic Equation of State of Nuclear Matter for Supernova Explosion”. In: *Progress of Theoretical Physics* 100.5 (1998), p. 1013. DOI: [10.1143/ptp.100.1013](https://doi.org/10.1143/ptp.100.1013).
- [220] H. Shen et al. “Relativistic Equation of State for core-collapse supernova simulations”. In: *The Astrophysical Journal Supplement Series* 197.2 (2011), p. 20. DOI: [10.1088/0067-0049/197/2/20](https://doi.org/10.1088/0067-0049/197/2/20).
- [221] Andrew W Steiner, Matthias Hempel, and Tobias Fischer. “Core-collapse supernova equations of state based on neutron star observations”. In: *The Astrophysical Journal* 774.1 (2013), p. 17.
- [222] Hans-Thomas Janka. “Conditions for shock revival by neutrino heating in core-collapse supernovae”. In: *Astronomy and Astrophysics* 368.2 (2001), p. 527. DOI: [10.1051/0004-6361:20010012](https://doi.org/10.1051/0004-6361:20010012).
- [223] Hans-Thomas Janka, Tobias Melson, and Alexander Summa. “Physics of Core-Collapse Supernovae in Three Dimensions: A Sneak Preview”. In: *Annual Review of Nuclear and Particle Science* 66.1 (2016), p. 341. DOI: [10.1146/annurev-nucl-102115-044747](https://doi.org/10.1146/annurev-nucl-102115-044747).
- [224] R. Buras et al. “Two-dimensional hydrodynamic core-collapse supernova simulations with spectral neutrino transport. I. Numerical method and results for a 15 M star”. In: *Astronomy and Astrophysics* 447 (2006), p. 1049. DOI: [10.1051/0004-6361:20053783](https://doi.org/10.1051/0004-6361:20053783).
- [225] Tuguldur Sukhbold et al. “Core-Collapse Supernovae from 9 to 120 Solar Masses Based on Neutrino-powered Explosions”. In: *The Astrophysical Journal* 821.1 (2016), p. 38. DOI: [10.3847/0004-637x/821/1/38](https://doi.org/10.3847/0004-637x/821/1/38).
- [226] T. Ertl et al. “A two-parameter criterion for classifying the explodability of massive stars by the neutrino-driven mechanism”. In: *Astrophys. J.* 818.2 (2016), p. 124. DOI: [10.3847/0004-637x/818/2/124](https://doi.org/10.3847/0004-637x/818/2/124).

- [227] A. Mirizzi et al. “Supernova neutrinos: production, oscillations and detection”. In: *La Rivista del Nuovo Cimento* 39.102 (2016), p. 1. DOI: [10.1393/ncr/i2016-10120-8](https://doi.org/10.1393/ncr/i2016-10120-8).
- [228] M. Rampp and H.-T. Janka. “Radiation hydrodynamics with neutrinos: Variable Eddington factor method for core-collapse supernova simulations”. In: *Astronomy and Astrophysics* 396.1 (2002), p. 361. DOI: [10.1051/0004-6361:20021398](https://doi.org/10.1051/0004-6361:20021398).
- [229] A. Marek et al. “Exploring the relativistic regime with Newtonian hydrodynamics: An improved effective gravitational potential for supernova simulations”. In: *Astronomy and Astrophysics* 445 (2006), p. 273. DOI: [10.1051/0004-6361:20052840](https://doi.org/10.1051/0004-6361:20052840).
- [230] Hans-Thomas Janka. “Explosion Mechanisms of Core-Collapse Supernovae”. In: *Annual Review of Nuclear and Particle Science* 62.1 (2012), p. 407. DOI: [10.1146/annurev-nucl-102711-094901](https://doi.org/10.1146/annurev-nucl-102711-094901).
- [231] Bernhard Müller, Hans-Thomas Janka, and Andreas Marek. “A New Multi-Dimensional General Relativistic Neutrino Hydrodynamics Code for Core-Collapse Supernovae II. Relativistic Explosion Models of Core-Collapse Supernovae”. In: *The Astrophysical Journal* 756.1 (2012), p. 84. DOI: [10.1088/0004-637x/756/1/84](https://doi.org/10.1088/0004-637x/756/1/84).
- [232] R. Bollig. “Self-Consistent Boltzmann Neutrino Transport in Three-Dimensional Core-Collapse Supernova Simulations”. In: *Diploma Thesis, Technische Universität München* (2013).
- [233] J. von Groote. “Neutrino-Driven Supernova Explosions in Three Dimensions”. In: *PhD Thesis, Technische Universität München* (2014).
- [234] T. Fischer et al. “Proton-neutron Star Evolution and the Neutrino Driven Wind in General Relativistic Neutrino Radiation Hydrodynamics Simulations”. In: *Astronomy and Astrophysics* 499 (2009), p. 1. DOI: [10.1051/0004-6361/200810527](https://doi.org/10.1051/0004-6361/200810527).
- [235] L. Hüdepohl. “Neutrino Signal of Electron-Capture Supernovae from Core Collapse to Cooling”. In: *PhD Thesis, Technische Universität München* (2013).
- [236] A. Weiss et al. *Cox and Giuli’s Principles of Stellar Structure*. Cambridge Scientific Publishers, 2004.
- [237] Irene Tamborra et al. “Neutrino signature of supernova hydrodynamical instabilities in three dimensions”. In: *Physical review letters* 111.12 (2013), p. 121104.
- [238] Ken’ichiro Nakazato, Kohsuke Sumiyoshi, and Hideyuki Suzuki. “Neutrino signal from the formation of black hole: A probe of equation of state of dense matter”. In: *Physical Review D* 78.8 (2008), p. 083014.
- [239] Ken’ichiro Nakazato et al. “Supernova Neutrino Light Curves and Spectra for Various Progenitor Masses and Metallicities”. In: *The Astrophysical Journal* 745.2 (2012), p. 197.
- [240] Ken’ichiro Nakazato et al. “Impact of progenitor’s metallicity on the explosive nucleosynthesis in core-collapse supernovae: Evolution and nucleosynthesis in massive stars with metallicities $Z = 0, 0.004, \text{ and } 0.02$ ”. In: *The Astrophysical Journal Supplement Series* 205.2 (2013), p. 20.
- [241] K. Nakazato et al. “Supernova Neutrino Light Curves and Spectra for Various Progenitor Stars: From Core Collapse to Proto-neutron Star Cooling”. In: *Astrophys. J. Suppl.* 205.2 (2013). DOI: [10.1088/0067-0049/205/1/2](https://doi.org/10.1088/0067-0049/205/1/2).
- [242] Bruce Fryxell et al. “FLASH: An adaptive mesh hydrodynamics code for modeling astrophysical thermonuclear flashes”. In: *The Astrophysical Journal Supplement Series* 131.1 (2000), p. 273.
- [243] Sean M. Couch, MacKenzie L. Warren, and Evan P. O’Connor. “Simulating Turbulence-aided Neutrino-driven Core-collapse Supernova Explosions in One Dimension”. In: *The Astrophysical Journal* 890.2 (2020), p. 127. DOI: [10.3847/1538-4357/ab609e](https://doi.org/10.3847/1538-4357/ab609e).
- [244] Sean M Couch and Christian D Ott. “The importance of turbulence in core-collapse supernova explosions”. In: *The Astrophysical Journal* 799.1 (2015), p. 5.
- [245] Quintin A Mabanta and Jeremiah W Murphy. “The role of turbulence and rotation in setting the explodability of massive stars”. In: *The Astrophysical Journal* 856.1 (2018), p. 22.

- [246] MacKenzie L. Warren et al. “Constraining Properties of the Next Nearby Core-collapse Supernova with Multimessenger Signals”. In: *The Astrophysical Journal* 898.2 (2020), p. 139. DOI: [10.3847/1538-4357/ab97b7](https://doi.org/10.3847/1538-4357/ab97b7).
- [247] Drew Clausen, Anthony L Piro, and Christian D Ott. “Impact of binary interactions on the dynamics of core-collapse supernovae”. In: *The Astrophysical Journal* 799.2 (2015), p. 190.
- [248] Masaru Shibata, Kenta Kiuchi, and Yu-ichiro Sekiguchi. “Truncated moment formalism for radiation hydrodynamics in numerical relativity”. In: *Progress of Theoretical Physics* 125.6 (2011), p. 1255.
- [249] Christian Y Cardall, Eirik Endeve, and Anthony Mezzacappa. “Conservative moment equations for neutrino radiation transport with limited relativity”. In: *Physical Review D* 87.10 (2013), p. 103004.
- [250] Evan O’Connor. “An Open-Source Neutrino Radiation Hydrodynamics Code for Core-Collapse Supernovae”. In: *Astrophys. J. Suppl.* 219.2 (2015), p. 24. DOI: [10.1088/0067-0049/219/2/24](https://doi.org/10.1088/0067-0049/219/2/24).
- [251] Adam Burrows et al. “Three-dimensional supernova explosion simulations of 9-, 10-, 11-, 12-, and 13-M stars”. In: *Monthly Notices of the Royal Astronomical Society* 485.3 (2019), p. 3153.
- [252] E. Margaret Burbidge et al. “Synthesis of the Elements in Stars”. In: *Rev. Mod. Phys.* 29 (4 1957), p. 547. DOI: [10.1103/RevModPhys.29.547](https://doi.org/10.1103/RevModPhys.29.547).
- [253] S. E. Woosley et al. “The r-Process and Neutrino-heated Supernova Ejecta”. In: *Astrophysical Journal* 433 (1994), p. 229. DOI: [10.1086/174638](https://doi.org/10.1086/174638).
- [254] Shin-ichiro Fujimoto et al. “Heavy-Element Nucleosynthesis in a Collapsar”. In: *Astrophysical Journal* 656.1 (2007), p. 382. DOI: [10.1086/509908](https://doi.org/10.1086/509908).
- [255] Tianshu Wang and Adam Burrows. “Nucleosynthetic Analysis of Three-dimensional Core-collapse Supernova Simulations”. In: *The Astrophysical Journal* 962.1 (2024), p. 71. DOI: [10.3847/1538-4357/ad12b8](https://doi.org/10.3847/1538-4357/ad12b8).
- [256] M. Arnould. “Possibility of synthesis of proton-rich nuclei in highly evolved stars. II.” In: *Astronomy and Astrophysics* 46.1 (1976), p. 117.
- [257] F. Kappeler, H. Beer, and K. Wisshak. “s-process nucleosynthesis-nuclear physics and the classical model”. In: *Reports on Progress in Physics* 52.8 (1989), p. 945. DOI: [10.1088/0034-4885/52/8/002](https://doi.org/10.1088/0034-4885/52/8/002).
- [258] Philip A. Seeger, William A. Fowler, and Donald D. Clayton. “Nucleosynthesis of Heavy Elements by Neutron Capture.” In: *Astrophysical Journal Supplement* 11 (1965), p. 121. DOI: [10.1086/190111](https://doi.org/10.1086/190111).
- [259] M. Arnould, S. Goriely, and K. Takahashi. “The r-process of stellar nucleosynthesis: Astrophysics and nuclear physics achievements and mysteries”. In: *Physics Reports* 450.4-6 (2007), p. 97. DOI: [10.1016/j.physrep.2007.06.002](https://doi.org/10.1016/j.physrep.2007.06.002).
- [260] David L. Lambert. “The p-nuclei: abundances and origins”. In: *Astronomy and Astrophysics* 3.3-4 (1992), p. 201. DOI: [10.1007/BF00872527](https://doi.org/10.1007/BF00872527).
- [261] M. Arnould and S. Goriely. “The p-process of stellar nucleosynthesis: astrophysics and nuclear physics status”. In: *Physics Reports* 384.1 (2003), p. 1. DOI: [https://doi.org/10.1016/S0370-1573\(03\)00242-4](https://doi.org/10.1016/S0370-1573(03)00242-4).
- [262] C. Fröhlich et al. “Nucleosynthesis in neutrino-driven supernovae”. In: *New Astronomy Reviews* 50.7-8 (2006), p. 496. DOI: [10.1016/j.newar.2006.06.003](https://doi.org/10.1016/j.newar.2006.06.003).
- [263] I. Jr. Iben and A. Renzini. “Asymptotic Giant Branch evolution and beyond”. In: *Annu. Rev. Astron. Astrophys.* 21 (1983), p. 271.
- [264] J. Pruet et al. “Nucleosynthesis in Early Supernova Winds. II. The Role of Neutrinos”. In: *The Astrophysical Journal* 644 (2006), p. 1028. DOI: [10.1086/503891](https://doi.org/10.1086/503891).
- [265] C. Fröhlich et al. “Neutrino-Induced Nucleosynthesis of $A > 64$ Nuclei: The νp Process”. In: *Phys. Rev. Lett.* 96 (14 2006), p. 142502. DOI: [10.1103/PhysRevLett.96.142502](https://doi.org/10.1103/PhysRevLett.96.142502).
- [266] Almudena Arcones and Friedrich-Karl Thielemann. “Origin of the elements”. In: *The Astronomy and Astrophysics Review* 31.1 (2022). DOI: [10.1007/s00159-022-00146-x](https://doi.org/10.1007/s00159-022-00146-x).

- [267] Takami Kuroda et al. “Core-collapse Supernova Simulations and the Formation of Neutron Stars, Hybrid Stars, and Black Holes”. In: *The Astrophysical Journal* 924.38 (2022). DOI: [10.3847/1538-4357/ac31a8](https://doi.org/10.3847/1538-4357/ac31a8).
- [268] Alexander Heger et al. “How Massive Single Stars End Their Life”. In: *The Astrophysical Journal* 591 (2003), p. 288. DOI: [10.1086/375341](https://doi.org/10.1086/375341).
- [269] Christopher L. Fryer. “Mass Limits For Black Hole Formation”. In: *The Astrophysical Journal* 522.413 (1999). DOI: [10.1086/307647](https://doi.org/10.1086/307647).
- [270] Takami Kuroda et al. “The Final Fate of Massive Stars”. In: *The Astrophysical Journal* 924.38 (2022). DOI: [10.3847/1538-4357/ac31a8](https://doi.org/10.3847/1538-4357/ac31a8).
- [271] Takami Kuroda et al. “Role of Phase Transition in Core-Collapse Supernovae”. In: *The Astrophysical Journal* 924.38 (2022). DOI: [10.3847/1538-4357/ac31a8](https://doi.org/10.3847/1538-4357/ac31a8).
- [272] Tobias Fischer and et al. “Phase Transition Dynamics in Core-Collapse Supernovae”. In: *The Astrophysical Journal* 894 (2020), p. 9. DOI: [10.3847/1538-4357/ab7c27](https://doi.org/10.3847/1538-4357/ab7c27).
- [273] Amanda Baxter et al. “SNEWPY: A Data Pipeline from Supernova Simulations to Neutrino Signals”. In: *Journal of Open Source Software* 6.67 (2021), p. 3772. DOI: [10.21105/joss.03772](https://doi.org/10.21105/joss.03772).
- [274] Jost Migenda et al. “sntools: An event generator for supernova burst neutrinos”. In: *Journal of Open Source Software* 6.60 (2021), p. 2877. DOI: [10.21105/joss.02877](https://doi.org/10.21105/joss.02877).
- [275] Tuan Do et al. “Relativistic redshift of the star S0-2 orbiting the Galactic center supermassive black hole”. In: *Science* 365.6454 (2019), p. 664.
- [276] A. Strumia and F. Vissani. “Precise quasielastic neutrino/nucleon cross-section”. In: *Phys. Lett.* B564 (2003), pp. 42–54. DOI: [10.1016/s0370-2693\(03\)00616-6](https://doi.org/10.1016/s0370-2693(03)00616-6).
- [277] A. Kurylov, M. J. Ramsey-Musolf, and P. Vogel. “Radiative corrections to low-energy neutrino reactions”. In: *Phys. Rev.* C67 (2003), p. 035502.
- [278] John F. Beacom, Will M. Farr, and Petr Vogel. “Detection of supernova neutrinos by neutrino-proton elastic scattering”. In: *Phys. Rev. D* 66 (2002), p. 033001.
- [279] Gerard 't Hooft. “Predictions for neutrino - electron cross-sections in Weinberg’s model of weak interactions”. In: *Phys. Lett.* 37B (1971), pp. 195–196. DOI: [10.1016/0370-2693\(71\)90050-5](https://doi.org/10.1016/0370-2693(71)90050-5).
- [280] John N. Bahcall, Marc Kamionkowski, and Alberto Sirlin. “Solar neutrinos: Radiative corrections in neutrino - electron scattering experiments”. In: *Phys. Rev.* D51 (1995), p. 6146. DOI: [10.1103/PhysRevD.51.6146](https://doi.org/10.1103/PhysRevD.51.6146).
- [281] E. Kolbe, K. Langanke, and P. Vogel. “Weak reactions on C-12 within the continuum random phase approximation with partial occupancies”. In: *Nucl. Phys. A* 652 (1999), p. 91. DOI: [10.1016/S0375-9474\(99\)00152-9](https://doi.org/10.1016/S0375-9474(99)00152-9).
- [282] T.W. Donnelly and R.D. Peccei. “Neutral Current Effects in Nuclei”. In: *Phys. Rept.* 50 (1979), p. 1. DOI: [10.1016/0370-1573\(79\)90010-3](https://doi.org/10.1016/0370-1573(79)90010-3).
- [283] Riya Gaba et al. “Supernova Neutrino Signal Using SNOwGLoBES”. In: *Springer Proc. Phys.* 304 (2024), p. 1162. DOI: [10.1007/978-981-97-0289-3_324](https://doi.org/10.1007/978-981-97-0289-3_324).
- [284] Richard C. Schirato and George M. Fuller. *Connection between supernova shocks, flavor transformation, and the neutrino signal*. 2002. arXiv: [astro-ph/0205390](https://arxiv.org/abs/astro-ph/0205390).
- [285] Luca Lista. *Statistical Methods for Data Analysis in Particle Physics*. Second Edition. Vol. 941. Lecture Notes in Physics. Cham, Switzerland: Springer International Publishing, 2017. DOI: [10.1007/978-3-319-62840-0](https://doi.org/10.1007/978-3-319-62840-0).
- [286] K. Abe et al. “Supernova Model Discrimination with Hyper-Kamiokande”. In: *The Astrophysical Journal* 916.1 (2021), p. 15. DOI: [10.3847/1538-4357/abf7c4](https://doi.org/10.3847/1538-4357/abf7c4).
- [287] Pauli Virtanen et al. “SciPy 1.0: Fundamental Algorithms for Scientific Computing in Python”. In: *Nature Methods* 17 (2020), p. 261. DOI: [10.1038/s41592-019-0686-2](https://doi.org/10.1038/s41592-019-0686-2).

-
- [288] Jost Migenda. “Supernova Model Discrimination with Hyper-Kamiokande”. 2019. URL: <https://etheses.whiterose.ac.uk/25941/>.
- [289] T. Totani et al. “Future detection of supernova neutrino burst and explosion mechanism”. In: *The Astrophysical Journal* 496 (1998), p. 216. DOI: [10.1086/305351](https://doi.org/10.1086/305351).